UNIVERSITY OF SOUTHAMPTON

FACULTY OF ENGINEERING AND THE ENVIRONMENT

Engineering Materials

Developments in advanced high temperature disc and blade materials for aero-engine gas turbine applications

by

Stewart Everitt

Thesis for the degree of Doctor of Engineering

March 2012

UNIVERSITY OF SOUTHAMPTON

ABSTRACT

FACULTY OF ENGINEERING AND THE ENVIRONMENT

ENGINEERING MATERIALS

Doctor of Engineering

DEVELOPMENTS IN ADVANCED HIGH TEMPERATURE DISC AND BLADE MATERIALS FOR AERO-ENGINE GAS TURBINE APPLICATIONS

by

Stewart Everitt

The research carried out as part of this EngD is aimed at understanding the high temperature materials used in modern gas turbine applications and providing QinetiQ with the information required to assess component performance in new propulsion systems. Performance gains are achieved through increased turbine gas temperatures which lead to hotter turbine disc rims and blades. The work has focussed on two key areas: (1) *Disc Alloy Assessment of High Temperature Properties*; and (2) *Thermal Barrier Coating Life Assessment*; which are drawn together by the overarching theme of the EngD: *Lifing of Critical Components in Gas Turbine Engines*.

Performance of sub-solvus heat treated N18 alloy in the temperature range of 650°C to 725°C has been examined via monotonic and cyclically stabilised tensile, creep and strain controlled low cycle fatigue (LCF) tests including LCF behaviour in the presence of a stress concentration under load-control. Crack propagation studies have been undertaken on N18 and a particular super-solvus heat treatment variant of the alloy LSHR at the same temperatures, in air and vacuum with 1s and 20s dwell times. Comparisons between the results of this testing and microstructural characterisation with RR1000, UDIMET® 720 Low Interstitial (U720Li) and a large grain variant of U720Li have been carried out. In all alloys, strength is linked to a combination of γ' content and grain size as well as slow diffusing atoms in solid solution. High temperature strength improves creep performance which is also dependent on grain size and grain boundary character. Fatigue testing revealed that N18 had the most transgranular crack propagation with a good resistance to intergranular failure modes, with U720Li the most intergranular. Under vacuum conditions transgranular failure modes are evident to higher temperature and ΔK, with LSHR failing almost completely by intergranular crack propagation in air. For N18 significant cyclic softening occurs at 725°C with LCF initiation occurring at pores and oxidised particles. An apparent activation energy technique was used to provide further insights into the failure modes of these alloys, this indicating that, for N18 with 1s dwell, changes in fatigue crack growth rates were attributed to static properties and for LSHR, with 20s dwell in air, that changes were attributed to the detrimental synergistic combination of creep and oxidation at 725°C. Microchemistry at grain boundaries, especially $M_{23}C_6$ carbides, plays an important role in these alloys.

Failure mechanisms within a thermal barrier coating (TBC) system consisting of a CMSX4 substrate, PtAl bond coat, thermally grown oxide (TGO) layer and a top coat applied using electron beam physical vapour deposition have been considered. TGO growth has been quantified under isothermal, two stage temperature and thermal cyclic exposures. An Arrhenius relation was used to describe the TGO growth and produce an isothermal TGO growth model. The output from this was used in the QinetiQ TBC Lifing Model. Thermo-mechanical fatigue test methods were also developed including a novel thermocouple placement permitting substrate temperature to be monitored without disturbing the top coat such that the QinetiQ TBC Lifing Model could be validated.

The importance of material, system specific knowledge and performance data with respect to a particular design space for critical components in gas turbine engines has been highlighted. Data and knowledge regarding N18, LSHR and TBC systems has been added to the QinetiQ's databank enhancing their capability for providing independent advice regarding high temperature materials particularly in new gas turbine engines.

List of contents

List of figures

List of tables

DECLARATION OF AUTHORSHIP

I, *Stewart Everitt*,

declare that the thesis entitled

Developments in advanced high temperature disc and blade materials for aero-engine gas turbine applications

and the work presented in the thesis are both my own, and have been generated by me as the result of my own original research. I confirm that:

- this work was done wholly or mainly while in candidature for a research degree at this University;
- where any part of this thesis has previously been submitted for a degree or any other qualification at this University or any other institution, this has been clearly stated;
- where I have consulted the published work of others, this is always clearly attributed;
- where I have quoted from the work of others, the source is always given. With the exception of such quotations, this thesis is entirely my own work;
- I have acknowledged all main sources of help;
- where the thesis is based on work done by myself jointly with others, I have made clear exactly what was done by others and what I have contributed myself;
- parts of this work have been published as:

Reed, P.A.S., Wisbey, A., Everitt, S., Di Martino, I. and Brooks, J.W. (2007) 'High temperature fatigue and creep performance of N18 alloy' eds. Strang A., Banks, W.M., McColvin, G.M., Oakley, J.E., and Vanstone, R.W. *Proceedings of the Seventh International Charles Parsons Turbine Conference: Power Generation in an Era of Climate Change, 11-13 Sept. 2007, University of Strathclyde, Glasgow, UK,* IOM Communications Ltd, London, UK, 309-319.[1]

Everitt, S., Starink, M.J., Pang, H.T., Wilcock, I.M., Henderson, M.B. and Reed, P.A.S. (2007) 'A comparison of high temperature fatigue crack propagation in various sub-solvus heat treated turbine disc alloys' *Materials Science and Technology*, **23** (12) 1419-1423.[2]

Everitt, S., Starink, M.J. and Reed, P.A.S. (2008) 'Temperature and dwell dependence of fatigue crack propagation in various heat treated turbine disc alloys.' eds. Reed, R., Green, K.A., Caron, P., Gabb, T., Fahrmann, M.G., Huron, E.S. and Woodard, S.R. *Proceedings of the Eleventh International Symposium on Superalloys, 14-18 Sept. 2008, Seven Springs, Champion, Pennsylvania, USA*, TMS, 741 - 750.[3]

Basoalto, H., Everitt, S. and Vermeulen, B. (2009) 'Final Report on Thermal Barrier Coating Lifing Model.' QinetiQ Ltd. QinetiQ/08/01042 31 March 2009.[4]

Signed: ……..
Date: 23rd March 2012

Acknowledgements

I have enjoyed the whole process of the EngD immensely, having now reached the end of the journey, I would like to acknowledge those who have helped, assisted, encouraged, supported or otherwise cajoled me and therefore helped to ensure that I got this far – there were a lot of you, thank you!

Specifically I would like to thank both of my academic supervisors Professor Philippa Reed and Professor Marco Starink for the assistance, support, guidance and forbearance they have provided, their professionalism and tolerance providing something to aspire to.

I am grateful too for the encouragement from my Industrial Supervisors, Professor Jeffery Brooks, Dr. Hector Basoalto, Dr. Andrew Wisbey and Dr Irene Di Martino, especially for their support at conferences and time given to answer all the questions I asked.

My fellow students, initially providing advice to me, then as I progressed and people moved on, me providing advice and help to them. Here I would like to thank Dr. Andrew "Instron" Moffat for passing on his knowledge on just about everything I wanted to know. Dr. Toby Balla for his almost permanent enthusiasm, Kath Soady, Tom Mbuya and Christian Schöttle for answering as many questions as they asked.

Many individuals at the University of Southampton have helped, I would especially like to thank, Gwyneth Skiller the Materials Research Group Secretary who could just make things happen, and the technical staff, Clive Stafford, Chris Williams, Rob Barnes, Erik Roszkowiak and Dave Beckett for their help and assistance in the various laboratories.

I would also like to acknowledge and thank sponsors and other individuals who made this all possible: QinetiQ Ltd for sponsoring the EngD project; Engineering and Physical Sciences Research Council for sponsorship of the EngD; University of Birmingham for courses and funding conferences; University of Southampton for the technical modules and funding conferences; SNECMA Moteurs for the supply of sub-solvus N18 material; NASA and Tim Gabb for the supply of super-solvus LSHR and supporting discussions.

Thanks also to my Mum and Dad without whom none of this would have been possible.

Many of my friends and colleagues have also helped me get this far; Clive Buckland for starting the learning bug a long time ago in Kinloss, John Haylock for encouraging me "to go for it", Jim Hennessy for support throughout and Ian Johnstone for helping me see the funny side and proof reading my final draft , thank you all!

My dog Amber deserves a special mention for giving me an excuse to get away from the computer, and my cat Teazer for reminding me to get up from the computer and feed her.

Finally, my especial love and thanks go to my partner Dot, for her unconditional support and tolerance through the long hours of study, research and writing.

Abbreviations and Symbols used

Abbreviations

AMC	acceptable means of compliance
APB	antiphase boundary
APS	air plasma spray
ARMINES	Association pour la Recherché et le Développement des Méthodes et Processus Industriels
BC	bond coat
BCT	body centred tetragonal
BEI	backscattered electron imaging
BLING	bladed ring
BLISK	bladed disk
BS	British Standard
C&W	cast and wrought
CDF	cumulative distribution function
CIH	Cheltenham Induction Heating
CRSS	critical resolved shear stress
CSS	cyclic stress strain
CTE	Coefficients of Thermal Expansion
$\Delta CTOD$	crack tip opening displacement range
CVD	chemical vapour deposition
DB	diffusion bonding
DBTT	ductile brittle transition temperature
DC	direct current
DefStan	UK MoD Defence Standard
DERA	Defence Evaluation Research Agency
DMHT	dual microstructure heat treatments
E&I	extruded and isothermally forged
EASA	European Aviation Safety Agency
EBPVD	electron beam physical vapour deposition
EBSD	electron back-scatter diffraction
EDM	electrostatic discharge machining
EDS	energy dispersive spectrometry
EDX	energy-dispersive x-ray spectroscopy
EngD	Engineering Doctorate
EPSRC	Engineering and Physical Sciences Research Council
ESR	electro-slag remelting
FADEC	full authority digital engine control

FCC	face centred cubic
FCG	fatigue crack growth
FEA	finite element analysis
FEG SEM	field emission gun scanning electron microscope
FOD	foreign object damage
GTCCL	Gas Turbine Critical Component Lifing
HCF	high cycle fatigue
HIP	hot isostatic pressing
HP	high pressure
HTLA	high temperature low activity
IDZ	interdiffusion zone
IP	in phase
JSF	Joint Strike Fighter
LCF	low cycle fatigue
LEFM	linear elastic fracture mechanics
LG	large grain
LSHR	Low Solvus High Refractory alloy
LTHA	low temperature high activity
NASA	National Aeronautics and Space Administration
OICC	oxide induced crack closure
ODS	oxide dispersion strengthened
ONERA	Office National d'Etudes et de Recherchés Aerospatiales
OP	out of phase
PAPVD	plasma assisted physical vapour deposition
pd	potential difference
PDF	probability density function
PICC	plasticity induced crack closure
PM	powder metallurgy
PO_2	partial pressure of oxygen
PPB	prior particle boundaries
PSCDTL	predicted safe cyclic damage tolerance lives
PSCL	predicted safe cyclic life
PSII	predicted safe inspection interval
PSLS	photo-stimulated luminescence spectroscopy
PSZ	partially stabilised zirconia
RCF	relative cumulative frequency
RICC	roughness induced crack closure
SAGBO	stress accelerated grain boundary oxidation

SEI	secondary electron imaging
SEM	scanning electron microscope
SENB	single edge notch bend
SFE	stacking fault energy
SHIM	scanning helium ion microscope
SNECMA	Societe Nationale d'Etude et de Construction de Moteurs d'Aviation
SPF	superplastic forming
TBC	thermal barrier coating
TC	top coat
TCP	topologically close packed
TEM	transmission electron microscope
TGA	thermogravimetric analysis
TGO	thermally grown oxide
TMF	thermo-mechanical fatigue
U720Li	UDIMET® 720 alloy Low Interstitial variety
UMAT	User defined MATerial (routine)
UTS	ultimate tensile strength
VAR	vacuum arc remelting
VIM	vacuum induction melting
WD	working distance

Symbols

$\frac{da}{dN}$	crack growth rate per cycle
$\frac{da}{dt}$	crack growth rate (with respect to time)
D_g	grain boundary diffusivity parameter
E	elastic modulus
E_{app}	apparent activation energy
H_v	Vickers Hardness
K	stress intensity factor
K_{max}	maximum value of stress intensity factor
K_{min}	minimum value of stress intensity factor
ΔK	stress intensity factor range
ΔK_{th}	threshold stress intensity factor range
N	number of cycles
N_f	number of cycles to specimen fracture
P	load
$PIDL$	proportional, integral, differential and lag parameters
R	load ratio
R_a	average roughness
R_s	surface roughness
T_m	melting temperature
V_f	volume fraction
a	crack depth
B	bend specimen breadth
D	notch depth
S	span
W	bend specimen width
ε	strain
ε_n	normal growth strains
ε_t	parallel growth strains
$\Delta\varepsilon$	strain range
$\Delta\varepsilon_p$	plastic strain range
σ	applied stress
σ_{min}	minimum applied stress
σ_{max}	maximum applied stress
σ_y	yield stress
ν	Poisson’s ratio

1 Introduction

To define the scope of this Engineering Doctorate (EngD), this chapter presents an introduction to the research objectives, followed by an outline of the research programme carried out both at the University of Southampton and at QinetiQ Ltd. The overarching theme of the EngD is also stated. This is followed by a brief introduction to the business of the industrial sponsor, QinetiQ Ltd and a description of the EngD programme structure.

1.1 Introduction to Research Objectives

In the earliest days of the gas turbine engine its viability relied on the abilities of the materials used in its construction to withstand the stresses that arise from pressure increases in the working fluid within the engine and from the forces developed on rotational components during operation. According to the Carnot cycle[5], the work output from a heat engine depends on the temperature difference that can be achieved in the working fluid. So, concurrently with the evolved stresses, the materials used had to withstand the high temperatures that arise in these heat engines in order to develop useful power (and efficiency). With a further complication arising from the continuous flow nature of the gas turbine engine which does not permit time for cooling.

Since then the gas turbine engine has developed. Over the years these developments have taken into account advances in engine design, examples include moving from separate individual combustion chambers via can-annular to annular construction and in general a move from centrifugal to axial flow compressors with a tendency to use turbofan engines, civil operators using large by-pass ratios for efficiency and military operators using lower by-pass ratios in order to balance rapid power production with efficiency which can be traded between range of operations and loitering capability as required. Multi-spooled engines have been developed which optimise speed and power extraction considerations for the various linked compressor and turbine stages, although latterly this tendency for mechanically complex engines has been reversed due to the increased use of computational design tools which amongst other things permit blade aerofoil optimisation, with development of advanced materials and suitable advanced manufacturing techniques enabling the realisation of these designs, leading to developments such as BLISKS (bladed disks) and BLINGS (bladed rings). In parallel with these developments, advances in control system technology has seen the development of full authority digital engine controls (FADEC) reducing the need for complex and relatively slow hydro-mechanical control and monitoring systems.

Although the design of a modern gas turbine engine is the outcome of the application of systems engineering design techniques and teamwork, the realisation of many of the explicit or perhaps implicit design requirements has been achieved as a result of

developments in materials, materials processing and manufacturing techniques. For instance, static components used in high temperature areas have seen the development of superalloys manufactured in sheet form and an increased use of ceramic coatings to assist in prolonging the life of these components. Lower temperature areas have seen an increase in the use of structural composites, especially shrouds towards the front of the engine, including those used to contain fan blade failures. Specialist manufacturing techniques including diffusion bonding and superplastic forming (DB/SPF) using high temperature inert gas inflation have been developed for the production of hollow titanium fan blades used in engines such as the Rolls-Royce Trent. High temperature rotating components have developed along differing paths as related to their operational requirements. Turbine discs have seen the optimisation of cast and wrought products and a move to those manufactured using powder metallurgy techniques, which permit the use of more exotic refractory elements, higher strength and fatigue requirements leading to improvements in alloy compositions, refining and densification techniques such as hot isostatic pressing (HIP). Heat treatment schedules have also been further developed to optimise alloy characteristics depending on usage and location. Turbine blades have seen perhaps more developments, moving from wrought blades, to investment casting, to directional solidification, to single crystal blades often manufactured as hollow sections to reduce mass and with additional cooling holes and galleries which allow air to be used to keep the blade at a suitable operating temperature such that an acceptable working life is achieved. A further development is the use of high temperature ceramic coatings which help to insulate a metal blade from the temperature of the turbine gas stream.

When considering using the gas turbine engine as an aircraft propulsion system, the aircraft / engine designer has to balance the various and often conflicting and interlinked requirements that arise, including: mass of engine; power output; efficiency, which impacts on cost of operations directly (and via the mass of fuel required to be carried to achieve a certain range of operation); and perhaps more importantly safety via the life of the engine which is driven by the life of individual components within the engine and is often linked to either operation cycles (engine start to engine shut down) or operating hours.

In some respects the basic requirements for a gas turbine engine have changed little from those required for the earliest engines, all the requirements discussed earlier are still present. The accumulation of the various mainly incremental changes has seen the operating envelope of a modern gas turbine change such that temperatures and pressures have increased significantly leading to more efficient engines. At the same time manufacturing techniques have developed and in combination with improvements in lifing methodology this has led to more reliable and safer engines. Yet, there is still (and always will be) a drive towards more efficient engines which can remain installed for

longer periods whilst being safe to operate, there is a trade off here as life may be exchanged for efficiency by lowering operating temperatures and *vice-versa*.

In order to realise higher efficiencies and longer installed engine lives, consideration of those components which currently limit higher temperature operation is necessary. Due to high energy failure modes and the critical nature of rotating high temperature components, these (in many cases) are the turbine assemblies. Higher efficiencies, in a heat engine mean by necessity, higher operating temperatures especially those seen at the turbine. Higher gas flow temperatures at the turbine, not only mean higher temperature at the turbine blade, but also higher temperatures at the turbine disc and particularly at the turbine disc rim. The focus of this research will concentrate on the materials used in these areas of the gas turbine and hence those that are most likely to be enablers for operation at high temperatures.

In the case of the turbine blade, these are already operating in gas flow temperatures that exceed the melting point of the blade metallic material because of the advances made in blade cooling techniques and some use of thermal barrier coating systems (TBCs). The full capability of TBCs has not yet been realised, principally this is because there is a large amount of scatter observed in working lifetimes. Further research is required into TBC coated turbine blade life assessment and prediction such that maximum life can be predicted and hence realised.

For a turbine disc, higher temperatures at the rim will mean higher temperatures at the bore. The impact of this increase in temperature across the whole disc needs to be considered to ensure accurate lifing assessments can be made. Traditionally this has meant ensuring sufficient material strength is retained at the bore of the disc and that a suitable fatigue life could be achieved. Higher disc rim temperatures will impact on these aspects, but may also introduce other failure regimes, such as creep and oxidation and where the synergistic interactions between failure mechanisms is required to be understood in detail.

1.2 Research Objectives

This EngD is intended to provide QinetiQ with the information required to assess the component performance in new propulsion systems such as the F135 and F136 engines to be used in the Joint Strike Fighter (JSF) where performance gains are achieved through increased turbine gas temperatures which lead to hotter disc rims and blades. Specifically the research is aimed at giving an understanding of the high temperature materials used in modern turbine applications.

Therefore the overall objective of the EngD is:

To consider developments in advanced high temperature disc and blade materials for aero-engine gas turbine applications of interest to QinetiQ.

Encompassed within this overall objective, two discrete areas of research were identified, each having its own objectives:

- Disc alloy assessment – high temperature properties
- Thermal barrier coating (TBC) life assessment and modelling

The objectives for and outline of each of these research areas is expounded upon below.

1.2.1 Disc Alloy Assessment – High Temperature Properties

The objectives and outline for the disc alloy assessment research area are presented in the following sections.

1.2.1.1 Disc Alloy Assessment - Objectives

- Elucidate the links between microstructural features and high temperature mechanical behaviour (strength, creep and fatigue) in a range of turbine disc alloys, with a principal focus on the micromechanisms of fatigue under cyclic and time dependent conditions.
- Analyse the effect that the underlying alloy composition and development have on these links, including what trade offs are made to obtain a balance of properties in order to define and reach an optimised microstructure.
- Use of appropriate lifing approaches for turbine discs that take account of the high temperature mechanical behaviour and particular alloy composition and microstructures.

1.2.1.2 Disc Alloy Assessment - Outline

The disc alloy assessment phase considers the super-solvus heat treated LSHR and sub-solvus heat treated alloys N18, RR1000 and UDIMET® 720 Low Interstitial (U720Li) including an experimental large grain (LG) variety developed by a previous QinetiQ - University of Southampton research programme, U720Li LG.

LSHR (Low Solvus High Refractory) alloy is a powder metallurgy (PM) turbine disc material, developed by National Aeronautics and Space Administration (NASA)[6]. The super-solvus heat treated version provided an opportunity to assess the effects that this heat treatment has on microstructure evolution and the failure mechanisms that occur during fatigue crack propagation. Access to LSHR became available only in the last nine months of the EngD following discussions with NASA[7] that arose during attendance and presentation at the Superalloys 2008 conference[3].

N18 is a PM turbine disc material, developed for the Societe Nationale d'Etude et de Construction de Moteurs d'Aviation (SNECMA) M88 engine used in the RAFALE aircraft, however it differs from other new generation PM turbine disc alloys in both composition and heat treatment, and thus provides the opportunity to assess the differing effects of precipitate morphology and grain size. A full mechanical test programme has been carried out on N18 in conjunction with QinetiQ[1].

Material characterisation of LSHR and N18 has included grain size measurement and microstructure characterisation such as γ' mapping; measurement of material properties including hardness and for N18 studies into oxidation rates. Fatigue crack propagation rate tests have been carried out at 650ºC and 725ºC in both air and under vacuum conditions, for N18 using two different trapezoidal cycles with a 1s and 20s dwell at maximum load, for LSHR, only a 20s dwell at maximum load was used as a relatively small number of LSHR test specimens (six) were available. For N18, QinetiQ carried out tensile, creep and low cycle fatigue (LCF) testing at their laboratories in Farnborough.

In all cases the analysis of the results obtained and comparison with existing in-house data on RR1000 and the U720Li variants has been carried out at Southampton. Details of the tests carried out, their results and subsequent analysis and discussion via comparison with the other alloys as well as potential future work are discussed later in this thesis.

1.2.2 Thermal Barrier Coating Life Assessment

The objectives and outline for the TBC life assessment and modelling research area are presented in the following sections.

1.2.2.1 TBC Life Assessment and Modelling - Objectives

- Consider failure mechanisms within TBCs, especially those at a mesoscale and particularly in terms of thermally grown oxide (TGO) layer growth.
- Provide TGO growth data as inputs for physics based lifing models under development by QinetiQ.
- Further develop thermo-mechanical fatigue (TMF) testing at QinetiQ in order to provide a method for validating the physics based lifing model developed concurrently.

1.2.2.2 TBC Life Assessment and Modelling - Outline

At the time of the industrial placement with QinetiQ at their Farnborough site, an opportunity to work within the Gas Turbine Critical Component Lifing (GTCCL) programme was available, this was a collaborative programme between QinetiQ and the University of Cranfield for which the United Kingdom (UK) Ministry of Defence (MoD) was the customer. One work package of this research programme was particularly relevant to the

EngD and included the life assessment and modelling of TBCs; this work package formed the basis for the final 12 months of the EngD.

The TBC life assessment and modelling research considered the life assessment and modelling of a partially stabilised zirconia (PSZ) top coat applied to CMSX4 substrate coated with a platinum aluminide bond coat. Experiments were designed to consider the effects of various thermal exposure tests on representative specimens to determine the failure modes of the TBC system and to determine growth rates of the TGO layer in order to inform a physics based lifing model under development by QinetiQ.

Further development and refinement of a TMF test capability was carried out such that TMF testing could be carried out using a loading cycle representative of that seen by an in-service turbine blade in order to provide validation for the QinetiQ lifing model.

1.3 Overarching Theme of the EngD

QinetiQ provide independent advice with regard to the lifing and performance of high temperature components operating within gas turbine engines. This EngD has contributed knowledge to two key areas relevant to the performance of high temperature components:

- High temperature properties and performance of turbine disc materials LSHR and N18 and the implications for lifing approaches.
- The characterisation of TBC performance and development of TMF testing techniques that can be used to inform and validate physics based lifing models.

The characterisation of both disc material and development of validated lifing methodologies is essential if QinetiQ are to continue to provide lifing advice using verifiable and validated data.

1.4 QinetiQ Ltd

To enable the EngD to be put in context from an industrial sponsor perspective, a brief introduction to QinetiQ is appropriate, from their website:

"QinetiQ is a leading international provider of technology-based services and solutions to the defence, security and related markets. We develop and deliver services and solutions for government organisations, predominantly in the UK and US, including defence departments, intelligence services and security agencies. In addition, we provide technology insertion and consultancy services to commercial and industrial customers around the world." [8]

Part of QinetiQ's business is to provide independent advice on lifing of components within gas turbine engines to the UK MoD and other commercial customers. To ensure

independence its expertise is underpinned by its own independent research and participation in collaborative research projects.

1.5 Engineering Doctorate

This EngD was carried out under the auspices of the University of Southampton and is jointly sponsored by QinetiQ and the Engineering and Physical Sciences Research Council (EPSRC).

The EngD is a four-year postgraduate degree designed to provide a more vocationally orientated Doctorate in Engineering with a significant taught component centred on a research project or projects defined in conjunction with the Industrial Sponsor.

Three years were spent at the University of Southampton, during which all taught courses were studied with 12 months completing a research programme at QinetiQ.

Progress of the EngD was monitored via six monthly project review meetings held jointly with QinetiQ and the University of Southampton. These meetings were also used to steer the direction of the project.

2 Literature Review

In the following sections a review of the literature relevant to this project is presented. Literature regarding the two different materials considered in this project, *Nickel Based Superalloys for Turbine Disk Applications* and *Thermal Barrier Coatings for Turbine Blades* is presented first, followed by a literature review of *Fatigue*. Finally, a review of *Lifing of Critical Components in Gas Turbine Engines* is presented to provide context for the EngD.

2.1 Nickel Based Superalloys for Turbine Disk Applications

Superalloys are metallic materials based on iron, cobalt or nickel that have been developed for use at high temperatures and high applied stresses. At high temperatures, they typically exhibit high strength, long fatigue and creep lifetimes in addition to good corrosion and erosion resistance. Superalloys are used where these properties are required such as in the final compressor stages and hot sections of gas turbines used in aircraft and in land based power generation facilities.

2.1.1 Composition and Physical Metallurgy

A nickel base superalloy consists of an austenitic face centred cubic (fcc) matrix phase, gamma (γ), comprising a solid solution, the constitution of which depends on the alloying elements present. An ordered nickel rich, $Ni_3(Ti, Al)$ precipitate, gamma prime (γ'), is the major strengthening precipitate and is largely responsible for the high temperature strength of the material[9,10]. Other precipitates may also be formed, depending on the alloying elements present. These elements and their potential effects are presented below.

The major alloying addition in many nickel base superalloys is Cr in the range of 10-20 wt %[9]. This is added to improve the high temperature corrosion and oxidation resistance of the alloy which is achieved by the formation of a strongly adhering, diffusion-resistant and therefore protective Cr_2O_3 oxide layer. Too little Cr can lead to poor corrosion / oxidation performance of the alloy, whereas too much increases the probability that the deleterious sigma (σ) phase will form. Cr also partitions preferentially to form the γ matrix with Ni, hence too much Cr will mean that less γ' will form.

In order to form the γ' phase, Al and Ti up to about 8 wt % are present in the alloy. The γ' volume fraction is directly related to the amount of Al and Ti that the alloy contains[11]. Nb and Ta can replace Al in forming γ' and may increase the solution temperature of γ' permitting strengthening effects to persist to higher temperatures. In some Ni-Cr-Fe superalloys, such as Inconel 718, high additions (greater than 4 wt %) of Nb can lead to the precipitation of another hardening phase, gamma double prime, γ'', Ni_3Nb[9].

The solubility of Al and Ti in the γ phase is decreased by the addition of Co and Fe, which may increase the amount of γ' precipitated for a given amount of Al, Ti. However, decreasing Fe also increases net alloy strength, whereas Co facilitates hot working of alloys containing high proportions of Al and Ti[9]. Increasing the amount of Co in the alloy reduces the creep rate and increases creep-rupture life at high temperatures[12].

Al, Cr, W and Mo all rate as good solid-solution strengtheners. At high temperatures, above 0.6 T_m (melting temperature), strengthening becomes more affected by the diffusion of vacancies and atoms and hence the amount of climb and thermally activated cross-slip present. The rate of diffusion may be inhibited by the presence of slowly diffusing refractory elements such as Mo and W. These two elements as well as Ta and Nb (discussed previously), dissolve to some extent into the γ' lattice, increasing the lattice parameter, solvus temperature and volume fraction of the γ'[9]. Additionally Mo and W determine the type of complex carbides formed in addition to Cr, Ni, Co and Fe.

Simple carbides of the form MC (where M represents a metallic element) are created from Hf, Ta, Nb and Ti, although Mo and W may also be present. These carbides are a source of carbon during later heat treatments and in service. The quantity of Nb and Ta present determines the stability of the carbides and reduces their breakdown during solution treatments[9].

B is an essential trace element (50-500 ppm) in superalloys as its presence at grain boundaries blocks the onset of grain boundary tearing under creep rupture loading[9], increasing creep rupture lives, although 0.2 % strain creep lives are reduced by the addition of both C and B[13].

2.1.2 Microstructure

Several strengthening mechanisms combine to give nickel base superalloys their high strengths. These include solid solution strengthening, precipitation hardening from intermetallics such as γ' or carbides and dispersoid hardening. The magnitudes of these strengthening mechanisms are influenced by alloy composition, heat treatments and thermo-mechanical processing[9].

2.1.2.1 Strengthening Precipitates

The main precipitate in nickel base superalloys is, γ', $Ni_3(Ti, Al)$, an ordered FCC crystal structure (type $L1_2$) which may be coherent with the γ matrix. The form of the γ' depends on the lattice mismatch (which also depends on size), generally forming spherical particles with mismatches up to 0.2%, cubes between 0.5-1.0% and plates above 1.5% [9,11]. Composition of the γ' can vary depending on the exact constitution of the alloy, as mentioned previously Ti and Al are especially important γ' formers.

The ordered γ' phase is generally present at three different size scales. Primary γ' are typically the coarse precipitates remaining after initial alloy production which are not dissolved during solution treatment and are present along grain boundaries. Primary γ' is incoherent with the γ matrix. Secondary γ' are typically intragranular precipitates formed during the ageing heat treatment, which are coherent with the γ matrix and may have a spherical or cubic to butterfly shape dependent on size. Tertiary γ', the finest precipitates are again intragranular and coherent with the γ matrix but spherical in shape[10,14] and are thought to form during cooling from heat treatment (see more detailed discussion in paragraph 2.1.2.5.)

Another strengthening precipitate, γ'' (Ni_3Nb) occurs in Nb containing Ni-Cr-Fe superalloys such as Inconel 718. γ'' has a metastable ordered body-centred-tetragonal (BCT) crystal structure (type DO_{22}). γ'' has a disc shape morphology and is coherent with the matrix. During extended ageing this transforms to the stable orthorhombic Ni_3Nb delta (δ) phase[9].

2.1.2.2 Carbides

When early studies of nickel base superalloys showed that carbides were detrimental to the ductility of the alloys, C was removed from the alloys to counteract this tendency only to find that creep life and ductility were reduced with a C content of less than 0.03%. Carbides in the correct morphology and location are beneficial for the rupture strength at high temperatures and affect ductility[9].

Primary carbides take the form MC, where M is a refractory or reactive metal atom such as Hf, Ta, Nb, and Ti. They adopt an FCC crystal structure (the NaCl structure) and have a coarse cubic or script morphology and are generally very stable. Discrete primary carbide particles are formed heterogeneously throughout the alloy at both intergranular or intragranular sites and often interdentritically when the alloy initially freezes from the melt. Mo or W can be substituted for M in the carbide and in doing so the bond strength of the carbide is weakened permitting its decomposition to more stable lower carbides (in most alloys this is predominantly $M_{23}C_6$) during heat treatments at temperatures where the lower carbides tend to be stable (typically between about 750°C to 1000°C). The addition of Ta and Nb counter this effect making the primary carbide more stable up to temperatures around 1200°C to 1260°C. The breaking up of primary carbides provides a source of C during heat treatment and throughout the service life of the alloy[9].

During heat treatments and service the primary carbides act as a source of C below about 1000°C by decomposing and yielding carbon, permitting reactions with the γ matrix to occur to form lower carbides in accordance with the following reactions:

$$MC + \gamma \rightarrow M_{23}C_6 + \gamma' \qquad \textbf{Equation 1}$$

$$MC + \gamma \rightarrow M_6C + \gamma' \qquad \textbf{Equation 2}$$

The $M_{23}C_6$ carbides are Cr rich and have a complex cubic crystal structure often forming irregular discontinuous blocky particles (although occasionally plates or regular geometries may be formed). These particles have a tendency to occur at grain boundaries where they inhibit grain boundary sliding, improving the rupture strength of the alloy. Final failure during rupture is normally by fracture or decohesion of these particles. The quantity of $M_{23}C_6$ carbides is increased for moderate to high Cr content alloys. The cellular form of $M_{23}C_6$ has been shown to initiate premature rupture failures and as such is an undesirable feature, alloys with high γ' content at grain boundaries are resistant to the formation of cellular $M_{23}C_6$. Another carbide M_6C is formed when Mo or W content of the alloy is high, it is often more stable than $M_{23}C_6$ at high temperatures and is useful as a grain boundary precipitate to control grain size when processing wrought alloys[9].

The carbides formed at the grain boundaries and the γ' formed at the same time encapsulates the grain boundary carbides in a relatively ductile creep-resistant layer. However Cr will be depleted from the γ matrix as the γ' is formed and the solubility of γ' will be increased near the grain boundary leading to denuded zones in this area[9].

2.1.2.3 Borides

Cadel *et al*[15] found through atom probe studies combined with TEM that in N18 the γ' precipitates are Al and Ti enriched, whilst Cr, Co and Mo preferentially partition to the γ matrix. They also observed intergranular borides: M_2B (M = Cr, Mo) arranged in clusters along the grain boundary, with 1 nm thick Ni and Co enriched films (when compared with the borides) separating adjoining boride particles. Grain boundary segregation (~1 nm thick films) of B, Mo and Cr were also observed.

2.1.2.4 Other Phases

Topologically close packed (TCP) intermetallic phases such as sigma (σ), mu (μ) and Laves phases can form during heat treatments, but more often during service at elevated temperatures. These phases tend to nucleate on carbides with similar crystal structures to the TCP phase, *i.e.* $M_{23}C_6$ has a similar crystal structure to σ and M_6C to μ. They then grow through the alloy matrix taking up the refractory metals as they do so causing solute depletion, this leads to losses of both solid solution strengthening and the ability to form an oxide resistant coating, Cr_2O_3[9].

The TCP phases generally have a hard plate-like morphology. These plates often act as crack initiation sites and encourage crack propagation. The σ phase in particular can reduce ductility leading to low temperature brittle failure of the material. Higher temperature effects include a reduction in rupture strength as failure can occur along the σ plates in addition to intergranular paths. The reductions in high temperature rupture

strength, fatigue lives and corrosion resistance means that the formation of the TCP phases is considered undesirable in the alloy[9].

Numerous other phases may be present in nickel base superalloys including nitrides, sulphides and phosphides. And in addition to the above, some such as eta (η) and nitrides may also form with a hard plate like morphology[9].

2.1.2.5 Microstructure and Processing Routes

Turbine discs are typically manufactured using either a cast and wrought route or by using powder metallurgy (PM) techniques.

For the cast and wrought process triple melting is employed in order to obtain a high quality material. Initially Vacuum Induction Melting (VIM) is used as this has the advantages of degassing the alloy (reducing levels of N_2 and O_2) in turn preventing the oxidation of reactive elements (Al, Ti, Zr and Hf) and removing low melting point contaminants such as Pb and Bi. Finally desulphurisation is carried out by adding lime (CaO) to the melt. Post VIM the material is not mechanically sound and contains refractory particles arising from both erosion of refractory lining of the crucible and reaction with it:

$$2Al + 3MgO \rightarrow Al_2O_3 + 3Mg \qquad \textbf{Equation 3}$$

Electro-slag remelting (ESR) is used as the second refining melting process although it is prone to heavy element partitioning leading to a phenomenon known as “freckling” leading to a heterogeneous material being produced. As the final stage, vacuum arc remelting (VAR) is used as this permits the production of a more homogeneous and larger diameter ingot. Following a post casting annealing heat treatment the final ingot has a grain size measured in 10s of mm, which is too large to forge effectively. In order to reduce the grain size to the order of 10s of μm an ingot conversion process known as “cogging” is carried out, the thermal-mechanical work involved in this process breaks down the as cast structure. The “cogging” process typically involves squeezing a hot ingot 20 to 30 times along its length, and repeating this after rotating the ingot through 90°, 45° and again through 90° and then returning the characteristically octagonal ingot to the furnace. The deformation thus caused, gives rise to recrystallisation with a finer grain structure. The whole process being repeated until the required ingot diameter is achieved. To reduce an ingot from 60cm to 30cm diameter many (typically around 10) of these “heats” may be required. In the later heats the temperature of this cogging process is kept to below the relevant (often γ′) solvus in order to limit grain growth post deformation. The ingot may now be forged into a disc, usually by a three stage process: upsetting by open die forging, followed by blocking using a closed die process and finally finishing using a closed die process[5].

However, as nickel base superalloys have developed and their high temperature strength increased, forging has become increasingly difficult. This is because much of the high temperature strength has been maintained by increasing the γ' solvus (thus reducing γ' dissolution at higher temperatures). To successfully forge these materials forging temperatures would have to be increased leading to incipient melting and accelerated tool wear. To overcome this PM techniques have been used which also imparts improved uniformity to the initial ingot, but at an increased cost. The PM process uses an inert gas (often Argon) to atomise a clean master melt produced via VIM, this produces alloy powder spheres between 30-300μm in diameter. To obtain a usable material this powder has to be consolidated which requires full bonding across the inevitable oxide films on the powder particles. In order to consolidate it the powder is subjected to high temperature and pressure and is deformed usually by hot isostatic pressing (HIP) and then extruded to obtain the fine grain sizes required for forging. The extrusion has the additional benefit of dispersing any non-metallic inclusions that are present in the material. These may arise from the ceramic nozzle through which the high pressure inert gas is blown or from the tundishes holding the initial melt, the inclusions arising tend to be smaller than the sieve sizes used during the PM process to eliminate any particles that may lead to inclusions. Finally a near net shape forging may be produced using isothermal forging techniques, during which the material can exhibit superplastic behaviour due to its small grain size, high stresses and low deformation rates[5]. Additionally the PM process route makes the manufacture of some nickel base alloy compositions possible and may involve the introduction of exotic elements and phases or dispersoids not normally found in casting alloys such as yttria (Y_2O_3).

To obtain good high temperature properties in nickel base superalloys various further heat treatment processes are employed following the initial production of the component shape. For turbine discs this heat treatment is normally a solution treatment followed by one or more ageing heat treatments[9]. By varying the process parameters further control can be exercised over the grain size, carbides and type and distribution of precipitates as well as size distribution of γ' particles, which can be bimodal or even trimodal. Clearly the choice of cast and wrought or PM processing route will affect the subsequent response of microstructure to these heat treatments with for instance mixtures of coarse and fine grain sizes and “necklace” structures obtained by thermo-mechanical processing routes [11].

Sub-solvus solution treatment refers to solutionising the superalloys below the γ' solvus, thus leaving undissolved and relatively coarse primary γ' precipitates usually on grain boundaries. Sub-solvus solution treatment temperatures are normally in the range of 1040°C to 1170°C and this is carried out in order to dissolve some of the phases, principally γ' and carbides, prior to their controlled precipitation during subsequent heat

treatment[9,16]. The undissolved primary γ′ particles pin the grain boundaries and therefore limit the grain growth. Subsequent ageing and cooling results in a trimodal γ′ size distribution[17].

Super-solvus solution treatments heat the alloy to above the γ′ solvus temperature, and all the γ′ is therefore dissolved. In this case carbides and borides are relied upon to pin the grain boundaries, limiting grain growth, but not to the same extent as primary γ′ thus resulting in larger grains[18]. At and above the γ′ solvus temperature of the alloy the γ′ phase is completely dissolved in the γ matrix and only two sizes of γ′ are precipitated on cooling, secondary and tertiary γ′[17].

The type of solution treatment and cooling rate affect the kinetics of grain growth and γ′ precipitation and morphology. On cooling γ′ precipitates uniformly throughout the alloy, with secondary γ′ precipitation and growth occurring prior to the precipitation of tertiary γ′ which may occur during the latter part of the cooling cycle or on subsequent ageing of the alloy, although the precipitation of tertiary γ′ may be suppressed if cooling rates are high enough, *i.e.* greater than 100°C min^{-1} for RR1000. Both secondary and tertiary γ′ appear to be sensitive to cooling rate, faster rates leading to smaller γ′ sizes and lower volume fractions[18].

Ageing heat treatments are carried out below the γ′ solvus temperature in order to precipitate and develop the major strengthening phases[9]. Those alloys that have experienced a higher cooling rate during the solution treatment have a higher hardness than those with a slower cooling rate[18]. Faster cooling causes less secondary γ′ to precipitate retaining a higher proportion of γ′ forming elements in solution ready to precipitate as tertiary γ′ on subsequent ageing. Some coarsening and splitting of the secondary γ′ has been reported for alloys subject to a super-solvus heat treatment[18]. Peak hardness was found to occur early in the ageing process when the maximum amount of tertiary γ′ had precipitated. Once this had occurred any further ageing led to tertiary γ′ precipitation coarsening causing a reduction in the measured hardness values[18].

For turbine discs, double ageing heat treatments may be used to obtain duplex γ′ structures providing a balanced combination of high strength and good creep resistance. It is claimed that, by the combination of a high temperature ageing process that produces high creep extensions and a low temperature treatment which reduces creep rate into a two stage heat treatment process, it is possible to obtain better creep characteristics than are obtained by a simple precipitation treatment[16].

Other heat treatments to provide dual microstructure in turbine discs are currently under development. These use insulation and heat sinks to prevent the bore and web of the

disc being heated above the γ′ solvus temperature during heat treatment, whilst the rim can be raised above the γ′ solvus temperature. This provides coarse grains at the rim for high creep and dwell crack growth resistance and fine grain microstructures at the bore and web of the disc for high strength and fatigue resistance[19].

Typical turbine disc heat treatment routes for materials of interest in this study are:

Employed by Rolls-Royce for U720 and U720Li[20],

4h 1105°C → oil quench → 24h 650°C → air cool →16h at 760°C → air cool

Employed by Rolls-Royce for RR1000[21],

4h 1120°C → fan air cool → 24h 650°C → air cool → 16h 760°C → air cool

Employed by SNECMA for N18[22],

4h 1165°C → air cool → 24h 700°C → air cool → 4h at 800°C → air cool

Employed by NASA for LSHR

1.5h 1135°C → furnace cool → 1171°C → air cool → 4h 855°C → air cool → 8h at 775°C → air cool[7]

2.1.2.6 Stability of Nickel-Base Superalloys

In view of their use at high operating temperatures the stability of nickel-base superalloys is considered separately; several issues have been reported in the literature.

2.1.2.6.1 γ′ and γ″ Coarsening

During low cycle fatigue (LCF) testing, Nimonic 90 with a low γ - γ′ misfit showed only minimal evidence of γ′ coarsening[23]. Other nickel-base superalloys typically have a higher volume fraction of γ′ and much higher γ - γ′ mismatch leading to an increase in the amount of γ′ coarsening[23]. For instance, René 80 has a γ′ volume fraction of 50% and a mismatch of 0.2% and under similar strain controlled LCF testing in René 80 and René 77 the γ′ coarsened rapidly. As a result stress in the material lowers, leading to a more damage tolerant material in spite of the aggressive environment and increased dislocation density, the strain life of René 80 for example increasing above 760°C to higher values than those found at 25°C[23]. In Nimonic 115 and UDIMET® 500, the precipitation of σ phase leaves the surrounding matrix rich in γ′ formers, leading to precipitation of γ′ on the σ plates, but there is no evidence of associated γ′ particle coarsening. While prolonged ageing in alloy 718 leads to the coarsening of the strengthening γ″ phase, this alters the mechanism for dislocation motion from precipitate shearing to Orowan bowing[24].

2.1.2.6.2 TCP Phase Formation

The precipitation of the deleterious σ phase in Nimonic 115 and UDIMET® 500 has been mentioned earlier, it should be noted that the quantity of σ phase present increases with temperature seen in service[25]. After prolonged exposure to temperature, in RR1000 intergranular σ phase forms at grain boundaries causing an increase in the rate of crack growth propagation[26].

2.1.2.6.3 Grain Boundary Changes

Carbide precipitation on grain boundaries, twin boundaries and slip bands occurred during testing of WASPALOY® at 700°C – 800°C[27]. This was reported to be strain induced, its formation leading to local stress concentrations at the grain boundaries. Combining the effect of the stress concentrations with environmental effects and the brittle nature of the carbides can lead to boundary cracking in an intergranular manner at 800°C[23]. Similar carbide behaviour is found for Nimonic 90 with the fracture surfaces at higher temperature being intergranular or along the twin boundary facets decreasing the life of this alloy[23]. In alloy 718, the increased resistance to fatigue crack propagation due to overageing arising from long term high temperature exposure in service, has been ascribed to the reduced local stress concentrations between slip bands and grain boundaries and increased resistance to oxygen penetration due to the increased activation energy for diffusion[24]. Grain boundary pinning can be performed by other species such as Yttria in the oxide dispersion strengthened (ODS) alloy PM1000, preventing the growth of subgrains and recrystallized grains during solution treatment, although some 10% of grains do overcome this pinning effect to grow[28].

2.1.3 Deformation Behaviour

Deformation behaviour is particularly important in Ni-based superalloys. The type, action and interaction of different deformation mechanisms generally control the mechanical properties of the material such as strength, creep, fatigue *etc*. Important mechanisms and their interactions are considered further below.

2.1.3.1 Dislocation and γ' Interactions

During plastic deformation in nickel based superalloys dislocations interact with the strengthening γ' precipitates. This can occur by one of the following processes; precipitate cutting, Orowan bowing between precipitates or dislocation climb around precipitates[29]. Dislocation glide processes including precipitate cutting and Orowan bowing are not diffusion controlled processes whereas climb of dislocations is controlled by diffusion and hence is thermally activated, typically dominating at higher temperatures and relatively low stresses. At higher temperatures cross-slip processes are also experienced which may allow γ' precipitates to be bypassed.

The size and spacing of precipitates affects how dislocations move through the material. Figure 1 shows the relationship between the critical resolved shear stress (CRSS) required for precipitate cutting and for precipitates to be bypassed via Orowan bowing. The increase in CRSS for precipitate cutting with precipitate size coarsening is due to the increase in CRSS required to cut through the larger precipitates. A particular precipitate will grow via diffusion at the expense of smaller precipitates in its vicinity, thus increasing the average distance between precipitates with precipitate coarsening. As this distance increases the CRSS required for Orowan bowing and looping to occur decreases. Therefore, at some intermediate precipitate size, the mechanism for dislocation movement through the material will change from a precipitate cutting to an Orowan bowing and looping process due to these respective changes in CRSS with precipitate size for the two processes.

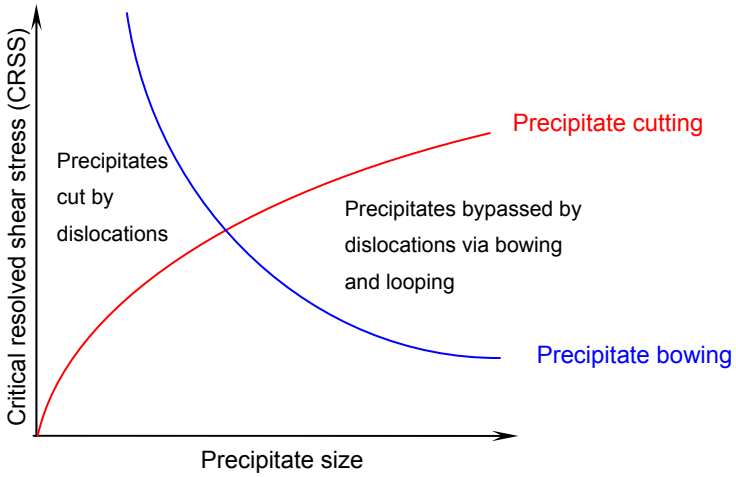

Figure 1 Representation of the variation of critical resolved shear stress (CRSS) required for precipitate cutting and precipitate bowing to occur.

A single dislocation cutting through a γ' precipitate will form a high energy anti-phase boundary (APB) due to the ordered nature of the γ', to minimise this, a second dislocation following closely will limit the extent of the APB. This phenomenon is known as dislocation pairing. The combined cutting effect of the paired dislocations leads to a reduced cross-sectional area of precipitate available for strengthening along this plane. This reduction in strength in this plane allows further dislocation pairs to cut the precipitate at a lower stress level causing further softening and concentration of slip in that particular plane[27,30], and slip heterogeneity (or planar slip) results.

When dislocations pass between precipitates by Orowan bowing, dislocation loops are left around the individual precipitates. This increases the effective diameter / area of the precipitate in that plane leading to a reduced effective spacing between precipitates making further dislocation bypass via Orowan bowing less likely in that particular plane[31]. For further precipitate bypassing to occur, dislocations either have to move to adjacent

planes within the same slip system when the strain is low or at higher strains cross-slip to other systems is possible[30,32] thus this in turn may promote wavy or homogeneous slip.

2.1.3.2 Planarity of Slip

At lower temperatures slip occurs heterogeneously in Nickel based superalloys. Slip is concentrated in slip bands that arise because of the low stacking fault energy (SFE) and the minimisation of an APB arising from coherent γ' precipitate cutting by paired dislocations[33,34] as discussed in the previous section. Low SFE values are promoted by Co additions which stabilise the hexagonal close packed stacking fault. A low SFE permits the separation of the paired screw dislocations into two sets of paired partial dislocations each separated by a larger area stacking fault. The resulting screw and edge mixed nature of the partial dislocations are no longer able to cross slip, thus further promoting planar deformation at low temperatures.

At higher temperatures, above 760°C, a further slip system becomes operative on {100} planes and along <011> directions (cube slip). This permits the long trailing partial dislocations described earlier to cross-slip causing some extremely efficient tangling to occur making them virtually immobile. This thermally activated entanglement of the screw dislocations is known as Kear-Wilsdorf locking and only occurs in the γ' precipitate due to their ordered nature permitting the formation of an APB. This phenomenon causes the anomalous high temperature increase in strength of the γ' precipitate and associated high temperature strength related to the volume fraction (V_f) of the γ' of Ni-base superalloys. As temperature continues to increase, slip on {100} planes becomes easier reducing the effects of Kear-Wilsdorf locking.

The degree of homogeneity of slip can be measured by the density of slip bands or the average spacing of slip bands[32,35]. Greater strain localisation (more heterogeneous slip behaviour) is indicated by widely spaced more intense slip bands. Whereas a higher density of less intense slip bands is associated with more homogeneous slip. Higher temperatures promote cross slip as well as dislocation climb leading to more homogeneous and wavy slip at higher temperatures. Cross slip is promoted by coarser γ' size (if bowing is promoted), low APB energy and high SFE. High loading frequencies also promote homogeneous slip[36]. Planar slip tends to be more reversible but gas adsorption or oxide formation on a fresh slip step can mechanically reduce any slip reversibility and promote wavy slip. In a vacuum, gas adsorption and oxidation cannot occur leading to more reversible and hence heterogeneous slip[37].

2.1.3.3 Effects of Slip Behaviour on Mechanical Properties

When a material is cyclically loaded strain localisation will tend to occur[38], this leads to an increase in the dislocation density in that area and results in the formation of a slip band.

Heterogeneous slip *per se* will tend to cause a reduction in toughness due to slip band impingement on grain boundaries but does not necessarily have a significant effect on yield strength[39,40].

Fatigue properties are strongly influenced by the slip characteristics that occur under differing operating conditions, the importance of these effects vary depending on the particular fatigue regime. For instance, during initiation and stage I crack growth slip character is particularly important. The intrusions associated with an intense persistent slip band can deepen to become an initiation site for a fatigue crack[38]. Stage I crack growth occurs along a slip band by slip band decohesion and is promoted by planar slip. Slip processes may however be more reversible during planar slip leading to less damage accumulation.

The intense slip bands created by heterogeneous slip cause dislocation pile up at grain boundaries creating stress concentrations in the grain and at the grain boundaries they impinge upon. These localised stresses can assist the propagation of intergranular cracks which grow without absorbing much energy[30,42] leading to premature intergranular failure[41,42] or in the case of coarser slip bands, transgranular failure[41]. Decohesion of the $M_{23}C_6$ grain boundary carbides interface with matrix may be caused in a similar manner[32]. The wider distribution of these localised stresses associated with more homogeneous slip will tend to reduce the stress between a grain boundary and the impinging slip band and minimise associated intergranular cracking in Nickel base superalloys[24].

Heterogeneous slip may reduce the effective crack tip driving force by enhancing extrinsic shielding mechanisms such as roughness induced crack closure (RICC), crack branching and crack tip deflection[41]. This can act in addition to the intrinsic reduction in fatigue damage due to increased reversibility of slip thus leading to an increase in fatigue crack propagation resistance[41,43,44].

2.1.3.4 Frequency Effects

In studies of alloy 718 by Ghonem and Zheng[45] slip line density was found to increase in proportion to the loading frequency. The higher slip line density in the crack region caused by high frequency loading leading to a more homogeneous slip behaviour. Additionally it was found that crack tip conditioning occurred if high frequency loading had been carried out prior to low frequency tests. Crack growth under these conditions was reduced and the slip line density found to be increased from that under pure low frequency tests, but less than the slip line density produced by high frequency tests, the preconditioning also produced increased crack growth resistance to environmental degradation in an oxidising environment as discussed further in the next section.

2.1.3.5 Environmental Effects

Diffusion of oxidising species to grain boundaries can occur along slip bands, more intense slip bands providing a lower resistance to diffusing oxidising species[46]. The effects of frequency can be correlated with environmental performance through the effect that homogeneity of slip has on environmental interactions.

There are two principal environmental interactions associated with slip behaviour: oxidation shielding nodes and grain boundary oxygen diffusivity, further discussion follows:

2.1.3.5.1 Oxidation Shielding Nodes

The assumption in this concept is that the slip density is the controlling parameter involved in the build up of Cr_2O_3 taking place at nodes that occur at the intersections of slip lines and grain boundaries within the crack tip region. Higher loading frequencies lead to a more homogeneous slip due to a higher slip line density within this region. This increase in slip line density on a potential grain boundary crack path has the following consequences: (i) there is a decrease in the amount of dislocation pile up due to the reduction in stress concentrations at the grain boundary arising from the increased probability of slip line matching occurring; (ii) increased transport along slip bands of Cr from the matrix, leads to an increase in this element's concentration along the potential path. When compared with areas free of slip line / grain boundary interaction, the higher stress levels and higher concentration of Cr available at the nodes provide these regions with the kinetics required for faster Cr_2O_3 build up. This beneficial build up of Cr_2O_3 at the nodes shields these regions from subsequent oxidation. Thus the higher slip line density present within the crack tip zone would lead to higher grain boundary resistance to environmental degradation during intergranular cracking, leading to lower crack growth rates[45,47].

2.1.3.5.2 Grain Boundary Oxygen Diffusivity

The rates of intergranular oxygen diffusion along grain boundaries can be characterised using the grain boundary diffusivity parameter, D_g, this is related to the stress and strain states that exist along grain boundaries of interest[48]. As discussed previously, during high frequency loading stress levels at grain boundaries are lower due to the increased slip line density and the attendant slip line matching at grain boundaries. Due to the low stresses at the grain boundaries and as D_g is a stress related parameter, it has been assumed to show only minimal variation[24,47]. Conversely during low frequency loading, stress levels at grain boundaries are higher as slip line density is lower and D_g has a correspondingly greater magnitude[47].

During high frequency loading, due to higher slip line density, the concomitant effects of increased oxidation shielding and minimal variation in D_g result in limited acceleration of

intergranular diffusion rate and hence lower oxygen penetration depth. Under these loading conditions crack tip oxidation has little effect on crack tip damage and therefore crack growth is dominated by cycle dependent effects. For low frequency loading not only does D_g increase, but due to the lower slip line density less oxidation shielding should occur and hence an expected increase in grain boundary diffusivity and associated increased oxygen penetration depth could result in an increase in crack tip damage. The effects arising from both the environmental interactions discussed above have been observed in IN718 during studies investigating the effects of high and low frequency loading carried out by Ghonem and Zheng[45] and Zheng *et al*[47].

2.1.4 Microstructure of Alloys of Interest

This section introduces the four disc alloys, N18, LSHR, RR1000 and U720Li, and different variants that are the subject of this work. A brief introduction to each of the alloys is provided and to aid comparisons between the alloys, data on alloy composition, heat treatments, microstructure characterisation and mechanical properties are presented in Table 5 to Table 8 respectively. Typically all alloys have been produced by PM routes followed by either a sub-solvus heat treatment and ageing leading to a tri-modal γ' distribution, incoherent primary γ' on the grain boundaries with secondary and tertiary γ' coherent with the γ matrix or in the case of LSHR a super-solvus heat treatment and ageing leading to an essentially unimodal γ' distribution coherent with the γ matrix. To provide context from an alloy designer's point of view, a brief summary of the patent for each alloy where available is also presented.

2.1.4.1 N18

N18 was developed by the SNECMA for the M88 engine installed in the RAFALE fighter aircraft. The stated aims of the development programme were to produce an alloy with improved creep and static strength at medium temperatures and damage tolerance capability at 650°C[49,50].

2.1.4.2 N18 Patent Claims

The composition of N18 lies within that prescribed by US Patent 5104614[50] granted to SNECMA; Association pour la Recherché et le Développement des Méthodes et Processus Industriels (ARMINES); Tecphy and the Office National d'Etudes et de Recherchés Aerospatiales (ONERA). The patent presents the background behind the development of the alloy which includes some of the rationale for including specific elements within the composition specification range. A summary of the pertinent items and claims is contained below.

2.1.4.2.1 Field of Application

The intended field of application is the discs of turbo-machines which encounter temperatures of up to 750°C.

2.1.4.2.2 Context, Prior Art and Background

Desirable qualities in the material would include good tensile properties, such as yield strength and elongation up to 750°C; a high creep strength and absence of any sensitivity to the presence of notches up to 750°C under creep conditions and a resistance to low cycle fatigue. There should also be a good resistance to crack propagation when the effects of environment and prolonged hold times are considered. In order to achieve these qualities it is claimed that PM materials are the most suitable.

It is claimed that previous materials have either: provided low fatigue crack propagation rates with a low sensitivity to the environment, yet their yield strength and resistance to creep were inadequate. Or elevated yield strength was achieved but sensitivity to notching under creep conditions, fatigue crack propagation rates and sensitivity to environmental effects were not acceptable.

Within the patent it is also noted that improvements can also be made via microstructural routes for *e.g.* coarse grains or necklace structure reducing fatigue crack propagation rates at expense of yield strength.

2.1.4.2.3 Alloy Composition

The compositional range contained within the patent[50] is presented in Table 1. The rationale for including these ranges of elements as stated in the patent is presented below, a summary of this information is contained at Appendix 1.

Table 1 N18 Patent compositional range.

	Cr wt%	Co wt%	Mo wt%	Nb wt%	Ta wt%	Ti wt%	Al wt%	Hf wt%	C ppm	B ppm	Zr ppm	Ni
range	11-13	8-17	6-8	0-1.5	0	4-5	4-5	0-1	0-500	0-500	0-500	Bal

2.1.4.2.4 γ Phase Stabilisers and Solid Solution Strengtheners

Mo and W are solid solution strengtheners of γ. Mo is preferred as its preferential partitioning to the γ phase means the ratio of Mo in γ compared with γ' is 2-3 times that if W is used. Mo also reduces the sensitivity to notches under creep conditions at 650°C, although the performance of smooth test pieces under creep conditions is lowered. The density penalty when using Mo is also less.

Cr is necessary to provide oxidation resistance and strengthening. For the ranges of Al, Ti, and Mo specified, Cr at levels greater than 13wt% leads to abundant precipitation of

intergranular carbides which leads to a deterioration in ductility and sensitivity to notching and cracking. Amount of Cr should lie between 11-13wt%.

A minimum of 8wt% Co is required to promote creep resistance, but due to the high levels of Al and Ti at least 14wt% is used. Co also reduces the γ' solvus and is therefore limited to a maximum of 17wt% to maintain the volume fraction of γ' for use at temperature.

No V is present, although it increases strength, associated fatigue crack growth rates at 650°C are excessive.

2.1.4.2.5 γ' Formers

Nb and Ta increase the yield strength under creep conditions for smooth test pieces, but increase sensitivity to notching and are detrimental to fatigue crack growth rates at 650°C. Ta will increase the density of the disk more than Nb and for this reason Ta is not included in the specification and the amount of Nb is limited to 1.5%.

Due to the low Nb content, to obtain the required yield strength, γ' volume fraction should be 50% minimum and the ratio of Al and Ti to obtain this should be 1:1. Ti when compared with Al provides more strengthening of the γ' above 650°C but also increases the γ' solvus which can make practical use of the alloy difficult. The maximum amount of Al + Ti should be 10wt% maximum.

2.1.4.2.6 Carbide and Boride Formers

B and C may improve resistance to creep, but as Cr and Mo are used and to avoid excessive formation of borides and carbides they both should be limited to 500 parts per million (ppm), but with a preferential maximum of 200ppm.

Hf provides complementary hardening, up to 1wt% maximum as it reduces the solidus and raises the γ' solvus.

2.1.4.2.7 Other Elements

Zr is included to counteract potential weakening due to possible sulphur content, but is limited to 500ppm to avoid forming phases with a low melting point.

Mg, Ca, Si and Y may be present in trace levels without detriment to the alloy.

2.1.4.3 LSHR

Following on from joint United States (US) Government and industry research programmes, LSHR, (so named using the acronym from Low Solvus High Refractory alloy), was developed by the National Aeronautics and Space Administration (NASA) in a search for a material that would meet a longer term requirement for turbine disks able to operate with higher rim temperatures (704°C and above)[6]. LSHR was selected from a number of experimental disk alloys with modified chemistries by screening them with

respect to the mechanical properties they achieved at high temperatures and selecting the alloy with a promising balance of properties.

2.1.4.4 LSHR Patent Claims

The composition of LSHR lies within that specified by US Patent 6974508[51].

2.1.4.4.1 Technical Field

Invention relates particularly to “a nickel base superalloy having a unique combination of versatile heat treatment processing capabilities and superior mechanical properties at elevated temperatures up to 760-815°C”.

2.1.4.4.2 Context, Prior Art and Background

Requirements for a gas turbine disk are outlined with differing temperatures, stress states, fatigue, creep and strength requirements from bore to rim. Materials peak temperatures of 760-815°C for aerospace and space applications with commercial operations in cruise operating at moderately elevated temperatures for long periods of time. The Patent states the need for an alloy capable of providing improved physical and mechanical properties at these high temperatures and / or elevated temperatures and extended time periods.

The Patent discusses previous attempts to obtain improved strength and time dependent properties including: (1) increasing content of strengthening γ' precipitates by increasing certain elements which stabilise and preferentially reside in γ' phase; (2) increasing the inherent strength and time-dependent properties of the γ' phase by increasing the amounts of certain refractory elements to take the place of Al atoms in the $L1_2$ crystal lattice of γ' and (3) increasing the strength and time-dependent properties of the γ phase by providing more refractory atoms to take the place of Ni atoms in the FCC crystal lattice. However, these approaches have resulted in alloys with disadvantages or limitations. For example and in general, super-solvus alloys with coarse grain microstructures optimised for use at high temperatures (704°C to 815°C) are difficult to heat treat, require high solution temperatures (above 1160°C) and are difficult to quench without forming cracks. Despite having a large grain size the alloys tend to have inadequate creep, tensile and fatigue properties approaching 815°C. Whereas sub-solvus with fine grain microstructures optimised for use at 704°C do not have adequate creep, tensile and fatigue properties approaching 815°C, neither do they respond well to alternative coarse grain heat treatments partly because of their high gamma prime solvus temperatures. In both cases dual microstructure heat treatments are difficult to apply successfully and although these type of heat treatments could be applied to the more recent “Balanced sub-solvus / super-solvus” class of alloys these too do not exhibit adequate tensile and creep properties at the required temperatures.

There exists a need for a high temperature, versatile disk superalloy with higher strength and creep resistance at maximum rim temperatures which retains dwell crack growth resistance at lower temperatures with sufficient phase stability to enable expected use for several thousand hours.

2.1.4.4.3 Disclosure and Best Mode of the Invention

Various objectives are detailed within the Patent. A general overarching objective of being able to achieve improved combinations of properties in applications used under high temperature conditions is presented. This is followed by more specific objectives, including:

- A low γ' solvus permitting heat treatments to produce;
    - uniform coarse grain microstructures to maximise strength and time dependent properties up to about 815°C.
    - uniform fine grain microstructures for high strength up to 704°C.
- Enable dual microstructures to be obtained via solution heat treatments;
    - higher treatment temperatures at rim, leading to coarse grain microstructures capable of withstanding temperatures up to about 815°C
    - lower treatment temperatures at bore, leading to fine grain microstructures capable of withstanding temperatures up to 704°C
- Capable of being produced using conventional powder metallurgy
- Less likelihood of quench cracks forming over a wide range of cooling rates
- A range of properties is produced for a range of cooling rates from 40°C min^{-1} to 167°C min^{-1}

2.1.4.4.4 Alloy Composition

The composition of the alloy is initially presented as a range of compositions which is refined into an “exemplary embodiment” of the composition presented in Table 2. Comments on the role of various elements have been taken from the Patent and are presented below.

Table 2 LSHR Patent composition.

	Cr	Co	Mo	Nb	Ta	Ti	Al	W	C	B	Zr	Ni
wt%	12.52	20.70	2.73	1.45	1.60	3.50	3.46	4.33	0.029	0.028	0.049	Bal

2.1.4.4.5 Solvus Temperature

Increases in Co and Cr were found to reduce the γ' solvus temperature, whereas Ta was found to increase it. A balance of these elements was selected to achieve a solvus temperature of 1150°C to 1160°C.

2.1.4.4.6 γ Phase Stabilisers and Solid Solution Strengtheners

W was found to provide the largest increase in tensile strength and yield strength at both 815°C and 704°C for the alloy. Mo did so to a lesser degree but adversely affected ductility and density.

2.1.4.4.7 γ' Formers

Too high a γ' content increases the tendency for quench cracking to occur a target V_f of 50% to 55% was selected in combination with a solvus temperature of 1150°C to 1160°C as an optimum balance between a tendency to quench crack and providing good creep resistance. A higher ratio of Al compared to Ti was found to increase the tendency to quench crack and a target ratio of Al : Ti of 0.94 to1.0 was chosen as a balance to the improved creep life performance a higher ratio provides.

Nb also improves tensile strength and yield strength but to a lesser degree than W, but was found to adversely affect ductility and density. The addition of Nb also improved creep life at 704°C and a range of above 1, but below 2.1 wt% was selected as a compromise between creep, tensile, ductility and quench cracking performance.

2.1.4.4.8 Carbide and Boride Formers

The role of carbides and borides is not discussed in the patent.

2.1.4.4.9 Phase Stability

The material has been subjected to extended exposures at 704°C for up to 1200 hours and 815°C for up to 600 hours without significant quantities of deleterious (σ, μ, η or P) phases forming.

2.1.4.4.10 Production and Heat Treatments

The alloy can be produced using conventional PM techniques, extruded into billet form and isothermally forged using conventional forging temperatures and strain rates. Figure 15 from the patent shows an exemplary route from alloy chemistry creation to final shape machining and is reproduced below in Figure 2.

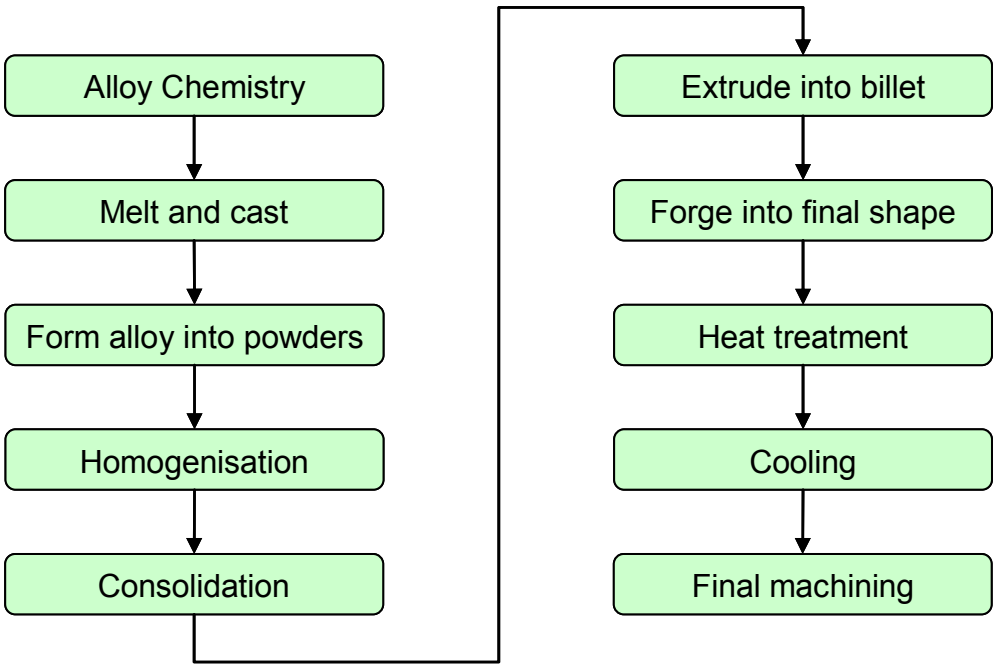

Figure 2 Exemplary processing steps for LSHR (Fig 15 of LSHR patent[51]).

2.1.4.4.11 Heat Treatments and Microstructure

Heat treatment routes required to produce three different types of microstructures are discussed within the Patent; (1) A coarse grain microstructure produced by heating above the γ' solvus for between 0.1 to 3 hours; (2) A fine grain microstructure obtained by heating the alloy to between 30°C and 45°C below the γ' solvus for between 0.5 and 3 hours. The alloy having a potential for quenching at rates of between 40°C min^{-1} and 167°C min^{-1}. And (3) dual microstructure heat treatments using higher solution heat treatment temperatures at the disc rim, to produce a coarser grain microstructure and lower solution heat treatment temperature at the bore to produce finer grain microstructures.

Subsequent heat treatments of 760°C to 835°C for between 1 to 10 hours, optimally followed by 650°C to 759°C for between 2 and 24 hours are presented as residual stress relieving heat treatments in order to improve machinability and also produce the necessary mechanical properties. Different temperatures and times may be used at the disc rim compared with the disc bore.

Wide ranges of mechanical property values are provided, this range being ascribed to the versatile range of cooling rates (40°C min^{-1} to 167°C min^{-1}).

2.1.4.5 RR1000

RR1000 has been developed by Rolls-Royce. The alloy is claimed to have a fatigue crack propagation resistance equal to WASPALOY®, tensile strength higher than WASPALOY® (at least 1400 MPa at 550°C) and therefore a higher operating temperature than WASPALOY® or any of the UDIMET® 720 family of alloys[52].

2.1.4.6 RR1000 Patent Claims

The composition of RR1000 lies within that specified by US Patent 5897718[52]. The following summarises the pertinent claims made within the patent including the background behind the development and some of the rationale for including some elements within the composition. With more production and heat treatment information it appears to be a more detailed patent than that applied for N18.

2.1.4.6.1 Field of Application

Wrought and heat treated products made from nickel base superalloys (e.g. compressor and turbine discs) up to one meter in diameter.

2.1.4.6.2 Context, Prior Art and Background

Previous alloys have included: WASPALOY® (1967) but this had limited strength and high temperature performance; UDIMET® 720 (1986) which proved to be unstable due to the formation of topologically close packed (TCP) phases; UDIMET® 720Li (1990), a PM alloy had reduced Cr, B and C in order to prevent the formation of TCP phases;

Cast and Wrought (C&W) UDIMET® 720Li (1994), which has properties close to those obtained by the PM version, has adequate strength, although its fatigue crack propagation resistance is lower than that provided by WASPALOY® and its maximum operating temperature is approximately 650°C.

2.1.4.6.3 Preferred Alloys

Using the above background as context, a preferred alloy will have a fatigue crack propagation resistance similar to that provided by WASPALOY® (without an attendant loss of property balance). A preferred alloy will have a UTS $\geq$ 1400 MPa at 550°C and a creep strain < 0.1 total plastic strain after 40h at 725°C under a load of 500 MPa. The weight fraction of γ' at 725°C will be 45± 2% (providing a balance between tensile strength and fatigue crack propagation resistance). A preferred alloy will also have a degree of instability and the potential to form grain boundary carbides such as M_6C and / or $M_{23}C_6$ (less stable alloys exhibit a greater resistance to fatigue crack propagation). There will be a limit to the TCP phases post wrought and heat treatment of < 7wt% at 725°C and the TCP solvus will preferentially be 40°C below the solvus for the M_6C or $M_{23}C_6$ phases. Finally a preferred alloy will have a higher operating temperature than both WASPALOY® or the UDIMET® 720 family of alloys.

2.1.4.6.4 Alloy Composition

The compositional range contained within the patent[52] is presented in Table 3. The alloys covered by the patent are characterised by their inclusion of Ta and combination of ranges of Cr, Mo, Ti and Al. The rationale for including these ranges of elements as

stated in the patent is presented below, a summary of this information is contained at Appendix 2.

Table 3 RR1000 Patent composition range.

wt%	Cr	Co	Mo	Ta	Nb	V	Fe	Mn	Ti	Al	Hf	W	Re	C	B	Si	Y	Zr	Ni
min	14.35	14	4.25	1.35	0	0	0	0	3.45	2.85	0.5	0	0	0.012	0.01	0	0	0.05	Bal
max	15.15	19	5.25	2.15	0.5	0.1	1	0.15	4.15	3.15	1.0	2	1	0.033	0.025	0.2	0.1	0.07	

2.1.4.6.5 γ Phase Stabilisers and Solid Solution Strengtheners

Co in the range of 15-18.5wt% has no significant effect on tensile or creep strength. 15wt% generates a minimum stacking fault energy which promotes planar deformation and the potential for improved fatigue crack propagation resistance.

Cr content is raised to improve fatigue crack propagation resistance without the formation of excessive TCP phases.

Mo is beneficial for tensile strength and ductility at high temperatures, the amount is controlled to balance the high Cr content with respect to the formation of TCP phases.

Re has a strong benefit on creep resistance, although is not included in any of the example alloys listed within the patent.

2.1.4.6.6 γ' Formers

Ta increases the tensile strength of the alloy, but segregates to form very stable TaC, its amount is controlled to allow MC carbides to breakdown in order to promote the formation of grain boundary carbides.

Both Ti and Al control the weight fraction of γ' and have the most effect on the γ' solvus. Their amounts are increased to counter reduced Ta so that tensile strength is maintained whilst γ' weight fraction and TCP phase formation are kept within limits.

Al is balanced with respect to Ti content to control the γ' weight fraction, amount of Al is limited to reduce the propensity for TCP phase formation.

Nb is included with less than 0.5 wt%, but preferably should not be used and is not included in any of the example alloys.

2.1.4.6.7 Carbide and Boride Formers

B is reduced to levels which are beneficial to creep, fatigue crack propagation resistance and tensile strength.

C is included at levels to promote hot ductility and high temperature creep resistance.

Hf improves all properties!

2.1.4.6.8 Other Elements

Although included in the patent specification, the roles of V, Fe, Mn, W, Si and Y are not discussed within the patent.

Zr has been increased to 0.06 wt% due to the beneficial effect it has on stress rupture lives and creep resistance.

2.1.4.6.9 Production and Heat Treatments

Possible methods of billet production, forging and heat treatments are also presented in the patent as summarised below.

2.1.4.6.10 Billet Production

Larger forgings are likely to be made via the PM route and consolidated (below γ' solvus) using HIP and extrusion or HIP and "cog". Smaller items can be produced using a cast and wrought route involving a triple melt process and conversion to ensure the final product is homogeneous.

2.1.4.6.11 Forging

The alloy may be formed under isothermal or hot die conditions within the following constraints. Up to the γ' solvus minus 60°C at a strain rate between $1x10^{-4}$ and $1x10^{-2}s^{-1}$ or up to the γ' solvus minus 120°C at a strain rate between $1x10^{-2}$ and $5x10^{-1}s^{-1}$.

2.1.4.6.12 Heat Treatments and Microstructure

Partial or fully solutionising heat treatments should be carried out at temperatures between γ' solvus minus 40°C and γ' solvus minus 20°C for between 0.5 and 8 hours Cooling must be carried out to avoid cracking whilst maintaining the alloy tensile response *i.e.* a rate of between 0.2 and 10°C s^{-1}. With ageing at temperatures of between 650°C and 900°C for 10 to 30 hours.

A relatively coarse grain size is associated with good fatigue crack propagation resistance, a range of 6-45 μm is preferred with that in the range of 25-35μm particularly preferred, although a non-uniform (including duplex) grain structure may be satisfactory.

A heat treatment window exists between the σ phase solvus (827°C) and $M_{23}C_6$ solvus (897°C). An ageing heat treatment in this window encourages the formation of a desired $M_{23}C_6$ phase without forming the deleterious TCP phase.

Primary γ' is retained throughout manufacturing to prevent grain boundary migration. The alloys have a fine grained microstructure and good fatigue crack propagation resistance. Creep and fatigue crack propagation resistance may be improved by increasing grain size. It is difficult to generate controlled and reproducible structures using super-solvus heat treatments. Because the alloys have good fatigue crack propagation resistance a super-solvus heat treatment to generate a coarse grain size in order to achieve good

fatigue crack propagation resistance is not required and it is possible to dispense with this expensive super-solvus and other heat treatments.

2.1.4.7 U720Li

Although a specific patent for U720Li has not been sighted, the following provides a summary overview of the alloy from the literature.

UDIMET® 720 (U720) was initially developed as a blade alloy for land based turbines[53] for long term service use of up to 10000 hours at temperatures up to 900°C[54]. With strength and stress rupture lives comparable to IN738 between 593°C and 871°C, U720 offered unique and superior stress corrosion resistance in low temperature (704°C) sulphate / chloride environments thought to be due to the carbides (TiC, $Cr_{23}(C, B)_6$) and borides (Mo_2B_3) precipitated on the grain boundaries during ageing heat treatments interrupting the normally preferential diffusion paths along grain boundaries[53]. The formation of these carbides and borides during heat treatments are also thought to contribute to U720 improved toughness after exposure times of 10000 hours by inhibiting further carbide and boride precipitation[53]. The alloy exhibits remarkable mechanical properties, approaching those of PM alloys when used in a fine grain size form, this in combination with its workability, the alloy was seen as having high potential for use in gas turbine engines as a disc alloy in cast and wrought form (C&W) at elevated tempertures[54]. Early testing on different grain size variants however revealed that strength rupture lives did not live up to predictions, initially this was ascribed to the high amounts of borides and carbides that were present at the grain boundaries[55]. Later studies showed that these carbides and borides had a similar structure to σ phase formed at grain boundaries making the detection of σ phase difficult. The attendant propensity for brittle failure and cracking of σ phase and reduction in ductility arising from excessive precipitation of $M_{23}(C, B)_6$ carbides at the grain boundaries leading to the worse than expected creep rupture strength properties[54]. For this reason the elements associated with forming the interstitial borides and carbides (B and C) were reduced along with the Cr content, of which too high a percentage can lead to the formation of σ phase. Due to the reduced interstitial element content, this later variant of U720 that was developed to reduce the propensity to precipitation of phases such as σ[56] has become known as U720 Low Interstitial (U720Li). Although in many cases its use may only be determined from analysis of the chemical composition of the alloy. The elemental composition of both U720 and the initial U720Li developed is shown in Table 4.

Table 4 U720 and U720Li Compositions (weight %)[54].

wt %	Cr	Co	Mo	Ti	Al	W	C	B	Zr	Ni
U720	18.0	14.7	3.0	5.0	2.5	1.25	0.035	0.033	0.03	Bal
U720Li	16.0	14.7	3.0	5.0	2.5	1.25	0.010	0.015	0.03	Bal

Later development of the alloy has included analysis of the tensile, stress rupture and LCF properties at room and high temperatures for sub-solvus and super-solvus heat treated and aged specimens of PM alloy in the Extruded and Isothermally forged (E&I) and PM and HIP conditions[57] and these studies conclude that subject to further analysis that the As-HIP alloy performance is comparable to that produced by PM (E&I) route and may be suitable for engine use. Early material was prone to segregation and hence variable microstructure although this was improved with triple melt (VIM – ESR – VAR) techniques providing a cost effective source for C&W alloy for both small and large (840 mm and 500 kg) turbine discs[58]. Its PM form has been shown to be cost effective when compared with C&W form and offers superior homogeneity[59]. The outstanding balance of strength, temperature and damage tolerance properties of U720Li has led to its use in turbine components in a large number of civil and military gas turbines[59].

2.1.4.8 U720Li LG

To permit comparisons to be made with regard to grain size, data from previous work[20,21] on a microstructural variant of 'as received' U720Li produced by the Defence Evaluation Research Agency (DERA) to have larger grain sizes whilst maintaining similar size distributions of the γ' precipitates has been included. To differentiate it from 'as received' U720Li, this variant is referred to as U720Li Large Grain (LG).

2.1.4.9 Alloy Summaries

To aid comparison to be drawn between the various alloys, summaries of information appertaining to them is presented in tabular form as detailed below:

Table 5 Alloy compositions (weight %) from literature

Table 6 Alloy heat treatments and reported γ' solvus from literature

Table 7 Microstructure characterisation and grain boundary phases from literature

Table 8 Mechanical properties from literature

Table 5 Alloy compositions (weight %) from literature.

Alloy	Co	Cr	Mo	Al	Ti	Hf	C	B	W	Fe	Zr	Ta	Nb
N18[60]	15.7	11.5	6.5	4.35	4.35	0.50	---	---	---	---	---	---	---
LSHR[61]	20.7	12.5	2.7	3.5	3.5	---	0.03	0.03	4.3	---	0.05	1.6	1.5
RR1000[52]	14.0-19.0	14.35-15.15	4.25-5.25	2.85-3.15	3.45-4.15	0.5-1.0	0.012-0.033	0.01-0.025	---	0.0-1.0	0.05-0.07	1.35-2.15	---
U720Li & LG[20]	14.57	15.92	2.98	2.44	5.18	---	0.023	0.016	1.35	0.08	0.042	---	---

Table 6 Alloy heat treatments and reported γ′ solvus from literature.

Alloy	γ′ solvus	Solution heat treatment		Ageing heat treatments*	
N18	1193°C[49]	4h 1165°C	air cool	24h 700°C	4h 800°C
LSHR	1155°C[6]	1.5h 1135°C (sub solvus) followed by 1171°C (super solvus)	furnace cool air cool	4h 855°C	8h 775°C
RR1000	1160°C[52]	4h 1120°C	fan air cool	24h 650°C	16h 760°C
U720Li	1160°C [62,63]	4h 1105°C	oil quench	24h 650°C	16h 760°C
U720Li-LG	1160°C[62, 63]	4h 1135°C	air cool	24h 650°C	16h 760°C

(* all ageing heat treatments were followed by an air cool, Where two references are given a rounded average of reported values are included in the table.)

Table 7 Microstructure characterisation and grain boundary phases from literature.

	N18	LSHR	RR1000[21]	U720Li[21]	U720Li-LG[21]
Grains					
Range (μm)	10-20[60]	---	2.3-16.0	2.1-13.1	4.8-41.3
Average (μm)	15[163]	32.5 [64]	7.4	6.4	15.4
Size standard deviation	---	---	2.8	1.8	6.5
Mean relative circularity	---	---	0.66	0.65	0.66
Primary γ′ precipitates					
Range (μm)	2.5-6.1[119]	N/A	0.4-6.3	0.5-6.9	0.9-7.6
Mean (μm)	4.3[119]	N/A	1.75	1.99	2.52
Size standard deviation	-	N/A	0.9	0.9	0.9
Mean relative circularity	-	N/A	0.70	0.70	0.72
V_f (%)	5[60]	N/A	8.7	18.9	8.6
Secondary γ′ precipitates					
Range (nm)	130-290[119]	---	40-200	51-150	81-300
Mean (nm)	210[119]	60 (median) [65]	140	102	190
Tertiary γ′ precipitates					
Range (nm)	10-30[119]	---	6-30	1-45	6-30
Mean (nm)	20[119]	11 (median) [65]	18	16	17
Coherent γ′ at 250°C					
V_f (%)	~45[60]	58 [65]	40.5[21]	29.4[21]	39.7[21]
Grain boundary phases					
Composition	M_2B[15]	$M_{23}C_6$ [65] MC [64] $(W,Mo,Cr)_3B_2$ [64]	$M_{23}C_6$ [52]	Predominantly $M_{23}(C,B)_6$ [54] Small amounts MB_2, M_3B_2 [54]	---

Table 8 Mechanical properties from literature.

	N18	LSHR	RR1000	U720Li	U720Li-LG
σ_y at 650°C (MPa)	1050[60]	1017 [64]	1035[21]	980[62]	850[62]
Hardness (Hv 30)	---	---	457±4.8[21]	458±2.9[21]	445±1.2[21]

2.2 Thermal Barrier Coatings for Turbine Blade Applications

This section of the literature review considers Thermal Barrier Coatings (TBCs) for turbine blade applications. To set the scene an introduction to TBCs is presented first. This is followed by a description of the materials used in a TBC system and their properties and finally by a review of the failure modes and mechanisms in TBC systems.

2.2.1 Introduction to Thermal Barrier Coating Systems

The introduction considers the purpose behind TBC systems and the benefits that their use provides. The scope of this aspect of the literature review is also considered here to further develop and justify the objectives within the TBC life assessment and modelling phase of the EngD at section 1.2.2.1.

2.2.1.1 Purpose and Benefits of Thermal Barrier Coating Systems

In the introduction to this EngD it was stated that, "…there is still (and always will be) a drive towards more efficient engines…" The Carnot cycle was discussed briefly in the context of this drive for higher efficiencies, which in a heat engine means by necessity higher operating temperatures, especially those seen at the turbine and especially the turbine blades. Turbine blade temperature performance has improved over the last seven decades[66] due to a combination of materials and manufacturing developments. In order to enhance this performance further, TBC Systems are used to insulate the substrate of state of the art turbine blades such that an increased operating temperature of the coated blade can be achieved, see Figure 3, thus maintaining suitable materials properties. The current state of the art turbine blade is typically a single crystal nickel base superalloy containing refractory (Ta, W, Re) solute additions for solid solution strengthening and with a high V_f of γ' for precipitate strengthening. To allow sufficient γ' to form and to allow the solvent to dissolve the refractory elements and prevent the formation of deleterious phases such as σ, the levels of Cr and Al are reduced. As discussed previously, Cr and Al are required for oxidation resistance in nickel base superalloys, this reduction in Cr and Al content leads to an increased susceptibility to oxidation. So in addition to the role of increasing operating temperature of the coated blade, TBC Systems have a role to play in protecting the blade from increased oxidation rates and environmental attack.

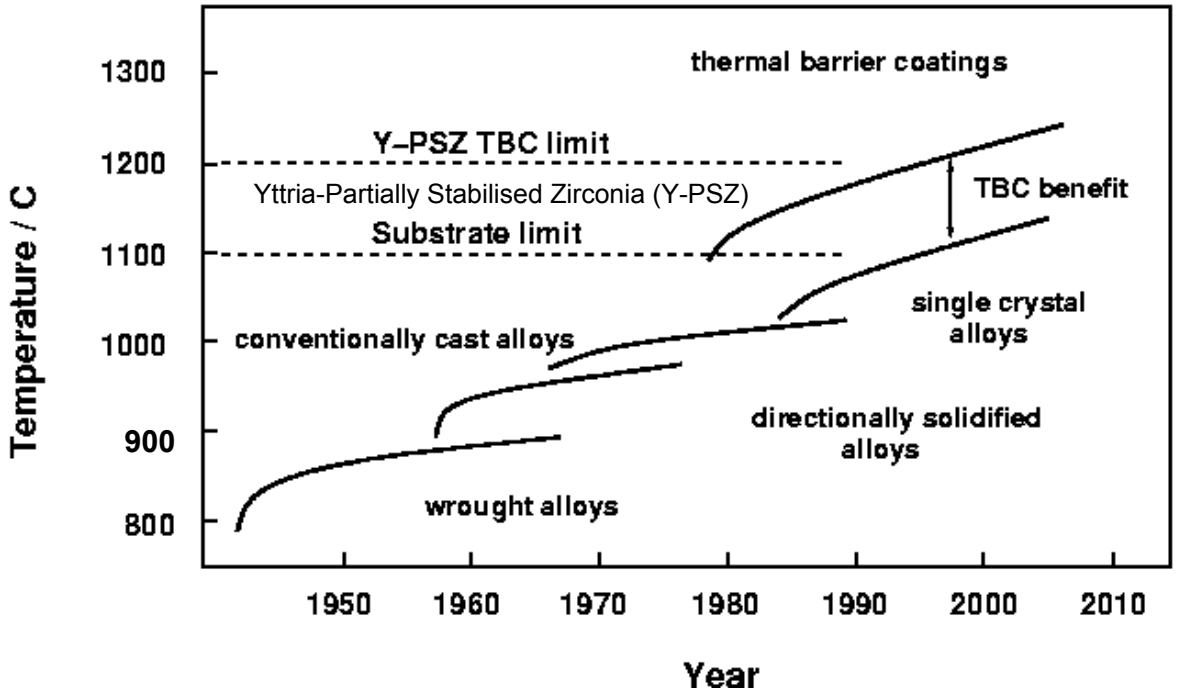

Figure 3 Increase of operational temperature of turbine components made possible by alloy development, manufacturing technology and TBCs[66].

2.2.1.2 Focus of the Thermal Barrier Coating Systems Literature Review

The focus of this aspect of the literature review is based around the objectives for this aspect of the research, *i.e.*:

- Consider failure mechanisms within TBCs, especially those at a mesoscale and particularly in terms of thermally grown oxide (TGO) layer growth.
- Provide TGO growth data as inputs for physics based lifing models under development by QinetiQ.

Initially an overview of TBC Systems was carried out to provide a framework and context for the research, this is presented in the next section.

2.2.2 Description and Material Properties of Thermal Barrier Coatings

In the following section an overview of the functionality and structure of TBCs is presented. The layered structure introduced here is then described in more detail in the subsequent sections.

2.2.2.1 Overview of Thermal Barrier Coating Systems

The main role of a TBC has been described above as: to insulate the substrate such that increased operating temperatures of the coated blade can be achieved. In an ideal world rather than use a TBC, a single material that could withstand higher temperatures than nickel base super alloys would be used to manufacture a blade (or even a BLISK) for instance silicon nitride (Si_3N_4)[67]. Although an area of active research, such materials do not currently have sufficient overall performance to be used in the demanding applications

of an aero-engine. This leads to the concept of some form of insulating material being applied to a turbine blade (or substrate), with the aim of shielding or separating the substrate from deleterious conditions, principally:

- High temperatures, so that:
    - the substrate does not melt;
    - the mechanical properties of the material are not significantly degraded;
- Oxidising environment, to prevent or reduce oxidation and other forms of corrosion that occur at high temperatures.

In order to achieve this, an insulating Top Coat (TC), normally of Yttria (Y_2O_3) Partially Stabilised Zirconia (Zr_2O_3) (YPSZ) is used to thermally insulate the substrate (blade). Unfortunately, YPSZ, as deposited on the substrate using Electron Beam Physical Vapour Deposition (EBPVD), is quite porous to oxygen, and as the substrate has little inherent protection to oxidation (for reasons mentioned earlier), the substrate requires a coating to protect it from oxidation and to act as a transition layer to improve compatibility due to differences in material properties. This protective coating serves another purpose, that is to provide an interface layer that can bond to the substrate and to which the top coat can bond onto, hence it is known as the Bond Coat (BC). The BC provides oxidation protection to the substrate via a protective oxide layer that forms between the BC and TC when the BC is subjected to oxidising (high temperature) conditions, this layer is the Thermally Grown Oxide (TGO). The complete structure is annotated on a micrograph of a TBC System tested during this work in Figure 4. The microstructure and properties of the various layers of the TBC System are discussed in more detail in subsequent sections.

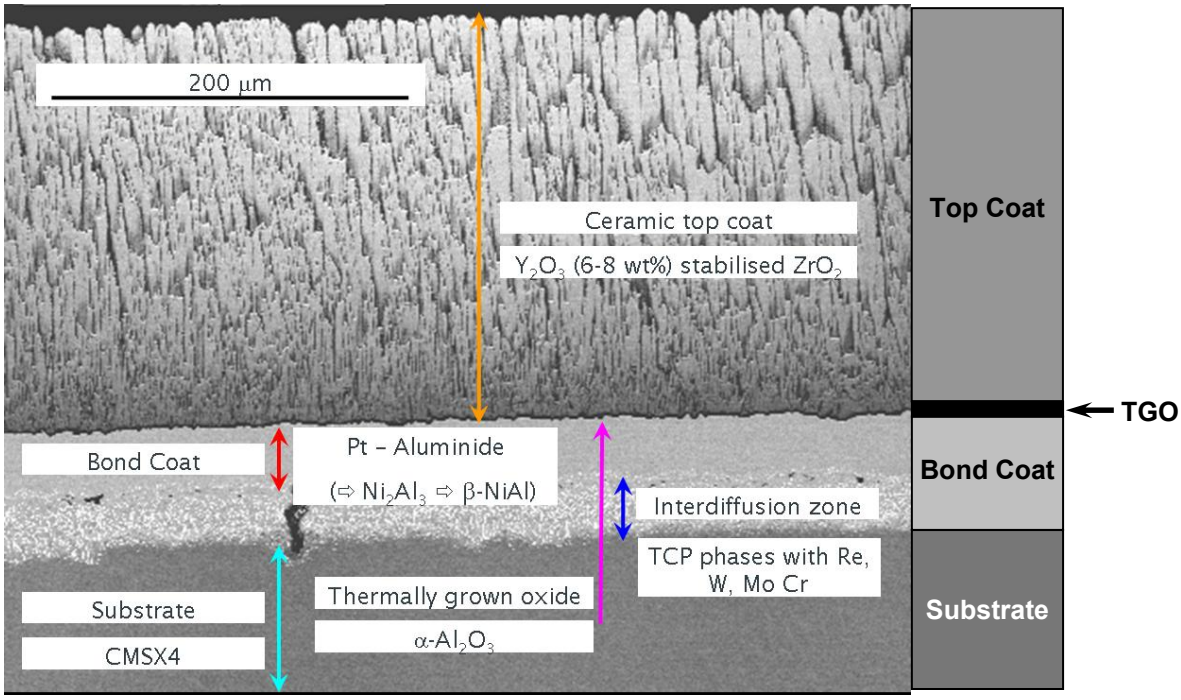

Figure 4 EBPVD Thermal Barrier Coating System (FEG SEM BEI Mode, 30 hours isothermal exposure at 1000°C in air, See Results Section 5.2.1.1).

2.2.2.2 Properties and Microstructure of Thermal Barrier Coating Systems

Having provided an overview of the structure of a TBC System, this section describes each of the component layers in more detail. A consideration that is important across all the layers of a TBC System is that of compatibility. To minimise interfacial stresses between the various layers the coefficients of expansion for each of the materials should be sufficiently similar. In addition the bond strength between each of the layers has to be sufficient to withstand failure during anticipated service conditions. Although for ease of presentation this review is presented in terms of each layer, from a materials engineering perspective, it is necessary to consider the TBC as an integrated materials system rather than simply a thermally insulating material coating on a structural alloy component[67].

2.2.2.2.1 Substrate

Figure 3 summarises the development of blade alloys and their associated manufacturing technology for gas turbine engines from their introduction as wrought alloys, progressing through conventionally cast and directionally solidified to arrive at single crystal alloys. Although Figure 3 represents this progress in terms of manufacturing technology, materials development has occurred concurrently to enable these methods of manufacture and provide improvement in blade performance. Materials development through generations of single crystal blade alloys has continued with Cr content reducing in 2nd generation single crystal alloys onwards and with Re first introduced into this generation of alloys. Cr levels were further reduced in 3rd generation single crystal alloys with increased Re with Ru introduced in 4th generation blade alloys[5]. With no grain boundaries, the absence of grain boundary modifying elements, C, B, in general, is not

surprising. Solid solution strengtheners, Co, Cr, Ta, W and Re are used to provide more creep resistance, with the amount used limited to prevent formation of TCP phases. γ' forming elements, Al, Ti, and Ta, are used to optimise the creep properties of the alloy which typically means a γ' volume fraction of around 70%.

2.2.2.2.2 Bond Coat

By using coatings, substrate and surface related properties can be separated. This permits the BC to be optimised in terms of its environmental protection capability without being constrained by the underlying high strength and creep performance requirements of the underlying substrate[68]. Nicholls goes on to say that; "the primary aim of the coating / surface treatment is to produce a stable slow growing surface oxide capable of providing a barrier between the coating alloy and the environment." The selection of a particular BC depends on the complex interactions between coating, substrate and required protective surface layer forming reactions. Desirable features of a BC are listed in Table 9:

Table 9 Desirable features of an Oxidation / Corrosion Resistant Coating[68].

Coating Property	Requirement	Location		
		Surface	Bulk	Interface
Oxidation / Corrosion Resistance	Low rates of scale formation	X		
	Uniform surface attack	X		
	Thermodynamically stable surface oxide	X		
	Ductile surface scales	X		
	Adherent surface scales	X		
	High concentration of scale forming elements within the coating to act as reserve for scale repair	X	X	
Interface Stability	Low rate of diffusion across interface at operating temperatures			X
	Limited compositional changes across interface			X
	Absence of embrittling phase formation during service			X
Good Adhesion	Matched coating and substrate properties to minimise coating mismatch and stress generation at coating interfaces		X	X
	Optimum surface condition before coating			X
	Growth stresses during coating formation should be minimised		X	X
Mechanical Strength	Coating must withstand all stress (creep, fatigue and impact loading) that is generated at component surface during service		X	
	Well matched thermal expansion coefficients between coating and substrate to minimise thermal stressing and thermal fatigue		X	X

There are two types of bond coat used in TBC systems:

- Overlay coatings
- Aluminide or Chromia diffusion coating

Overlay coatings are often referred to as M-Cr-Al-Y, where M is normally Ni or Co or a combination of the two. They are applied by vapour deposition onto the substrate and do not need diffusion to form. An advantage of M-Cr-Al-Y coatings lies in their ability to be tailored to a particular substrate by altering the amounts of Cr or Al such that mechanical properties are compatible with the substrate. The addition of Y enhances further the corrosion resistance of the coating.

This research considers PtAl coatings, so the literature review will focus on this area. Diffusion coatings are applied using either pack cementation or Chemical Vapour Deposition (CVD) techniques. Aluminide coatings have relatively high Ductile Brittle Transition Temperatures (DBTT) (where DBTT is defined as the temperature for a 1% strain to cause a crack) and as such the mechanical properties are not amenable to extensive modification. For example, low temperature high activity (LTHA) PtAl has a DBTT of >840°C *cf.* high temperature low activity (HTLA) PtAl which has a DBTT of 760°C whereas an overlay coating can have a DBTT as low as 235°C (Co-18Cr-9Al-Y)[68]. The PtAl BC relies on diffusion to produce a stable slow growing oxide (α-alumina (Al_2O_3)) as a protective thermally grown oxide (TGO) layer. The thickness of TGO layer increases with length of exposure at high temperature, which is discussed further in section 2.2.2.2.3. The PtAl BC acts as an Al reservoir for the TGO. Due to diffusion the BC forms two distinct layers: an interdiffusion zone (IDZ) and β-(Ni, Pt) Al rich layer as shown in Figure 4.

2.2.2.2.3 Thermally Grown Oxide

As mentioned previously, the TGO is an important part of the overall TBC system. It is this layer of α-alumina (Al_2O_3) that provides a barrier and effectively slows both the inward diffusion of O_2 and outward diffusion of Al. The growth rate of the TGO is controlled by both inward diffusion of O_2, mostly along grain boundaries towards the TGO-metal interface (internal oxidation) and outward diffusion of Al cations along the boundaries of alumina particles towards the TGO-ceramic interface (external oxidation), as shown schematically in Figure 5[69].

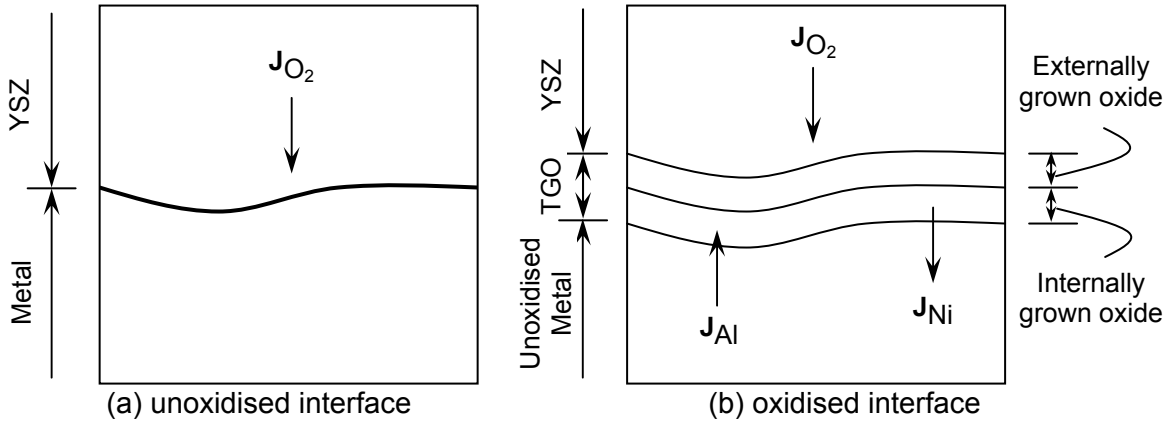

Figure 5 Schematic representation of the internal and external oxidation processes in a ceramic-metal system[69].

The depth of internal oxidation is limited to the depth where the amount of dissolved oxygen becomes too low for the primary aluminium oxide to form, whereas the external oxidation will continue as long as Al cations can diffuse outward through the TGO (and the partial pressure of O_2 at the TGO-ceramic interface is maintained at the required level[69]).

In a study by Spitsberg and More[70] that considered the effects of oxidising the BC prior to topcoat application, they found that if the O_2 partial pressure is very low, the resulting oxide surface has a "saw-toothed" structure with gaps in between the individual α-alumina grains with an average grain size of 0.2μm. At relatively high O_2 partial pressures, much thicker oxide formed which experienced cracking on cooling. At intermediate partial pressures of O_2 they found that the largest grain size of 5μm α-alumina formed which in turn resulted in the most durable TBC system with performance increased by a factor of 2 - 2.5.

2.2.2.2.4 Ceramic Top Coat

The main purpose of the top coat (TC) is to insulate the underlying substrate from high temperatures, as such a material with low thermal conductivity is required. When compared with other materials[71], Zirconia (ZrO_2) exhibits low thermal conductivity, ~2 W/mK, without this being strongly temperature dependent, as is often seen in other ceramics, see Figure 6, for a comparison with other ceramic materials. This low thermal conductivity is achieved by disrupting both the phonon (lattice vibration) and photon (radiation) transport through the material[72].

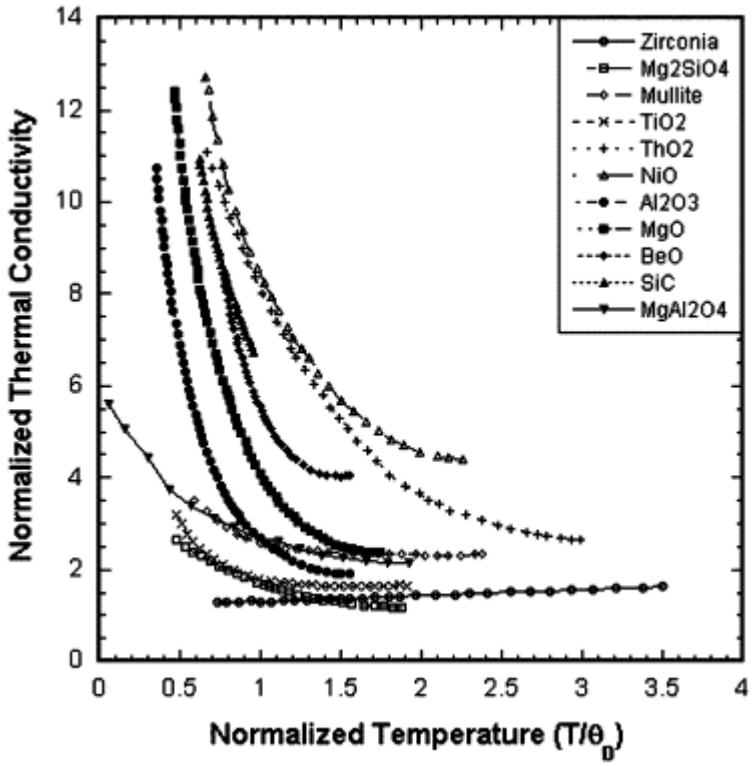

Figure 6 The temperature dependence of the thermal conductivity of a variety of polycrystalline oxides[71], redrawn from data presented by Kingery[73].

Pure Zirconia is not generally used as a TC in modern TBCs as at around 1200°C it exhibits a martensitic phase transformation from its tetragonal to monoclinic crystal structure, this phase transformation causing an increase in volume of around 5%[74]. This volumetric expansion can lead to spalling and earlier failure of the ceramic. The tetragonal phase can be stabilised by adding yttria (Y_2O_3) allowing a tetragonal prime only phase to form which is metastable down to room temperatures as can be seen from the zirconia – yttria phase diagram presented in Figure 7. Around 6% to 8% of yttria is normally used to partially stabilise the zirconia (YPSZ), as this range of concentrations was found to provide the best lifetime performance in terms of cycles to failure in early NASA burner rig tests[75], see Figure 8.

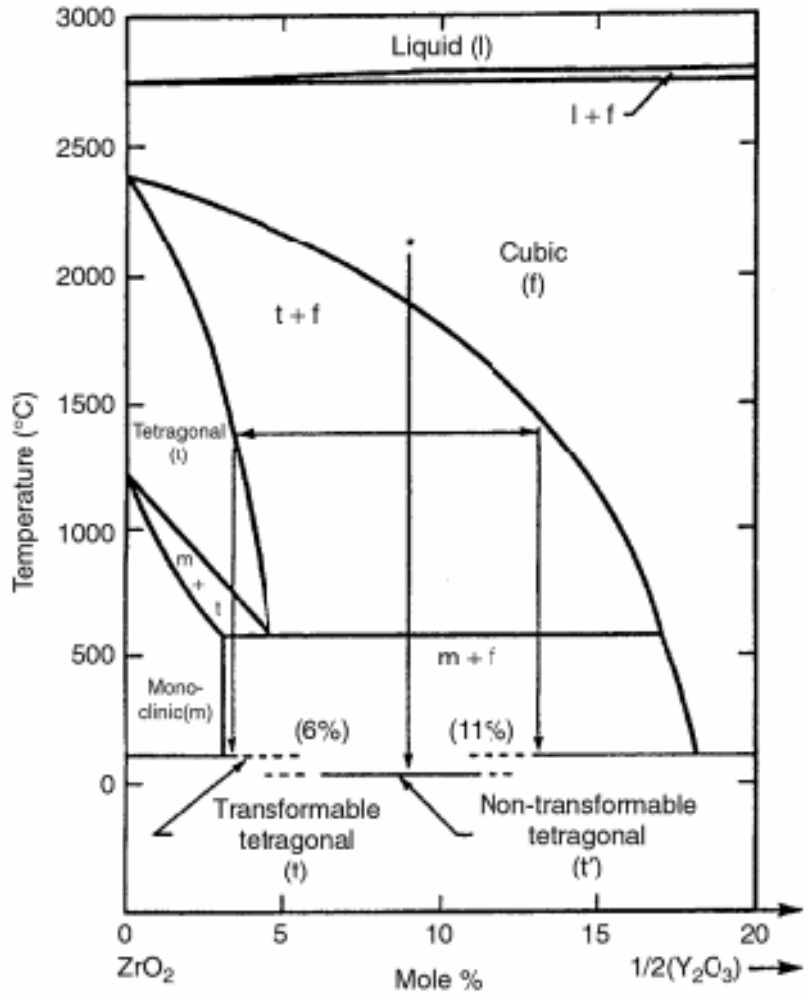

Figure 7 Phase diagram of ZrO_2-Y_2O_3 system (after Scott[76]).

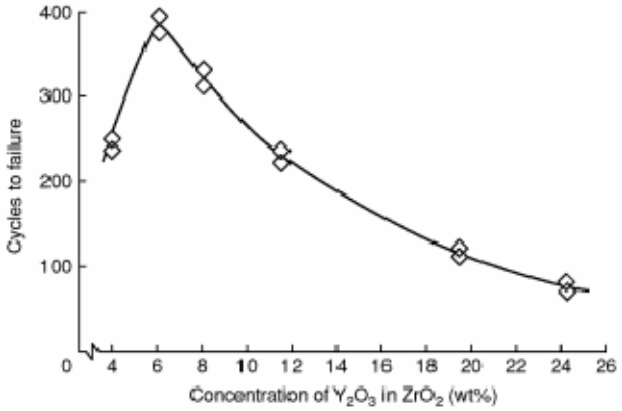

Figure 8 Effect of Concentration of Y_2O_3 in ZrO_2 on lifetime in burner rig tests undertaken by NASA[75].

An air cooled blade insulated with a YPSZ TC applied by EBPVD can lower the temperature at the blade metal to TC interface by 170°C[77], thus providing several potential benefits in the form of materials property retention. These include reduced creep rates or increased creep rupture life, retained strength, with additionally a reduction in temperature providing an order of magnitude reduction in the rate of corrosion[68].

2.2.2.2.5 Deposition of Top Coat

In general the TC is applied either using air plasma spray (APS) or by EBPVD. The particular method used determining the type of microstructure developed, see Figure 9, and hence the particular properties of the TC.

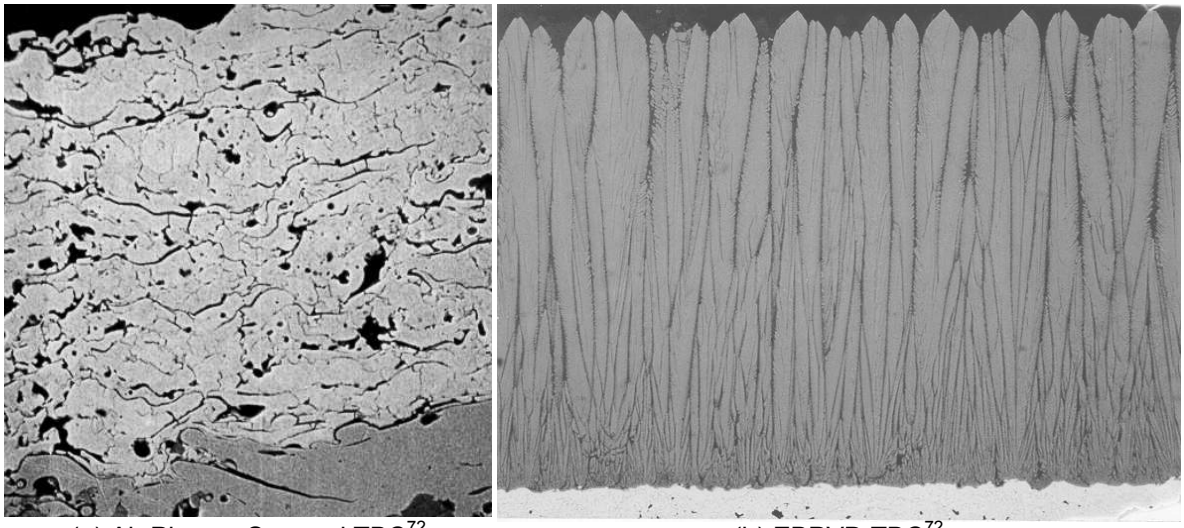

(a) Air Plasma Sprayed TBC[72] (b) EBPVD TBC[72]

Figure 9 Thermal Barrier Coating microstructure applied using (a) Air Plasma Spray and (b) Electron Beam Physical Vapour Deposition.

The structure of TC applied by APS (Figure 9 (a)) shows a microcrack network corresponding to poor contact between the different splats.

The structure of TC applied by EBPVD is columnar, as shown in Figure 9 (b), which provides strain tolerance by providing a measure of compliance, although this is reduced when sintering occurs at higher temperatures for longer exposures. The strain tolerance, excellent surface finish and good erosion resistance provided by EBPVD permits the TC to be used on blades and vanes leading to either reduced requirement for cooling, or increased hot gas temperature. TC applied by APS provides reduced thermal conductivities 0.8 W/mK *cf.* 1.5 to 1.9 W/mK for EBPVD[72] due to the further disruption of phonon and photon transport that the discontinuities of YPSZ perpendicular to the heat flux create. Although similar reductions in the thermal conductivity have been achieved using colouring (dopant atoms) and layered EBPVD (Plasma Assisted Physical Vapour Deposition (PAPVD)) coatings[72].

2.2.3 Integrity of Coatings

The benefits of a TBC system have been discussed in previous sections. One method of maximising efficiency benefits would be to increase the hot gas flow temperatures such that the substrate below the TC was operating at its peak temperature for an appropriate balance between service lifetime and efficiency. Under these conditions, should the TC fail there would be no insulation from these higher gas flow temperatures and the substrate would be exposed to temperatures above its melting point which would

obviously lead to loss of structural properties and failure. For this reason integrity of the TC is paramount during service and understanding its failure modes is essential if an appropriate lifing methodology is to be developed for aero-engine components with a TBC system. This section considers the dominant mechanisms associated with the failure of TBC systems.

The greatest changes in a materials sense occur around the TGO in a TBC system. This is where the transition from a diffusible and matched BC to an oxide layer occurs. Behaviours of the various layers are very different as some of the properties would indicate, (see Table 10). Discrete layers of materials mean that strain compatibility is required if the system is to function as a single "material", yet this requirement for compatibility will most likely lead to stress evolution (assuming delamination does not occur) in an area that is least able to deal with it. Further to this, surfaces are the most likely areas to contain the most significant flaws. These flaws coupled with evolved stresses will mean that crack initiation and growth in or around the interface layers is likely, with in some circumstances the interface providing a pre-determined preferential route for crack growth.

Table 10 Summary of Thermal Barrier Coating System Component Material Properties (after Evans *et al* [78]).

Property	Bond Coat (BC)	Interface BC to TGO	TGO	Top Coat
Young's Modulus (GPa)	200	---	350 – 400	0-100
Coefficient Thermal Expansion (C^{-1} ppm)	13 - 16	---	8 - 9	11 - 13
Toughness or adhesion energy (J m^{-2})	---	Mode I adhesion energy Segregated: 5 – 20 Clean: > 100	Mode I fracture toughness: 20	Delamination toughness: 1 – 100
Yield Strength Room Temp. (MPa)	300 - 900	---	---	---
Growth Stress (GPa)	---	---	0 – 1	---
Misfit Compression (GPa)	---	---	3 - 4	---

The mechanisms of failure of TBC systems can be grouped into three main categories: chemical, thermo-mechanical and foreign object damage (FOD)[78]. A summary of these mechanisms is shown in Figure 10.

Chemical mechanisms leading to failure include Al depletion, Figure 10(a) and Ni diffusion through the TGO Figure 10(b). These lead to the formation of (CoNi)(CrAl)[79] and $NiAl_2O_4$[80] spinels respectively, which can lead to spallation of the top coat due to the brittleness of the spinel and stresses due to the volume changes in its formation or reduction. The failure mechanism due to FOD, Figure 10(c), is compaction of the TC or cracking and removal of the TC with the associated hot area beneath these areas leading to failure[81].

Chemical

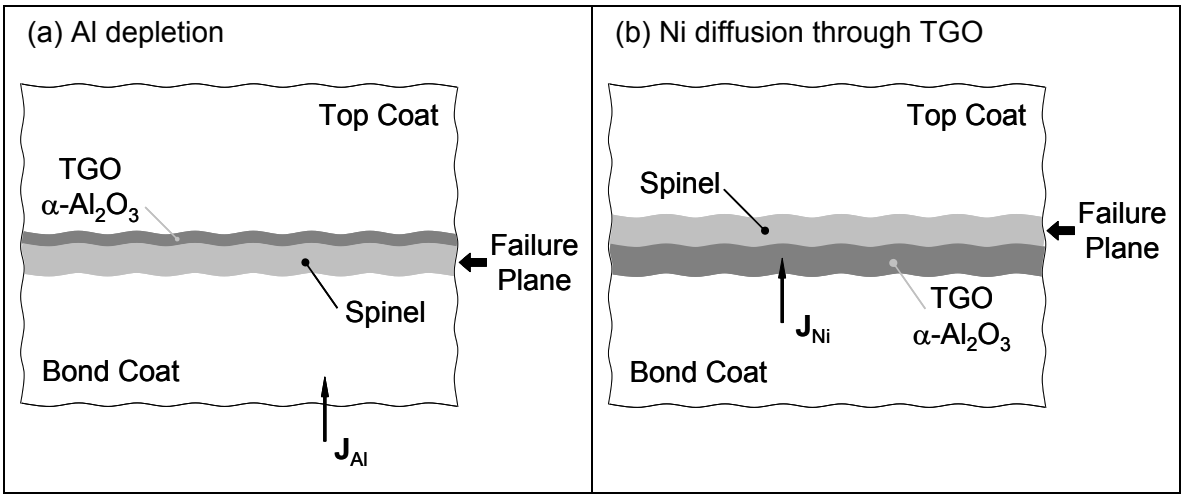

(c) Foreign Object Damage

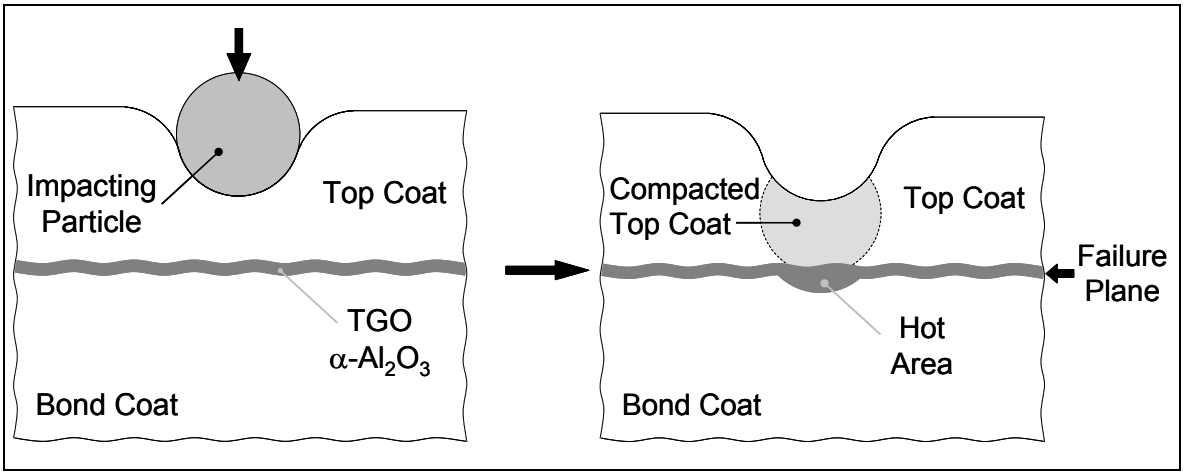

Thermo-mechanical

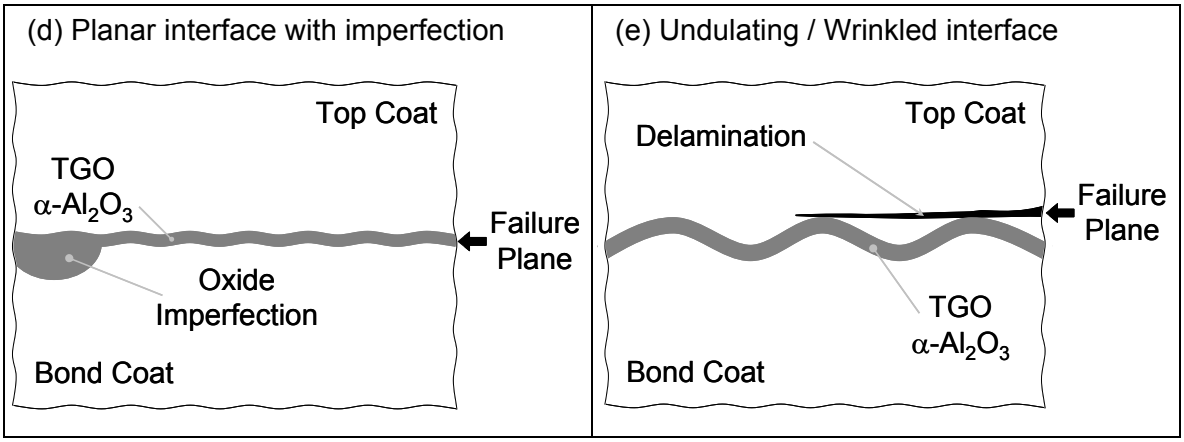

Figure 10 Summary of dominant failure mechanisms for TBC systems (after Evans *et al* [78]).

However, the objectives of this research are to "consider failure mechanisms within TBCs, especially those at a mesoscale and particularly in terms of thermally grown oxide (TGO) layer growth" in order to inform a lifing model for TBC Systems subjected to TMF. These are the conditions shown in Figure 10(d) and (e), both imbedded oxides and undulations or rumpling of the TGO can be seen as imperfections that continue to grow in service and

as such produce localised stresses that lead to crack initiation, propagation and eventual failure by large scale buckling. Although compliant, the TC retains sufficient stiffness to suppress small scale buckling[78]. Growth and rumpling of the TGO layer in relation to stress evolution within the TBC system are considered further in the following sections.

2.2.3.1 Stress Evolution

The Coefficients of Thermal Expansion (CTE) for materials used in TBC systems with an EBPVD TC are provided in Table 10. It can be seen that the CTE for the TGO is lower than that of both the BC and TC. The implications of this thermal mismatch are that due to the large temperature range of operation, significant stresses will arise in each of the layers that form the TBC system, assuming that compatibility in terms of strain is maintained, *i.e.* failure by buckling or delamination does not occur. The nature of these stresses is complex and variable, as the actual values will depend on the operating temperature range and where this is in relation to the temperature at which the BC and TC were applied. Further complication arises from the growth of the TGO, (especially under thermal cyclic conditions), which is continuously forming as the component is used, this sets up further stress states in addition to those seen due to thermal mismatch, the growth of the TGO layer is discussed in the next section.

2.2.3.2 Stresses Arising From Growth of TGO Layer

The growth of the TGO layer is described in section 2.2.2.2.3, and is typically parabolic in nature[78]:

$$h^2 = 2k_p t \qquad \textbf{Equation 4}$$

Where, h, is the thickness of the TGO, t, time and k_p, the parabolic rate constant.

The parabolic relation arising from the diffusion controlled reaction that forms Al_2O_3 as described previously. Stresses in the TGO arise due to volume expansion associated with the formation of Al_2O_3, this volume expansion not only increases the thickness of the TGO, but also the width (in-plane growth) as Al_2O_3 will also be formed at the boundaries of the individual grains that make up the TGO. During operation of a gas turbine engine, the temperature at the TGO, although reduced due to the presence of the thermally insulating TC, will increase the rate of formation of the TGO. During thermal cycling of the engine or at shut down, the whole blade will cool down and as it does so, because the CTE for the TGO is significantly lower than that in the BC (see Table 10), the thinner TGO will effectively be compressed by the BC. Measurements of these stresses have been made using photo-stimulated luminescence spectroscopy (PSLS) by Tolpygo and Clarke[82], with a graph of their results reproduced in Figure 11.

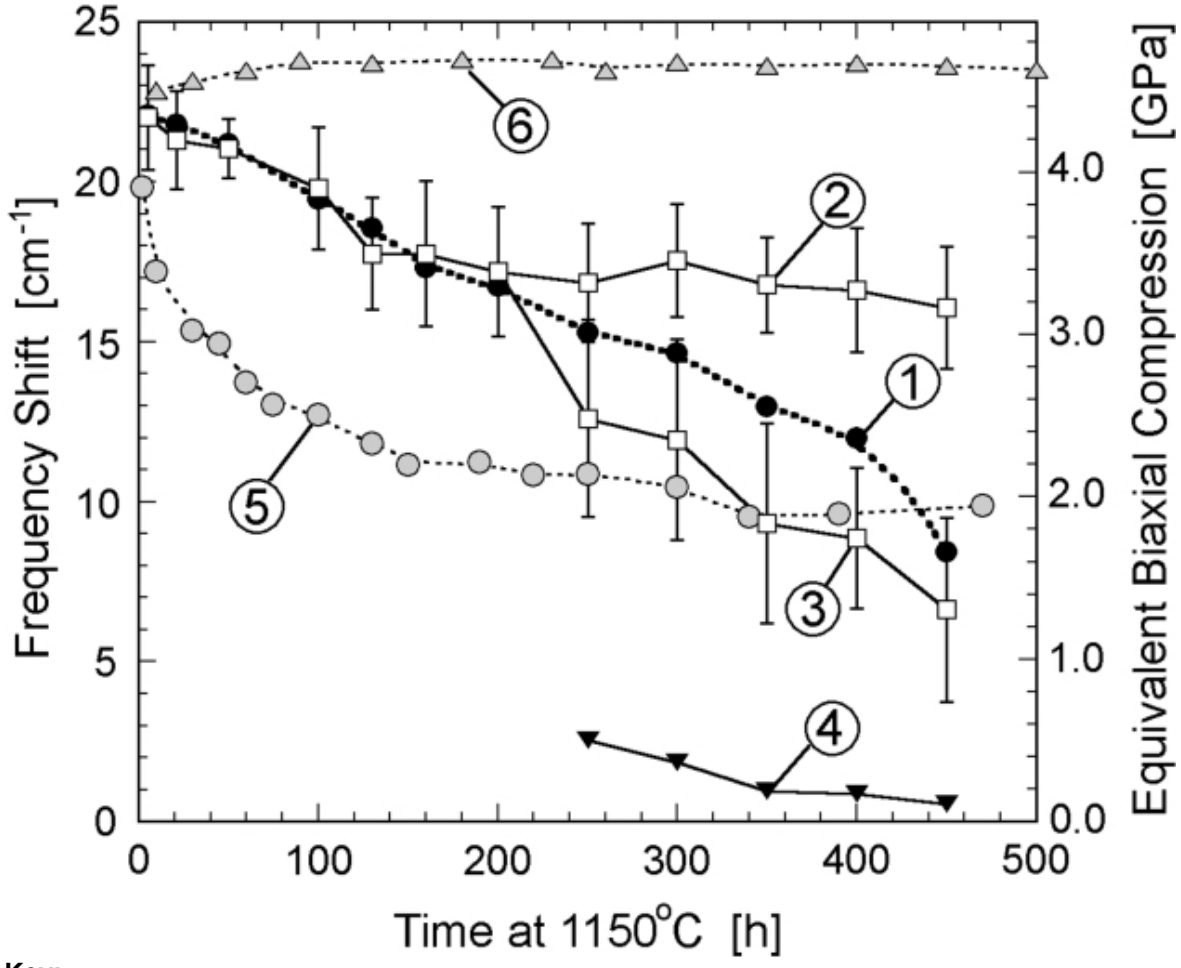

Key:

(1) Average stress underneath 60 μm Top Coat (TC)
(2) Local stress values for the visually intact regions on the same sample
(3) Local stress values for the visually separated regions on the same sample
(4) Stress in fractured or spalled fragments of the TGO
(5) Average stress on similar samples without TC
(6) Average stress on similar samples with 130 μm TC and fully intact TC–TGO interface

Figure 11 Frequency shift of Cr^{3+} luminescence and equivalent biaxial compression in Al_2O_3 scales during cyclic oxidation at 1150°C (1 h cycles)[82].

From Figure 11, it can be seen that the equivalent bi-axial stresses evolved can be as high as -4.6 GPa, for a fully adherent TC-TGO interface with a flat BC, curve (6). With curve (5) showing the equivalent bi-axial stress that exists if stress relaxation due to rumpling and potentially plastic deformation of the BC and / or TGO in the form of creep has occurred.

2.2.3.3 Rumpling of the TGO Layer

Undulations in the BC and subsequently grown TGO exist as part of the deposition process. These undulations increase in amplitude under thermal cycling due to a process known as ratcheting[83]. The effects of these undulations can be seen in the TC in the form of wrinkling in test coupons exposed at 1150°C for 250 and 450 cycles of 1 hour duration, however, in contrast to this under isothermal conditions wrinkles in the TC were not seen

after 500 hours exposure[82].This increase in undulation amplitude induces out of plane tensile strains in the TC which can lead to cracking as shown in Figure 12.

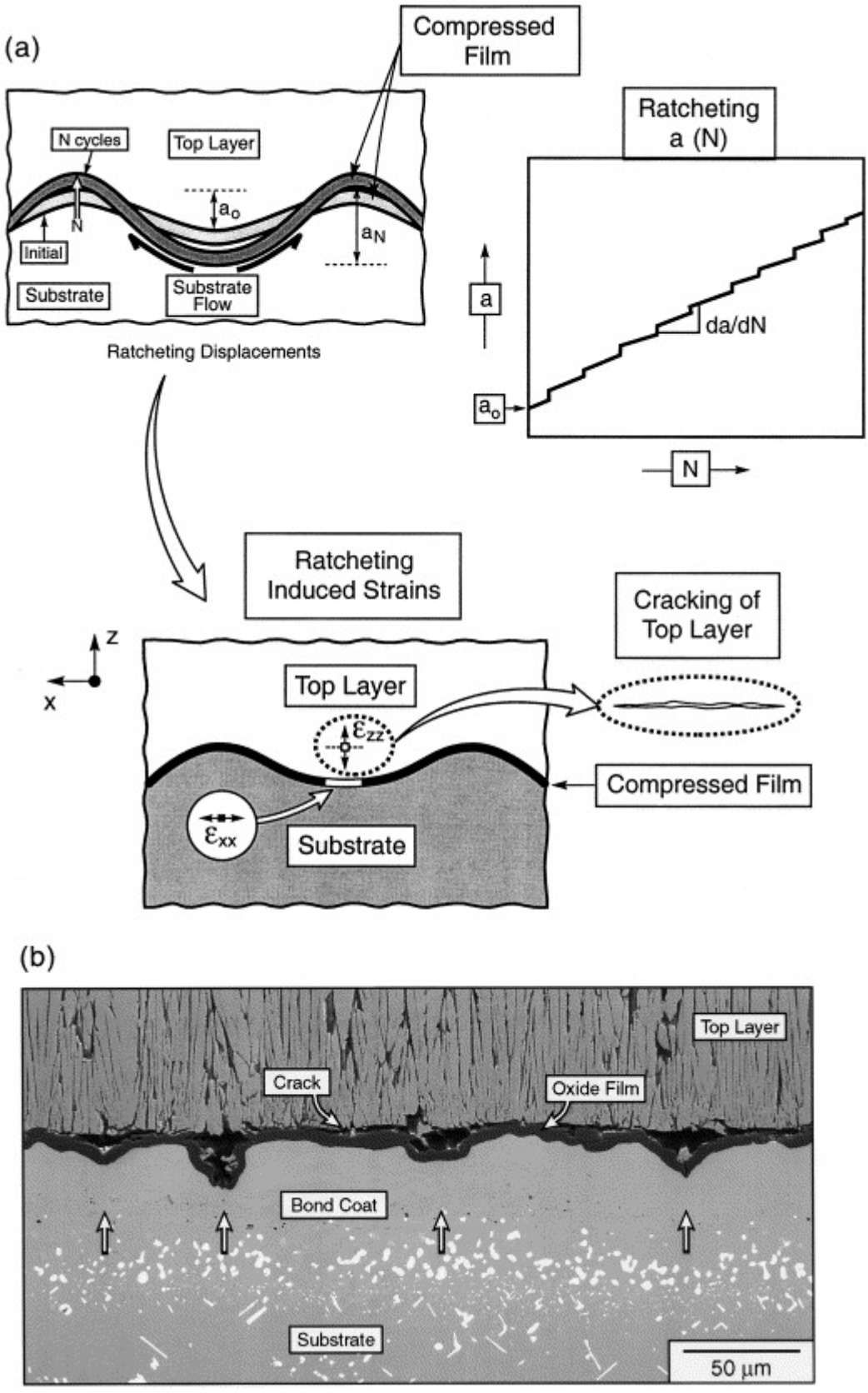

Figure 12 Ratcheting in thin compressed films (a) Schematic representation and (b) Undulations created by ratcheting arrowed[83].

Figure 12 also shows that the TGO and BC remain adherent but have separated from the TC in the arrowed locations. By comparing Figure 11 curve (1) with curve (6), it can be seen that a thicker TC reduces the propensity for ratcheting to occur possibly by mechanically restraining the growth of undulations. Although if ratcheting starts, it will continue with thermal cycling, eventually it will cause local separation of the TGO from the TC as rumpling progresses. Finally, further separation of the TGO from the TC over a large enough area will lead to large scale buckling and TC spallation.

2.2.3.4 Life Time Prediction of Thermal Barrier Coating Systems

In the foregoing sections an overview of TBC systems with a Pt aluminide BC and EBPVD TC has been presented. The complex and dynamic nature of such TBC systems means that life predication is problematic, especially if such predictions are to be used to determine the installed lives of TBC systems used as prime reliant coatings in gas turbine engines.

Early attempts at life prediction tended to focus on a critical TGO thickness as a life determining feature[84]. These only accounted for TGO thickness rather than the evolution of stress and its role in crack formation and propagation. Evans *et al*[78], have produced TC durability (mechanism) maps that plot TC thickness against modulus ratio (in plane / out of plane moduli), see Figure 13, with the implication that there is an optimum TC thickness for a given TC modulus anisotropy[78], although as the TGO grows the "fail safe" region becomes smaller.

As a summary, the following physical issues would need to be addressed in a life prediction method.

1. The growth of the TGO, both in terms of thickness and laterally which would require knowledge of the contributing diffusion processes including any limits on TGO growth and TGO grain size.
2. Details of the temperature and load cycles to which the TBC is subjected.
3. Initial state of the TBC system, including physical dimensions and presence of heterogeneities that could lead to undulations and stress concentrations.
4. The impact of ratcheting on pre-existing undulations.
5. Effects of cyclic plasticity and creep on the evolution or relief of stress and effects of stress concentrations and undulations in both BC and TC, as well as sintering in the TC.
6. Changes in materials properties resulting from for example Al depletion or cation diffusion, other phase changes or due to the ductile brittle transition experienced by the TC on cooling to room temperature.

7. The strains and stresses evolved due to the combined effects of the above under dynamic thermal and load cycling conditions.
8. Determination of relevant failure mechanisms, likely to be crack initiation, short crack growth, crack coalescence, propagation leading to small scale decohesion, decohesion coalescence and finally failure by large scale buckling and spallation.

Many of these are summarised schematically by Clarke and Levi[67] and reproduced in Figure 14.

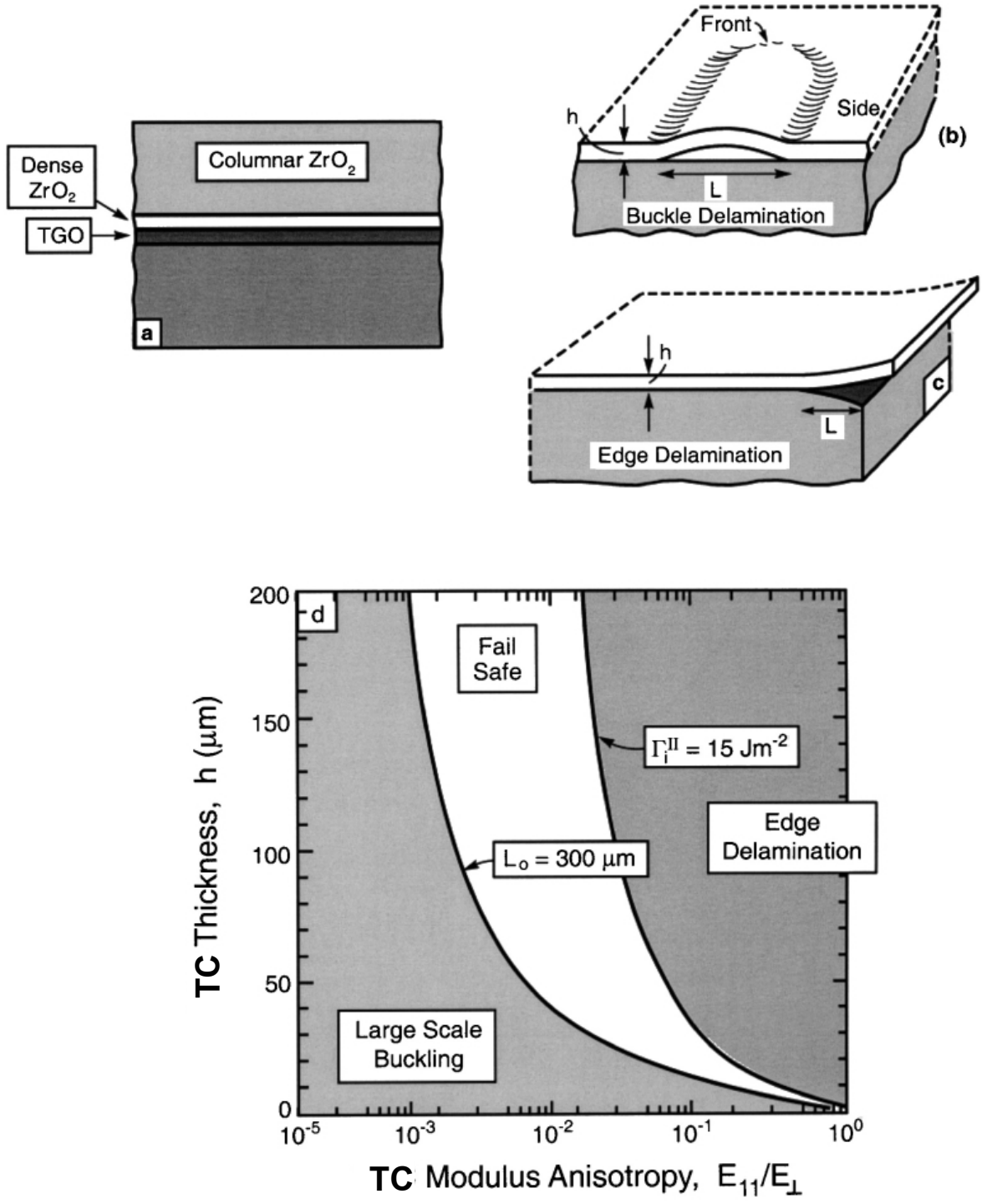

Figure 13 Top Coat durability map indicating the domains for large scale buckling and edge delamination[78].

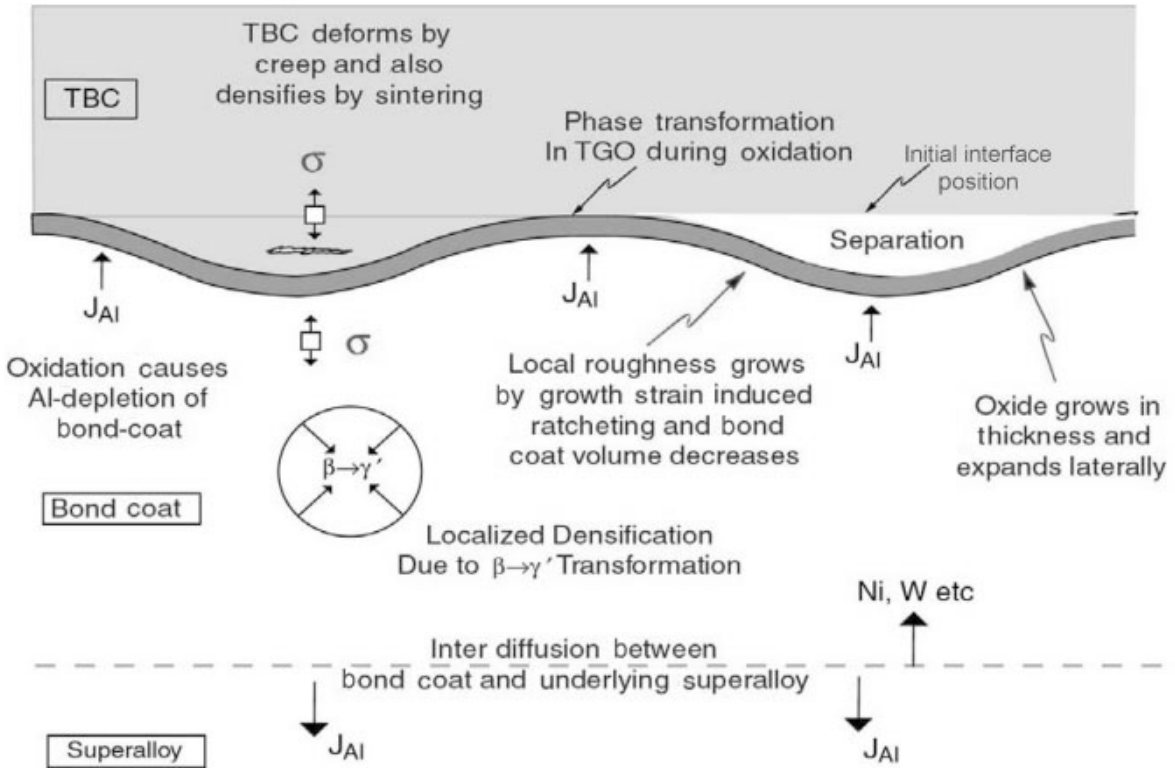

Figure 14 Schematic summary of the concurrent processes occurring in the bondcoat, TGO and Top Coat, during use at high temperatures[67].

2.3 Fatigue

Fatigue in materials is defined as a type of failure that occurs due to fluctuating stresses in the material. In these conditions, it is possible for failure to occur at stresses much lower than the yield stress or ultimate tensile stress of the material which would cause failure under static loading conditions. It is estimated that 90% of metallic materials fail due to fatigue followed by rapid final failure occurring suddenly and without warning[85].

The total fatigue life of a component may be considered to comprise three different stages:

1. **Initiation**

Where small cracks form at a site subject to a high stress concentration caused by defects such as microscopic flaws in a material, these flaws may be associated with persistent slip bands, grain boundaries, twin boundaries, inclusions, microstructural and compositional inhomogeneities[38] or at discontinuities in the component such as presented by a notch.

2. **Short and Long Crack Growth**

Once initiation has occurred, this is followed by the rapid growth of a short crack under the local stress / strain conditions that led to the initiation, the crack grows incrementally with each stress / strain cycle. The short crack may then experience transient acceleration and retardation depending on local crack tip conditions such as closure effects or grain boundary interactions, growth occurs predominantly by single shear and is termed stage I

growth. As the crack length increases, the plastic zone at the crack tip encompasses many grains, long crack growth now occurs via simultaneous or alternating flow along two slip systems and is termed stage II growth[38].

3. **Final Fracture**

Eventually final fracture occurs when the crack reaches a critical size, sufficient either to cause plastic collapse in the uncracked ligament or to achieve the critical stress intensity factor (K) for fast fracture at the maximum load.

The time spent at each stage depends on a range of factors including the environment, material, loading conditions and initial flaw size. The merits of quantifying the life at each stage also depend on the lifing approach appropriate for the component.

2.3.1 Characterisation of Fatigue Behaviour

Fatigue can be described using either a phenomenological continuum approach to characterise the total fatigue life (initiation and propagation lives combined) or by using a defect tolerance approach that describes the fatigue life in terms of the time taken to reach a critical flaw size in the presence of a pre-existing (fatigue) flaw in the material[38]. Total fatigue life can be characterised using either a stress-life or strain-life approach, normally considered to be synonymous with High Cycle Fatigue (HCF) and Low Cycle Fatigue (LCF) respectively, where components subject to HCF are expected to have a life greater than 10^4 to 10^5 cycles and LCF components lower than this[85]. The total fatigue life approaches and a defect tolerant approach in the form of Linear Elastic Fracture Mechanics (LEFM) are discussed further below.

2.3.1.1 High Cycle Fatigue

High Cycle Fatigue (HCF) can be characterised using an empirical stress-life approach to total fatigue life, *i.e.* effectively combining the fatigue cycles that lead to fatigue damage, initiation and propagation to final failure. This approach can be used in components that are designed typically to be unconstrained and experience low amplitude stresses within the elastic limit of the material used such that long lifetimes are achieved[38]. This approach leads to the concept of an “endurance” limit which described the stress amplitude below which the material is expected to have an “infinite” fatigue life, assuming no pre-existing defects are present. This “endurance” limit is shown in the stress / life plot also known as an S-N curve in Figure 15 below. Mild steel and materials that harden by strain-ageing generally exhibit an endurance limit (shown by the solid line). Whereas, other materials including high strength steels and aluminium alloys do not exhibit an “endurance” limit, for these materials the “endurance” limit is often taken to be the stress amplitude at which life times of 10^7 cycles can be achieved.

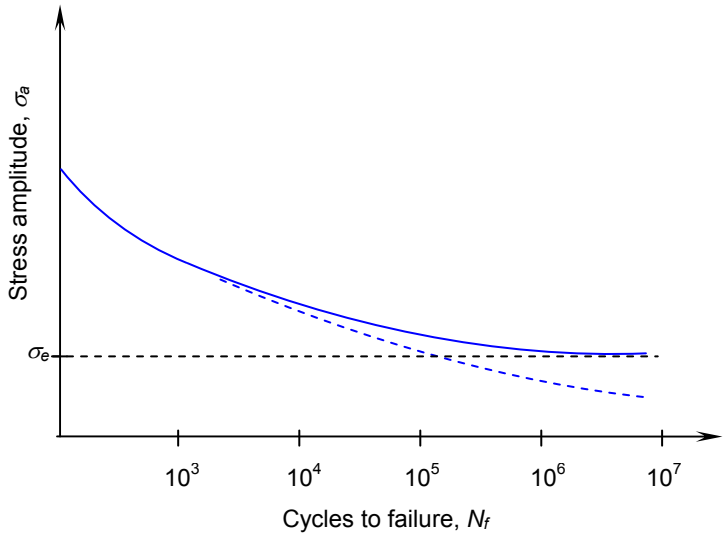

Figure 15 Typical S-N curve.

By replotting Figure 15 on a log-log scale, a linear relationship is often observed. The Basquin[86] relation between stress amplitude, σ_a, for a fully reversed constant amplitude fatigue test and number of load reversals to failure, $2N_f$, is given by Equation 5.

$$\frac{\Delta\sigma}{2} = \sigma_a = \sigma'_f (2N_f)^b \qquad \textbf{Equation 5}$$

Where, σ'_f is the fatigue strength co-efficient and *b* is known as the fatigue strength exponent or Basquin exponent.

2.3.1.2 Low Cycle Fatigue

Unconstrained design for many real engineering components is not practical and many experience localised constraint and plastic flow, especially at stress concentrations. For these situations a strain-life approach to fatigue is more appropriate[38]. Both Coffin[87] and Manson[88] found a linear relationship when the logarithm of plastic strain amplitude, $\Delta\varepsilon_p/2$, was plotted against the logarithm of number of load reversals to failure, $2N_f$, as shown in Equation 6.

$$\frac{\Delta\varepsilon_p}{2} = \varepsilon'_f (2N_f)^c \qquad \textbf{Equation 6}$$

Where, ε'_f is the fatigue ductility co-efficient and *c* is known as the fatigue ductility exponent.

Given that the total strain amplitude, $\Delta\varepsilon/2$, can be expressed in terms of plastic strain amplitude (Equation 9) and elastic strain amplitude, $\Delta\varepsilon_e/2$ as shown at Equation 7.

$$\frac{\Delta\varepsilon}{2} = \frac{\Delta\varepsilon_e}{2} + \frac{\Delta\varepsilon_p}{2} \qquad \textbf{Equation 7}$$

Equation 5, Equation 6 and Equation 7 can be combined to produce an equation for characterising total fatigue life in terms of the elastic and plastic components of total strain, as shown in Equation 8.

$$\frac{\Delta\varepsilon}{2} = \frac{\sigma'_f}{E}(2N_f)^b + \varepsilon'_f(2N_f)^c \qquad \textbf{Equation 8}$$

2.3.1.3 Linear Elastic Fracture Mechanics

Various fracture mechanics approaches have been developed to correlate fatigue crack growth with loading conditions, the most commonly used is the Linear Elastic Fracture Mechanics (LEFM) approach. This correlates the far-field applied stress and flaw length to the local stresses in the region of the crack tip.

The LEFM approach can be illustrated by the classical example of a sharp through thickness crack of length 2a in a thin elastic plate as illustrated in Figure 16.

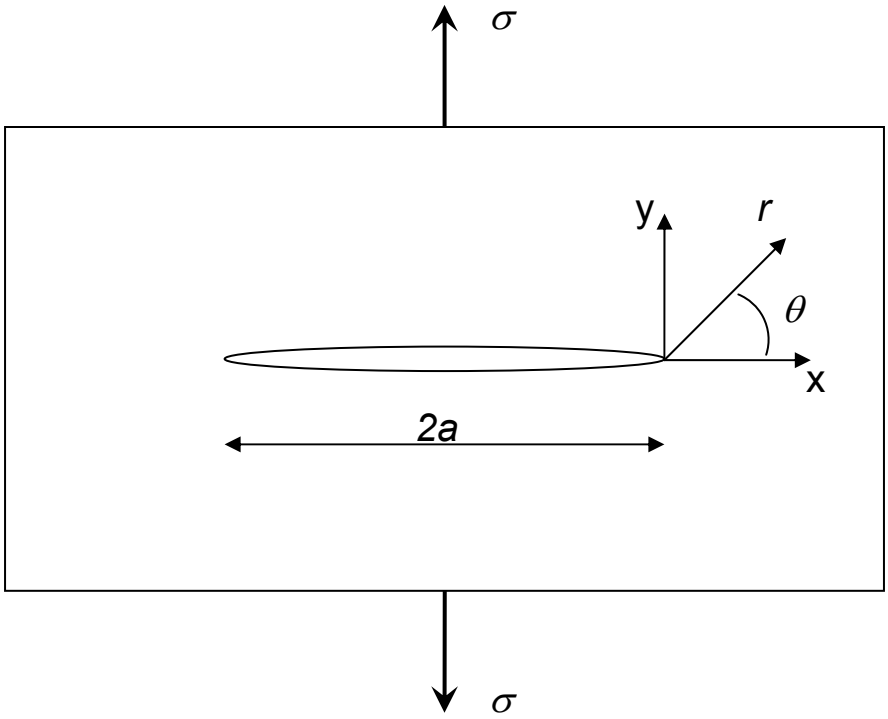

Figure 16 Sharp crack in thin elastic plate normal applied stress, σ.

In LEFM, the local stresses at co-ordinates (r, θ), as defined in Figure 16, close to the crack tip are given, to a first approximation, by:

$$\sigma_{xx} = \sigma\left(\frac{a}{2r}\right)^{\frac{1}{2}}\left[\cos\frac{\theta}{2}\left(1-\sin\frac{\theta}{2}\sin\frac{3\theta}{2}\right)\right] \qquad \textbf{Equation 9}$$

$$\sigma_{yy} = \sigma\left(\frac{a}{2r}\right)^{\frac{1}{2}}\left[\cos\frac{\theta}{2}\left(1+\sin\frac{\theta}{2}\sin\frac{3\theta}{2}\right)\right] \qquad \textbf{Equation 10}$$

$$\sigma_{xy} = \sigma\left(\frac{a}{2r}\right)^{\frac{1}{2}}\left[\sin\frac{\theta}{2}\cos\frac{\theta}{2}\cos\frac{3\theta}{2}\right] \qquad \textbf{Equation 11}$$

Thus the stresses tend to infinity as r tends to zero, and this holds for any sharp crack under load. Although the LEFM approach predicts that stresses tend to infinity as *r* tends to zero, in practice this does not occur due to plastic yielding, i.e. the LEFM approach becomes invalid in a localised area at the crack tip.

The stress intensity factor, *K*, was introduced to describe the elastic stress field near to the crack tip, the general form of the equation relating *K* to the load and flaw size is given by:

$$K = \sigma_f \sqrt{\pi\, a} \quad f\left(\frac{a}{W}\right) \qquad \textbf{Equation 12}$$

where σ_f is the far-field applied stress, *a* is the flaw size and $f\left(\frac{a}{W}\right)$ is the compliance function which allows for differing component geometry and shape. *K* is a useful parameter as it describes the local crack tip stress state and is easily calculated from specimen dimensions and external loading conditions. (It is tabulated for various geometries.) This means that in theory if two cracks with a different geometry have the same value of *K*, then they will have identical local crack tip stress fields.

K is only valid for the characterisation of near crack-tip stress fields when small-scale yielding conditions exist, that is when the yielding at the crack tip is sufficiently small when compared to the constraining material around the plastic zone, which is behaving elastically. If plastic deformation becomes greater, then alternative methods, using other parameters such as the *J*-integral, would have to be used to characterise local loading conditions and resulting fatigue growth.

As the stress intensity factor range, ΔK describes the conditions of the crack tip cyclic stress field, it has been adopted to characterise fatigue crack growth instead of the stress range $\Delta\sigma$. Plots of the crack growth rate per cycle, $\frac{da}{dN}$ versus ΔK (both on a logarithmic scale) generally show a sigmoidal variation with three distinct regimes as shown in Figure 17.

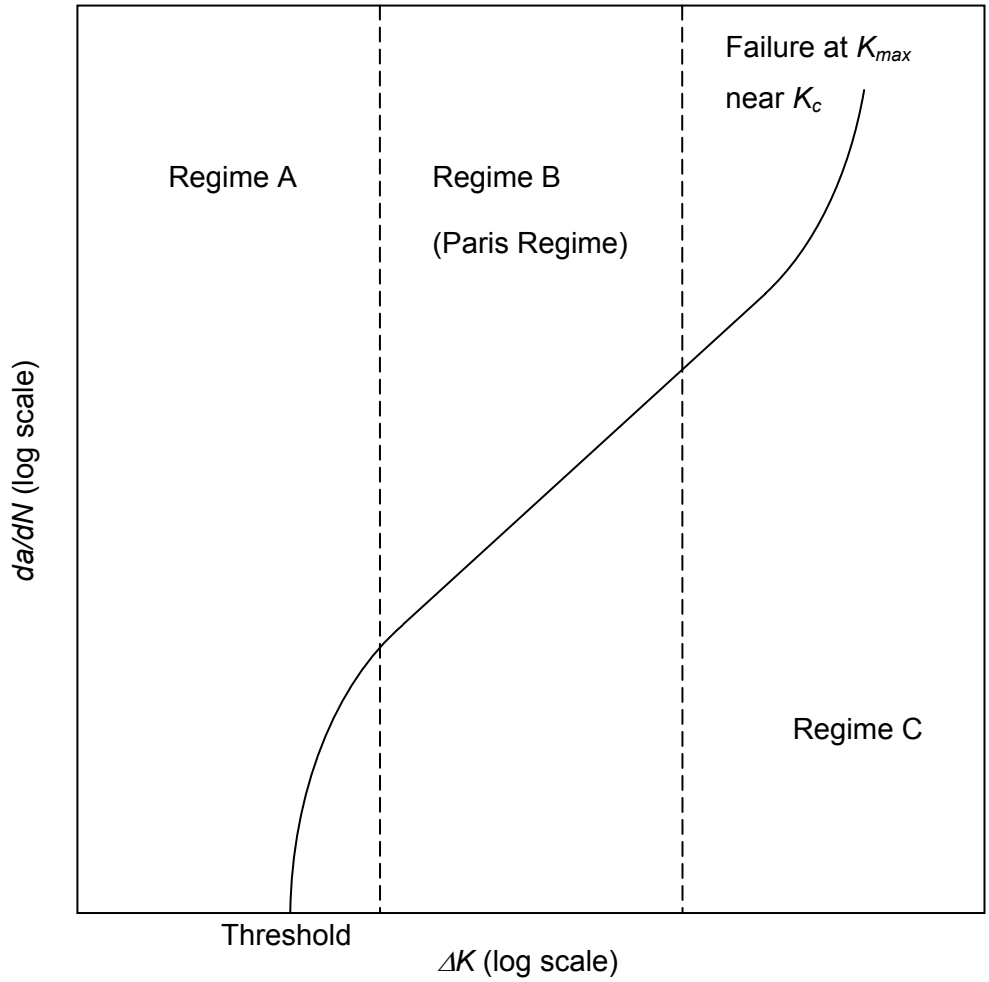

Figure 17 Typical *da/dN* versus *ΔK* curve showing different regimes of fatigue crack propagation.

Regime A is where the average crack growth increment per cycle is smaller than the lattice spacing. Below the threshold stress intensity factor range, ΔK_{th} cracks remain either dormant or grow at undetectable rates[38]. In this region crack closure levels are high and the effects of microstructural, load ratio and environmental factors is large. Regime B is known as the Paris regime as it exhibits a linear variation of $\log \frac{da}{dN}$ with $\log \Delta K$ described by the Paris equation:

$$\frac{da}{dN} = C\Delta K^{m} \qquad \textbf{Equation 13}$$

where *C* and *m* are materials constants determined experimentally. High ΔK values in regime *C* cause crack growth rates to accelerate rapidly due to increasing contributions from static failure modes quickly leading to failure.

2.3.2 Crack Closure

Crack closure is the term used to describe load transfer in the wake of a growing crack, it may be induced by plasticity ahead of the crack tip, Plasticity Induced Crack Closure, (PICC), surface roughness, Roughness Induced Crack Closure, (RICC) or formation of

oxide, Oxide Induced Crack Closure, (OICC). These mechanisms effectively reduce the ΔK experienced by the crack tip by increasing the minimum stress intensity at which the crack closes.

2.3.3 Initiation and Short Crack Growth Behaviour

The initiation of fatigue cracks and short crack growth behaviour is important with respect to turbine discs as most of their operational life is spent within these regimes[89,90,91,92]. High relative mass and rotational speeds lead to high stresses in turbine discs and limit critical crack lengths to relatively small sizes beyond which fast fracture will occur, the majority of the fatigue life of a disc is thus spent in the short crack growth regime[93,94]. With the drive to increase strengths of disc alloys, the stress to which such components are subjected continues to increase. The implications of this are that the critical flaw size reduces further, and the use of long crack data will lead to increasingly non-conservative lifetime calculations[95]. Microstructure and environment have been shown to play an important role in crack initiation and short crack growth, especially for cracks with a similar size to the scale of the characteristic microstructural features[90,96]. The precise definition of a short crack varies between authors, but in general it is considered to be the length below which individual effects of microstructural features are important rather than their average effects, *i.e.* where non-continuum mechanics are operating. Suresh[38] defines short cracks as follows:

1. Microstructurally small flaws – where the fatigue crack size is comparable to the scale of the characteristic microstructural dimension, *e.g.* the grain size for monolithic materials or the interparticle spacing for particulate –reinforced composites.
2. Mechanically small flaws – cracks are either engulfed by the plastic strain field of a notch or for which the near tip plasticity is comparable to the crack size.
3. Physically small – although physically larger than the characteristic microstructure and scale of local plasticity these cracks are typically smaller than 1 to 2 mm, and may exhibit reduced closure.
4. Chemically small – the crack propagation rate below a certain size of crack is dependent upon environmental stress corrosion fatigue effects whereas nominally it could be analysed by linear elastic fracture mechanics.

2.3.3.1 Crack Initiation in Nickel-Base Superalloys

Naturally occurring cracks will occur at the least resistant points within the microstructure of a material, *i.e.* at defects or slip bands in favourably orientated grains[97]. In such cases the number of cycles to initiate a crack is reduced[92,98]. A variety of initiation mechanisms operate in nickel base superalloys and depend strongly on various factors including

temperature, microstructure and environment. At room temperature fatigue crack initiation can occur from slip bands[96,99,100], twin boundaries[96,99,100], grain boundaries[98,100,101], carbides[102,103,104] due to cracking at inclusions and precipitates[90,100,105], pores[110,] or at other defects[103,104,105]. At higher temperatures crack initiation has been reported as occurring from slip bands[94,102] , grain boundaries[106,107], twin boundaries[108], inclusions[64,104,108,109] and pores[64,110].

Stage I cracking along persistent slip bands promoted by heterogeneous slip is the predominant mechanism for fatigue crack initiation at room or relatively low temperatures[96,102,]. Such cracks will initiate at approximately 45° to the principal stress axis, *i.e.* in the crystallographic plane most favourably orientated for experiencing the maximum resolved shear stress. Initiation at slip bands is more extensive in microstructures with a coarse grain and fine coherent γ' precipitates as both of these characteristics give rise to heterogeneous slip[103,111], whereas finer grained microstructures with coarse coherent γ' show little tendency to initiate fatigue cracks in this manner. Larger grains imply a longer slip band which will accumulate a larger amount of irreversible slip and hence accrue more dislocation damage making crack initiation more likely[94]. Slip in these larger grains is further promoted by the lower constraint that is offered by them[112]. Whereas finer grains are known to promote homogeneity by slip dispersion at grain boundaries reducing the stress concentrations that may be present due to an impinging slip band[100], unless the finer grains are favourably aligned, in effect becoming a large grain[99].

It is also possible for cracks to initiate at grain boundaries or annealing twins due to an impinging slip band which may cause local decohesion leading to crack initiation[90,98]. Crack initiation at inclusions or precipitates have also been reported[98,100], these generally arise from the differing thermal expansion coefficients or strengths of the inclusions or precipitates compared with the matrix material leading to the generation of local tessellated stress[113] fields during cooling, although crack initiation may also be caused by a slip band impinging onto an inclusion[112]. Larger inclusions tend to be more susceptible to decohesion or cracking[98] the exact mechanism depending on the relative strengths of the inclusion and the matrix interface with the inclusion.

Crack initiation may also occur at carbides, due to oxidation at higher temperatures[103,109], cracking[102] or due to the impingement of slip bands[103] leading to carbide / matrix interface decohesion.

In the NASA alloy LSHR, heat treatment, temperature and strain range also had an effect on initiation due to slip, in super-solvus heat treated material noticeable slip offsets occurring in relatively large grains at the surface at 426°C, whereas at 704°C this only occurred at strain ranges ($\Delta\varepsilon$) of 0.6 to 0.8, with slip at $\Delta\varepsilon$ = 0.6 only occurring in internal

grains[64]. At room temperature Goto and Knowles[90] found cracking of TiN particles in U720Li during the early stages of cyclic testing were responsible for later crack initiation. Other studies of U720Li and U720Li LG by Pang and Reed found that porosity was the dominant high temperature initiation mechanism[62] and the main initiation mechanism at room temperature for etched specimens, although for U720Li, this was more balanced with initiation at slip bands also occurring in polished specimens[110]. A limited amount of RR1000 testing was carried out by the same study[110] (two specimens at both room and elevated temperatures), in all cases cracks were found to initiate from porosity. For N18, cracking from inclusions is stated as being of most concern[49]. In work by Guedou *et al*[114] on N18, during strain controlled LCF tests a large scatter in service life was reported, with crack initiation occurring from defects such as pores or ceramic inclusions, with surface defects being the most detrimental at high loading levels for 70% of crack initiation sites. The majority (85%) of surface initiations occurring around pores in the material indicating that pores are statistically more numerous than ceramic inclusions. This was attributed to the improved powder cleanliness and high solutioning temperature which causes the coarsening of argon bubbles trapped in the powder particles during atomisation. At lower loading levels large inclusions are the primary cause of crack initiation.

2.3.3.2 Short Crack Growth

The short crack growth regime is the crack growth period between crack initiation and the long crack growth regime. Suresh[38] states that to apply LEFM to a crack, then its growth regime must conform to the concept of similitude, *i.e.* continuum mechanics are operating. In the short crack growth regime, due to the size of the crack, it is susceptible to the individual and combined effects of: microstructural features in the crack path[91, 98], the absence of crack closure[95, 115,116] and chemical attack[98]. This means that the crack does not experience larger scale averaging effects and as such non-continuum mechanics operate in this regime, it is therefore not appropriate to use traditional LEFM to characterise short crack growth[38].

Typically short crack growth is characterised by:

1. Considerable scatter and fluctuations in the growth data[117].
2. For the same ΔK, on average higher growth rates than that experienced in the long crack growth regimes[90,95,98,102].
3. Short cracks grow below the ΔK_{th} measured for long crack growth[95,98,102].

Stage I crack propagation generally occurs by single shear in the direction of the primary slip system and occurs when the crack and associated plastic deformation zone are less than a few grain diameters in length[38]. A combination of this and the concentration of deformation into intense slip bands leads to short cracks growing in a highly

crystallographic manner, often parallel to the {111} planes[98]. This single slip mechanism results in a zigzag crack path and a predominantly faceted fracture surface.

The scatter and fluctuations associated with short crack growth data is mostly due to the interactions between the plastic zone surrounding the crack tip and microstructural features[96,118], *i.e.* crack propagation can be decelerated, arrested or its path may change direction when the plastic zone encounters a microstructural barrier[94,112], such as a grain boundary, precipitate / inclusion or twin boundary. Grain boundaries can cause crack arrest or deceleration by acting as a hard barrier[100] or because of the misorientation of crystallographic planes between neighbouring grains[100,118], leading to alteration of the crack path, the greater this misorientation, the higher the deceleration of the crack[98,118]. The lower the angle of misorientation, the easier slip can traverse the grain boundary[99]. Indeed no crack growth deceleration has been observed at the grain boundary between two grains separated by a low angle grain boundary, in this case the grain system behaved as one equivalent large grain[99]. When a short crack encounters an inclusion or precipitate, temporary crack arrests have been observed. This has been noted by Goto and Knowles[90], who observed a sudden decrease in short crack propagation rates when the crack encountered primary γ' precipitates. Changes in short crack growth direction arising from orientation changes at annealing twins or from non-parallel slip planes cause retardation of short crack growth rates[100,102] and are considered as soft barriers to short crack growth[100].

The high mean short crack growth rates as compared with long crack growth rate data have been associated with the lack of crack closure effects in short crack growth studies[60,98,119]. This effect is exacerbated in short cracks because of the short wake behind the crack and the typically high applied stresses that are used in short crack growth studies. The high applied stresses result in extensive monotonic plasticity and crack growth at an effectively high value of R[35,95]. With regard to the crack wake, there is a critical distance typically ranging from 200 μm to 20 μm behind the crack tip below which RICC does not occur[95], although this can be specific to a particular alloy system.

2.3.3.3 Convergence with Long Crack Behaviour

As the length of the short crack increases more grains are encountered and as compatibility between the randomly orientated grains must be maintained, deformation within the plastic zone becomes constrained and small crack growth rates are expected to merge with long crack growth rates[120]. The convergence of short and long crack growth behaviour is thought to occur when the short crack begins to sample the material as a continuum[102]. A general indication that this has occurred is the change in crack growth rate during the transition from stage I to stage II crack growth[96] which is also related to the transition from facetted to striated growth[95]. The convergence of the rates of short and

long crack growth in disc alloys has been observed to occur when the crack length has typically spanned eight to ten microstructural elements[96,100,102]. Other studies have noted convergence of short and long crack growth data when the crack tip plastic zone size exceeds the grain size of the materials[35,120]. These are essentially the same conditions, as the crack tip plastic zone size often exceeds the grain size when the crack has grown across approximately eight to ten grains[102]. Although in one study on ASTROLOY®, convergence of the short and long crack growth data occurred at approximately 20 grain diameters[95].

2.3.3.4 Effect of Temperature

With increasing temperature, the time required for a crack to initiate may be reduced or increased depending on the exact mechanisms in operation[104,121]. As slip becomes more homogeneous with increasing temperature slip band cracking may be supressed[121], with a further rise in temperature, oxidation becomes more significant which may reduce crack initiation resistance[104]. Higher short crack growth rates have been observed at elevated temperatures when compared with room temperature, this increased rate is usually associated with a change in slip character indicated by the fracture surface changing from a highly faceted to a flatter surface[102].

2.3.3.5 Environmental Effects

Increased crack initiation periods and reduced short crack growth rates have been observed during vacuum tests, especially at elevated temperatures[32,122]. Oxygen penetration along persistent slip bands has been cited to enhance stage I crack initiation and stage II crack growth and penetration of oxygen along grain boundaries was associated with increased intergranular crack growth rates in Rene 80, MAR-M-200, IN738 and IN718[32].

2.3.4 Threshold and Near Threshold Long Crack Growth

The threshold and near threshold crack growth regime for a long crack is represented in Figure 17 by regime A, this is outside of the Paris regime. Regime A shows the response of a long crack to a reducing ΔK, *i.e.* the long crack is pre-existing, and the applied load is reduced to determine the threshold behaviour. In this regime, the crack either propagates slowly or there is insufficient driving force for the crack to propagate at all. The value of ΔK at which the crack stops growing or where its growth rate is imperceptible is termed the threshold value and represented by ΔK_{th}. Crack growth in this regime occurs typically by crystallographic stage I type growth at room temperature, facetted fracture surfaces are exhibited and crack growth is sensitive to microstructure, temperature and environmental effects. As the crack length is much greater than the plastic zone size around the crack tip and the microstructural element size, the assumptions used in LEFM are valid and ΔK

can be used to characterise crack growth in this regime. A transition from structure sensitive near threshold crack growth to structure insensitive long crack growth occurs when the plastic zone size around the crack tip exceeds the grain size of the material[11,33], beyond this transition a much flatter structure is observed[11].

2.3.4.1 Effect of Load Ratio

In fine grain material, ΔK_{th} and crack growth rates appear to be independent of load ratio, however in larger grain material increasing R tends to lower the value of ΔK_{th} and increases crack growth rates[123].

2.3.4.2 Effect of Temperature

Studies comparing fine and coarse grain materials have reported that as temperature increases ΔK_{th} has reduced for coarse grained materials, yet remained substantially unchanged for fine grained materials[123,134]. This has been ascribed to the coarse grained material's propensity to RICC. As the temperature increases, coarser grained materials exhibit a flatter fracture surface, albeit with some crystallographic features, leading to reduced RICC[123,134]. Whereas for the fine grain material little change was apparent in the fracture surface explaining why the value of ΔK_{th} remains unchanged[123,134]. Conflicting results for increasing ΔK_{th} attributed to OICC at higher temperatures due to increased oxidation rates at these higher temperatures have also been reported[124,125]. Initially it appears that the tendency is for ΔK_{th} to reduce due to the reduction in RICC, but as oxidation processes become more influential and the amount of oxide increases, OICC leads to an increase in the value of ΔK_{th}.

2.3.4.3 Environmental Effects

Higher ΔK_{th} has been observed in room temperature studies on Nimonic AP1 carried out under vacuum conditions[126], this was attributed to crack face rewelding under vacuum conditions, further reducing the ΔK seen by the crack tip more so than that attributed to crack closure effects as the crack is effectively being held closed by the welded material until the weld is broken. This phenomenon does not occur in air due to the formation of a protective Cr_2O_3 layer on the crack faces as the crack grows.

Higher ΔK_{th} was also found during a study on U720 carried out at room temperature under vacuum conditions by Loo-Morrey and Reed[127]. When compared with tests carried out under air conditions, stage I cracking was found to be enhanced and the fracture surface was much rougher due to the increased reversibility of slip under vacuum conditions. There was limited evidence of fretting or rewelding of the crack, so the increased ΔK_{th} was not a result of RICC. The higher ΔK_{th} under vacuum conditions was attributed to extrinsic

shielding due to crack branching and the formation of secondary cracks resulting in the crack tip experiencing an effectively reduced ΔK.

2.3.5 Long Cracks and their Growth Behaviour

A short crack has been defined in section 2.3.3. A long crack is therefore one whose length is large compared with the size of the microstructural elements or plastic zone. Due to the length of the crack, in general the effects of the microstructure can be averaged and models using continuum mechanics assumptions applied. In discussion, long crack growth behaviour is usually considered to be the crack growth regime represented by region B in Figure 17 which can be described by the Paris equation (Equation 13). Long crack growth does occur outside of this regime, but in these cases its description normally contains a caveat in terms of the applicability of the Paris law *e.g.* threshold behaviour to represent growth in Figure 17 region A.

Fatigue crack growth is a complex process involving the concomitant and sometimes interrelated involvement of a number of parameters, these include; ΔK, R, temperature, frequency, hold time and environment. As a generalisation, crack growth regimes can be categorised as either cycle-dependent or time-dependent. Typically low temperatures, high loading frequencies and an inert-atmosphere lead to cycle-dependent crack growth. Whereas high temperatures, low loading frequencies and deleterious environment generally lead to time-dependent crack growth[128,129].

In the cycle-dependent regime, crack growth rate per cycle, $\frac{da}{dN}$, is dependent principally on the characteristics of the loading cycle, *i.e.* ΔK and load ratio, R, which is defined as:

$$R = \frac{\sigma_{min}}{\sigma_{max}} = \frac{K_{min}}{K_{max}} \qquad \textbf{Equation 14}$$

Temperature has an indirect effect on cycle-dependent crack growth via its effect on the yield strength and modulus of the material, as can be seen from the expression for crack tip opening displacement (CTOD), δ[130]:

$$\delta = \frac{K_I^2}{\sigma_{YS} E} \qquad \textbf{Equation 15}$$

Where for a particular stress intensity factor, K, a reduction in yield stress, σ_{YS}, and / or Young's Modulus, E, will lead to a larger crack opening displacement, δ, and hence faster crack growth. The behaviour of an individual alloy will be dependent upon the particular behaviour of σ_{YS} and E at elevated temperatures.

Crack propagation in the cycle-dependent regime is typically characterised by a transgranular crack path[11] often with evidence of striations. The remaining parameters,

frequency, hold time and environment, are essentially related to the time-related regime and have little effect on the cycle-dependent crack growth processes.

Creep and environment factors are the main processes by which time-dependent fatigue occurs in nickel-base superalloys. Creep is defined as the time dependent deformation of a material under load at elevated temperature, its effects increasing with higher temperatures and stresses. Environmental effects include oxidation and corrosion, which are time dependent processes due to the chemical reactions involved and access paths to reactants. As such both are thermally activated and lead to temperature and time dependent crack growth. Crack growth typically occurs in an intergranular manner in the time-dependent regime[124].

There is typically no sudden changeover from cycle-dependent to time-dependent crack growth, there are therefore intermediate frequencies and temperatures at which crack growth occurs due to creep-fatigue-environmental effects and a mix of both transgranular and intergranular crack propagation occur. This intermediate regime is termed the mixed mode regime.

The separate effects attributed to fatigue, creep and environment in fatigue crack propagation can be elucidated by carrying out testing under different conditions. Testing in vacuum as opposed to air will permit the effects of environment to be excluded thus leaving either pure fatigue or creep-fatigue responsible for crack propagation. High frequency testing in a vacuum will permit the fatigue performance of the material to be assessed in the absence of creep and environmental effects, while the application of longer hold times at maximum load will permit the creep-fatigue performance to be determined. Care must be used in the application of such data to in service situations as the interactions between creep, environment and fatigue are complex and a straightforward superposition of the performance in each regime is unlikely to provide the correct life prediction. Characterisation of in-service fatigue crack growth is difficult and complex, the exact combination of load, environment and creep will affect the crack propagation. In some cases the individual parameters may oppose each other leading to retardation or possibly arrest in crack growth, whilst in others their effects may be augmented leading to crack growth acceleration[128].

As creep is an inelastic deformation process, any parameter defined using LEFM such as ΔK is not going to be valid when the process is active. In attempts to characterise creep-fatigue, models have been devised that separate crack growth rates into their separate fatigue and creep aspects or portioning the crack driving forces into elastic and inelastic components. The most basic model is a straightforward summation of the components of crack propagation rates due to fatigue and those due to creep[129,131] *i.e.*

$$\frac{da}{dN} = \left(\frac{da}{dN}\right)_c + \left(\frac{da}{dN}\right)_f$$ **Equation 16**

The suffixes *c* and *f* are used to represent the crack growth rates due to creep and fatigue respectively. This model only works well when the assumptions it is based on are valid, *i.e.* when there is no interaction between the creep and fatigue processes occurring in the material, as is reflected by the limited amount of correlation to experimental results[129].

When interaction between the fatigue and creep processes occur at the crack tip differing responses in the fatigue crack growth rate may be seen. Creep crack growth may accelerate crack growth rates whereas stress relaxation may result in a reduction in driving force and a retardation of crack growth rate. However, in general, the combination of creep and fatigue will tend to increase crack growth rate through the material and a model based on simple superposition will tend to underestimate fatigue crack growth rates. In addition, other effects such as RICC[129], OICC or those due to synergistic interactions are not considered in this simple model.

Better correlation with experimental data has been obtained by Gayda *et al*[132] using a time integration approach, taking the general form of:

$$\frac{da}{dN} = \left(\frac{da}{dN}\right)_f + \int\left(\frac{da}{dt}\right)dt$$ **Equation 17**

The crack growth rates due to pure fatigue in the absence of creep and environmental effects are represented by the suffix, *f*, values for this can be found experimentally by high frequency testing in a vacuum. The contribution to crack growth made by the time dependent mechanisms is represented by the integral term, to calculate this, data from tests representative of similar creep-fatigue conditions are required. Good correlation with experimental data has been obtained when the effects of environment are not significant[132].

2.3.5.1 Effect of Load Ratio

For a given temperature, increasing *R* generally lowers the value of ΔK_{th} and increases crack growth rates[33,133]. This effect has largely been attributed to crack closure mechanisms, RICC[33,134] and oxide induced crack closure at elevated temperatures[134]. When the crack growth data are plotted against an effective stress intensity range, ΔK_{eff}, rather than ΔK, the majority of the results obtained for differing load ratios fall within a small range of scatter and a similar value of ΔK_{th} is seen[133]. The effective stress intensity factor range, ΔK_{eff} is defined as:

$$\Delta K_{eff} = K_{max} - K_{closure}$$ **Equation 18**

K_{max} is the maximum applied stress intensity factor, and $K_{closure}$ is the stress intensity factor below which crack face contact will occur. ΔK_{eff} is relevant only when the value of $K_{closure}$ is greater than K_{min}.

2.3.5.2 Effect of Temperature

In air increasing temperature generally leads to an increase in crack growth rates[134,135], with smaller increases occurring for those tests carried out in a vacuum[124]. Crack growth rate increases in the cycle dependent crack growth regime were reported to be minimal[117,136]. These increases could largely be accounted for in terms of increased CTOD caused by the reduction in yield strength and Young's modulus that occurs with temperature in addition to the change of slip behaviour that occurs at higher temperatures. Larger increases in crack growth rates were reported in the time dependent crack growth regime, as in addition to the processes present in the cycle dependent regime, the effects of creep and environmental processes become more pronounced[124,128]. Although at higher temperatures reductions in crack growth rates have been seen[124,135]. This has been attributed to either crack tip blunting, or coarsening of the strengthening γ' precipitates[135]; leading to a reduction of local stress concentrations and hence reduced associated intergranular cracking due to the more homogeneous slip processes present at higher temperatures.

Crack growth rates in N18 have been reported to increase by a factor of 3 to 4 between 400°C and 650°C, and by a further factor of 1.5 between 650°C and 700°C[114].

2.3.5.3 Frequency Effects

Crack growth rates are generally not affected by loading cycle frequency at room temperature, with effects only being observed at elevated temperatures[124,137]; these being more predominant in tests carried out in air than those carried out under vacuum or inert conditions[124,132,137].

High loading frequencies imply that the material is operating within the cycle dependent crack growth regime; transgranular propagation is normally observed and crack growth rates are largely independent of frequency due to a lack of time dependent processes in operation, as can be seen from the good correspondence of high temperature crack growth rates with those seen at room temperature and under vacuum conditions[137,138]. No frequency effect was noted in N18 at 650°C down to around 0.1 Hz[114].

As loading frequency is lowered the contribution to crack growth from time dependent processes becomes more significant. This is seen to occur when the loading frequency falls below what is termed the transitional frequency; crack growth now occurs in the mixed mode regime, further reductions in loading frequency eventually leading to time dependent crack growth. At high temperatures, in both the mixed and time dependent

modes, crack growth rate for a particular ΔK is seen to increase as the loading frequency is reduced[131,137]. This usually corresponds with a transition from transgranular to mixed transgranular and intergranular or even intergranular crack propagation through the material. Crack growth rates for N18 increase by a factor of about 3 when the loading frequency is lowered to $3x10^{-3}$ Hz, with transgranular crack growth occurring up to 550°C, a mixed mode between 600 to 650°C and 0.5 Hz frequency, with intergranular crack growth occurring at lower frequencies, less than 0.1 Hz or higher temperatures, although no mechanism is cited for the changes[114].

The higher crack growth rates seen at lower frequencies have been attributed to an increased contribution from environmental damage[132,138] or creep[139] or the concomitant effects of both these processes[140,141]. At low loading frequencies testing conditions become closer to those seen during static load testing, hence the increased contribution from creep processes and explaining the sensitivity to dwell times imposed at maximum or minimum load. The diffusion of embrittling species to crack tips from elsewhere in the material may explain the increased environmental damage seen at low frequencies[140] as more time is available for their diffusion and as the crack is held open for longer, a less tortuous path exists for oxygen to reach the crack tip for longer period.

A frequency mechanism map clearly demonstrates the influence of frequency on crack growth rates and is obtained by plotting the crack growth rates obtained at a particular ΔK against loading frequency, an example taken is reproduced in Figure 18 [131].

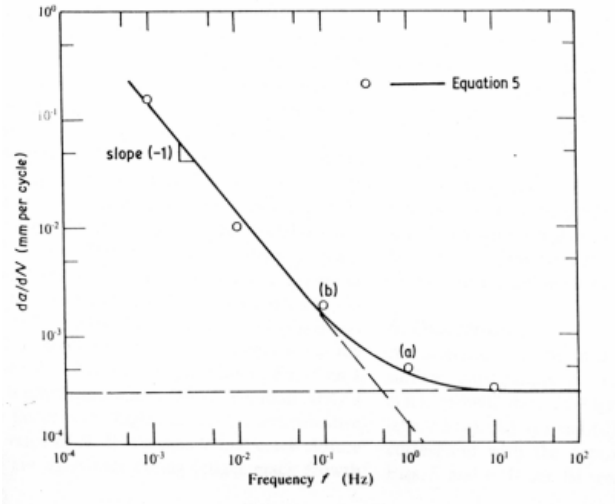

Figure 18 Frequency mechanism map, alloy AP1, 700°C, ΔK = 20 MPa√m and R = 0.7.

In the cycle dependent regime (above 10 Hz) a constant crack growth rate is seen indicating that crack growth rate is independent of frequency[131,138]. In this case, below around 0.1 Hz the slope approaches a value of -1, corresponding to fully time dependent behaviour.

2.3.5.4 Environmental Effects

As discussed in the previous section, crack growth rates for alloys tested in air in the time dependent crack growth regime are generally higher when compared with tests carried out in a vacuum or inert environment. Crack growth in this regime tended to be intergranular with the effects of air becoming more significant during lower frequency, longer dwell times or at higher temperatures due to more time being available for the diffusion of embrittling species to the crack tip. Although once $\frac{da}{dN}$ attains a certain value the contribution arising from these time dependent processes will become more limited. It has also been observed that for tests carried out in air at various temperatures and with various dwell times, the slope of the $\frac{da}{dN}$ versus ΔK plot remains almost constant[46,142]. As intergranular crack growth dominates under various test conditions, oxygen embrittlement along grain boundaries could explain the similar slopes observed.

The effect of environment is more pronounced in fine grained microstructures (within the long crack growth regime). This is attributed to the increased grain boundary area in such microstructures which in turn increases the susceptibility to grain boundary related crack growth processes and hence the effect attributed to the environment. Intergranular crack growth processes that are normally associated with these fine grained microstructures are generally suppressed when tests are carried out in a vacuum[47,142]. Although work by Andrieu and Pineau[143] on N18 found that despite similar grain sizes, variations in fatigue crack growth rate did occur due to the microstructural differences arising from the different cooling rates experienced at the surface of a turbine disc when compared with the bulk of the disk. Their paper considers the interplay between oxidation and mechanical loading processes by considering three different methods of exposing the test specimen to oxygen, these were: Type I, triangular waveform 180s/180s with an injection of air to achieve a partial pressure of oxygen (PO_2) of 1mb for 20s at a variable phase angle (ϕ) within the loading cycle; Type II, a trapezoidal waveform 10s-300s-10s with an injection of air to achieve a PO_2 of 1mb for a variable time period (t_{ox}) at the beginning of the hold time; Type III, a similar load cycle to type II, with the air injected to achieve a PO_2 of 1mb for the remainder of the hold cycle after a time delay (t_{del}). Intergranular crack growth paths and high growth rates were found when ϕ was between 40 and 180s, confirming that a combination of load and oxidation processes are required to initiate intergranular embrittlement. However after 180s, *i.e.* load is beginning to decrease from its maximum value, crack growth rate begins to decrease, falling to a constant value around 220s, and this out of phase region only experiencing transgranular crack growth. The change in crack growth rate being attributed to the change of oxidation process from a duplex oxide scale (formed under an air environment) to chromium oxide scale formed under low PO_2.

During the type II test, fatigue crack growth rate increased as t_{ox} increased, but differences were noted between the surface and bulk of the disk, the bulk of the disk fatigue crack growth rates being insensitive to t_{ox} of less than 60s and a difference at the fastest crack growth rates of an order of magnitude. A similar difference was noted during type III testing. The crack growth rates for the bulk of the disk being insensitive to values of t_{del} greater than 60s, whereas the surface of the disk needed much longer delay times before crack growth insensitivity was noted. Andrieu and Pineau argue that these phenomena can be explained by the dynamic coupling required to initiate intergranular embrittlement, but that oxygen intergranular diffusion is not involved in the damaging processes. They postulate that the damaging process can be attributed to another diffusing species whose diffusion is enabled by the super-saturation of vacancies created during the oxidation process. They also carried out further tests using a 10s-300s-10s trapezoidal wave form where the specimen is unloaded by a percentage of the maximum load at the beginning of the hold time. The hold time effect was found to disappear and a change of fracture mode from intergranular to transgranular occurred after a 20% reduction of the peak load, this was attributed to crack tip relaxation and the creation of a compressive zone at the crack tip, the extent of which is controlled by the amount of unloading, the critical size of this compressive zone was calculated to be 6 μm. The earlier differences in fatigue crack growth rates between surface and bulk disk material can be explained in terms of creep performance and as the surface material has superior creep performance to the bulk material, then by reducing creep performance, *i.e.* permitting "beneficial" creep to occur, it is argued that oxidation assisted cracking resistance will be improved.

2.3.6 Thermo-mechanical Fatigue

The focus of this aspect of the literature review is to provide an overview of TMF based around the relevant objective for this aspect of the research, *i.e.*:

- Further develop TMF testing at QinetiQ in order to provide a method for validating the physics based lifing model developed concurrently.

A description and overview is presented in the following section in order to introduce the terminology and test methodology associated with TMF.

2.3.6.1 Description and Overview

TMF is the combined fatigue damage that occurs in a component due to is exposure to cyclic mechanical strains and thermal cycles simultaneously[144]. In terms of damage rates the synergistic combination of the effects attributed to both temperature and strain are often greater (although not always) than the damage that would be seen under the separate application of these conditions.

It is normal to consider the extreme modes of TMF that occur, in-phase (IP) and out-of-phase (OP) as shown schematically in Figure 30.

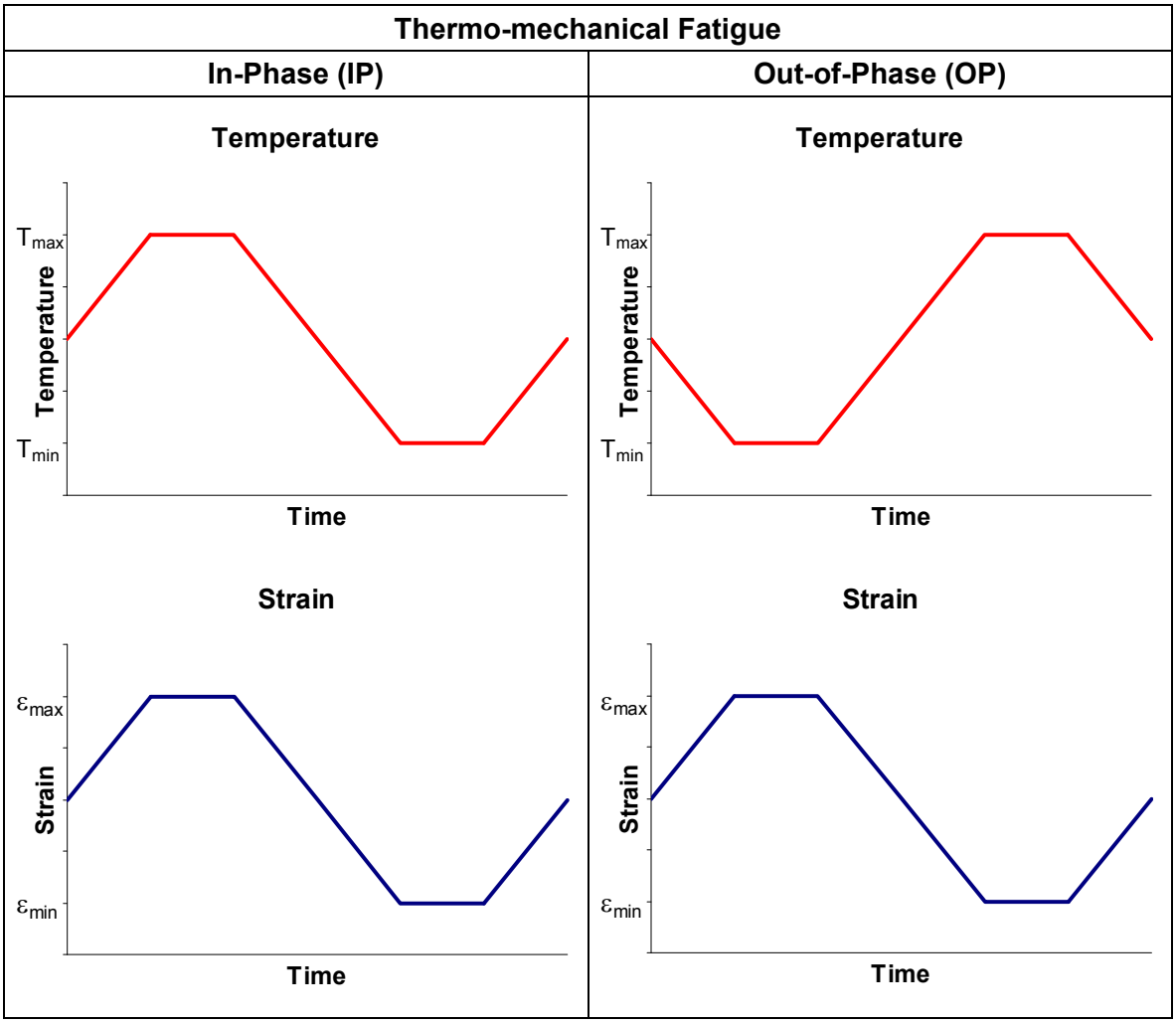

Figure 19 In-phase and Out-of-phase TMF Strain-Temperature cycles.

In these idealised extreme modes, under IP loading conditions the maximum tensile strain occurs at the same time as the peak temperature and maximum compressive strain at the minimum temperature. This contrasts with the OP cycle, where maximum tensile strain occurs at the minimum temperature and maximum compressive strain at the peak temperature. Phasing effects are difficult to generalise, and are dependent on the materials involved and the exact nature of the cycle used. In terms of stress versus strain, traditional “peanut” diagrams are presented in Figure 20.

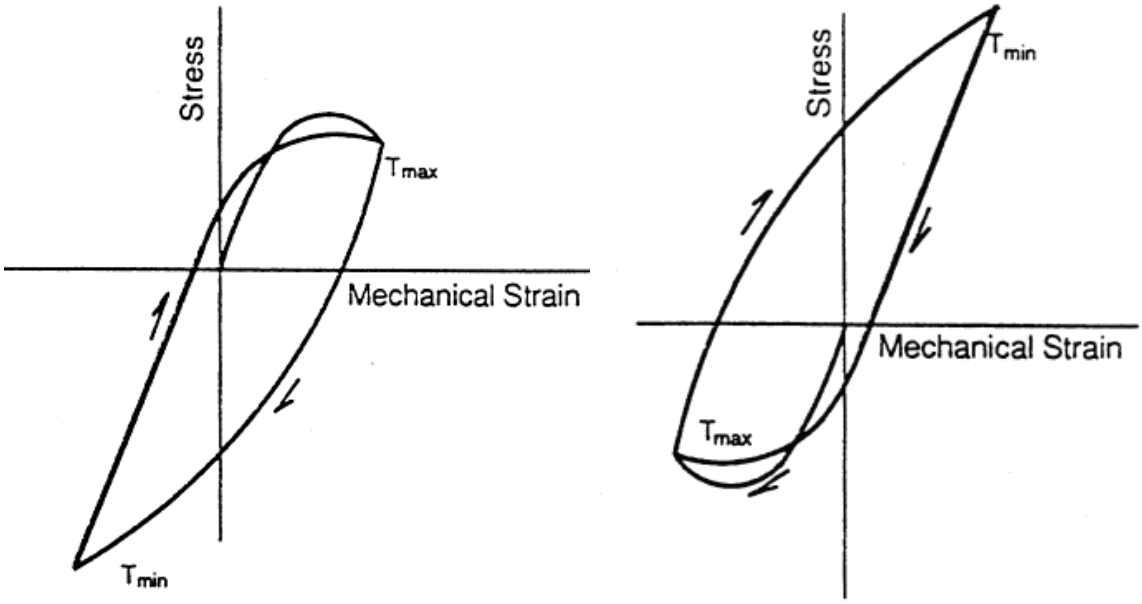

(a) TMF In-phase cycle **(b) TMF Out-of-phase cycle**

Figure 20 Stress versus strain under TMF loading cycles[145].

2.4 Lifing of Critical Components in Gas Turbine Engines

The overarching theme of the EngD was introduced in section 1.3. In order to place the methodologies, knowledge and data created by this EngD into the context of the independent advice provided by QinetiQ to UK MoD with regard to the lifing and performance of high temperature components operating within gas turbine engines, an overview of the various procedures used to life gas turbine parts and components is required. QinetiQ provides advice to UK MoD, as such only the requirements for military gas turbines operated by the MoD will be considered in this section.

2.4.1 Lifing of Military Gas Turbines for UK MoD

The UK MoD Design and Airworthiness requirements for Service Aircraft are contained within UK MoD Defence Standard (DefStan) 00-970 Part 11[146]. With the fundamental airworthiness requirements contained within Section 3 which is based on the European Aviation Safety Agency (EASA) Certification Specifications for Engines[147]. Specifically the DefStan requires the Engine Designer to carry out a Safety Analysis to define which components and parts in the engine are critical, insofar as their failure would be Catastrophic (prevents continued safe flight or landing) or Critical (jeopardises continued safe flight and landing, results in mission abort) in terms of operation of the aircraft[146]. The lives of these engine critical parts must be determined in accordance with an acceptable means of compliance (AMC) such the probability of their failure is Extremely Remote (Defined for passenger carrying transport aircraft as a probability range of between 10^{-7} to 10^{-9} per hour, and for other aircraft between 10^{-5} to 10^{-7} per hour). A lifing procedure considered to be an AMC is contained at Annex A to DefStan 00-970 Part 11, and describes the following approaches to lifing[146]:

1. Traditional Safe Life
2. Databank
3. Damage tolerance
4. Retirement for cause

A brief overview of each of these is presented in the following sections (all information is from the DefStan[146]).

2.4.2 Traditional Safe Life Approach

This approach establishes a predicted safe cyclic life for a component or part following cyclic testing of representative parts. Tests are carried out until either:

1. Critical crack length is reached (dysfunction) *i.e.* when material fracture toughness is exceeded or remaining ligament tensile strength is exceeded.
2. If the area is found to be crack free on inspection, then a crack is assumed to occur at the limit of the inspection method used on the next cycle, and if this is greater than 0.38 mm radius, the established life adjusted to reflect this. Or an approved statistical approach may be used.

Where testing of a component cannot be carried out the life of the component may be determined using calculated stresses and temperatures and material properties appropriate to a minimum strength part, but in this case only half of the calculated life may be used.

In all cases the probability of a component exceeding ⅔ of its dysfunction life is to be ≤ 1:750 with 95% confidence.

2.4.3 Databank Approach

Rather than carrying out a specific test to determine a particular life, in this approach a materials databank is used. This databank has been created previously using correlated data from laboratory testing of materials, including results from previous tests carried out on critical features in a particular material. Lives for minimum property parts are determined using statistical techniques.

2.4.4 Damage Tolerance Approach

This is a specific approach detailed in the DefStan[146], and should not be confused with Damage-Tolerant also known as Retirement for Cause Approach as discussed by Reed[5] which is presented in the next section.

This requirement is additional to the previously discussed lifing approaches. It is a specific requirement that applies to those components that are susceptible to failure from

surface damage, as determined by analysis or previous service experience. The damage tolerant lifetime will be determined by analysis or test validated by specimen or component tests. This testing or analysis considering the number of cycles it takes to propagate an initial flaw to dysfunction under representative loading conditions. These Predicted Safe Cyclic Damage Tolerance Lives (PSCDTL) have the same safety margins applied as previous tests, and should not exceed the lives published as result of applying the previous lifing approaches. A probabilistic approach can be used, and in this case a ⅔ factor is not required. Engine overspeed conditions must be considered during determination of component lifing.

2.4.5 Retirement for Cause

Within the UK, this approach is not routine and requires specific approval to use. Its use allows the utilisation of components that would otherwise be retired as they have reached their Predicted Safe Cyclic Life (PSCL). Parts which pass a rigorous inspection may be returned for service for a specified Predicted Safe Inspection Interval (PSII). No part that is known to contain a crack that could result in a critical failure within the service life can be returned to service.

2.5 Literature Review Summary

A summary of the literature review is presented in the following sections.

2.5.1 Turbine Disc Considerations Summary

Nickel superalloys used to manufacture turbine discs are complex alloys often containing in excess of 11 alloying elements in addition to Nickel. They generally have an austenitic γ matrix which is strengthened by an intermetallic γ' precipitate of varying morphologies related to processing route and heat-treatments. As operating temperature and stress level requirements in turbine discs have increased volume fractions of γ' have increased in disc alloys and processing is generally carried out using powder metallurgy (PM) techniques. N18 is a typical PM superalloy in this respect which has been designed specifically for a medium sized turbo-fan used to power a military aircraft. LSHR on the other hand has, as the name suggests, been designed to have a Low Solvus and High Refractory properties enabling dual microstructures to be achieved, coarse grained at rim and fine grain at bore to optimise the disc for the different conditions it experiences due to the differences in operating temperatures and stresses seen between the bore and rim.

The γ' precipitates in the alloy provide the anomalous high temperature strength response seen in Ni based superalloys which is due to the thermally activated entanglement of screw dislocations known as Kear-Wilsdorf locking.

Although there is a large body of literature published regarding superalloys, due to complexity both in terms of the alloys themselves and the complex conditions in which they are used there are aspects about which only an empirical understanding has been reached. This is perhaps because the complete role and inter-reactions of all constituent elements is not fully understood or because in any complex operating environment, which will often consist of differing ΔK, load ratios, temperatures, frequencies, hold times and environments, often compromises have to be made.

To provide good creep resistance and long fatigue crack growth resistance a large grain size is preferred but this leads to a lower strength alloy. For higher strength a small grain size is preferred, this also providing better resistance for short fatigue crack propagation (as may predominate in a notch fatigue situation). The conditions in a turbine disc require high strength at the bore of the disc where the temperatures are somewhat lower than those seen at the rim. At the rim due to higher temperatures, creep becomes an issue. More recent dual microstructure heat treatments have been developed as a solution to this dichotomous requirement. From the study of the patents for some of these alloys, it has been seen that a degree of instability in the material properties of the alloys is being sought to provide suitable chemical and mechanical conditions at grain boundaries.

In addition to these basic design parameters imposed on the material, other issues such as the effect of grain boundary chemistry need to be understood such that the effects on oxygen diffusivity to the crack tip or alloying species may be accounted for and the switchover from perhaps beneficial behaviour such as OICC to crack tip oxidation embrittlement can be predicted in the complex environments within which superalloys are used. It is perhaps the interactions of these many concomitant processes and environments that pose the greatest problems to overcome in terms of understanding, modelling and using superalloys.

2.5.2 Turbine Blade Coating Considerations Summary

The literature review has in the main been focused on Electron Beam Physical Vapour Deposition (EBPVD) applied Top Coat (TC) and Pt Aluminide Bond Coat (BC) as the area of specific interest to this project.

Thermal Barrier Coating (TBC) systems offer the benefit of insulating turbine blades (and other parts of gas turbine engines) such that they may be operated at higher temperatures than previously seen and yet retaining the blade's underlying structural properties and performance at these elevated temperatures. Insulation of the blade is achieved by applying a TC of Zirconia partially stabilised with Yttria to the blade using EBPVD. The efficiency of this coating is enhanced by creating a thermal flux by providing cooling air via channels within the blade. As single crystal blades have developed, the content of those elements that provided protection against corrosion at high temperatures have been

reduced. The columnar structure achieved by EBPVD application provides the TC with some strain compliance, yet as a whole the TC preserves enough stiffness to resist failure by small scale buckling. As the TC is effectively transparent to oxygen and it does not adhere well to the blade surface directly, a BC is applied to the blade. This serves to protect the blade surface from corrosion by forming an α-alumina (Al_2O_3) Thermally Grown Oxide (TGO) layer which is both strongly adherent with a low rate of diffusion across its interface. The TGO is grown initially prior to TC application, as the TC adherence to the TGO is improved when compared to its application to the BC directly.

The TGO layer continues to oxidise in service, growing in thickness and laterally in a parabolic nature. The strains induced by such growth during thermal cycling lead to rumpling of the TGO induced by a process known as ratcheting. The imperfections created by rumpling as well as other oxide imperfections in conjunction with the stresses created due to differing Coefficients of Thermal Expansion (CTE) and growth of the oxide layer provide sites for crack nucleation. Once this has occurred crack propagation, coalescing and local decohesion of the TC occurs until a critical size is reached at which large scale buckling and spallation of the TC from the blade surface occurs. Once spallation of the TC occurs the blade may be subject to temperatures in excess of its melting point with structural failure a real possibility.

Early attempts at predicting life using TGO thickness alone have not been successful and although durability maps have been produced these are largely empirical in nature. In order to use TBC systems as a prime reliant coating system a method of predicting life using the physical characteristics of the TBC system is required.

2.5.3 Fatigue Summary

Fatigue is a failure mode that arises from fluctuating stresses in a material such that failure can occur at stresses much lower than either the yield stress or ultimate tensile stress of the material. Cracks initiate at sites of high stress concentration, followed by a period of short crack growth, which depending on the particular conditions at the crack tip may result in further crack growth or crack arrest occurring. Coalescence with other cracks may occur ultimately leading to the creation of a long crack which would typically grow in accordance with the Paris equation. Linear Elastic Fracture Mechanics (LEFM) can be used to correlate fatigue crack growth with loading conditions by relating the far-field applied stress and flaw length to the local stresses at the crack tip, introducing the concept of change in stress intensity factor, ΔK. As a crack grows the stress intensity at its tip increases, accelerating the crack growth rate. Final fracture occurs when the crack length reaches a critical size, either causing plastic collapse in the uncracked ligament or when the critical stress intensity factor is reached. For long cracks there is a stress intensity threshold, ΔK_{th} below which cracks do not appear to grow. However, initiation

and short crack growth may occur at these stress intensities. Load transfer may occur in the wake of a growing crack leading to crack closure, this may be induced by plasticity, roughness or oxide formation, with the effect at the crack tip of reducing the change in stress intensity factor.

Fatigue behaviour can be characterised using either a stress-life (High Cycle Fatigue (HCF)) or strain-life (Low Cycle Fatigue (LCF)) approaches where LCF lifetimes are usually lower than 10^5 cycles. For HCF, by plotting the stress amplitude against cycles to failure on log-log scales, a linear relationship known as the Basquin relation is observed, for LCF the equivalent expression is known as the Coffin-Manson relation.

Much of the lifetime of turbine discs is spent within the initiation and short crack regimes. Increasing strength of materials, allows higher stresses to be applied and therefore reduces the length at which a flaw size becomes critical, under these conditions long crack growth data may provide non-conservative lifetime predictions. Crack initiation in Nickel-base superalloys can occur at various sites depending on temperature, microstructure and environment. At higher temperatures initiation can occur from slip bands, grain boundaries, twin boundaries, inclusions and pores. Short cracks generally grow at faster rates than long cracks as due to their size the crack tip is susceptible to the effects of local microstructure, absence of crack closure and chemical attack. Although there is considerable scatter and variations in short crack growth rates mostly due to the interactions between the plastic zone surrounding the crack tip and local microstructural features, which can lead to crack arrest. Thus short cracks do not experience the larger scale averaging effects of a long crack and as such are not described well by LEFM. Short crack growth rates tend to converge with those of long cracks when the crack length has spanned eight to ten microstructural elements, *i.e.* typically when the plastic zone size exceeds the grain size of the material.

Higher temperatures cause slip to become more homogeneous suppressing cracking at these sites, conversely oxidation becomes more significant reducing crack initiation resistance. At higher temperatures in coarse grain materials ΔK_{th} is reduced due to the propensity for roughness induced crack closure (RICC). Generally in air, for long crack growth increasing temperature leads to increased crack growth rates, with smaller increases seen for those tests carried out under vacuum conditions. This can mostly be explained by the indirect effect of temperature on an individual alloy's yield stress or Young's Modulus at elevated temperatures. Increases in crack growth rate tend to be lower for cracks within the cycle dependent regime and higher for those within the time depended regime due to the more pronounced effects of creep and oxidation, although reductions in crack growth have also been seen attributed to crack tip blunting or coarsening of the γ' precipitates.

Environment is also significant, with increased initiation periods and reduced short crack growth rates observed during vacuum tests, especially at elevated temperatures. In threshold or near threshold conditions, crack face rewelding has led to higher values of ΔK_{th} being observed. In long cracks environmental effects such as oxidation, corrosion and creep are the predominant processes causing crack growth in the time dependent regime. As creep is an inelastic process LEFM is not strictly valid when this occurs. In air the effects become more significant at longer hold times or at higher temperature as diffusion of embrittling species to the crack tip is enhanced, although as the crack growth rate increases these effects are reduced.

In fine grain material, ΔK_{th} is independent of load ratio, R, increasing R in larger grain material tends to increase ΔK_{th} and increase crack growth rates in near threshold and Paris regimes.

At room temperature changes in load cycle frequency generally have little effect on crack growth rates, at higher temperatures effects are more pronounced, especially for tests carried out in air. As loading frequency is lowered contribution from time dependent processes, creep and / or oxidation, become more significant, with crack growth rate for a particular ΔK, increasing as loading frequency is reduced.

Thermo-mechanical fatigue (TMF) is the combined fatigue damage that occurs due to cyclic mechanical strains and thermal cycles simultaneously. In terms of damage rates the synergistic combination of the effects attributed to both temperature and strain are often greater than the damage that would be seen under the separate application of these conditions.

Fatigue crack growth is a complex process involving the concomitant and often interrelated involvement of a number of parameters, including ΔK, R, temperature, frequency, hold time and environment. With the specific impact of these parameters varying depending on a particular alloys chemical composition and heat treatment which determines (for a particular chemistry) the alloy's morphology and grain boundary characteristics. In general crack growth regimes are categorised as either cycle-dependent typically due to low temperatures, high loading frequencies and inert atmospheres and fracture surfaces often exhibit a transgranular crack path, or time-dependent normally arising from high temperatures, low loading frequencies and deleterious environments leading to intergranular crack propagation. The transition from one regime to another does not occur suddenly, hence there is intermediate mixed-mode regime where crack propagation occurs by a mixture of transgranular and intergranular processes.

The separate effects on fatigue crack propagation attributed to fatigue, creep and environment may be determined individually by carrying out testing under different test

conditions. Although, using this data to predict performance under service conditions must be carried out with care. The interactions between environment, creep and fatigue are complex and simple superposition of the individual effects is unlikely to predict the correct life.

2.5.4 Lifing of Critical Components Summary

The UK MoD has determined that the following approaches are acceptable for determining the life of critical components fitted to its engines:

1. Traditional Safe Life (life to first crack)
2. Databank
3. Damage tolerance (an additional requirement to (1) and (2) specifically for components which are susceptible to failure arising from surface damage.
4. Retirement for cause (also known as damage tolerant)

It is within the context of the independent advice provided by QinetiQ to UK MoD with regard to the lifing and performance of high temperature components operating within gas turbine engines that this EngD is presented.

3 Materials

Initially details of the *Turbine Disc Materials* are presented, followed by details of the *Thermal Barrier Coating Materials*.

3.1 Turbine Disc Materials

In this section the compositions, heat-treatments and supply of specimens are considered, first for N18, then LSHR and finally for the three comparison materials previously analysed and tested at the University of Southampton.

3.1.1 N18

N18 is a PM alloy and was supplied by SNECMA to QinetiQ. The section supplied comprised half a hot isostatically pressed and forged, heat treated "pancake" (disc precursor), with parts of the material that QinetiQ required for the tensile, creep and LCF tests removed. A cutting plan is presented at Appendix 3 which also shows the details of the test specimen dimensions and notches.

The chemical composition was analysed by IncoTest for QinetiQ[148], the results of the analysis are reproduced in Table 11 with the compositions of the comparison materials. The heat treatments of all materials are reproduced in Table 12.

3.1.2 LSHR

LSHR is also a PM alloy and was supplied by NASA to the University of Southampton as pre-heat treated standard blanks measuring 2.1 inches by 0.57 inches square. These specimen dimensions were chosen to permit direct comparison with data on similar sized specimens already available to NASA. Specimen dimensions are provided on the cutting plan at Appendix 4.

3.1.3 Comparison Materials

N18 and LSHR are compared against three PM disc material variants that have previously been researched at the University of Southampton: RR1000; UDIMET® 720 Low Interstitial (U720Li) and U720Li Large Grain (U720Li LG) variety, compositional details of these materials are presented in Table 11.

Table 11 Alloy chemical compositions (weight %).

	Cr	Co	Mo	Ti	Al	C	B	W	Hf	Zr	Fe	Ta	Nb
N18[148]	11.1	15.4	6.44	4.28	4.28	0.022	0.008	-	0.50	0.019	-	-	-
LSHR[7]	12.5	20.7	2.7	3.5	3.5	0.03	0.03	4.3	-	0.05	-	1.6	1.5
RR1000[21]	14.35 to 15.15	14.0 to 19.0	4.25 to 5.25	3.45 to 4.15	2.85 to 3.15	0.012 to 0.033	0.01 to 0.025	-	0.5 to 1.0	0.05 to 0.07	0.0 to 1.0	1.35 to 2.15	-
U720Li & LG[20,21]	15.92	14.57	2.98	5.18	2.44	0.023	0.016	1.35	-	0.042	0.08	-	-

Table 12 Alloy heat treatments.

N18[148]	4h 1165°C →	air cool →	24h 700°C →	air cool →	4h 800°C →	air cool
LSHR[7]	Sub-solvus	1.5h 1135°C →	furnace cool	Followed by Super-solvus on next line		
	1171°C →	air cool →	4h 855°C →	air cool →	8h at 775°C →	air cool
RR1000[21]	4h 1120°C →	fan air cool →	24h 650°C →	air cool →	16h 760°C →	air cool
U720Li [20,21]	4h 1105°C →	oil quench →	24h 650°C →	air cool →	16h 760°C →	air cool
U720Li LG[20,21]	4h 1135°C →	air cool →	24h 650°C →	air cool →	16h 760°C →	air cool

3.2 Thermal Barrier Coating Materials

Two types of CMSX4 test specimen were used for the TBC research. “Button” specimens and “dog bone” specimens, the supply of both of these specimens including their TBC is considered in the following sections.

3.2.1 Button Specimens

CMSX4 “Button” specimens, 20mm diameter x 5mm thick, (Figure 21) were coated by Cranfield University using their own proprietary coatings. The coatings consisted of a sputtered CN-91-equivalent Platinum Aluminide bondcoat, and a CN33-type EBPVD applied Thermal Barrier Coating (TBC) with a nominal thickness of 200µm. The buttons were supplied to Cranfield by QinetiQ, ground flat to 1200 grit.

Figure 21 Typical Coated CMSX4 "Button" specimen (approximately 20mm x 5mm).

The buttons were initially cleaned in acetone to remove any packing tape and then grit blasted at 30psi with 220 mesh grit to provide a controlled surface roughness. The platinum was deposited by sputter deposition, (which differs from the standard commercial practice of electroplating). The specimens were sputtered at $1x10^{-1}$ mBar. Platinum was then diffused under vacuum at 1140°C for 1 hour. Aluminising was carried out using a vapour aluminising process using a chromium-aluminium alloy source material and an aluminium fluoride halide activator. The process ran at 1030°C for five hours in an Argon-10% Hydrogen atmosphere. After aluminising the specimens were ultrasonically cleaned in hot water for 30 minutes to remove any deposits or salts from the specimens. The buttons were then heat treated at 1140°C for 1 hour to interdiffuse the coating and form a single-phase microstructure. Immediately prior to loading the specimens into the EBPVD coater, the specimens were given a light grit blast to provide a controlled roughness and clean surface for the TBC process. The TBC consisted of standard white Yttria partially stabilized Zirconia (7wt% Yttria, balance Zirconia) and was applied using the EBPVD process carried out under an oxygen partial pressure of $1x10^{-2}$ mBar at 1000°C for 83 minutes. After the coating process, the specimens were processed through a 1 hour at 1100°C oxidation cycle in an air muffle furnace, this allowed further development of the Thermally Grown Oxide (TGO) and served as a quality check to ensure there were no short-life specimens.

3.2.2 "Dog Bone" Specimens

A CMSX4 "dog bone" type specimen (Figure 22) was supplied by Chromalloy already coated with a commercial proprietary Chromalloy TBC system.

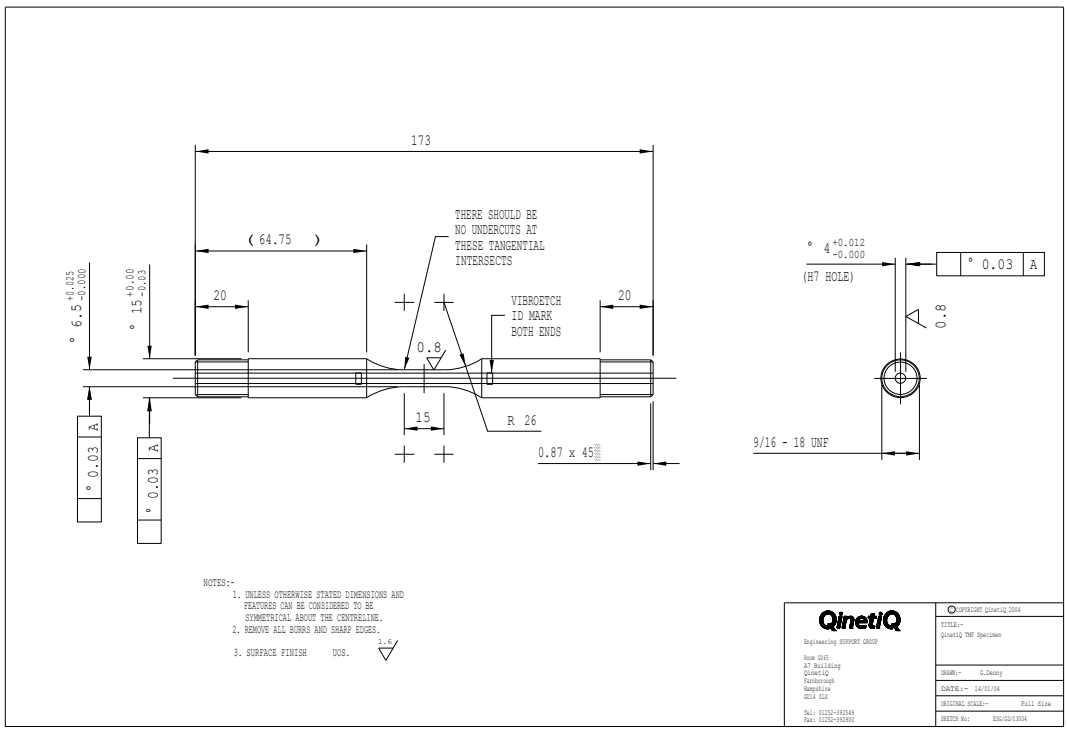

Figure 22 "Dog bone" specimen, QinetiQ Sketch ESG/GD/03004 (creep and TMF tests).

4 Experimental Methods

Here the various experimental methods are presented, the first section regarding *Testing of Turbine Disk Alloys N18 and LSHR*, followed by a section that describes the *Testing and Analysis of Thermal Barrier Coatings*.

4.1 Testing of Turbine Disk Alloys N18 and LSHR

In this section the experimental methods used during the turbine disk alloy research aspect of the project are presented. As an introduction, the test matrices for N18 and LSHR are considered. This is followed by a detailed description of the procedures and methods used for materials characterisation and testing and includes those tests carried out by QinetiQ at Farnborough on N18.

4.1.1 Test Matrices for N18 and LSHR

The test matrix used for N18 is summarised in Table 13 and was devised taking into account availability of material and to enable comparisons to be made with other materials. In addition it had further value for QinetiQ in terms of expanding their material properties database and as unseen data for their Neural Network Model[149]. The tensile, creep and LCF tests would be carried out by QinetiQ.

Table 13 N18 test matrix (QQ represents tests carried out by QinetiQ).

Test type		**Test Environment and Temperature (°C)**					
		Air				Vacuum	
		Room Temp	650	700	725	650	725
Tensile		QQ	QQ	-	QQ (750°C)	-	-
Creep	σ_1 = 330 MPa	-	-	-	QQ	-	-
	σ_2 = 560 MPa	-	-	-	QQ	-	-
	σ_3 = 800 MPa	-	QQ	-	-	-	-
	σ_4 = 900 MPa	-	QQ	-	-	-	-
Fatigue Crack Propagation Rate, $\frac{da}{dN}$, 1-1-1-1 trapezoidal wave form		-	1	-	1	1	1
Fatigue Crack Propagation Rate, $\frac{da}{dN}$, 1-20-1-1 trapezoidal wave form		-	1	-	1	1	1
Low Cycle Fatigue	ε_1 = 0.7 %	-	QQ	QQ	QQ	-	-
	ε_2 = 0.75 %	-	QQ	-	QQ	-	-
	ε_3 = 0.85 %	-	QQ	QQ	QQ	-	-
	ε_4 = 1.0 %	-	QQ	-	QQ	-	-
	ε_5 = 1.2 %	-	QQ	-	-	-	-
Polished U-notch fatigue test, 1-1-1-1 trapezoidal wave form		-	2	-	2	2	2

LSHR became available following discussions with NASA at the Superalloys 2008 Conference. A limited amount of material was available for testing, with NASA being particularly interested in FCG rates under vacuum conditions. The 1-20-1-1 trapezoidal wave form was chosen such that the interactions of creep and oxidation and their effect on FCG rate could be assessed. The LSHR test matrix is presented in Table 14.

Table 14 LSHR test matrix.

Test type	Test Environment and Temperature (°C)			
	Air		Vacuum	
	650	725	650	725
Fatigue Crack Propagation Rate, $\frac{da}{dN}$,1-20-1-1 trapezoidal wave form	1	1	1	1

4.1.2 Microstructure Characterisation of N18 and LSHR

The microstructure was characterised by using specimen sections mounted in Bakelite and polished to a ¼ μm finish using standard metallographic techniques. Specimens were then etched with various γ' etches:

Nimonic etch (40ml H_2O, 10ml HNO_3, 50ml HCl, 2.5g $CuCl_2$);

Kalling's reagent (80ml HCl, 40ml CH_3OH, 40g $CuCl_2$);

In both cases typical etching times were 10 seconds.

An electrolytic etch consisting of 10% Orthophosphoric acid in H_2O was also used. In this case nickel wires were used as electrodes with the specimen as the anode and the cathode a stainless steel washer held 1mm from the surface of the specimen and a voltage of 2 V, a longer etching time of 25 seconds was used.

Micrographs were obtained using both an Olympus BH2 optical microscope and Prosilica GE1350C Camera and a JSM 6500F field emission gun scanning electron microscope (FEG SEM) which was also able to clearly resolve secondary γ' precipitates in N18 and the coherent γ' in LSHR.

The micrographs were analysed using ImageJ software to determine the grain size and average circularity, incoherent (grain boundary) primary γ' size and volume fraction and secondary γ′ size. The equivalent circle diameter (*DCircle*) for particle sizes was determined where:

$$DCircle = \sqrt{\frac{4A}{\pi}} \qquad \textbf{Equation 19}$$

Where *A* is the area of the particle.

Circularity of particles was also determined using:

$$Circularity = \frac{4\pi A}{P^2}$$ **Equation 20**

Where *A* is the area of the particle and *P* the particle perimeter.

Characterisation of tertiary γ' and grain boundaries was performed on thin foils of N18 produced by electro-jet polishing using a 34% 2-n-Butoxyethanol and 6% perchloric acid (60% solution) in methanol solution at -40°C at 24 V. The foils were examined on a JEOL JEM 3010 Transmission Electron Microscope (TEM). This enabled sizes and size range distributions of the secondary and tertiary γ' to be further defined.

4.1.3 Hardness Testing of N18 and LSHR

Hardness testing was carried out with a Vickers hardness tester using a 10kg mass in order to estimate the yield stress. To avoid introducing compliance effects from the Bakelite during hardness testing specimens were mounted in a thin layer of Bakelite and polished such that a 1μm finish on the metal was achieved on both sides of the specimen. Eight measurements were taken in each case and the mean value reported.

4.1.4 Tensile Testing of N18

All tensile testing on N18 was carried out by QinetiQ at Farnborough. Tensile test specimens were cut from the disc precursor in the radial direction such that the longitudinal axis of the specimens was parallel with the disc radial direction. Standard bar tensile test specimens, with a 3.99 mm diameter and 22 mm parallel gauge length were produced. These were tested at room temperature, 650°C and 750°C in accordance with British Standard (BS) 4 A4[150], i.e. an initial constant strain rate of ~$10^{-4}s^{-1}$ was applied up to the 0.5% proof strength and thereafter a constant cross-head speed was applied (to give a strain rate of approximately $10^{-3}s^{-1}$) until failure occurred.

4.1.5 Creep Testing of N18

All creep testing on N18 was carried out by QinetiQ at Farnborough. The creep specimens were cut using the same method as that used for the tensile test specimens. Bar test pieces with a 20 mm parallel gauge length and 3.99 mm diameter were produced for creep testing with extensometer retaining ridges at the ends of the gauge length. Creep testing was based on the standard BS10291 and was performed under constant stress loading conditions of 800 and 900 MPa at 650°C and 330 and 560 MPa at 725°C in air. The strain versus time deformation behaviour was measured up to specimen rupture.

4.1.6 Long Crack Fatigue Growth Rate Testing of N18 and LSHR

N18 and LSHR fatigue testing was carried out in air and vacuum at 650°C and 725°C using the principles contained within BS ISO 12108:2002[151]. Fatigue testing was carried out using an Instron 8501 servo-hydraulic testing machine fitted with an ESH Ltd. high

temperature vacuum chamber. Heating was provided by four high intensity quartz lamps. The temperature of the specimen was monitored and controlled to an indicated ± 1°C using a Eurotherm 815 thermo-controller and an R-type (platinum + 13% rhodium / platinum) thermocouple spot welded to the specimen within the hot zone. For vacuum testing, the above equipment was augmented with an Edwards rotary vacuum pump, Balzers TPU240 turbomolecular vacuum pump and TCP380 electronic drive unit linked to Balzers Pirani and cold cathode pressure gauge heads and TPG300 pressure gauge and controller, which allowed the ESH Ltd. test chamber to be evacuated to an indicated pressure of 1 x 10^{-5} mb. Testing was carried out in three point bend conditions on single edge notched bend specimens (SENB) of nominal cross section 10mm x 10mm, 65mm long for N18 and 53mm long for LSHR, each with a span of 40mm. Crack length was monitored using the direct current (DC) electrical potential difference (pd) method using two point and four point probes and corrected post-test using a linear correction factor obtained from optical measurements of initial and final crack length measurements. As this technique measures the pd across the crack, insulating ceramic rollers are required to transmit loads. The arrangement is shown diagrammatically for a two point probe in Figure 23, and for a 4 point probe pre and post test in Figure 24. The 4 point probe was used for all except the initial tests as this system automatically compensates for changes in material resistivity due to temperature and therefore requires less adjustment when pre-cracking is carried out at room temperature and final grow out at higher temperatures.

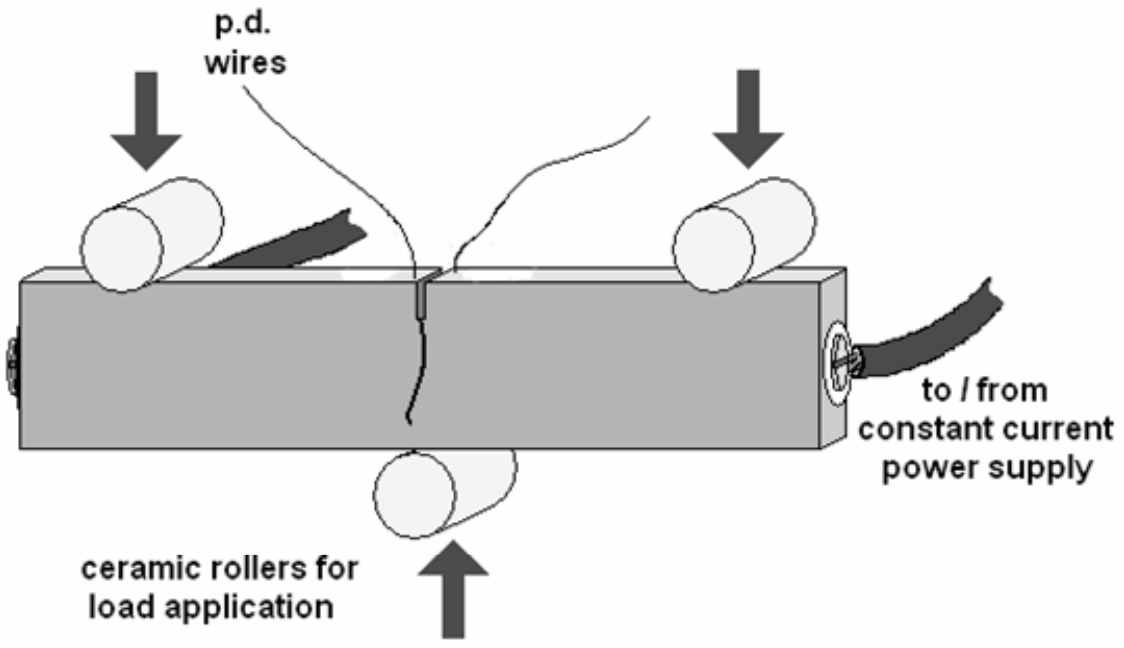

Figure 23 Schematic showing direct current potential drop crack measurement using a 2 point probe.

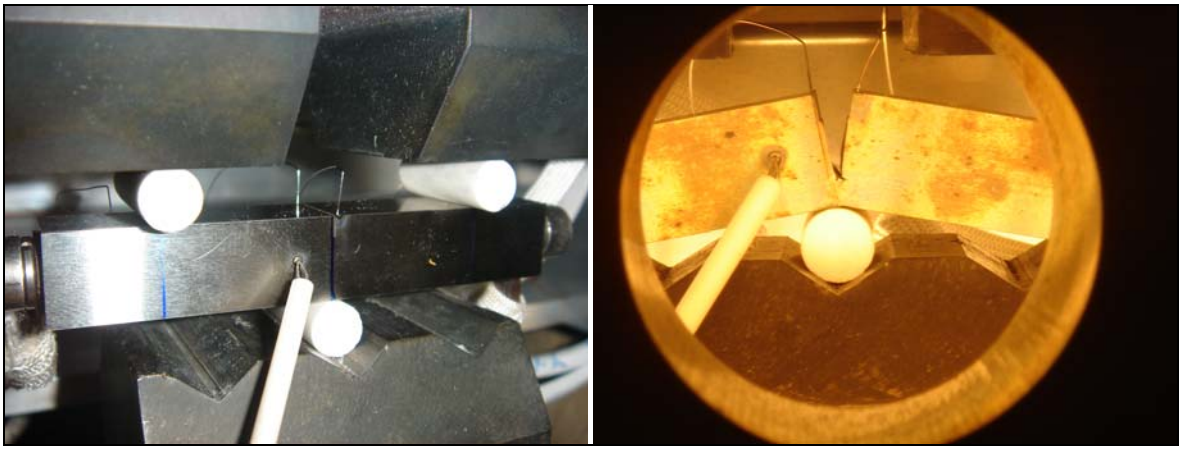

Figure 24 Direct current potential drop crack measurement using 4 point probe, pre and post test.

This method of crack measurement requires an initial calibration; this was done using an aluminium foil analogue of the width of the specimen (30 times real size, but negligible breadth). Using this analogue the relationship of crack length / specimen width to potential difference drop / datum potential difference (*a/W* versus V/V_0) for the electrical discharge machined (EDM) notch was determined. The sensitivity to positioning of the pd wires in comparison with the notch edge for two point pd probes was also established with the results for a four point probe placed at the edge of the slot and 900mm away added for reference. The results from this analogue are presented in Figure 25.

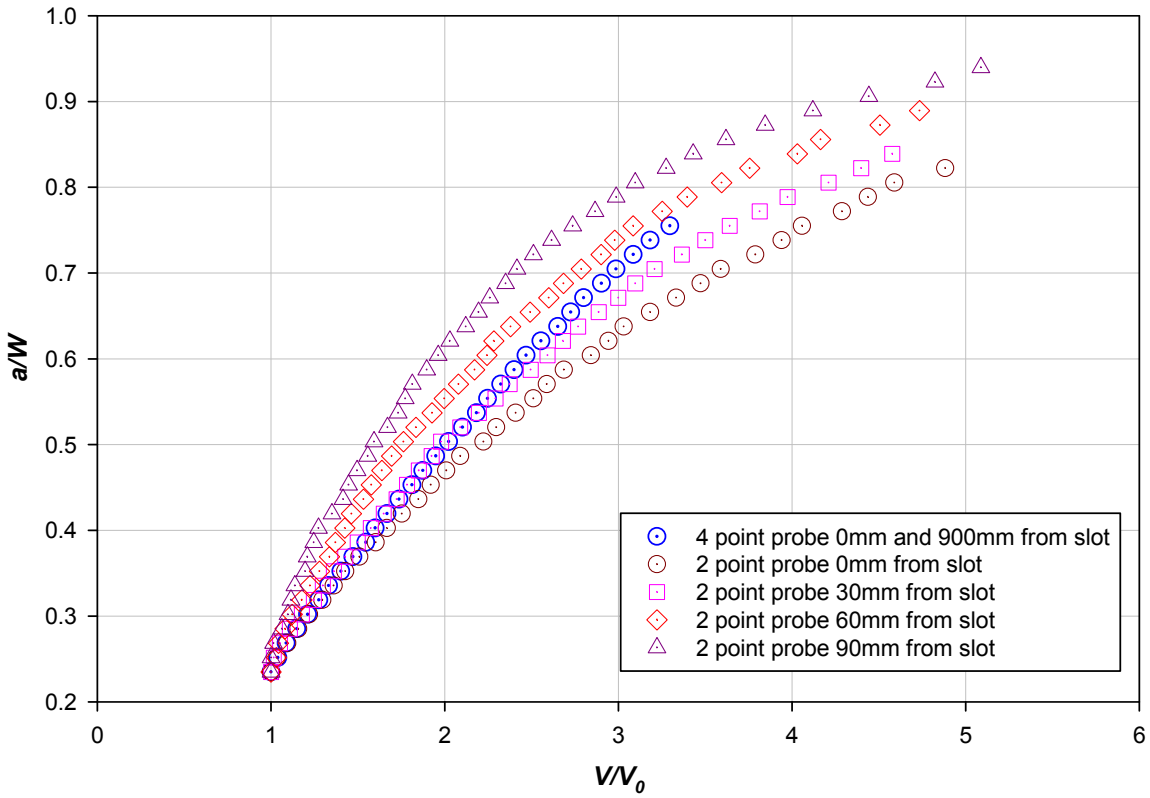

Figure 25 Foil analogue relationship between *a/W* and V/V_0.

The variation in positioning of the pd wires in relation to the slot edge was assessed, it was found that these could be positioned consistently between 0 and 0.6 mm of the slot edge. The curves in Figure 25 were also compared to those used by a previous researcher (H.T. Pang). Following this comparison, the polynomial fitted to the results for the pd wire placed at the edge of the slot was chosen for the initial tests to enable the pre-cracking measurements and growth out to be calculated, although this had to be corrected post testing using physical measurement of the crack length at the beginning of the growth out stage and the final crack length.

During crack grow out pd information was recorded using WINDAQ software via a DATAQ DI-700 USB data acquisition unit connected to a standard personal computer. At higher temperatures, the data gathered via this system appeared somewhat noisy and was smoothed using the following technique: The data was divided into overlapping segments. The data curve in each segment was locally smoothed using a tri-cube weighting function and polynomial regression (Loess function within Sigmaplot). The inter-quartile portion of the smoothed data was used to generate a complete smoothed pd curve, apart from the first and last segment where the first and last quartiles of the data respectively were additionally used. Using this smoothed curve, actual crack growth rate and ΔK were calculated to permit the results to be plotted graphically.

4.1.6.1 Long Crack Fatigue Testing in Air of N18 and LSHR

For tests carried out in air, pre-cracking was carried out using a triangular wave form, with R=0.1, a frequency of 20Hz and an initial ΔK of 20 MPa$\sqrt{m}$, which was stepped down in 10% increments after the crack had grown through at least four plastic zone sizes until $\Delta K \approx$15 MPa$\sqrt{m}$ was achieved. This ensured that crack growth out would occur from a microscopically sharp crack away from any residual effects induced in the machining of the notch. The specimen was heated to the required temperature (650°C or 725°C). The cyclic loading was changed to the appropriate trapezoidal waveform 1-1-1-1 or 1-20-1-1 for N18 and 1-20-1-1 for LSHR, R=0.1 and the crack allowed to propagate to failure under constant load (increasing ΔK conditions).

4.1.6.2 Long Crack Fatigue Testing in Vacuum of N18 and LSHR

Vacuum tests were conducted in a similar manner to the air tests as described in paragraph 4.1.6.1, with the following exceptions. At the end of the pre-cracking stage the ESH Ltd. chamber was evacuated until a pressure equal to or less than 5 x 10^{-5} mb was attained. Heating was then applied to raise the specimen to the required test temperature (650°C or 725°C), this led to out-gassing of the chamber and specimen resulting in an increase in pressure. Crack grow out using the required trapezoidal waveform 1-1-1-1 or 1-20-1-1 for N18 and 1-20-1-1 for LSHR was only commenced once the vacuum had recovered to less than 5 x 10^{-5} mb. The crack was then allowed to propagate to failure

under constant load (increasing ΔK conditions). For LSHR in order to obtain crack grow out, ΔK had to be increased to approximately 18 MPa√m.

4.1.7 Low Cycle Fatigue Testing of N18

All LCF testing on N18 was carried out by QinetiQ at Farnborough. The LCF specimens were cut using the same method as that used for the tensile test specimens. Specimens for LCF testing were produced in bar form with a parallel gauge length of 14 mm and a diameter of 6 mm. These specimens had a ground and polished surface finish within the gauge length. The LCF testing was performed under strain controlled conditions at 650°C, 700°C and 725°C, using a strain ratio (i.e. minimum strain / maximum strain) $R = 0$. A 1-1-1-1 trapezoidal waveform, 0.25 Hz, was used to cyclically strain the specimens. Full loop load and deformation behaviour was captured during this testing to enable the initial and stabilised cyclic deformation conditions to be evaluated.

4.1.8 U-Notch Fatigue Testing of N18

To assess the fatigue performance of N18 in the presence of a stress concentration, fatigue testing was carried out on 8mm x 8mm x 50mm specimens with a "U" notch. The nominal dimensions of the notch in these specimens are shown in Appendix 3. The notch type was chosen to provide an elastic stress concentration of around 2, *i.e.* representative of that seen in the fir tree root fixings used to secure blades to turbine discs. The U-notch was cut using EDM and the surface ground using a locally manufactured arbour and polished using dental felts and 1μm diamond polishing paste. Grinding and polishing was carried out in a jig in order to limit dimensional changes during this process. Testing in air and under vacuum conditions was conducted at 650°C and 725°C using the same equipment as described earlier (section 4.1.4). Tests were carried out in three point bend with a span of 40mm and under constant load conditions. The load was calculated to produce a maximum stress, σ_{max}, defined as the net section bending stress at the plane of the notch root calculated using simple beam theory. Testing was conducted at 650°C with σ_{max} = 1020 MPa and 1105 MPa and at 725°C with σ_{max} = 935 MPa and 1020 MPa.

4.1.9 Fractography of N18 and LSHR

Fractography for all completed tests on N18 and LSHR was carried out at the University of Southampton. Overviews of the fracture surfaces were obtained using a Wild Macroscope and Moticam 2000 camera. Micrographs of failed specimens were obtained using an Olympus BH-2 optical microscope and Prosilica GE1350C camera and a JSM 6500F field emission gun scanning electron microscope (FEG-SEM). For FCG rate tests micrographs at differing levels of ΔK were obtained. A Zeiss Orion scanning helium ion microscope (SHIM) was also used to obtain micrographs of a single N18 FCG specimen.

To permit analysis of structure of the material in the vicinity of the crack surface N18 specimens were sectioned as shown in Figure 26. To maintain the integrity of the fracture surface and provide edge retention during sectioning specimens were plated with Ni using Watt's Solution (500 ml H_2O, 150g $NiSO_4$ $6H_2O$, 20g $NiCl_2$ $6H_2O$, 20g) at a temperature of 65°C, a 99.9% pure Ni anode, and passing a current of 0.4A at 4V for 90 minutes. The experimental apparatus is shown in Figure 27.

After plating with Ni, specimen is first sectioned along the red plane and then the shaded blue plane.

The shaded blue plane is then mounted and polished for microscopy.

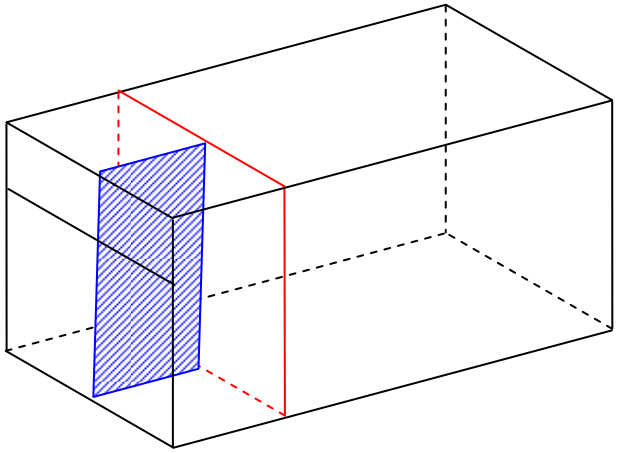

Figure 26 Sectioning of SENB Fracture surface.

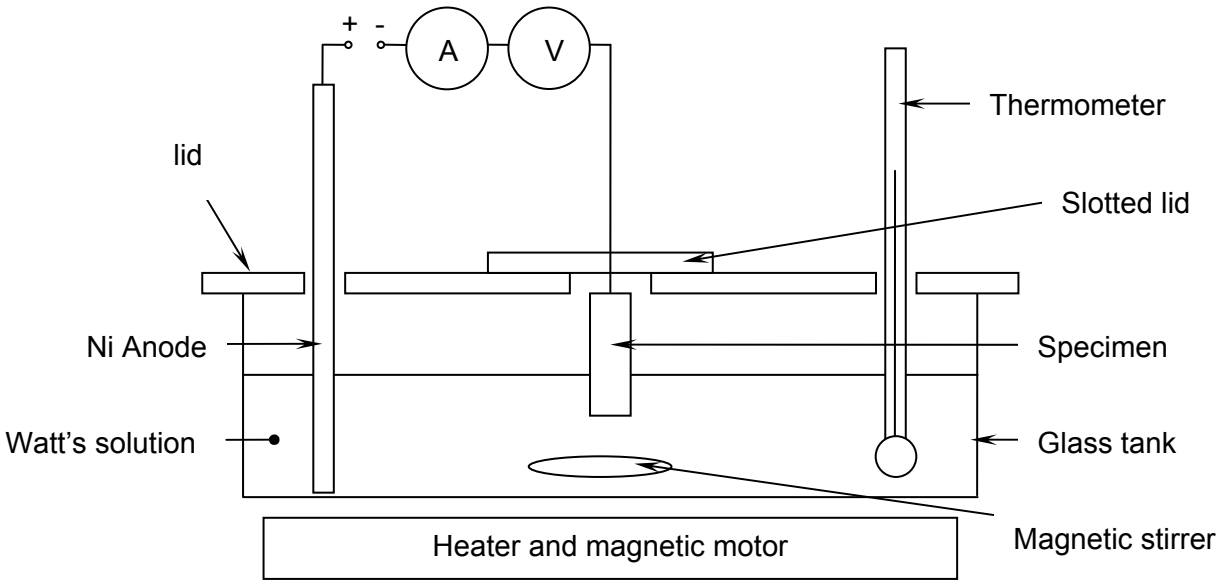

Figure 27 Nickel plating apparatus.

4.2 Testing and Analysis of Thermal Barrier Coatings

In this section the experimental methods used during the thermal barrier coating research aspect of the project are presented. Initially the test matrices for TGO growth characterisation are introduced with a detailed description of the procedure and method used during TGO characterisation. This is followed by the test matrix and a description of the procedure and method used for TMF testing of the TBC coated "dog bone" specimens.

4.2.1 TGO Growth Characterisation Experiments

The purpose of these experiments is to define and characterise the TGO growth behaviour at a mesoscale in terms of thickness and morphology for the TBC system in order to provide an initial calibration for the TBC lifing model under development at QinetiQ. The TBC lifing model aims to model typical in service conditions that a TBC coated blade would be subject to (further details of TMF cycle used are contained later in the TMF test description). In this case TMF Data could have been obtained by carrying out a series of tests under TMF conditions, however, TMF testing is time consuming and the number of tests that would be required to calibrate the model for the various TMF parameters would have been prohibitive. In order to overcome this, the test matrix was designed such that the various components of a TMF cycle (*i.e*. thermal, thermal cyclic and load) were separated and considered in isolation and hence the TGO layer growth behaviour for each component of the TMF cycle could be elucidated. Although by separating the individual components in this way the concomitant effects of the various components of the TMF cycle may not be defined or even occur, which must be kept in mind throughout the model development and subsequent interpretation of the later TMF tests. However, by separating out the various components of the TMF cycle further information on the impact of changes to each of these TMF cycle components with regard to the TGO layer growth kinetics could be established.

Exposure tests were carried out in air under the following conditions:

1. Isothermal
2. Two stage temperature exposures
3. Thermal cyclic
4. Creep (thermal exposure plus load)

Two types of test specimens were used for these tests. For (1), (2) and (3) CMSX4 “button” specimens, coated with the Cranfield TBC system as described in paragraph 3.2.1 were used. For the creep test (4), a CMSX4 “dog bone” as discussed in paragraph 3.2.2 was used. A brief description of the test methods and test matrices used follows for each condition.

4.2.1.1 Isothermal Exposures

Isothermal exposures in air were carried out by placing “button” specimens in a furnace at each of the temperatures and times specified in Table 15.

Table 15 Isothermal exposure test matrix.

Exposure time (h)	Temperature (°C)				
	950	1000	1050	1100	1150
30	●	●	●	●	●
100	●	●	●	●	●
300	●	●	●	●	●
1000	●	●	●	●	●
3000	●	●	●	●	●

4.2.1.2 Two Stage Temperature Exposures

Two stage temperature exposures in air were carried out by placing “button” specimens in a furnace at the “first stage” temperature and then subsequently at the “second stage” temperature for the exposure times specified in Table 16.

Table 16 Two stage temperature exposures test matrix.

First Stage				
Temperature	1000°C	1050°C	1100°C	1100°C
Exposure	300 h	300 h	100 h	300 h
Second Stage				
Temperature	950°C	950°C	950°C	950°C
Exposure	1000 h	1000 h	1000 h	1000 h

4.2.1.3 Thermal Cyclic Exposures

Thermal cyclic exposure tests in air were carried out by automatically inserting and removing “button” specimens into and from a furnace at the temperature and for the number of cycles specified in Table 17. A typical cycle (for 1100°C) is shown in Figure 28.

Table 17 Thermal cyclic exposures test matrix.

Cycles	Temperature (°C)			
	1000	1050	1100	1150
300	●	●	●	●

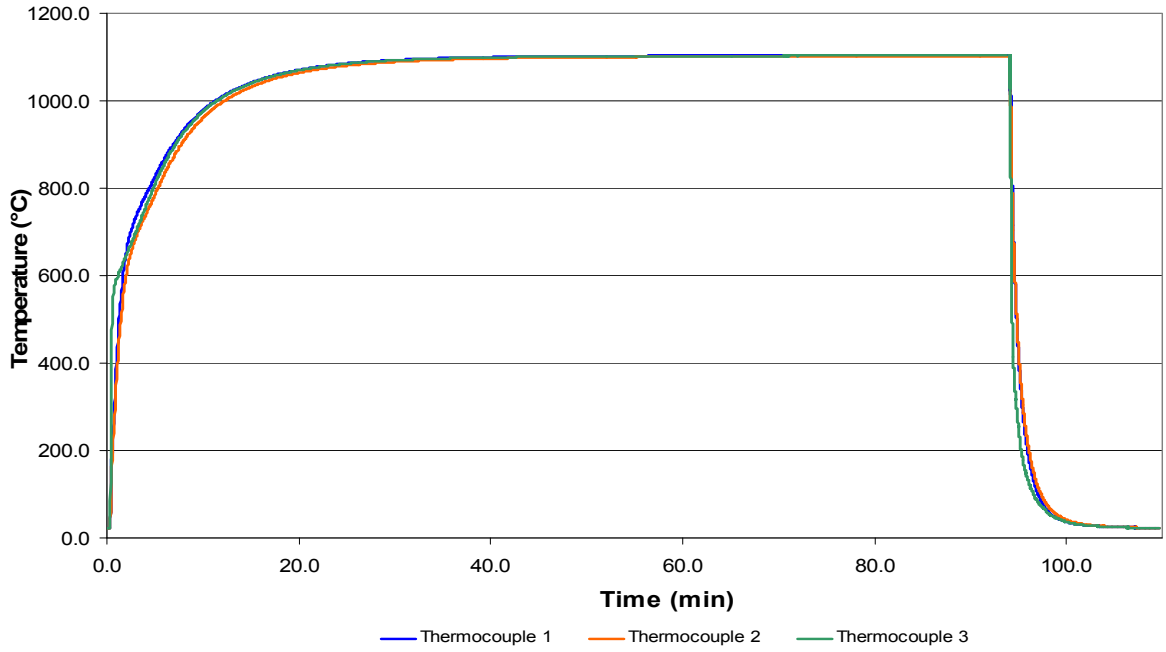

Figure 28 Thermal cyclic rig - Typical cycle 1100°C.

4.2.1.4 Creep

In order to assess the combined effects of load and temperature, a “dog bone” specimen was subjected to a stress of 100 MPa at 1000˚C for 300 hours in a Mayes TC 20 creep test rig.

4.2.1.5 Measurement of the Thermally Grown Oxide layer

On completion of the tests, specimens were sectioned, mounted in Bakelite and prepared for examination in a FEG SEM using standard metallographic techniques (grinding with 240 grit paper until plane, then followed by 1200 and 2500 grit papers with a final polish using colloidal silicon suspension (OPS))[152] by University of Cranfield. Micrographs were obtained using Leo 1550 and JEOL JSM 6500F FEG SEMs in Secondary Electron Imaging (SEI) and Backscattered Electron Imaging (BEI) modes. Image analysis was carried out using ImageJ software, initially by manually measuring the thickness of the TGO layer and later by using user defined macros within ImageJ.

4.2.2 Thermo-mechanical Fatigue Testing of Thermal Barrier Coating

The purpose of the TMF testing of TBC coated specimens is to provide data on an EBPVD TBC system under realistic load/temperature cycles representative of those experienced by turbine blades in service to enable future model developments, with an ultimate aim of validating the model under development by QinetiQ. A series of TMF tests on TBC coated “dog bone” specimens (previously described in paragraph 3.2.2) were carried out. On completion of testing the TGO growth behaviour in terms of thickness and morphology was characterised as described previously at paragraph 4.2.1.5. Prior to presenting the TMF test matrix, details of the TMF test cycle are presented. Both are then

followed by a description of the test equipment used, TMF test requirements for TBCs, the temperature measurement and control systems used during the TMF testing.

4.2.2.1 Thermo-mechanical Fatigue Cycle of an HP Blade

Previous work by QinetiQ under project "RE804 – Structural Integrity and Lifing Studies"[153] considered a high pressure (HP) turbine blade (Figure 29). Finite Element Analysis (FEA) was used to obtain and describe the TMF cycle experienced by the blade, with the most damaging profile seen at the blade trailing edge, see Figure 30. Of the two TMF cycles shown, PT1 was chosen for the TMF testing as the HP blade was exposed to both the highest temperature (875°C) and the highest stress (260 MPa) at a higher temperature (750°C) when compared to cycle PT2. To simplify control of the TMF rig this cycle was converted to a strain versus temperature cycle, and simplified to the idealised cycle shown in Figure 31. There is also a time aspect to the TMF cycle. The original length of the complete cycle[154] was 37920 seconds which included a dwell a temperature of 36000 seconds. In order to keep the overall timescale of a TMF test within reasonable bounds, this dwell at high temperature was reduced to 600 seconds with the complete cycle lasting 1420 seconds, see Figure 32 for details.

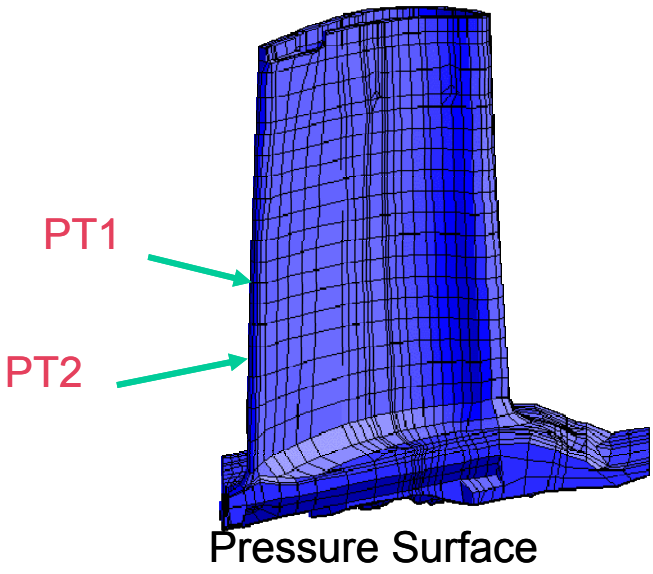

Figure 29 HP turbine blade, area analysed by QinetiQ using Finite Element Analysis[153].

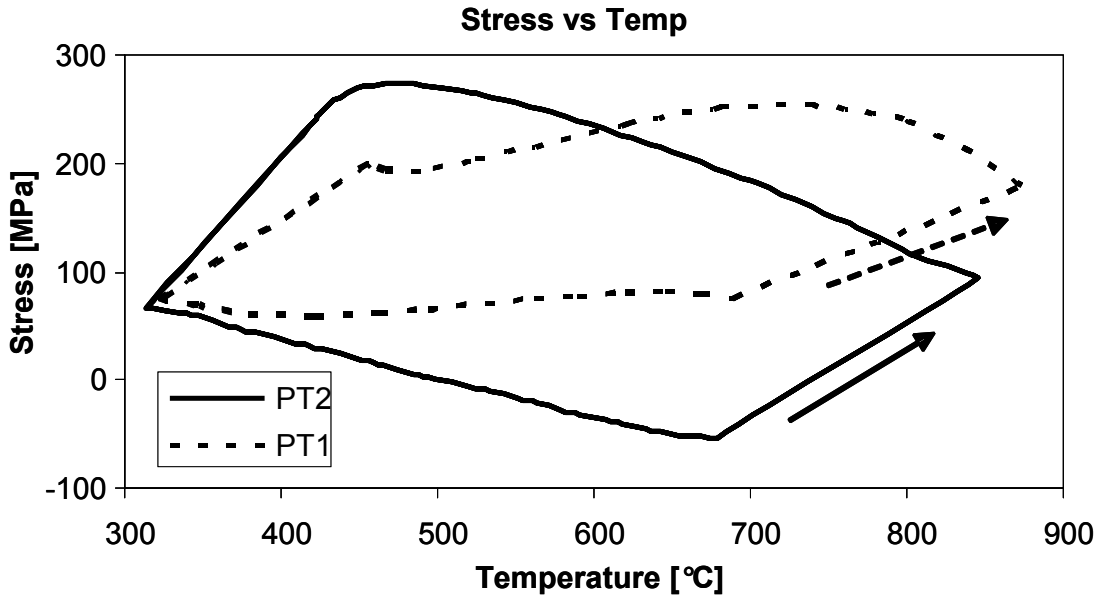

Figure 30 Thermo-mechanical fatigue profile determined by QinetiQ FEA for points PT1 and PT2 on HP turbine blade[153].

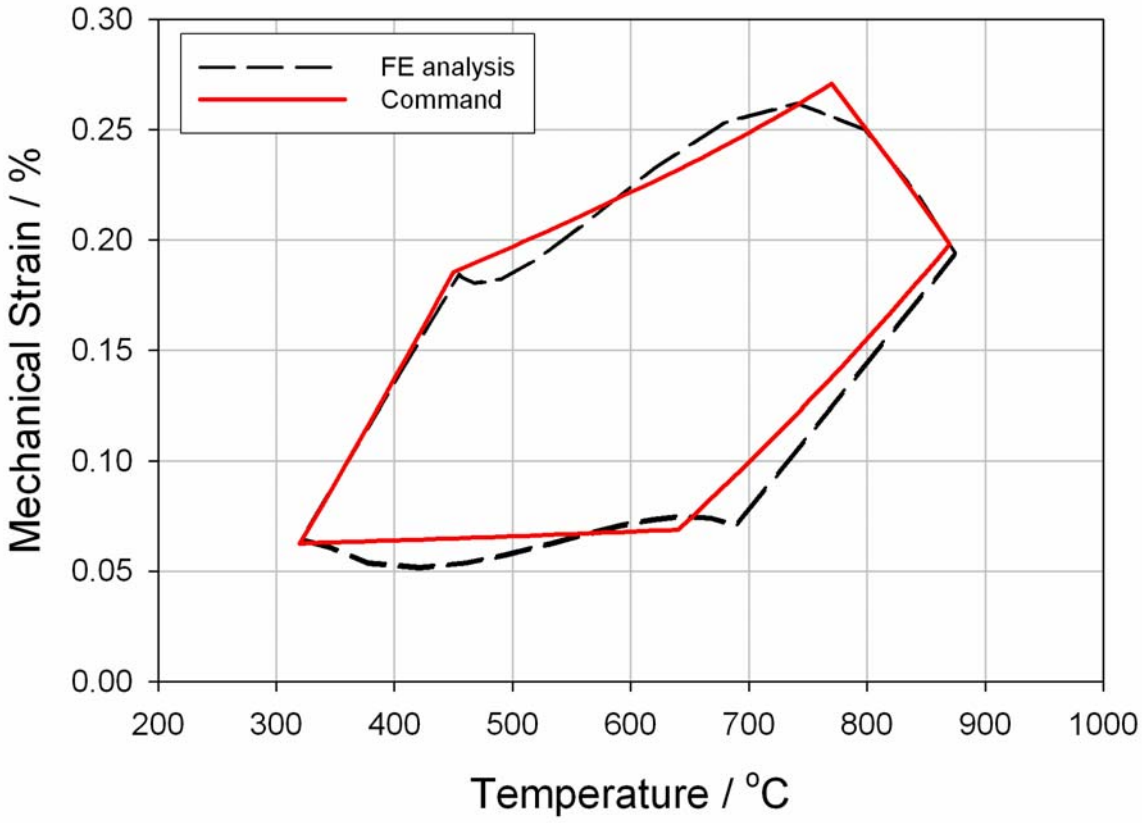

Figure 31 TMF Cycle arising from FEA and Idealised version for command, Strain versus Temperature.

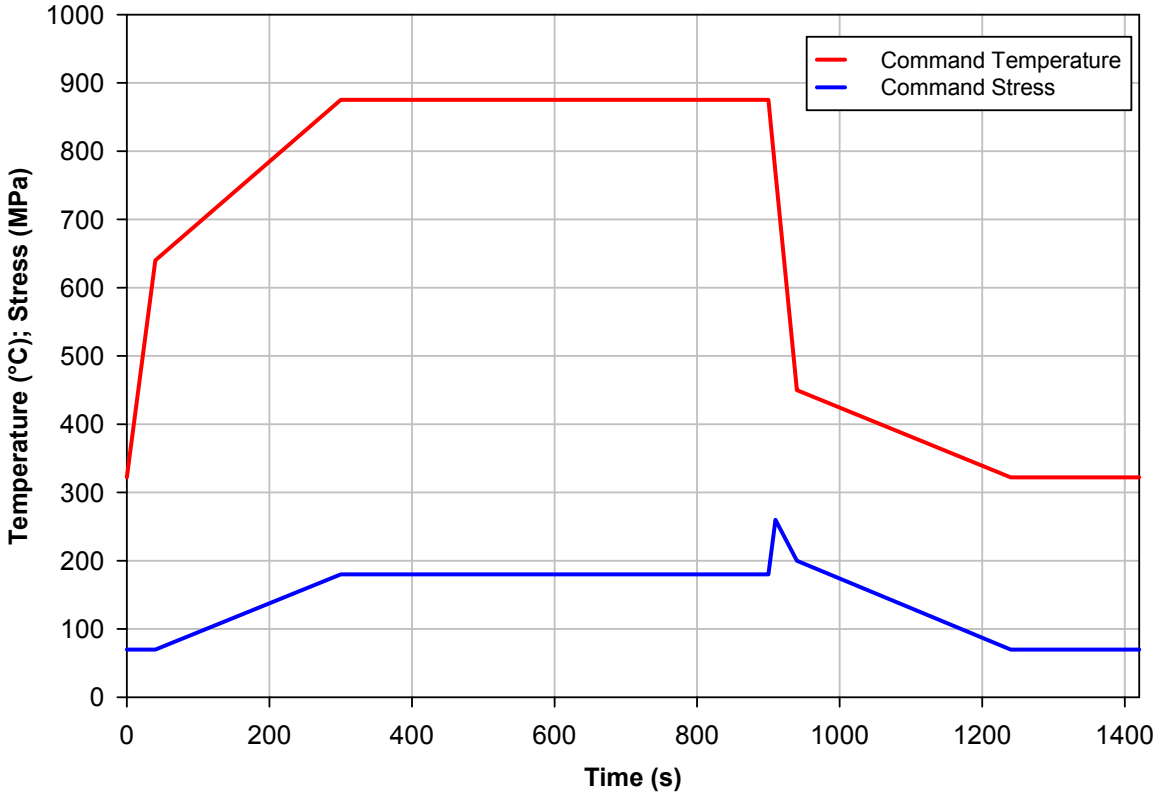

Figure 32 TMF Cycle arising from FEA, Idealised, Temperature and Stress versus Time.

4.2.2.2 TMF Test Matrix

TMF testing using the TMF cycle shown in Figure 32 was carried out on "dog bone" specimens. The aims of the tests were to provide data with regard TGO growth under realistic TMF conditions experienced in service. In order to increase the likelihood of TBC spallation occurring (and hence be able to define the TGO thickness at which this occurred), pre-exposure of some specimens was carried out at 1000°C in air to increase the initial thickness of the TGO layer. The target number of cycles and amount of pre-exposure for each test specimen are shown in Table 18.

Table 18 TMF test matrix.

Pre-exposure at 1000°C in air (h)	TMF Cycles
Nil	1000
100	1000
300	1000
900	1000

4.2.2.3 TMF Test Rig

The TMF tests were carried out on a TMF testing rig consisting of an Instron 8862 electromechanical loading rig with water cooled hydraulically operated grips controlled by an Instron Fast Track 8800 Tower. This basic loading rig was augmented such that test specimens were heated by a Cheltenham Induction Heating (CIH) system using water cooled copper coil(s) and cooled using forced air fed through the centre of the cylindrical

test specimen. Use of a personal computer (PC) running Instron MAX software (version 6.7) permitted simultaneous and co-ordinated control of both the Instron loading rig and CIH system and hence load and temperature at the specimen. A schematic of the arrangement, excluding loading rig and PC controller is provided in Figure 33.

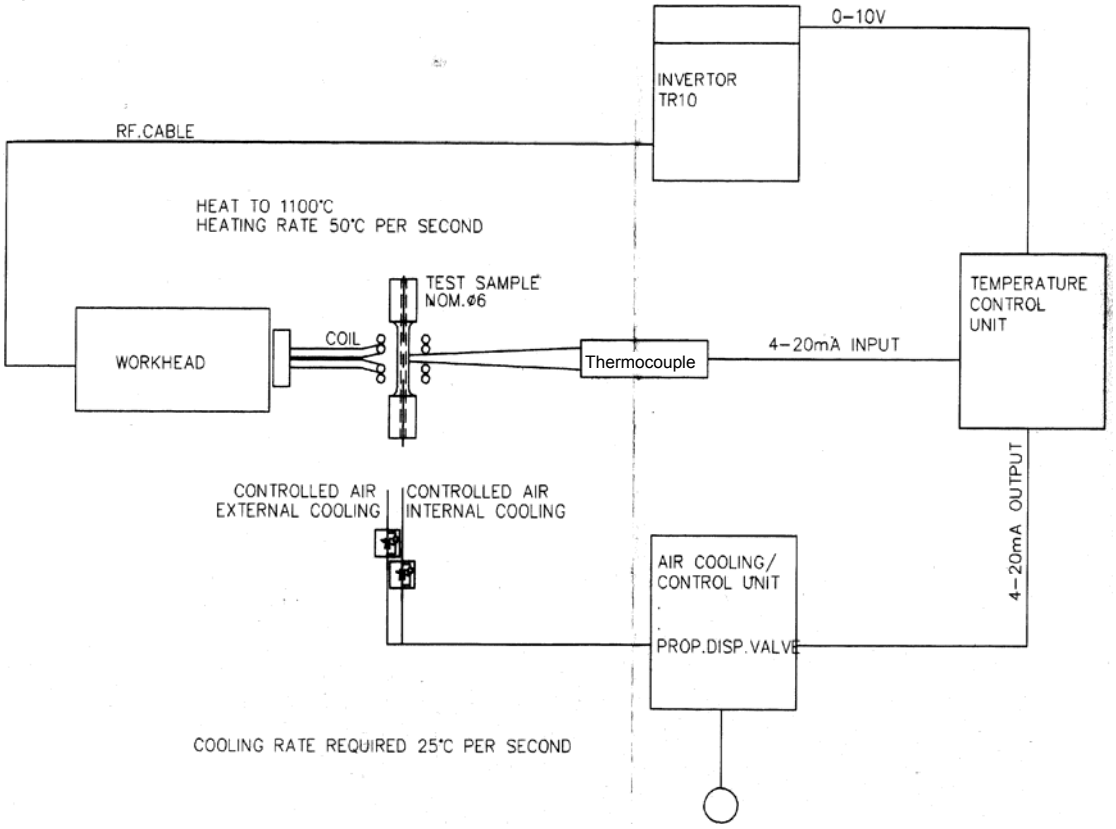

Figure 33 Schematic of TMF Test Rig, excluding PC control and Instron load rig.

4.2.2.4 TMF Testing Requirements for TBCs

Traditional induction heating generates heat from the inside of the specimen, which would, if used, lead to an inverse temperature gradient over the TBC compared to that seen in service, see Figure 34 (after Sourmail[155]). To overcome this issue a susceptor manufactured from Nimonic 115 (T_m = 1304°C), as shown in Figure 35 and Figure 36, was used as an intermediate device to transfer heat to the test specimens once the susceptor had been heated by an induction coil. In this configuration the maximum working temperature of the susceptor (around 1250°C) becomes the limiting aspect of the system. In order to establish a temperature gradient between the TBC top coat and the CMSX4 substrate, the bore of the specimen was cooled with air at a minimum flow rate. The flow rate of cooling air could be increased automatically above this minimum limit in order to increase the cooling rate of the specimen when required.

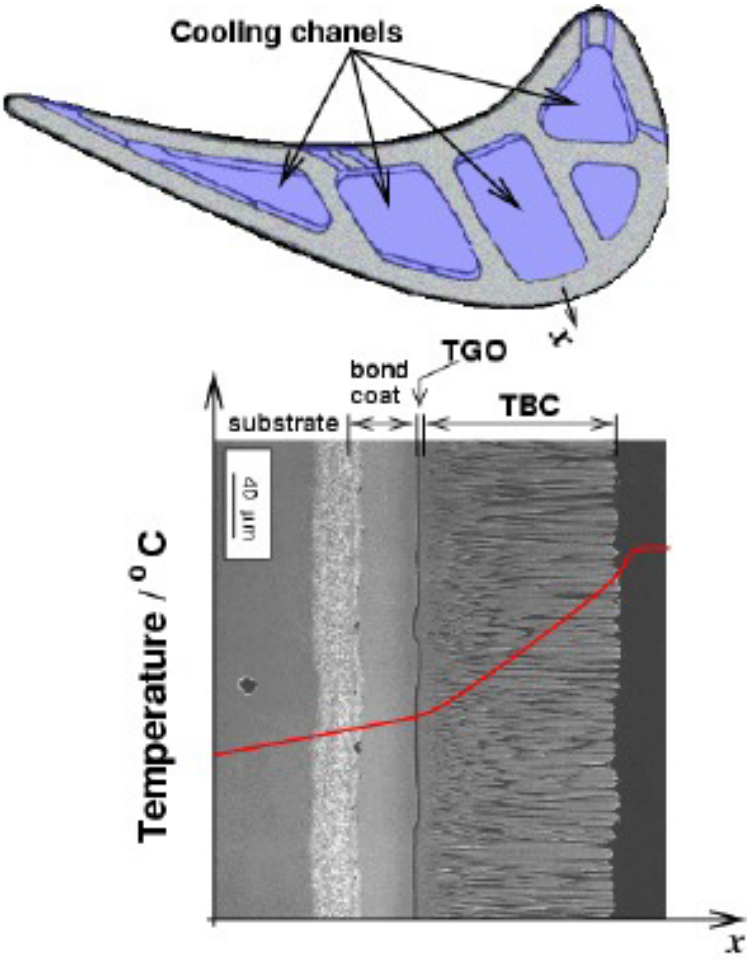

Figure 34 Schematic of temperature profile across a turbine blade with TBC applied [155].

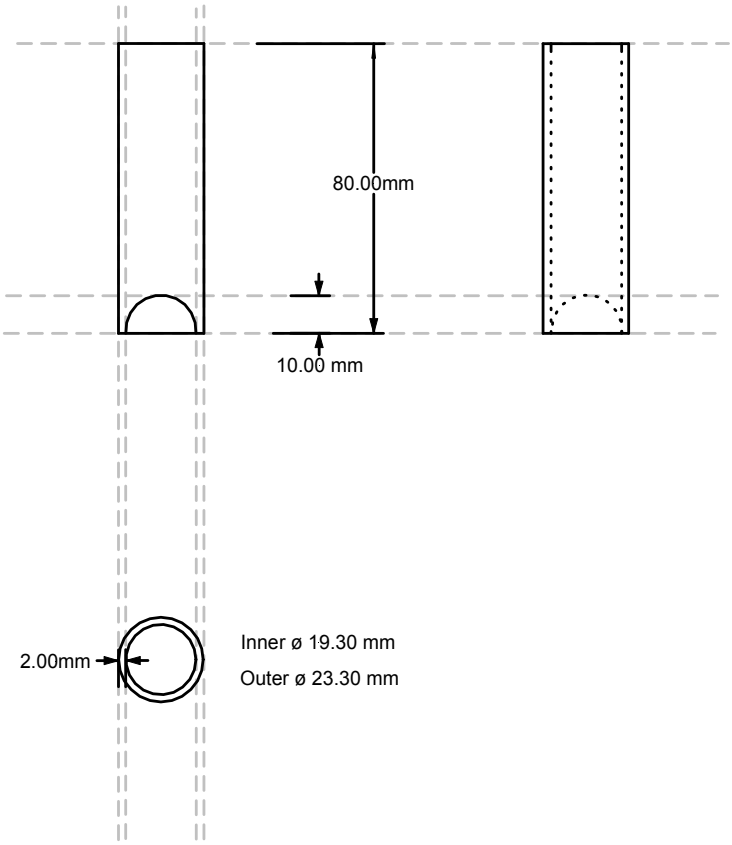

Figure 35 Final design of susceptor for TMF testing.

Figure 36 Nimonic 115 susceptor with heating coil close to maximum working temperature of 1250°C.

4.2.2.5 Temperature Measurement

Temperature sensing at the specimen was required for control and data gathering purposes. The substrate temperature was selected as the system control temperature as this temperature could if required be compared directly to the material performance of the blade surface modelled under previous work. As a susceptor was being used, optical pyrometry, which relies on line of sight, could not be used. However, even if this issue could be overcome, pyrometry cannot be used with TBCs as they are infra-red transparent and therefore it would not be possible to distinguish between the surface or substrate temperature. It was also important that any method used did not damage the TBC top coat, as it would not be possible to isolate the effects of this damage from other damage mechanisms under investigation. To overcome these issues and limitations a new method for thermocouple placement was implemented. A 0.25mm diameter thermocouple was used and a 0.3 mm diameter hole was drilled using electric discharge machining (EDM) to accommodate it. The hole started outside of the TBC coated area of the TMF “dog bone” specimen (above the shoulder) and terminated at the mid point of the specimen gauge length just below the substrate surface as shown in Figure 37. FEA was used to analyse the effect of this hole by carrying out an anisotropic elastic calculation using the elastic parameters representing CMSX4. As can be seen from Figure 38, it was

found that the hole does not significantly perturb the stress state along the gauge length of the specimen. A 0.25 mm diameter K-type mineral insulated thermocouple was inserted in this hole as shown in Figure 39(a) and used to monitor the substrate temperature. TBC top coat temperature was monitored using an R-type thermocouple that was manufactured to have a thin sensing junction and securing loops that permitted mechanical attachment to the “dog bone” specimen with Refrosil (asbestos replacement containing string), see Figure 39(b). To determine whether remote temperature sensing could be used to control the temperature at the substrate for the first TMF test a thermocouple was attached to the TMF “dog bone” at the shoulder of the specimen as shown in Figure 39(c). Another K-type thermocouple was attached to the inner surface of the “dog bone” specimen bore to permit monitoring of this temperature (not shown). Figure 39(d) shows the additional support provided to all thermocouples by a stainless steel strip spot welded to the specimen, this was to ensure sufficient robustness during specimen installation in the testing machine. Data was gathered using the MAX software on the controlling PC and an additional standalone PC running POD data logging software.

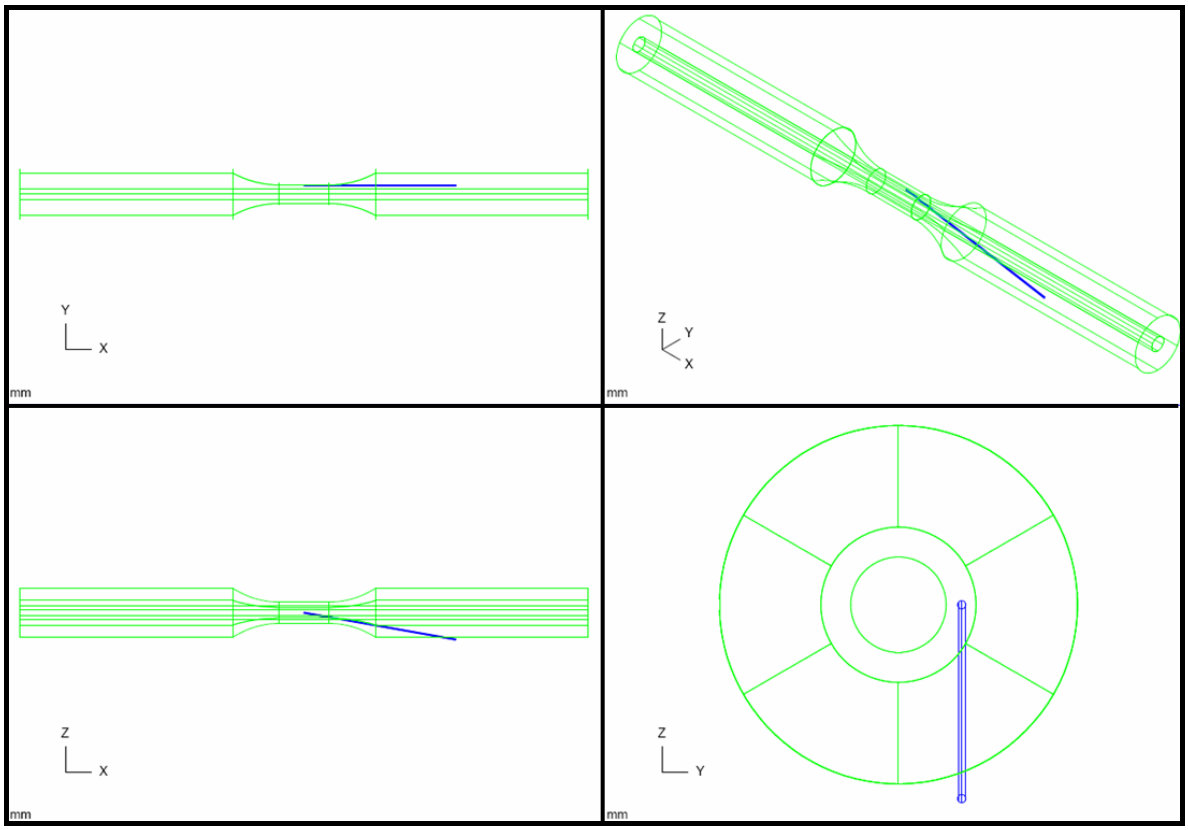

Figure 37 EDM drilling of "dog bone" specimen from above shoulder to mid-point of gauge length.

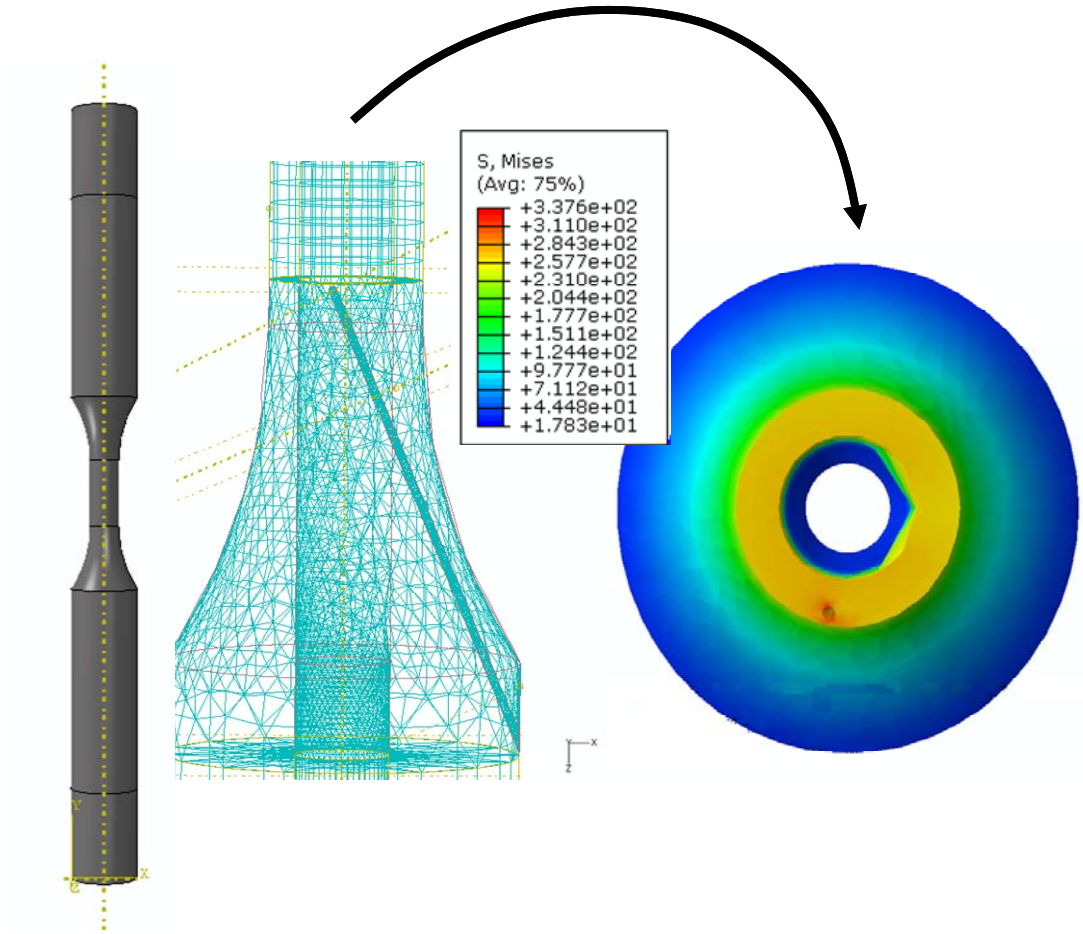

Figure 38 FEA of TMF "dog bone" specimen with the newly designed EDM hole. Note stress perturbation at the hole is minimal.

(a)

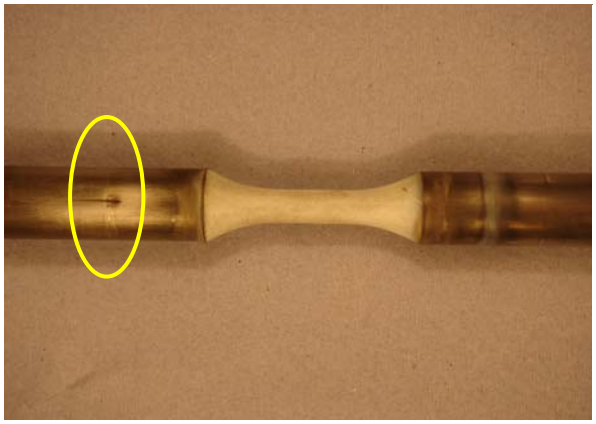

Entry hole of substrate thermocouple (T/C)

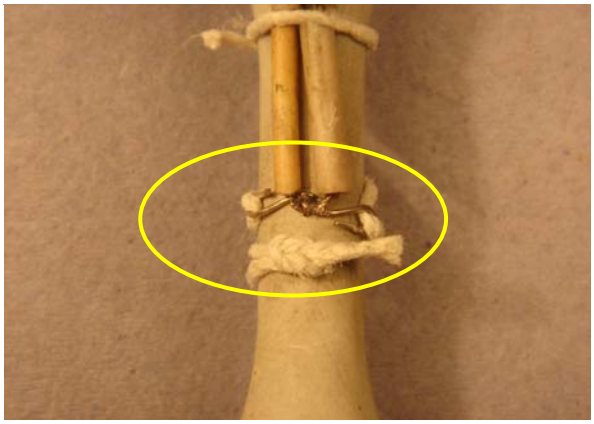

TBC top coat T/C with attachment loops (b)

(c)

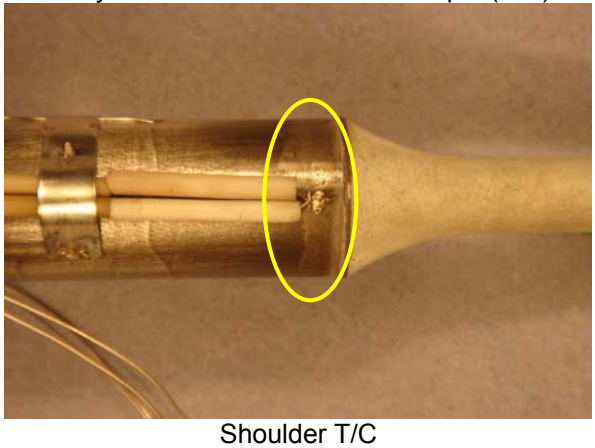

Shoulder T/C

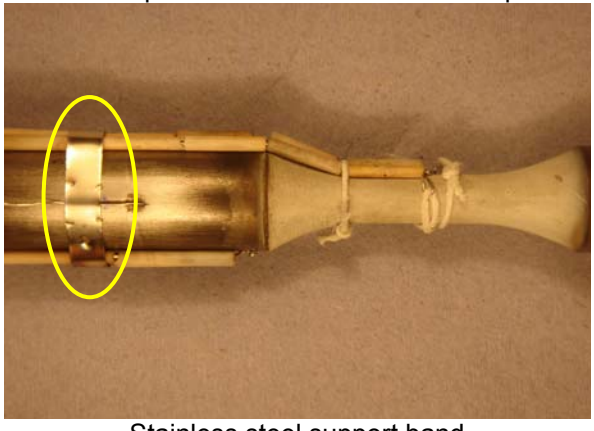

Stainless steel support band (d)

Figure 39 TMF "dog bone" specimen thermocouple positions.

4.2.2.6 TMF Test Rig Control

The idealised TMF cycle shown in Figure 32 was used to control the TMF test rig in both the stress and temperature control channels. The stress channel control was provided using the standard transducer feedback and actuator control system within the Instron 8862 electromechanical loading rig. The control algorithm parameters (proportional, integral, differential and lag (*PIDL*)) were optimised for the test specimen shape and material using the in-built tuning algorithm within the MAX software. Control of the temperature channel used the substrate thermocouple monitoring the substrate temperature, as described in paragraph 4.2.2.5. This temperature measurement was provided to: (1) a Eurotherm 900 EPC controller for heating control via the CIH Induction heater; and; (2) a Eurotherm 2408 controller for cooling air control. Both Eurotherm controllers Set Points (SP) were defined remotely and dynamically by the MAX software. The auto-tune algorithms for these two channels did not optimise the *PIDL* parameters for these controllers and had to be established experimentally and set manually. As the control response varied with temperature of the test, gain scheduling within the Eurotherm controllers was used to limit the effects of this. Gain scheduling permits different *PIDL* calibrations to be established for different temperature bands with changeover occurring automatically.

5 Results

In this section, the *Results of N18 and LSHR Testing and Comparison with RR1000, U720Li and U720Li LG* are presented first. These are followed by the *Results of Thermal Barrier Coating Testing and Analysis*.

5.1 Results of N18 and LSHR Testing and Comparison with RR1000, U720Li and U720Li LG

In this section the results from the N18 and LSHR testing carried out by the University of Southampton and QinetiQ are presented. In addition to these results and to enable comparisons against other materials to be made, the results from previous research carried out at the University of Southampton and QinetiQ are also provided. This additional data is drawn from H.T. Pang's PhD thesis[21] and a report by Hide *et al* [20].

Therefore, in addition to N18 and LSHR, two other materials with a total of three microstructural variants are presented in the following paragraphs, these are: RR1000, U720Li and U720Li LG.

For ease of reference and comparison all results figures and tables are presented in section 9.

5.1.1 Microstructure

In this section the results from the microstructure analysis are presented, with those for N18 first, followed by LSHR and finally for the three comparison materials.

5.1.1.1 Microstructure of N18

The microstructures of N18 revealed by Orthophosphoric etch, Kalling's Reagent and Nimonic etch are shown in Figure 40(a), Figure 41(a) and (b) and Figure 41(c) to (f) respectively. Using ImageJ, grain size *DCircle* diameter has been found to lie in the range of 1.5 – 24.5 μm with a mean and standard deviation of the grain size distribution of 8.7 ± 4.7 μm. (Figure 56 and Table 25). Mean relative circularity for the grain size was found to be 0.62 (Figure 57). In both the optical and FEG-SEM micrographs, incoherent primary γ′ can be inferred at the grain boundaries, its *DCircle* diameter has been determined to lie within the range of 0.4 – 5.1 μm with a mean of 2.19 ± 0.98 μm (standard deviation of the grain size distribution) (Figure 60 and Table 25). With the mean relative circularity was determined to be 0.6 (Figure 61). If the grain and primary γ′ *DCircle* measurement data for N18 is combined (Figure 67) and compared with the same combined measurements available from the Electron Backscatter Diffraction (EBSD) analysis (Figure 54) which has been produced from the EBSD grain (and primary γ′) size map shown in Figure 50 it can be seen to be comparable. The pole figures available from this analysis shown in Figure

51 show that crystal orientation within the alloy appears to be random indicating texturing effects are not present.

At higher magnifications, Figure 41(e) and (f), it can be seen that secondary γ' form a typical ogdoadically-diced cube structure; with a range of 5 to 568 nm (Figure 62), and mean *DCircle* diameter of 188 ± 112 nm (Table 25). At these highest magnifications the tertiary γ' can be resolved. In the specimens of N18 etched with Kalling's Reagent shown in Figure 41 (a) and (b), grain boundaries are defined, primary γ' on grain boundaries can be seen, and the differing contrast shows up annealing twins. The higher magnification electropolished specimen of N18 (Figure 42) shows a grain boundary between two primary γ' with secondary and tertiary γ' also revealed. A plain polished specimen of N18 is shown in Figure 49, the contrast between the darker γ' and lighter γ matrix indicating that the γ matrix contains more of the heavier elements when compared with the γ' precipitates. Much of the grain boundaries and γ / γ' interfaces also appear very light, this could be explained due to the formation of borides ($(MoCr)_2B$) discussed by Cadel *et al*[15] at grain boundaries or it could be due to the partitioning of Hf as Hafnia to the grain boundaries, although Energy-dispersive X-ray spectroscopy (EDX) analysis did not detect Hf at the grain boundaries nor were the results for B conclusive, probably due to the low atomic mass of B. TEM micrographs of N18 are presented in Figure 41 (g) and (h). Using these micrographs, the sizes of the tertiary γ' was found to be in the range of 13 to 48 nm, see Figure 66, with a mean of 25 nm.

5.1.1.2 Microstructure of LSHR

The microstructures of LSHR are revealed by Orthophosphoric acid, Kalling's Reagent, Nimonic etch and electro polishing in Figure 40 (e) and (f), Figure 43 (a) and (b), Figure 43 (c) and (d) and Figure 43 (e) to (h) respectively. Immediately obvious are the much coarser grains present in LSHR shown by the comparison of the same scale micrograph in Figure 40 (e) with the other alloys presented in Figure 40 (a) to (d). Also there is no primary γ' present as may be expected following a super-solvus heat treatment. Grain boundaries are clearly delineated in the micrographs of specimens etched with Kalling's Reagent (Figure 43 (a) and (b)), and have a quite straight un-serrated appearance. Some twinning can be seen in these micrographs; although this is much clearer in the micrographs of the electro polished specimens presented in Figure 43 (e) and (f). Grain size *DCircle* diameter were determined using ImageJ and found to lie in the range 3.6 to 116.4 μm (Figure 58 and Table 25) with a mean value of 35.9 μm and standard deviation of 21.2 μm. Mean relative circularity of 0.7 (Figure 59) is slightly higher than N18, which is perhaps to be expected from a higher temperature heat treatment. Grain size data and pole figures from EBSD analysis are presented in Figure 52 and Figure 53 respectively. This permits a comparison of the grain size data to be carried out with the ImageJ

measured data presented in Figure 58 showing some correlation to that obtained using EBSD in Figure 55, a smaller specimen was measured using ImageJ when compared with EBSD and this goes some way to explaining the lack of a full correlation between the two figures. As with N18 the pole figures indicating that there are no texturing effects and random crystal orientation. Secondary γ' is revealed on the higher magnification micrographs of LSHR etched with Nimonic etch, Figure 43 (c) and (d) and electro polished specimens Figure 43 (g) and (h). The secondary γ' appears to be more spherical than that seen in N18 although this is not borne out by the relative circularity measurements which are presented for N18 in Figure 63, and LSHR in Figure 65 indicating an ellipsoid shape for the LSHR secondary γ' particles. The secondary γ' *DCircle* diameter ranges from 12 to 168 nm (Figure 64 and Table 25) with a mean *DCircle* diameter of 76nm and standard deviation of 29 nm. Closer examination of the highest magnification micrographs (Figure 43 (d) and (h)) reveals little evidence of tertiary γ' consistent with some examples in the literature for this particular combination of heat treatment and cooling rates[61], TEM foils were therefore not produced for this alloy.

5.1.1.3 Microstructure of Comparison Materials: RR1000; U720Li and U720Li LG

Optical, SEM and TEM micrographs for RR1000, U720Li and U720Li LG are shown in Figure 44, Figure 45 and Figure 46 respectively. These at: (a) highlight the grain boundaries and show incoherent primary γ′ at the grain boundaries; (b) show the primary γ' size by etching the alloy; (c) show secondary γ' sizes from TEM replicas and (d) show the tertiary γ' size from TEM replicas. As a summary, the grain, primary γ', secondary γ' and tertiary γ′ sizes and distributions are reproduced from previous work[21] in Table 25. To allow visual comparisons to be made micrographs showing similar features of each of the alloys have been presented by feature at the same scales. Optical micrographs after Orthophosphoric acid etching showing the grain and primary γ' sizes are presented in Figure 40. SEM micrographs providing details of the secondary γ' morphology and size are shown in Figure 47. Details of the tertiary γ' sizes and distribution can be seen in the TEM micrographs presented in Figure 48.

5.1.1.4 Comparison between the Microstructure of N18, LSHR, RR1000, U720Li and U720Li LG

Using Table 25, it can be determined that RR1000 and U720Li have similar grain sizes as well as primary, secondary and tertiary γ′ sizes. The grain size values of N18 fall between those of RR1000 / U720Li and U720Li LG, especially when the larger outlying grains are taken into account. LSHR clearly has the largest grains on average over twice as large as those seen in U720Li LG and outliers being nearly three times larger than the largest seen in the other alloys. The primary γ' sizes for all the sub-solvus heat treated alloys are all of

a similar size. The secondary γ' size of N18 is found to have a relatively coarse distribution compared with U720Li variants and RR1000, although its mean size is similar to that seen in U720Li LG. By comparison with the other alloys presented here, the secondary γ' in LSHR has the smallest mean diameter. The tertiary γ′ observed in N18 is again somewhat coarser than reported in these other PM alloys.

5.1.2 Hardness Testing of N18 and LSHR

The room temperature hardness of N18 was measured as 424.2 ± 3 Hv10, somewhat lower than the hardness of any of the comparison materials shown in Table 26.

For LSHR, the room temperature hardness was measured as 463.6 ± 5.7 Hv10, which is similar to RR1000 and U720Li (see Table 26).

5.1.3 Tensile Testing of N18 and Comparison Materials

The results of the N18 tensile testing carried out by QinetiQ are provided in Figure 68 and are summarised with reported results for LSHR, RR1000, U720Li and U720Li LG in Table 27, the data from which has been plotted in Figure 69 (the data for LSHR presented in this table has a different heat treatment[64] to that supplied by NASA for long crack fatigue testing). A tensile test result for a single temperature (704°C)[61] is available for LSHR with a similar heat treatment to that applied to the long crack fatigue specimens, (this is shown on the graph in Figure 69).

Tensile testing revealed only a modest decrease in 0.2% proof stress between 20°C and 750°C in N18. A slightly larger decrease is reported for LSHR[64] between the same temperatures. However the U720Li reported values[62] indicate a higher 0.2% proof stress at 20°C than N18, but a lower value at 650°C. This indicates that although the strength was initially higher in U720Li the strength falls off more rapidly with increasing temperature. When compared with N18 and LSHR, the 0.2% proof stress of RR1000 falls the most from 650°C to 750°C. The UTS of the N18 and LSHR drop more significantly with increasing temperature, LSHR slightly less than N18, indicating a reduced work hardening capacity at higher temperatures, although this capacity is better for LSHR than N18 due to the relative divergence of 0.2% proof stress and UTS when compared with N18.

N18 LCF testing results are presented in sub-section 5.1.6. As full stress / strain curves were obtained during these tests, it is possible to ascertain if cyclic softening occurs between the first cycle and 50% lifetime cycle at both 650°C and 725°C. It is therefore pertinent to introduce these curves and the cyclically stabilised yield stress data in this sub-section.

Analysis of the stress-strain response during loading for the LCF testing is carried out in section 5.1.6, this indicated that only a small amount of cyclic softening, approximately 28

MPa, was exhibited by the material at 650°C (see Figure 115). However, at 725°C (Figure 116), significant cyclic softening was observed, approximately 66 MPa.

5.1.3.1 Tensile Testing Fractography for N18

Tensile test fracture surfaces were compared at room temperature, 650°C and 750°C see Figure 70. At room temperature a typical cup-cone type fracture was observed with limited shear lips formed at the specimen sides (a) whereas at the higher temperatures far larger shear lips were produced together with significantly increased oxidation (c) and (e). Ductile rupture processes were observed in all specimens (b), (d) and (f).

5.1.4 Creep of N18 and Comparison Materials

Creep strain against time curves for N18 tests carried out by QinetiQ at 650°C at 800 MPa and 900 MPa and 725°C at 330 MPa and 560 MPa are presented in Figure 71, with the total creep rupture life data for N18 and U720Li[1] presented in Table 28. Very little primary or secondary creep was observed in N18. The creep tests revealed that N18 was more creep-resistant when compared with U720Li, with significantly longer creep rupture lives observed at directly comparable stress levels at both 725°C and 650°C. To permit comparisons to be drawn creep rupture lifetimes for LSHR [64] and RR1000[156] were obtained from the literature and presented in Table 29 and Table 30 respectively although it should be noted that the heat treatment conditions for these examples are different to the comparison materials established earlier. A creep result for a single temperature (704°C)[61] is available for LSHR with a similar heat treatment to that applied to the long crack fatigue specimens, (this is shown on the graphs in Figure 152 and Figure 153).

5.1.4.1 Creep Fractography for N18

Creep test rupture surfaces obtained at 650°C at 900MPa (lifetime = 623hrs) and 725°C at 560MPa (lifetime = 364hrs) were examined. The longer lifetime test at 650°C showed two regions of stable creep crack growth, which can be seen in Figure 72(a). Both regions of stable crack growth were linked to initiation from a heterogeneous particle, probably an oxide inclusion, which can be seen in (c) and (d). In the stable crack growth regions some evidence of intergranular failure modes was observed (e) and (f) although in comparison with the overload rupture surface (b), it could be seen that it also showed evidence of void formation/cavitation processes typical of ductile rupture processes and no stark difference in failure mode was observed between the two regions. The creep rupture surface at 725°C (g) showed no distinctive differences in the overload failure region (h), and no region of stable crack growth was observed, as was found in the longer lifetime test.

5.1.5 Long Crack Fatigue Propagation of N18, LSHR and Comparison Materials

To permit comparisons in fatigue crack growth (FCG) performance between the various tested conditions, graphs of *da/dN* versus ΔK were plotted using the results from the FCG tests carried out in air and vacuum at 650°C and 725°C under both 1-1-1-1 and 1-20-1-1 trapezoidal loading conditions. These graphs are initially presented by alloy and then used to compare the performance of the N18, LSHR, RR1000, U720Li and U720Li LG.

5.1.5.1 Long Crack Fatigue Propagation of N18

FCG curves obtained from testing N18 using a 1-1-1-1 and 1-20-1-1 trapezoidal load cycle are presented in Figure 73 and Figure 74 respectively, with both load cycles combined in Figure 75.

For the 1s dwell tests (Figure 73), under both air and vacuum conditions, as expected there is an increasing crack growth rate with increasing ΔK and for the higher temperature tests in the same environment a slight increase in crack growth rate is seen when compared with the lower temperature test. At ΔK=25 MPa√m the crack growth rate under vacuum conditions is about a fifth of that seen for tests carried out in air, although this separation is reduced to around a factor of two at ΔK=45 MPa√m. There is also an increase in the slope of the *da/dN* versus ΔK curves for the vacuum tests when compared to the slope seen for the air tests such that the crack growth rates are converging with increasing ΔK. The discontinuity which can be seen in the air test carried out at 725°C is due to the test tripping off and being restarted.

For the 20s dwell tests (Figure 74), (as expected) there is increasing crack growth rate with increasing ΔK but with a more marked increase in crack growth rate for the higher temperature tests when compared with the lower temperature test carried out in the same environment. At ΔK = 25 MPa√m crack propagation rates for tests carried out in air are increased by about a factor of four and five for 650°C and 725°C respectively when compared to those tests carried out in vacuum conditions, at ΔK = 45 MPa√m this is reduced slightly to about factors of three and four for the same temperatures. Although the reverse of this trend is seen if temperature effects only are considered for both the air and vacuum tests, Figure 88(c). In effect the crack growth rates for each temperature in both air and vacuum are diverging with increasing ΔK. There is also an increase in slope of the *da/dN* versus ΔK curves for each vacuum test, but only when each temperature is compared in isolation.

When the 1s and 20s dwell tests are compared (Figure 75), it is apparent that in both air and vacuum tests the most pronounced change in crack growth rate occurs at 725°C when a 20s dwell is used. It can also be seen that the increase in magnitude of the crack

growth rate with the change in environment for all four testing conditions is similar The combination of both of these changes in testing conditions can be seen in the highest crack growth rate for N18 at 725°C in air using a 1-20-1-1 trapezoidal load cycle.

5.1.5.2 Long Crack Fatigue Propagation of LSHR

LSHR was tested using a 1-20-1-1 trapezoidal load cycle, these graphs are presented in Figure 76. Note that the *da/dN* axis is a different scale to previously presented graphs. To permit comparisons with other materials to be made more easily, the graphs have been replotted in Figure 77 using a *da/dN* scale range between $1x10^{-8}$ and $1x10^{-4}$ as presented previously for N18.

For the tests carried out under vacuum conditions the initial ΔK was increased to 20 MPa√m in order to obtain crack grow out. For all conditions there is an increasing crack growth rate with increasing ΔK, with a large increase in crack growth rate for the higher temperature test carried out in air when compared with the test at lower temperature. The shape of the curve for the test carried out in vacuum at 650°C is atypical in that failure of specimen occurs at much lower ΔK. Ideally this test would have been repeated to confirm this result, it does, however, have a segment which appears to be in the Paris regime between ΔK ~ 23 MPa√m and 40 MPa√m, whereas, the vacuum test carried out at 725°C is in this regime between ΔK ~ 25 MPa√m and 60 MPa√m. For the tests carried out in air the crack growth rate increases between 650°C and 725°C at ΔK = 25 MPa√m by about a factor of 38 and at ΔK = 45 MPa√m by about a factor of 32. The effect that temperature has on the crack growth rate under vacuum conditions is much less pronounced, the rate increases by about a factor of around two between 650°C and 725°C at both ΔK = 25 MPa√m and ΔK = 45 MPa√m. At these same levels of ΔK, the effect of environment can also be seen by comparing the crack growth rates achieved in vacuum with those in air, here, about a factor of eight increase is seen at 650°C at ΔK = 25MPa√m and about a factor of 136 at 725°C at ΔK = 25MPa√m with the factors falling to four and 74 as ΔK is increased to 45 MPa√m. Except for the test carried out in vacuum at 650°C, discussed earlier, there are no significant changes in slope between the air or vacuum curves or due to a change in temperature.

5.1.5.3 Long Crack Fatigue Propagation of Comparison Materials: RR1000; U720Li and U720Li LG

The results of the previous fatigue crack propagation studies[20,21] for RR1000, U720Li and U720Li LG at 650°C and 725°C in air and vacuum are reproduced graphically for the tests using a 1-1-1-1 trapezoidal load cycle in Figure 80 and a 1-20-1-1 trapezoidal load cycle in Figure 81, with the data from both of these graphs being combined in Figure 82.

For those tests carried out using a 1-1-1-1 trapezoidal waveform (Figure 80), crack growth rates increase for all alloys with increased ΔK under all test conditions. The fatigue crack growth rate for RR1000 is similar at 650°C in air and under vacuum conditions. Increasing the temperature in air increases the fatigue crack growth rate for all alloys, but for RR1000 increasing the temperature in a vacuum improves the crack growth rate, this effect will be discussed later. Under vacuum conditions the best performing alloy is U720Li LG at 650°C. The best performing alloy in air, in terms of fatigue crack growth rate, is RR1000 at 650°C with U720Li having the fastest crack growth rate at 725°C. The fatigue crack growth rate of RR1000 at 725°C is similar to that of U720Li LG at 650°C. When compared to crack growth rates in vacuum, at ΔK = 25 MPa√m the crack growth rates for RR1000 and U720Li LG in air increase by a factor of around one and three respectively, whereas at ΔK = 45 MPa√m, this factor remains the same for U720Li LG but falls to around 0.5 for RR100. For U720Li there is an increase in fatigue crack growth rate by a factor of about two due to the increase in temperature from 650°C to 725°C at ΔK = 45 MPa√m, whereas the crack growth rate at ΔK = 25 MPa√m is similar at both temperatures.

With the dwell increased to a 1-20-1-1 load cycle (Figure 81), in general fatigue crack growth rates increase with increasing ΔK and increasing temperature. Under vacuum the slowest fatigue crack growth rates are exhibited by U720Li and U720Li LG at 650°C. In this environment, the performance of RR1000 is similar at both temperatures. Increasing the temperature to 725°C increases the fatigue crack growth rates of both U720Li and U720Li LG by about a factor of four and eight respectively at ΔK = 45 MPa√m and in both cases the slopes increase in a similar fashion. The situation is different with the change of environment to air, here the performance of RR1000 and U720Li LG is comparable at 650°C with U720Li having the fastest fatigue crack growth rate at this temperature. Increasing temperature to 725°C, increases the fatigue crack growth rate of RR1000 by a factor of around seven at ΔK = 45 MPa√m. Approximately double this rate of increase is seen for U720Li LG at the same ΔK, however, *cf.* RR1000, the performance of U720Li LG is improved at lower values of ΔK and higher fatigue crack growth rates are seen at higher values of ΔK. The fastest fatigue crack growth rates under 1-20-1-1 load cycle conditions are seen in U720Li at 725°C in air, an increase of around a factor of 43 at ΔK = 25 MPa√m and around a factor of 27 at ΔK = 45 MPa√m when compared to the crack growth rate of the same material at 650°C under the same conditions.

5.1.5.4 Comparisons Between Long Crack Fatigue Propagation of N18, LHSR, RR1000, U720Li and U720Li LG

In order to permit further comparisons between N18, LSHR and the comparison alloys to be made, further graphs showing fatigue crack growth rates have been plotted for

comparing N18 and LSHR in Figure 78 and Figure 79 and for progressively more aggressive test conditions combining both 1-1-1-1 and 1-20-1-1 loading cycles at a single temperature and environment. The following graphs are presented for tests carried out under 1-1-1-1 and 1-20-1-1 loading cycles: Vacuum at 650°C and 725°C in Figure 83 and Figure 84 respectively; Air at 650°C in Figure 85 and 725°C in Figure 86. A final comparison graph is presented in Figure 87. This permits a comparison of the fatigue crack growth rates to be carried out between the conditions normally considered the most benign (650°C in vacuum using 1-1-1-1 load cycle) and the most aggressive (725°C in air using 1-20-1-1 load cycle) for those tested. (Throughout the comparisons, it should be borne in mind that LSHR has only been tested under 20s dwell conditions and results for a 1s dwell in this material are not presented.)

For tests carried out in vacuum at 650°C (Figure 83), the crack growth rates of all alloys under both load cycles increased in a similar manner as the value of ΔK increased. The alloys with the lowest crack growth rates are LSHR with a 1-20-1-1 load cycle and U720Li LG with a 1-1-1-1 load cycle. RR1000 with a 1-1-1-1 load cycle had the fastest crack growth rate, although to put this into context the lowest and highest crack growth rates only vary by a factor of about four for a particular ΔK, between ΔK = 25 MPa√m and ΔK = 45 MPa√m. For both N18 and RR1000 the fatigue crack growth rate reduced when the load dwell was increased from 1s to 20s.

Under vacuum conditions at 725°C (Figure 84), the variance between the alloys, for a particular ΔK, between ΔK = 25 MPa√m and ΔK = 45 MPa√m, increased to a factor of around 6. Under these conditions RR1000 when tested with a 1s dwell was the best performing alloy. N18 and U720Li LG both with a 20s dwell had the highest fatigue crack growth rates, joined by U720Li above ΔK = 23 MPa√m.

For the air tests carried out at 650°C (Figure 85), the slopes of all the fatigue crack growth curves are reasonably similar. Over the range of ΔK = 25 MPa√m to ΔK = 45 MPa√m the fatigue crack growth rates vary by approximately factors of seven and five respectively. Again the best performing alloy is RR1000 using a 1s dwell and the alloy with the highest crack growth rate is U720Li when a 1s dwell is used. At ΔK < 30 MPa√m N18, U720Li and U720Li LG for a particular ΔK exhibit a reduced crack growth rate when the dwell is increased from 1s to 20s.

At 725°C in air (Figure 86), the best performing alloy is RR1000 under 1-1-1-1 and 1-20-1-1 load cycle test conditions at ΔK = 45 MPa√m. With an applied 1-20-1-1 load cycle, LSHR and U720Li have the highest crack growth rates. The difference in fatigue crack growth rates between 1s and 20s dwell conditions varies considerably at ΔK = 25 MPa√m, for U720Li the crack growth rate changes by a factor of about 33, falling to seven

for RR1000 and only two for N18 and U720Li LG. In all cases the increases in dwell, increased fatigue crack growth rates.

Finally, in Figure 87, a comparison between the results for vacuum tests using a 1s dwell at 650°C are compared with 20s dwell tests carried out in air at 725°C. Here, for a particular ΔK, the range of fatigue crack growth rates are distributed over three orders of magnitude. Under the most aggressive conditions for fatigue crack growth *i.e.* under 1-20-1-1 load cycle in air at 725°C but at ΔK = 25 MPa√m, then the alloys performance is ranked best to worst as U720Li LG > N18 > RR1000 > LSHR > U720Li (see Table 31).

5.1.5.5 Summary of Long Crack Fatigue Propagation Results

As can be seen from the previous paragraphs, it is difficult to systematically compare the fatigue crack propagation performance of the various alloys, any comparison or ranking will depend on a particular performance criterion being declared important for the environment found in a particular application, *e.g.* beneficial effects of creep such as crack tip blunting versus failure creep. For this reason the performance of the various alloys has been summarised in several tables and figures: The performance rankings for the alloys in terms of crack growth rate (*da/dN*) at ΔK = 25 MPa√m and ΔK = 45 MPa√m are presented in Table 31; the effect on fatigue crack growth rate (*da/dN*) from changes in test environment, temperature and dwell time between ΔK = 25 MPa√m and ΔK = 45 MPa√m compared in tabular from in Table 32 with the same comparison presented graphically in Figure 88; and finally a summary of the Paris Law coefficients, *C* and *m*, are presented in Table 33.

5.1.5.6 Long Crack Fatigue Fractography of N18, LSHR and Comparison Materials

In the following sections optical overviews and micrographs of the fracture surfaces of the long crack fatigue tests are presented for N18, LSHR and the comparison alloys.

5.1.5.6.1 Optical Overviews of N18 and LSHR Long Crack Fatigue Specimens

Optical overviews of the fracture surfaces of the N18 test specimens for the tests carried out under 1-1-1-1 and 1-20-1-1 are presented in Figure 89 and Figure 90 respectively and those for the LSHR 1-20-1-1 load cycle tests are presented in Figure 91. Various features are identified, with numbers corresponding to the following features:

1. Edge of EDM slot
2. Pre-cracking region
3. Application of heat, end of pre-cracking
4. Fatigue crack grow out region
5. Start of final crack
6. Break open area post failure

It can be seen from the fracture surfaces that all cracks are not symmetrical to varying degrees, indicating that the crack propagation has not been uniform across the breadth of the test specimen. The 1-1-1-1 load cycle 650°C specimen in both environments having the least uniform crack propagation for N18 and the 725°C air test the worst for the LSHR 20s dwell specimen. In general, the effect of variations in the crack growth rate can be accounted for by using a mean crack length based on three measurements taken at the 25%, 50% and 75% positions across the breadth of the specimen, as shown in Figure 89(a). With the crack length measured from the edge of the specimen in direction of the arrow and using this information to correct the crack length determined using the pulsed DC pd measurement technique. For the LSHR 20s dwell test carried out in air at 725°C, Figure 91 (b), the extent of the non-uniform crack growth measured between the front and rear faces of the test specimen was found to be 0.32 x Breadth (*B*) of the specimen, which invalidates this test in accordance with the symmetry requirements of BS ISO 12108[151] Section 8.5 where a 0.25*B* limit is stipulated.

For the N18 specimens tested in vacuum with a 1s dwell, Figure 89 (c) and (d), the difference in the amount of oxidation on the pre-cracking portion of the specimen between the 650°C and 725°C specimens is due to specimen heating only being applied for the 725°C test once the test chamber had been evacuated. This same specimen experienced a hydraulic supply failure which effectively unloaded the specimen, a beach mark line can be seen on the specimen and the event also identified by the discontinuity on the *da/dN* versus ΔK graph (Figure 73). The oxidation on the N18 20s dwell tests carried out in vacuum, Figure 90 (c) and (d), was caused by the unexpected loss of vacuum when the specimen failed at the end of these tests. On the LSHR 20s dwell vacuum specimens; apparent bright spots or 'polishing' can be seen on the 650°C specimen, Figure 91(c), which may be an indication of crack welding and the 725°C, Figure 91(d), surface appears to have signs of fretting.

5.1.5.6.2 Fractography Micrographs of N18 Long Crack Fatigue Specimens

Micrographs of the fracture surfaces at increasing levels of ΔK for both temperature tests in air for N18 using a 1-1-1-1 load cycle are presented in Figure 92. At the lowest temperature and ΔK (Figure 92(a)) the fracture surface suggests that transgranular failure is the main type of failure. As the temperature is increased (right hand column) or ΔK is increased the type of failure increasingly becomes intergranular, with the most severe conditions (Figure 92(f)) leading to a mixture of transgranular and intergranular crack propagation. In Figure 92(f), extensive signs of secondary cracking can also be seen. 1-20-1-1 load cycle tests carried out in air are presented in Figure 93. Figure 93(a) shows that at the lowest temperature and ΔK a mixed transgranular and intergranular failure occurs, somewhat similar to that seen for the 1s dwell at a similar ΔK but higher

temperature. Increasing the temperature or ΔK increases the amount of intergranular crack propagation, but even the most severe condition (Figure 93f) shows some signs of transgranular failure.

Micrographs of the fracture surfaces at increasing levels of ΔK and temperatures of 650°C and 725°C tests in vacuum for N18 subjected to a 1s dwell are presented in Figure 94. Here the lowest temperature and ΔK Figure 94(a) shows a transgranular failure surface. As ΔK and temperature are increased the failure mode becomes a mixture of intergranular but mostly transgranular crack growth with some secondary cracking seen at the highest temperatures and ΔK, Figure 94(e) and Figure 94(f), although the proportion of intergranular cracking seen appears to be significantly less than seen with the tests carried out in air. The fracture surfaces of the 20s dwell tests carried out under vacuum conditions are shown in Figure 95. Crack propagation for the lower temperature tests (left column) remain mostly transgranular, but as the temperature and ΔK is increased crack propagation becomes mostly intergranular at the highest ΔK and temperature.

During pre-cracking, rupture of primary γ' particles was noticed as shown in Figure 96. In Figure 97, micrographs of sections through nickel plated fatigue crack fracture surfaces for both 650°C and 725°C, under air, vacuum and 1-1-1-1 load cycle conditions for similar ΔK are shown. At 650°C in air, a secondary crack grows from a primary γ' interface with the matrix and propagates along a grain boundary Figure 97(a), under vacuum conditions at the same temperature there is little evidence of secondary cracking. For tests carried out at 725°C in air, a secondary crack around a primary γ' is shown Figure 97(b). Whereas for the tests carried out under vacuum conditions at this temperature there is little evidence of secondary cracking in the sectioned specimens even at higher ΔK Figure 97(d). Micrographs of secondary cracking for tests carried out in air at 650°C are shown in Figure 98. Secondary cracking appears to occur along slip planes Figure 98(a), enlarged, the crack changing direction as primary γ' is encountered in Figure 98(b). In Figure 98(c) and Figure 98(f) secondary cracks appear to have propagated along the primary γ' / γ matrix interface, while Figure 98(d) and Figure 98(e) reveal propagation of secondary cracks along grain boundaries. Further micrographs of secondary cracking for tests carried out in air at 725°C are shown in Figure 99. The secondary cracking appears to occur at grain boundaries or between primary γ' particles Figure 99(a). The secondary crack in Figure 99(b) is enlarged in Figure 99(c) where there may be an indication that this crack is propagating along a grain boundary. The two cracks shown in Figure 99(d) are enlarged in Figure 99(e) and Figure 99(f). Micrograph Figure 99(e) shows a secondary crack propagating through the boundary between two primary γ'. The straight crack in Figure 99(f) may have propagated along a twin boundary, but appears to have arrested at the grain boundary.

5.1.5.6.3 Fractography Micrographs of LSHR Long Crack Fatigue Specimens

Micrographs of the fracture surfaces of the LSHR 1-20-1-1 load cycle tests carried out at both 650°C and 725°C in air are presented in Figure 100. Even under the most benign conditions Figure 100(a), the crack propagated in a mostly intergranular manner, although there are some signs of transgranular failure throughout the tests carried out at 650°C. Increasing ΔK leads to extensive secondary cracking at both temperatures, with the most severe conditions Figure 100(f) leading to crack propagation almost completely in an intergranular manner.

In Figure 101, fracture surface micrographs of LSHR tested under vacuum conditions with a 20s dwell at 650°C and 725°C are presented. In contrast to the air tests, fatigue crack propagation at the lower temperature progresses by transgranular failure processes, although there is extensive secondary cracking present at higher values of ΔK Figure 101(e). Increasing the temperature leads to an increase in the amount of intergranular failure, especially at the highest ΔK causing a mixture of transgranular and intergranular failure modes under these conditions.

5.1.5.6.4 Fractography Micrographs of RR1000 Long Crack Fatigue Specimens

Micrographs of the fracture surface of RR1000 at increasing ΔK and temperatures of 650°C and 725°C for 1s dwell tests carried out in air are presented in Figure 102. For the most benign conditions (top left) a mixed but more transgranular mode of crack propagation is observed. As conditions worsen with increasing ΔK and temperature (right and down) the mode of crack propagation becomes increasingly intergranular and increasing severity of secondary cracking becomes apparent. For 20s dwell tests carried out under otherwise similar conditions, the micrographs of the fracture surfaces are shown in Figure 103. Increasing the dwell has led to an increase in the amount of intergranular crack propagation, although the tests carried out at 650°C (left column) still have a significant amount of transgranular crack propagation. By the time the highest ΔK and temperature, (f), is reached, crack propagation becomes almost wholly intergranular in nature.

Micrographs at comparable temperatures and ΔK of the fracture surfaces for the RR1000 fatigue crack propagation tests carried out under vacuum are presented in Figure 104. These show transgranular crack propagation at the lowest temperature and ΔK Figure 104(a), becoming mixed transgranular and intergranular with increasing temperature and ΔK Figure 104(c), (d), (e), where there is also some signs of secondary cracking. Compared with the air tests (Figure 102) the signs of secondary cracking are significantly reduced. Micrographs of the fracture surfaces for 20s dwell tests for comparable conditions (Figure 105) show that although the increase in dwell has a smaller effect than

it does for the tests carried out in air (Figure 103), increasing the dwell increases the amount of intergranular failure and secondary cracking present.

5.1.5.6.5 Fractography Micrographs of U720Li Long Crack Fatigue Specimens

For U720Li the fracture surfaces for the tests carried out in air showing differing ΔK for both the 650°C and 725°C 1-1-1-1 load cycle tests are reproduced in Figure 106. Even under the most benign conditions (top left) the crack propagates through this material in an intergranular manner and continues to do so at increasing levels of ΔK and temperatures. Again increasing signs of secondary cracking can be seen as the conditions worsen. The effect of a 1-20-1-1 load cycle can be seen in Figure 107 where the amount of secondary cracking has increased significantly.

The fracture surfaces for the tests carried out on U720Li under vacuum conditions and 1-1-1-1 load cycle are shown in Figure 108, apart from the very lowest ΔK Figure 108(a) and (b), which appear to exhibit mixed intergranular and transgranular crack growth, the remaining fracture surfaces appear to show predominantly intergranular crack growth with an increasing amount of secondary cracking as both temperature and ΔK are increased.

5.1.5.6.6 Fractography Micrographs of U720Li LG Long Crack Fatigue Specimens

From Figure 109, it can be seen that the crack propagation mode in the large grain variety of U720Li LG is initially quite transgranular when a 1s dwell is applied. This becomes increasingly intergranular as the temperature increases or ΔK is increased. Signs of secondary cracking are evident in most of the micrographs. Increasing the dwell to 20s (Figure 110) increases the amount of secondary cracking and amount of intergranular crack propagation present.

U720Li LG fracture surfaces under vacuum and 1-1-1-1 load cycle conditions are shown in Figure 111. At low ΔK (18 MPa$\sqrt{m}$) and medium ΔK (25 MPa$\sqrt{m}$) and 650°C Figure 111(a) and (c), crack growth appears to be mostly transgranular becoming mixed transgranular and intergranular at the highest ΔK (38 MPa$\sqrt{m}$) Figure 111(e) shown for this temperature. At 725°C at the lowest ΔK Figure 111(b) crack growth is mixed transgranular and intergranular which becomes predominantly intergranular at higher ΔK Figure 111(f). Figure 112 presents the available micrographs of the 20s dwell fracture surfaces at 650°C under vacuum conditions, when compared with comparable 1s dwell fracture surfaces (Figure 111), there appears to be little change in crack propagation mode due to the increase in dwell.

5.1.6 LCF of N18 and Comparison Materials

For the N18 LCF tests carried out by QinetiQ, the number of cycles to failure against total strain range can be seen in Figure 113 for N18 at 650, 700 and 725°C and are compared

with data from the literature for U720Li at 650°C in Figure 114 (this data includes information from short crack, runout and acetate replica tests from which strain ranges have been estimated by finite element analysis)[21]. Tests at 700°C and 650°C show little difference in LCF behaviour in N18, but increasing the test temperature to 725°C does seem to lower fatigue lives somewhat. The U720Li LCF behaviour is comparable to the N18 at 650°C at higher strain ranges, but significantly worse at the lower strain ranges (which may be expected to be more initiation controlled).

Analysis of the stress-strain response during loading for the LCF testing at 650°C revealed that the cyclically stabilised stress was achieved after 5-20 cycles except for the very lowest strain ranges (where the 0.2% proof stress value was not quite achieved in the first loading cycle). Comparison of the cyclically stabilised maximum stress values achieved at the different applied strain ranges with a typical stress-strain curve for the first loading step indicated that only a small amount of cyclic softening, approximately 28 MPa, was exhibited by the material at this temperature (see Figure 115). LCF testing at 725°C however revealed that significant cyclic softening was observed, approximately 66 MPa, as can be seen when the typical stress-strain curve for the first loading step is compared with the cyclically stabilised stress-strain curve at half life for an exemplar specimen (Figure 116). The stabilised stress / strain data derived from these tests is particularly useful, it will be used later in discussing the long crack fatigue response, where is it used to determine $\Delta CTOD$, which will change due to the test temperature and the amount of cyclic softening present at that particular temperature. The data can be used to produce Cyclic Stress Strain (CSS) curves which are useful for modelling the cyclic response of N18 when the material is subject to constraint or stress concentration such that plastic deformation occurs as is the case in most real engineering applications.

5.1.6.1 LCF Fractography of N18

Fractography from the LCF specimens for 650°C at $\Delta\varepsilon = 0.7$ and $\Delta\varepsilon = 1.2$ is shown at Figure 117 and that for 725°C at $\Delta\varepsilon = 0.7$ and $\Delta\varepsilon = 1$ in Figure 118. Typically crack propagation comprised ~ 10-30% of the overall fracture surface, dependent on the strain level applied. In Figure 117(c) initiation at a sub-surface pore with an attendant halo can be seen. Numerous particles were observed on the fracture surfaces, particularly near the edges of the specimens. Whilst some of these are thought to be contamination from the testing procedures, several are thought to be inherent inclusions (including γ') in the material and appeared to be initiation sites as shown in Figure 117(d) and Figure 118(c) and (d). The number of initiation sites increasing with an increase in temperature or an increase in $\Delta\varepsilon$. At both testing temperatures it was seen that close to the initiation region the fatigue fracture surface was generally relatively smooth, indicating predominantly transgranular crack propagation mechanisms were in operation with a slight increase in

fracture surface roughness (indicating intergranular crack growth modes were starting to operate) observed close to the final overload failure region. Examples of this can be seen in Figure 117(e), (g), (f) and (h) at 650°C and Figure 118(e), (g), (f) and (h) at 725°C. At 725°C generally a slightly more intergranular crack growth mode was apparent than observed in comparable regions at 650°C.

5.1.7 U-Notch Fatigue of N18

The results of the N18 U-notch fatigue testing, in terms of total lifetime to failure are presented on an *S-N* plot in Figure 119. In general, this shows that increasing the applied stress, raising temperatures and testing in air all tend to reduce fatigue life; such that the test carried in air at 725°C with an applied stress (calculated for the uncracked ligament) of 1020 MPa had the lowest life of all the specimens tested. Exceptions to this generalisation are the tests carried out in air at 650°C.

5.1.7.1 U-Notch Fractography of N18

Optical overviews of the fracture surfaces of the U-notch test specimens are presented in Figure 120 and Figure 121 for tests carried out in air and vacuum conditions respectively. The primary crack initiation site is marked with a yellow arrow (unless the crack initiated at a corner). For the air tests, Figure 120, it can be seen that increasing the stress, increases the severity of ratchet lines (some examples marked with red lines), which provides an indication that cracks are initiating over a larger proportion of the notch and propagating further before they coalesce with other cracks to form the ratchet line. The effects are similar for tests carried out at 650°C (Figure 120(a) and (c)) and for those tests carried out at 725°C (Figure 120(b) and (d)). The tests carried out in vacuum, Figure 121, are somewhat different, any ratchet lines on the specimens tested at 650°C are much less pronounced (see Figure 121(a) and (c)) with ratchet lines only becoming prominent on those specimens tested at 725°C (see Figure 121(b) and (d)). It would appear that the specimen tested at 650°C in vacuum with an applied stress of 1020 MPa failed due to a crack that initiated at corner of the notch and the side of the specimen, potentially indicating that a stress concentration was present here and thus likely to lead to a reduced initiation phase for the crack and hence the lifetime of the specimen.

More detailed fractography was carried out in the FEG SEM and is presented in Figure 122 to Figure 129 and commented on further below.

For the test carried out in air at 650°C with an applied stress of 1020 MPa, the development of the primary crack is presented in Figure 122. The initiation point of the crack Figure 122(a), appears to be from an oxidised area possibly γ' and initially propagates in a transgranular manner, a higher magnification of the initiation area is presented in Figure 122(b) showing secondary cracking within the oxidised initiation site.

As the crack propagates, about half way between initiation and final fracture, Figure 122(c) and (d) it traverses pores approximately 10 μm in diameter, remaining mainly transgranular in nature, becoming more intergranular as the crack approaches final failure Figure 122(e) with typical fast fracture occurring Figure 122(f) as the specimen fails. In the same specimen in Figure 123(a) increased oxidation products can be seen at the grain boundaries, possibly indicative of improved diffusion rates at these locations, this highlights the grain boundaries within the U-notch. Different rates of oxidation were also seen at the original primary γ' sites, which give the specimen an appearance of being "Thermal etched". Higher magnification in Figure 123(b) shows what appears to be a higher volume of oxidation product. Does this just arise from the surface exposure or is it extruding at the surface as no constraint is provided? If the latter, this would lead to internal stresses being created at the internal grain boundaries which in turn will tend to assist cracks propagating along these routes, as the effective ΔK seen here would be increased. EDX analysis of the oxidation products at grain boundaries indicated high levels of Cr, Ti and Al. During the FEG SEM analysis, what appeared to be a "sealed" surface pore was located, Figure 124. It is not clear if the pore is sealed from oxidation occurring during the test or from polishing artefacts introduced prior to testing. There does appear to be a semi-circular "halo" around the crack, highlighted in Figure 124(b) using a yellow line. This type of effect is more normally associated with sub-surface cracks growing under vacuum conditions, but in this case may be due to oxidation of the material around the pore leading to a change in its appearance.

At the higher temperature of 725°C in air with the same applied stress of 1020 MPa, initiation of the primary crack is shown in Figure 125(a). It does not appear to be from a pore, so an oxidised particle is more likely. Reasonably close to the initiation site the crack is propagating via a mixture of transgranular and intergranular modes as shown in Figure 125(b), with the crack propagation mode becoming more intergranular as the crack length and hence ΔK increases (Figure 125(c)), with typical final failure occurring as shown in Figure 125(d). "Thermal etching" at the grain boundaries of the same specimen is shown in Figure 126(a), this appears to be more extensive than that seen at 650°C under the same conditions (Figure 123) with a crystalline phase appearing to be forming at or over the grain boundaries / primary γ' (areas of interest are circled in yellow), a higher magnification view presented in Figure 126(b). EDX analysis identifies this as having a high atomic % content of Co, C and O, with Ni and Cr also present in smaller amounts. If the M:C ratio for each sample volume is calculated, values of 3.2, 3.4 and 0.9 are obtained. These compare well with MC with a ratio of 1 and $M_{23}C_6$ with a ratio of 3.8, but do not take account of the presence of O in the analysis, neither does it consider the extensive nature of the phase. A similar phase appears to be able to form in the bulk of the alloy, as shown in Figure 127(a), with its location with respect to the U-notch shown in

Figure 127(b), where the darker microstructure appears to have a friable appearance, perhaps caused by oxidation and may explain changes to local crack growth rates.

Under vacuum conditions at 650°C and 1105 MPa, crack initiation occurs from a pore (Figure 128(a) and (b)), which might be expected if tests in air obtain earlier initiation from oxidation of γ' and perhaps benefit from oxide filling of pores, reducing their ability to act as a stress raiser. In the vacuum test, crack propagation is more transgranular in nature, apparently cutting through primary γ' as well as grains which can be seen in Figure 128(c). As in the air tests, with increasing ΔK, the crack propagation becomes more intergranular, but less so than the air test, with some signs of secondary cracking, Figure 128(d) refers. Final fracture is again typical as shown in Figure 128(e). Given that this was a vacuum test, it was initially surprising to see apparent “Thermal etching”, however, when the extent is compared to that seen in the air tests, there appears to be less volume at the grain boundaries, which might be explained if the compound is a carbide rather than oxide.

An increase in temperature to 725°C at the higher stress of 1020 MPa, led to an increase in the number of initiation sites, see Figure 121. The main crack appears to initiate from one area, where one of the initiation sites appears again to be at a pore, Figure 129(a). Initial crack growth (Figure 129(b)) is more intergranular than that seen at 650°C and becomes predominantly intergranular as ΔK increases, as can be seen in Figure 129(c) with typical final failure being shown in Figure 129(d). At this temperature and stress, Figure 129(e) shows extensive secondary cracking in the U-notch, this is likely to be indicative of slip band initiation of cracks under these conditions. Figure 129(e) and (f) show what appears to be “thermal etching”, but in this case it does appear to be much more subdued, with little volume of any compound as polishing scratches are still clear to see.

5.2 Results of Thermal Barrier Coating Testing and Analysis

In this section the results from the TBC testing carried out at QinetiQ are provided. Initially the results from the TGO growth characterisation studies are presented followed by the TBC TMF testing results. For ease of reference and comparison results figures and tables are presented in section 9.

5.2.1 TGO Growth Characterisation

The results from the exposure tests including progress through the test matrix, representative images and TGO measurements are presented in the following paragraphs.

5.2.1.1 Measurement of Thermally Grown Oxide layer

Sample BEI and SEI mode micrographs are presented in Figure 130 and Figure 131 respectively. The images produced under BEI mode are generally better quality with a lower number of charging effects than seen under SEI mode. Due to the lower atomic number of the TGO layer, it was thought that BEI mode may be able provide a good contrast between TGO layer, top coat and bond coat, thus providing a method of defining the TGO layer thickness. Initial image analysis was carried out on this basis for the specimens exposed isothermally at 1000°C for 30, 300 and 1057 hours, see Figure 132 for images from the specimen exposed for 30 hours at 1000°C. Using ImageJ it was possible to isolate the apparent TGO, the thickness of which was then measured using an overlaid grid, see Figure 133. Later image analysis was automated using a macro within ImageJ to carry out this work and allow TGO thickness measurements to be carried out at single pixel intervals. When the BEI images were compared with those taken in SEI mode, it was found that cracking and polishing artefacts associated with specimen preparation were included within the apparent TGO thickness. For this reason SEI mode became the preferred imaging technique to determine the TGO thickness, with all other images examined in SEI mode.

5.2.1.2 Isothermal Exposures

The status and final exposure times of the isothermal tests are presented in Table 34. Image analysis and measurement of the TGO thickness was carried out as described in paragraph 5.2.1.1. The measurements of the TGO thickness are presented graphically; initially as an overall summary of TGO thickness versus exposure time for the various temperatures in Figure 134; and as relative cumulative frequency (RCF) plots with a fitted Gaussian normal cumulative distribution function (CDF) in Figure 135. (For ease of presentation the results from the specimen exposed for 30 hours at 1150°C has been included on the same graph as those exposed at 1100°C). A Gaussian normal distribution was chosen as the growth of the TGO layer is governed by diffusion and the variation in this process is associated with the “random walk” of species that occurs during Brownian motion. An alternative representation to describe the RCF data in the form of a probability density function (PDF) has been used and this is presented in Figure 136. (With the exception of the 1000°C and thermal cyclic exposures all graphs have the same scale on the TGO thickness axis to aid comparison.)

It is difficult to draw comparisons right across the spectrum of temperatures used in the isothermal exposures. In general, it can be seen from Figure 134 that as the exposure temperatures were increased, then, as expected, the survival time of the specimen before spallation occurred reduced. If the 1000°C specimens are excluded, it would appear from the graph that TGO spallation could be expected to occur when it reached a thickness of

somewhere around 4 μm to 5 μm. All surviving specimens isothermally exposed for 100 hours at temperatures from 950°C (Figure 135 (a)) to 1100°C (Figure 135 (d)), show increasingly thicker TGO layers as the exposure temperature increases. In general the fit of a Gaussian normal distribution curve is reasonable across the range of temperatures and exposure times. However, there are some apparent anomalies: In Figure 135 (b), the specimen exposed for 30 hours at 1000°C has (for the most part) a slightly thicker TGO layer than that the specimen exposed for 100 hours, although this could be due to several reasons, such as temperature fluctuation in the furnace due to other specimen removal and insertion, scatter in the TGO thickness at production and scatter in TGO growth rate or a combination of all three of these effects. In Figure 135 (c), the thickness of the TGO layer in the specimen exposed for 30 hours at 1050°C appears to have a more uniform layer thickness as some areas are not as thick as the “as received” specimen, the potential reasons discussed above could also explain this phenomenon, even so this will be returned to in the discussion. In Figure 136, in general as the exposure time increases and TGO thickness increases, the range of TGO thickness increases indicated by the wider and lower peak of the PDF.

5.2.1.3 Two stage temperature exposures

The status and final exposure times of the two stage temperature exposure tests are presented in Table 35. Image analysis and measurement of the TGO thickness was carried out as previously discussed and these results are presented graphically as an RCF and CDF in Figure 137, and PDF in Figure 138. The only specimen that spalled was the specimen exposed at 1100°C for 300 hours, this is consistent with the isothermal test carried out at the same temperature and time. Although all the exposures consisted of two stages, the second stage exposure in all cases was very similar at 950°C for around 1000 hours. Unexpectedly, the lowest temperature first stage exposure, 1000°C for 306 hours, developed the thickest TGO. Whilst the other two specimens, with initial cycles of 1050°C / 300 hours and 1100°C / 100 hours developed almost identical TGO thickness profiles.

5.2.1.4 Thermal Cyclic Exposures

The status and final number of cycles of the thermal cyclic exposure tests are presented in Table 36. Image analysis and measurement of the TGO thickness was carried out as previously discussed and these results are presented graphically as an RCF and CDF in Figure 139, and PDF in Figure 140. The fit of a Gaussian normal distribution curve is reasonable for both the 1000°C and 1050°C specimens, however, this is not the case for the specimen exposed at 1100°C. This was attributed to an increase in the apparent TGO thickness due to a crack through the complete TGO layer in this specimen, which has essentially failed, but retained its TC.

5.2.2 Thermo-mechanical Fatigue Testing

When compared to the commanded cycle, the results from TMF testing show that the TMF control system with manually adjusted *PIDL* control parameters conformed well, as can be seen from Figure 141 in terms of strain versus temperature and Figure 142 in terms of stress and temperature versus time. There are two areas where there is some room for improvement. (1) as strain is increasing from 0.25 to 0.27 the cooling rate from 875°C down to 769°C is slightly too slow and (2) as strain is reducing from 0.27 to 0.19 a small temperature overshoot occurs. Figure 143 shows the same information for cycle number 1346 indicating that the TMF test cycle is highly repeatable. In Figure 144, the TBC TC temperature is shown, this is not the controlled temperature so some lead and lag when compared with the substrate temperature is expected. During the dwell with the substrate at 875°C, the TBC top coat is around 1045°C a temperature difference of approximately 170°C.

The status and final number of cycles of the TMF tests is presented in Table 37. Figure 145 and Figure 146 show sections through the TMF test specimens with no pre-exposure and 100 hours pre-exposure in air at 1000°C respectively. The substrate thermocouple hole is shown in these two figures; the variability in position of the hole should be noted. In Figure 146 the thermocouple remained in the specimen as it expanded due to oxidation and a section through it can be seen. The TMF test that had been pre-exposed for 300 hours at 1000°C in air started spalling at 754 cycles, images of this spallation are presented in Figure 147

Image analysis and measurement of the TGO thickness was carried out as previously discussed and these results are presented graphically as an RCF and CDF in Figure 148, and PDF in Figure 149.

6 Discussion

The discussion of results commences with those pertaining to the *Turbine Disc Alloy Assessment* research followed by those related to the *Thermal Barrier Coating Life Assessment* research. Once these have been discussed, a further discussion regarding the *Lifing of Critical Components in Gas Turbine Engines* is undertaken to put the various results and discussions into context of the overarching theme of the EngD.

6.1 Turbine Disc Alloy Assessment

The discussion of the disc alloy assessment aspects of the project is presented in a progressive manner. Initially the chemical compositions and the heat treatments that lead to the various alloy microstructures are discussed. This is followed by a discussion of monotonic properties and environmental responses of the alloys which progresses onto the more complex cyclic behaviours. Where necessary the discussion is shaped by the expected operating environment for a turbine disc. Each section of the discussion starts with a summary or signpost to the relevant results of the alloys studied, N18 and LSHR or the comparison alloys, RR1000, U720Li and U720Li LG.

6.1.1 Microstructure and Heat Treatment

Although the chemical composition of the alloy is important, in terms of the behaviour and performance of an alloy, it is the microstructure created by a combination of the chemical composition and the heat treatment schedules that are applied that permit optimisation of the alloy for use in the operating environment it has been selected or designed for. These heat treatment schedules are usually applied on the basis of how they (beneficially) modify the alloy microstructure given its composition and the thermal - mechanical processing that has taken place up to that point in a component's history.

Compositions of all the alloys discussed here are summarised in Table 11, the heat treatment schedules applied in Table 12 and a summary of their characterisation is presented in Table 25. To permit further comparison of the alloys, their compositions in weight % have been converted to atomic percent (at%) in Table 19 after making the assumption that the balance of all the alloys is Ni.

Table 19 Alloy chemical compositions (atomic %).

	Cr	Co	Mo	Ti	Al	C	B	W	Hf	Zr	Fe	Ta	Nb	Ni
N18	11.98	14.66	3.77	5.01	8.90	0.10	0.04	-	0.16	0.01	-	-	-	55.37
LSHR	13.96	20.41	1.63	4.24	7.54	0.15	0.16	1.36	-	0.03	-	0.51	0.94	49.07
RR1000	15.71 to 16.67	13.53 to 18.44	2.52 to 3.13	4.10 to 4.96	6.01 to 6.68	0.06 to 0.16	0.05 to 0.13	-	0.16 to 0.32	0.03 to 0.04	0 to 1.02	0.42 to 0.68	-	57.40 to 47.77
U720Li & LG	17.26	13.94	1.75	6.10	5.10	0.11	0.08	0.41	-	0.03	0.08	-	-	55.13

From the data in Table 19, the mean relative atomic mass (ram) of the alloys has been calculated and is presented in Table 20.

Table 20 Mean relative atomic mass of alloys.

	Mean ram
N18	56.10
LSHR	58.09
RR1000	56.94 to 57.21
U720Li & LG	56.39

6.1.1.1 γ' Formers

A simple estimate of the maximum amount of γ' that can be formed in each alloy can be calculated using the chemical composition of γ', Ni_3(Al, Ti, Ta, Nb), by considering the total at% of γ' formers (Al, Ti, Ta, Nb) from Table 19, if a stoichiometric composition of γ' is assumed. The results from this calculation are presented in Table 21.

Table 21 Maximum γ' content (at%).

Alloy	**Maximum γ' (at%)**	**γ' V_f from Table 7**
N18	55.65	60
LSHR	52.93	58
RR1000	42.16 to 49.26	49.2
U720Li and U720Li LG	44.79	48.3

Given that the main constituents of the alloys are γ' and γ which both have an fcc packing structure with similar lattice parameters (which permits secondary and tertiary γ' to be coherent with the matrix) the maximum γ' in at% can also be considered to be a first order estimate of the maximum V_f of γ' present in the alloys. Although these V_fs are somewhat lower than those presented in Table 7. N18 and LSHR have the highest V_f of γ' and this should be expected to contribute to retained strength at higher temperatures. Such a high content of γ' (and associated hardening effects) could lead to a propensity for quench cracking. To reduce the likelihood of this occurring the Ti / Al ratio for both N18 and LSHR is kept relatively low at 0.56. Although in U720Li and U720Li LG, Al content is limited to reduce the potential for TCP phases forming.

The amount of Al and Ti available to form γ' may be reduced by the solubility of these elements in the γ matrix this phenomenon is discussed in the next section.

6.1.1.2 γ Phase Stabilisers and Solid Solution Strengtheners

Although Al and Ti are required to form γ', both are soluble in the γ matrix. Al is a strong solid solution strengthener of the γ matrix whereas Ti provides less solid solution strengthening, their solubility in γ can be limited by the addition of Co, Cr and Fe to the alloy[157] by reducing the sites available for the Al atoms to reside. If these three elements (Cr, Co, Fe) are considered RR1000 provides both the upper and lower range boundaries of between 28.35 and 35.15 wt%. Although if at% is considered, N18 has the lowest total amount, 26.64 at% with RR1000 upper range providing the maximum amount at 36.13 at%. However, for a fair comparison to be made, then these figures need to be put in context. In the previous section, the maximum amount of γ' that one of the alloys could contain was estimated, this can also be used to estimate the amount of γ phase of the alloy and hence ratios of elements in comparison to γ content, as presented in Table 22.

Table 22 Alloy maximum γ', grain boundary elements and γ content (at%) (2 sig fig).

Alloy	Maximum γ'	Grain Boundary elements	γ	(Cr+Co+Fe) / γ (%)	Cr / γ (%)	(Mo + W) / γ (%)
N18	56	0.31	44	60	27	8.6
LSHR	53	0.34	47	74	30	6.4
RR1000	42 to 49	0.30 to 0.65	58 to 50	51 to 72	27 to 33	4.4 to 6.3
U720Li and U720Li LG	45	0.22	55	57	31	3.9

With the Cr, Co, Fe content compared against the γ content of the alloys in terms of at%, it can be seen from Table 22 that the ratio of these elements to γ is close for N18, RR1000 and U720Li and U720Li LG at 60%, 61% (mean) and 57% respectively whereas at 74% LSHR has a much higher ratio. This is explained by the higher Co content of LSHR added to reduce the γ' solvus[51], which promotes hot working. Thus in relative terms γ' formation due to the solubility of Al and Ti in γ is unlikely to be markedly different in N18, RR1000 and U720Li and U720Li LG, with perhaps relatively more γ' forming in LSHR as the solubility effects are reduced further.

From Table 11, it can be seen that the Cr content of the alloys ranges from 11.1 wt% for N18 to 15.92 wt% for U720Li and U720Li LG and Co content ranging from 14.0 wt% for RR1000 to 20.7 wt% for LSHR. With the lowest levels of Cr, N18 could be expected to perform less well when a protective oxide (Cr_2O_3) layer is required to enhance performance at high temperatures within an oxidising environment. Although this protective oxide layer can only form where Cr is present and in general this is within the γ matrix, hence a further comparison of Cr against γ content is appropriate. From Table 22, it can be seen that N18 does indeed have the lowest Cr content when compared to γ content in at%, but at 27%, even though this figure is lower than those for LSHR (30%),

RR1000 (30% mean) and U720Li and U720Li LG (31%), the difference has less significance than comparisons made using the wt% Cr content would suggest.

Mo and W provide solid solution strengthening of the γ matrix, with Mo preferentially partitioning to the γ matrix when compared with W[50]. Both Mo and W diffuse slowly enabling the retention of solid solution strengthening of the γ matrix above 0.6 T_m[157] beneficially affecting tensile strength and ductility at high temperatures[52]. Mo is preferred in N18 as it is stated to reduce notch sensitivity during creep tests[50], whilst in LSHR W is used as it provides the largest increase in yield strength at high temperatures[51]. As previously, if the total amounts of Mo and W are compared with the amount of γ matrix in terms of at% (Table 22), then it can be seen that N18 has the highest relative amount at 8.6% with U720Li and U720Li LG the lowest at 3.9%. Potentially, this is an indicator of improved high temperature behaviour from N18 when compared with U720Li or U720Li LG.

6.1.1.3 Carbides and Borides

Carbides and Borides tend to form at grain boundaries, at these locations they are able to inhibit grain boundary sliding and improve rupture strength[9]. They also retard grain boundary diffusion[157] which will be beneficial in retarding the effects of failure mechanisms which rely on this route being available, such as Stress Accelerated Grain Boundary Oxidation (SAGBO) often reported in IN718, but also seen in other alloys such as UDIMET® 700[158].

Excessive $M_{23}C_6$ carbides can lead to a continuous film at grain boundaries which can lead to σ-phase formation due to the similarities in crystal structure[5]. This was the phenomenon that caused unpredicted failures within U720[54] which led to development of U720Li[56] which is therefore less likely to be seen in the variants studied here.

Both Ta and Nb tend to form very stable primary carbide (MC), potentially limiting the availability of C to decompose into lower carbides ($M_{23}C_6$ or M_6C). This does not present an issue for N18 or U720Li and U720Li LG as these alloys do not contain Ta or Nb. RR1000 does not contain Nb either and its Ta content is limited to permit primary carbides to decompose into lower carbides[52], this “instability” is seen as a beneficial attribute of the alloy to permit the formation of grain boundary carbides. LSHR contains both Ta and Nb which could limit decomposition and retain C within primary carbides and thus limit the amount of $M_{23}C_6$ formed.

Carbides may be especially important in limiting the grain growth of LSHR during the super-solvus heat treatment. Prior to this heat treatment taking place, carbides will exist at the grain boundaries of the post sub-solvus heat treated LSHR. Although no primary gamma prime is present, the existence of carbides at these prior particle boundaries

(PPB) during super-solvus heat treatments may limit the extent of grain growth during the super-solvus heat treatment[9].

All the alloys studied contain B and either form[54,64,15] or are expected to form borides which will limit grain boundary diffusion and prevent grain boundary sliding thus enhancing the creep rupture lives of all of the alloys.

6.1.1.4 Grain Boundary Refining Elements

In addition to the carbides and borides formed at the grain boundaries, other elements in addition to these particles, notably B, Zr and Hf do refine the behaviour of the alloys at the grain boundaries. With trace levels of B retarding the γ' to η reaction and creation of cellular η at the grain boundaries with an attendant increase in notched stress rupture strength of the alloy[157].

Decker[157], also summarises the beneficial effects of B, Zr and Mg have with regard to preventing zones of γ denuded of γ' forming and hence improving creep performance in UDIMET® 500 to the extent that life is increased 13 times, elongation by a factor of 7 and rupture stress 1.9 times. Zr is specifically mentioned in the N18 patent[50], where its role as a getterer is implied for the presence of S, but the amount of Zr added to N18 is limited to prevent the formation of low T_m phases.

Of the alloys studied only two, N18 and RR1000, contain Hf, this reactive element in addition to forming carbides is expected to act as a getterer (in a similar manner to Zr[5]) absorbing tramp elements especially at the grain boundaries which in turn should reduce diffusion rates at these locations. In cast superalloys Hf alters the crystallisation of carbides, by suppressing the solidus and liquidus of the alloy, permitting angular primary carbides to form earlier with Hf, surrounded by γ', this limits the formation of deleterious script carbides later at the grain boundaries (as the majority of the C has been consumed) thus improving the ductility of the grain boundaries. The shape of grain boundaries is also changed by the changes to the solidification process, leading to convoluted grain boundaries in cast alloys. A further benefit is obtained due to Hf affinity for C and as such to form carbides, in that the other elements in the alloy are not depleted and remain to carry out another function, such as Mo can provide solid solution strengthening[159]. In single crystal alloys, Hf improves the adherence of oxides[160], Al_2O_3 grows around the boundaries of internal oxides, elongated intrusions into the alloy can form leading to improvement of the oxide adherence via pegging into the microstructure.

In N18, several effects in the alloy are attributed to the addition of Hf[50], it reduces the solidus, increases the γ' solvus and provides complementary hardening. The reduction in solidus is acceptable in a disc alloy, however the increase in γ' solvus leads to a compromise between the formability of the alloy which will be reduced and the retention of

strength at high temperatures which should be increased by reducing the amount of γ' returning to solution at higher temperatures. Although Hf can provide dispersion hardening[161], for the amount of Hf present in N18, the complementary hardening is more likely to be provided by grain boundary modification rather than dispersoids.

For RR1000 the role of Hf is stated as[52], "…improves all properties." With no specific information with regard to how it does this, although the effects of including Hf in RR1000 are likely to be similar to those in N18.

Work by Huron *et al* noted that Hf additions were promising but there was a risk of hafnium oxides affecting LCF initiation life as the particles acted as initiation sites and further work in this area was dropped[162]. They also found that B and Hf interacted to reduce FCG.

6.1.1.5 Heat Treatments

All of the alloys were subject to sub-solvus solution heat treatments as summarised in Table 12. In the case of LSHR this was to condition the alloy prior to a super-solvus solution heat treatment. In all cases, following the final solution heat treatment, the alloys were subject to a two stage ageing heat treatment.

For N18, the sub-solvus heat treatment was carried out relatively close (28°C below) the γ' solvus. Most of the γ' could be expected to be solutionised, but some primary γ' would be retained which would limit the grain growth at the solution temperature. A relatively slow cool (50°C min^{-1} to 100°C min^{-1} [163]), will allow some (secondary) γ' to precipitate out of solution. The two stage ageing treatment initially at a relatively high (when compared with the other sub-solvus solution heat treated alloys) 700°C for 24 hrs is expected to coarsen the size of the secondary γ' and nucleating further (tertiary) γ'. With a (relatively) high second ageing temperature of 800°C, the exposure is limited to four hours, this will coarsen the tertiary γ' and secondary γ' further leading to a tri-modal distribution of γ'. The 24 hr exposure at 700°C is relatively long for the temperature which may lead to increased secondary γ' size in comparison to the other sub-solvus heat treated alloys which is seen for N18 (Table 25). These ageing treatments providing some indication of the maximum operation temperatures for the alloy, *i.e.* for N18 somewhere between 700°C and 800°C.

RR1000, U720Li and U720Li LG were all subjected to similar types of sub-solvus solution heat treatments, with the following differences: The RR1000 solution temperature was 40°C below its γ' solvus and was cooled more quickly following this. This would imply less γ' was solutionised, but more was held in solution pending the ageing heat treatments. This would leave relatively more primary γ' available to restrict grain growth, possibly leading to reduced grain size for RR1000. For U720Li the solution temperature was 55°C below its γ' solvus, similar to RR1000, more primary γ' would be expected when

compared with N18 and U720Li LG and thus a smaller grain size due to the pinning effect provided by the increased primary γ'. U720Li LG was solution treated at 25°C below its γ' solvus (similar to N18), so similar grain sizes to N18 might be expected. The ageing heat treatments for these three alloys were the same, 650°C for 24 hrs and 760°C for 16 hrs, so again a tri-modal distribution would be expected for each alloy, however their maximum operation temperatures would lie somewhere between 650°C and 760°C.

The super-solvus heat treated LSHR is obviously different to the other alloys discussed previously. LSHR initially has a sub-solvus heat treatment 20°C below its γ' solvus for 1.5 hrs from which it is allowed to cool in the furnace. This presumably is a conditioning heat treatment which ensures that the γ' is of an even size and distribution throughout the alloy and uses the remaining primary γ' to establish a grain size and system of grain boundaries that will determine the positions of borides and carbides which will remain in these PPB locations during subsequent super-solvus heat treatment and provide some restriction to grain growth once all the primary γ' has been solutionised. The super-solvus heat treatment is 16°C above the γ' solvus for LSHR, all primary γ' will be dissolved and grain growth will be somewhat limited by exposure time and the pinning effect of the carbides and borides on the PPB discussed earlier, although it is well known that the pinning effects of these particles is not as great as provided by primary γ' and therefore larger grains would be expected. For the LSHR tested as part of this work, it was then subject to a fast cool (FC) of 202°C min^{-1}, this can lead to two effects. Firstly, the γ' is held in solution rather than precipitating out, as experienced in RR1000 with cooling rates greater than 100°C min^{-1} [18] and secondly grain boundaries tend to be straight rather than serrated[61] potentially due to the limited precipitation of γ' [164,165]. For LSHR the initial ageing heat treatment was at a higher temperature of 855°C for 4 hrs than the second ageing heat treatment of 775°C for 8 hrs. This would lead to secondary γ' being nucleated and grown initially, with further growth occurring during the second ageing heat treatment. As the second ageing heat treatment is at a lower temperature than the first, there is unlikely to be any further γ' to nucleate at this temperature. This particular heat treatment profile therefore leads to a single distribution of secondary γ' for LSHR. As previously, the ageing heat treatment range provides an indication of the maximum operating temperature of LSHR of somewhere between 775°C and 855°C due to alloy stability considerations.

6.1.1.6 Grain and γ' Sizes and Distributions

The grain and γ' sizes are summarised in Table 25 and will have a significant influence on the mechanical properties of the alloys such as yield strength, creep and fatigue resistance.

As discussed at section 6.1.1.5, N18, RR1000, U720Li and U720Li LG were all given sub-solvus solution treatments and LSHR a super-solvus solution treatment preceded by a sub-solvus conditioning heat treatment. The γ' solvus temperatures for N18, U720Li , RR1000 and LSHR being given in the literature (Table 6) as about 1193°C[49], 1160°C[62,63] and 1160°C[52] and 1155°C[6] respectively. U720Li-LG and N18 have been solution treated relatively close to their γ' solvus temperature when compared with RR1000 and U720Li, which has resulted in more resolutionising of primary γ' for U720Li LG and N18. LSHR has been solution treated above its γ' solvus, as such, all of the primary γ' has been dissolved back into the alloy. The reduced amount of primary γ' is expected to result in faster grain growth, which can be seen most clearly in the super-solvus heat treated LSHR in Figure 40. For the sub-solvus heat treated alloys, however, the largest grain sizes are observed for U720Li LG. For RR1000 the grain size is still quite fine despite some reduction in primary γ' when compared with U720Li. It would seem that additional grain boundary pinning processes (such as carbides) are in operation for this alloy. This may also apply to N18 which has a larger outlier grain sizes than RR1000, but also some very fine grains, Figure 41 (h) indicates the possible presence of fine grain boundary particles (which are thought likely to be borides[15]) and these may also explain the retention of a finer grain size *cf.* U720Li LG. Although for N18 the mean measured grain size is somewhat lower at 8.7 ± 4.2 μm compared with 15 μm seen elsewhere[163].

More γ' forming elements will be left in solution because of this reduced volume fraction of primary γ' these are therefore available to form secondary and potentially tertiary γ' during subsequent thermal processing. The secondary γ' mean sizes for N18 and U720Li LG are similar at 188 nm and 190 nm respectively. With RR1000 being smaller at 140 nm and U720Li almost half the size at 102 nm, possibly reflecting insufficient concentration of γ' in solution to permit the secondary γ' to coarsen in size. With LSHR the situation is a little different, the mean γ' size is 76 nm which is likely to be a result of the lack of nucleation during cooling following its solution heat treatment and therefore effectively missing a potential coarsening heat treatment stage.

As expected for LSHR from the heat treatment schedule of a fast cool from solution temperature, with a high temperature ageing heat treatment followed by a lower temperature one, practically no tertiary γ' was seen. In the sub-solvus heat treated alloys with the same ageing heat treatment schedules, RR1000, U720Li and U720Li LG, these alloys had similar sizes with an average of around 17 nm. The tertiary γ' measured in N18 was larger at 25 nm potentially from the higher temperatures used in ageing the alloy.

6.1.2 Oxidation Behaviour

In parallel with the disc alloy aspects of this work, oxidation studies were carried out at two temperatures 650°C and 725°C on N18, RR1000 and U720Li by Reynolds[166] (LSHR did not become available until towards the end of the project), relevant extracts are included here to facilitate later discussions.

6.1.2.1 Oxidation of Superalloys

Due to the presence of Al, Cr and Ni, various stable oxides can form, such as Al_2O_3, Cr_2O_3 and NiO. In terms of affording protection to the underlying alloy, the more stoichiometric the oxide, the better. Of the three expected oxides, the most stoichiometric is Al_2O_3, followed by Cr_2O_3 which both form tightly adhering protective oxide layers that limit the cation diffusion outwards of metallic species and inward anion diffusion of oxygen once a thick enough protective layer has formed. NiO on the other hand has a high concentration of nickel vacancies which forms very quickly but as a friable weakly bonded oxide offering little protection[5], given this, it is unfortunately one of the common oxides that form at the tip of an advancing fatigue crack[167]. When exposed to air at high temperature a disc superalloy will develop an external Cr_2O_3 layer which gives protection against rapid oxidation[168]. The presence of reactive elements such as Ti and Al can lead to the formation of internal oxides such as TiO_2 and Al_2O_3 beneath the Cr_2O_3 layer[169], and Ti has also been seen to form oxides outside the scale in a range of alloys including UDIMET® 720 (U720), ASTROLOY® and WASPALOY®[169,170].

6.1.2.1.1 UDIMET® 720 and RR1000 Previous Studies

Chen *et al* [170] conducted a study on chromia forming superalloys which included U720 which has a 2% higher Cr content *cf.* U720Li and ASTROLOY® which has a very similar composition (including Cr, Ti, Mo, Al and Co contents that are the same or very close) to RR1000 so their oxidation behaviours were assumed to be comparable in the Reynolds' study[166].

In the studies by Chen *et al* [170] the initial stages of oxidation in U720 were influenced by the microstructure of the alloy. The γ' phase within the grains oxidised at a high rate, probably forming Ti rich oxide. The oxide that formed clearly delineated the original γ' microstructure and included greater oxide products at grain boundaries where diffusion kinetics are improved, this could explain the thermal etching seen in the U-notch tests, for those tests carried out in air, although the diffusion kinetics may go some way to explaining the vacuum tests also. After 1000 hrs the oxide provided more general coverage, but was still slightly thicker at grain boundaries. In ASTROLOY® increased oxidation over grain boundaries and at carbide-alloy interfaces was observed. After extended exposure at 750°C the oxide scale was fine grained and slightly undulating.

6.1.2.2 Oxidation Study of N18, RR1000 and U720Li

The oxidation study by Reynolds[166] involved heating small, polished, different specimens in air at 650°C and 725°C and measuring their increase in mass after 1, 4, 16, 64, 256 and 1024 hrs and from this calculating the mass gain per surface area. Specimens were examined in the SEM following oxidation and pertinent features identified using Energy Dispersive Spectrometry (EDS). The results and conclusions of this study are summarised below.

The mass change / surface area versus exposure time seen for N18, RR1000 and U720Li are presented graphically in Figure 150. It should be noted that each data point is produced from a single specimen, so weight gain is not cumulative for each alloy. It has been proposed that the weight gains seen up to 16 hrs may be attributable to difference in atmospheric conditions and thermogravimetric analysis (TGA) would be required to determine whether this was the case or not. The performance of the alloys is summarised in terms of ranking in Table 23.

Table 23 N18, RR1000 and U720Li Oxidation Performance Ranking Summary[166].

← Increasing mass gain

Alloy	U720Li	RR1000	U720Li	N18	RR1000	N18
Temperature	650°C	650°C	725°C	650°C	725°C	725°C

Increasing oxidation resistance →

From Figure 150, it can be seen that for almost every exposure time that the mass of the 650°C specimens for each material was higher than those heated to 725°C and by the 1024 hr exposure time the differences in temperature were even more apparent.

EDS results were used to determine whether a particular element in the scan was high (1.1 x normal elemental content of alloy to 3 x normal elemental content of alloy) or very high (> 3 x normal elemental content of alloy). The results of this analysis are presented in Table 24.

Table 24 Oxidation Study - Summary of percentage of EDS scans that contained high or very high amounts of an element[166].

			Element																			
			Cr		Ti		Mo		Co		Al		Hf		Zr		Ta		Fe		Nb	
Temp	Material	Scans	H	VH	H	VH	H	VH	H	VH	H	VH	H	VH	H	VH	H	VH	H	VH	H	VH
725°C	RR1000	27	37	0	44	0	33	19	7	0	15	0	0	7	0	7	11	15	0	11	0	0
	N18	21	43	5	38	14	10	0	48	10	14	0	19	5	0	0					0	0
	U720Li	18	44	0	56	6	6	0	6	0	22	0			0	0						
650°C	RR1000	15	53	20	40	27	40	0	7	0	33	7	0	0	0	0	7	27	0	0	0	0
	N18	14	86	0	21	29	7	0	64	7	43	0	0	0	0	0					0	0
	U720Li	5	100	0	0	100	20	0	0	0	100	0			0	0						

Key:
H – high elemental content (1.1 x normal elemental content of alloy to 3 x normal elemental content of alloy)
VH - very high (> 3 x normal elemental content of alloy)
■ Element not in alloy specification

From Table 24, it can be seen that all alloys contained either a high or very high amount of Ti and Cr at the surface, the amount reducing slightly from 650°C to 725°C. RR1000 had a significant amount of particles containing Mo on the surface, with these increasing with increasing temperature. For N18, a significant number of particles on the surface contained Co, with the numbers decreasing with increasing temperature.

6.1.2.2.1 Chromium and Titanium Oxides

The most common elements seen on the surface of the specimens were Cr and Ti in all alloys at both 650°C and 725°C. Al was also seen in high amounts but more commonly at the lower temperature. The Ti is expected to have originated from either γ' or Ti – carbides, whilst the Cr may well have originated from the γ matrix or Cr-carbides.

The distribution of Cr between the matrix and Cr-carbides is known to influence the oxidation behaviour by the diffusion of Cr towards the oxidation front[171] with grain boundaries providing preferential diffusion paths to the surface of the alloy. High amounts of Ni were almost always present in the Cr-rich particles in all of the alloys implying the oxides formed are $NiCr_2O_4$ in agreement with the findings of Chen *et al* [170].

Ti when found was usually the predominant element indicating the oxide being formed was likely to contain Ti rather then other metallic elements, the most likely Ti-oxide to be formed during oxidation of superalloys is TiO_2[169,170].

6.1.2.2.2 N18

Following exposure at 650°C large Ti-rich and Al-rich particles formed at the grain boundaries and are likely to have formed from the primary γ' found at these locations. Smaller particles formed across the surface of grains, again these had a high Al and Ti content possibly indicating oxidised secondary γ' precipitates.

Interestingly, the surface of the specimen exposed at 725°C for 1024 hrs was completely different to that exposed at 650°C, less roughness and generally flat with oxide particles rich in Cr and Ni, probably $NiCr_2O_4$. For this particular specimen a high amount of Ti was only found once from seven scans and Al not detected at all. This indicates that differing oxidation processes could be occurring at the different temperatures. A possible explanation for this could be that at the higher temperature diffusion rates of the elements that form protective oxide films have been increased leading to a protective oxide film being formed impeding oxygen diffusion.

6.1.2.2.3 RR1000 and U720Li

Similar to N18, both alloys were more heavily oxidised at lower temperature, with RR1000 showing superior oxidation resistance with only the longest exposure times providing signs of substantial oxidation.

6.1.2.3 Oxidation Mass Change

The specimens gain mass during oxidation as the surfaces react with oxygen from the atmosphere, typically as shown by the two main types of oxidation reaction:

$$MC\ (s) + O_2\ (g) \rightarrow M_aO_b\ (s) + CO_2\ (g) \qquad \textbf{Equation 21}$$

$$M\ (s) + O_2\ (g) \rightarrow M_xO_y\ (s) \qquad \textbf{Equation 22}$$

The oxidation of a carbide (Equation 21) leads to a mass gain for the formation of a solid metal-oxide, but with a debit for the formation of CO_2 gas. Whereas the oxidation reaction shown at Equation 22 leads to a gain in mass as no gas is formed during the reaction.

Previous studies[170] attribute mass gains to the formation of Cr_2O_3, TiO_2 and internal oxides, neglecting the transitional development of other oxides during the initial stages of the oxidation process. The reactions for the formation of Cr_2O_3 and TiO_2[172] are shown at Equation 27 and Equation 28 respectively, with the internal oxide reaction, thought to be Al_2O_3, shown at

$$4Cr + 3O_2 \rightarrow 2Cr_2O_3 \qquad \textbf{Equation 23}$$

$$TiC + 2O_2 \rightarrow TiO_2 + CO_2 \qquad \textbf{Equation 24}$$

$$4Al + 3O_2 \rightarrow 2Al_2O_3 \qquad \textbf{Equation 25}$$

As the alloys were seen to gain more mass at 650°C, this implies that one of the above reactions had a faster rate at the lower temperature, perhaps due to the lack of protective oxide scale forming.

6.1.2.4 Oxidation Summary

In terms of mass gain, N18 gained the least mass, followed by RR1000 and U720Li.

Each alloy was more heavily oxidised at 650°C than at 725°C. This was attributed to the formation of TiO_2 at a higher rate at the lower temperature perhaps due to a more protective oxide film forming at 725°C.

6.1.3 Monotonic Properties

In the following section the results from the tensile strength and creep tests for N18 are discussed and put into context with regard to LSHR and comparison materials using information from the literature.

6.1.3.1 Tensile Strength

The results from the N18 tensile strength tests are presented in Figure 68, this data and data for LSHR, RR1000, U720Li and U720Li LG is summarised in Table 27 and graphically in Figure 69.

Using this information, the strength ranking at 650°C of the alloys is as follows:

N18 = RR1000 > LSHR (super-solvus) > U720Li > U720Li LG.

Although if the strength data for sub-solvus solution treated LSHR[64] is considered, see Table 38 and plotted in Figure 151, then the strength ranking becomes:

LSHR (sub-solvus) > N18 = RR1000 > LSHR (super-solvus) > U720Li > U720Li LG.

If the data for LSHR with a similar heat treatment to that received for long crack fatigue testing is considered (704°C)[61] then there would appear to be an increase in strength for LSHR, but without other test details it is not possible to confirm trends further.

Strength is a measure of a materials ability to impede the motion of dislocations. As discussed previously, there are several mechanisms acting in combination by which this is achieved in superalloys, including solid solution strengthening of the matrix, precipitation hardening via γ' and grain size effects.

N18 has a reported γ' volume fraction of typically around 55-57%[173] which compares well with the first order prediction of 56% in Table 22, compared with around 48% predicted in U720Li [46], with solution treatment closer to its γ' solvus, this should lead to less primary γ' and hence to an increase in the amount of secondary γ' (which may be coherent with the matrix) which in turn will lead to a strengthening of the alloy, especially at higher temperatures. This strengthening effect will be balanced by the reduced number of grain boundaries available to impede dislocation motion resulting from the larger grain size due to there being less primary γ' available to restrict grain growth. Assuming that solid solution strengthening is optimised for all the alloys, (which may not be the case as the ratio of solid solution strengtheners to γ ranges from around 61% in the U720Li variants to 80% in LSHR), and that in relative terms it contributes the least to overall strength when

compared with the effects of (1) overall coherent V_f of γ'; (2) spacing between γ' and (3) the fineness of the coherent γ'. Then for the 0.2% proof stress at 650°C it can be seen that the balance between grain size effects and coherent γ' for N18, LSHR (super-solvus) and RR1000 is about equal. Whereas for U720Li, with a similar grain size to RR1000, its strength is somewhat lower due to there being less coherent γ' predicted (29.4% vs. 40.5% respectively[21]). Although if U720Li LG is compared with RR1000 where the coherent γ' predictions are similar (39.7% vs. 40.5%[21]) or even U720Li which has a lower coherent γ' content, then this would seem to indicate that grain size (Hall-Petch) has a more significant contribution to strength at this temperature. This is further supported by the differences in the 0.2% proof stress between super-solvus and sub-solvus heat treated LSHR where the sub-solvus heat treated material will have lower coherent γ' and smaller grains and has a higher reported strength[64].

Increasing the temperature from 650°C to 750°C leads to the 0.2% proof stress performance of RR1000 falling more than N18, with super-solvus LSHR retaining its strength. The sub-solvus heat treated LSHR performance falls by a similar amount to N18, but the differential between the two of around 100 MPa is retained in favour of LSHR (sub-solvus). This is a potential indication of the effect of the higher amount of coherent γ' within N18 and LSHR (super-solvus), but still shows the apparent importance of grain size in terms of its contribution to strength.

The capacity for work hardening for LSHR (sub-solvus and super-solvus) and N18 can be seen by comparing their 0.2% proof stresses with that of their ultimate tensile strength (UTS). For all three alloys the capacity for work hardening falls as the temperature is increased from 650°C to 750°C.

6.1.3.2 Creep

Within the literature only a single stress / lifetime combination at each of 650°C, 704°C and 760°C was available for LSHR[64], with a further single stress / lifetime at 704°C[61] for LSHR with the same heat treatment as applied to the specimens used in long crack fatigue testing. For RR1000 only a single temperature, 725°C, was available[156] with two stress / lifetime data points. Due to the difference in testing temperatures and stresses and low number of data points, the creep information was plotted as stress against log time against equivalent data derived from the tensile strength tests for each of the materials in Figure 152. This derivation makes the assumption that tensile testing can be considered a high stress creep test of short duration. With typical applied strain rates of 10^{-3} s^{-1} applied up to 0.5% proof stress and then 10^{-4} s^{-1} to failure in accordance with British Standard BS 4 A4[150]. As an example with failure occurring at 25% elongation an approximate time for tensile tests would be 0.7 hours. Curves were fitted to both sets of

data for each material / temperature combination to permit comparisons between the materials to be made.

With regard to performance at 650°C, the alloys can be ranked in terms of stress / hours to rupture from best to worst performance as follows:

LSHR > N18 > U720Li

At 725°C with the anticipation that the performance of LSHR lies between its performance at 704°C and 760°C, and potentially closer to 760°C, then the ranking is similar:

LSHR > N18 = RR1000 > U720Li

Creep and oxidation occur principally along grain boundaries due to the preferential diffusion paths they offer, and this weakens the grain boundary and provides a weaker path along which cracking can occur. Such creep and grain boundary oxidation effects will be reduced by the larger grain size (and hence decrease in amount of grain boundary area), but may also be expected to vary with alloy composition and grain boundary character.

The improved creep performance of N18 compared with U720Li is likely to be due to a combination of reduced grain boundary area, possibly an improved grain boundary microstructure and the improved high temperature deformation resistance (higher proof stress). For the creep testing conditions studied, failure mechanisms would appear to be principally tertiary mechanisms. Weber *et al* [174] reported improved creep resistance for N18 when grain size was increased, indicating the importance of grain boundary failure modes in creep in this alloy. The grain boundary character will therefore control these failure modes and the grain boundary borides and the species segregation reported[15] may be expected to have an effect on grain boundary failure. B film segregation to grain boundaries may improve grain boundary strength through two mechanisms: (1) increased disorder at the grain boundary increases dislocation mobility, hence reducing pile-ups at the grain boundary[175] (2) Grain boundary cohesion is reinforced by the formation of strong interatomic bonds with B[176]. In addition to these possible mechanisms, the role of the borides, their distribution and mechanical properties are likely to affect the operation of grain boundary sliding or decohesion modes. Fine distributions of pinning grain boundary carbides and borides have been advocated in improving intergranular failure resistance at high temperatures in more recently developed alloys[177]. The importance of the grain boundary character in determining high temperature mechanical properties can also be seen in the fatigue performance.

With regard to the performance of LSHR at 725°C see Figure 153, (and anticipating that the performance of LSHR lies between its performance at 704°C and 760°C, and potentially closer to 760°C); as (1) the creep performance of the sub-solvus variant of

LSHR [64] is comparable to N18 and RR1000 ; then (2) the improved performance of the super-solvus variant when compared with N18 and RR1000 appears to be due to the increase in grain size. LSHR (both super-solvus and sub-solvus) failed from intergranular surface initiated cracks due to environmental attack at grain boundaries[64]. Increasing temperature led to an increasing amount of secondary cracking and grain boundary cavitation with final overload due to transgranular microvoid coalescence[64], similar to the final failure modes seen in N18. In RR1000 most of the creep was tertiary in nature, specimens that had been subject to long term ageing had a substantially reduced creep life with some reduction in ductility[156]. As N18 has a larger grain size than RR1000, similar performance in creep may indicate that other grain boundary improvements must be taking place in RR1000 compared with those in N18. These could be carbides or the small amounts of σ which forms (by design[52]) at the grain boundaries which will lead to a reduction in grain boundary sliding and diffusion at these locations leading to improved creep performance, although Turan *et al*[156] state that σ has little effect on creep performance and it is the dissolution of the fine tertiary γ' during the long ageing process that leads to higher initial creep strains being seen in their specimens and leading to reduced rupture lives. With secondary γ' (the size of which is unaffected by the long ageing time their specimens were subjected to) controlling creep rate during intermediate strains.

6.1.4 Crack Propagation Behaviour

In this section, the crack propagation behaviour of the alloys is discussed. Initially a summary of results is presented, followed by a discussion on the modes of crack propagation and then the effects of environment, temperature and dwell. Microstructural and alloy chemistry are then considered followed by an analysis using an apparent activation energy approach.

6.1.4.1 Summary of Results

The fatigue crack propagation performance of N18, LSHR, RR1000, U720Li and U720Li LG has been summarised in several tables and figures: The performance rankings for the alloys in terms of crack growth rate (da/dN) at ΔK = 25 MPa$\sqrt{m}$ and ΔK = 45 MPa$\sqrt{m}$ for the various combinations of environment, temperature and dwell time are presented in Table 31. With the effect on fatigue crack growth rate (*da/dN*) due to changes in test environment, temperature and dwell time between ΔK = 25 MPa$\sqrt{m}$ and ΔK = 45 MPa$\sqrt{m}$ compared in tabular from in Table 32 and graphically in Figure 88. A summary of the Paris Law coefficients, *C* and *m*, are presented in Table 33.

6.1.4.2 Crack Propagation Modes

If the fractography of the failed specimens is considered, for tests carried out in air and 1s dwell, at low ΔK (~20 MPa$\sqrt{m}$) N18 at 650°C (Figure 92(a)) exhibits the most transgranular failure on the fracture surface, followed by U720Li-LG (Figure 109(a)). RR1000 (Figure 102(a)) exhibits mixed intergranular and transgranular failure modes under these conditions whilst U720Li, Figure 106(a), shows mostly intergranular failure. At the increased temperature of 725°C and increased ΔK, the mode of failure becomes increasingly intergranular for N18 ((Figure 92(d), (f)), U720Li LG (Figure 109(d), (f)) and RR1000 (Figure 102 (d), (f)), which provides an indication that the grain boundary oxidation and creep processes discussed earlier predominate, especially when this it contrasted with the fractography from the tests carried out under vacuum conditions (N18,Figure 94; RR1000,Figure 104; U720Li, Figure 108 and U720Li LG, Figure 111) where transgranular crack growth is evident to higher values of temperature and ΔK when compared to the equivalent tests carried out in air.

For a 20s dwell, the failure modes are increasingly intergranular for tests carried out in both air and under vacuum conditions for all the alloys previously discussed. In very approximate terms increasing the dwell time increases the amount of intergranular failure by a similar amount to the increase in temperature from 650°C to 725°C. Apart from a small amount of transgranular failure at 650°C, LSHR exhibits almost exclusively intergranular failure when tests are carried out in air (Figure 100) this is sharply contrasted by the transgranular failure this alloys sees under vacuum conditions (Figure 101). Although with increased temperature and ΔK, the failure mode does become more intergranular as can be seen in Figure 101(b), (d) and (f). The intergranular failure providing further evidence of grain boundaries providing a preferential path for crack propagation, especially in the case of such a high V_f alloy. This is perhaps an indication that the performance of both grain boundary and the grains need to be balanced overall to produce an optimum alloy. In Figure 101(e), very straight secondary cracks can be seen in LSHR tested under vacuum conditions at 650°C at the highest ΔK, these are cracks are probably following slip planes. However, this type of cracking is not seen at 725°C in the same alloy perhaps indicating that a transition to wavy slip occurs between 650°C and 725°C in this alloy.

The comparisons carried out above rely on qualitative analysis and comparison of micrographs of the fracture surfaces, in order to produce quantitative evidence analysis of the roughness of the fracture surfaces of N18 and LSHR was carried out by an intern, (Thompson[178]), using Alicona MeX® software. In brief, the Alicona MeX® software uses three images of the same fracture surface taken at -5°, 0° and +5° angle of tilt. The magnification of the fracture surfaces is selected to provide a representative range of

surface features, in this case 800x magnification was chosen for N18 and 100x magnification for LSHR due to its larger grain size. From these images average roughness, R_a, and surface roughness, R_s, were calculated. Where R_s is a dimensionless value equal to the true area S of the fracture surface divided by its apparent projection area A[179]. R_a measurements were made along lines which formed a grid over the surface, see Figure 154, with the reported R_a an average of these measurements. A cut-off length of 4μm was used for N18 and 16μm for LSHR. R_s measurements were calculated for the complete surface, which can be represented in three dimensional form as shown in Figure 155. The results from these measurements of R_a and R_s are presented in Table 39 and graphically in Figure 156 and Figure 157 for N18 and LSHR respectively.

Apart from a general trend of roughness increasing with ΔK seen in N18 and a convergence of R_a to around 500 nm seen in LSHR, there is little apparent correlation between roughness and other test conditions. This may be due to slight variation in the Working Distance (WD) of the microscope, the cut off length selected in MeX®. If the range of R_a is normalised with respect to mean grain size then the range seen in N18 is similar to that of LSHR (8.6 to 18.5 and 11.9 to 17.5 respectively), but, as only two data sets are being considered, further studies would be required to confirm this relationship.

6.1.4.3 Environment, Temperature and Dwell Effects

The crack propagation observed in the N18 fatigue crack propagation tests show that N18 has good resistance to intergranular cracking modes, although some increase in intergranular cracking is seen at higher ΔK levels and temperatures, although not to the same levels seen in other alloys. Increased intergranular cracking linked to oxidation attack along grain boundaries could perhaps lead to the creep processes being distributed over a larger volume of material rather than being concentrated at the crack tip. This would imply that creep would then have a diminished role compared with its role during fatigue crack propagation under vacuum conditions leading to a fatigue crack growth process dominated by oxidation. N18 shows far better resistance to fatigue crack propagation at 725°C than U720Li. Prior work on U720Li[46] in air and vacuum has indicated that the fast intergranular crack propagation mode observed in U720Li is principally oxidation-fatigue rather than creep-fatigue, as the time dependent effects seen at 725°C in vacuum are very small when compared with the time-dependent effects observed in air. The relative amounts of intergranular and creep fatigue crack propagation can be gauged by comparing fatigue crack propagation rates in air and vacuum (Table 32 and Figure 88 (a) and (j)) at low crack growth rates where there is sufficient time for time dependent processes to have an effect with higher crack growth rates where time dependent processes should have less significance. Comparison with tests conducted in vacuum has indicated that at these temperatures oxidation-fatigue

processes swamp pure creep-fatigue processes[62]. Other crack propagation studies in N18[143] have indicated increased intergranular crack growth modes with long hold times, with mostly transgranular crack growth modes observed at 650°C with lower hold times[60], in agreement with this work. At a ΔK of 25 MPa√m crack propagation rates in N18 are around four to five times faster at both 650°C and 725°C whereas for U720Li at 725°C there is a six fold increase in fatigue crack propagation rate between the tests carried out in vacuum and in air with a 1s dwell rising to a factor of 108 with a 20s dwell in air. At a higher ΔK of 45 MPa√m the difference between fatigue crack growth rates in air and vacuum for N18 falls to around a factor of two for a 1s dwell and to between three and four for 20s dwell. This is reflected by the change in slope of the *da/dN* versus ΔK curves between air and vacuum tests, where the higher m-value for the vacuum curves implies an increased contribution from monotonic damage (i.e. creep processes) which are likely to have a greater effect at higher ΔK levels. Alternatively the reduced m-values for the air curves could be a reflection of the more wavy slip processes created by a reduction in planar slip and grain boundary sliding due to some form of pinning effect caused by oxidation. For the 1s dwell tests curves the crack growth rate for N18 can be seen to converge around a ΔK of 60 MPa√m. This convergence may reflect the point where pure creep processes in vacuum are starting to have as much effect as combined creep and oxidation processes in air. Oxidation processes might be expected to have an equivalent effect at all ΔK levels, however, if Figure 87 (c) is considered, it can be seen that when increasing the dwell from 1s to 20s, under vacuum conditions at 725°C, the rate of FCG increases by a factor of approximately two irrespective of ΔK, whereas in air at the same temperature the crack growth rate increases by around a factor of two at a ΔK = 25 MPa√m and about a factor of four at ΔK = 45 MPa√m. This arises from the divergence of the slope for the air, 725°C, 20s dwell curve (Figure 75) from that of the other curves for tests in air towards the slope of the curves for tests carried out under vacuum conditions. This indicates that any benefit from oxidation processes in terms of reducing the contribution to the rate of FCG from monotonic and cyclic processes that occur without hindrance from oxidation under vacuum conditions (creep, grain boundary sliding and slip reversibility) is being reduced as ΔK is increased which can be explained by the increased amount of creep fatigue that will occur due to the increase in $\Delta CTOD$ arising from a reduction in strength of the alloy. An alternative beneficial process that could provide the same result would be OICC where at low ΔK this could lead to a significant reduction in the $\Delta CTOD$, but at higher ΔK and increased temperature the impact of OICC on $\Delta CTOD$ would be much less significant.

CTOD was defined previously at Equation 15, in order to take into account reversed plastic flow with a cyclic variation in stress intensity factor, ΔK, a cyclic crack tip opening

displacement, $\Delta\delta_t$, which is half of the total opening displacement, δ, experienced under a monotonic stress intensity factor and is defined as[38]:

$$\Delta\delta_t = \frac{\Delta K_I^2}{2\sigma'_Y E} \qquad \textbf{Equation 26}$$

Where, σ'_Y, is the cyclic yield strength and has been used to take account of any cyclic softening in the alloys. *da/dN* versus *ΔCTOD* have been plotted for N18 in Figure 158 and LSHR in Figure 159, cyclic softening data was only available for N18 from the LCF tests carried out at 650°C and 725°C by QinetiQ, for LSHR standard 0.2% yield strength at 650°C and 725°C was utilised. *da/dN* versus *ΔCTOD* have also been plotted for LSHR, by comparing Figure 159 with Figure 77, it can be deduced that the relatively small change in yield strength with temperature has little relative effect on the crack growth rates of the LSHR between 650°C and 725°C. However, the situation for N18 is different, if Figure 158 is compared with Figure 75, it can be seen that the crack propagation curves for tests carried out under vacuum conditions, with the exception of the 725°C 1-20-1-1 curve, tend to "collapse" onto each other. The effect is similar for the tests carried out in air, with smaller differences in *da/dN* between the crack growth rates for *ΔCTOD* when compared with those obtained using *ΔK*. The curves obtained for N18 from the tests carried out at 725°C under 1-20-1-1 load conditions in both air and vacuum are particularly interesting. They have similar slopes and vary from their peers (air and vacuum respectively) by similar amounts despite the tests being carried out in different environments. This appears to indicate that a process other than oxidation is increasing the crack growth rates at 725°C and 1-20-1-1 load conditions. To provide further insight, *da/dt* versus *ΔK* has been plotted in Figure 160 for N18. This allows comparisons to be made on the basis of crack growth rates with respect to time, rather than number of cycles. Comparing the 20s dwell tests against the 1s dwell tests indicates the presence of a beneficial process at both 725°C and 650°C during the 20s dwell tests, with the apparent benefit in reduced crack growth rate (*da/dt*) significantly increased at 650°C when compared to 725°C. As this benefit occurs for tests carried out in air and under vacuum conditions, it suggests that creep rather than oxidation is responsible for providing it, perhaps via crack tip blunting and thus reducing the effect of oxidation embrittlement at this point, or by reducing the effective *ΔK* due to stress relaxation. The reduced benefit seen at 725°C can perhaps be explained by a transition from crack tip blunting or stress relaxation caused by creep to increased CTOD due to the reduction in strength from both the reduced monotonic strength and via cyclic softening at this temperature as well as a reduced Young's Modulus. This would reduce, but not completely nullify, the benefits of crack tip blunting or stress relaxation and lead to increased crack propagation rates, at these particular dwell conditions. The hold time effect in N18 has been linked to

intergranular oxidation assisted embrittlement and creep strains due to stress relaxation during the hold time (where the stress relaxation has been found to be largely dependent on γ' size). Vacuum tests carried out by Andrieu and Pineau [143] and Weber *et al* on N18[174] showed significantly less effect of hold time at 650°C and the failure mode maintained a transgranular character. Under vacuum conditions, just prior to final failure the increase in crack length during the 20s dwell can be seen on the DATAQ data logger, see Figure 161, but here is likely to be due to rapid crack propagation as the critical crack length is approached.

For LSHR, its performance at 650°C and 725°C when tested under vacuum conditions (Figure 79) is somewhat better than N18, especially at lower values of ΔK. The macroscopic overviews presented in Figure 91(c) and (d) shows signs of what appear to be polishing and fretting respectively. These could indicate that crack re-welding has been occurring under vacuum conditions, which would effectively reduce the ΔK seen at the crack tip, hence leading to reduced crack propagation rates under these conditions. Although there does not appear to be any further evidence of this effect occurring in the micrographs from the FEG SEM shown in Figure 101. In air, LSHR does not perform as well when compared with N18, at 725°C under a 20s dwell load, the performance of LSHR is comparable with that of U720Li under the same conditions, although it should be borne in mind that this particular test for LSHR was not strictly valid in terms of crack front symmetry. Noting the almost completely intergranular failure that has occurred in this alloy (Figure 100), the reduction of performance in air is almost certainly due to increased oxidation-fatigue similar to that seen in U720Li. Other variants of LSHR that are cooled more slowly from the super-solvus heat treatment temperature produce serrated grain boundaries which will tend to impede the transport of oxygen along the grain boundaries, whereas, the particular alloy tested here does not have the benefit of these serrated grain boundaries due to the fast cooling it has received. This would perhaps explain (at least in part) the alloys relatively poor performance due to the comparatively unimpeded transport of oxygen to the crack tip along grain boundaries.

6.1.4.4 Microstructural Effects

N18 has improved resistance to intergranular cracking which is perhaps due to the reduced grain boundary area when compared with U720Li. Further evidence of this can be seen in the fatigue crack propagation rates at 650°C and 725°C for tests carried out under 1-1-1-1 loading cycles shown Figure 80, and even more pronounced for the tests carried out under 20s dwell conditions, Figure 81, where the large grain variety of U720Li (LG) has improved fatigue crack propagation performance in air over the as-received U720Li, yet, in the same figures, performance under vacuum conditions shows a much smaller difference in the performance of the two variants. The better crack propagation

performance shown in U720Li-LG when compared with U720Li can therefore be understood in terms of reduced grain boundary area.

RR1000 achieves the lowest crack propagation rate in air over all ΔK levels (except for low ΔK under a 20s dwell at 725°C, see Table 31) and yet has a grain size intermediate between U720Li and U720Li-LG. This shows that grain size alone cannot account for difference in the crack propagation rates across the alloys. The influence of additional factors such as alloy chemistry and coherent γ' distributions, which will strongly influence the alloys' flow strengths at elevated temperature will also play a role, and slip behaviour may play a role in transport of oxygen to the grain boundaries[47]. Previous short crack studies in some of these alloys at 650°C[110] have indicated that changes in the finer γ' distributions and the concomitant effects on slip behaviour only have a minor effect when compared with grain size effects. Alloy chemistry and heat treatments schedules will also play an important part in the control of oxidation rates along grain boundaries in LSHR, RR1000, N18 and the U720Li variants.

Secondary cracking tends to occur in all of the alloys tested in air at higher ΔK, as seen in N18 in Figure 92 and Figure 93, LSHR in Figure 100, RR1000 in Figure 102 and Figure 103, U720Li in Figure 106 and Figure 107 and U720Li LG Figure 109 and Figure 110. These secondary cracks will reduce the crack tip driving force seen at the crack tip, hence the effective ΔK seen at the crack tip. Although the use of ΔK to describe crack tip conditions may be valid in experimental specimens of similar dimension, validation of the use of ΔK may be required for differing sizes and conditions as ΔK may not be a valid descriptor for crack tip driving force under these differing conditions.

6.1.4.5 Alloy Chemistry

Grain boundaries are obviously sites of special interest with their capacity to resist crack propagation across them and because of the potentially quicker diffusion paths they offer for some species. The amount of grain boundaries will depend on the grain sizes of a particular material which is determined by the deformation history and heat treatment schedule that the alloy receives. Alloy behaviour at these grain boundaries can be modified by changes to an alloy's chemistry. For instance the changes to the chemistry of U720 to form U720Li were discussed earlier. Here the local microstructure at the grain boundaries was modified by reducing the C, B and Cr content of the alloy, simultaneously reducing the elements required to form carbides and borides and the tendency of the alloy to form the deleterious brittle σ phase at the grain boundaries, thus improving the fatigue crack propagation performance of U720Li when compared with U720.

Amongst the other differences in alloy chemistry, an important aspect is the addition of Hf to the RR1000 and N18 alloys and Ta to RR1000 and LSHR. These elements will modify

the MC carbides to become enriched in Hf and Ta and under certain conditions MC carbide with a wide range of compositions from Hf lean (Ti, Ta)C to Hf rich MC can form[180]. The decomposition of the MC carbides during heat treatment and exposure at high temperatures will cause the formation of lower carbides such as the Cr-rich $M_{23}C_6$ carbides which form predominantly at grain boundaries in a range of superalloys[181], including RR1000[177]. As C diffusion is orders of magnitude faster than diffusion of metallic alloying elements, and Ta and Hf diffusion is particularly slow, the rate of $M_{23}C_6$ formation is dependent mostly on the decomposition rate of the Ta and Hf containing MC carbides. Thus, in combination with heat treatment schedule, Ta and Hf additions offer the possibility of fine tuning the $M_{23}C_6$ distribution on grain boundaries and hence the microchemistry at the grain boundaries. In addition, the MC carbides will to some extent be located preferentially at grain boundaries, because they slow down grain growth. These carbides at grain boundaries are expected to influence fatigue crack propagation along grain boundaries through two mechanisms. Firstly, formation of substantial amounts of the Cr-rich $M_{23}C_6$ carbides at grain boundaries will cause local Cr depletion of the matrix at the grain boundaries and hence change local susceptibility to corrosion and the corrosion products formed, which will degrade FCG resistance in air. This effect is also influenced by the increased Mo content of RR1000, which will substitute for some of the Cr in the formation of $(Cr, Mo)_{23}C_6$. On the other hand, the presence of carbides at grain boundaries will reduce creep by grain boundary sliding, and this effect is especially important for finer grained alloys. Thus carbides at grain boundaries will improve FCG resistance in vacuum and can improve FCG resistance in air provided the detrimental effect of Cr depletion is kept limited. The beneficial effect will become more important if a dwell at high load is included. The producers of RR1000 have stated that the composition and heat treatment of RR1000 is optimised to provide the optimum grain boundary carbide distribution with optimum size of carbide grain boundary particles of 350 to 550 nm[177]. On the basis of the present discussion it is suggested that a key factor in the superior FCG resistance of RR1000 is the (near) optimised combination of heat treatment and Ta and Hf additions which produces a beneficial distribution of fine carbides at grain boundaries and a beneficial local chemistry at the grain boundaries. This optimisation ultimately proves more beneficial compared to the increased grain size of the U720Li LG variant, which is thought to have grain boundary particle distributions and chemistry that are not optimised for FCG resistance.

6.1.4.6 Activation Energy Analysis

Since the failure processes assessed in the previous discussion are essentially multi-mechanistic, clearly defining the dominant or rate-determining process is complex and open to many alternative interpretations. An alternative method of gaining information on the mechanisms involved in these tests is to assess the apparent activation energy of the

fatigue crack process, as proposed by Starink and Reed[182]. This method assumes that progress of many of the processes discussed so far is dominated by a thermally activated reaction and as such the rate is proportional to an Arrhenius term. Examples of such processes are, thermally activated dislocation motion (including creep), solid state reactions, gas-solid reactions (including oxidation), and other diffusion processes which may apply to fatigue crack propagation processes considered here. When adopted for fatigue crack propagation, the following relation can be derived[182]:

$$\frac{da}{dt} \propto k_{FCG}\ f(a) \exp\frac{-Q}{R_g T} \qquad \textbf{Equation 27}$$

Where d*a*/d*t* is the rate of crack growth, k_{FCG} is a term that contains all non temperature dependent terms, except for the length of the crack, f is a function depending only on the extent of the reaction completed, Q is the activation energy, R_g is the gas constant (8.31 J/mol.K) and T is the temperature. With the product of k_{FCG} and $f(a)$ being kept constant by defining a crack driving force appropriate for the material's loading condition, such as ΔK in this case. Thus, as the product k_{FCG} and $f(a)$ is kept constant, then the (apparent) activation energy, E_{app} can be obtained from two fatigue crack propagation tests at two temperatures, T_2 and T_1 by using[182]:

$$E_{app} = \frac{-R_g}{T_2^{-1} - T_1^{-1}} \ln\left(\frac{da}{dN}(T_2) \Big/ \frac{da}{dN}(T_1) \right) \qquad \textbf{Equation 28}$$

Which assumes that the loading cycles at the two temperatures are identical and as such d*a*/d*t* is proportional to d*a*/d*N*.

Using this method and by relating this apparent activation energy to the activation energies required for various mechanisms to occur it should be possible to identify which thermally activated mechanisms have been activated by the increase in temperature from T_1 to T_2. Three main groups of thermally activated mechanisms can be attributed to time-dependent crack growth behaviour at temperature: (1) localized oxidation at the crack tip and/or dynamic embrittlement (2) creep (especially at grain boundaries) (3) thermally activated modes of dislocation movement, which may influence, amongst others, the monotonic mechanical properties of the material, most notably the yield strength. The relative importance of these processes can change with temperature and crack tip stress cycle, affecting the apparent activation energy as it is assessed between different temperatures (unlike other thermally activated reactions where the activation energy generally undergoes very little change with temperature). Detailed derivations / discussions of the different expected apparent activation energies for the different underlying mechanisms, as well as experimental and mechanistic issues related to

linearity of the E_{app} versus *1/T* curves, were discussed by Starink and Reed[182], a summary of the values derived is presented in Table 40.

Activation energies for all five materials tested in air and vacuum under 1-1-1-1 and 1-20-1-1 load cycles for ranges of ΔK from 20 MPa√m to 60 MPa√m are presented as radar plots by ΔK in Figure 162 and graphically by alloy in Figure 163. To permit comparisons to be drawn between the full complement of alloys, the data available for ΔK = 30 MPa√m and 40 MPa√m is the most complete and this will be considered below in order to assist in identifying the thermally activated reactions that contribute to the change in fatigue crack propagation rate due to the temperature change from 650°C to 725°C.

In general, with the exception of RR1000, tests carried out under vacuum conditions and 1-1-1-1 tests in air have an E_{app} between 0 – 175 kJ/mol. Tests using 1-20-1-1 load cycle in air were more dependent on the particular alloy: RR1000 and N18, E_{app} = 150 - 200 kJ/mol; LSHR and U720Li E_{app} = 300 - 400 kJ/mol; U720Li LG in between these two groups. The least (detrimentally) to worst affected by the increase in temperature from 650°C to 725°C is as follows: RR1000, N18, U720Li LG, LSHR, U720Li. For RR1000 tests carried out in vacuum using 1-1-1-1 load cycle, E_{app} falls to -150 kJ/mol at ΔK = 50 MPa√m. This may be indicative of beneficial processes becoming thermally activated such as crack tip blunting due to creep or alternatively to a previously detrimental process no longer being active at the higher temperature. For instance a particular oxidation reaction may be active at lower temperatures, but as the temperature is increased a different (and less detrimental) reaction may replace it. To obtain maximum value the E_{app} results should be considered with the results obtained from fractographic analysis. Although some interesting observations for each of the alloys may be made by considering the E_{app} presented in Figure 162 and Figure 163 and comparing the values obtained with those in Table 40.

6.1.4.6.1 N18

For 1-1-1-1 load cycle tests carried out in air and vacuum are similar E_{app} = 0-50 kJ/mol are obtained. Too low a value to be oxidation related this potentially is due to a change in static properties (strength). With the 20s dwell tests in air and vacuum E_{app} = 100-150 kJ/mol again too low for oxidation, but potentially related to the longer hold time i.e. creep processes are contributing to the change in fatigue crack propagation rates.

6.1.4.6.2 LSHR

For 1-20-1-1 tests carried out in vacuum, at lower ΔK E_{app} ~ 110 kJ/mol with transgranular fatigue crack growth at low ΔK and lower temperature changing to more intergranular failure at higher ΔK and an E_{app} ~ -120 kJ/mol, implying that a beneficial process (in terms of fatigue crack propagation) is occurring at the higher temperature which may be blunting

of the crack tip due to creep. For the 20s dwell tests carried out in air, E_{app} = 350 – 400 kJ/mol. Potentially caused by creep and oxidation combining in a synergistic manner such that effect is more severe and hence fatigue crack growth rate is increased at the higher temperature.

6.1.4.6.3 RR1000

The activation energies for FCG for RR1000 and N18 tested in air using 1s dwells are much lower than any known diffusion process (at grain boundaries or in the bulk) and apparent activation energies for FCG in the U720Li variants. These activation energies for RR1000 and N18 also show a clear decreasing trend with increasing ΔK, and activation energies become nearly zero for ΔK = 50MPa√m. It is thought that these observations indicate that oxidation or creep is not the rate determining step in FCG for medium to high ΔK. (This is not to say the oxidation does not occur, it means that the oxidation that occurs is not significantly contributing to the FCG rate change when increasing T_1 to T_2.) In this case, where higher crack growth rates occur, pure cyclic (or mechanical) fatigue processes may be considered to predominate. For the 20s dwell tests carried out in air, E_{app} = 150 – 200 kJ/mol and indication that either creep or combination of grain boundary creep and oxidation dominated FCG are causing the increase in FCG rate. For 1-1-1-1 load cycle tests in vacuum, E_{app} has a clear decreasing trend with increasing ΔK and at ΔK = 50MPa√m, E_{app} = -150 kJ/mol, not oxidation related as the test is carried out under vacuum conditions but potentially beneficial creep effects with increasing ΔK are leading to the improved FCG with increased temperature. Whereas for the 20s dwell tests carried out under vacuum conditions the beneficial effects of creep are not seen due to the longer hold time giving an E_{app} ~ 0 kJ/mol.

6.1.4.6.4 U720Li variants

The activation energies measured for the 1-20-1-1 tests in air of the U720Li variants are between 250 to 350kJ/mol, which taken in conjunction with the fractography results and consideration of crack growth rate trends can be related to FCG dominated by oxidation. However, the apparent activation energies of U720Li LG and U720Li for 1-1-1-1 cycles in both air and vacuum are substantially lower (80-100kJ/mol), indicating that oxidation provides a much more limited contribution to the failure processes for this cycle the change in fatigue crack growth rate potentially being due to a change in the static properties (strength). Although U720Li LG has a slightly higher E_{app} ~150kJ/mol for 1-20-1-1 load cycle tests carried out in vacuum when compared with U720Li, this could be indicative of grain boundary creep, but its effects in terms of fatigue crack growth rate are minimised in U720Li LG because of the effective reduction in grain boundary area due to larger grains in this alloy.

The activation energies suggest that oxidation is not the rate determining process for FCG in RR1000, but for U720Li (the smaller grain variant studied here) oxidation related FCG is dominant for tests in air with a dwell. The figures also suggest that there is no significant change in the main mechanism for FCG for the two U720Li variants when atmosphere is changed from air to vacuum in the absence of a dwell (during the 1-1-1-1 test cycle). It should be noted that the apparent activation energy reflects the degree of thermal activation of a process, and is not a reflection of how much it may affect crack propagation resistance in an individual alloy. Hence the activation energy for crack propagation in air for U720Li-LG is similar to that of U720Li, which is consistent with oxidation-fatigue at grain boundaries being dominant for both materials, with the difference in FCG rate being determined predominantly by the reduced grain boundary area. In the case of RR1000 and N18 however, the improvement in grain boundary character discussed earlier (through manipulation of either carbides or borides on the grain boundaries) may be contributing to improved resistance to creep processes, but also oxidation processes, assuming any Cr depletion in forming the grain boundary particles is limited. This may be reflected in the low apparent activation energies for these alloys.

By contrast, for LSHR the grain boundary character is not enhanced by the particular super-solvus heat treatment used here. There is no pinning primary gamma prime and the fast cool leads to a reduction in serration of the grain boundary *cf.* serrated boundaries seen for heat treatment using a slower cooling rate. The grain boundary character may allow detrimental synergistic combination of creep and oxidation effects allowing increased FCG and indicated by the highest activation energies seen throughout the alloys tested.

6.1.4.6.5 Apparent Activation Energy Analysis for Oxidation

In addition to the change in mass study carried out as part of the oxidation analysis at section 6.1.2.3, an apparent activation energy analysis approach was applied to the mass changes over time to determine if this could elucidate further insights. The method makes the assumption that the progress of the process, in this case oxidation, is dominated by a thermally activated reaction and thus that such a rate is proportional to an Arrhenius term, the term “apparent” is used as more than one type of oxidation may be occurring and any derived activation energy will refer to this combination of processes. Equation 28 was used to determine the apparent activation energy, but in this case substituting the increase in mass seen at each of the temperatures (650°C and 725°C) instead of the crack growth rate *da/dN.*

In general, a correlation between this study and the fatigue crack propagation analysis was not found. The apparent activation energies were, at least for the longer exposed specimens, found to be negative which indicates that some form of beneficial reaction was

taking place and slowing the rate of mass gain. One such beneficial reaction could be the formation of a protective oxide layer, which effectively reduced the availability of oxygen at the oxidation front. Furthermore, the timescales seen during the FCG tests and oxidation experiments are completely different, for FCG, timescales for the formation of an oxide at the crack tip are in the order of seconds (1 to 20s in the experiments described here) compared with the maximum exposure of 1024 hrs for the oxidation experiment. Although the shorter time exposures during the oxidation experiments may be more relevant to FCG studies. These short time exposures seem to indicate that transitional and / or non-protective oxides may form after exposure for shorter timescales and / or lower temperatures. Further to this, under cyclic loading conditions the stress state at the crack tip is varying rather than unstressed as would be the case in the oxidation study, this varying stress state would tend to keep cracking any newly formed oxide layer, minimising any protective value it may provide.

6.1.5 Low Cycle Fatigue Behaviour

The crack propagation modes observed in both the N18 LCF and fatigue crack propagation tests are in agreement and show that N18 has good resistance to intergranular cracking modes, although some increase in intergranular cracking modes is seen at higher ΔK levels and temperatures.

In terms of LCF resistance, N18 shows only a slight effect of increasing test temperature from 650°C to 725°C, and this may be linked to the maintenance of quite high strength levels, and a modest change in crack propagation mechanisms expected. However, LCF lives are mostly dominated by initiation processes. Weber *et al* [174] have reported fatigue initiation from inclusions and porosity whereas Flageolet *et al*[14] testing N18 at 700°C under 1-1-1-1 or 1-50-1-1 loading cycles at R = 0.05 under constant stress control (σ_{max} = 775MPa) found initiation occurred from sub-surface porosity in air, but they saw intergranular damage that seemed to initiate at primary γ' precipitate interfaces (most noticeably in the vacuum tests). Similar fatigue initiation by intergranular cracking was reported by Pang *et al*[62] in a large grain variant of U720Li in notched fatigue specimens tested at 650°C under a 1-1-1-1 trapezoidal loading cycle, but again porosity was found to be the primary cause of initiation in the U720Li variants studied. It is not clear whether these observations relate to genuine porosity or cavities associated with oxide inclusions. In the N18 LCF tests, sub-surface porosity caused the initiation of a crack in the 650°C $\Delta\varepsilon$ = 0.7 specimen as shown in Figure 117(c), yet with higher strain ranges and temperatures edge initiation of cracks becomes apparent, the quantity of initiation sites increasing with strain range and temperature associated with the greater quantity of initiation sites that become feasible with higher strains and temperatures.

As discussed previously the cyclically stabilised maximum stress values achieved for the different applied strain ranges were compared with a typical first cycle stress-strain curve in order to determine the amount of cyclic softening that occurred in N18, this was found to be approximately 28 MPa at 650°C and 66 MPa at 725°C. During room temperature tests of WASPALOY® Stoltz and Pineau[183] determined that the type of cyclic response was dependent on the tertiary γ' size present in the alloy. Below a critical precipitate size (in this case 25nm, although V_f or interparticle spacing is not reported) precipitate cutting occurred that initially led to cyclic strengthening, but was followed by significant cyclic softening, which stabilised once the areas between the slip bands were saturated with dislocations. Above this critical size Orowan bowing and looping of precipitates occurred leading to cyclic strengthening of the alloy. At the critical precipitate size, both Orowan bowing and precipitate shearing were observed which led to a small amount of cyclic softening. From the results, the situation appears to be similar with N18, with a small amount of cyclic softening occurring in the alloy at 650°C which also has a mean tertiary γ' diameter of 25nm. At the higher temperature of 725°C more significant cyclic softening was observed in N18, this could be explained by an increased temperature increasing the rate of dislocation removal, such that further dislocations are created, shearing precipitates further prior to saturation occurring in the alloy.

6.1.6 Fatigue Behaviour in the Presence of a Stress Concentration (U-Notch)

The discussion on fatigue behaviour in the presence of a U-notch has been broken down into three separate areas. (1) *Stress Concentration* – where the choice of notch is discussed and its effect on the stresses in the test material. (2) *Crack Initiation and Short Crack Propagation* – here the initiation of a crack and its initial behaviour as a short crack are discussed. (3) *Long Crack Growth and Final Failure* – where the relevance of this type of crack growth is considered along with ultimate final failure.

6.1.6.1 Stress Concentration

The size and depth of U-notch was chosen to provide a monotonic stress concentration of approximately two, similar to that seen at the root of fir tree root fixings used to secure turbine blades to turbine discs.

Neuber published the first comprehensive book on stress concentrations in 1937[184]. The elastic stress concentration factor (for static elastic loading), K_t, is defined as:

$$K_t = \frac{\sigma_{max}}{\sigma_{nom}} \qquad \textbf{Equation 29}$$

Where:

σ_{max} is the peak maximum stress due to the stress concentration

σ_{nom} is the nominal stress in the net cross section of the material

The fatigue stress concentration factor, K_f, is related to K_t by a notch sensitivity factor, q, whose value is dependent on the particular material:

$$q = \frac{K_f - 1}{K_t - 1}$$ **Equation 30**

Often the value of K_f is much smaller than K_t, its actual value depending on the notch sensitivity of the material. This approach is only valid if the stress at the root of the notch is within the elastic limit of the material, *i.e.* there is no appreciable plastic yielding. Should there be appreciable plastic yielding at the notch root, then Neuber's[185] formula for non-linear material behaviour may be used to calculate the maximum stress and maximum strain in the notch root. Neuber established that K_t is the geometric mean of the stress concentration factor, K_σ, and strain concentration factor, K_ε:

$$K_t = \sqrt{(K_\sigma K_\varepsilon)}$$ **Equation 31**

or,

$$K_\sigma = \frac{K_t^2}{K_\varepsilon}$$ **Equation 32**

Where:

$$K_\sigma = \frac{\sigma_{max}}{\sigma_{nom}}$$ **Equation 33**

$$K_\varepsilon = \frac{\varepsilon_{max}}{\varepsilon_{nom}}$$ **Equation 34**

ε_{max} is the peak maximum strain due to the stress concentration

ε_{nom} is the nominal strain in the net cross section of the material, obtained by using σ_{nom} in conjunction with the material stress-strain curve.

This can be rewritten in terms of stresses and strains as:

$$\sigma_{max}\varepsilon_{max} = K_t^2 \sigma_{nom}\varepsilon_{nom}$$ **Equation 35**

This method could have been used to calculate the monotonic stress and strain within the notch root, however, the notch sensitivity factor, q, would still be required to convert K_t to K_f in accordance with Equation 30.

The initial maximum stress state of the root notch had been modelled[186] using Abaqus, details of the meshing, constraints and example maximum Von-Mises stress in the U-notch root are provided in Figure 164(a), (b) and (c) respectively. This has permitted the initial strain of the U-notch tests to be calculated to permit comparison with the LCF tests, see Figure 165.

In the testing for N18 discussed here, a cyclic load was used, the initial maximum value of which was chosen to provide a lifetime of between 10,000 to 50,000 cycles to failure, *i.e.* LCF, by inducing plastic deformation in the notch root. The material at the notch root will yield during the first load cycle creating a plastic zone, which may take several cycles to reach its maximum size depending on the material response to cyclic loading.

6.1.6.2 Crack Initiation and Short Crack Growth

For N18, when tested in air, crack initiation appears to be from oxidised particles (Figure 122(a) and Figure 125(a)) and pores (Figure 124), whilst for those tests carried out under vacuum conditions initiation appeared to be from pores (Figure 128(a), (b) and Figure 129(a)). In which case there will be more potential crack initiation sites available in air compared with the number available under vacuum conditions. This goes someway to explaining the shortened life (Figure 119) of the majority of the specimens tested in air. Additionally, in air, oxidation of γ' and other particles will occur, with the larger primary γ' being more angular and hence providing a higher stress concentration. Primary γ', and other particles such as carbides, often lie on the grain boundaries, which offer improved diffusion routes for oxygen and are likely to increase oxidation rates at these sites, hence initiation occurring in fewer cycles when compared with vacuum tests. For U720Li initiation was found to occur mostly at sub-surface pores, whilst U720Li LG further initiation sites were noted along grain boundaries, thought to be due to the increased oxidation activity occurring at these locations, which may have been assisted by SAGBO[21]. In N18, with the notch root experiencing similar $\Delta\varepsilon$, to that seen in the LCF tests, it may be a reasonable assumption that initiation will occur after approximately the same number of cycles (allowing for statistical variation) when compared to the same conditions for LCF. However, once nucleated, and as the crack starts growing through the width of the material, the driving force of the short crack, related to its length and applied stress will reduce as the nominal stress induced by bending reduces. This reduction in nominal stress is shown in Figure 166, where stresses seen in uncracked specimens of different geometries (plain bend bar, axial loaded specimen and notched bend bar) are compared. This comparison suggests two things: (1) the highest stresses in notched bend bars occur just below the surface of the notch, hence cracks are more likely to initiate in these areas; (2) as cracks grow away from the notch, the driving force from stresses imposed by bending are reduced at a faster rate than that seen in plain

bars. This could lead to reduced crack growth rate or even crack growth arrest if the stress reduces below a critical level, at least through the width of the material. These transient growth effects existing until the tip of the small flaw is relieved of the strain field associated with the notch tip deformation[38]. Further crack growth arrest in these small cracks could occur due to PICC, changes in microstructure, *i.e.* encountering a primary γ' or grain boundary. This would mean that many cracks across the breadth of the specimen would have to coalesce prior to there being sufficient reduction in material constraint for the driving force for the crack to propagate the crack through the width of the material. Which is supported by the multiple initiation sites as evidenced by the ratchet lines where cracks have coalesced (indicated by red arrows in Figure 124 and Figure 125). This reduced initial growth rate of short cracks in the strain field of notches combined with the reduced stress seen as the crack propagates due to the constant load nature of the tests effectively accounts for another aspect that leads to the increased life times of the U-notch tests in N18 when compared with the strain controlled uniaxial loaded LCF tests. In general, further improvement in lifetimes for those tests carried out under vacuum conditions was noted, reflecting the larger number of initiation sites activated when testing is carried out in air and some contribution from the increased propagation rates for 1-1-1-1 loading conditions in air (Figure 75). Cyclic softening has not been incorporated in the model that permitted the comparison against LCF lifetimes to be carried out. However, as N18 does cyclic soften at 650°C and 725°C, then an increase in strain range would be expected at both temperatures until the stress in the specimen balanced that due to the applied load, this would provide further improvement to the lifetimes when compared with the LCF tests.

6.1.6.3 Long Crack Growth and Final Failure

As discussed previously, the tests were carried out in three point bending under constant load conditions. Once the crack has grown sufficiently to move from mode I to mode II crack growth, microstructural features will have less of an influence over the crack propagation rate. As the multiple initial cracks coalesce, the test specimen becomes similar in nature to that used for long crack tests, with the U-notch in effect increasing the crack length, a. ΔK, would now be an appropriate parameter by which to describe the crack tip driving force. However, it is not clear where the transition from short crack to long crack growth has occurred, but if the short crack definitions from Suresh[38] are used then a length of 1 to 2 mm for a mechanically short crack could be appropriate. In this case, if the length of the U-notch is included as part of the crack length, the effective crack length, a = 3.25 mm. For a specimen of the geometry used for these tests and a nominal load of 6.2 kN, then $\Delta K \sim 70$ MPa$\sqrt{m}$. Figure 73 shows the limit of the Paris regime for long crack growth in N18. Although not shown, failure occurred shortly after this regime somewhere between $\Delta K \sim 60$ MPa$\sqrt{m}$ and $\Delta K \sim 70$ MPa$\sqrt{m}$, indicating that specimen

failure will occur when the crack grows to somewhere around 3.25 mm consistent with the approximate dimensions seen in Figure 120 and Figure 121. Significant crack growth in the true long crack regime is therefore not expected and hence little further contribution to lifetime would be forthcoming.

6.2 Thermal Barrier Coating Life Assessment Discussion

In the following sections, the results from the TGO layer evolution tests are discussed. This is followed by a brief discussion of the TBC lifing model developed by QinetiQ to provide some context. Finally a discussion of the TMF testing is presented.

6.2.1 Thermally Grown Oxide Layer Evolution Tests

The following paragraphs discuss the results from the TGO layer evolution experiments.

6.2.1.1 Measurement of Thermally Grown Oxide Layer

Initial measurements of the TGO layer were carried out on the specimens exposed at 1000°C for 30, 300 and 1057 hours by measuring the apparent TGO thickness from micrographs taken in BEI mode on the FEG SEM. When the BEI images were compared with those taken in SEI mode, it was found that cracking and polishing artefacts associated with specimen preparation were included within the apparent TGO thickness. For this reason SEI mode became the preferred imaging technique to determine the TGO thickness.

6.2.1.2 Isothermal Exposures

The TGO measurements are presented as graphs of RCF and CDF in Figure 135. In Figure 135 (c), the measured thickness of the TGO layer in the specimen exposed for 30 hours at 1050°C appears to have a more uniform layer thickness and in some areas the TGO in this specimen is not as thick as TGO layer in the "as received specimen", *i.e.* the 30 hour specimen has a lower distribution of thickness measurements when compared with the "as received" specimen; this is seen more easily (from a visual perspective) using the PDF curve in Figure 136 (c), but as a fitted curve, care should be exercised during interpretations. The reasons for the "as received" button having an increased TGO thickness distribution than would normally be expected for a specimen with no isothermal exposure were mentioned previously in the *Results* section. An alternative explanation might be that the thinner areas of a TGO will initially grow more rapidly as the TGO layer at these locations is not limiting the diffusion rates as much as a thicker TGO, however, for this to be the case a more skewed distribution of actual measurement on the RCF graphs would be expected, and this does not seem to be the case.

For longer time exposures an increase in thickness of the TGO layer is seen in conjunction with an increase in the distribution of this thickness. The increased

distribution can be linked to the stochastic nature of a diffusion driven process. With the exception of the 1000°C specimens exposed for 30, 300 and 1057 hours there is also a general increase in the thickness of the TGO layer with an increase in temperature for a given exposure time. This is to be expected, as the growth of the TGO layer is driven by diffusion[69,78]. In an attempt to reduce this data a simple Arrhenius based relationship was proposed initially of the form:

$$d(t,T) = A\exp\left(-\frac{Q}{RT}\right)\sqrt{t} + d_0 \qquad \textbf{Equation 36}$$

where $d(t,T)$, is the average TGO thickness (μm); T is the temperature during exposure; t is the time of exposure (at T); R is the ideal gas constant = 8.31 J/(mol.K); Q is the (effective, average) activation energy for diffusion of the diffusing species, A is a constant depending on, amongst others, the initial concentration of the diffusing species in the matrix through which it diffuses, the diffusion pre-exponential factor, size factors (mainly the distance between the TGO and Al containing phases) and d_0 is the initial thickness (μm) of the TGO layer prior to the measured thermal exposure, *i.e.* the TGO grown prior to application of the TC.

This relation was used to produce a global fit, using the least squares method, to the isothermal TGO growth data. Initially, all the isothermal TGO growth data except for the 1000°C specimens exposed for 30, 300 and 1057 hours, which appear to be anomalous when compared with other data points, and the results from the 1150°C specimen which were not available, were used to obtain the global fitting parameters. These are presented in Table 41 and were used within the model under development by QinetiQ. Once all isothermal TGO growth data was available, the revised parameters for the TGO global growth relation were established. The results of this fit are presented graphically in Figure 167. The actual data points for all the isothermal tests have also been plotted on this graph. On this graph with linear axes, a reasonable fit appears to have been achieved despite the global model nature of the model. However, if plotted on logarithmic scales, as in Figure 168, there are four specimens whose ranges of values do not fall within the prediction. These were the results from the specimens exposed for 30 hours at 1050°C and 1150°C and two specimens exposed at 1000°C for 300 hours and 1000 hours (which had been excluded from the initial fitting used of the global relation). The TGO growth lines from the model fall within the range of the TGO measurements for all other specimens. The global fit parameters from using all available isothermal data are provided in Table 42.

The TGO global growth model did not fit the two specimens exposed for 30 hours at 1050°C and 1150°C well. This could be that due to short exposure times there is little opportunity to overcome any variability in manufacture of the initial TGO thickness.

However, it is perhaps more likely, especially for the specimen exposed at 1100°C, that a poor fit is due to the lack of TGO growth data for these temperatures. For instance, there is only a single data point available for 1150°C and only a short 30 hour exposure, whereas for 950°C there are five measurements available. This provides a bias towards the 950°C data which may be reflected in the poor fit of 1150°C data point. Just applying a weighting to the small number of data points would not necessarily improve the results of the TGO global growth model, as this would not allow for any statistical variation in the sample and is likely to introduce bias in another direction. With regard to the apparent anomalous results for the specimens exposed at 1000°C, these could be anomalies, especially as the measurements were taken from a BEI rather than SEI mode micrograph. However, it is conceivable that there could be that a specific oxide or type of porosity formed in the TGO at 1000°C (but not seen at other temperatures) that permits more rapid diffusion at this temperature, permitting the TGO to grown in an accelerated manner, however, a search of the literature did not reveal any further information about this type of oxide formation.

A refinement to the relation introduced at Equation 36 to allow for the growth of the TGO layer during the preparation of the layered coating, *i.e.* prior to and during the TC application, was proposed. This took the form:

$$d_{TGO} = A\sqrt{t_{gr}\exp\left(-\frac{E}{RT_{gr}}\right)+t_{xp}\exp\left(-\frac{E}{RT_{xp}}\right)} \qquad \textbf{Equation 37}$$

where $d_{(TGO)}$ is the average TGO thickness (μm); t_{gr} is the time during initial TGO growth during the preparation of the layered coating; T_{gr} is the (average, effective) temperature during initial TGO growth in the preparation of the layered coating; T_{xp} is the temperature during exposure; t_{xp} is the time of exposure (at T_{xp}); R is the ideal gas constant = 8.31 J/(mol.K); E is the (effective, average) activation energy for diffusion of the diffusing species and A is a constant as previously described for Equation 36.

As future TGO growth is dependent on the thickness of the TGO layer and the reservoir of Al that the BC contains. These conditions can be described by the parameter d_0 in Equation 36, keeping the relation relatively simple. To introduce a further Arrhenius term to describe this initial TGO growth will only provide the same information for which the model will be calibrated. The reason behind this is that the TGO layer thickness increase attributed to a particular temperature will depend on the time of exposure at this temperature and the initial thickness of TGO present prior to commencing the exposure at the particular temperature. Thus a relation capable of determining the growth rate of the TGO during subsequent thermal exposure dependent on the thickness of the pre-existing TGO would have to be created. *i.e.* the second Arrhenius term in Equation 37 would need

to be dependent on the output from the first Arrhenius term to calculate TGO thickness. The current proposal in Equation 37 is based on superposition of thickness rather than dependence on thicknesses. Whereas in practice the initial TGO thickness would have to be converted to an equivalent exposure time for the subsequent thermal exposure temperature, with the TGO layer thickness growth being calculated from this equivalent point in time, examples of this are presented in the discussion of the *Two Stage Thermal Exposure* at section 6.2.1.3. For these reasons the proposal for the relation at Equation 37 was not pursued further.

6.2.1.3 Two Stage Thermal Exposure

Three specimens that were subject to a two-stage temperature exposure have been analysed, it is difficult to compare these directly, as the first stage of the thermal exposure was for different exposure times. However, the relation developed at paragraph 6.2.1.2 might be used to predict the TGO growth and to permit further comparisons to be made. As discussed in the previous section, predictions have been made based on the expected TGO thickness following the first stage temperature exposure and calculating an equivalent exposure time for this first stage exposure for the second stage temperature. The second stage exposure time has then been added to this equivalent first stage time to generate an expected final TGO thickness, the values obtained are presented in Table 43 and the method presented graphically in Figure 169. If these predictions are plotted on the PDF for the two stage thermal exposures, Figure 170, then it can be seen that predictions from the diffusion based relation tend to fall on the high side of measured values (within a single standard deviation) for the TGO thickness. In general, it would appear that growth of the TGO layer is less for two stage thermal exposures, than would be predicted by the equivalent TGO growth seen in isothermal exposures.

6.2.1.4 Thermal Cyclic Exposure

The thermal cycle used at 1100°C is shown in Figure 28, from this, it can be seen that the specimen is within 50°C of its maximum exposure temperature for 75 minutes. In 300 cycles, if a direct comparison is possible, this would equate to an isothermal exposure at the same temperature for 375 hours. The thermal cyclic exposures are compared with the isothermal exposures in Figure 171 on this basis. The 1000°C and 1050°C thermal cyclic specimens compare well with the TGO thickness global growth model, although as with the two stage thermal exposures, the TGO thickness is lower than predicted by the model, but within the a single standard deviation of the measured thicknesses on both specimens. Potentially further evidence that TGO growth rate is reduced by thermal cycling.

6.2.2 QinetiQ Thermal Barrier Coating Lifing Model

The QinetiQ Thermal Barrier Coating Lifing Model was developed by QinetiQ as part of the Gas Turbine Critical Component Lifing Programme which culminated with the issue of the final report[4]. An outline of the QinetiQ model is presented here to provide context for the preceding work on TGO layer evolution studies and the following discussion regarding the TMF testing of TBC Systems carried out during this research programme.

6.2.2.1 Aim of the QinetiQ Model

The aim of the QinetiQ Model was to produce a finite element model that could be used to predict lifetimes of TBC systems in service use, *i.e.* when they are exposed to TMF cycles within the operating environment experienced in a gas turbine engine. The model was designed to achieve this by taking into account the growth and morphology of the TGO as well as the constituent behaviour of each of the layers that go into creating a TBC system; substrate, BC, TGO and ceramic TC.

6.2.2.2 Constitutive Description

Elastic distortions arise due to modulus and thermal expansion mismatch between the substrate, BC, TGO and TC, as well as accounting for this, plasticity and creep in the TBC system should be taken into account by the model.

6.2.2.2.1 Thermally Grown Oxide Layer Growth Kinetics

The growth directions of the TGO are determined by those directions offering the least resistance to the volumetric expansion. This anisotropic growth has been shown experimentally by Huntz *et al.*[187] and has been modelled using finite element calculations to show that growth occurs parallel and normal to the interface[188], with the ratio between normal growth strains, ε_n, to the parallel growth strains, ε_t, is approximately 87[189]. The volumetric strain can be obtained from the Pilling-Bedworth ratio, approximately 1.28 for the reaction leading to the formation of the TGO. For the model the rate of growth was determined by the TGO global growth relation presented at section 6.2.1.2 using the parameters from Table 41. The anisotropic growth kinetics of the TGO were modelled in terms of a swelling strain rate tensor which was expressed in terms of a local reference system that followed the TGO morphology to ensure that the growth of the TGO remained perpendicular to the TGO / BC interface, see Figure 172.

6.2.2.2.2 Creep Response

An assumption was made that both the BC and TGO would undergo creep deformation with the implementation of this simplified by modelling creep using power laws, with creep parameters obtained from the literature[190,191.]

6.2.2.2.3 Plasticity

Plasticity in the BC was modelled assuming that it was ideally plastic, as this has been shown to be acceptable in lieu of visco-plastic analysis[192]. The TGO was assumed not to undergo plastic deformation. In order to keep the number of parameters affecting the lifetime of the TBC to a minimum, the TC was modelled as an isotropic material. Although this is clearly not a correct assumption as the material is highly anisotropic and it was recognised that this modelling simplification was likely to lead to significant effects in the predicted stresses near the TGO interfaces.

6.2.2.2.4 Creep and Plasticity Interaction

Cyclic plasticity and creep deformation interact with the concomitant effects determining the location and magnitude of evolved stresses that will ultimately lead to failure. To model elastic, plastic and creep strains together in complex materials at elevated and changing temperatures, where cyclic hardening, rate-dependency and strain ageing occur is non-trivial, and a User defined MATerial (UMAT) routine was developed by QinetiQ for this purpose.

6.2.2.3 Finite Element Model

The model of the TBC system is based on the morphology of the TGO layer shown in Figure 132(b), this system had a TC thickness of 200μm, an initial TGO thickness of 0.9μm and BC thickness of 67μm. As a UMAT was used, a three-dimensional model had to be constructed. The model relation to the test specimen geometry and mesh close to the TGO layer is shown in Figure 173.

The CMSX4 substrate behaviour is implemented by a constitutive description that describes the complex interactions of stress, temperature and orientation. A reference node on the substrate is coupled to the TBC model to impose constraints on those TBC surfaces without imposed boundary conditions such that the substrate behaviour, in the x_1 and x_3 directions, is supplied to the TBC model, as shown in Figure 174.

6.2.2.4 QinetiQ Model Results

The model has been used to carry out numerical calculations under isothermal, creep and cyclic temperature conditions[4].

Model predictions for the von Mises and radial stresses (S22) for isothermal exposure at 950°C and creep exposure at 950°C with an applied stress of 100 MPa are provided in Figure 175 and Figure 176 respectively. In each case large von Mises stresses are predicted in the TGO and within the TC close to the TGO / TC interface, these stresses are dominated by the S22 stress component. The largest radial stress is predicted to

occur around the trough of the undulation which is where cracking of the top coat / TGO interface would be expected to occur.

The predicted radial (S22) stress evolution at three locations (A, B and C) in the BC near to the interface with the TGO is given in Figure 177. The corresponding predicted radial (S22) stress in their pairs (H, I and J) within the TGO on the opposite side of the interface is shown in Figure 178. Initially, during heating to 950°C, the radial (S22) stress component increases linearly due to the differences in thermal expansion between the BC and TGO. Once the temperature stabilises, at 950°C, the stresses relax due to plastic yielding of the BC and creep of both the TGO and BC. After 581 hours the predicted radial (S22) stress in the BC has fallen to ±8 MPa (location A +ve, location C –ve).

The model prediction for the equivalent plastic and creep strains for the 950°C isothermal exposure is shown in Figure 179 and for the 100 MPa / 950°C creep condition in Figure 180. The model indicates that in both of these cases the inelastic strain accumulations are in the bond coat at the BC / TGO interface in the flank of the undulation with the maximum values of strain accumulation located close to the trough. In both the isothermal exposure and creep exposure, the maximum plastic strain predicted in the BC is approximately 0.003. The creep strains are predicted to be much higher at 1.3 and 0.8 respectively. The prediction for the isothermal exposure results in the largest amount of inelastic damage, which has accumulated along the whole of the flank of the undulation from the trough to the peak.

The results from the prediction of TGO growth under isothermal and creep conditions are presented in Figure 181 along with the initial state to permit comparisons to be made. Simulations of both conditions give rise to a thicker TGO layer, with the prediction for creep conditions showing an additional increase in amplitude of the undulation, thus increasing the effects of rumpling in the area.

The simulated TGO thickness under isothermal and cyclic temperature exposures at 1050°C is presented graphically in Figure 182. The model predicts slower TGO growth under cyclic conditions, even after allowing for the reduced time at temperature due to the cycle.

Figure 183 shows the predicted radial (S22) stress evolution in the BC at the BC / TGO interface. The isothermal simulation (black lines) shows little change to the stress state at this location, whereas for the thermal cyclic simulation (red lines with A and B superimposed), the stresses evolved approach asymptotically absolute values of about 400 MPa at point A, and 500 MPa at point C.

6.2.2.5 QinetiQ Model Discussion

The model's predictions of the location of the maximum stresses close to the trough of the undulation (Figure 175 and Figure 176) are consistent with the locations for initiation of cracks described in the literature[67,83], as shown in Figure 12 and Figure 14.

The predicted stress evolutions in adjacent pairs presented in Figure 177 and Figure 178 should be understandable in terms of local stress transfer. Pairs (A, H) and (C, J) are in line with the direction of the chosen predicted stress, similar magnitudes (and sign) might be expected if the assumptions applying to each layer were the same. However this is not the case, the TGO is assumed not to undergo plastic deformation but would experience swelling strains caused by the growth of the TGO, whereas the BC was assumed to be ideally plastic, which would provide a limit to the maximum applied stress before plastic deformation occurred. In Figure 178(a) very high radial (S22) stresses are predicted to be experienced by TGO close to the TGO / BC interface, these are of the order of 2 GPa and -14 GPa respectively. Although bi-axial compressive stresses of up to 4.6 GPa have been measured just below the TC[82], the predicted compressive stress is around a factor of three greater than this. The assumption that the TC is an elastic isotropic material may account for these excessive stresses. Indeed, this would agree with the detrimental effects that sintering of the TC has on TBC performance by virtue of increasing the TC stiffness (hence reducing its compliance), especially at higher temperatures[193].

The stress in the TGO at the TGO / TC interface is predicted as shown In Figure 175 and Figure 176, for isothermal exposures and creep exposures respectively. The build up of these stresses is due to the TGO growth strains discussed previously. The predicted maximum von Mises stresses in the TGO are 78 GPa and 50 GPa, yet when the radial (S22) stress only is considered these figures fall to 49 GPa and 32 GPa respectively. This appears to indicate that either one or both of the S11 and S33 stresses are significant in magnitude (although they too are likely to be compressive). As failure of the TBC normally occurs by cracking close to the TGO, then it is a tensile crack opening stress in these areas that becomes particularly relevant *i.e.* an opening stress perpendicular to TGO as shown in Figure 172 along the x'_2 axis.

The results of the thermal cyclic exposure tests were discussed at section 6.2.1.4, where it was observed that the TGO layer growth rate appeared to slow down during thermal cyclic exposures when compared with the growth rate modelled for isothermal exposures, see Figure 171. The initial results of the model agree with this observation, but further cyclic exposure tests would be required to validate this assertion.

6.2.3 Thermo-mechanical Fatigue

Over 4000 cycles of TMF testing had been completed by the time the last TMF specimen had been tested. The typical level of control achieved is shown in Figure 143 which shows the final cycle of the first TMF test specimen, indicating that the cycle is highly repeatable and representative of that requested by the controller.

Variability in position of the substrate thermocouple hole has been observed (Figure 145 versus Figure 146). In order to determine the effect of this variability the temperature of either the TC surface or the wall of the centre bore of the test specimen would need to be measured so that the temperature gradient across the complete specimen could be determined.

The insulating effect provided by the TC is shown In Figure 144, during the dwell the TBC top coat is around 1045°C with the substrate at 875°C, a temperature difference of approximately 170°C, this is consistent with differences published in the literature[77], although little information is available regarding the Chromalloy proprietary coating used on the "dog bone" specimens. However, this temperature difference, assumes that the substrate thermocouple measures the temperature of the TC / BC interface, *i.e.* that in the area of the TGO, this is not the case, as can be seen in Figure 145. But as two temperatures, thermal conductivities and distances are known, the temperature at the TC / BC interface can be calculated using heat flux, q (W/m^2):

$$q = \frac{(T_1 - T_2)\lambda_1}{d_1} \qquad \textbf{Equation 38}$$

Where: T_1 is the TC temperature, (K), T_2 is the TC / BC interface temperature, (K), λ_1 is the thermal conductivity of the TC, (W/mK) and d_1 is the thickness of the TC, (m).

As heat flux is constant throughout the system, then q is also given by:

$$q = \frac{(T_2 - T_3)\lambda_2}{d_2} \qquad \textbf{Equation 39}$$

In this case: T_2 is the TC / BC interface temperature, (K), T_3 is the substrate thermocouple temperature, (K), λ_2 is the thermal conductivity of the substrate, (W/mK) and d_2 is the distance from the TC / BC interface to the centre of the substrate thermocouple, (m).

As q is equal, putting Equation 38 = Equation 39, then:

$$\frac{(T_1 - T_2)\lambda_1}{d_1} = \frac{(T_2 - T_3)\lambda_2}{d_2} \qquad \textbf{Equation 40}$$

As all but T_2 are known (T_1 = 1318 K; T_3 = 1148 K; d_1 = 225 x 10^{-6} m; d_2 = 625 x 10^{-6} m; λ_1 = 1.7 W/mK[72] and λ_2 = 19 W/mK[194]), Equation 40 can be rearranged and solved to find

T_2. Which in the case of the “dog bone” specimen with no pre-exposure (Figure 145) the TC / BC interface temperature is calculated as 1182K or 909°C, a temperature difference of 136°C when compared with the TC temperature.

In the case of the “dog bone” specimen pre-exposed for 100 hours at 1000°C (Figure 146) and making the assumption that the TC temperature remains the same, then the TC / BC interface temperature can be calculated in a similar manner and is found to be 1167K or 894°C, a temperature difference of 151°C when compared with the TC temperature.

These simple calculations indicate the importance of the position of the substrate thermocouple, in this case the difference in position was approximately 294 μm, which leads to a temperature difference of 15°C at the TC / BC interface, the location of the TGO, hence potentially affecting its growth rate.

It would be useful to know the position of the substrate thermocouple prior to running a TMF test such that the thermal cycle could be adjusted to achieve the exact desired thermal profile. Although attempts were made to use ultrasonic non-destructive test (NDT) techniques to do this, they were not successful.

As expected the measurements of the TGO thickness, presented graphically in Figure 148 and Figure 149 show an increasing thickness of TGO with increased pre-exposure time for a given number of TMF cycles. Given the foregoing calculation, it is likely that the TGO layer in each specimen has experienced different temperatures during the TMF cycle, further comparison would require further measurements from other specimens post TMF cycling. The reference “as received” measurements refer to the Cranfield coated buttons and is shown to indicate how the Chromalloy TBC system clearly differs from this assumed starting position.

The TMF test specimen that had been pre-exposed for 300 hours at 1000°C in air started spalling at 754 cycles. From the close up image of this spallation, Figure 147(b), it appears that the TMF testing has induced cracking in the substrate. It is not clear if initial spallation of the TC led to the substrate cracking in this manner or the substrate cracking led to the failure of the TC by cracking and spallation. Further testing will be required to determine whether the substrate or TC deteriorated first.

The concept of using TMF testing to expose specimens to realistic service conditions has been validated and TGO thicknesses of tested specimens measured. However, as the TBC system on the Chromalloy “dog bone” specimens is different to that used to calibrate the model, validation of the model is not possible at this stage. In order to validate the QinetiQ TBC Lifing models “dog bone” specimens with a TBC of the same specification used to calibrate the model will be required.

6.3 Lifing of Critical Components in Gas Turbine Engines

The requirements for lifing of military aircraft engines mean that material performance data is required. For a *Traditional Safe Life Approach*, this data may be very specific as would be obtained by individual component testing or testing of a particular feature on a component to determine its safe cyclic life. If testing could not be carried out a detailed knowledge of the component's materials properties relevant to the environment in which it was used would be required in conjunction with the necessary knowledge that supports the application of this data. The *Databank* approach to lifing clearly relies on availability of relevant, accurate and verified materials property data. Additionally this approach requires methods to convert potentially raw laboratory data and apply it to components, where issues such as sub-optimum heat treatments due to the shape or design of the component, stress concentrations and size effects come into play. *Damage Tolerance* lifing in essence overlays consideration of damage caused by FOD or by operating an engine in an environment likely to cause surface degradation and wear onto the preceding requirements. This is to ensure that likely damage caused through usage and implications of this damage is taken into account in the lifing process, so yet another set of data and attendant knowledge of how to use it in conjunction with the other approaches would be required. The *Retirement for Cause* approach to lifing would additionally need details of both short and long crack growth rates in the alloy, critical crack length for a particular stress and details of the smallest flaw size that can be found using NDT techniques, such that inspection regimes can be implemented to ensure that critical component catastrophic failure does not occur. Probabilistic approaches can be used in place of some of the preceding techniques, additionally they require knowledge of types, size, shape and density of "defects" in the material, whether these are in the form of pores, particles (including desirable ones) or pre-existing cracks.

However, in addition to data, a wider knowledge and understanding of the material, its properties and behaviour, and how this behaviour might change with the interplay that can occur between failure mechanisms, is required to interpret the data and use it to make appropriate decisions regarding lifing. These decisions not only have to consider the expected operating environment, but also excursions from this. In particular for rotating critical components operating at high temperature, this would mean overspeed and over temperature conditions. As either new materials are put into service or old materials are put to new uses or have different heat treatments applied, then the data and knowledge required to provide advice needs to be obtained, developed and verified.

7 Summary and Conclusions

Research in two key areas has been undertaken as part of this EngD: *Turbine Disc Alloy Assessment* and *Thermal Barrier Coating Life Assessment and Modelling*. The requirement for these areas were driven by the needs of the Industrial Sponsor with respect to *Lifing of Critical Components in Gas Turbine Engines* and the independent advice that QinetiQ provides to the UK MoD.

Summaries and conclusions for each of these research areas are presented in the following sections. These are followed by a section that summarises and draws both areas of research together in the context of the Industrial Sponsor.

7.1 Turbine Disc Alloy Assessment

In effect, five disc alloy types have been considered within the research undertaken during this EngD, these are:

N18 – a sub-solvus heat treated PM alloy for which a full mechanical performance characterisation has been carried out including; microstructural evaluation; high temperature strength testing at 650°C and 750°C; creep performance determination at 650°C (800 MPa and 900 MPa) and 725°C (330 MPa and 560 MPa); assessment of fatigue performance at 650°C and 725°C, in air and vacuum, under LCF conditions (also at 700°C) at various $\Delta\varepsilon$ and long crack conditions, with 1s and 20s dwells, and behaviour in the presence of a U-notch (simulating the stress concentration of a fir tree root blade fixing). These results were used to make comparisons between N18 and the other alloys listed below.

LSHR – a super-solvus heat treated PM alloy, for which comparable studies of long crack fatigue performance have been undertaken at 650°C and 725°C with 20s dwell times in air and under vacuum conditions, with microstructural characterisation to provide information for analysis.

RR1000 – results from previous research, carried out on an early variant of this sub-solvus heat treated PM alloy, against which the other alloys' performance is compared.

U720Li – an as received commercial sub-solvus heat treated PM alloy, where the results of previous research have been used as a comparator for the other alloys.

U720Li LG – an experimental version of U720Li, previously created by DERA to research grain size variation effects, the results of previous research have been used here as a comparator for other alloys' performance, although the heat treatment was modified, it remained sub-solvus.

The combination of an alloy's chemical composition and heat treatment schedule (including thermal history) and microstructure are important. These are often created and optimised via heat treatments for a particular operating environment design space or to overcome previous shortcomings of other alloys. For this reason generalisations are difficult to make, as it is the individual performance under specific conditions that is often important.

In terms of microstructure, LSHR had the largest grain size (expected due to the super-solvus heat treatment), this was followed by U720Li LG, N18 and then both RR1000 and U720Li each essentially having the same grain size.

The alloys' strength performance has been ranked at 650°C:

N18 = RR1000 > LSHR (super-solvus) > U720Li > U720Li LG.

N18 and LSHR have the highest γ' V_f and are the highest strength alloys at 650°C, along with RR1000 whose performance has been attributed to its smaller grain size. Often information on elemental content of alloys is presented in terms of wt%, yet comparisons made using at%, especially with respect to solutes and solvents, for instance comparing the atomic ratio of Cr : γ provides more insight than wt% alone. When compared with U720Li and U720Li LG, the improved high temperature strength performance of N18 may be understood in terms of a high V_f of γ' coupled with an increased amount of slow diffusing solid solution strengthening elements (Mo and W). Whilst the good high temperature performance of LSHR, despite its large grain size, can be explained by a high Mo and W content in addition to a high content of other solid solution strengtheners, Cr, Co and Fe.

In terms of creep, the performance of the alloys has been ranked:

LSHR > N18 = RR1000 > U720Li

In this case better performance is due to a combination of high temperature strength, reduced grain boundary area (larger grains) and grain boundary character. Borides and carbides are important in all the alloys, with some declared "instability" designed into RR1000 to permit lesser carbides to form at grain boundaries modifying their sliding and diffusion behaviour. Although too much of a good thing can lead to deleterious phases forming due to the similarities in morphology between σ and $M_{26}C_6$ carbides, as in the original UDIMET® 720 alloy. In addition to borides and carbides, grain boundaries may be modified such that convoluted boundaries are encouraged to form due to presence of Hf or by the modification of cooling rates used in the heat treatment processes as is the case with some versions of LSHR.

Fatigue crack growth performance of the alloys is more difficult to rank as it depends on the interplay between many factors such as: ΔK, environment, dwell and temperature. For

the worst case considered (20s dwell at 725°C in air at high ΔK) the ranking of alloys in terms of lowest to highest *da/dN* is:

RR1000 ≥ N18 ≥ U720Li LG ≥ U720Li ≥ LSHR

The long crack behaviour of the alloys has been assessed and a technique using apparent activation energy applied to provide additional insights into the failure modes of the alloys. N18 exhibited the most transgranular failures indicating a good resistance to intergranular modes, with U720Li the most intergranular. With all alloys generally: (1) showing increasingly intergranular failure modes as temperature and ΔK increases; (2) transgranular modes of failure evident to higher values of temperature and ΔK under vacuum conditions; and (3) Increasing dwell from 1s to 20s appears to increase the amount of intergranular failure by approximately the same amount as increasing the temperature from 650°C to 725°C. However, a simple relationship between grain size and fatigue crack propagation resistance does not exist.

Qualitative examination of micrographs was used, as an attempt to quantify failure modes, using roughness measurements made with MeX® software provided little apparent correlation. The mode of failure for LSHR is almost completely intergranular in air, with oxidation fatigue rates similar to those seen in U270Li, yet performance under vacuum conditions improves as the failure mode changes to transgranular crack propagation under vacuum conditions indicating that grain boundary performance and strength are compromised in air, optimisation and balance of performance is key, which appears to have been achieved in this particular variant of RR1000. Although the relatively poor performance of LSHR may be exacerbated by the straight rather than serrated grain boundaries seen in this particular variant. Secondary cracking was also seen in many of the alloys especially at higher ΔK, this might lead to creep processes being distributed over a larger volume rather than concentrated at the crack tip and will diminish effective value of ΔK, and this may invalidate the assumptions made for LEFM to be valid. Creep fatigue was more significant under vacuum conditions, but swamped by oxidation effects in air, and more generally the time dependent effects in vacuum were smaller than those seen for tests carried out in air. Creep fatigue may actually be subdued in an air environment as slip systems may become pinned and grain boundary sliding inhibited by oxidation effects. For all the alloys except for U720Li LG, the largest change in crack growth propagation rate (*da/dN*) occurred when the environment changed from vacuum to air for the 20s dwell tests carried out at 725°C at ΔK = 25 MPa$\sqrt{m}$. For U720Li LG the largest increase in da/dN arose when the temperature was increased from 650°C to 725°C for the 725°C 20s dwell specimen tested in air at ΔK = 45 MPa$\sqrt{m}$. Changes in FCG rate in LSHR were not attributed to $\Delta CTOD$ yet for N18, the change in the alloy's strength explains the change in rates in all but the 20s dwell tests at 725°C in vacuum and

much of the change in performance that occurs in an oxidising environment. Beneficial creep processes perhaps in the form of stress relaxation or crack tip blunting, appear to be operating in N18 at 650°C and 725°C for the 20s dwell tests. Grain size and grain boundary area (although not beneficial to LSHR in air) are important in controlling intergranular crack growth processes, but not exclusively, as RR1000 shows. More important perhaps is the control of oxidation rates along grain boundaries and their cohesive strength. Microchemistry at grain boundaries therefore plays an important role in the performance of these alloys, from increasing the bond strengths with B (proposed in N18), to retarding grain boundary oxygen diffusion rates via grain boundary pinning with carbides or by creating serrated boundaries due to γ' growth around grain boundary carbides. $M_{23}C_6$ appears to be especially important, its formation may contribute to local Cr depletion which may lead to increased oxidation fatigue, but is offset by reduced grain boundary sliding especially in finer grain alloys, and at the same time it is thought to impede the diffusion of oxygen along these sites. As might be expected grain boundary character becomes more significant under dwell conditions.

Additional insight has been provided by using an apparent activation energy approach in combination with fractography. For N18 the approach indicated that changes in static properties are responsible for changes in FCG rates for 1s dwell tests carried out in air and under vacuum conditions, with beneficial creep processes occurring when the dwell was increased to 20s. In LSHR, the analysis pointing to the detrimental synergistic combination of creep and oxidation occurring to cause the accelerated FCG rate seen at 725°C in air under 20s dwell conditions. For RR1000 it showed that although processes such as oxidation are clearly occurring (as seen in micrographs) this process is not necessarily contributing significantly to FCG, and hence pure cyclic (mechanical) processes are assessed as occurring. Thus oxidation is not the rate determining process for RR1000, but it is for U720Li and U720Li LG, but in these cases the actual rate of FCG is determined by the grain boundary area, with the rate reduced in U720Li LG as it has a smaller grain boundary area when *cf.* U720Li.

For real world situations, fatigue is often strain controlled (Coffin-Manson), as such LCF tests are particularly useful in understanding an alloys performance. Under LCF conditions, N18 exhibits good resistance to intergranular cracking modes, with only a slight change in performance as temperature is increased from 650°C to 750°C, this was thought to be attributed to the maintenance of high strength levels. Failures in LCF are initiation life controlled, in N18 caused by sub-surface pores at lower $\Delta\varepsilon$ and temperature but the number of sites increasing and changing location to edge initiations at higher temperatures and $\Delta\varepsilon$. These tests also established that cyclic softening in N18 occurs very quickly and was quantified as a decrease of 28 MPa at 650°C and 66 MPa at 725°C, this is possibly explained by the increased temperature increasing the rate of dislocation

removal, permitting further dislocation creation and movement such that precipitates are sheared more often leading to reduced strengthening from the precipitate.

In combination with LCF, the U-notch tests can be used to understand material performance in the presence of a stress concentration representative of that caused by fir tree root fixings in turbine discs. For N18 testing revealed initiation occurred at oxidised particles or pores, with vacuum testing removing oxidised particles as potential initiation sites. This leaves a larger number of potential sites available for initiation in air but also stops pores closing due to oxidation. The improved life seen under vacuum conditions is due to lower numbers of potential initiation sites and subsequent crack growth being slower under vacuum conditions Particles that lie on grain boundaries offer improved routes for oxidation in air, hence grain size has an effect, but so do pore and particle distributions, including primary γ' content. In the constant load tests carried out, life may be increased by the effective strain reduction as a small crack tries to propagate away from the strain field associated with the U-notch, PICC may occur potentially leading to crack arrest (at least in some cases). For this reason care needs to be used in making comparisons with LCF data. Failure in the U-notch specimens appeared to be via coalescing of cracks along the edge of the U-notch, which then propagated through the thickness. Cyclic softening was not taken into account during the assessment which would have tended to increase the lifetimes over those seen under constant strain LCF tests. Due to the size of the U-notch test specimens, no appreciable long crack growth took place prior to final fracture, which may not be the case in real world applications.

7.2 Thermal Barrier Coating Life Assessment and Modelling

This research has considered the failure mechanisms within TBCs, especially those at a mesoscale and particularly in terms of TGO layer growth. TGO growth experiments have been carried out and the growth rate of the TGO has been determined under isothermal, two stage and thermal cyclic conditions. With both thermal cyclic and two stage thermal exposures leading to an apparently slower rate of TGO growth, although sufficient data is not available to quantify the difference in growth rates.

The TGO growth under isothermal conditions has been modelled by assuming an Arrhenius relation describes its growth with the data for all temperature exposures fitted to the relation using the least squares method. This global parametric TGO growth model was used to determine the growth rates of the TGO in the QinetiQ TBC Lifing Model. The TGO growth rate for specimens with two stage thermal exposures was not predicted well by the isothermal data, with predictions being on the high side of those seen during testing.

An outline of the QinetiQ TBC Lifing Model has been presented. The stress and strain predictions from the model provide supportive evidence for the TBC failure mechanisms

which are observed in practice. The model predicts high tensile (S22) stresses between the TC and TGO in the trough of the undulation, indicating that crack initiation is likely in this area. The QinetiQ TBC Lifing Model also predicts high compressive strains in the TGO, arising from the TGO growth strains, which are likely to be the source of ratcheting[83] and hence increased rumpling is also predicted by the model. Further development of the model should include the incorporation of the anisotropic behaviour of the TC, better physical property data for BC, TGO and TC including the ductile to brittle transition that PtAl bondcoats typically experience. Defining a criteria for small scale buckling, delamination growth and failure due to large scale buckling would provide the model with a method of determining that failure had occurred and hence useable lifetime of a component.

TMF testing at QinetiQ has been developed with the testing of pre-coated TBC specimens enabled by the introduction of a revised thermocouple location, which in conjunction with calibration of the *PIDL* settings for the TMF test controller, has permitted the accurate control of the temperature cycle with this being shown to be reproducible for 1000s of cycles. Although the location of the controlling thermocouple is critical, as a variance in its position by around 300 μm can lead to a change in temperature at the TGO of around 15°C, potentially affecting the TGO growth rate in this location. The TMF testing is ready to validate the QinetiQ TBC Lifing Model, but in order to be able to do this TMF "dog bone" specimens with a coating similar to that used to calibrate the model should be used.

7.3 Lifing of Critical Components in Gas Turbine Engines

To enable QinetiQ to provide independent advice to UK MoD with respect to the lifing and performance of components operating at high temperatures within military aircraft gas turbine engines, QinetiQ require: (1) Up to date knowledge and data regarding material performance and behaviour for the environment within which the materials are used; and (2) Suitable lifing techniques, with these being developed and verified where existing techniques either do not exist, are inappropriate or inadequate.

The research carried out during this EngD has contributed to both of the above requirements of the Industrial Sponsor. A focus on the wider requirements of QinetiQ formed the basis for research and contribution of knowledge in two key areas, these were:

- High temperature properties and performance of turbine disc materials LSHR and N18 and the implications for lifing approaches.
- The characterisation of TBC performance and development of TMF testing techniques that can be used to inform and validate physics based lifing models.

Research into these areas included the latest disc materials in use, N18 (SNECMA M88 engine in the French RAFALE aircraft), or under development, LSHR (NASA), and the

particular microstructures evolved from their individual heat treatment schedules. Performance data and knowledge of high temperature behaviour has been obtained for QinetiQ's materials property databank. In the case of LSHR this has been long crack fatigue performance with a 20s dwell in air, but particularly under vacuum conditions. For N18, a full mechanical characterisation and interpretation has been carried out, which was also used to verify the QinetiQ Neural Network Model[149]. In both cases, performance of these disc alloys has been considered at current disc rim operating temperatures (650°C) and also at a higher aspirational disc rim temperature of 725°C. The performance of N18 and LSHR has been compared with other materials previously researched at the University of Southampton, RR1000, U720Li and U720Li LG, using standard and novel techniques, such as Apparent Activation Energy Analysis, with some of the comparisons between N18 with the other alloys published[2,3]. The mechanistic understanding achieved from analysis and comparisons of microstructures and performance with other alloys has led to improved knowledge and understanding of alloy elemental content variations, implications of heat treatment and its variation, and the importance of either selecting a particular material for a chosen design space, or if a suitable material is not available, to designing one, but realising that any solution is likely to be a trade off between conflicting compositional requirements that drive performance requirements and that ultimately these have to be balanced to optimise the alloy.

The other key area of research was associated with TBCs and in particular the characterisation of TGO growth in a TBC system with a CMSX4 substrate, a PtAl bond coat and an EBPVD YPSZ top coat. The characterisation of TGO growth under isothermal, two stage temperature and thermal cyclic exposures was used to produce a global parametric fit of the isothermal TGO growth data. This global parametric model was used as a critical input to the QinetiQ TBC Lifing Model. Additionally the TGO growth analysis has provided further data for QinetiQ's materials property databank. The development of the TMF testing carried out under this area of research included the introduction of novel temperature measurement strategies and revised susceptor design. This provided QinetiQ with a robust and repeatable TMF testing capability with which the TMF seen by an in-service turbine blade could be replicated, and therefore a method which could be used to verify the QinetiQ TBC Lifing Model.

There are however, areas of research that were not pursued during this EngD, yet would have added additional insight or information with regards to the materials studied or techniques used, these are discussed briefly in the next section.

8 Further Work

Research programmes are by necessity time bounded and this is especially the case with a research degree. During the course of the research carried out during this EngD several areas that warranted further work became apparent. This further research would be aimed at either clarifying or addressing areas that may answer some of the questions raised by this work, or naturally extending it to create further knowledge. These areas of suggested further work are detailed below, with those pertaining to disc alloys presented first followed by those relevant to the TBC lifing aspects of the research.

8.1 Turbine Disk Alloy Assessment Further Work

In both N18 and LSHR, the high temperature performance was often inferred to be related to grain boundary character, although there is some research that covers this area, there is little relating to the specific details for both of the alloys and their particular heat treatments studied here. Grain boundary characterisation of N18 and LSHR (and RR1000, U720Li and U720Li LG) to determine the type of particles present (e.g. borides, carbides, σ) and the type of role they perform at the boundary, whether beneficial or detrimental would address this need. Grain boundary morphology and its effects on sliding and diffusion rates should also be considered as part of this activity.

During the apparent activation energy analysis grain boundary area effects were discussed and in some cases changes in fatigue crack propagation rate attributed to changes in grain boundary area. Following on naturally from the proposed grain boundary characterisation work, research into these grain boundary area effects could be used to discriminate between those effects related to grain size, those related to morphology of the grain boundary and those relating to grain boundary chemistry.

Some very simple calculations were used in this research to consider the relevant effects of elemental content in the alloy. It would be useful to further validate the arguments presented here by running full thermodynamic predictions for both N18 and LSHR.

Given the drive for higher turbine disc rim temperatures extending the work carried out here to other alloys or heat treatments would provide further knowledge about operations at these higher temperatures. The behaviour of the disc material in the vicinity of the blade fir tree root fixing is especially important, further analysis of behaviour in this area should be carried out for N18 and LSHR. Short crack initiation and growth studies in the presence of a stress concentration (U-notch used previously) would meet this requirement.

Super-solvus heat treatments have recently been applied to N18, a similar study of this particular alloy especially its comparison against sub-solvus heat treated N18 would

provide useful information with respect to the alloy behaviour due to the change in heat treatment. The same rationale would also apply in reverse to LSHR, where research into a sub-solvus variant of the alloy would provide further information regarding the sub-solvus heat treated behaviour of this alloy which could be used to elucidate further information from both the super-solvus and sub-solvus heat treatment studies.

To provide better creep performance at the disc rim and yet retain strength at the bore of the disc, dual microstructure heat treatments (DMHT) are being developed for N18 and LSHR to provide large and fine grain size in each of these respective areas. Although the behaviour of the material at the rim and bore is covered by either the work carried out as part of this EngD or further work suggested here, there is less information regarding the behaviour of the materials at the transition zone and whether or not this behaviour is significant. Further research in this area, including crack initiation and propagation under vacuum conditions is essential if DMHT discs are to be qualified for use.

8.2 Thermal Barrier Coating Life Assessment Further Work

The analysis of the “dog bone” creep specimen and TMF specimen pre-exposed for 300 hours at 1000°C has not been completed. Further SEM work to determine the thickness of the TGO in each specimen, even though the TMF specimen spalled, would complete the results for this aspect of the research.

During the TMF testing the susceptor was operating very close to its melting point. Significantly higher temperatures were unlikely to be obtainable using a Nimonic susceptor without melting the susceptor. As a semi-conductor, SiC can be used as a susceptor, a suggested improvement to permit higher temperature testing of TMF specimens with an applied TBC would be to use SiC as a material for the susceptor.

The QinetiQ TBC Lifing Model was calibrated using TGO growth rates arising from the exposure testing carried out on specimens coated with a University of Cranfield proprietary TBC system. To verify the model, TMF testing of specimens coated with the same TBC system should be carried out.

Only one TMF cycle was considered following on from previous work carried out by QinetiQ. It would be interesting to model a complete representative engine flight cycle using TMF including engine start up and shut down activities. This would consider the effects of the high DBTT of PtAl BC, (HTLA has a DBTT of 760°C), on rumpling and spallation.

The TBC life assessment work considered PtAl BC only, it would be useful to repeat the work for an overlay BC, adjust the parametric calibration of the model and determine the predicted behaviour of the system.

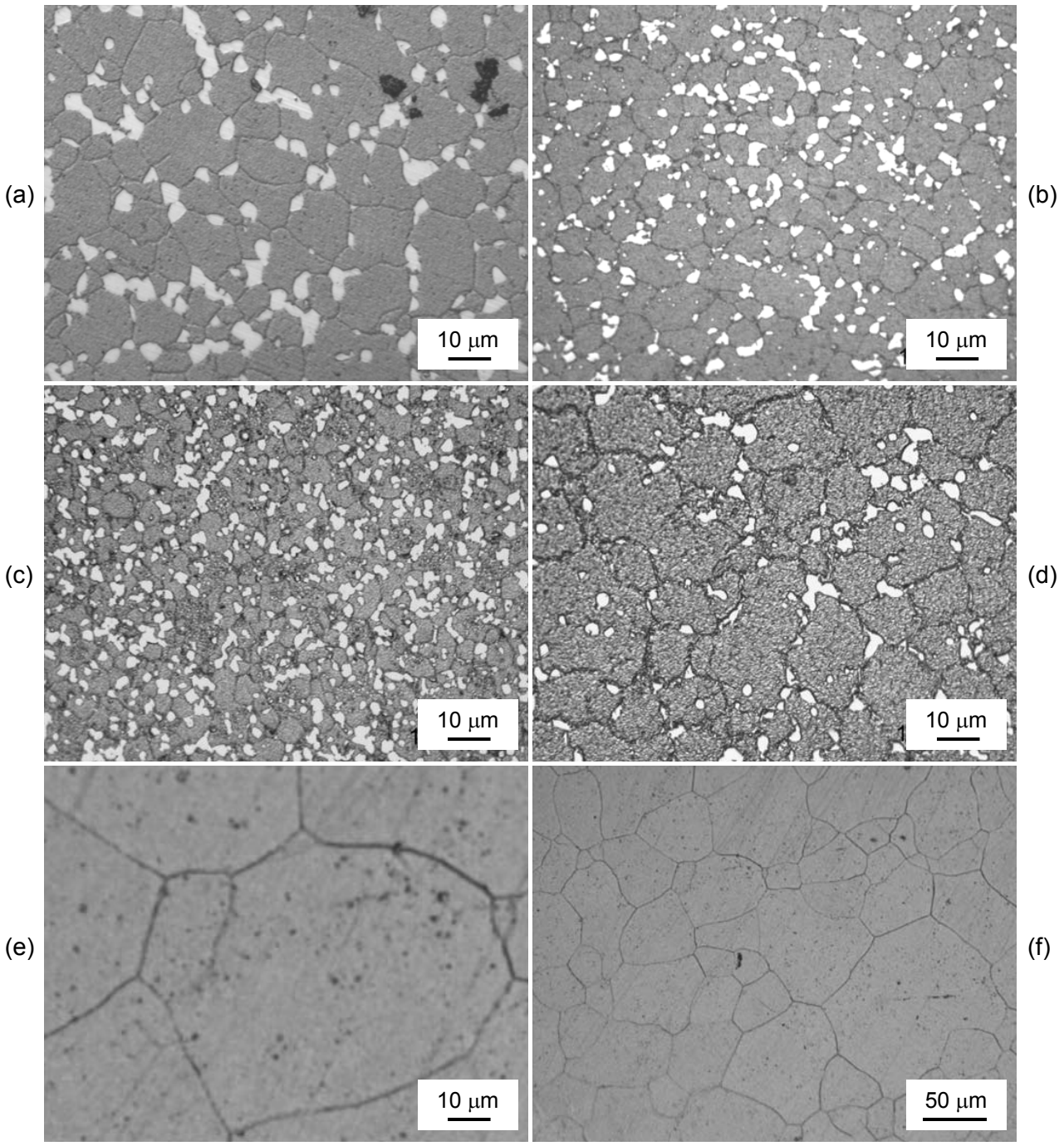

Figure 40 Optical micrographs: (a) N18; (b) RR1000[21]; (c) U720Li[21]; (d) U720Li LG[21]; (e) LSHR and (f) LSHR different scale. Orthophosphoric etch.

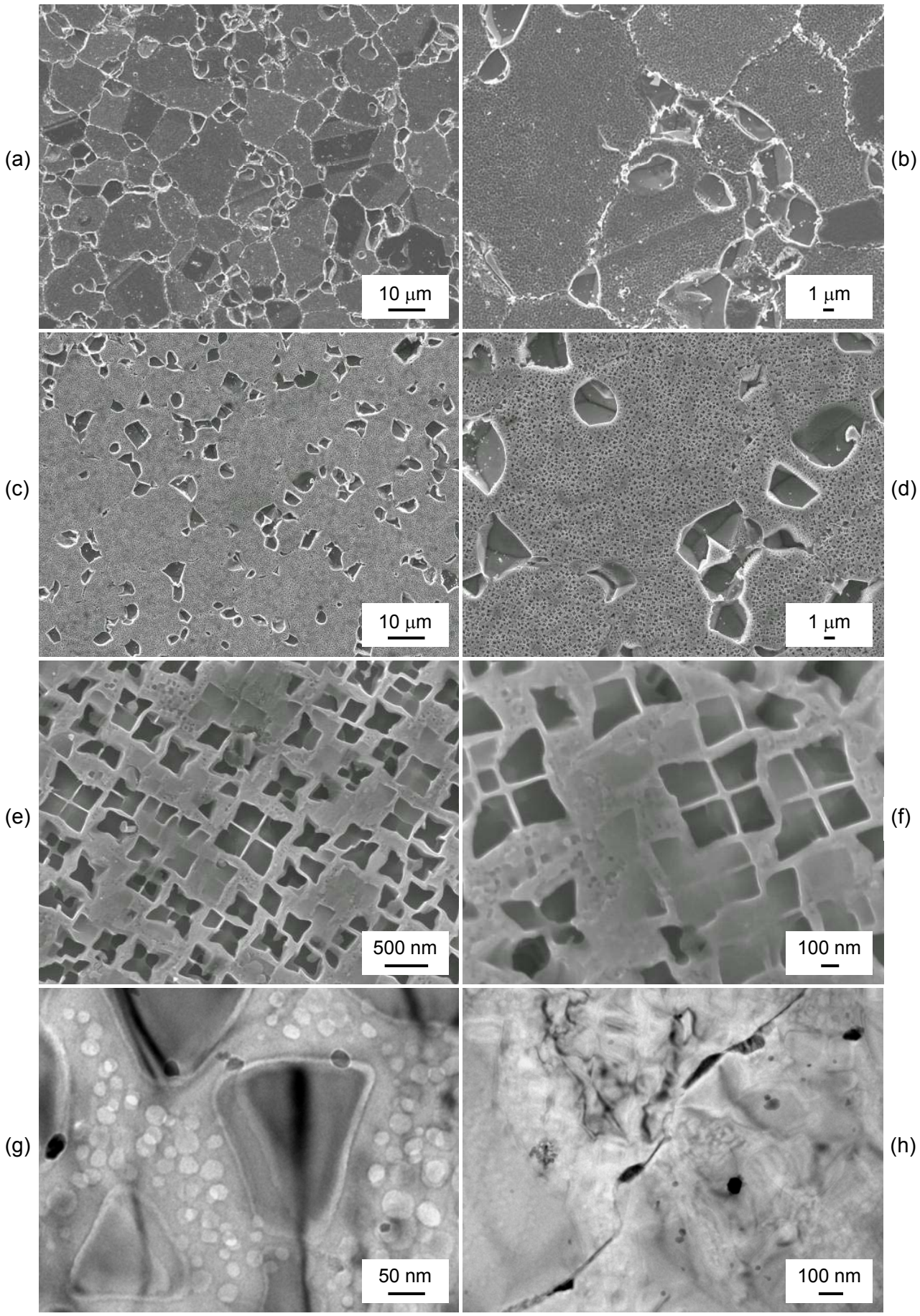

Figure 41 N18 microstructure: (a) to (f) FEG SEM SEI mode micrographs; (a) & (b) Kalling's Reagent; (c), (d), (e) & (f) Nimonic etch; (g) & (h) Bright field TEM images.

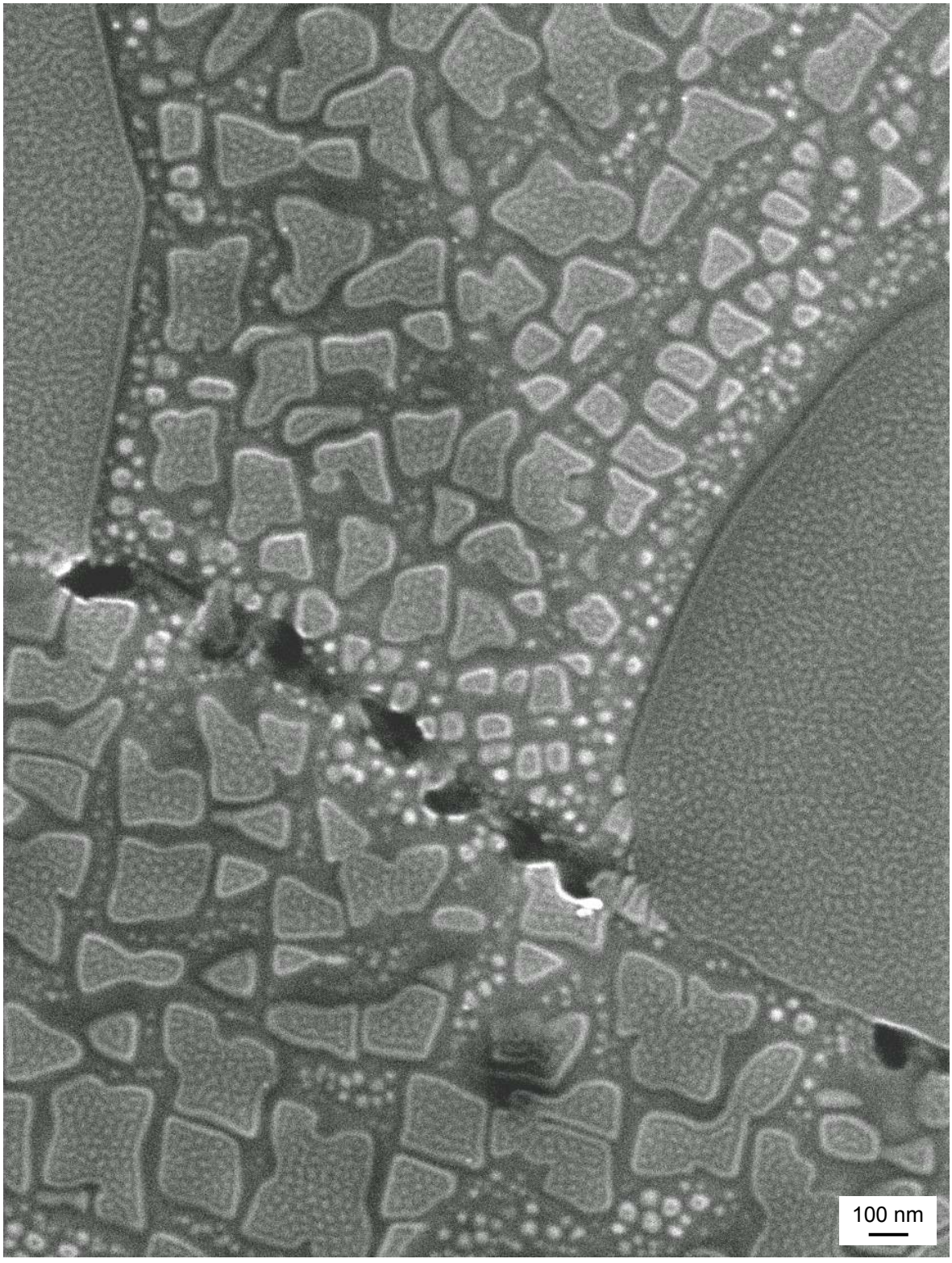

Figure 42 N18 microstructure, FEG SEM SEI mode, Electro polish.

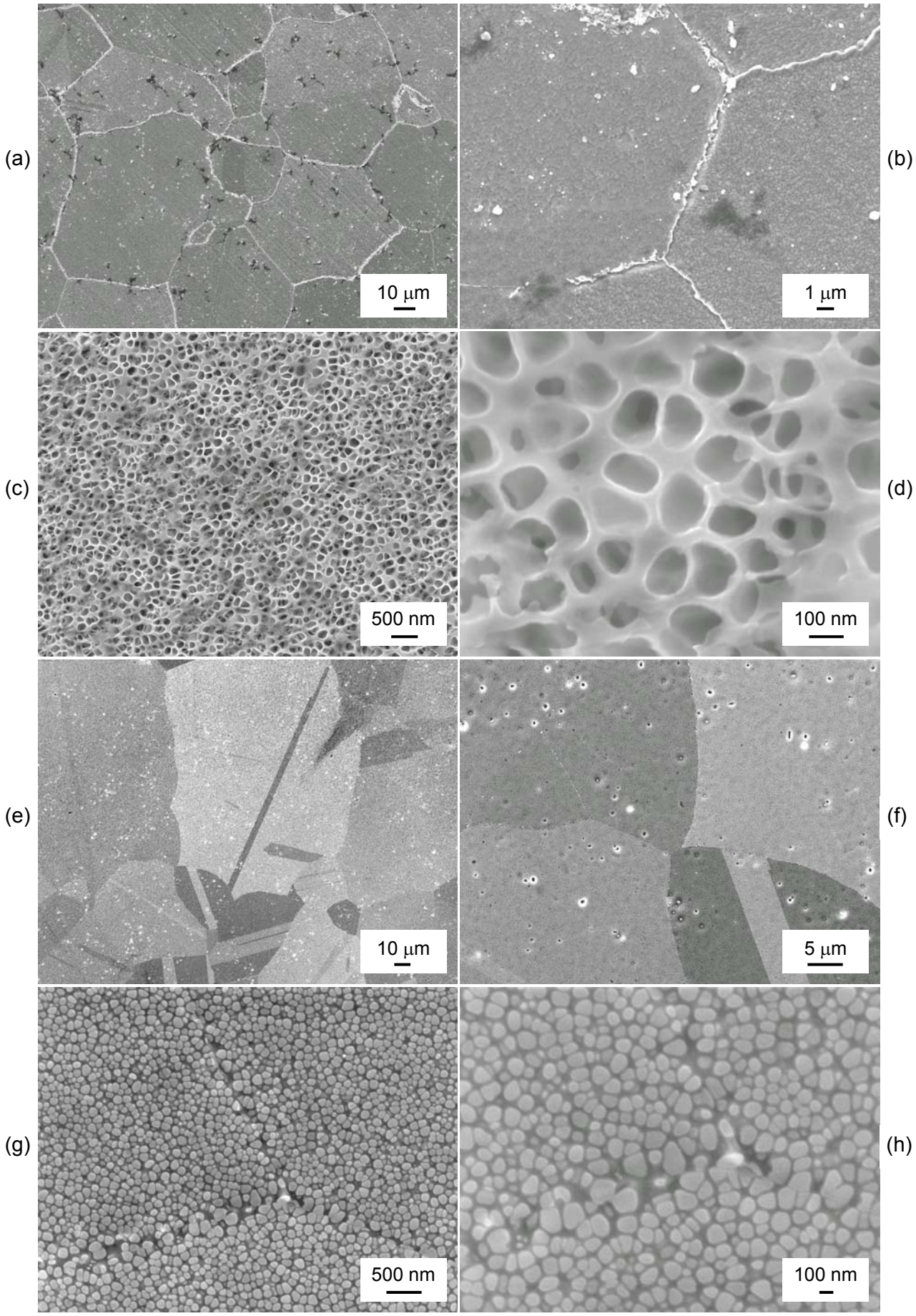

Figure 43 LSHR microstructure, FEG SEM SEI mode micrographs: (a) & (b) Kalling's Reagent; (c) & (d) Nimonic etch; (e), (f), (g) & (h) Electro polish.

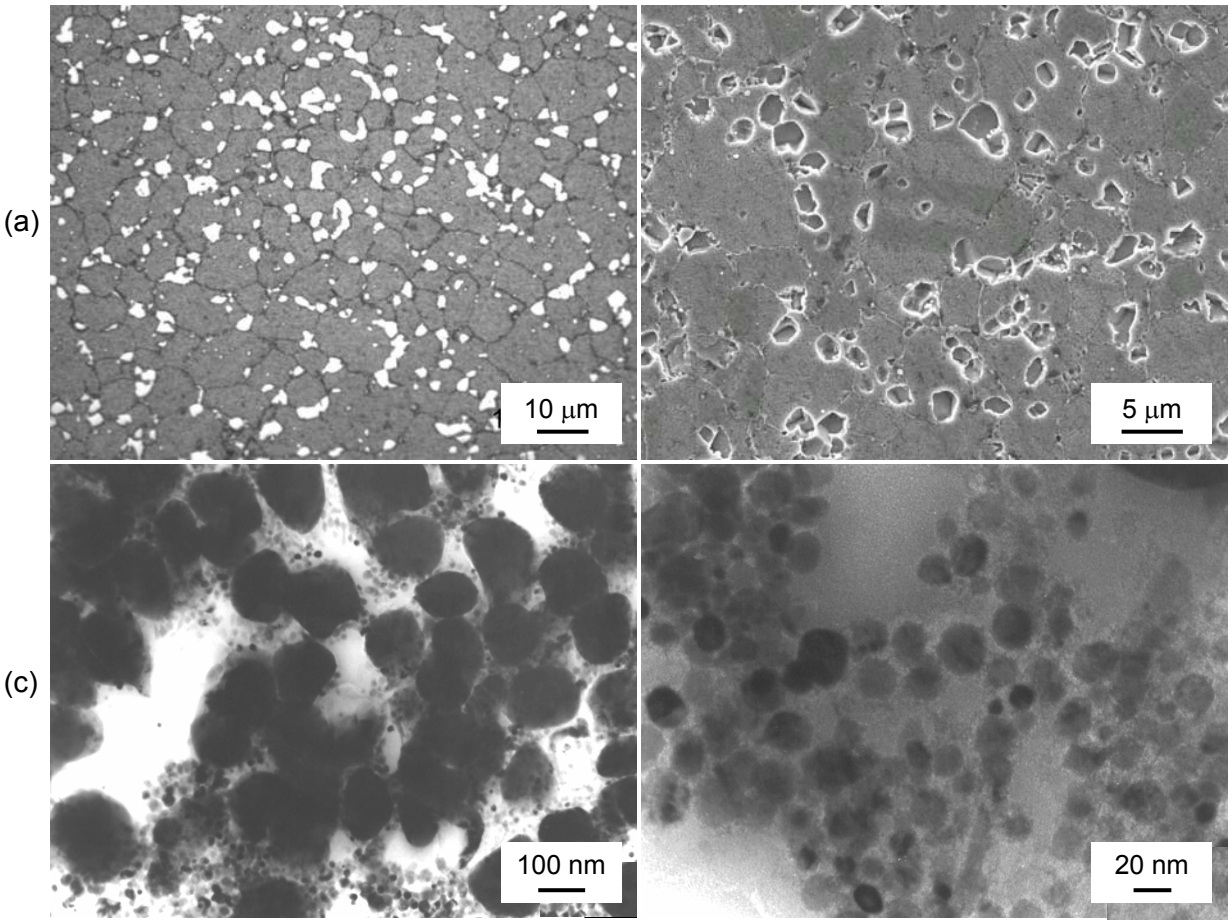

Figure 44 RR1000 microstructure: (a) Optical, Orthophosphoric etch; (b) FEG SEM SEI mode, Nimonic etch; (c) & (d) TEM bright field carbon replicas[21].

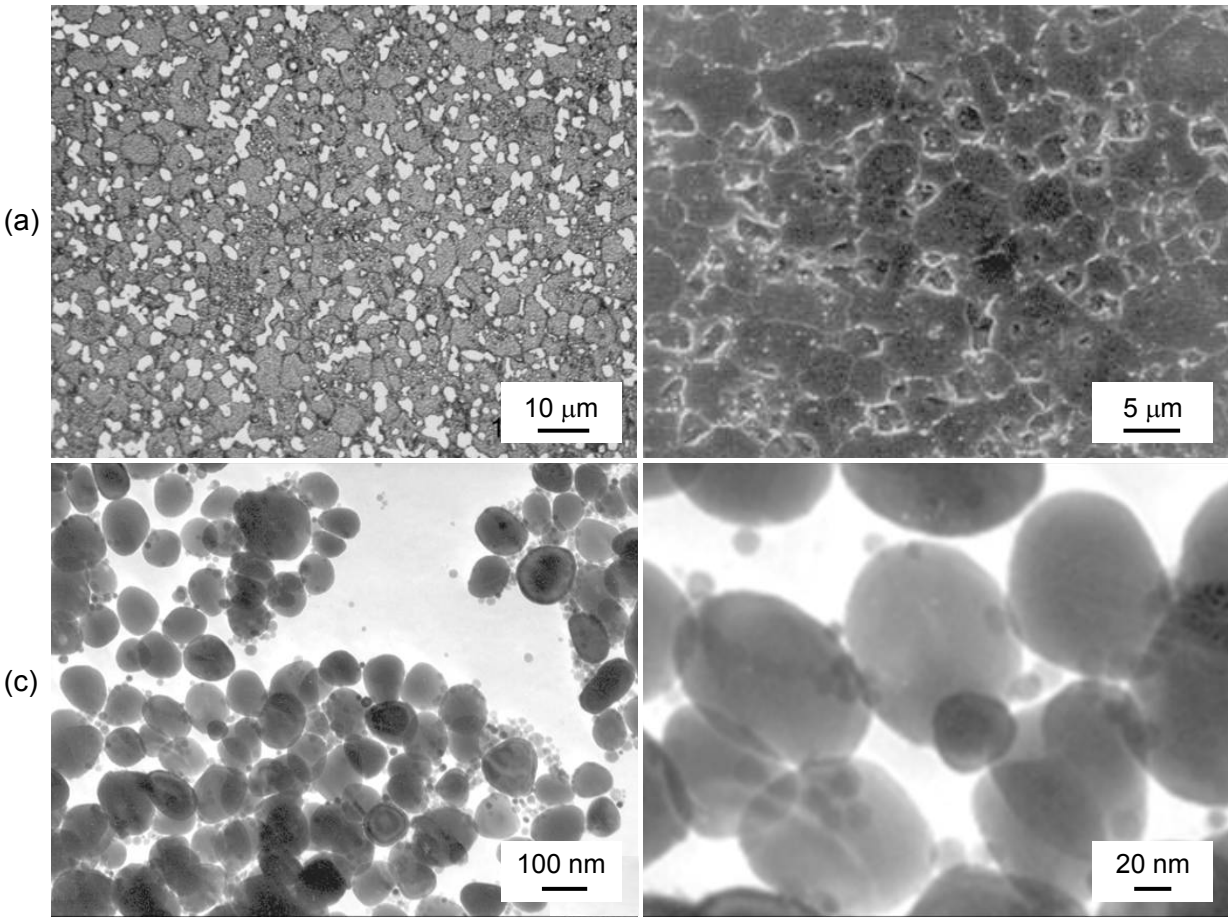

Figure 45 U720Li microstructure: (a) Optical, Orthophosphoric etch; (b) SEM SEI mode, Fry's Reagent[20]; (c) & (d) TEM bright field carbon replicas[21].

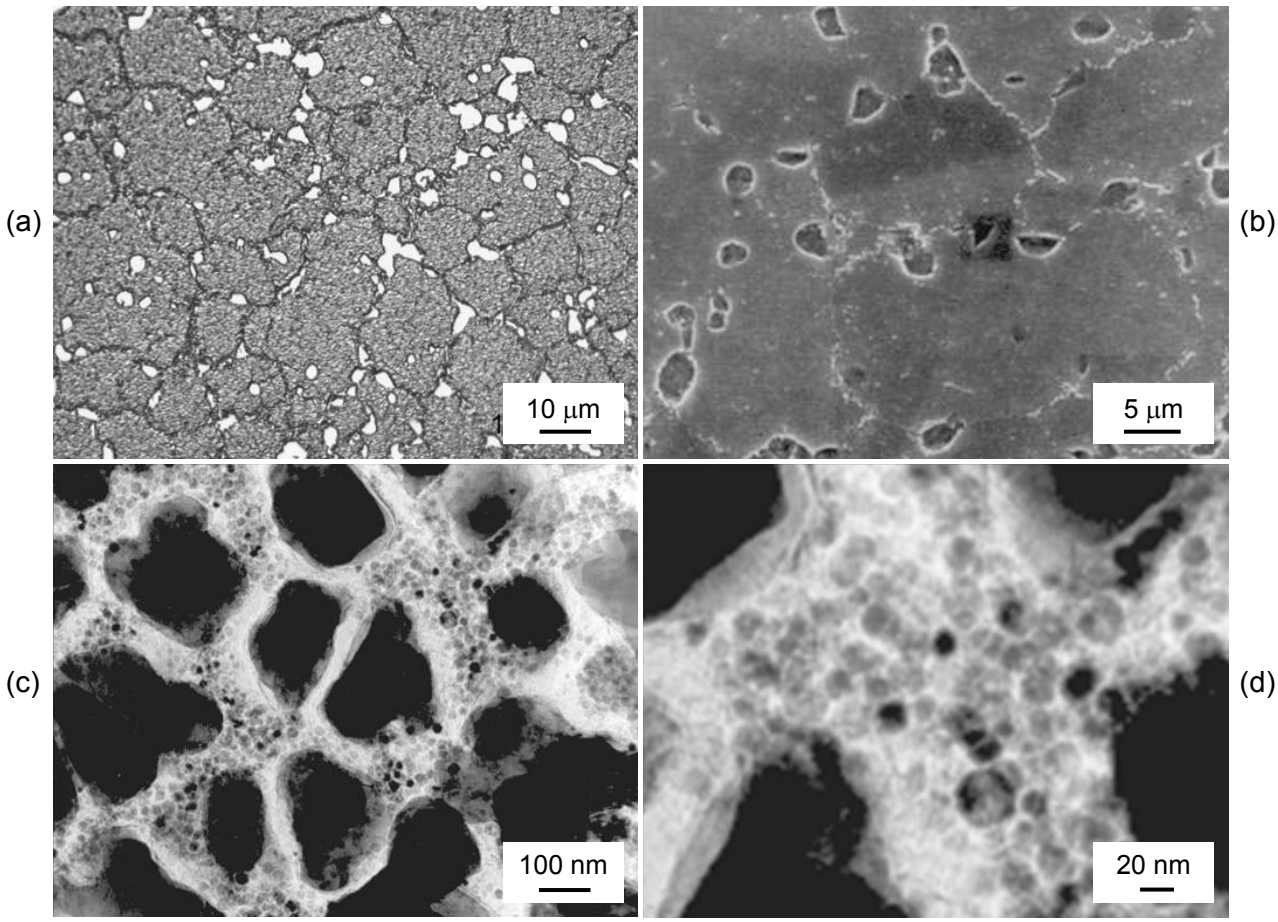

Figure 46 U720Li LG microstructure: (a) Optical, Orthophosphoric etch; (b) SEM SEI mode, Fry's Reagent[20]; (c) & (d) TEM bright field carbon replicas[21].

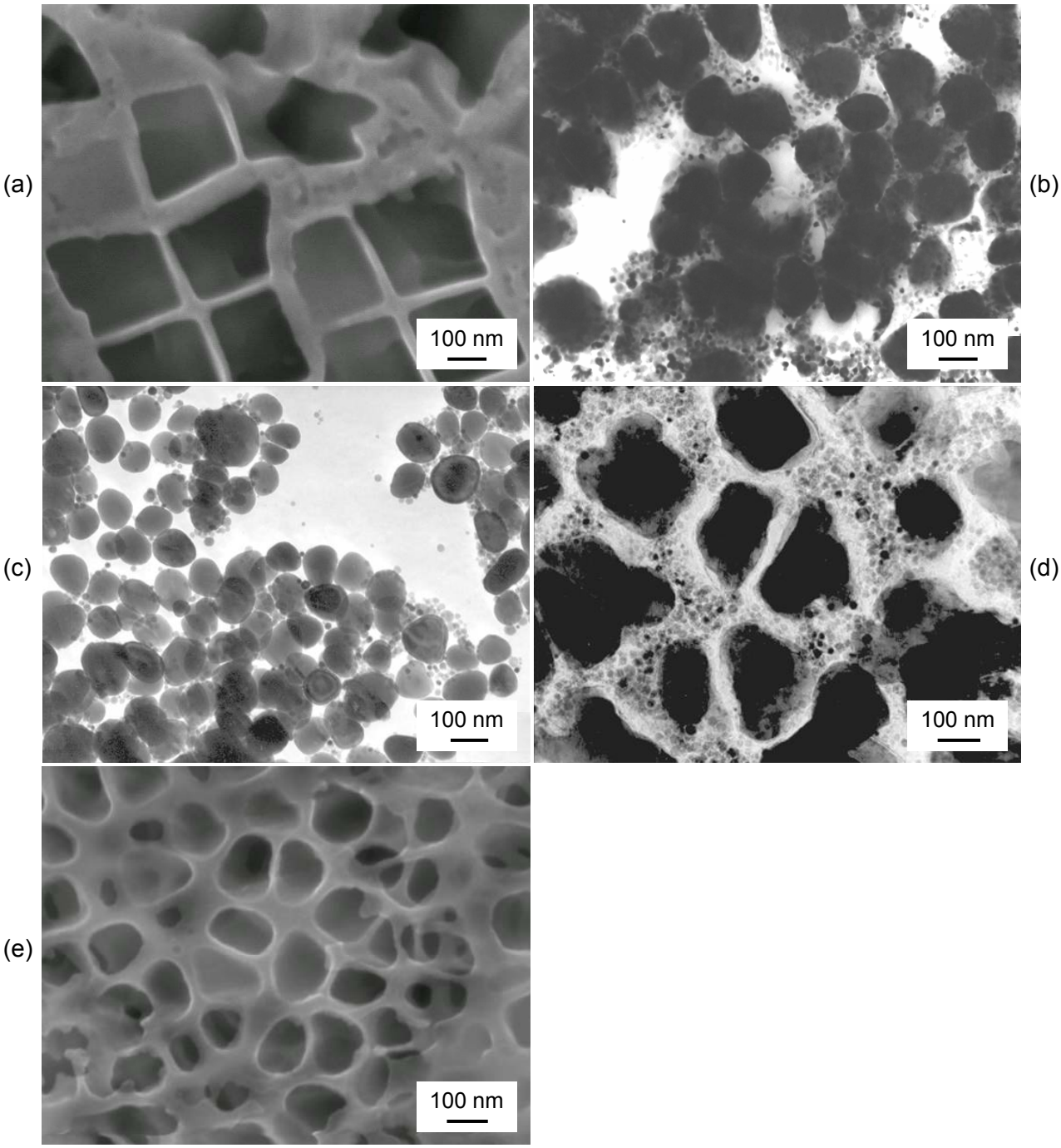

Figure 47 Comparison of secondary γ' similar scale: (a) N18, FEG SEM SEI mode, Nimonic etch; (b) RR1000, TEM bright field, carbon replica; (c) U720Li, TEM bright field, carbon replica; (d) U720Li LG, TEM bright field, carbon replica; (e) LSHR, FEG SEM SEI mode, Nimonic etch.

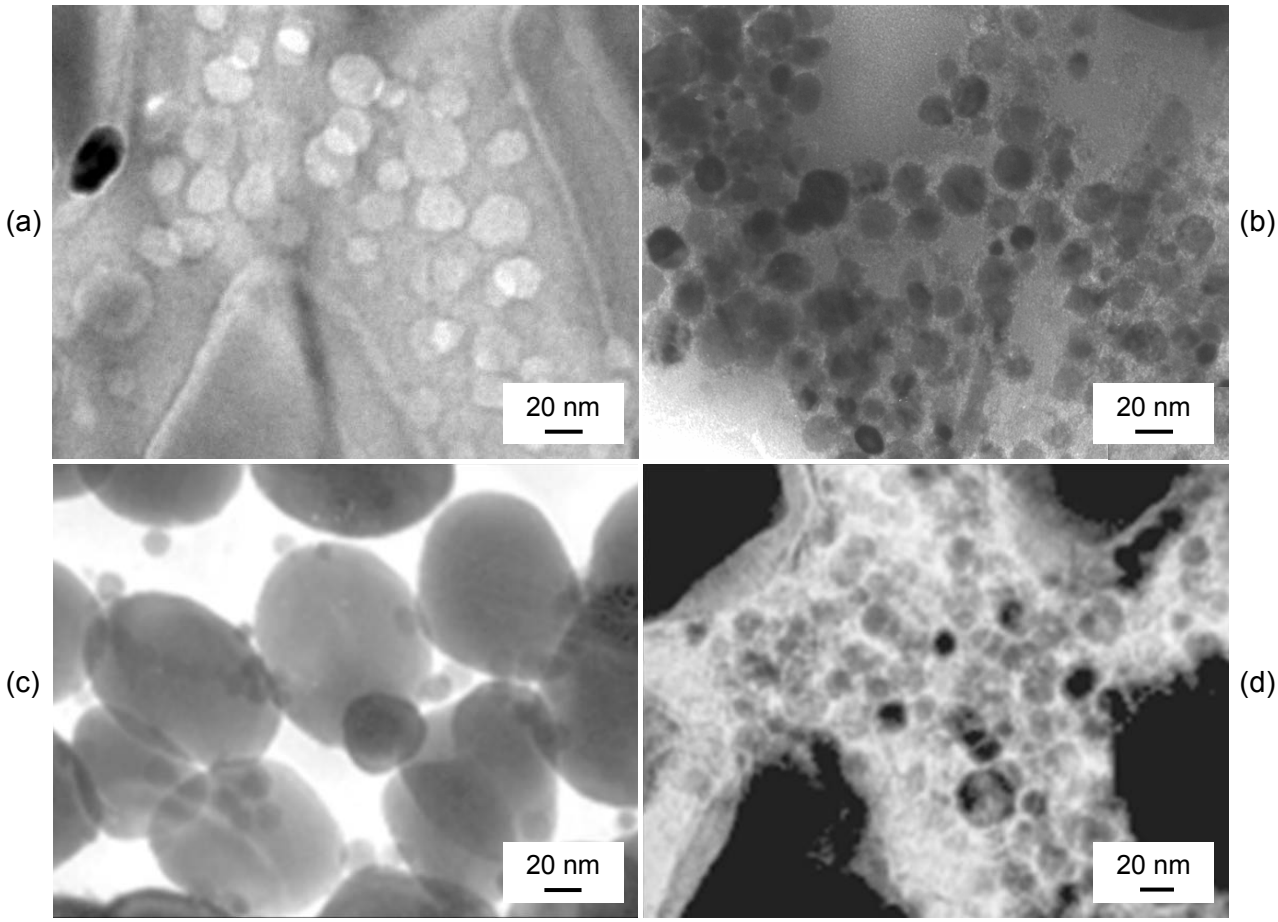

Figure 48 Comparison of tertiary γ' similar scale, TEM bright field: (a) N18; (b) RR1000, carbon replica; (c) U720Li, carbon replica; (d) U720Li LG, carbon replica.

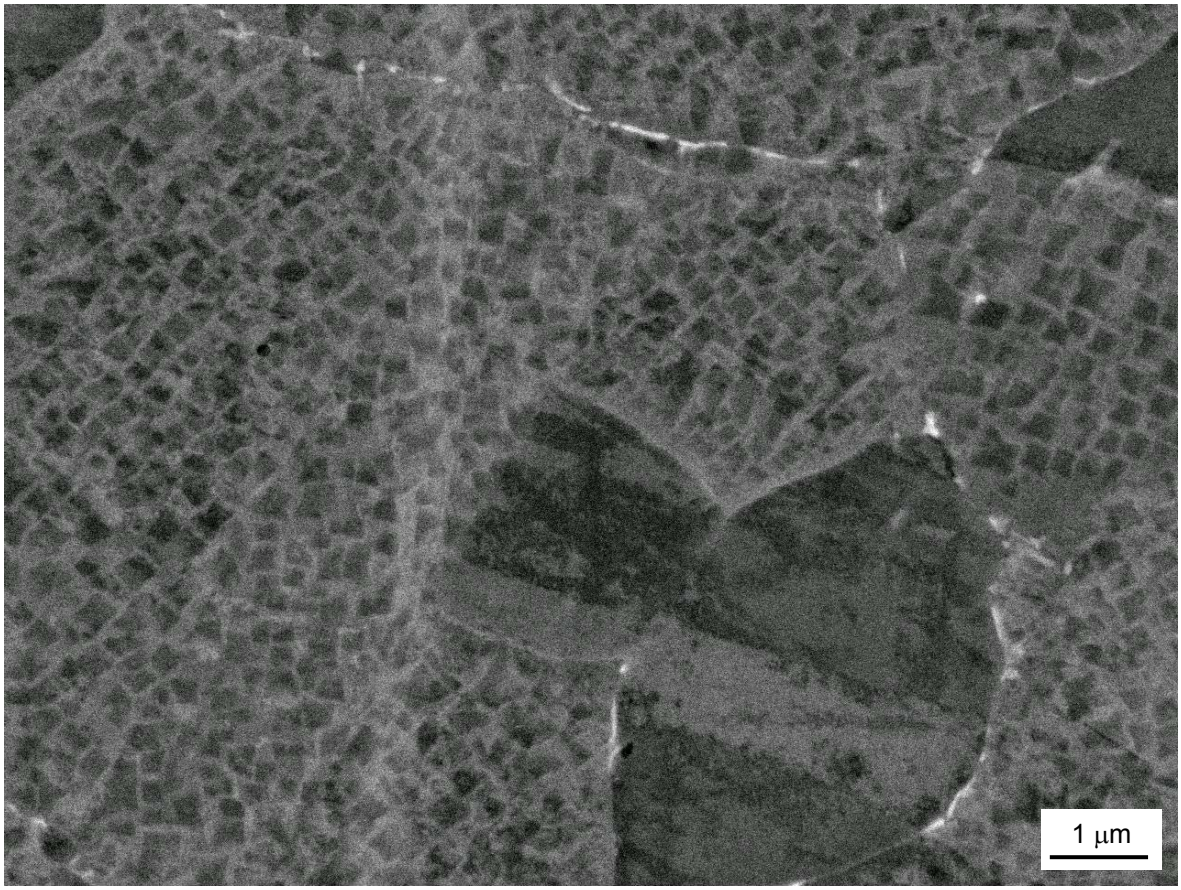

Figure 49 N18 Plain polish, FEG SEM BEI mode micrograph.

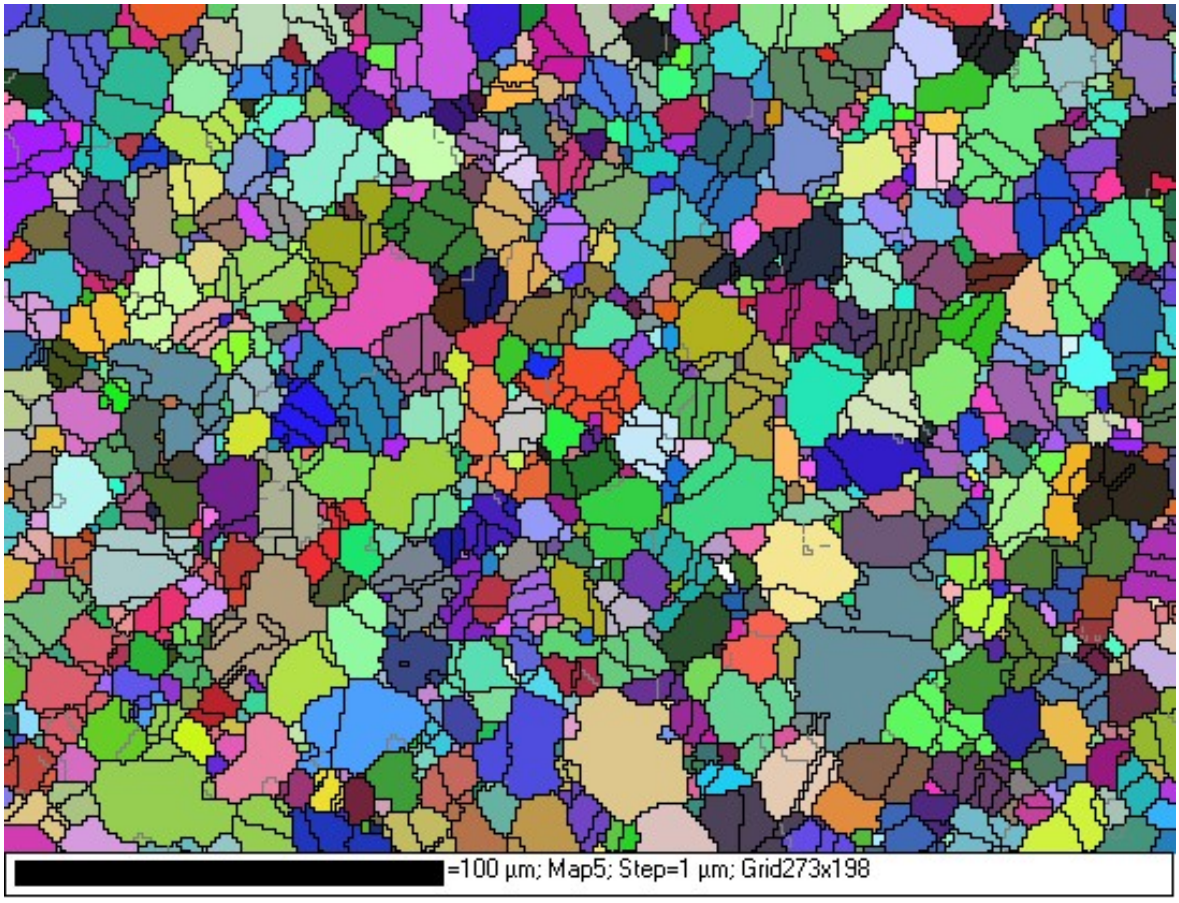

Figure 50 N18 EBSD Grain (and primary γ') size map.

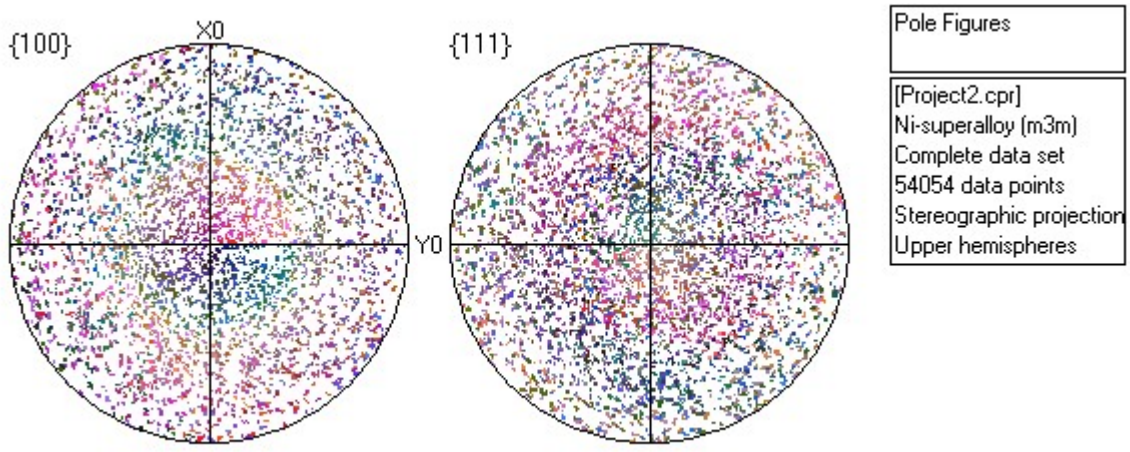

Figure 51 N18 EBSD Pole figures.

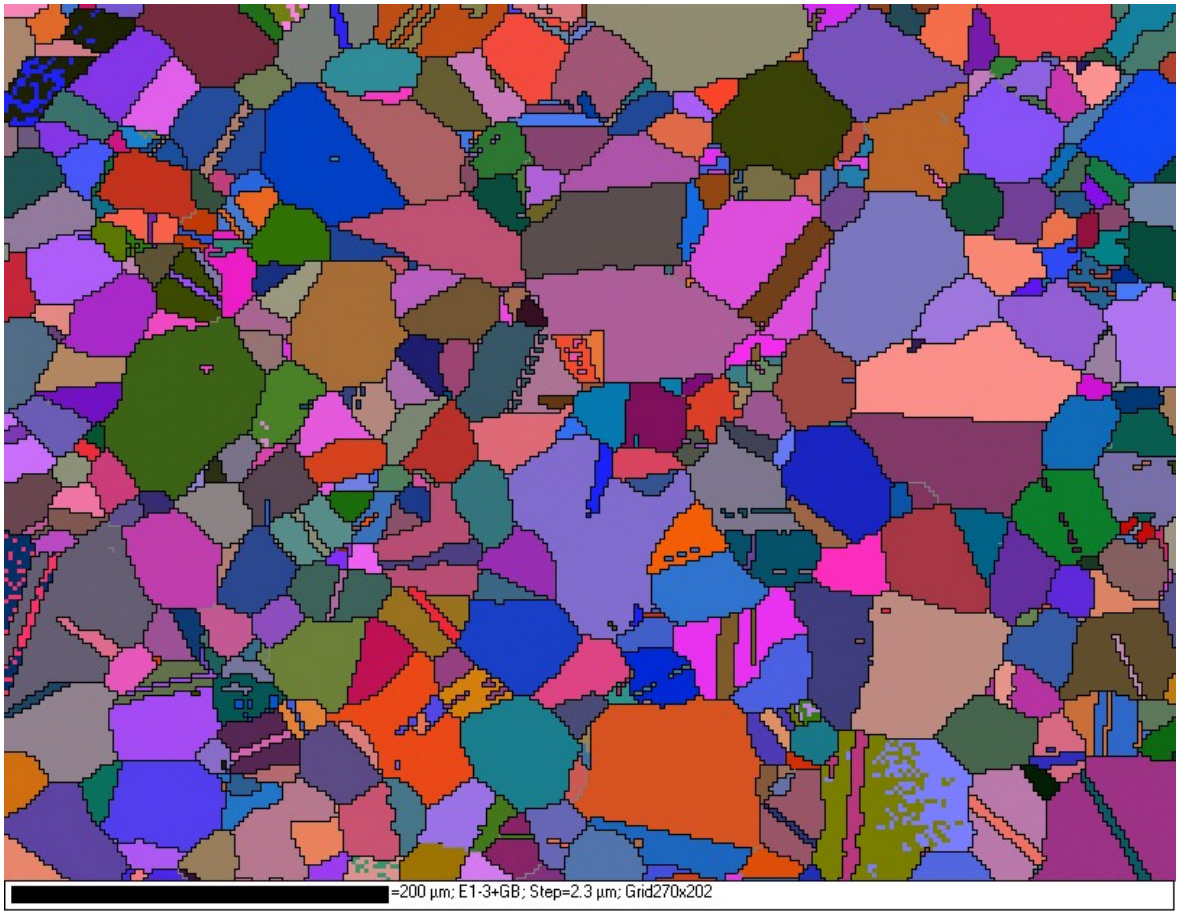

Figure 52 LSHR EBSD Grain size map.

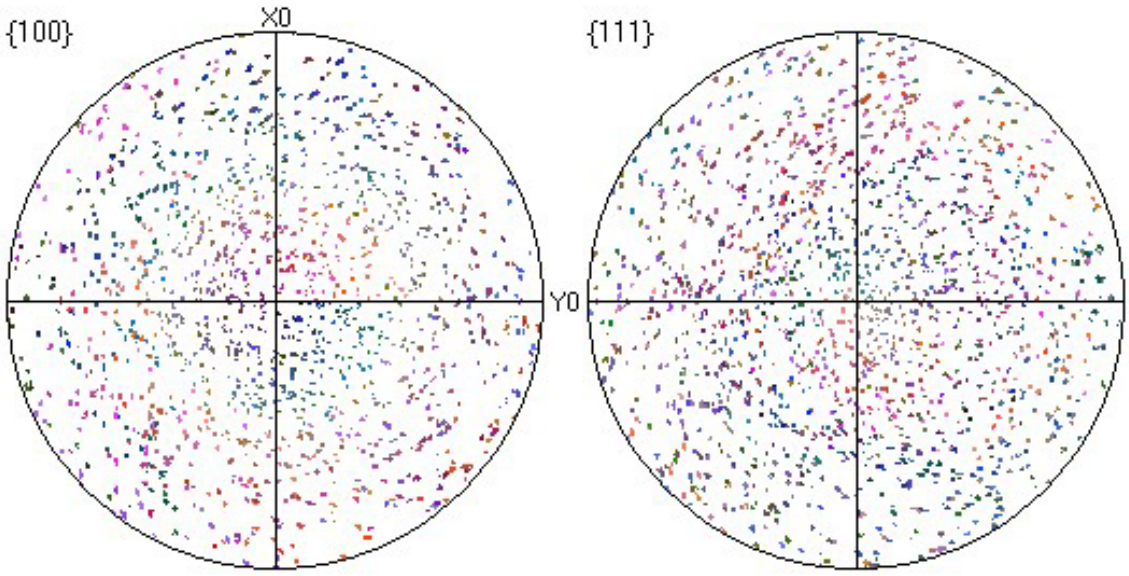

Figure 53 LSHR EBSD Pole figures.

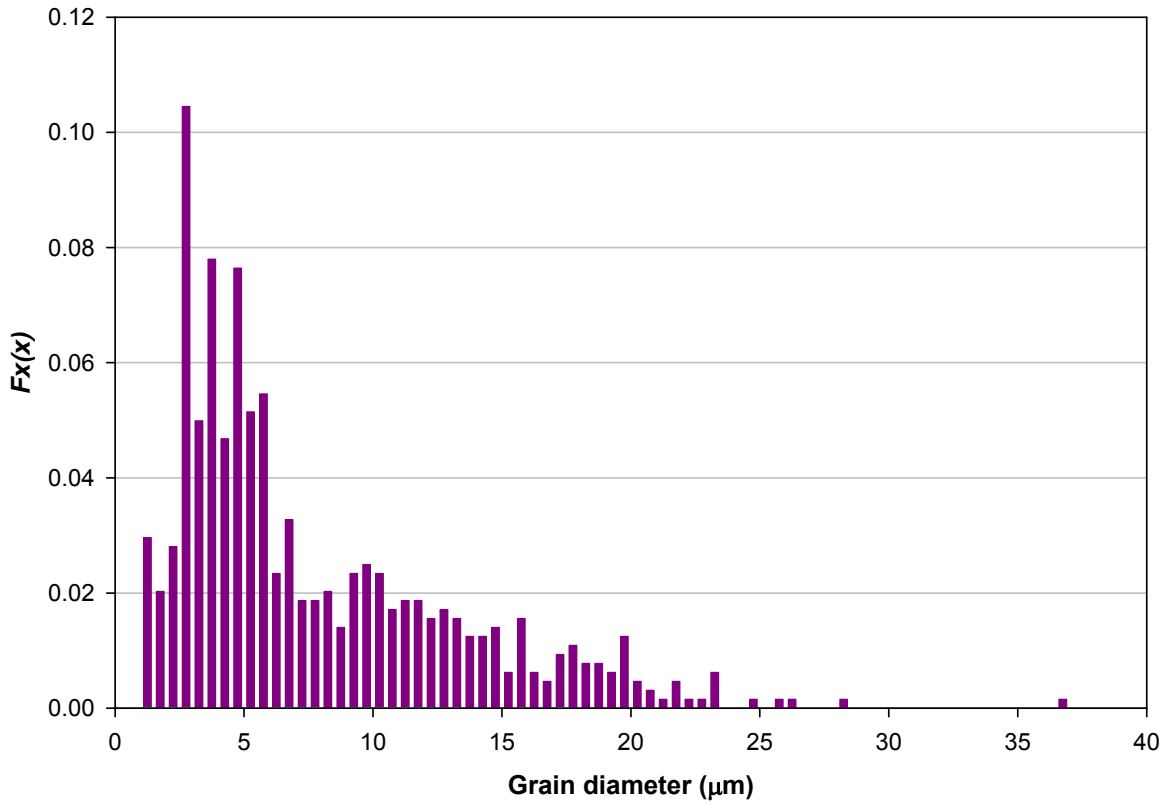

Figure 54 N18 EBSD Combined primary γ′ and grain size distribution.

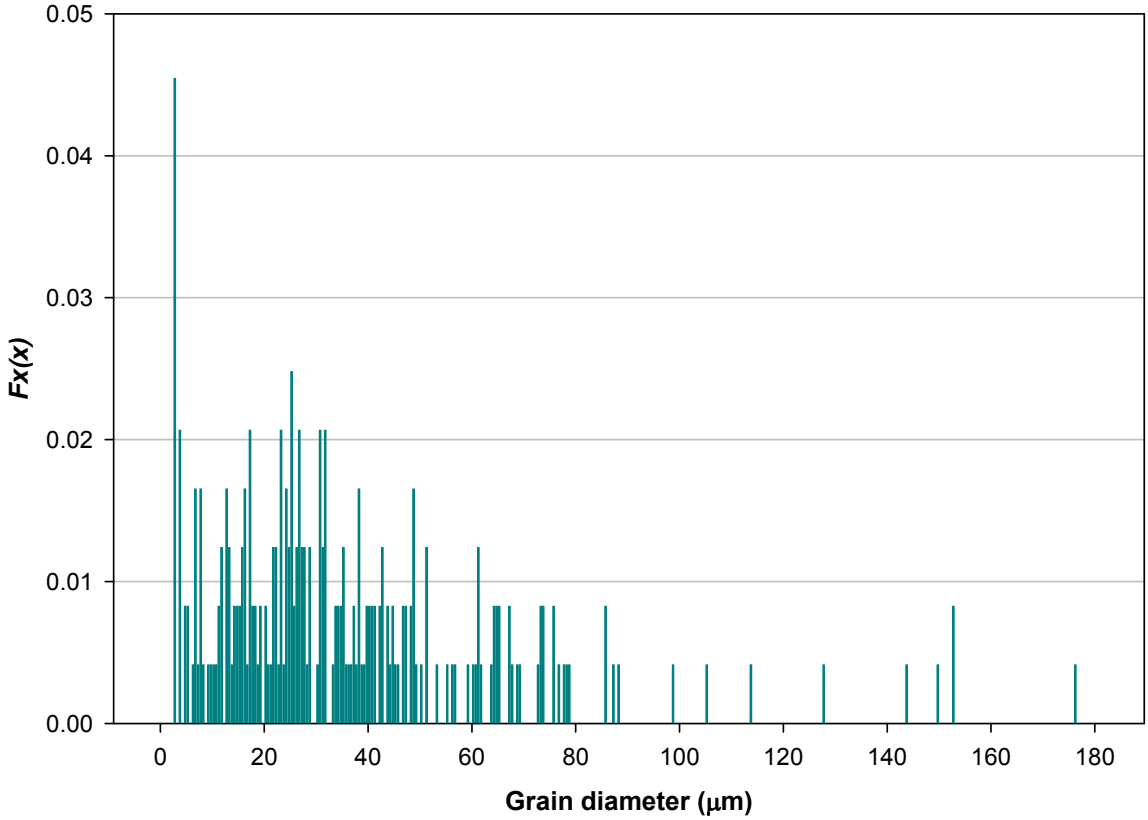

Figure 55 LSHR EBSD Grain size distribution.

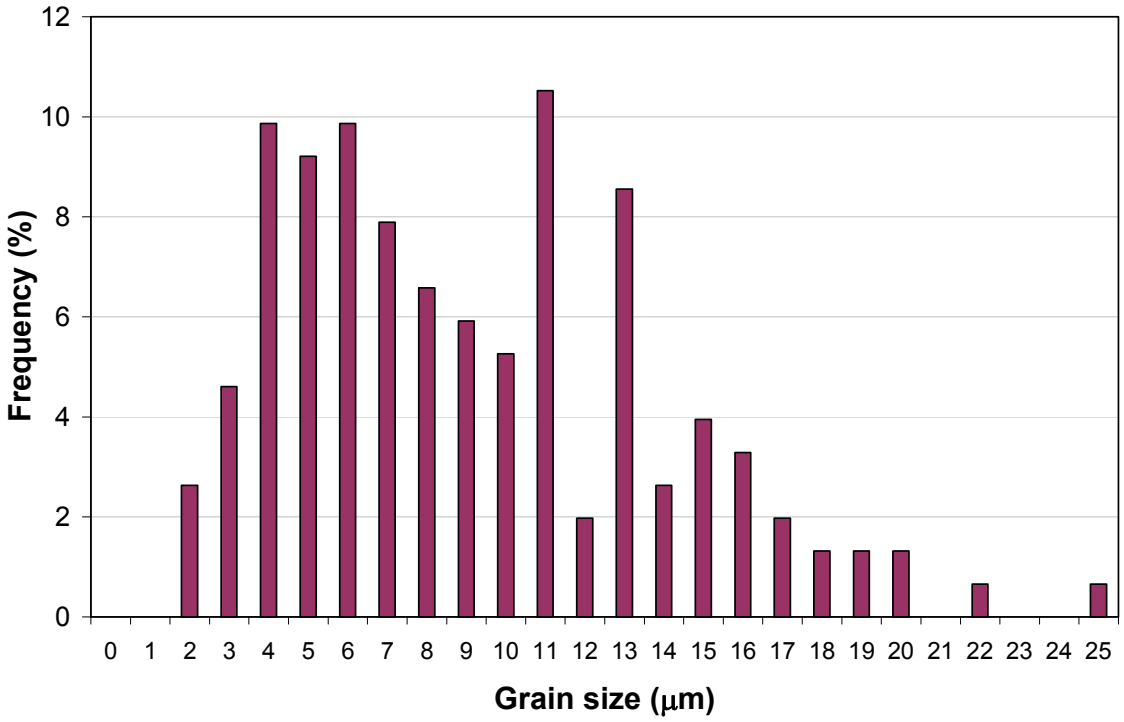

Figure 56 N18 Grain size distribution.

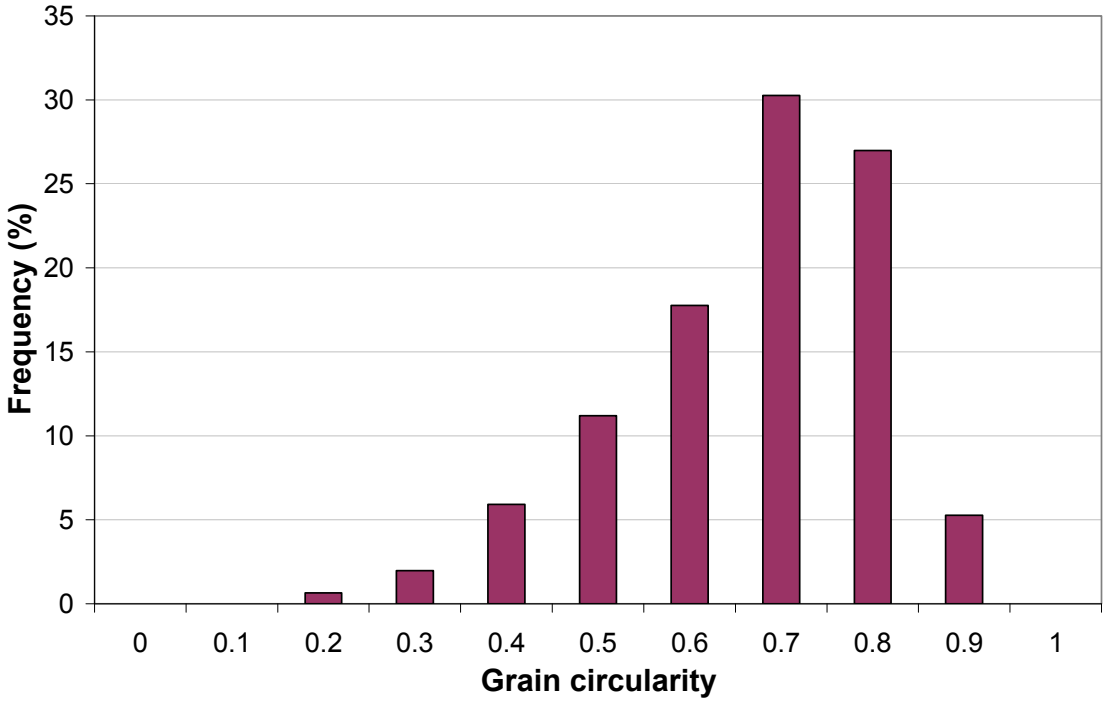

Figure 57 N18 Grain relative circularity.

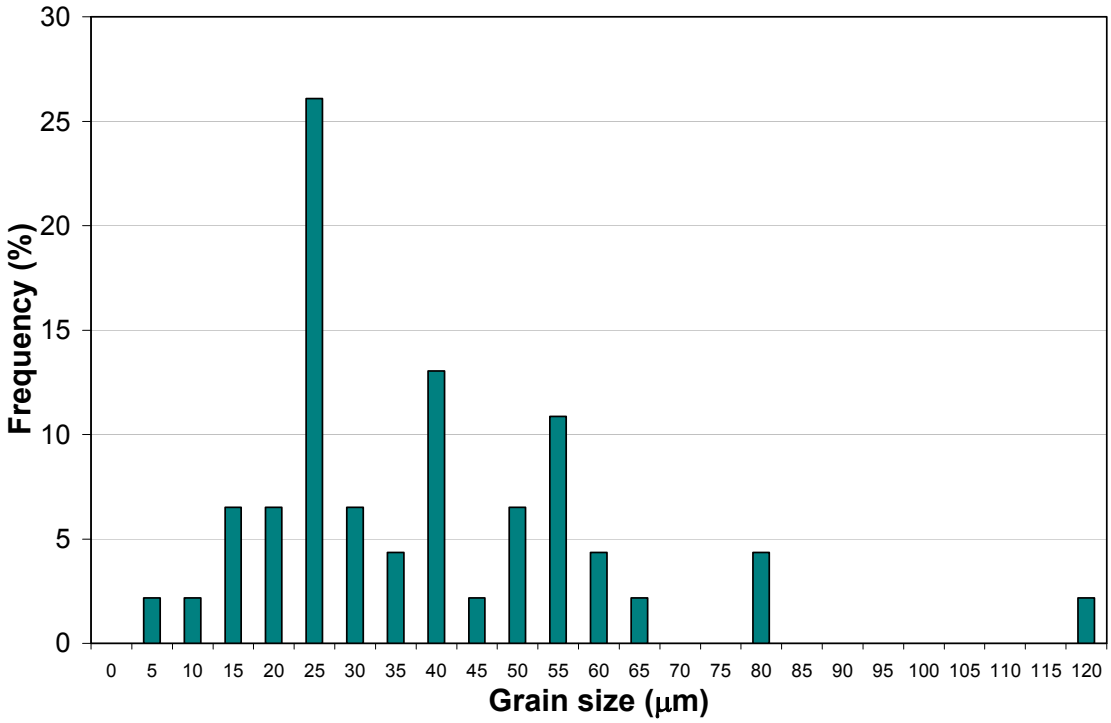

Figure 58 LSHR Grain size distribution.

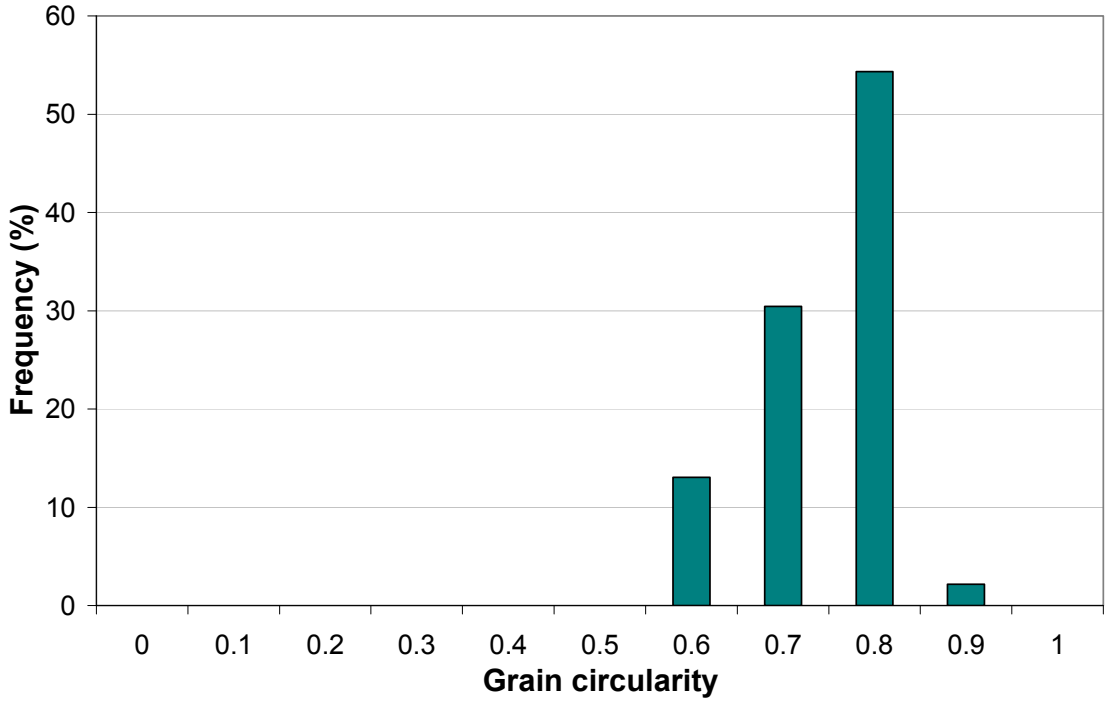

Figure 59 LSHR Grain relative circularity.

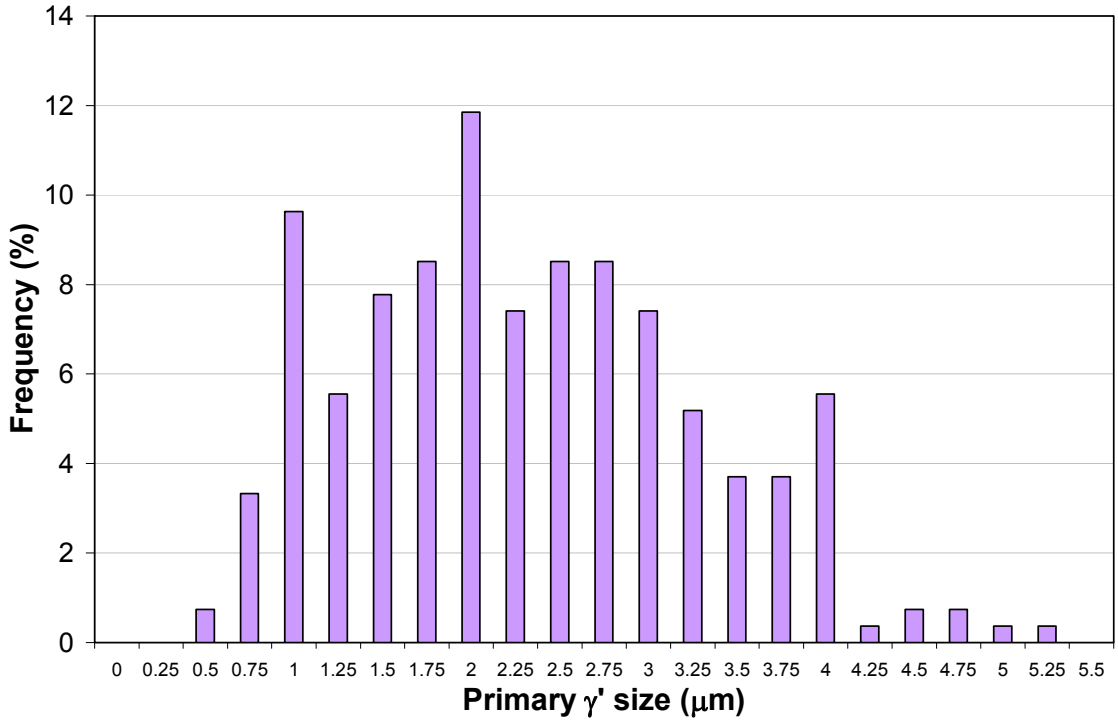

Figure 60 N18 Primary γ′ size distribution.

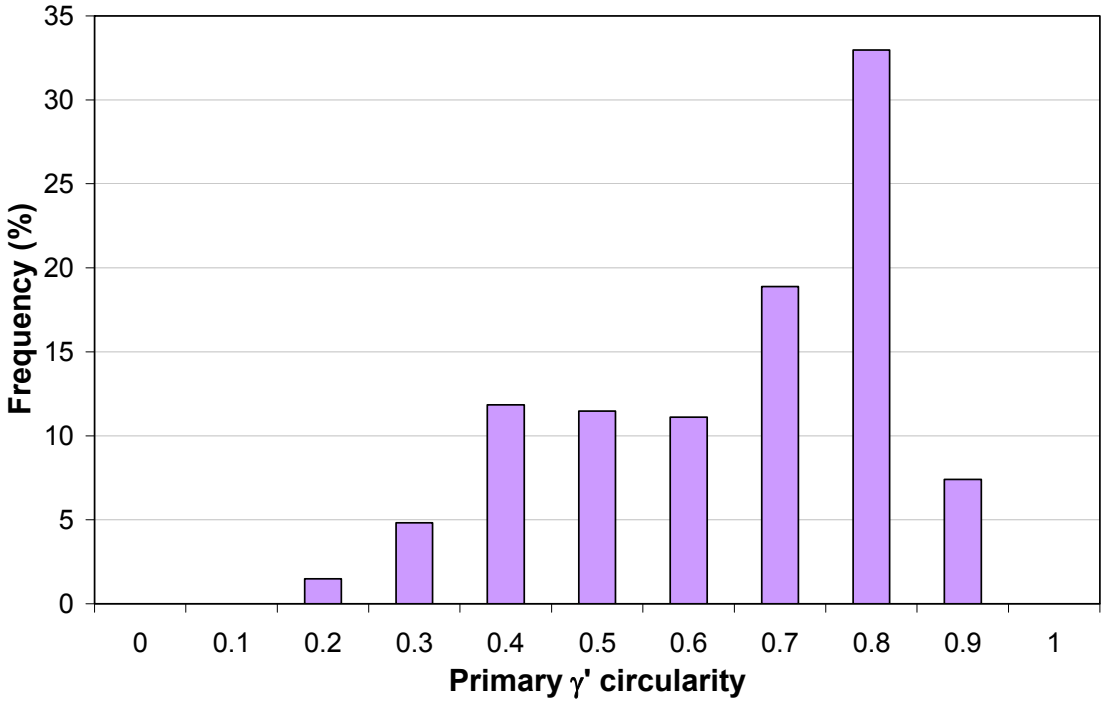

Figure 61 N18 Primary γ' relative circularity.

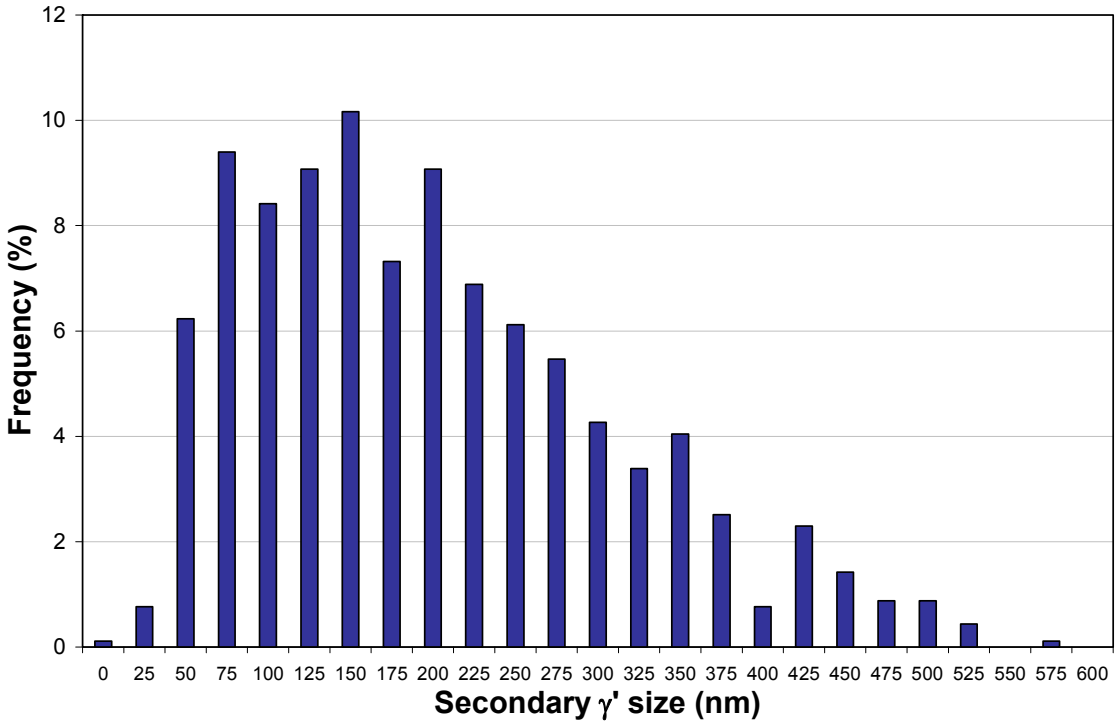

Figure 62 N18 Secondary γ' size distribution.

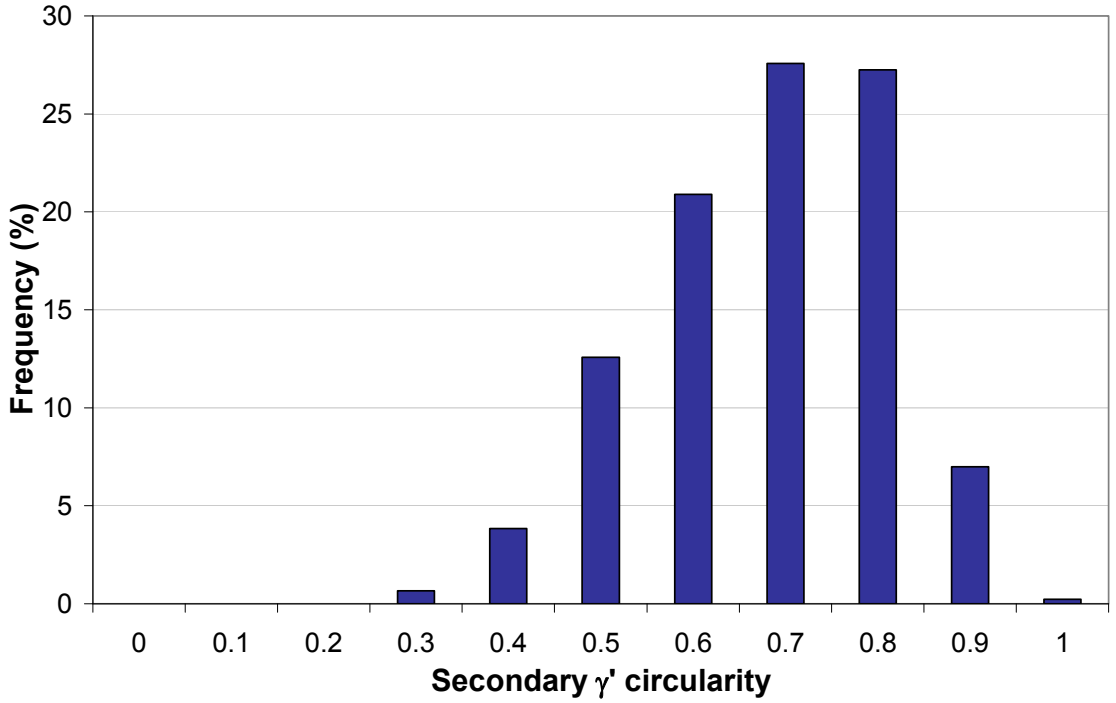

Figure 63 N18 Secondary γ' relative circularity.

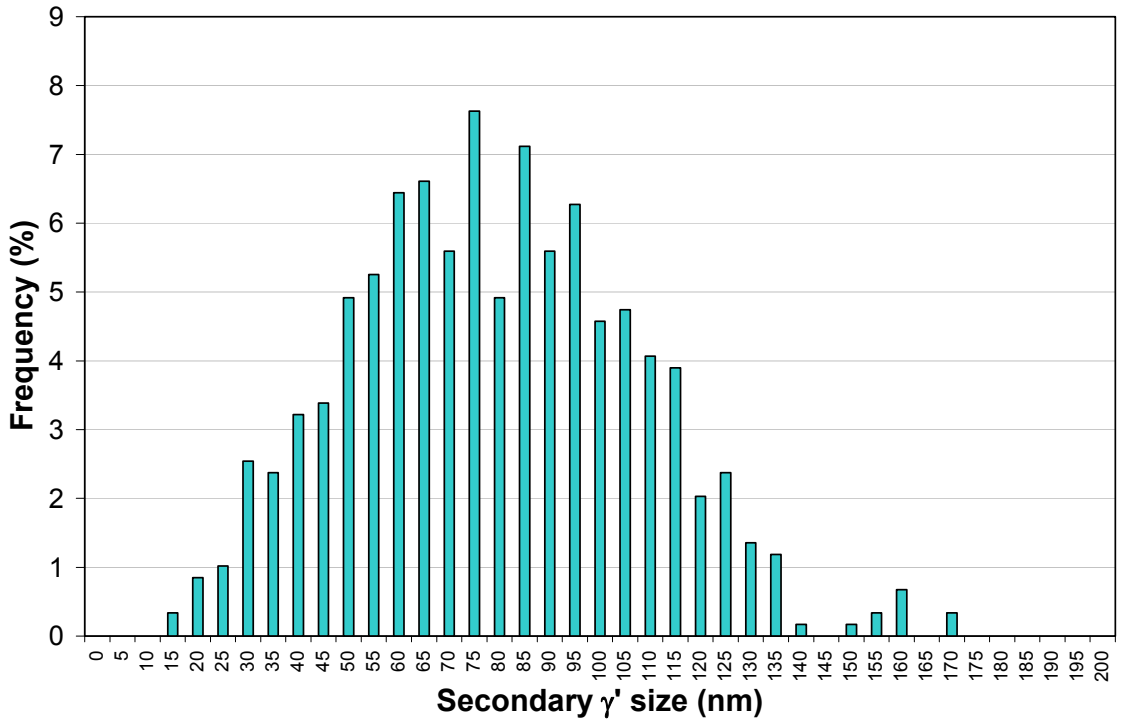

Figure 64 LSHR Secondary γ' size distribution.

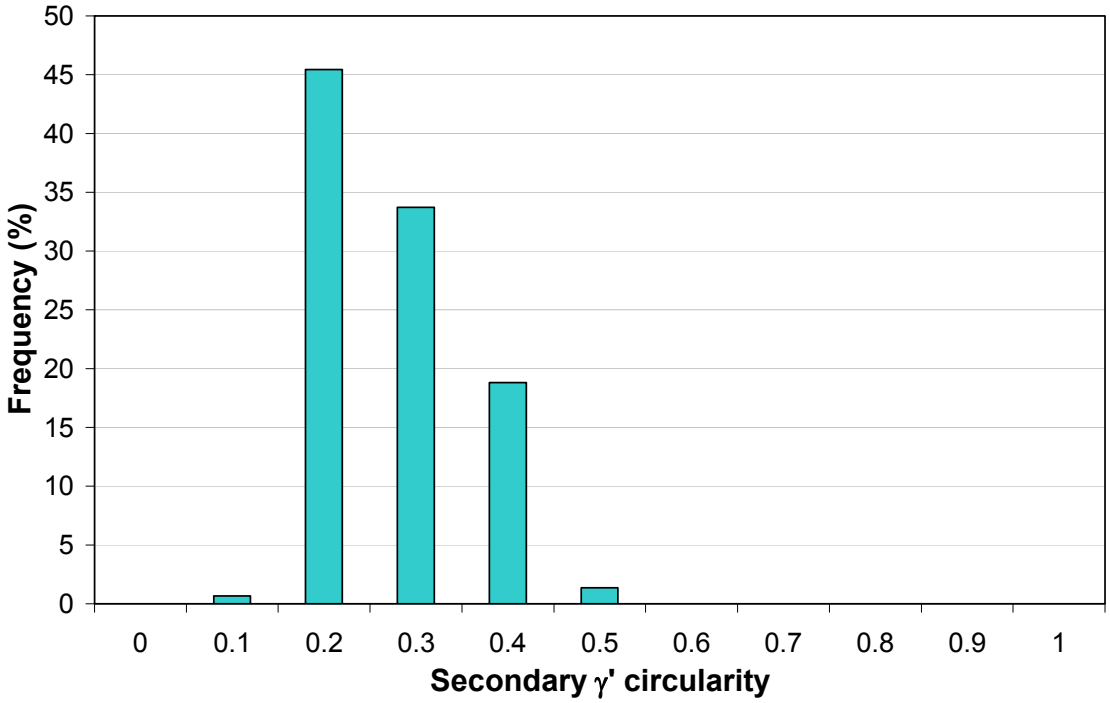

Figure 65 LSHR Secondary γ' relative circularity.

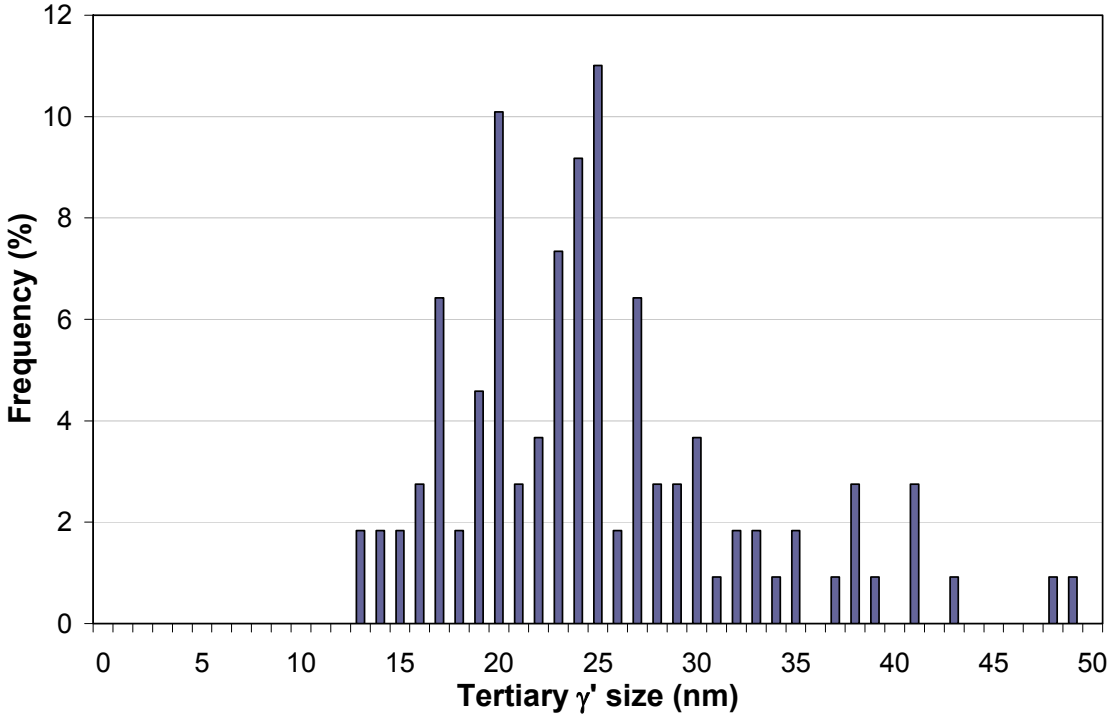

Figure 66 N18 Tertiary γ′ distribution.

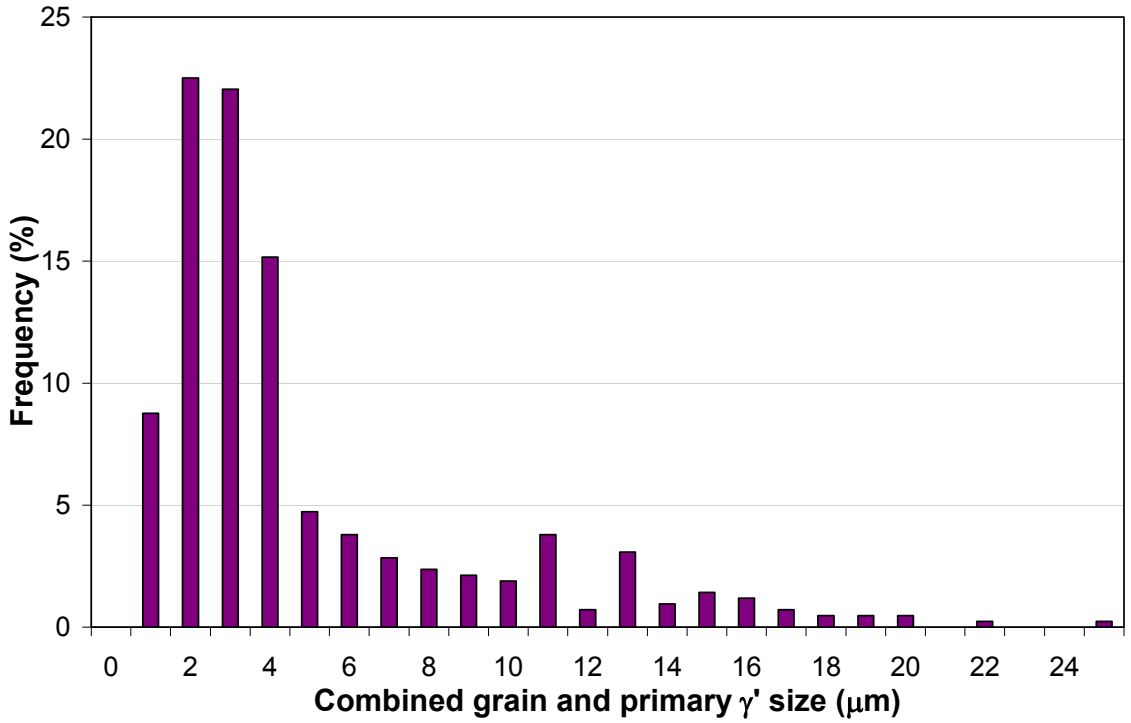

Figure 67 N18 Combined grain and primary γ′ size distribution.

Table 25 Comparison of grain and γ′ sizes and distributions between N18, LSHR, RR1000[21], U720Li[21] and U720Li LG[21].

	N18	**LSHR**	**RR1000**	**U720Li**	**U720Li-LG**
Grains					
Range (μm)	1.5 – 24.5	3.6 – 116.4	2.3 – 16.0	2.1 – 13.1	4.8 – 41.3
Mean (μm)	8.7 ± 4.7	35.9 ± 21.2	7.4 ± 2.8	6.4 ± 1.8	15.4 ± 6.5
Mean relative circularity	0.62	0.7	0.66	0.65	0.66
Primary γ′ precipitates					
Range (μm)	0.4 – 5.1	N/A	0.4 – 6.3	0.5 – 6.9	0.9 – 7.6
Mean (μm)	2.19 ± 0.98	N/A	1.75 ± 0.9	1.99 ± 0.9	2.52 ± 0.9
Mean relative circularity	0.6	N/A	0.70	0.70	0.72
Secondary γ′ precipitates					
Range (nm)	5 - 568	12 – 168	40 – 200	51 – 150	81 – 300
Mean (nm)	188 ± 112	76 ± 29	140	102	190
Tertiary γ′ precipitates					
Range (nm)	13 - 48	Significant amount not present	6 – 30	1 – 45	6 – 30
Mean (nm)	25		18	16	17

Table 26 Hardness values N18, LSHR, RR1000[21], U720Li[21] and U720Li LG[21].

	N18 (Hv10)	**LSHR** (Hv10)	**RR1000** (Hv30)	**U720Li** (Hv30)	**U720Li-LG** (Hv30)
Hardness	424.3±3	463.6±5.7	455.5±6.3	458±2.9	445±1.2

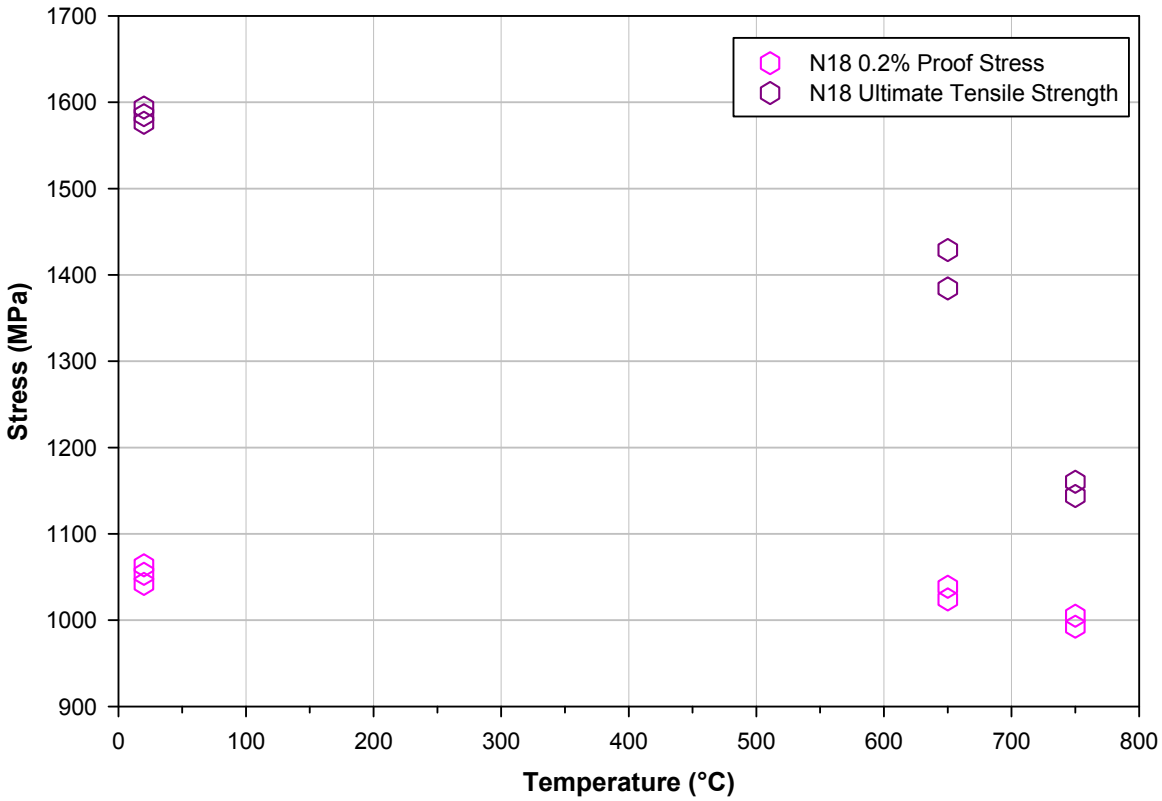

Figure 68 N18 Tensile test results, room temperature, 650°C and 725°C.

Table 27 Tensile strength data N18, LSHR, RR1000 and U720Li various temperatures.

Material	Tensile Strength Measure (MPa)	20°C	650°C	750°C	760°C
N18	0.2% proof stress	1053±9	1031±7	999±6	-
	UTS	1585±7	1406±22	1152±8	-
LSHR[64]	0.2% proof stress	1097	1017	-	1022
	UTS	1589	1494	-	1183
RR1000[21]	0.2% proof stress	-	1035	895	-
U720Li [62,195]	0.2% proof stress	1216	980	-	-
U720Li-LG[62]	0.2% proof stress	1181	850	-	-

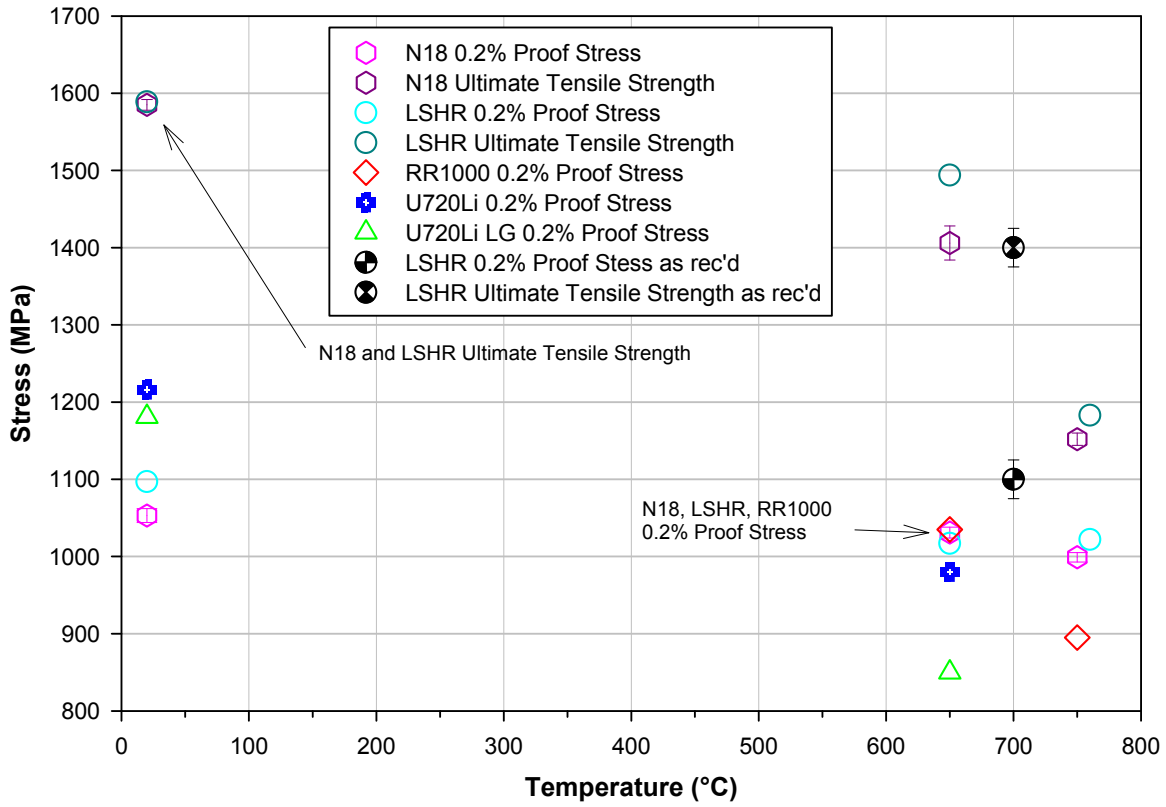

Figure 69 Tensile Strength Comparison between N18, LSHR, RR1000, U720Li and U720Li LG

(a)

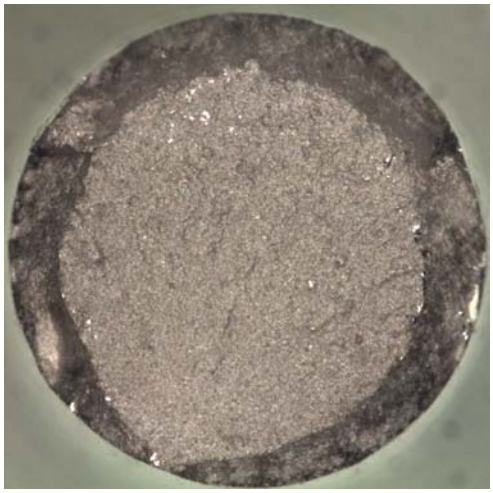

(b)

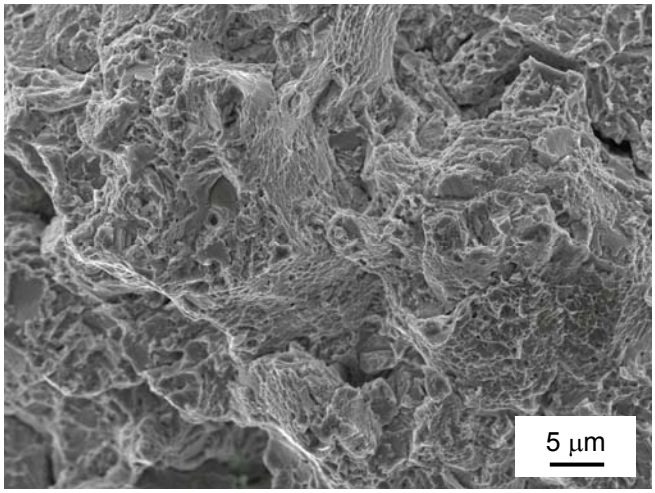

N18 tensile room temperature

(c)

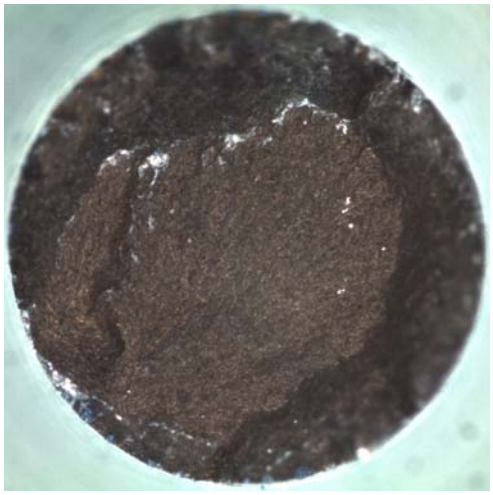

(d)

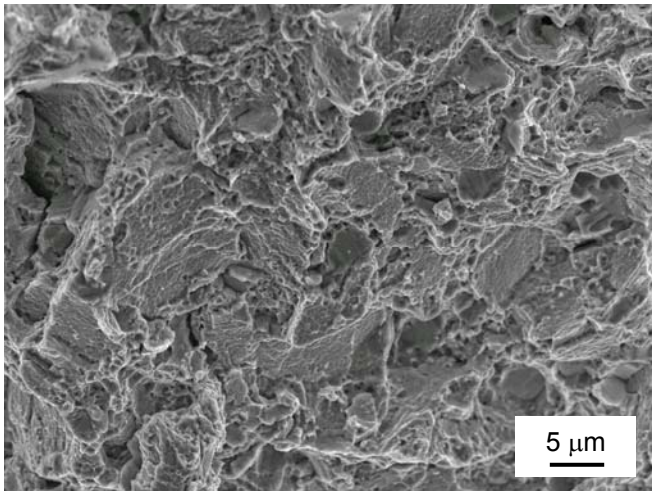

N18 tensile 650°C

(e)

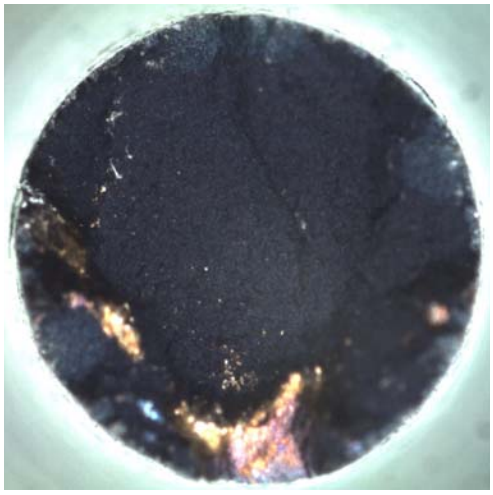

(f)

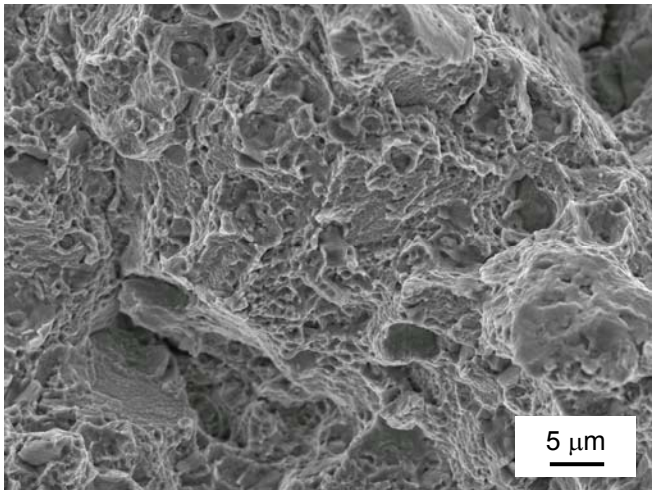

N18 tensile 725°C

Figure 70 N18 Tensile tests fractography, room temperature, 650°C and 725°C in air, macroscopic overviews and FEG SEM SEI mode micrographs.

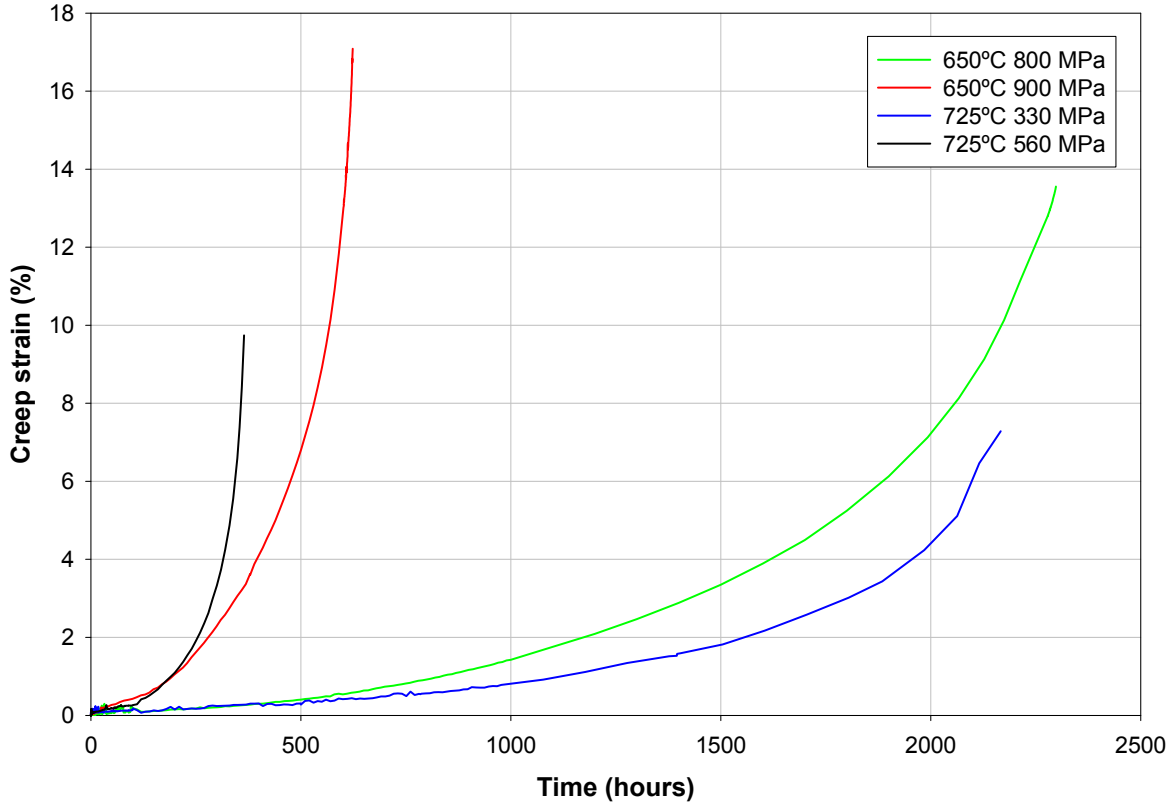

Figure 71 N18 creep curves, 650°C and 725°C.

Table 28 Creep rupture data for N18 and U720Li at 650°C and 725°C.

Temperature	**650°C**		**725°C**	
Stress (MPa)	**800**	**900**	**330**	**560**
N18 creep rupture times (hours)	2302	623	2445	364
U720Li creep rupture times (hours)[1]	690	257	588	66

Table 29 Creep rupture data for LSHR at 650°C, 704°C and 760°C.

Temperature	**650°C**	**704°C**	**760°C**
Stress (MPa)	**862**	**689**	**448**
LSHR creep rupture times (hours) [64]	3574	1872	1849

Table 30 Creep rupture data for RR1000 at 725°C.

Temperature	**725°C**	
Stress (MPa)	**460**	**525**
RR1000 creep rupture times (hours) [156]	923	482

(a)

N18 creep 650°C 900 MPa

(b)

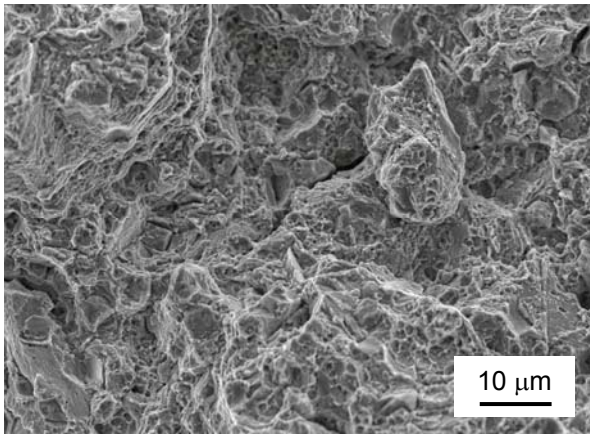

N18 creep 650°C 900 MPa overload

(c)

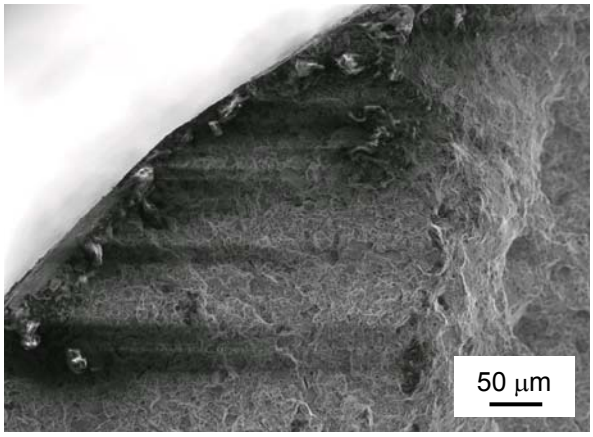

650°C smaller creep crack initiation

(d)

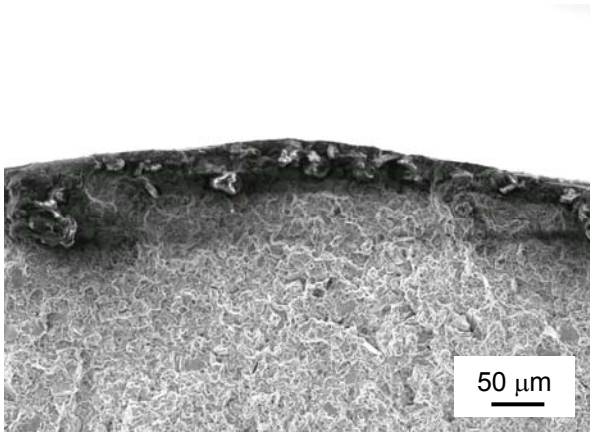

650°C larger creep crack initiation

(e)

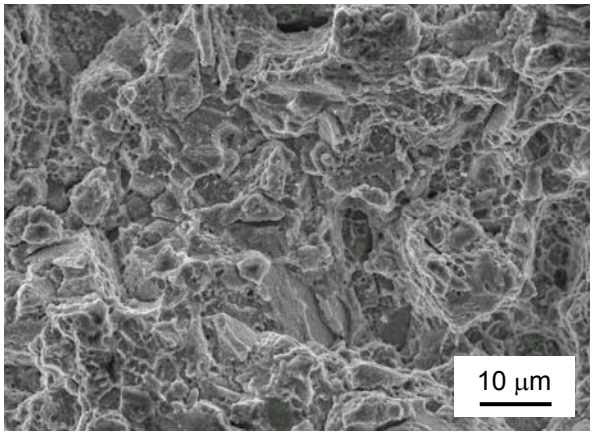

650°C smaller creep crack stable growth

(f)

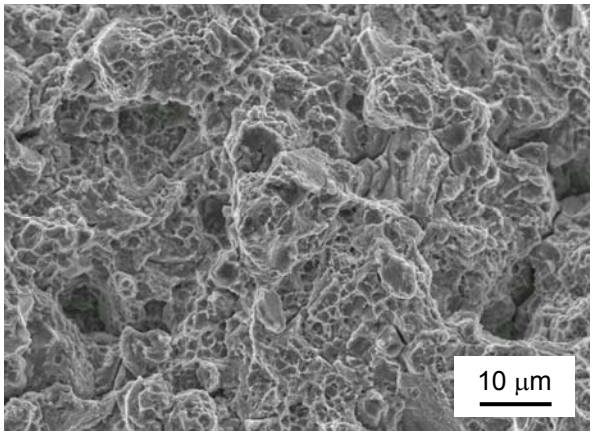

650°C larger creep crack stable growth

(g)

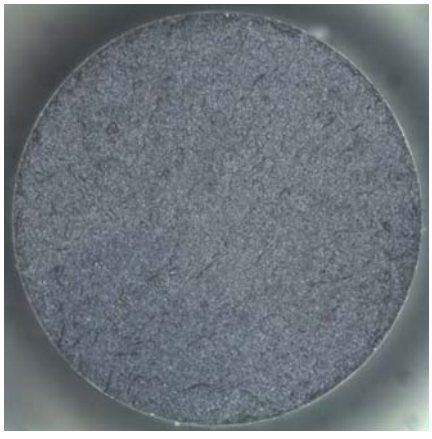

N18 creep 725°C 560 MPa

(h)

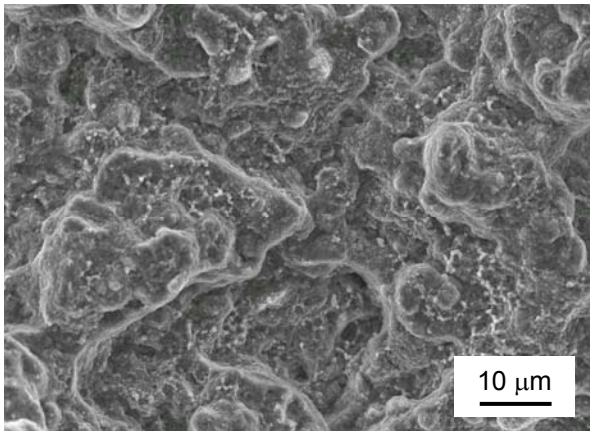

N18 creep 725°C 560 MPa overload

Figure 72 N18 Creep test fractography, 650°C 900 MPa and 725°C 560MPa in air, macroscopic overviews and FEG SEM SEI mode micrographs.

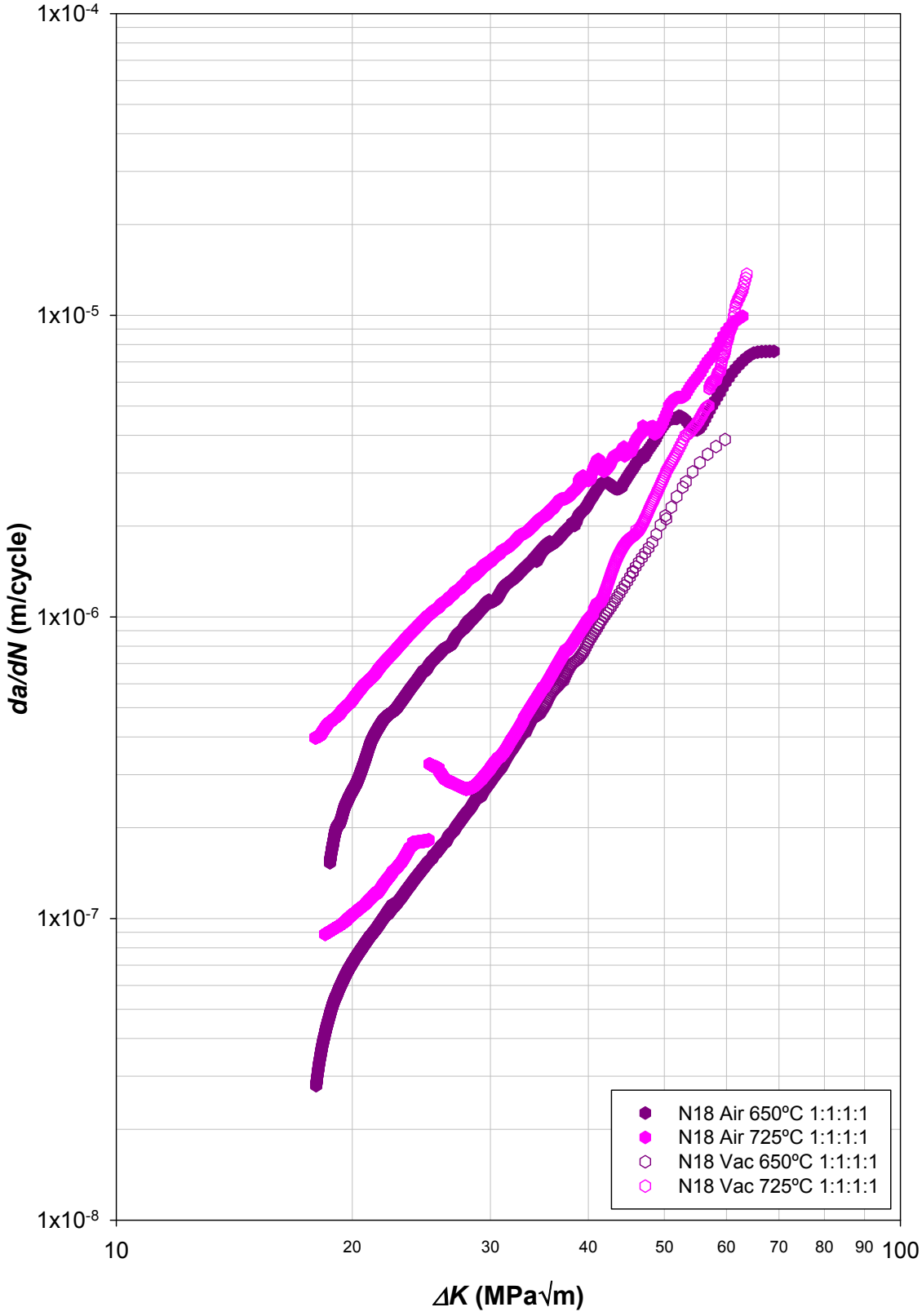

Figure 73 N18 *da/dN* vs. *ΔK*, in air and vacuum at 650°C and 725°C, 1-1-1-1 load cycle.

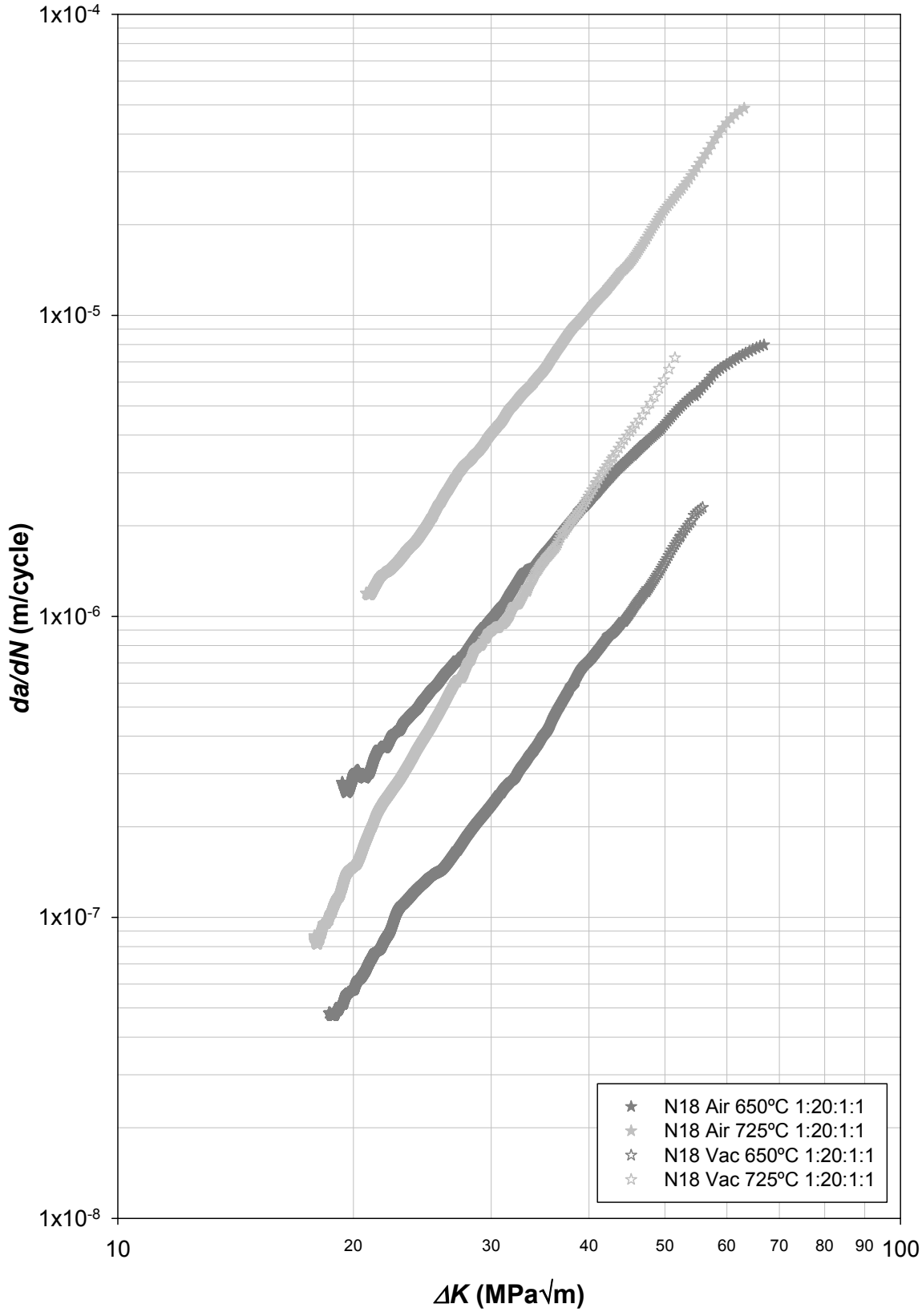

Figure 74 N18 *da/dN* vs. *ΔK*, in air and vacuum at 650°C and 725°C, 1-20-1-1 load cycle.

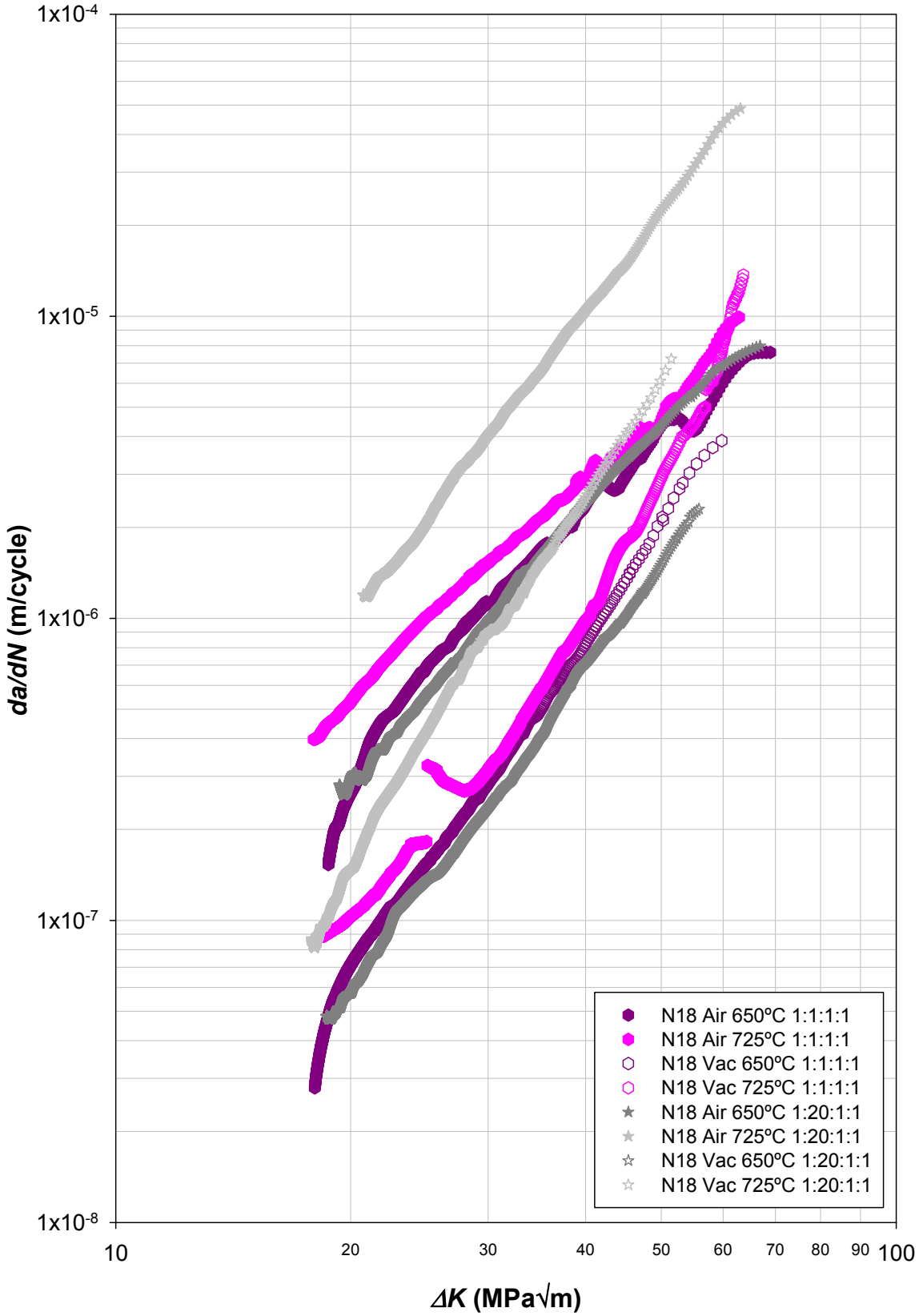

Figure 75 *N18 da/dN* vs. *ΔK*, in air and vacuum at 650°C and 725°C, 1-1-1-1 and 1-20-1-1 load cycles.

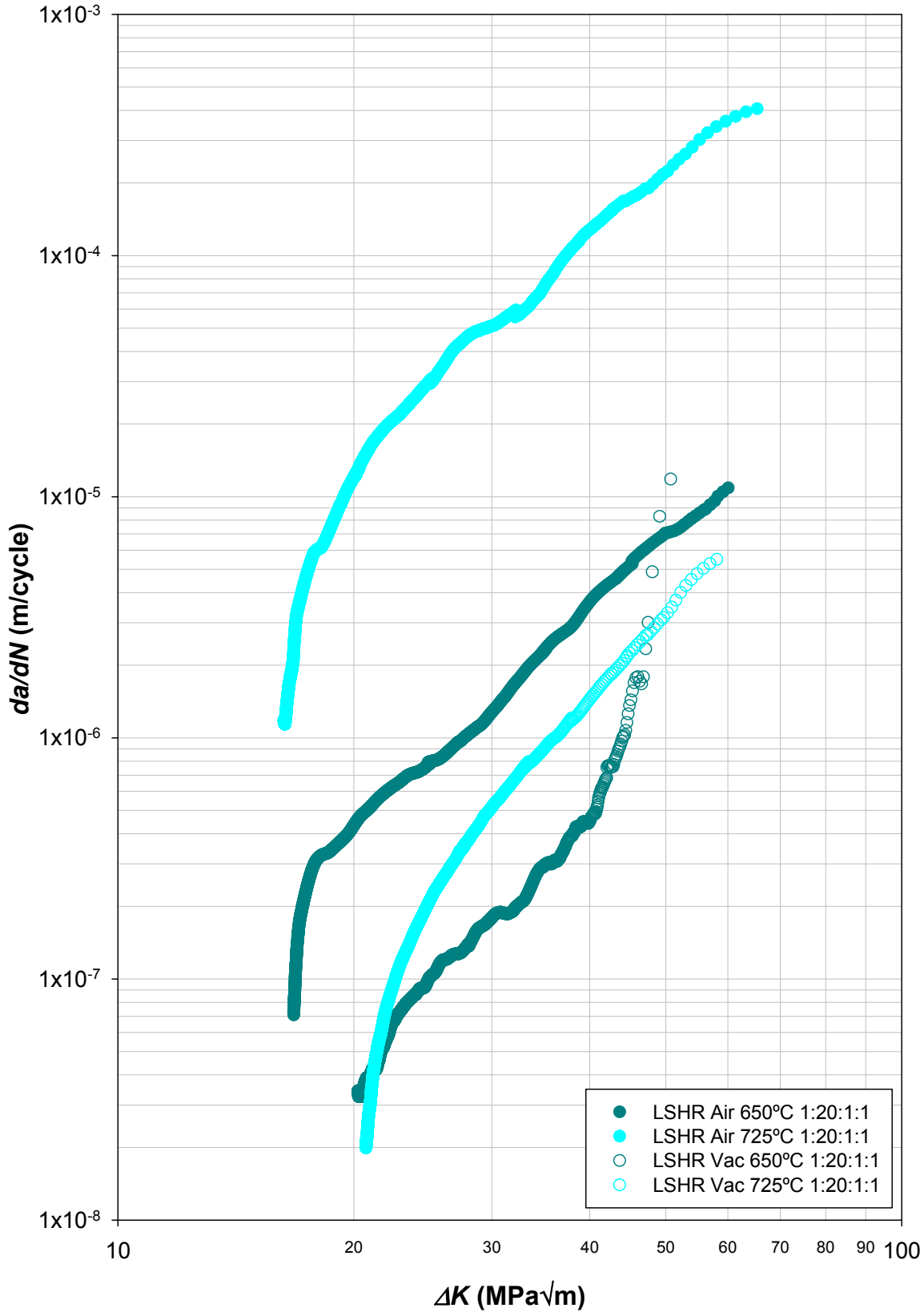

Figure 76 LSHR *da/dN* vs. *ΔK*, in air and vacuum at 650°C and 725°C, 1-20-1-1 load cycle.

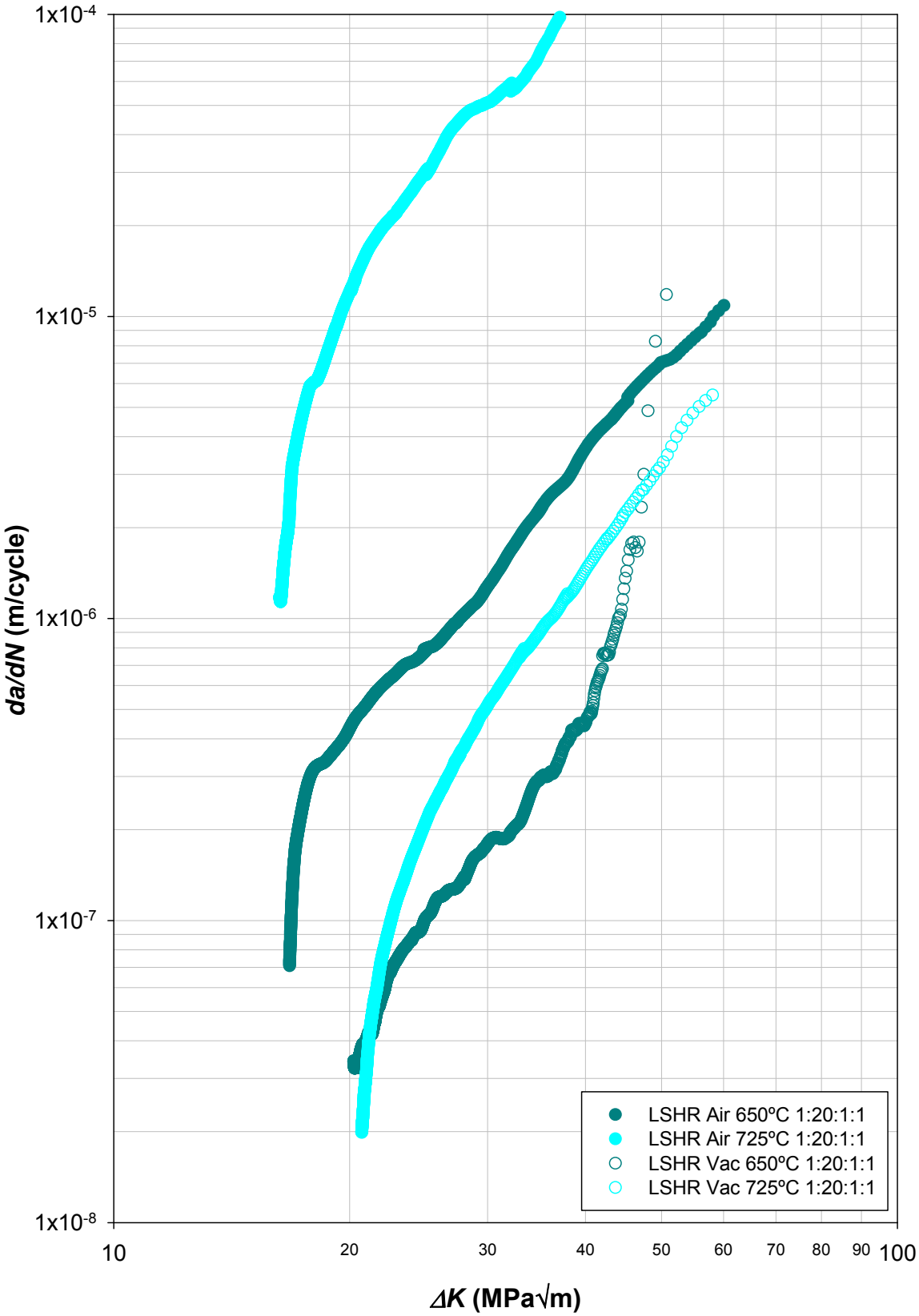

Figure 77 LSHR *da/dN* vs. *ΔK*, in air and vacuum at 650°C and 725°C, 1-20-1-1 load cycle (da/dN range limited to 1x10^{-4} to aid comparison with other graphs).

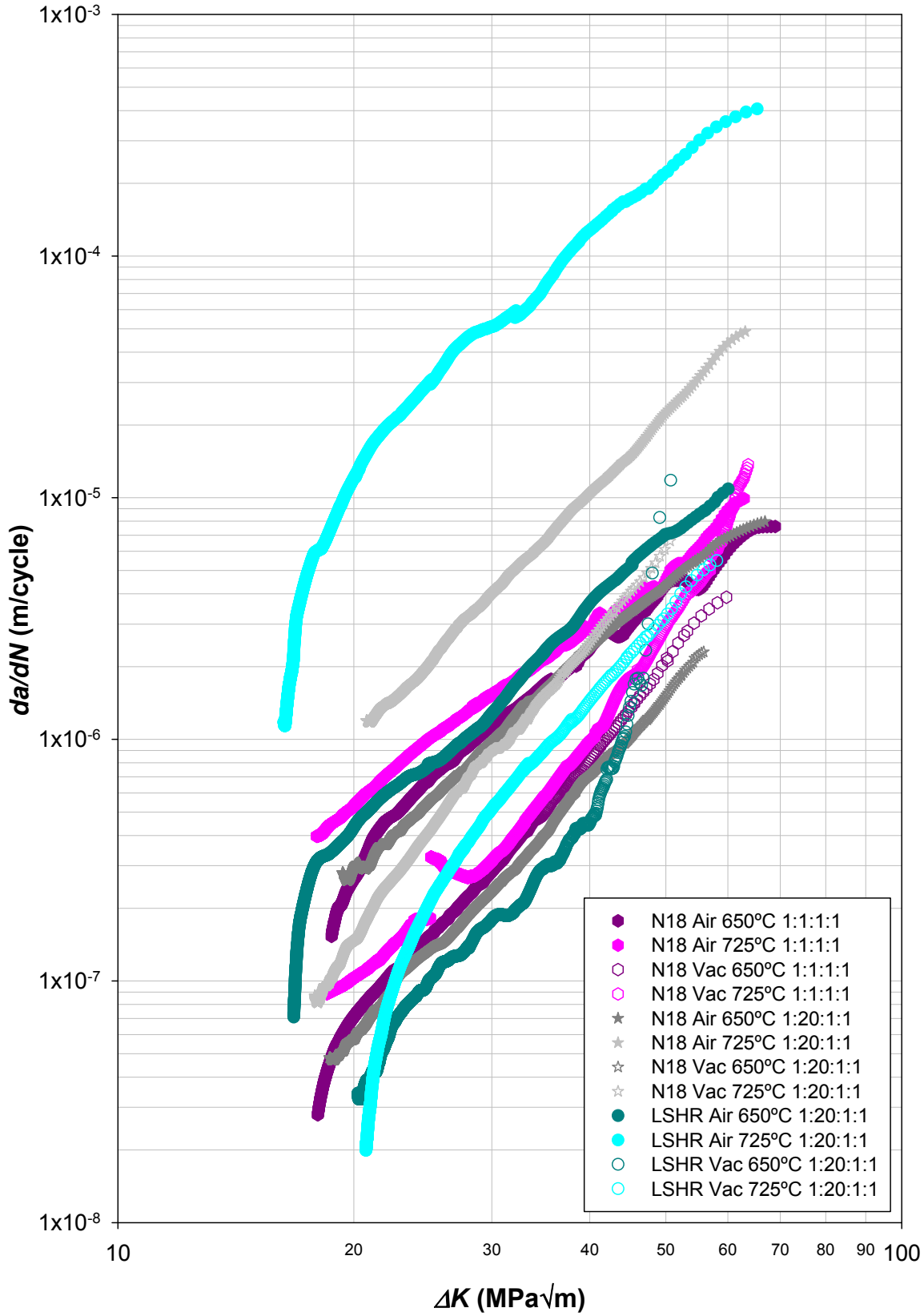

Figure 78 N18 and LSHR *da/dN* vs. *ΔK*, in air and vacuum at 650°C and 725°C, 1-1-1-1 and 1-20-1-1 load cycles.

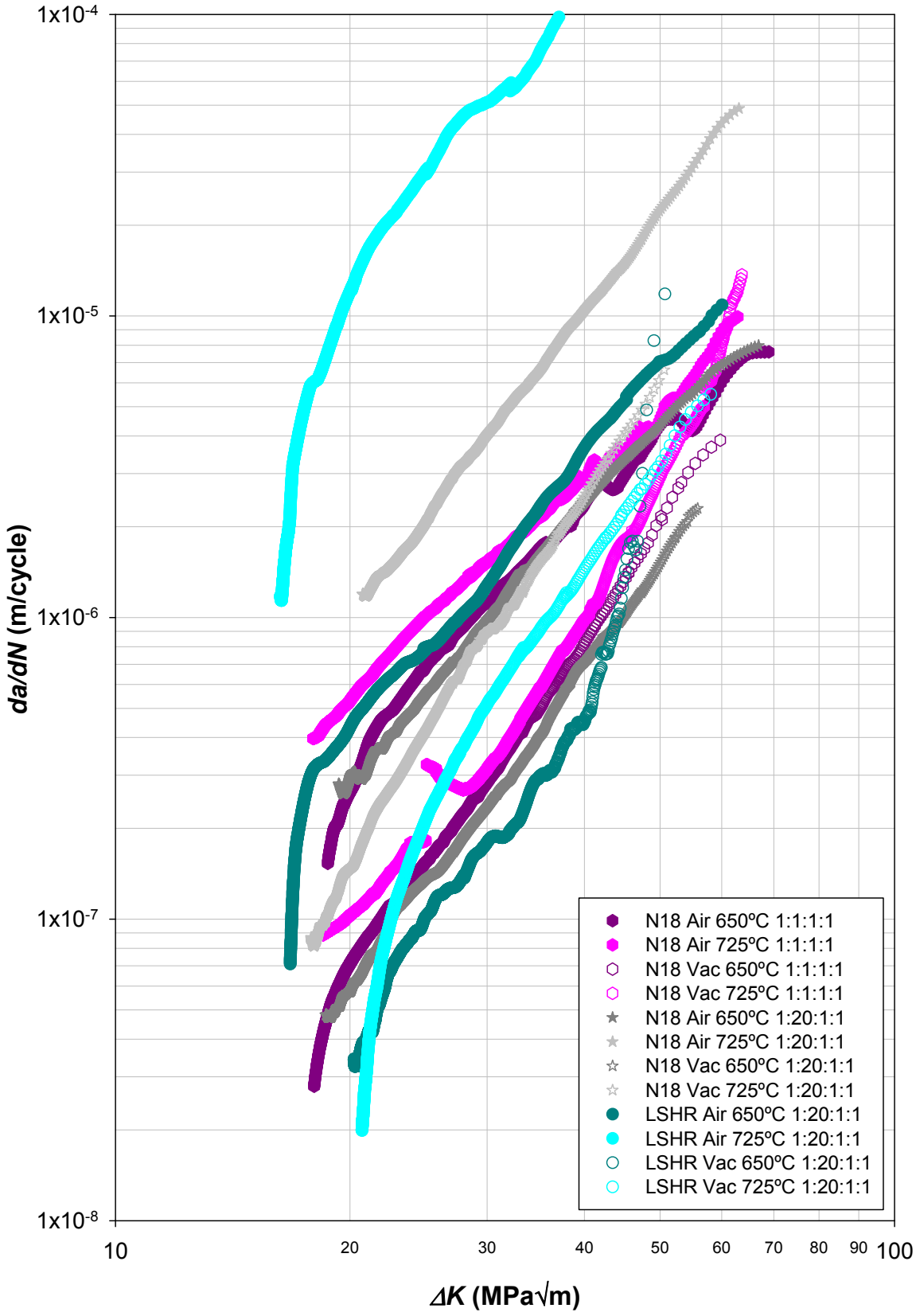

Figure 79 N18 and LSHR *da/dN* vs. *ΔK*, in air and vacuum at 650°C and 725°C, 1-1-1-1 and 1-20-1-1 load cycles (*da/dN* range limited to $1x10^{-4}$ to aid comparison with other graphs).

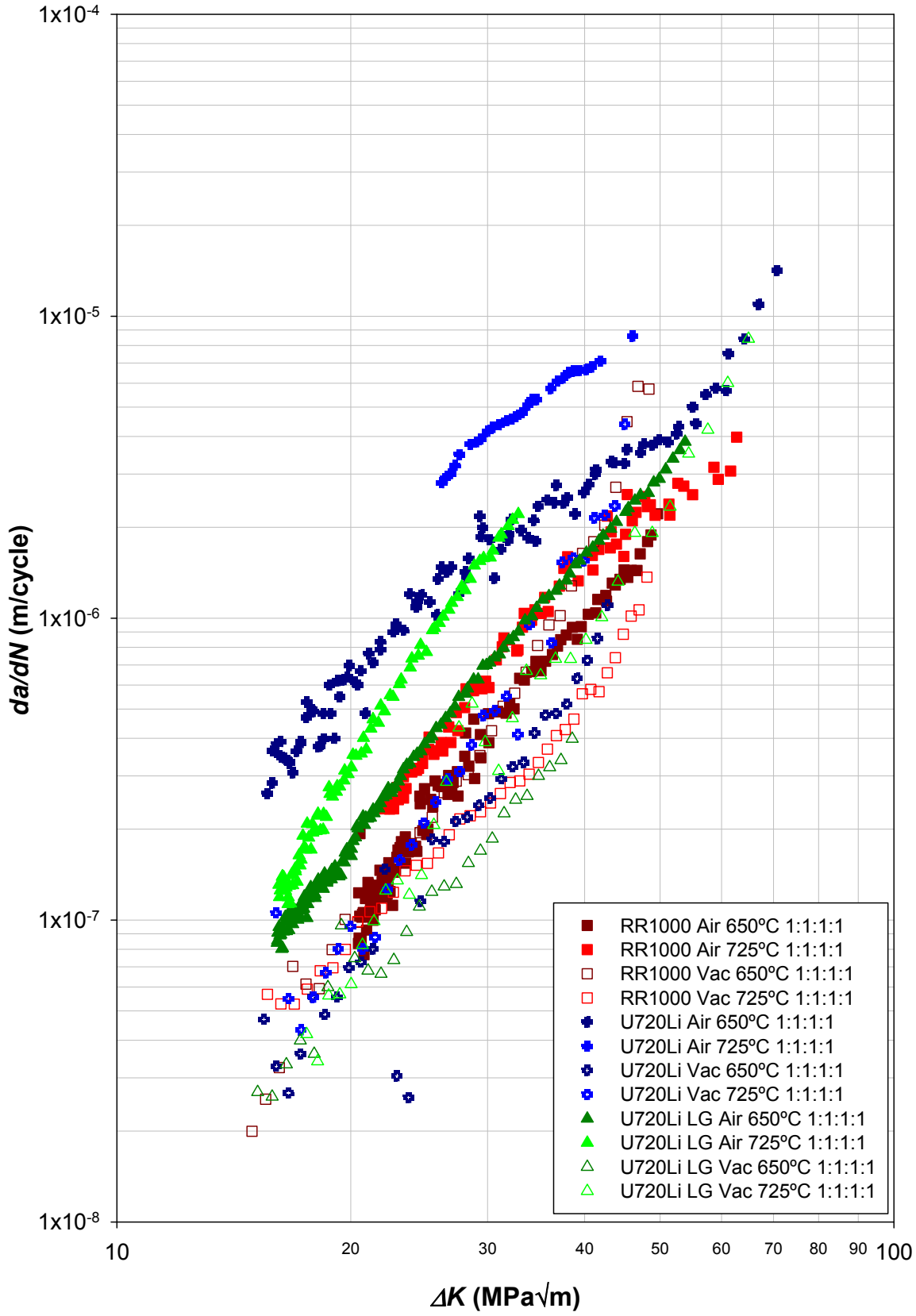

Figure 80 RR1000, U720Li and U720Li LG *da/dN* vs. *ΔK*, in air and vacuum at 650°C and 725°C, 1-1-1-1 load cycle[21].

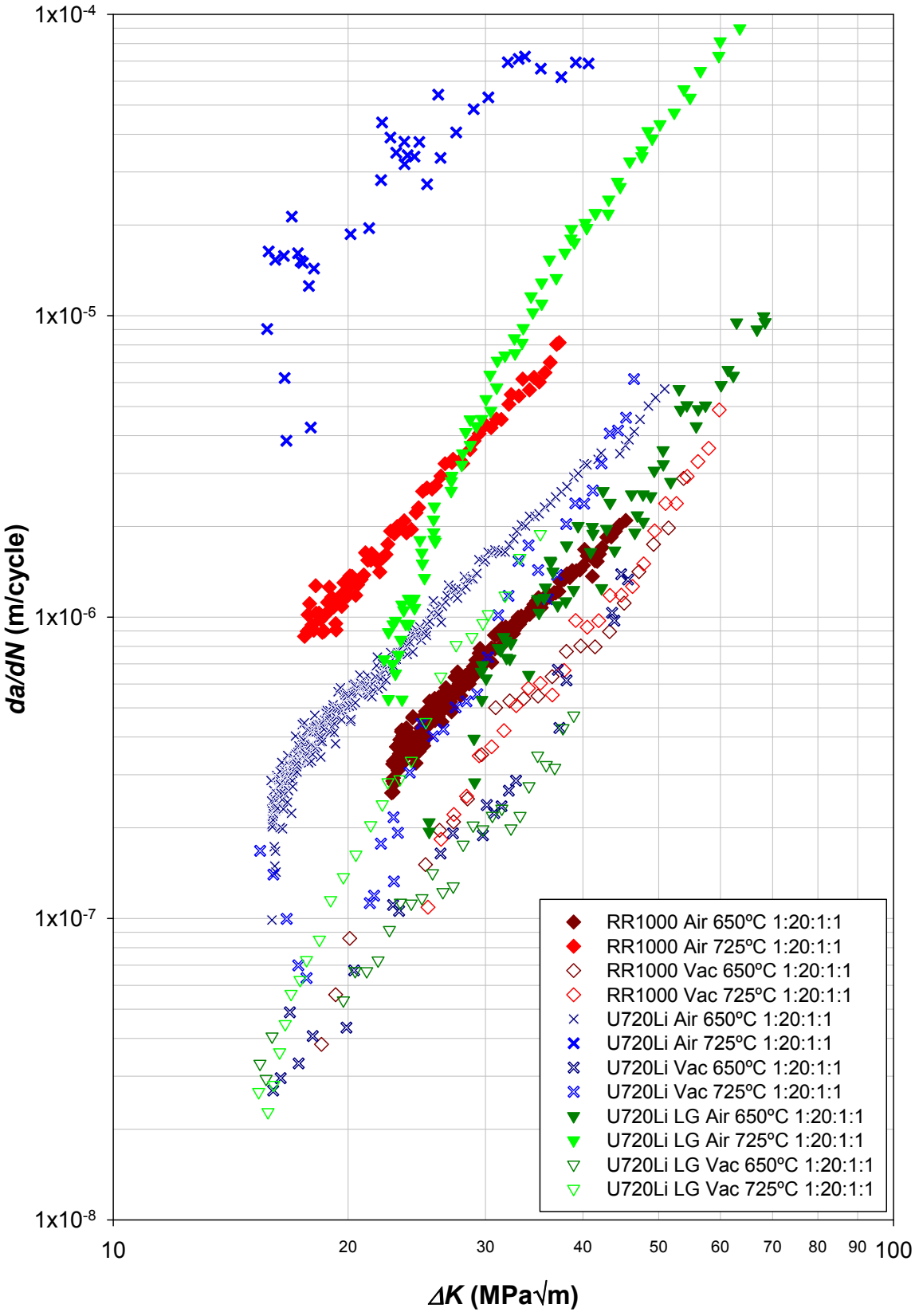

Figure 81 RR1000, U720Li and U720Li LG *da/dN* vs. *ΔK*, in air and vacuum at 650°C and 725°C, 1-20-1-1 load cycle [21].

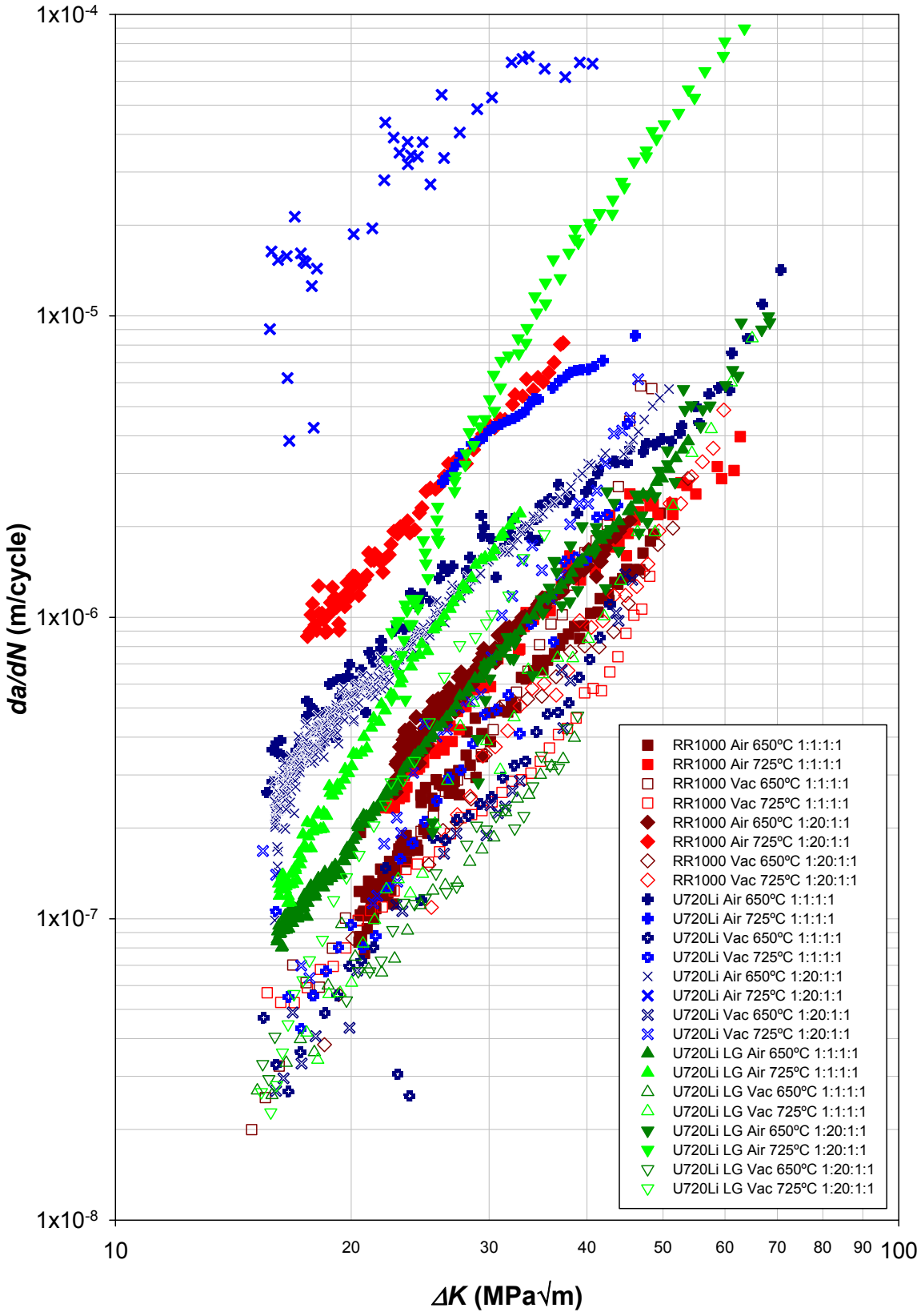

Figure 82 RR1000, U720Li and U720Li LG *da/dN* vs. *ΔK*, in air and vacuum at 650°C and 725°C, 1-1-1-1 and 1-20-1-1 load cycles [21].

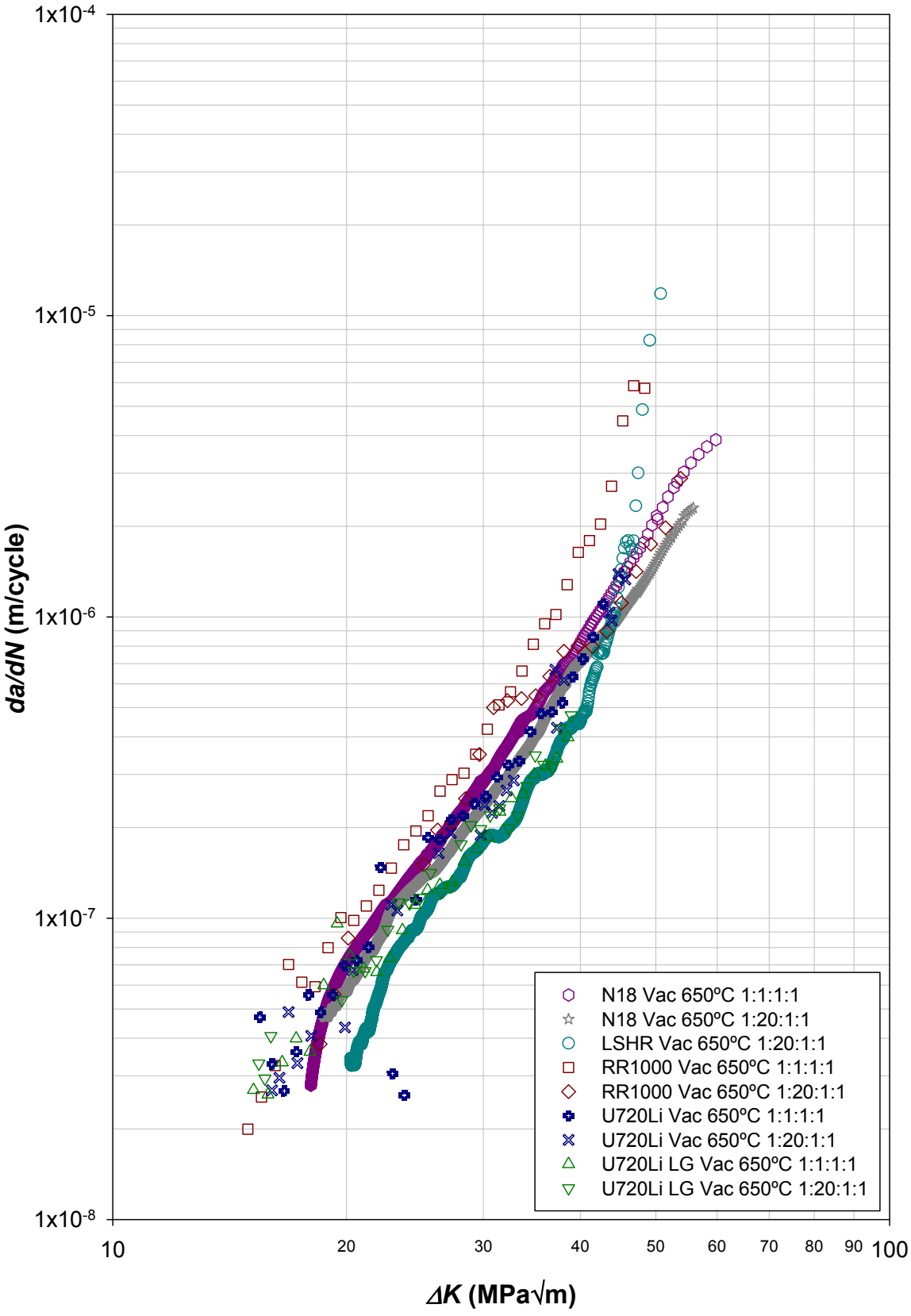

Figure 83 N18, LSHR, RR1000, U720Li and U720Li LG *da/dN* vs. *ΔK*, in vacuum at 650°C 1-1-1-1 and 1-20-1-1 load cycles.

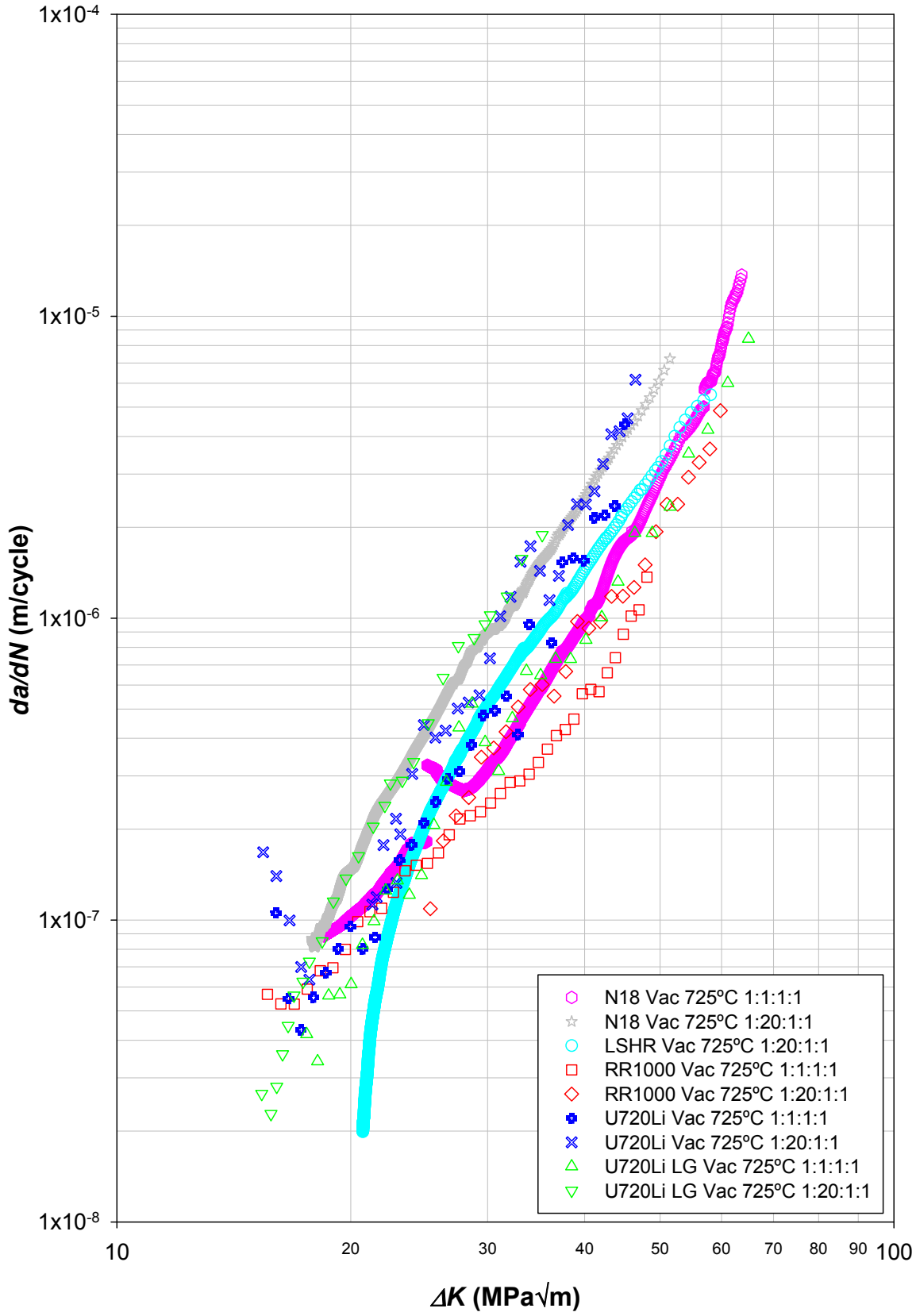

Figure 84 N18, LSHR, RR1000, U720Li and U720Li LG *da/dN* vs. *ΔK*, in vacuum at 725°C 1-1-1-1 and 1-20-1-1 load cycles.

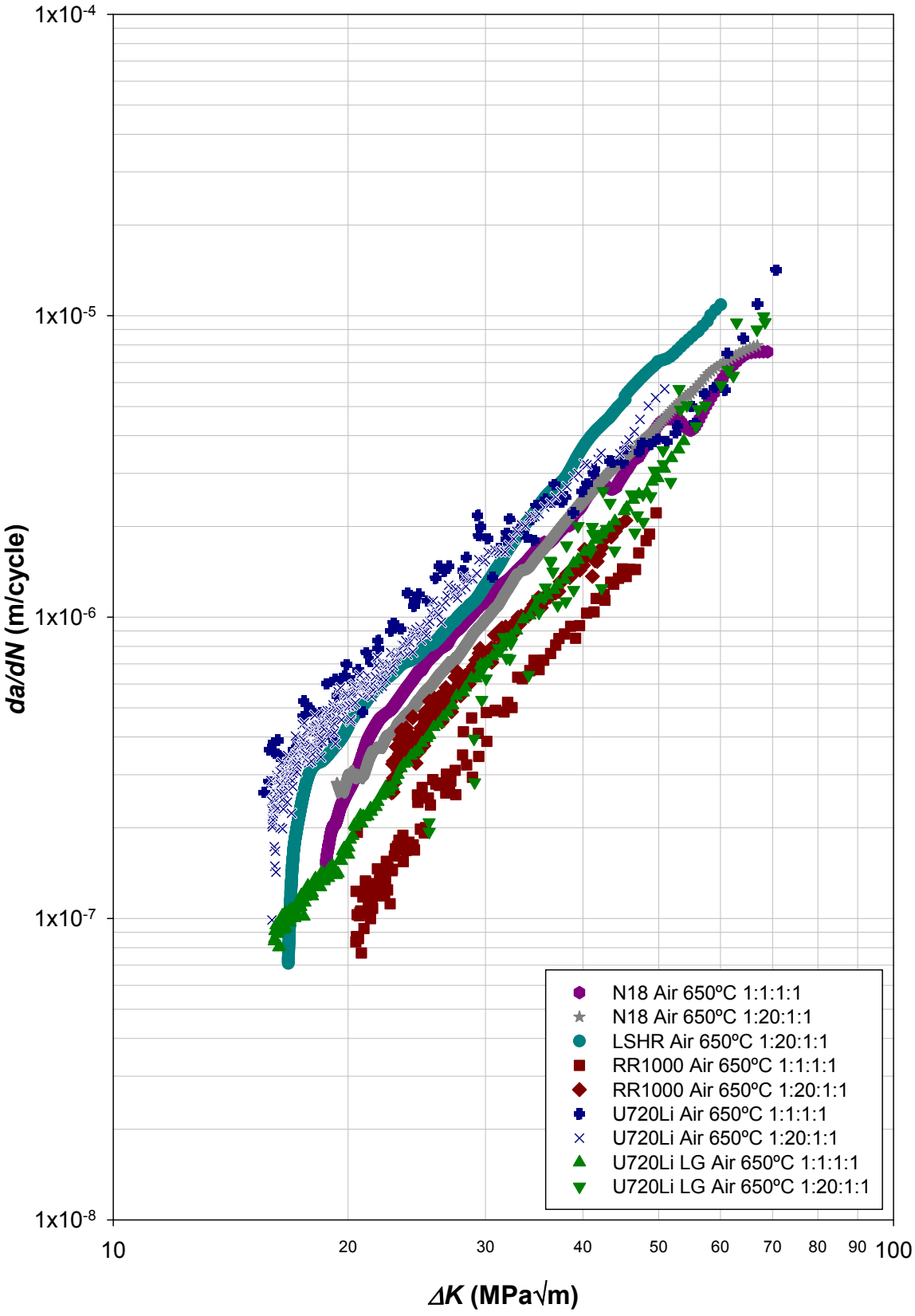

Figure 85 N18, LSHR, RR1000, U720Li and U720Li LG *da/dN* vs. *ΔK*, in air at 650°C 1-1-1-1 and 1-20-1-1 load cycles.

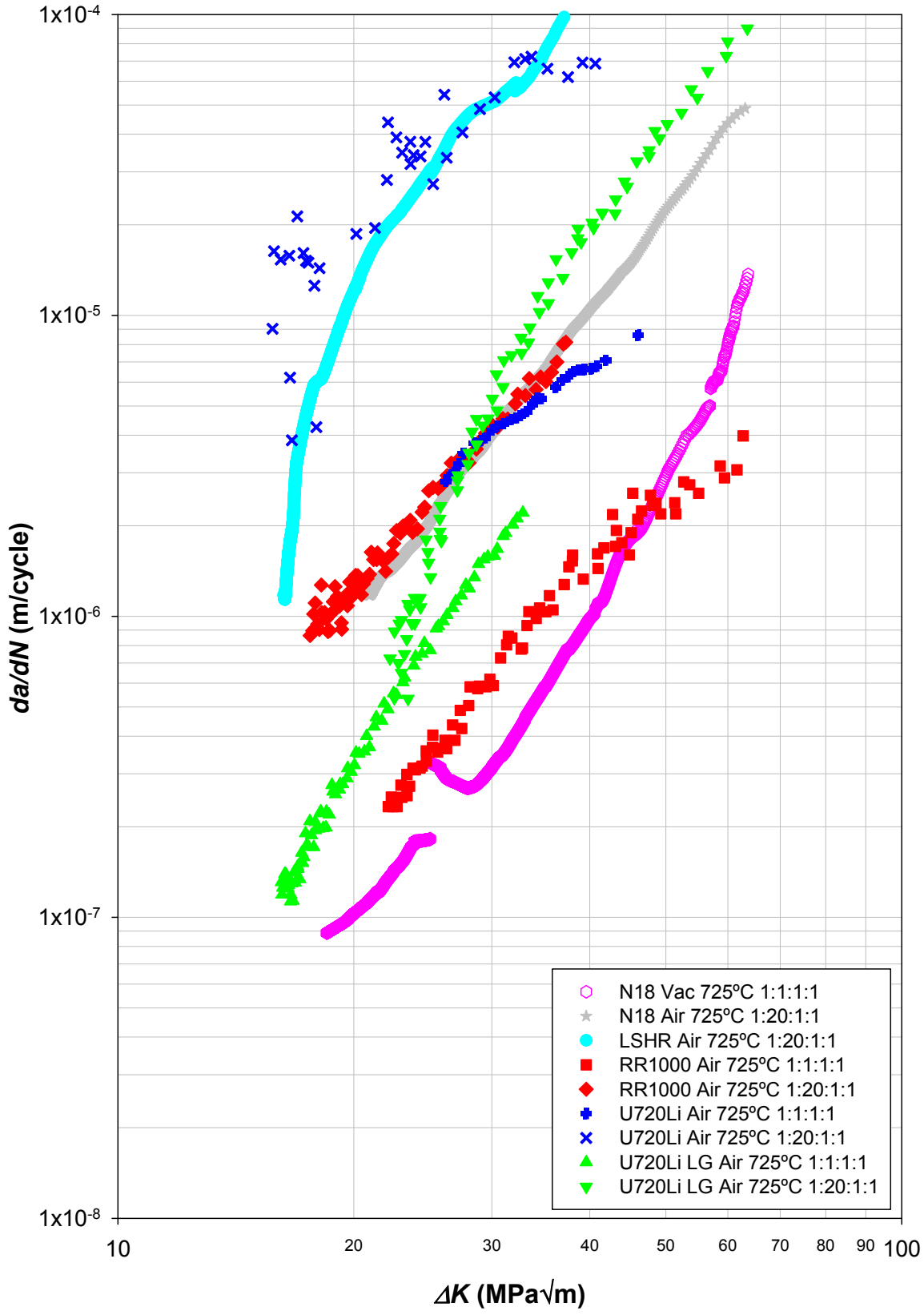

Figure 86 N18, LSHR, RR1000, U720Li and U720Li LG *da/dN* vs. *ΔK*, in air at 725°C 1-1-1-1 and 1-20-1-1 load cycles.

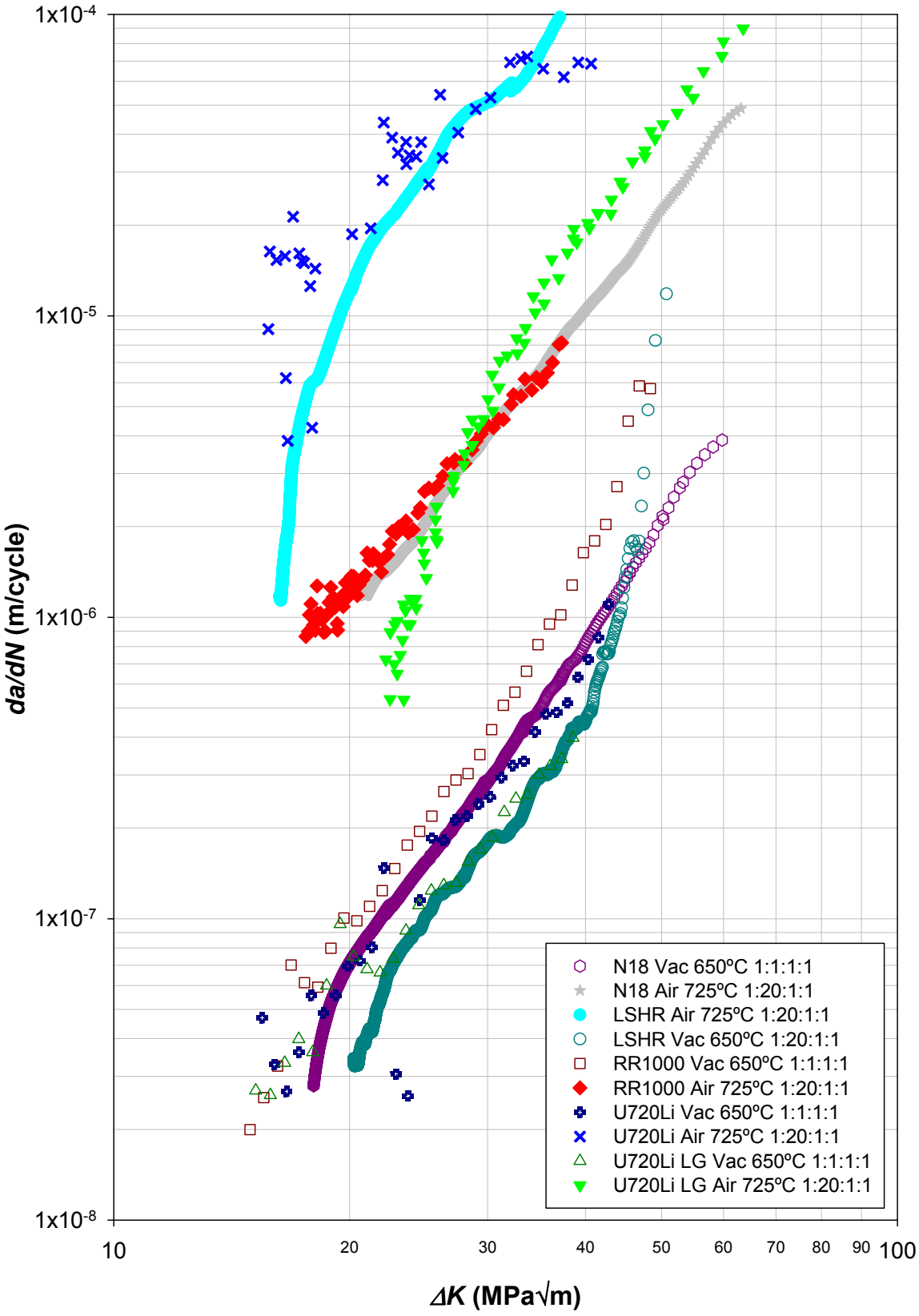

Figure 87 N18, LSHR, RR1000, U720Li and U720Li LG *da/dN* vs. *ΔK*, in vacuum at 650°C 1-1-1-1 load cycle and air at 725°C 1-20-1-1 load cycles (except for LSHR 1-20-1-1 in each case).

Table 31 Alloy *da/dN* performance rankings for tested conditions ΔK = 25 MPa√m and ΔK = 45 MPa√m.

Environment		Air							
Load cycle		1-1-1-1				1-20-1-1			
Temperature		650°C		725°C		650°C		725°C	
ΔK		25	45	25	45	25	45	25	45
da/dN	Lowest	RR1000	RR1000	RR1000	RR1000	U720Li LG	RR1000	U720Li LG	RR1000
	↓	U720Li LG	U720Li LG	U720Li LG	N18	RR1000	U720Li LG	N18	N18
	↓	N18	N18	N18	U720Li LG	N18	N18	RR1000	U720Li LG
	↓	U720Li	U720Li	U720Li	U720Li	LSHR	U720Li	LSHR	U720Li
	Highest					U720Li	LSHR	U720Li	LSHR

Environment		Vacuum							
Load cycle		1-1-1-1				1-20-1-1			
Temperature		650°C		725°C		650°C		725°C	
ΔK		25	45	25	45	25	45	25	45
da/dN	Lowest	U720Li LG	U720Li LG	RR1000	RR1000	LSHR	U720Li LG	RR1000	RR1000
	↓	N18	U720Li	U720Li LG	U720Li LG	U720Li LG	N18	LSHR	LSHR
	↓	U720Li	N18	N18	N18	N18	RR1000	U720Li	N18
	↓	RR1000	RR1000	U720Li	U720Li	U720Li	U720Li	N18	U720Li
	Highest					RR1000	LSHR	U720Li LG	U720Li LG

Table 32 Comparison of changes in fatigue crack growth rate due to changes in test environment, temperature and dwell time between ΔK = 25 MPa$\sqrt{m}$ and ΔK = 45 MPa$\sqrt{m}$.

N18																								
Comparison between	**Vacuum and Air**								**650°C and 725°C**								**1-1-1-1 and 1-20-1-1 load cycle**							
Condition 1	650°C				725°C				Air				Vacuum				Air				Vacuum			
Condition 2	1-1-1-1		1-20-1-1		1-1-1-1		1-20-1-1		1-1-1-1		1-20-1-1		1-1-1-1		1-20-1-1		650°C		725°C		650°C		725°C	
ΔK	25	45	25	45	25	45	25	45	25	45	25	45	25	45	25	45	25	45	25	45	25	45	25	45
X increase $\frac{da}{dN}$	5	2	4	3	5	2	5	4	1.5	1	4	5	1.5	1.5	3	4	1	1	2	4	1	1	2	2

LSHR																								
Comparison between	**Vacuum and Air**								**650°C and 725°C**								**1-1-1-1 and 1-20-1-1 load cycle**							
Condition 1	650°C				725°C				Air				Vacuum				Air				Vacuum			
Condition 2	1-1-1-1		1-20-1-1		1-1-1-1		1-20-1-1		1-1-1-1		1-20-1-1		1-1-1-1		1-20-1-1		650°C		725°C		650°C		725°C	
ΔK			25	45			25	45			25	45			25	45								
X increase $\frac{da}{dN}$			8	4			136	74			38	32			2	2								

RR1000																								
Comparison between	**Vacuum and Air**								**650°C and 725°C**								**1-1-1-1 and 1-20-1-1 load cycle**							
Condition 1	650°C				725°C				Air				Vacuum				Air				Vacuum			
Condition 2	1-1-1-1		1-20-1-1		1-1-1-1		1-20-1-1		1-1-1-1		1-20-1-1		1-1-1-1		1-20-1-1		650°C		725°C		650°C		725°C	
ΔK	25	45	25	45	25	45	25	45	25	45	25	45	25	45	25	45	25	45	25	45	25	45	25	45
X increase $\frac{da}{dN}$	1	0.5	3	2	2	2	16	12	1.5	1.5	6	7	1	0.5	1	1	2	1.5	7	7	0.5	0.5	1	1

U720Li																								
Comparison between	**Vacuum and Air**								**650°C and 725°C**								**1-1-1-1 and 1-20-1-1 load cycle**							
Condition 1	650°C				725°C				Air				Vacuum				Air				Vacuum			
Condition 2	1-1-1-1		1-20-1-1		1-1-1-1		1-20-1-1		1-1-1-1		1-20-1-1		1-1-1-1		1-20-1-1		650°C		725°C		650°C		725°C	
ΔK	25	45	25	45	25	45	25	45	25	45	25	45	25	45	25	45	25	45	25	45	25	45	25	45
X increase $\frac{da}{dN}$	7	3	7	3	6	2	108	22	1	2	43	27	1.5	3	3	4	1	1	33	12	1	1	1.5	1.5

U720Li LG																								
Comparison between	**Vacuum and Air**								**650°C and 725°C**								**1-1-1-1 and 1-20-1-1 load cycle**							
Condition 1	650°C				725°C				Air				Vacuum				Air				Vacuum			
Condition 2	1-1-1-1		1-20-1-1		1-1-1-1		1-20-1-1		1-1-1-1		1-20-1-1		1-1-1-1		1-20-1-1		650°C		725°C		650°C		725°C	
ΔK	25	45	25	45	25	45	25	45	25	45	25	45	25	45	25	45	25	45	25	45	25	45	25	45
X increase $\frac{da}{dN}$	3	3	1.5	3	5	5	4	6	2	3	8	13	1	2	3	8	0.5	1	2	4	1	1	3	4

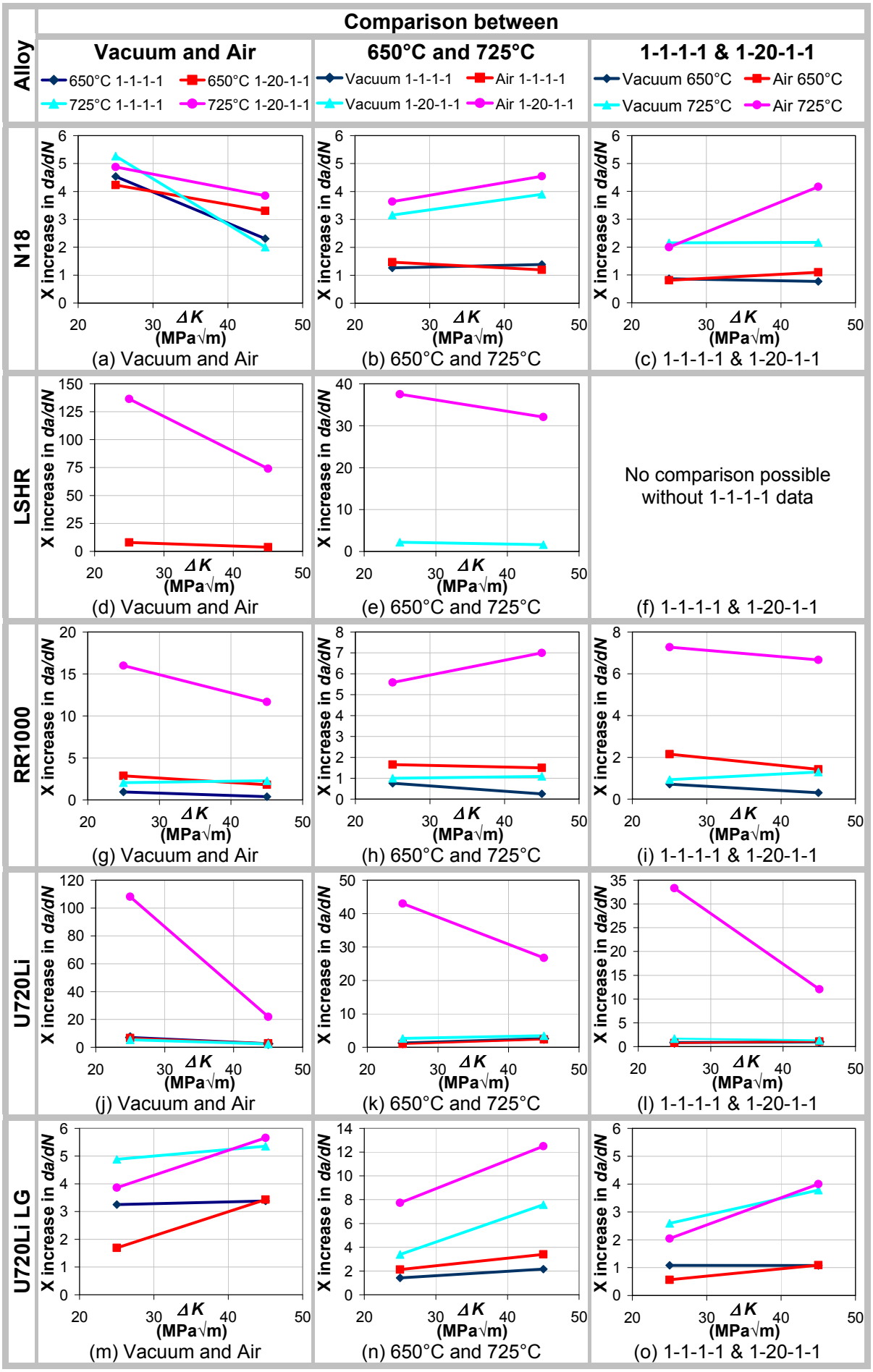

Figure 88 Comparison of changes in fatigue crack growth rate due to changes in test environment, temperature and dwell time between ΔK = 25 MPa√m and 45 MPa√m.

Table 33 Fatigue crack propagation values of *C* and *m* for N18, LSHR, RR1000, U720Li and U720Li LG.

Alloy	Environment	Dwell	Temp (°C)	*ΔK* min (MPa√m)	*ΔK* max (MPa√m)	*C*	*m*
N18	Air	1	650	25	60	2.49E-10	2.47
			725	20	58	3.41E-10	2.46
		20	650	23	52	2.75E-11	3.08
			725	22	54	3.53E-11	3.42
	Vac	1	650	23	54	1.29E-12	3.63
			725	29	57	1.47E-13	4.28
		20	650	20	55	1.84E-12	3.47
			725	19	52	5.50E-13	4.19
LSHR	Air	1	650	No data			
			725				
		20	650	19	50	5.98E-11	2.96
			725	19	43	4.33E-10	3.44
	Vac	1	650	No data			
			725				
		20	650	23	40	4.19E-12	3.13
			725	25	50	7.49E-13	3.93
RR1000	Air	1	650	22	48	5.29E-12	3.30
			725	23	62	5.34E-11	2.75
		20	650	23	45	8.26E-11	2.67
			725	18	37	1.85E-10	2.94
	Vac	1	650	15	48	2.13E-13	4.31
			725	16	44	4.16E-11	2.56
		20	650	19	54	2.56E-12	3.45
			725	25	60	8.90E-13	3.75
U720Li	Air	1	650	16	64	9.37E-10	2.17
			725	26	46	6.14E-09	1.90
		20	650	17	42	2.08E-10	2.61
			725	16	40	5.07E-08	2.03
	Vac	1	650	15	43	2.20E-12	3.42
			725	17	44	2.14E-13	4.29
		20	650	16	46	1.40E-12	3.56
			725	17	47	1.26E-13	4.57
U720Li LG	Air	1	650	16	54	1.27E-11	3.19
			725	16	31	7.69E-13	4.31
		20	650	29	69	1.09E-11	3.23
			725	24	60	6.52E-13	4.63
	Vac	1	650	15	39	1.29E-11	2.82
			725	17	65	6.89E-13	3.86
		20	650	15	39	1.42E-11	2.81
			725	15	35	1.61E-14	5.29

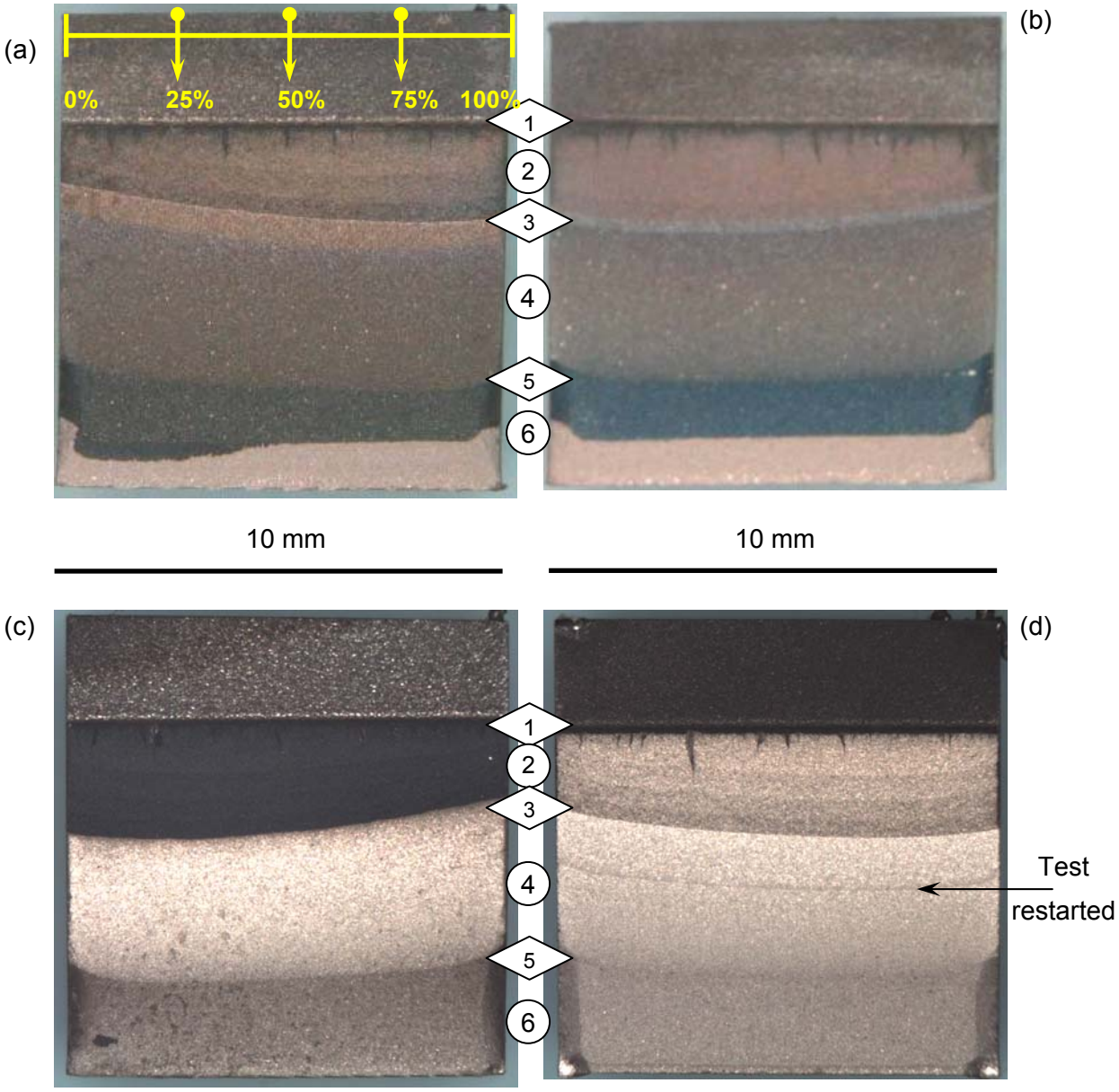

Figure 89 N18 Macroscopic overviews of SENB fracture surfaces, all 1-1-1-1 load cycle: (a) 650°C in air; (b) 725°C in air; (c) 650°C in vacuum and (d) 725°C in vacuum.

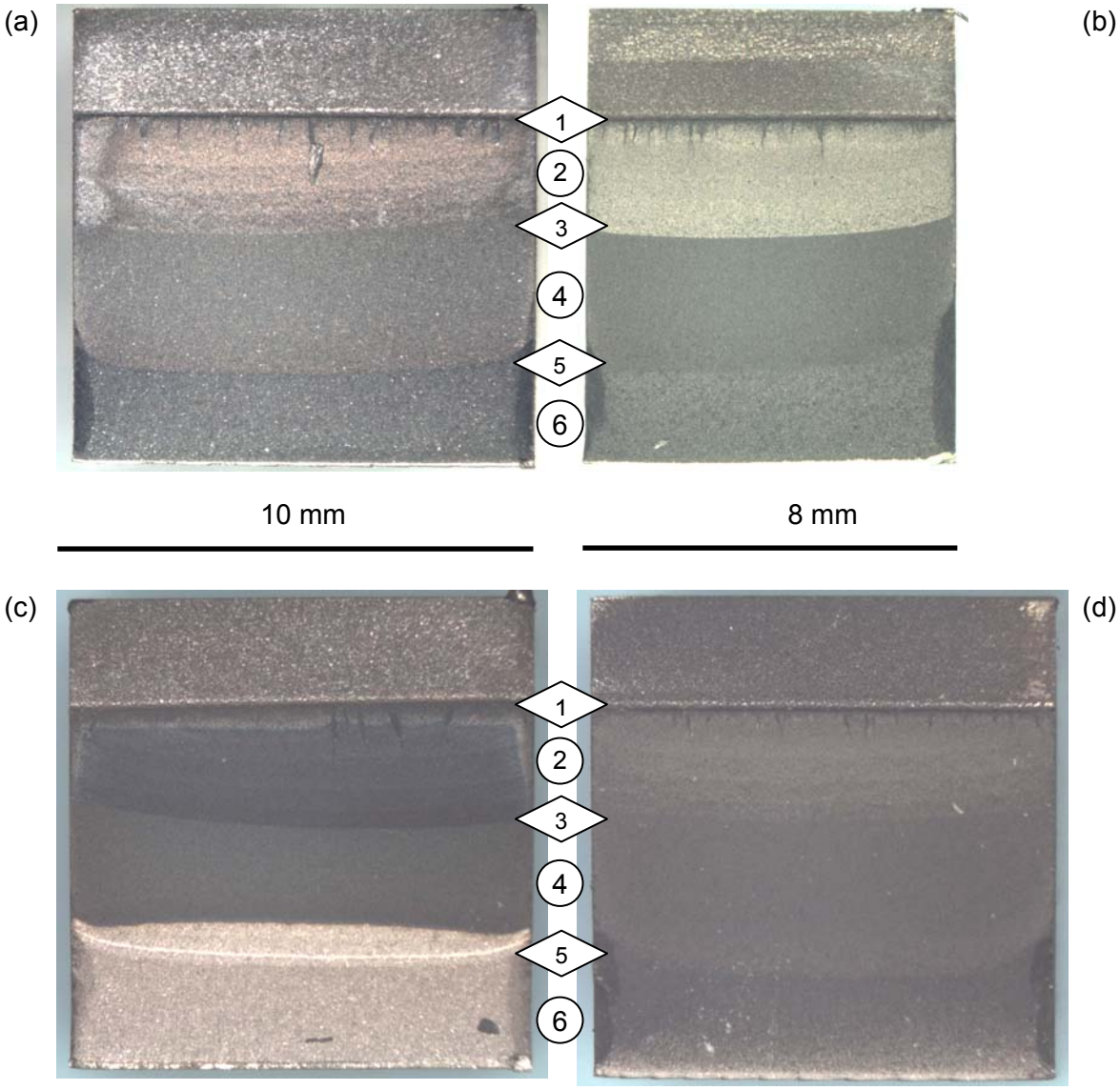

Figure 90 N18 Macroscopic overviews of SENB fracture surfaces, all 1-20-1-1 load cycle: (a) 650°C in air; (b) 725°C in air; (c) 650°C in vacuum and (d) 725°C in vacuum.

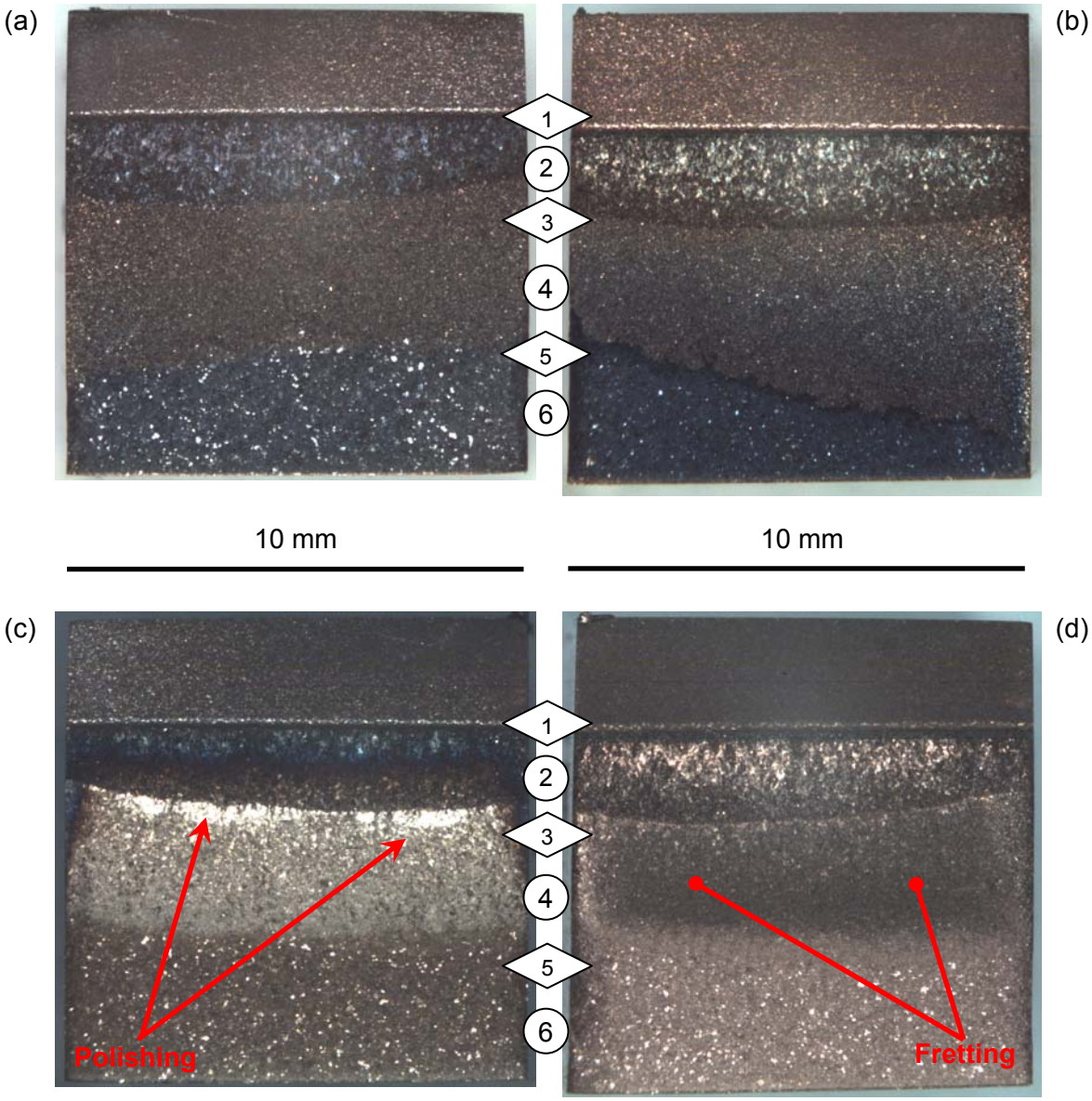

Figure 91 LSHR Macroscopic overviews of SENB fracture surfaces, all 1-20-1-1 load cycle: (a) 650°C in air; (b) 725°C in air; (c) 650°C in vacuum and (d) 725°C in vacuum.

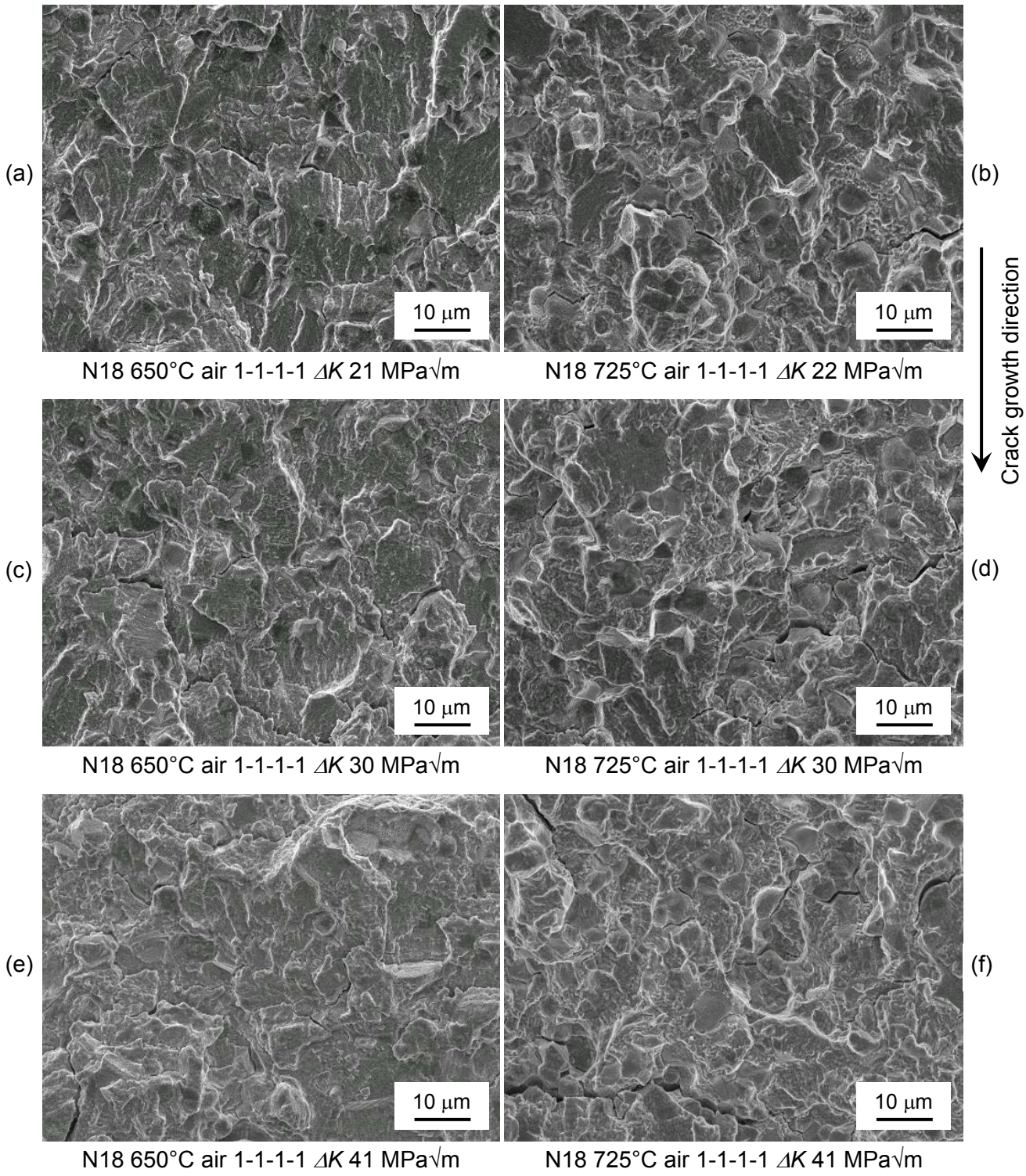

Figure 92 N18 SENB fracture surfaces, in air, 1-1-1-1 load cycle, increasing *ΔK*, increasing temperature, FEG SEM SEI mode.

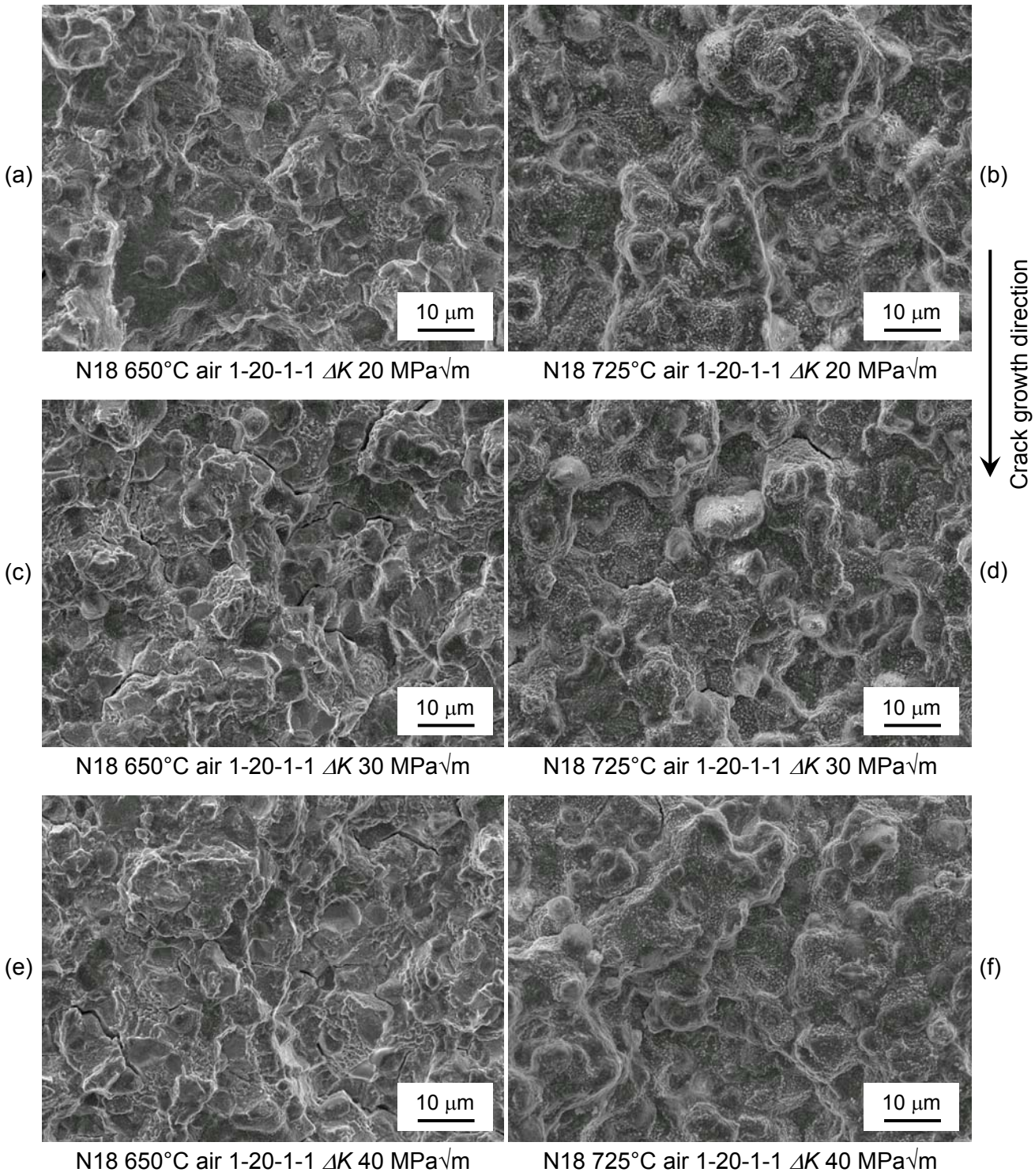

Figure 93 N18 SENB fracture surfaces, in air, 1-20-1-1 load cycle, increasing *ΔK*, increasing temperature, FEG SEM SEI mode.

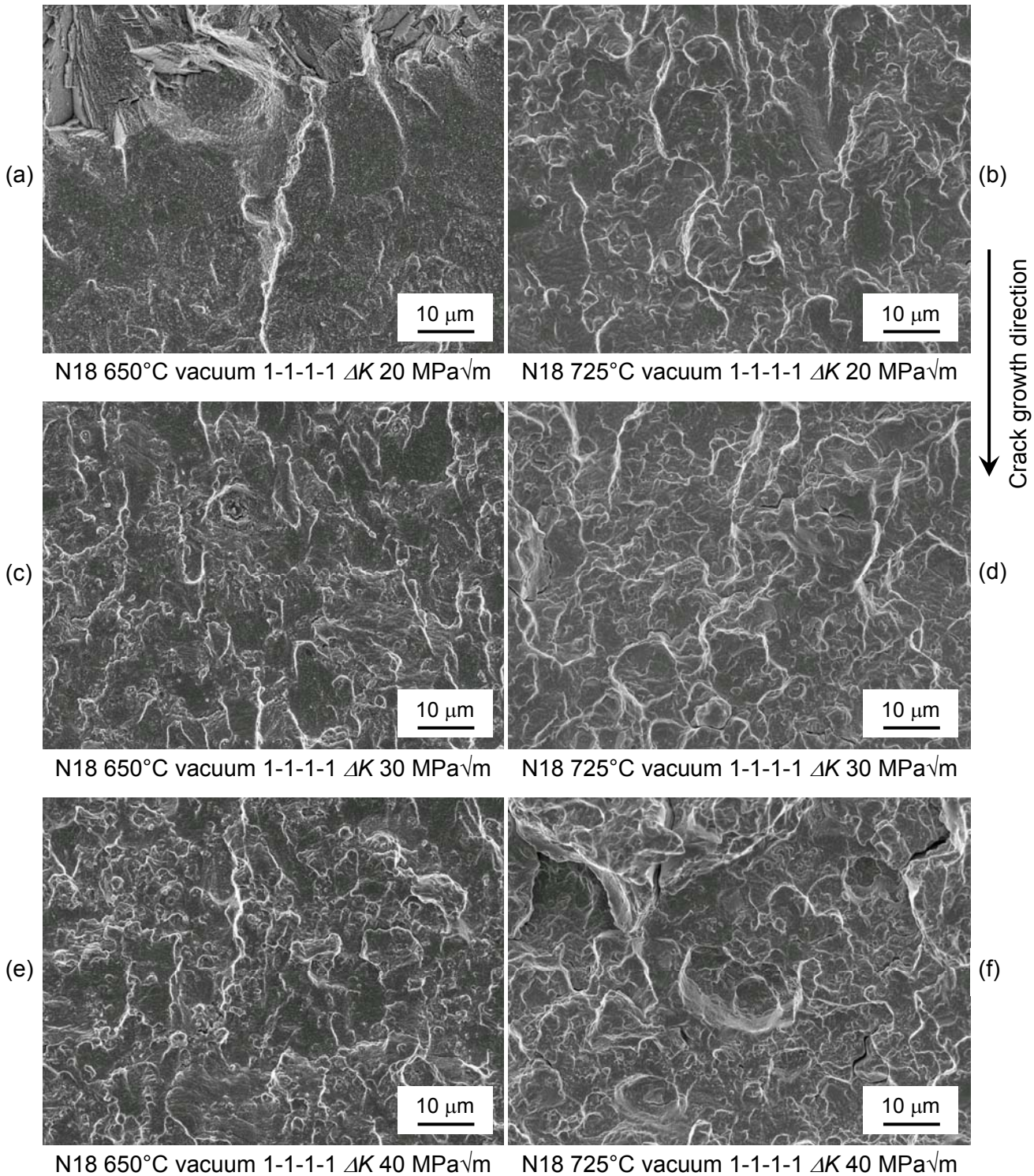

Figure 94 N18 SENB fracture surfaces, in vacuum, 1-1-1-1 load cycle, increasing *ΔK*, increasing temperature, FEG SEM SEI mode.

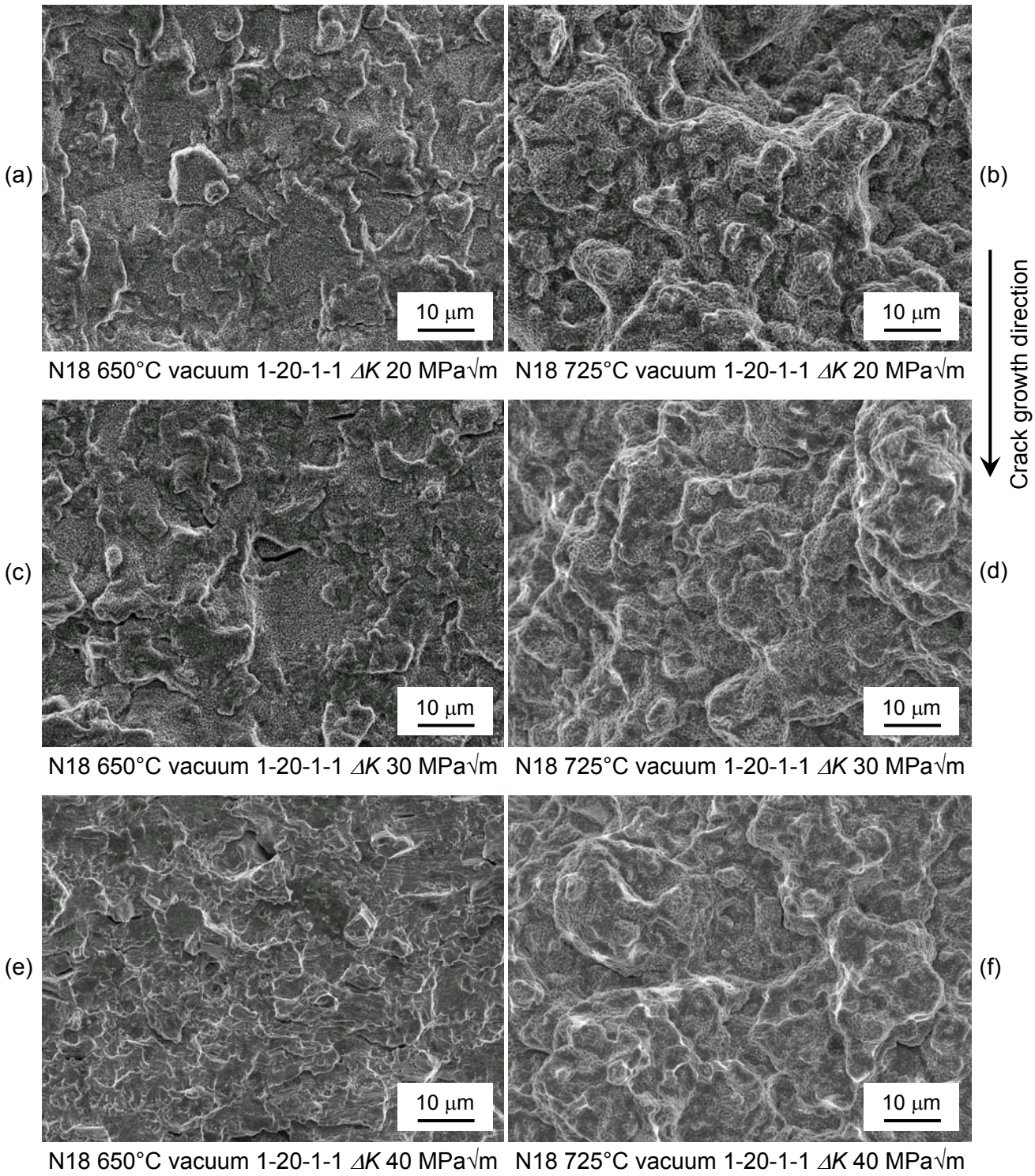

Figure 95 N18 SENB fracture surfaces, in vacuum, 1-20-1-1 load cycle, increasing *ΔK*, increasing temperature, FEG SEM SEI mode.

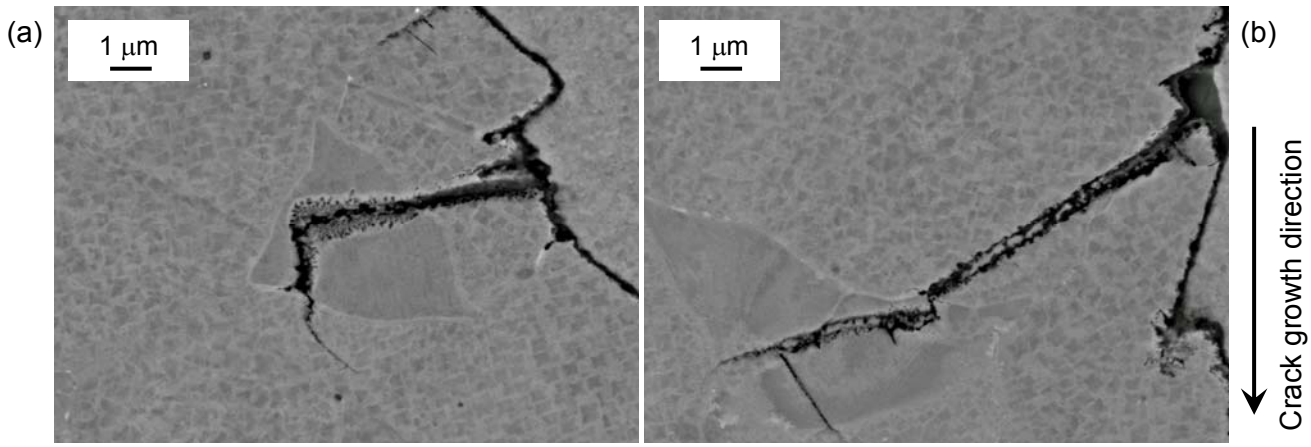

Figure 96 N18 Nickel plated and sectioned fatigue crack propagation specimens pre-cracking stage, FEG SEM BEI mode.

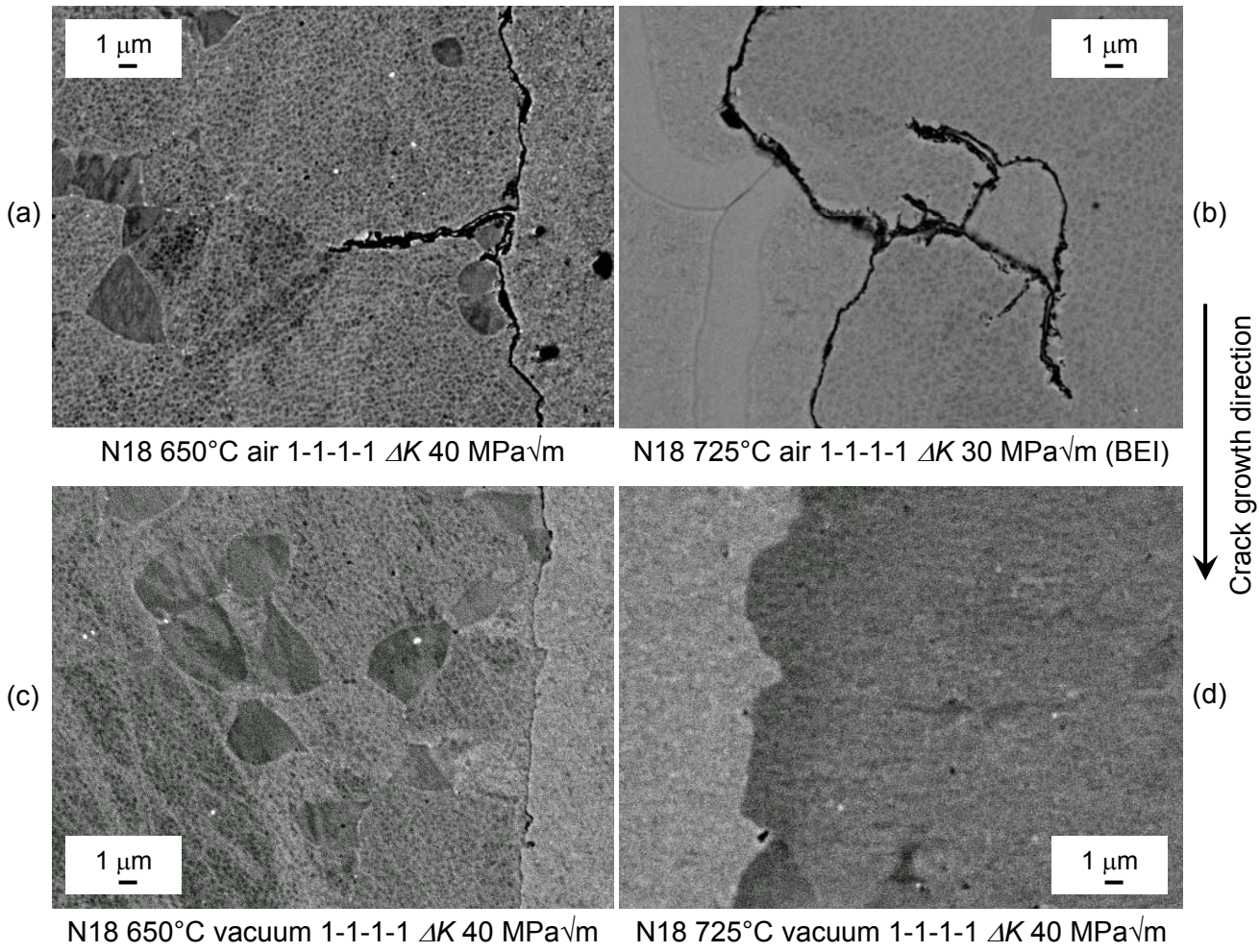

Figure 97 N18 Nickel plated and sectioned fatigue crack propagation specimens mid to high *ΔK*, 1-1-1-1 load cycle, FEG SEM BEI and SEI modes.

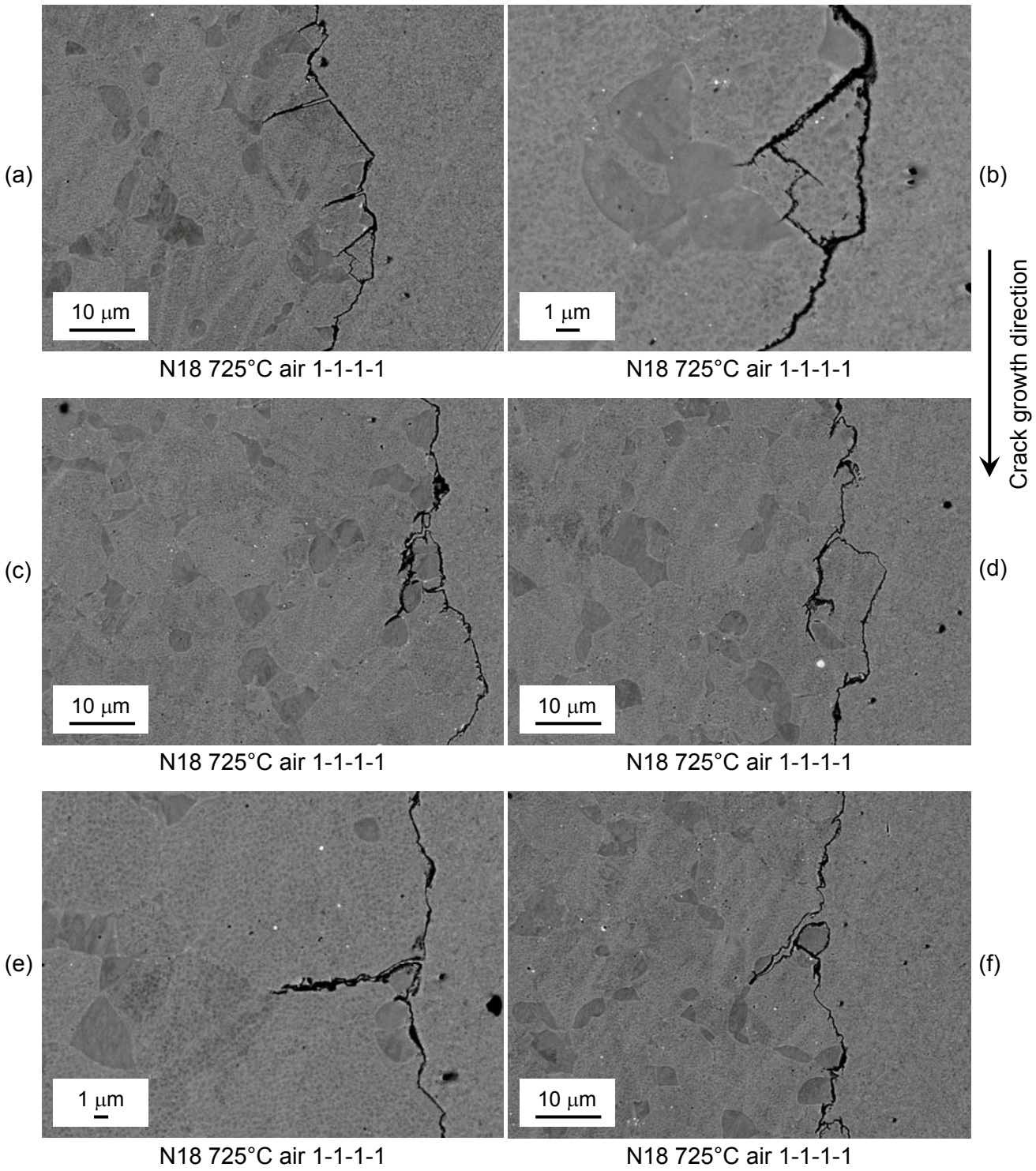

Figure 98 N18 Nickel plated and sectioned fatigue crack propagation specimens 650°C in air, 1-1-1-1 load cycle, secondary cracking, FEG SEM BEI mode.

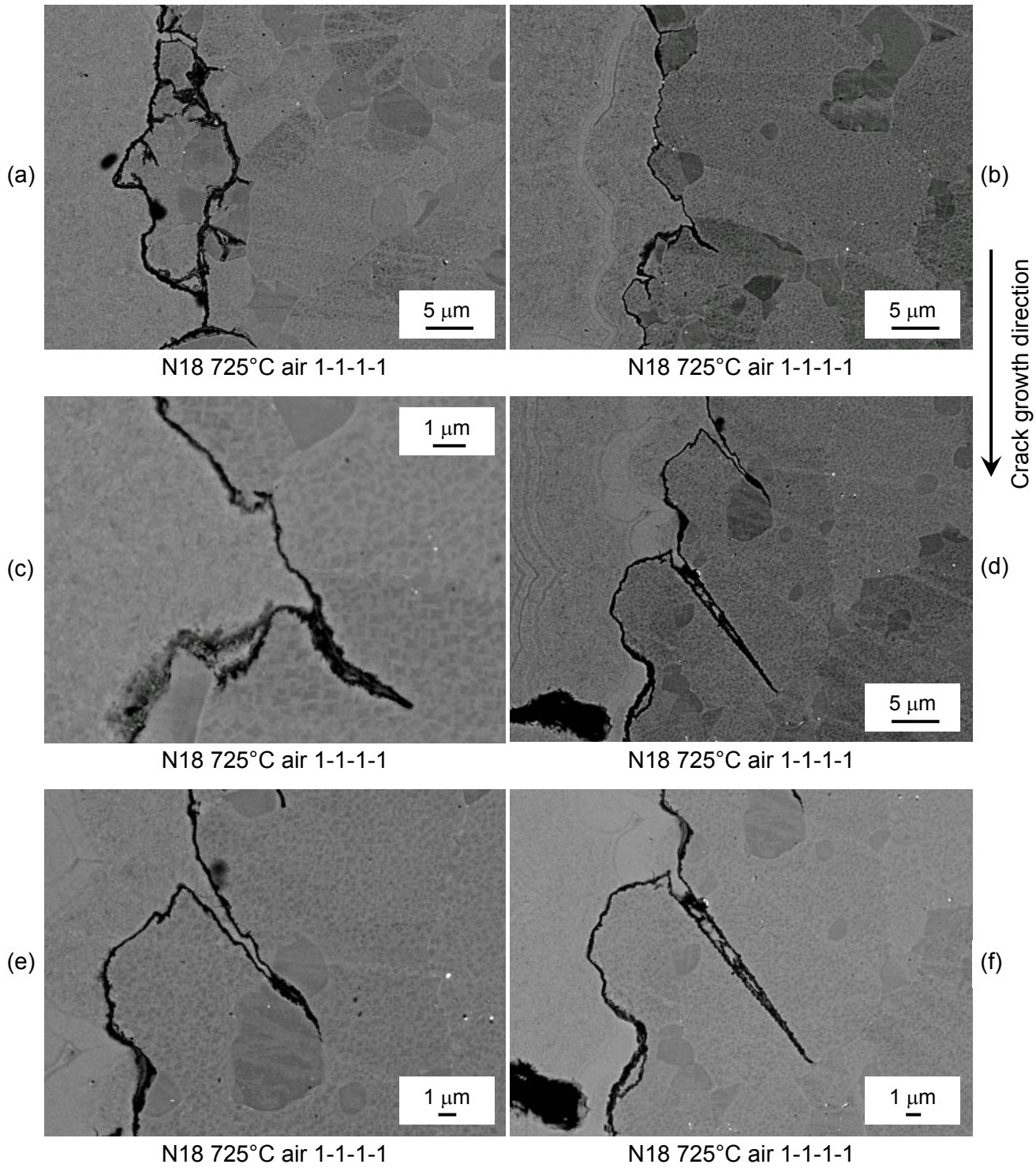

Figure 99 N18 Nickel plated and sectioned fatigue crack propagation specimens 725°C in air, 1-1-1-1 load cycle, secondary cracking, FEG SEM BEI mode.

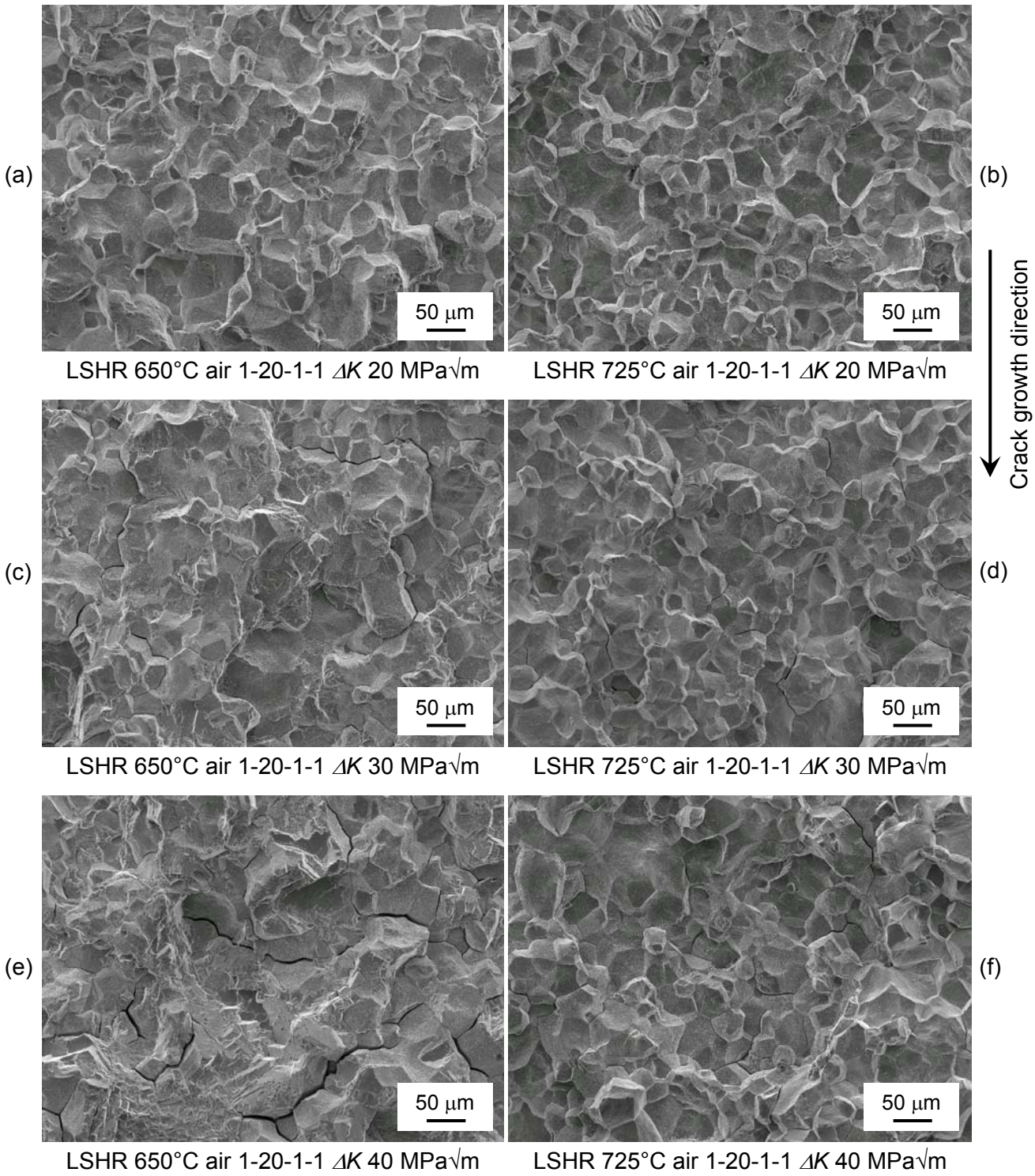

Figure 100 LSHR SENB fracture surfaces, in air, 1-20-1-1 load cycle, increasing *ΔK*, increasing temperature, FEG SEM SEI mode.

(Note that when comparing with other SENB fracture surfaces the magnification used for LSHR is reduced by a factor of around 7.)

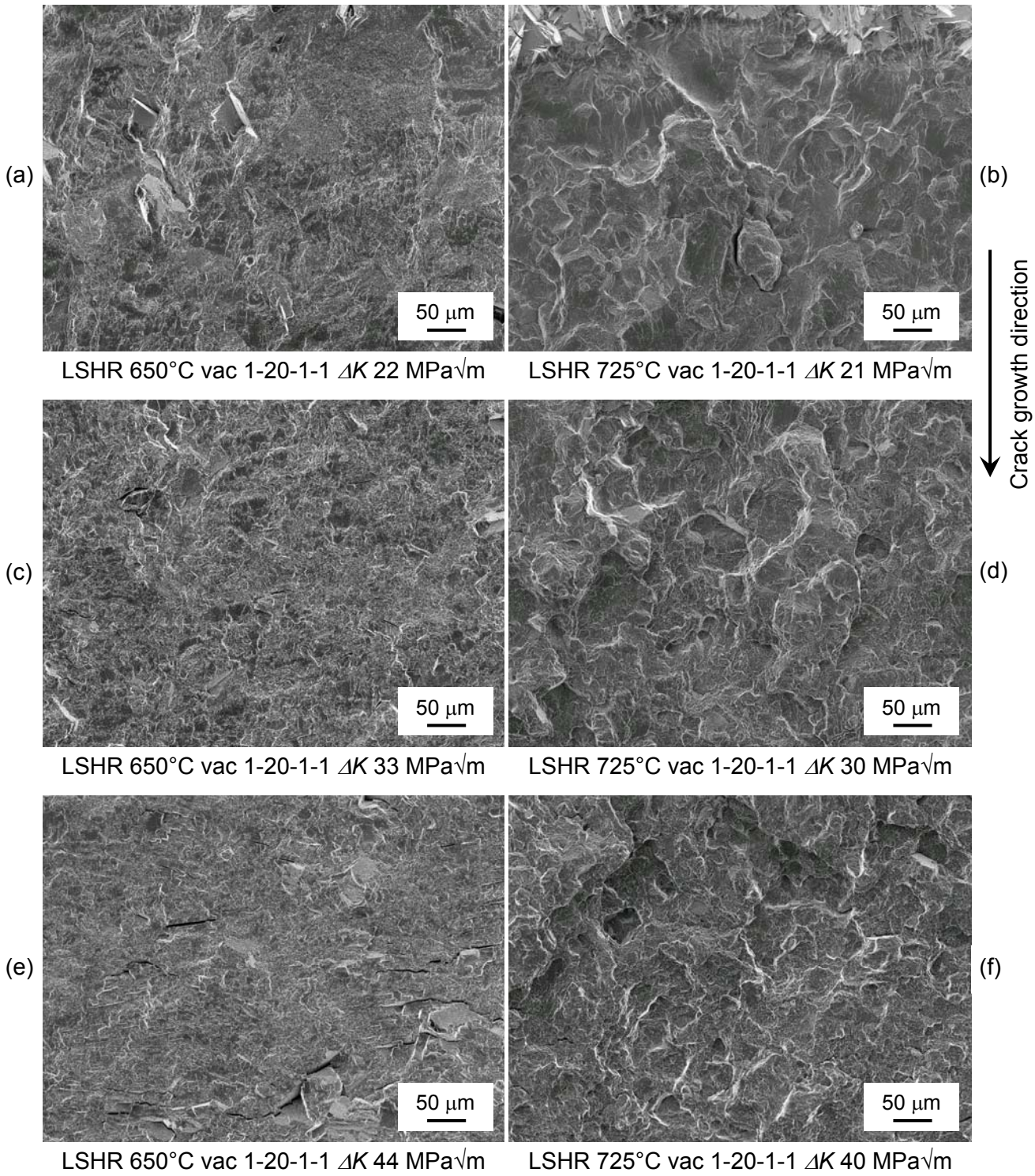

Figure 101 LSHR SENB fracture surfaces, in vacuum, 1-20-1-1 load cycle, increasing *ΔK*, increasing temperature, FEG SEM SEI mode.

(Note that when comparing with other SENB fracture surfaces the magnification used for LSHR is reduced by a factor of around 7.)

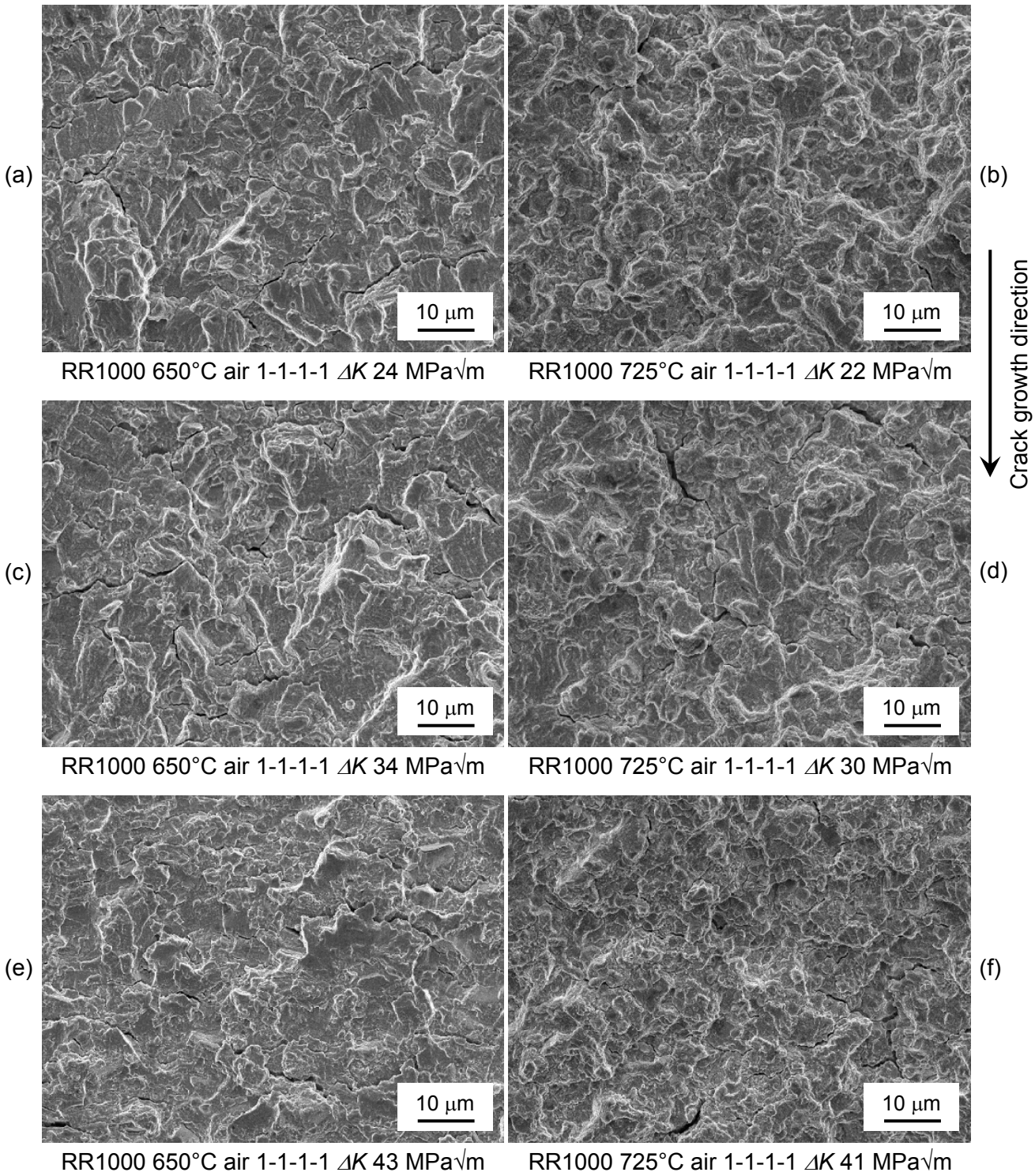

Figure 102 RR1000 SENB fracture surfaces, in air, 1-1-1-1 load cycle, increasing ΔK, increasing temperature, FEG SEM SEI mode[21].

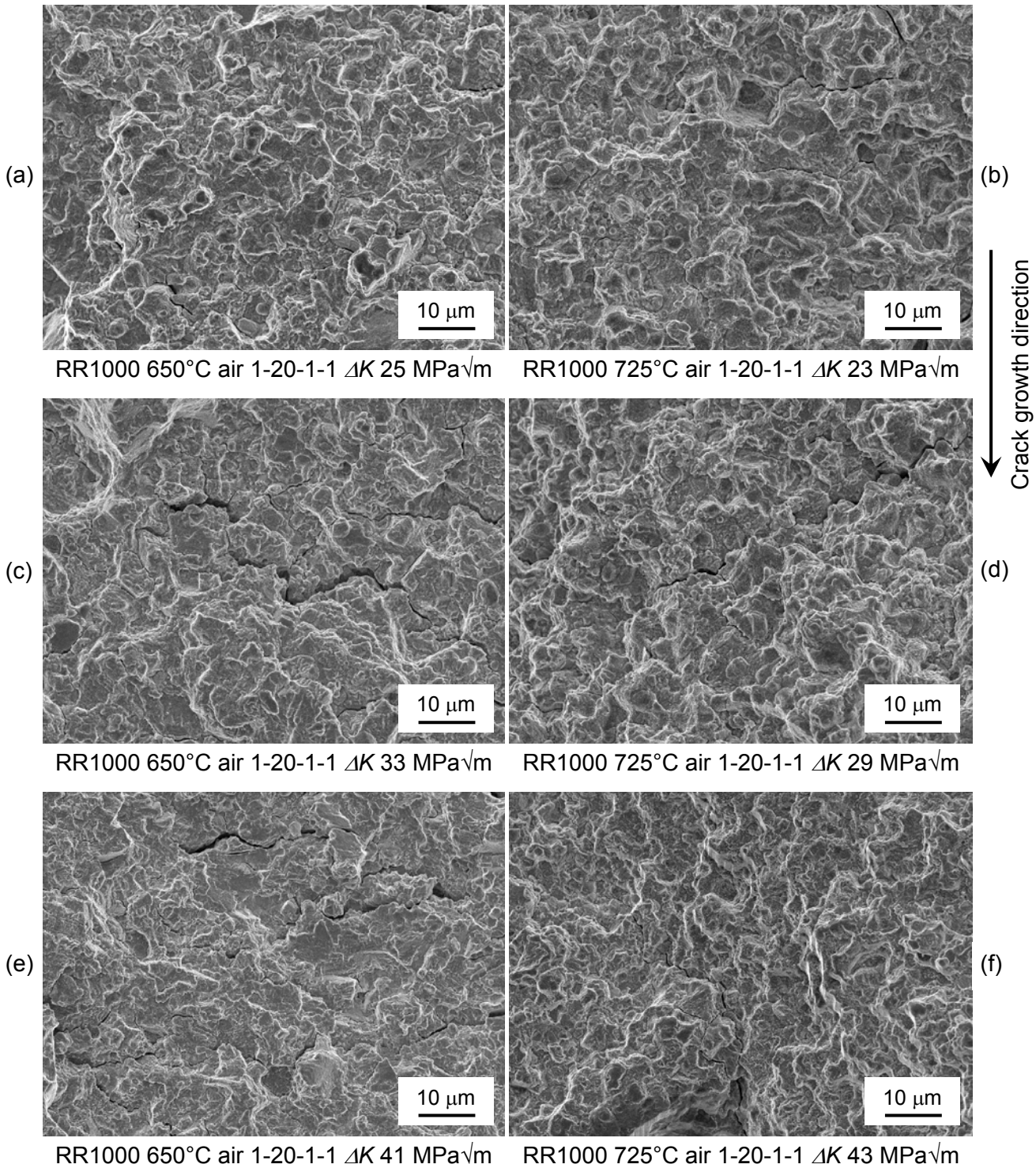

Figure 103 RR1000 SENB fracture surfaces, in air, 1-20-1-1 load cycle, increasing *ΔK*, increasing temperature, FEG SEM SEI mode[21].

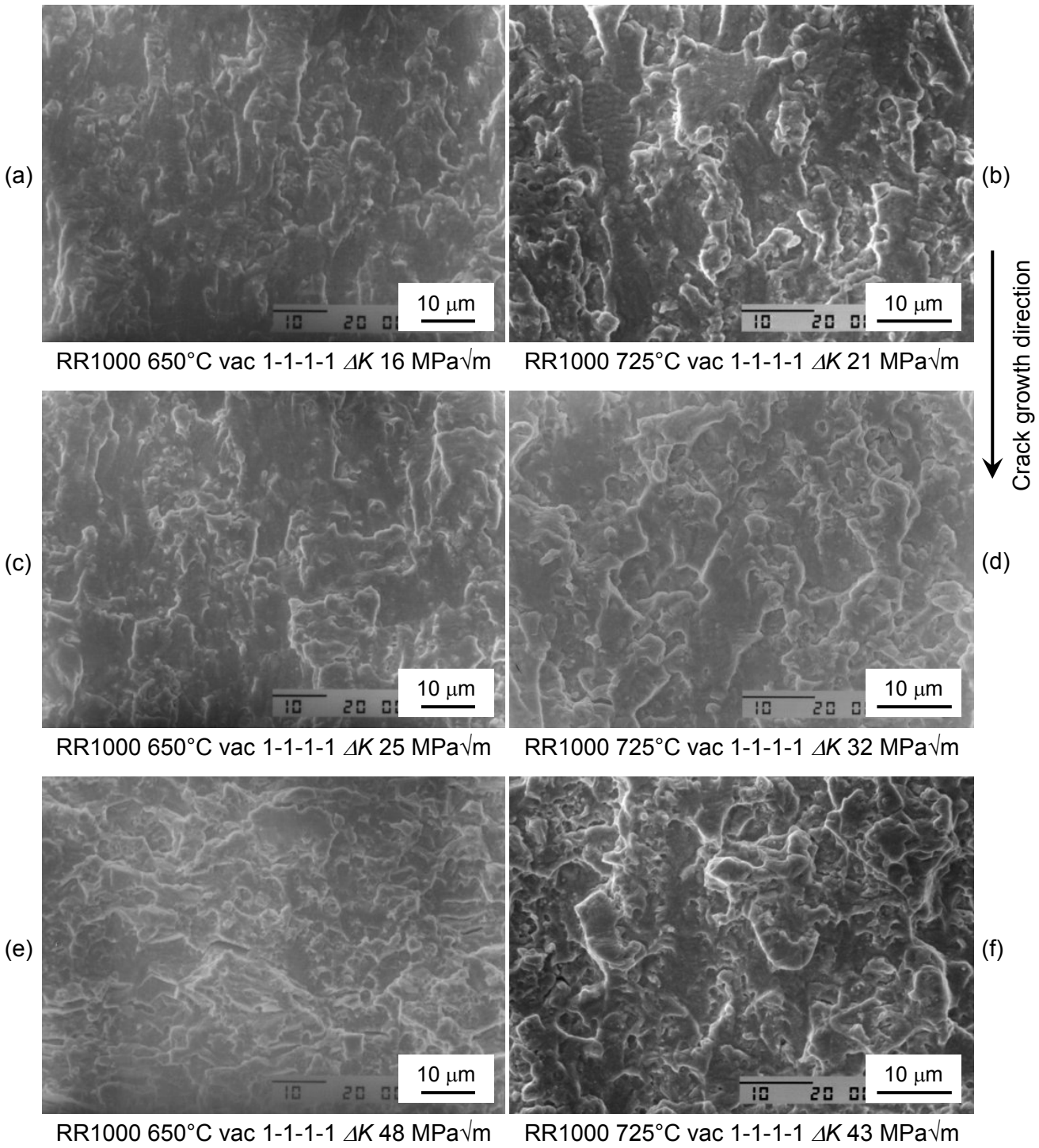

Figure 104 RR1000 SENB fracture surfaces, in vacuum, 1-1-1-1 load cycle, increasing *ΔK*, increasing temperature, SEM SEI mode[21].

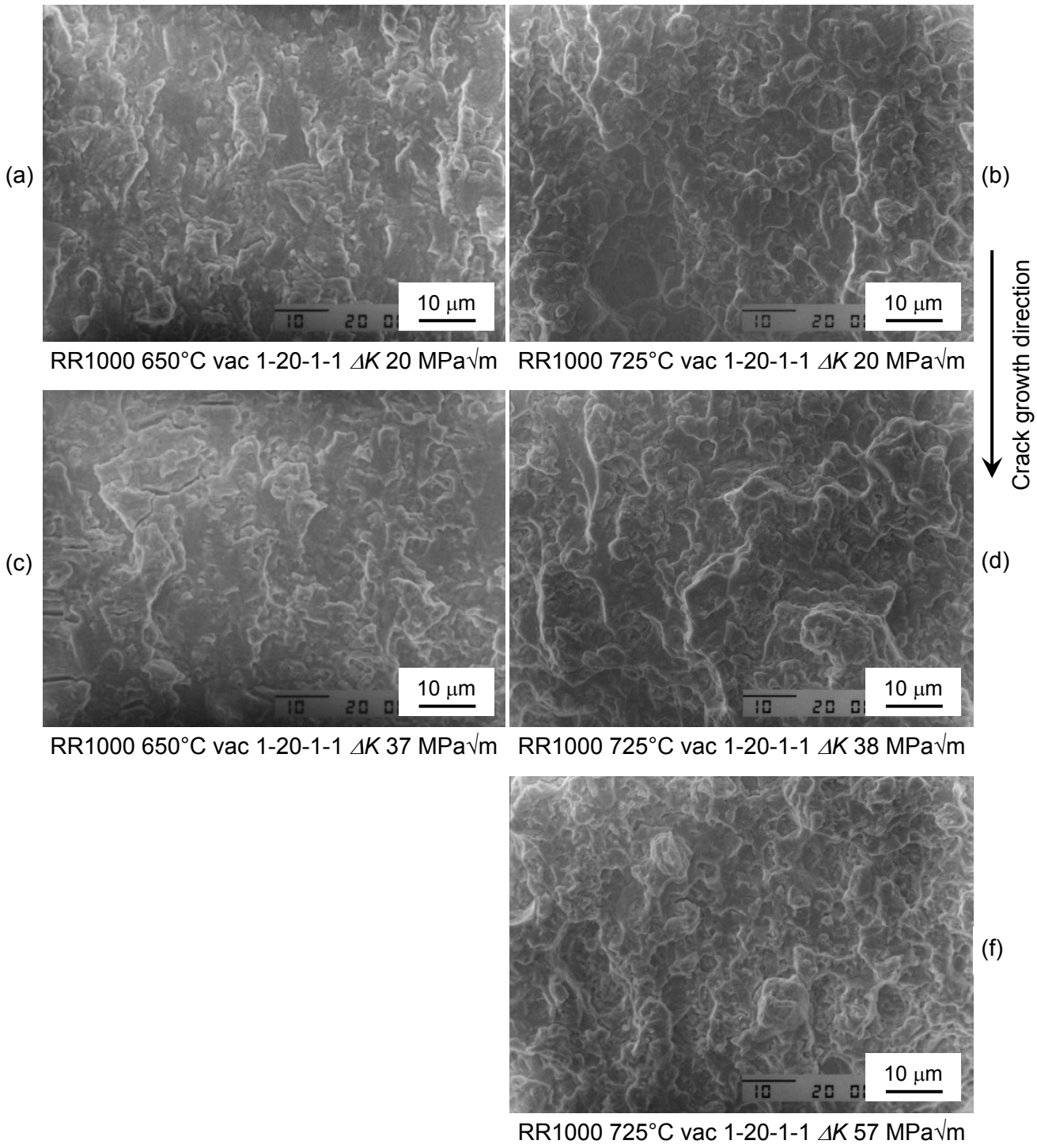

Figure 105 RR1000 SENB fracture surfaces, in vacuum, 1-20-1-1 load cycle, increasing *ΔK*, increasing temperature, SEM SEI mode[21].

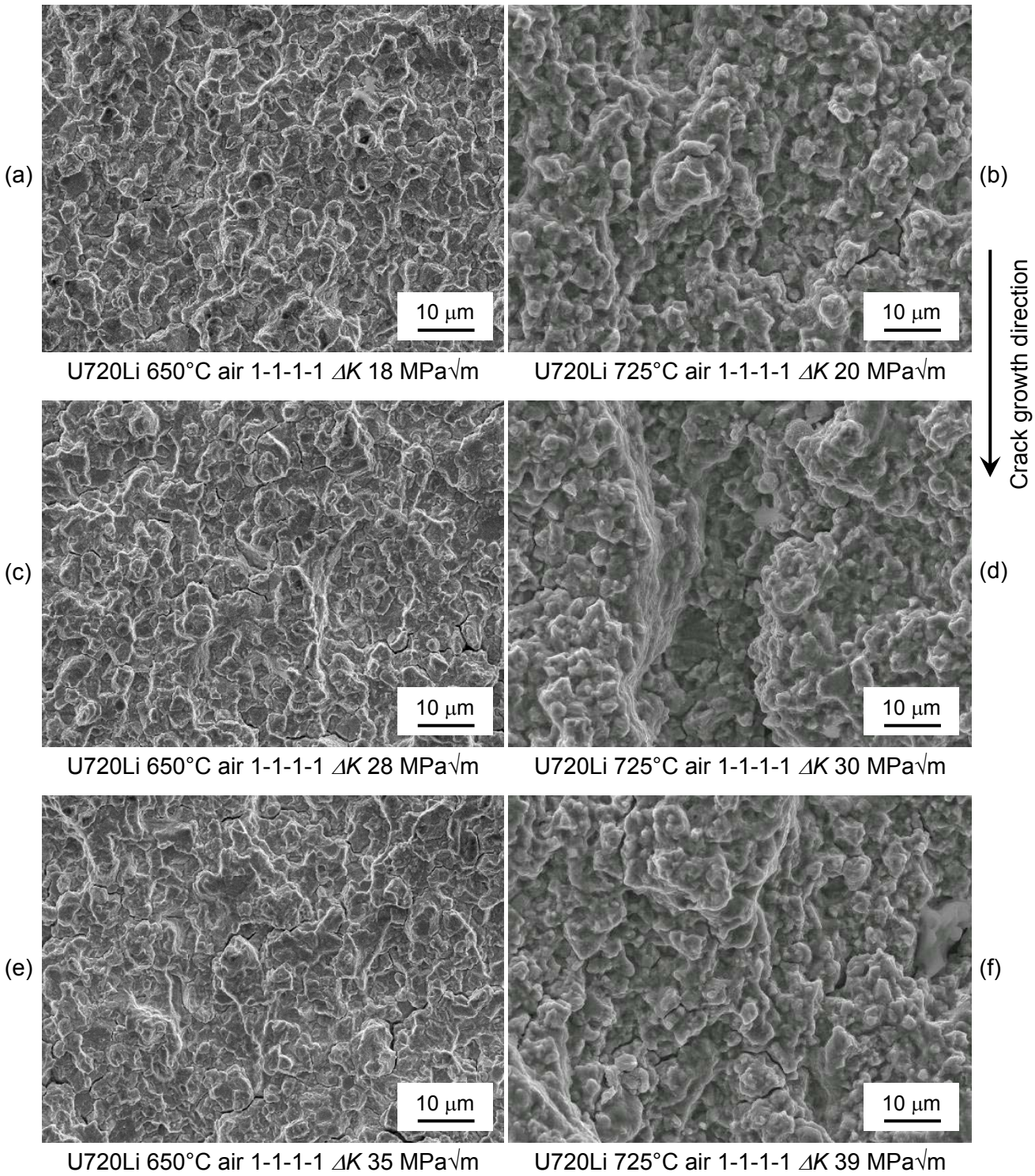

Figure 106 U720Li SENB fracture surfaces, in air, 1-1-1-1 load cycle, increasing *ΔK*, increasing temperature, FEG SEM SEI mode[21].

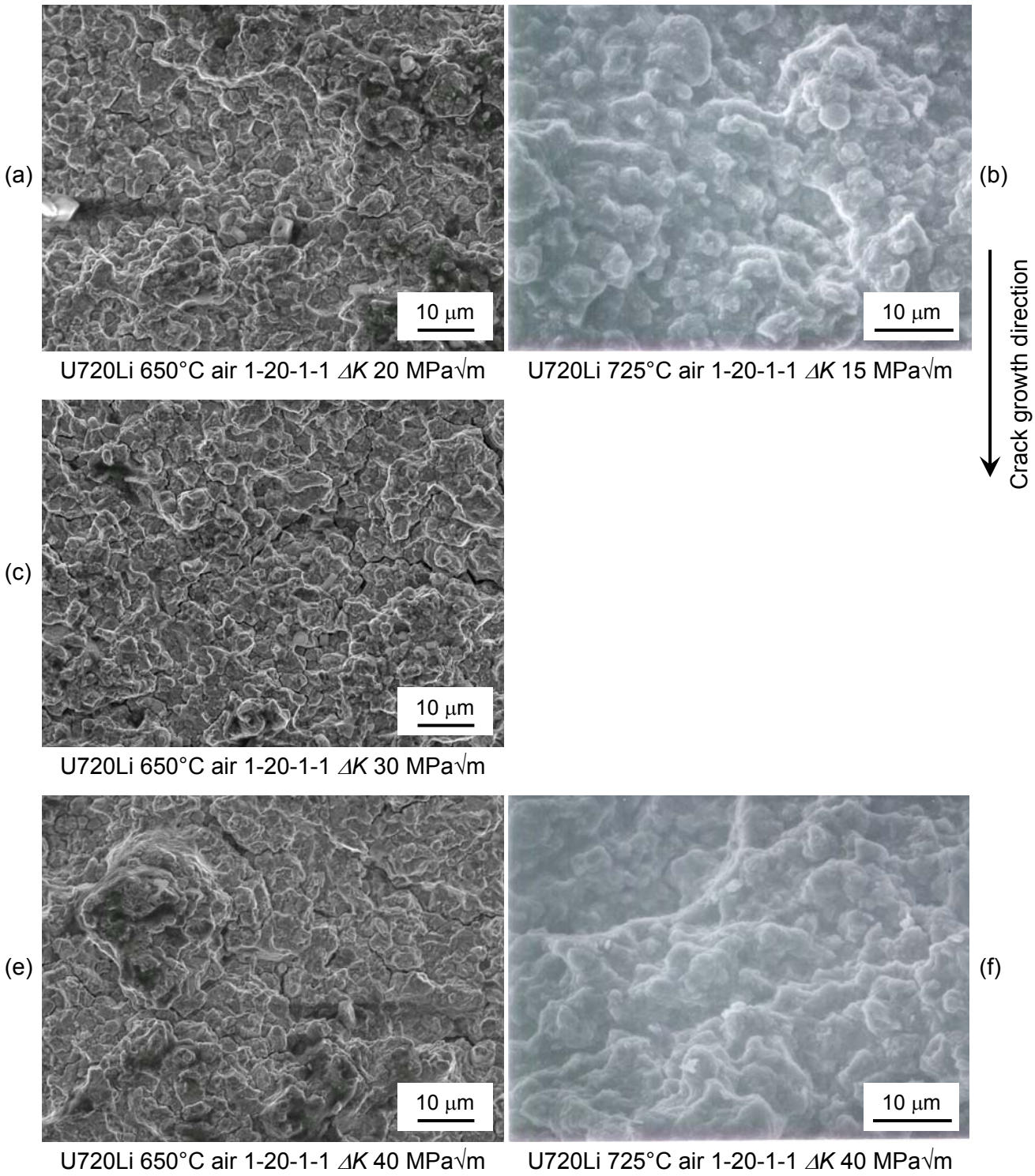

Figure 107 U720Li SENB fracture surfaces, in air, 1-20-1-1 load cycle, increasing *ΔK*, increasing temperature, FEG SEM and SEM SEI mode[196].

(images (b) and (f) are scanned archived photographs)

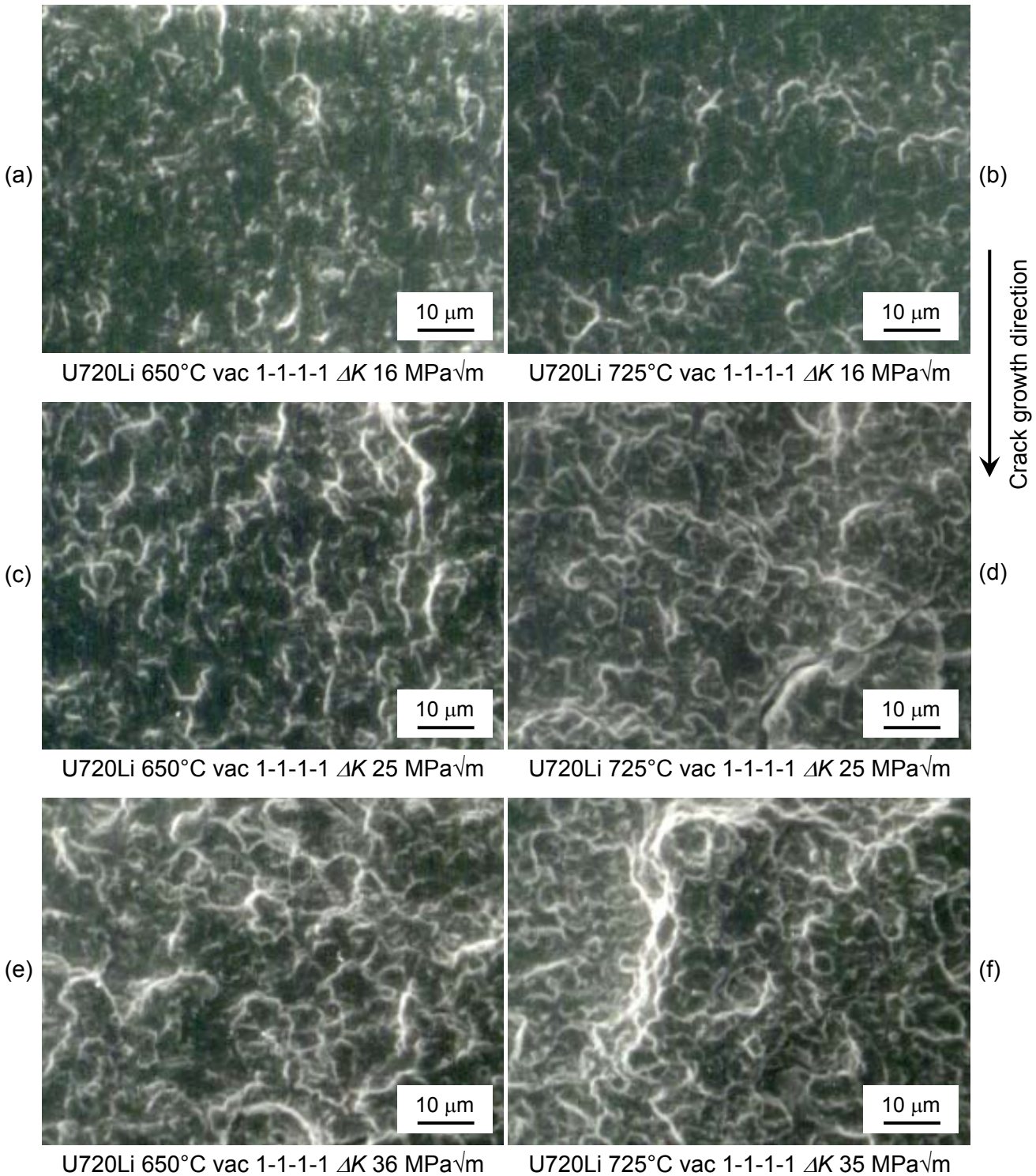

Figure 108 U720Li SENB fracture surfaces, in vacuum, 1-1-1-1 load cycle, increasing ΔK, increasing temperature, FEG SEM SEI mode[196].

(images are scanned archived photographs)

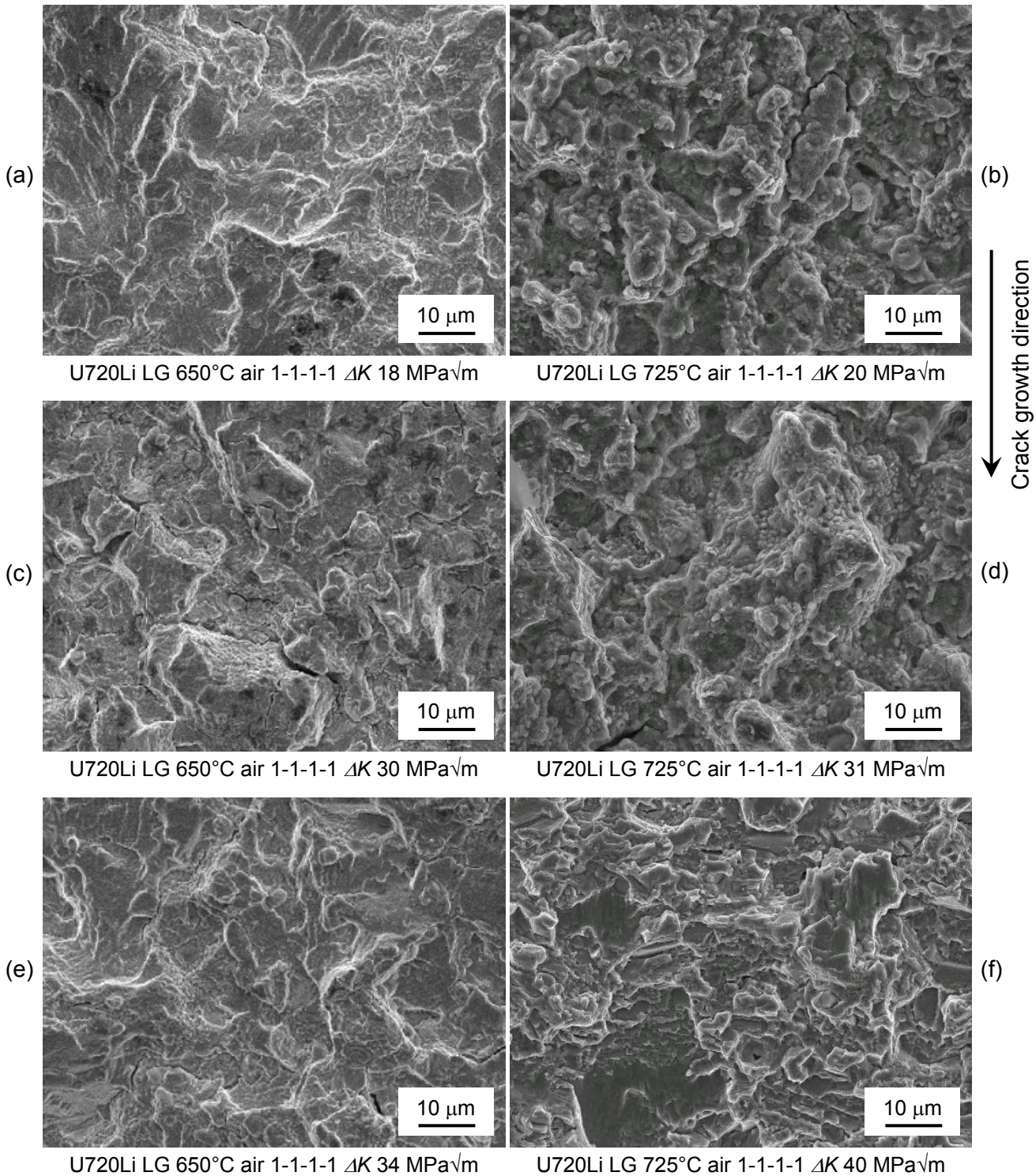

Figure 109 U720Li LG SENB fracture surfaces, in air, 1-1-1-1 load cycle, increasing *ΔK*, increasing temperature, FEG SEM SEI mode[21].

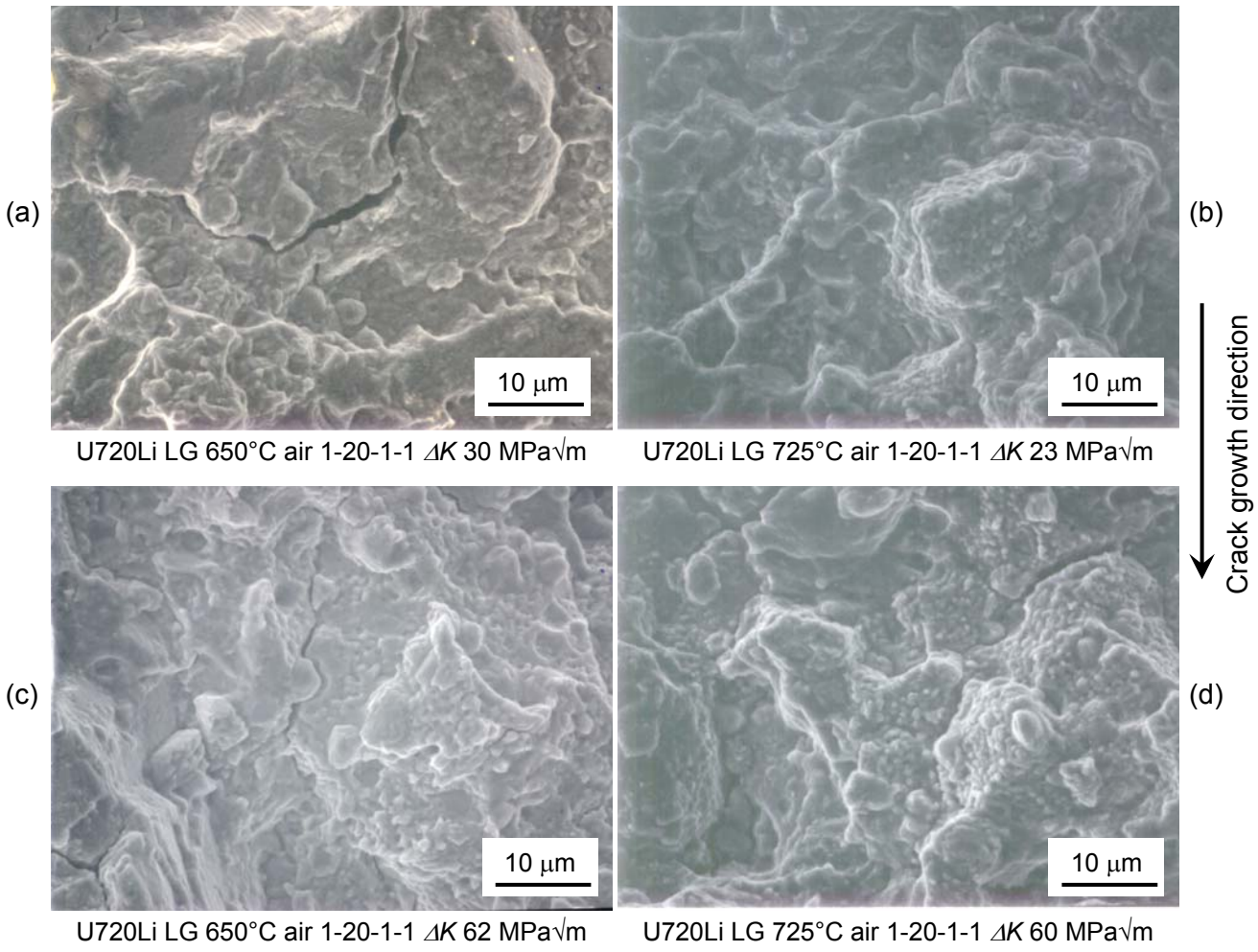

Figure 110 U720Li LG SENB fracture surfaces, in air, 1-20-1-1 load cycle, increasing *ΔK*, increasing temperature, SEM SEI mode[196].

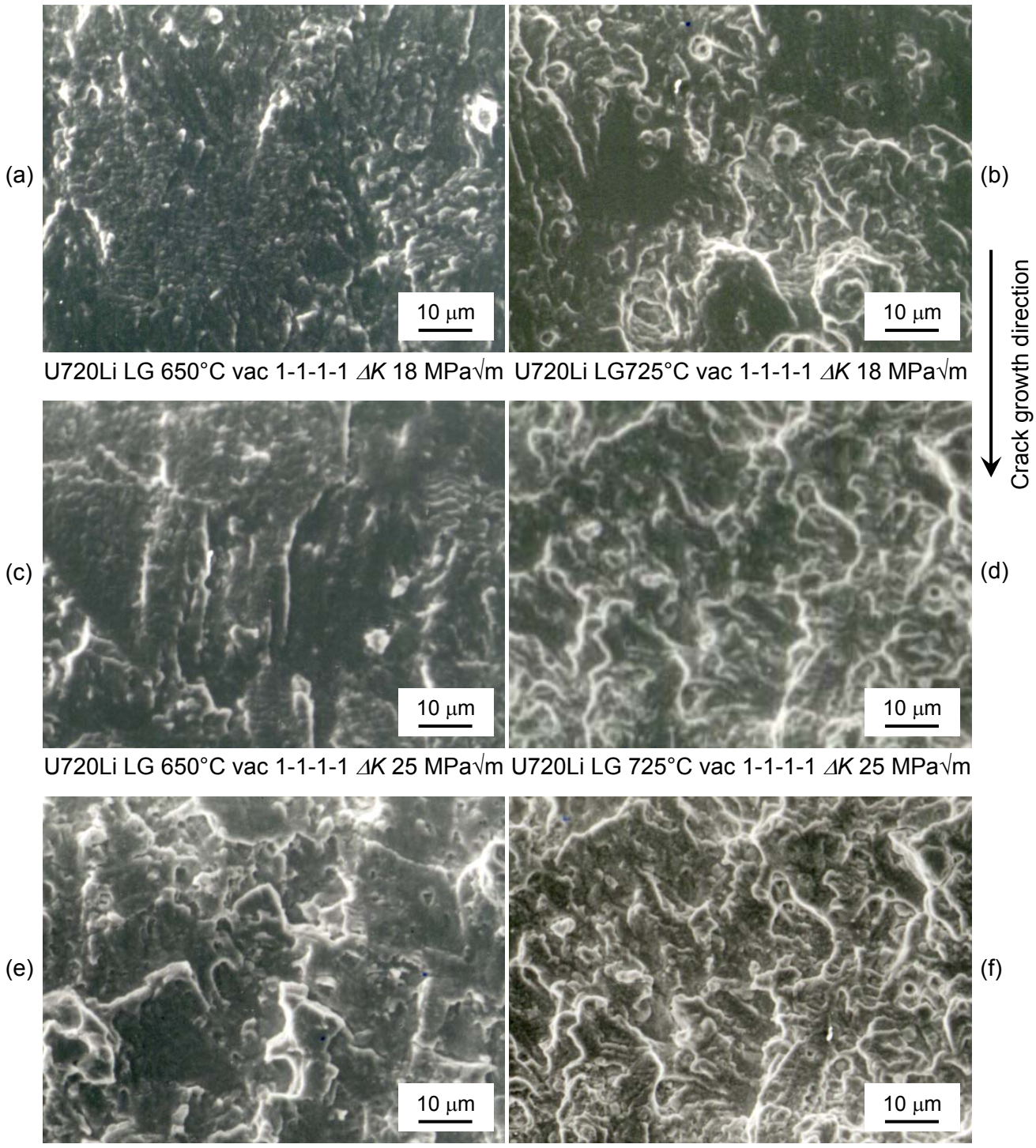

Figure 111 U720Li LG SENB fracture surfaces, in vacuum, 1-1-1-1 load cycle, increasing *ΔK*, increasing temperature, SEM SEI mode[196].

(images are scanned archived photographs)

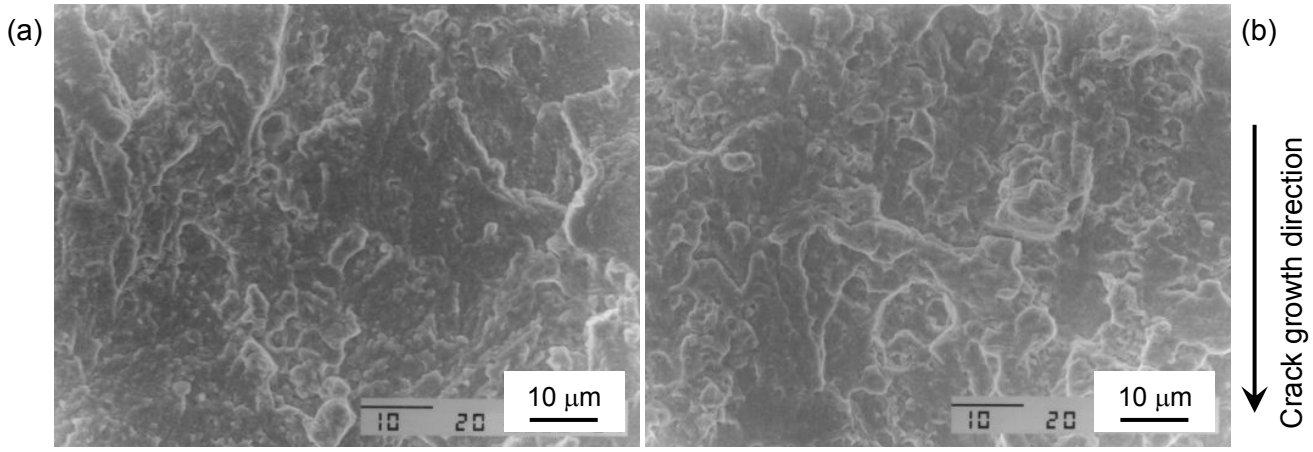

U720Li LG 650°C vac 1-20-1-1 ΔK 18 MPa√m U720Li LG 650°C vac 1-20-1-1 ΔK 35 MPa√m

Figure 112 U720Li LG SENB fracture surfaces, in vacuum, 1-20-1-1 load cycle, increasing ΔK, 650°C, SEM SEI mode[196].

(images are scanned archived photographs)

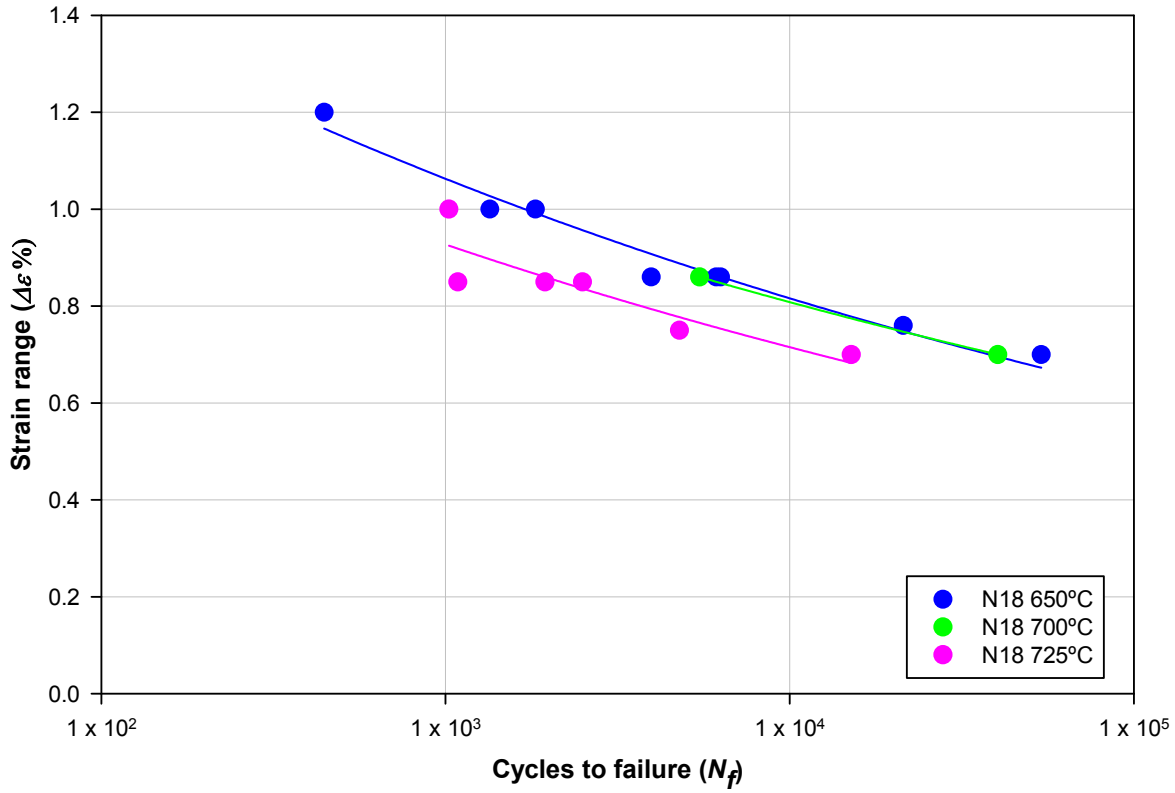

Figure 113 N18 LCF Strain range versus number of cycles to failure.

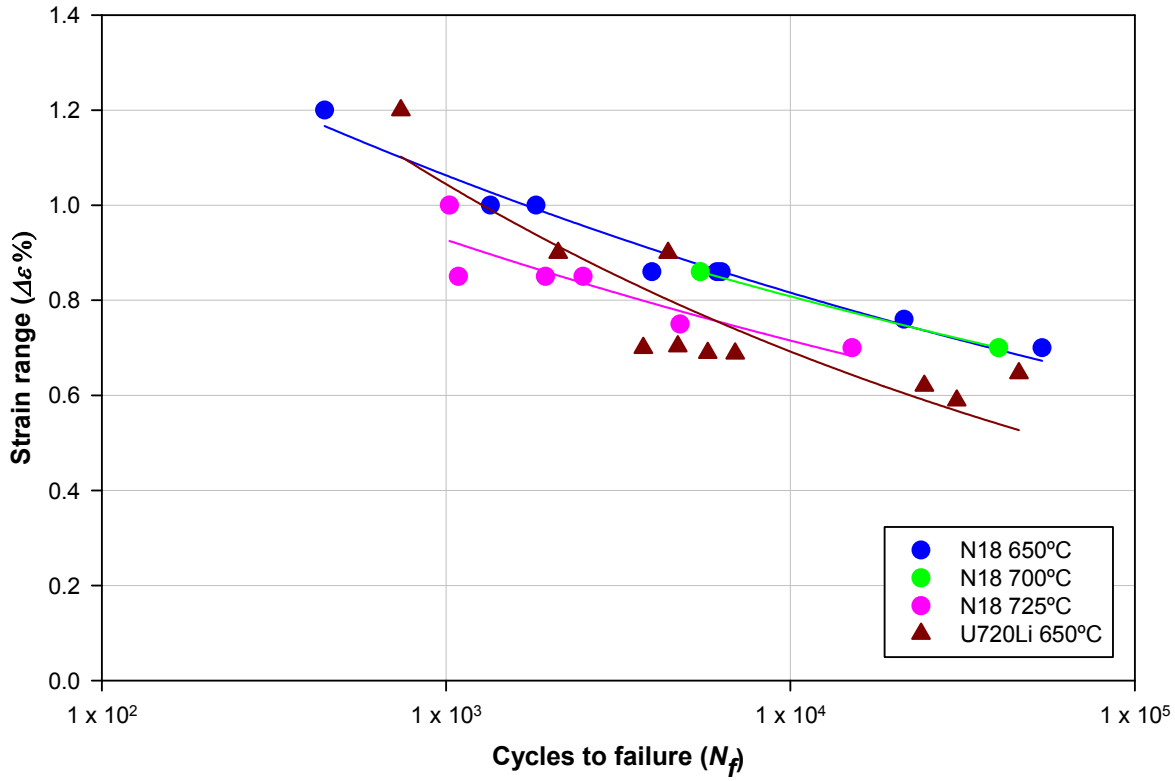

Figure 114 Strain range versus number of cycles to failure comparison between N18 and U720Li.

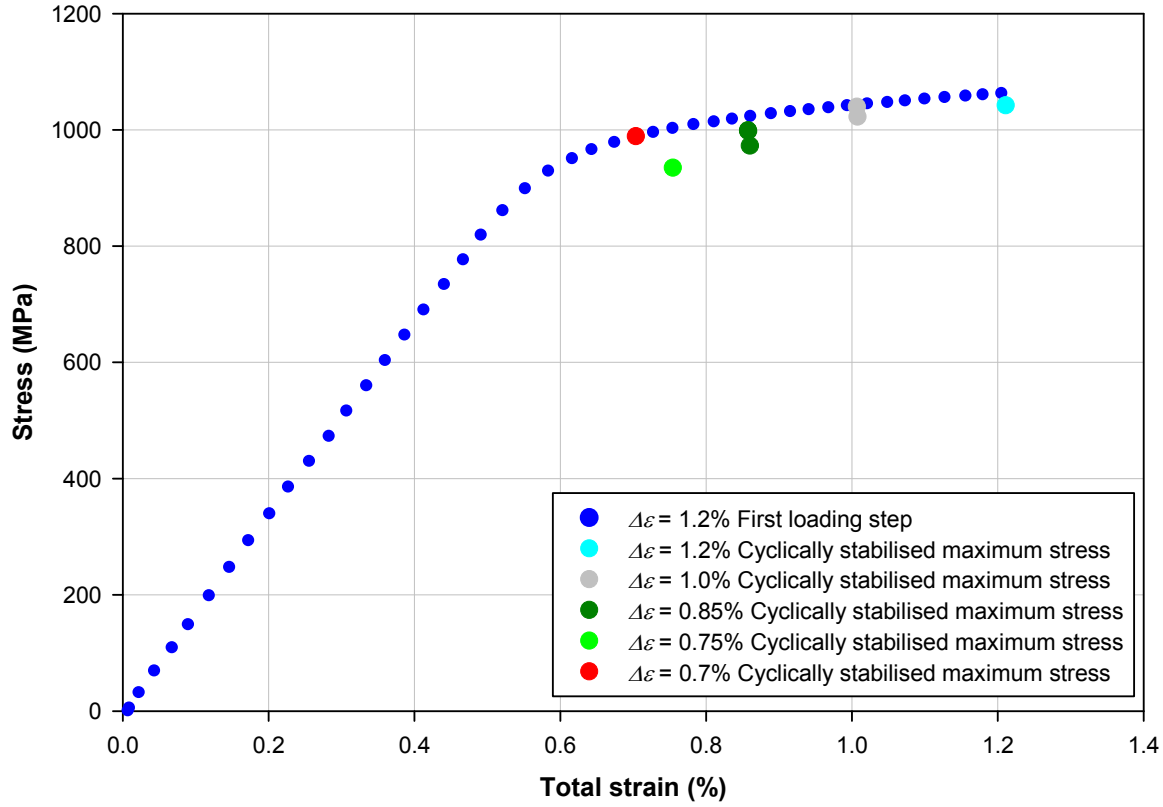

Figure 115 N18 LCF 650°C initial cycle *cf.* with cyclically stabilised maximum stresses.

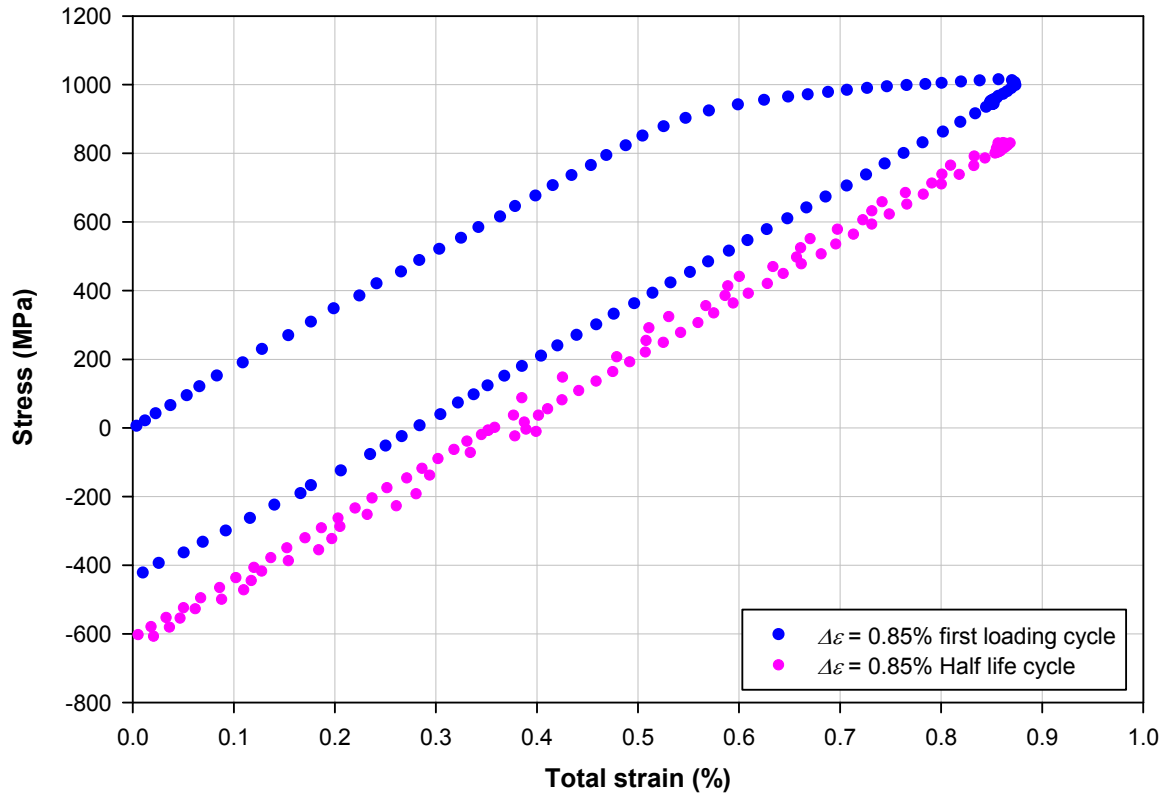

Figure 116 N18 LCF 725°C initial cycle *cf.* cyclically stabilised cycle $\Delta\varepsilon$ = 0.85%.

(a)

N18 LCF 650°C $\Delta\varepsilon$ = 0.7

(b)

N18 LCF 650°C $\Delta\varepsilon$ = 1.2

(c)

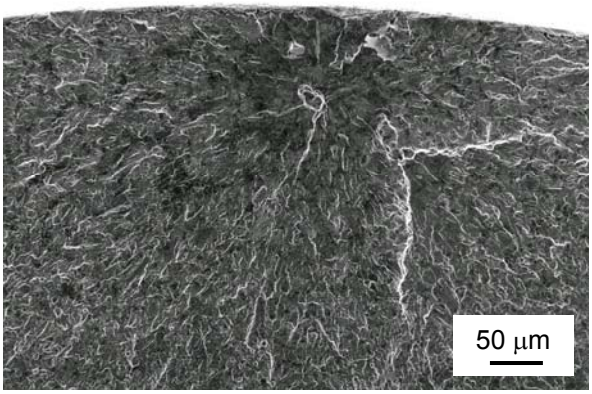

N18 LCF 650°C $\Delta\varepsilon$ = 0.7 initiation

(d)

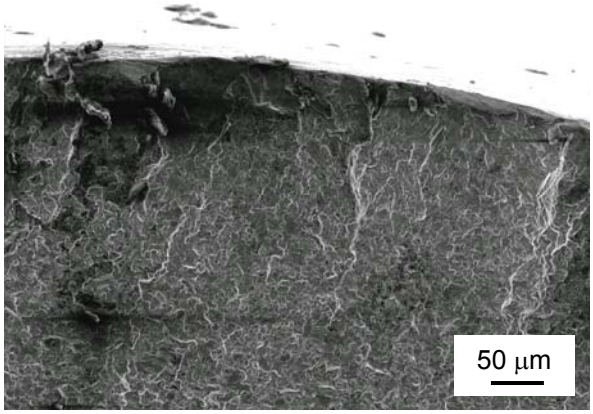

N18 LCF 650°C $\Delta\varepsilon$ = 1.2 initiation

(e)

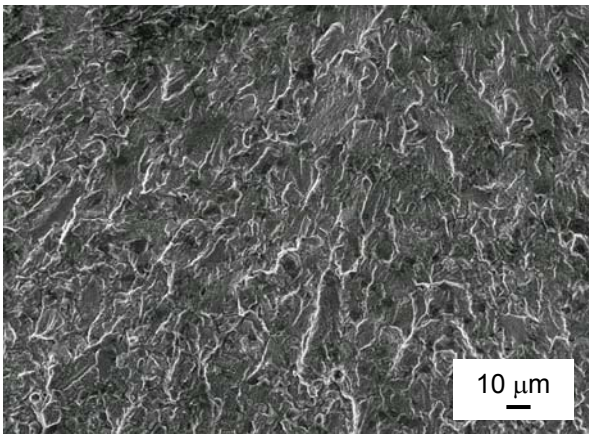

N18 LCF 650°C $\Delta\varepsilon$ = 0.7 low ΔK

(f)

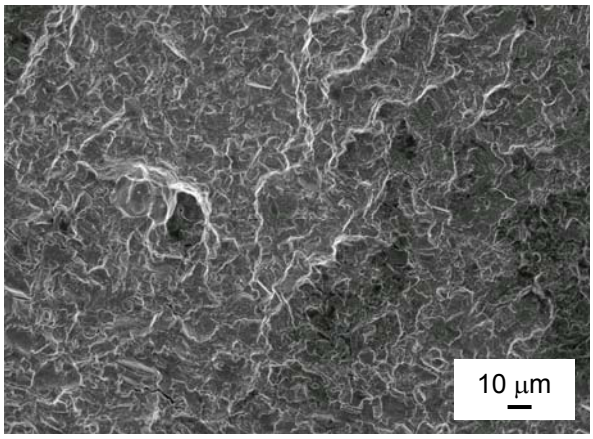

N18 LCF 650°C $\Delta\varepsilon$ = 1.2 low ΔK

(g)

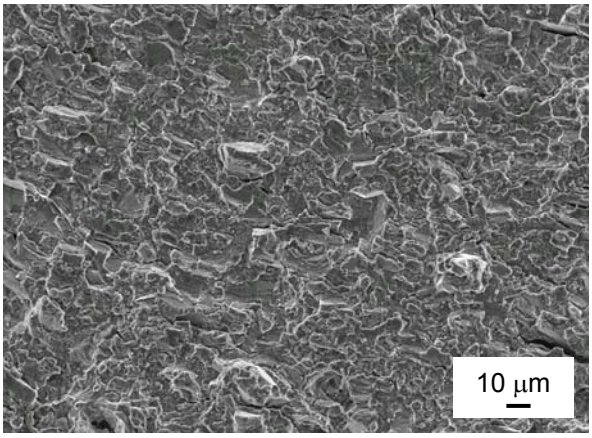

N18 LCF 650°C $\Delta\varepsilon$ = 0.7 high ΔK

(h)

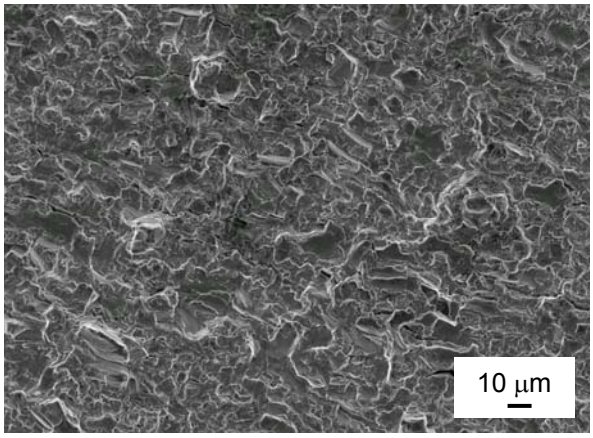

N18 LCF 650°C $\Delta\varepsilon$ = 1.2 high ΔK

Figure 117 N18 LCF 650°C in air, $\Delta\varepsilon$ = 0.7 and $\Delta\varepsilon$ = 1.2 fractography, macroscopic overviews and FEG SEM SEI mode micrographs.

(a)

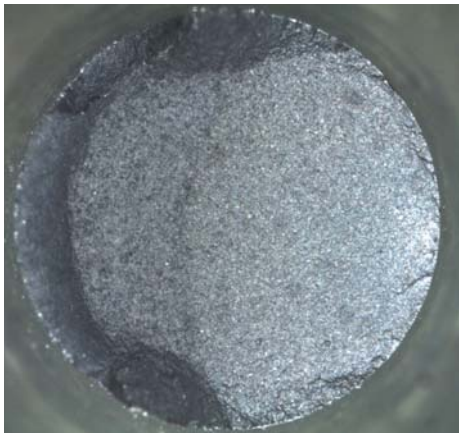

N18 LCF 725°C $\Delta\varepsilon$ = 0.7

(b)

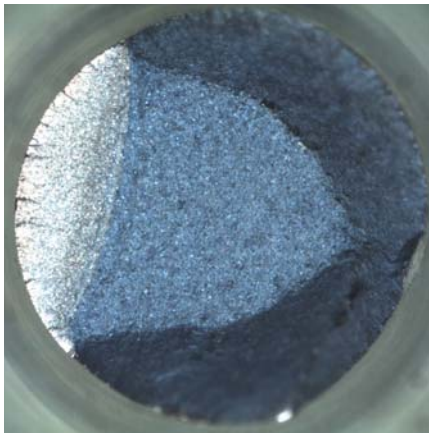

N18 LCF 725°C $\Delta\varepsilon$ = 1

(c)

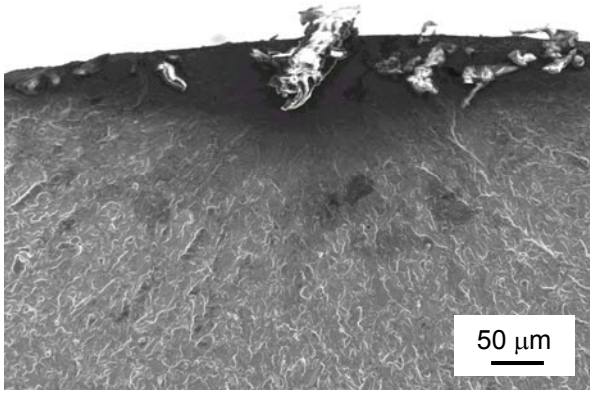

N18 LCF 725°C $\Delta\varepsilon$ = 0.7 initiation

(d)

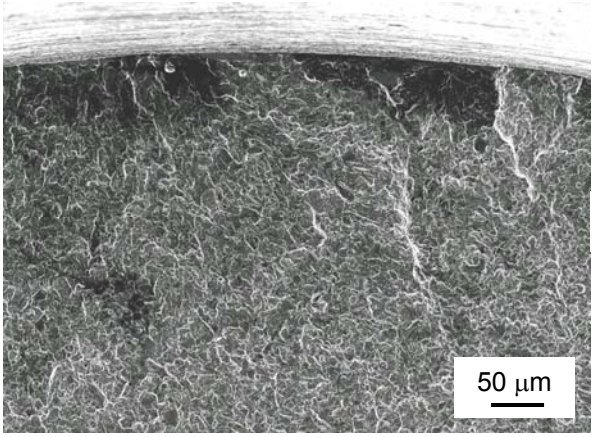

N18 LCF 725°C $\Delta\varepsilon$ = 1 initiation

(e)

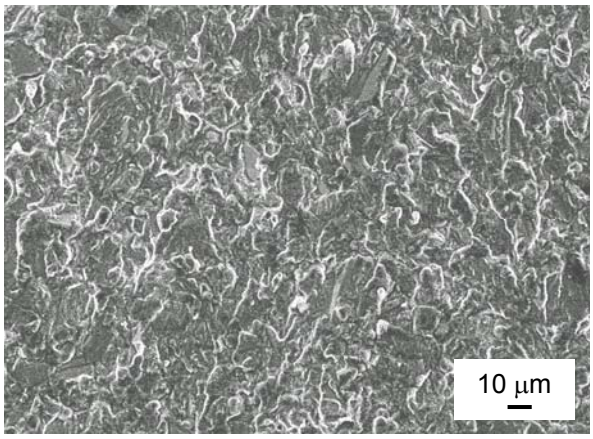

N18 LCF 725°C $\Delta\varepsilon$ = 0.7 low ΔK

(f)

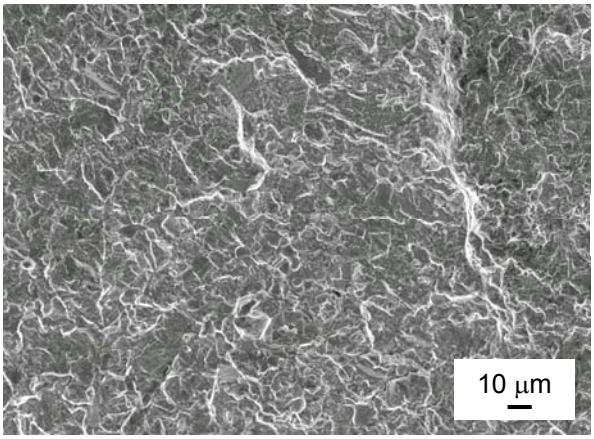

N18 LCF 725°C $\Delta\varepsilon$ = 1 low ΔK

(g)

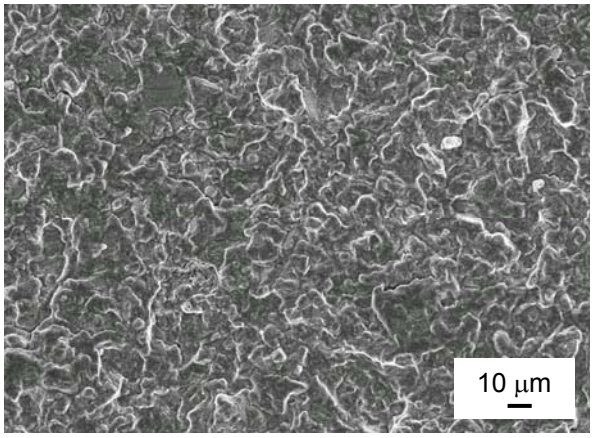

N18 LCF 725°C $\Delta\varepsilon$ = 0.7 high ΔK

(h)

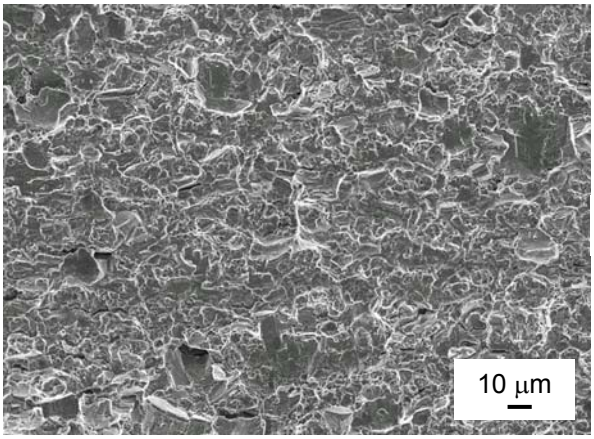

N18 LCF 725°C $\Delta\varepsilon$ = 1 high ΔK

Figure 118 N18 LCF 725°C in air, $\Delta\varepsilon$ = 0.7 and $\Delta\varepsilon$ = 1 fractography, macroscopic overviews and FEG SEM SEI mode micrographs.

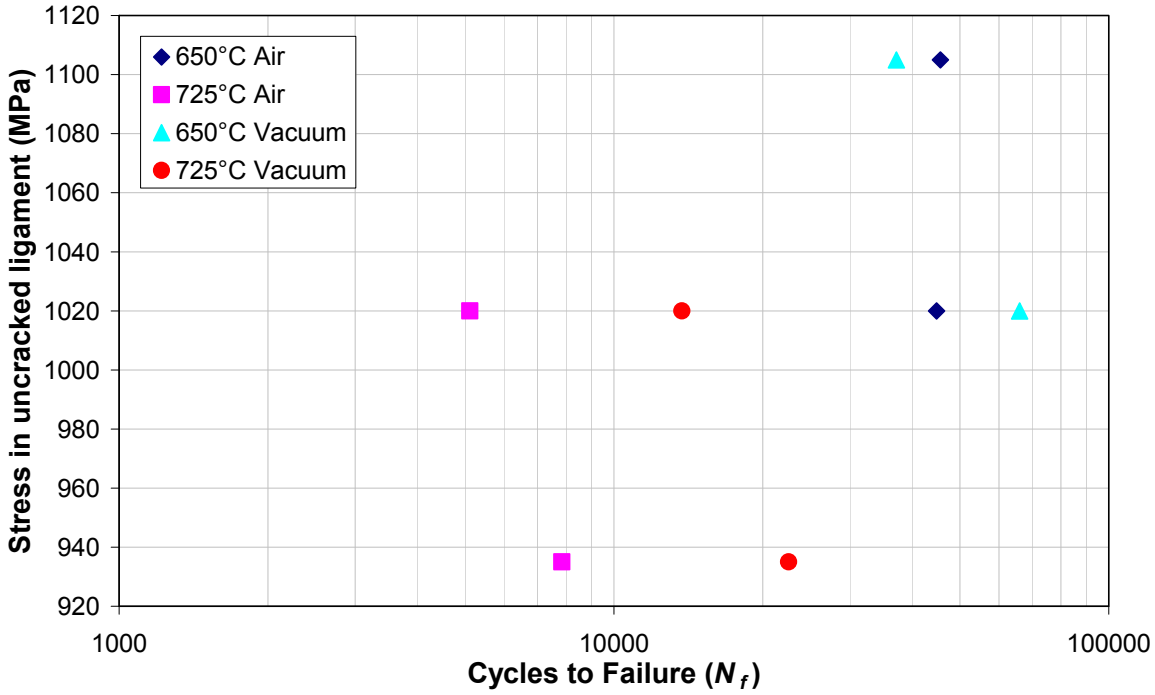

Figure 119 N18 U-notch fatigue, graph of stress in un-cracked ligament against cycles to failure.

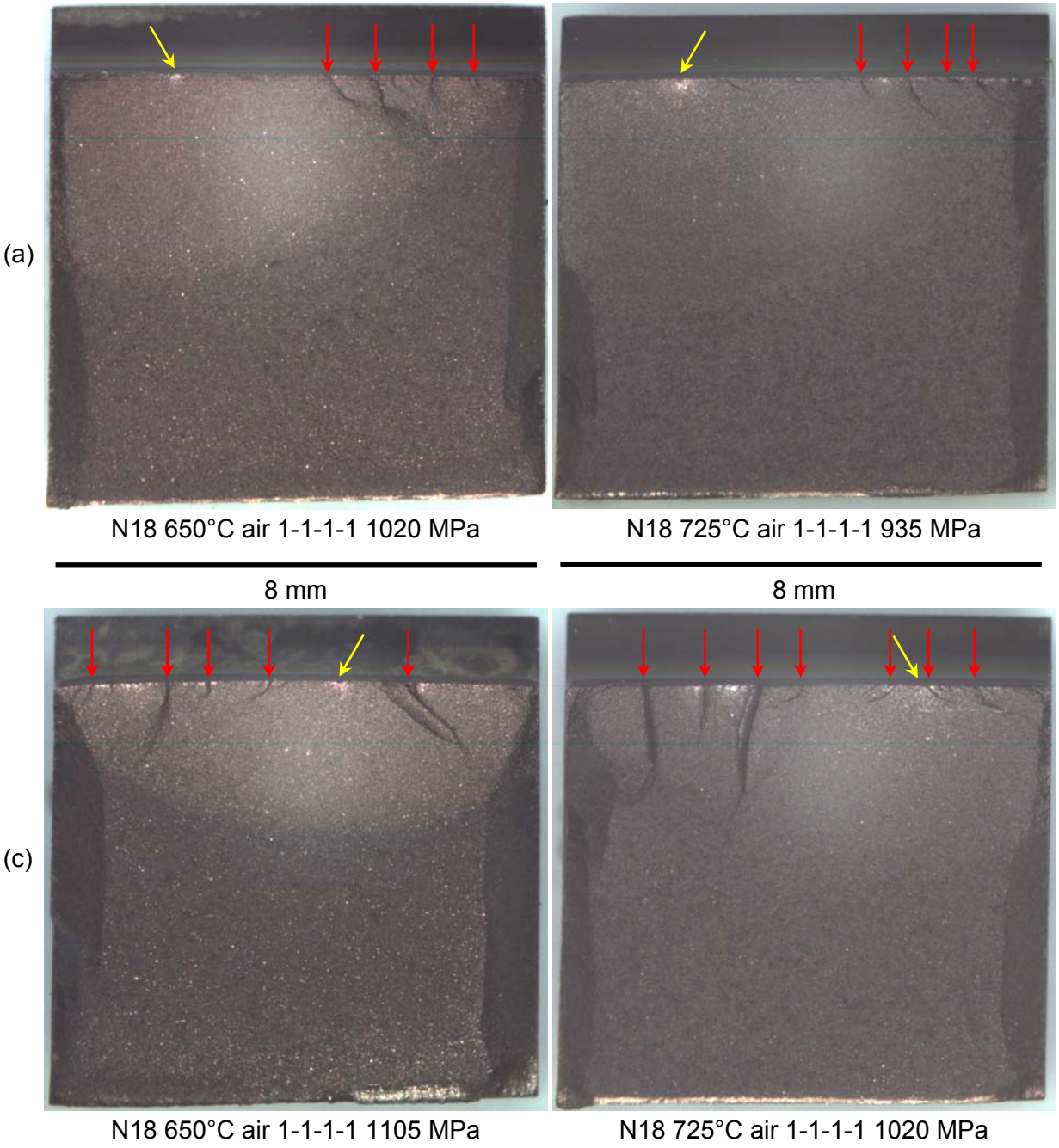

Figure 120 N18 U-notch fracture surfaces, in air, 1-1-1-1 load cycle, increasing stress, increasing temperature, optical overviews.

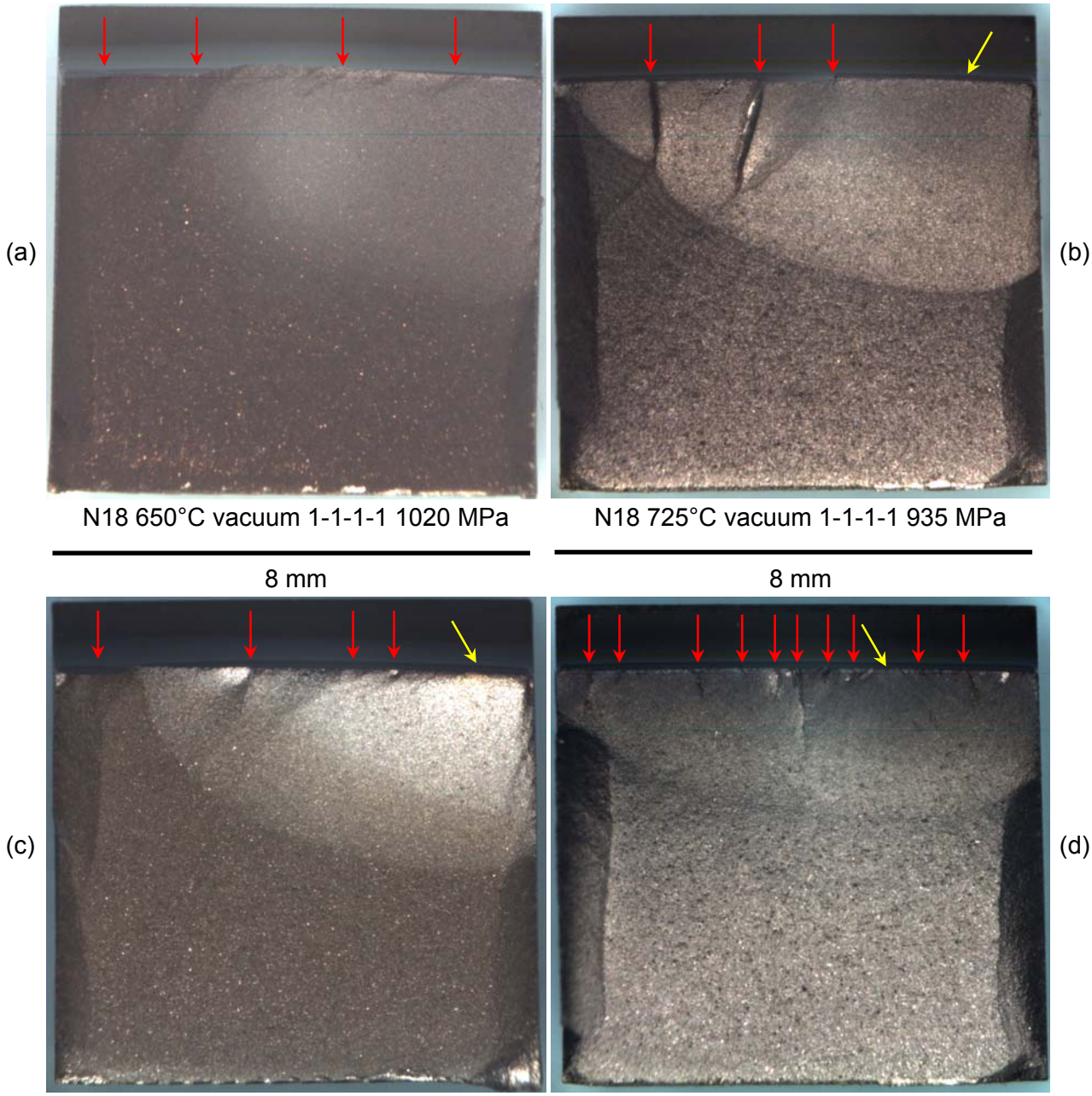

Figure 121 N18 U-notch fracture surfaces, in vacuum, 1-1-1-1 load cycle, increasing stress, increasing temperature, optical overviews.

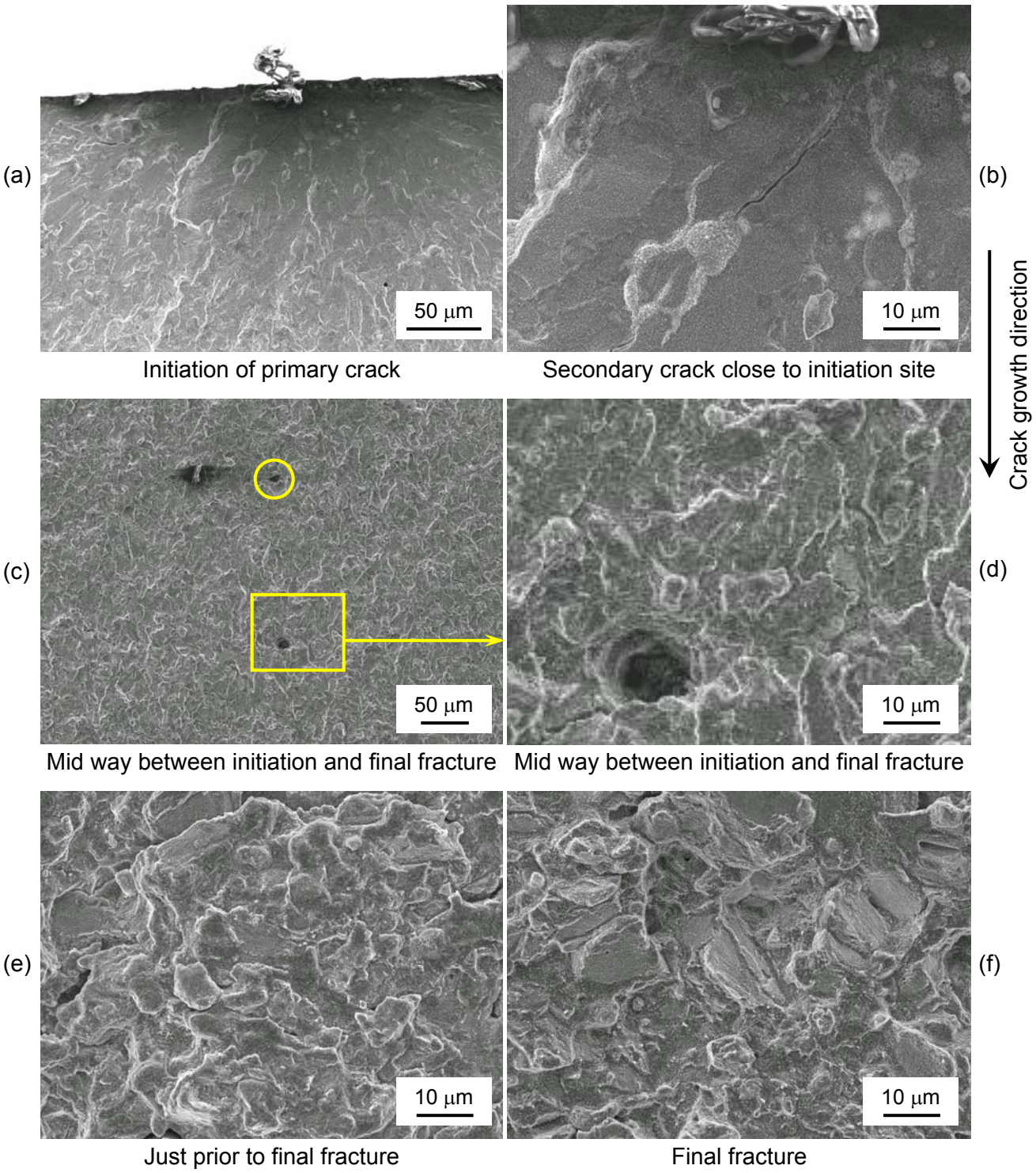

Figure 122 N18 U-notch fracture surfaces, crack initiation and propagation, in air, 1-1-1-1 load cycle, 650°C, 1020 MPa, FEG SEM SEI mode.

(a)

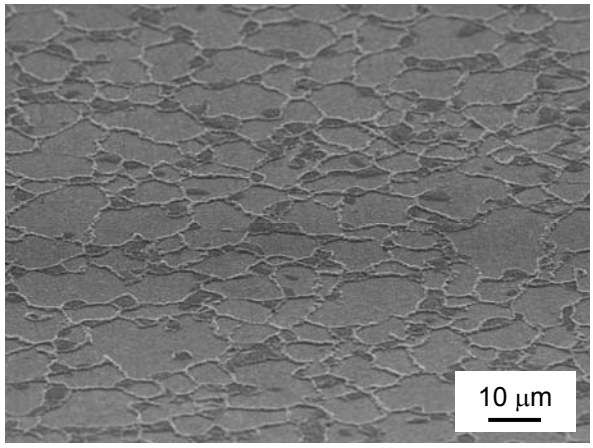

(b)

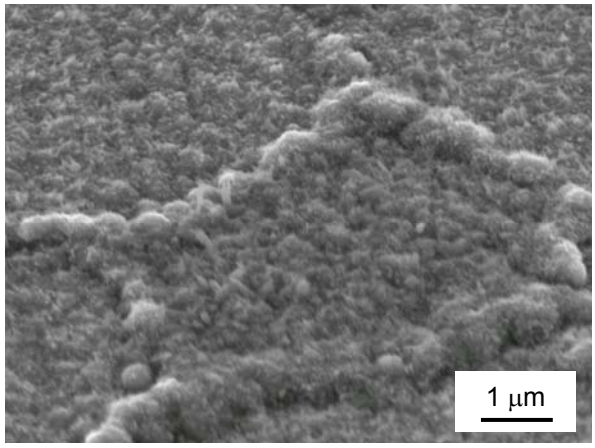

"Thermal etching" of grain boundaries Increased volume oxidation products at gbs

Figure 123 N18 U-notch fracture surfaces, "Thermal etching" of grain boundaries, in air, 1-1-1-1 load cycle, 650°C, 1020 MPa, FEG SEM SEI mode.

(a)

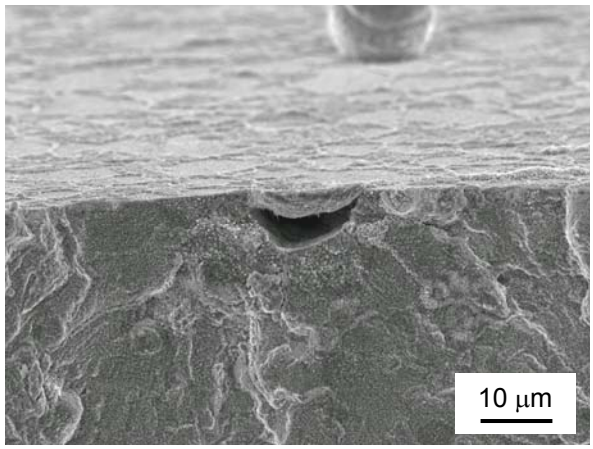

(b)

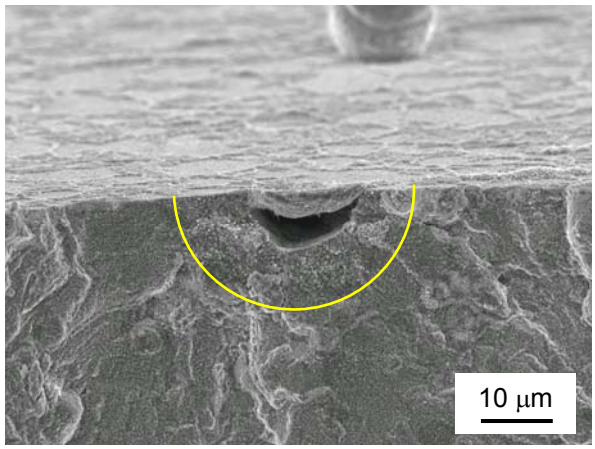

"Sealed" pore initiation site Halo marked

Figure 124 N18 U-notch fracture surfaces, crack initiation from "sealed" surface pore, in air, 1-1-1-1 load cycle, 650°C, 1020 MPa, FEG SEM SEI mode.

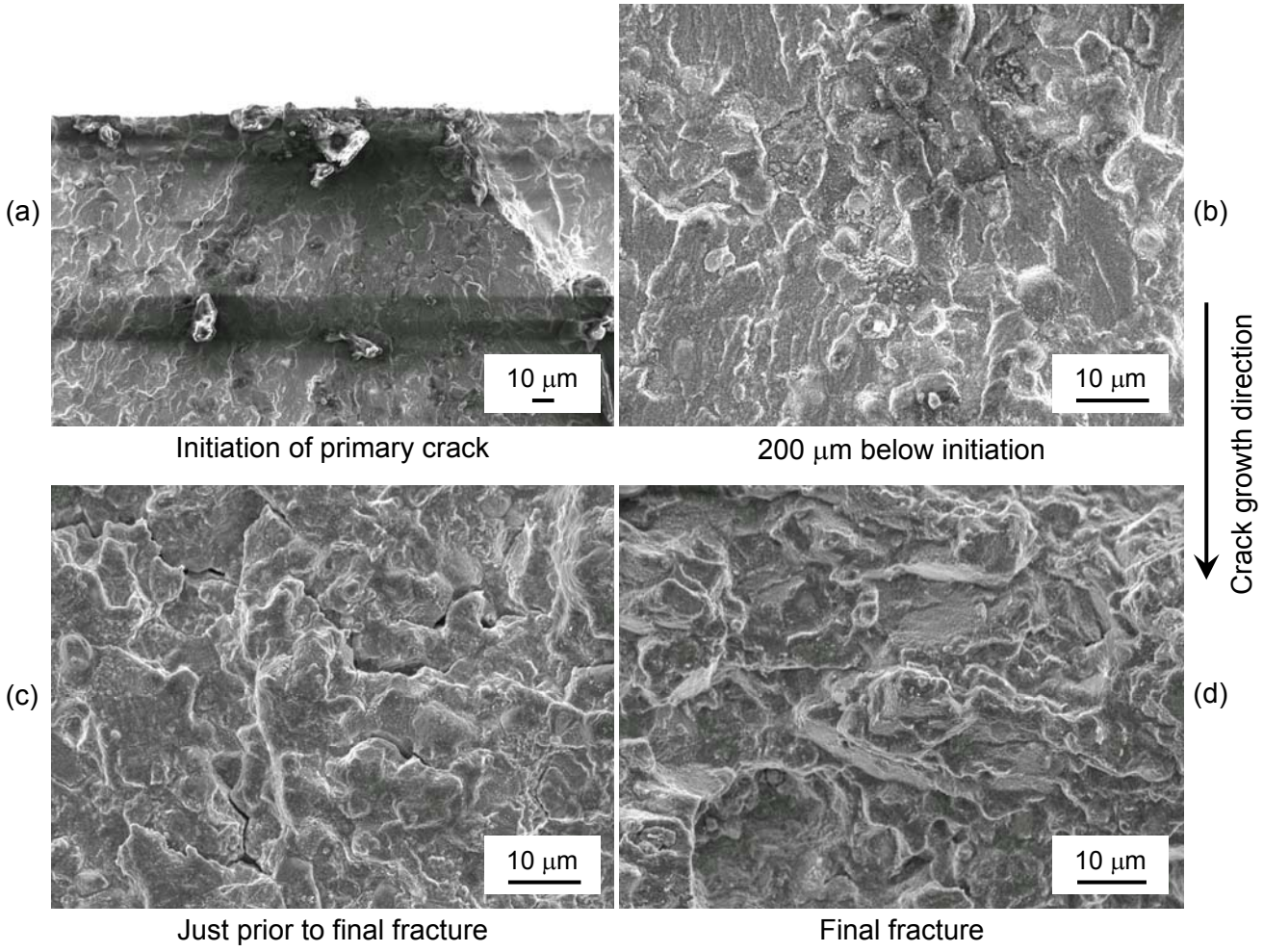

Figure 125 N18 U-notch fracture surfaces, crack initiation and propagation, in air, 1-1-1-1 load cycle, 725°C, 1020 MPa, FEG SEM SEI mode.

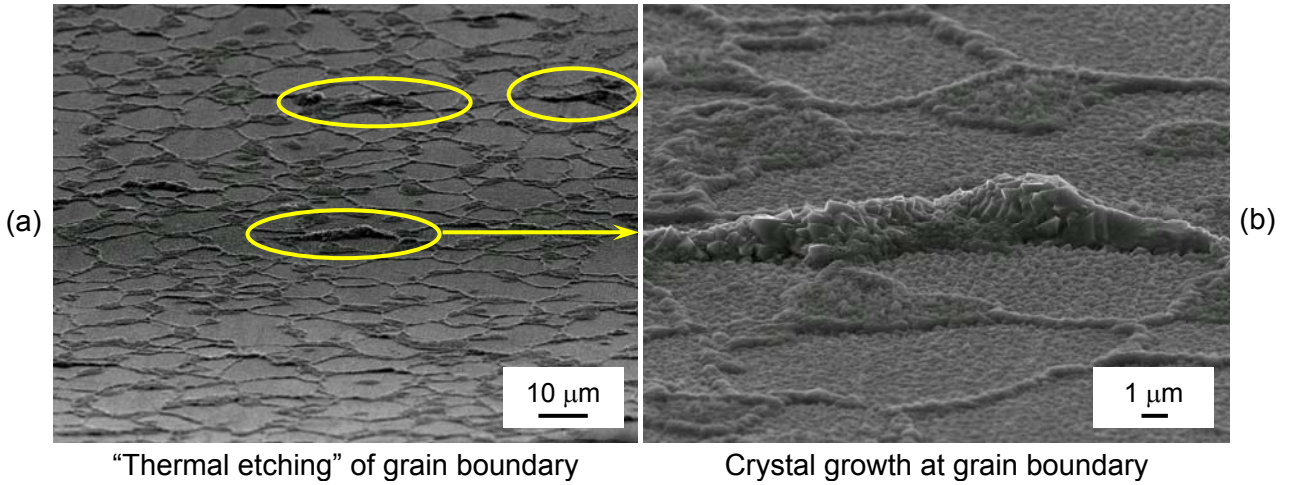

Figure 126 N18 U-notch fracture surfaces, "Thermal etching" of grain boundary, in air, 1-1-1-1 load cycle, 725°C, 1020 MPa, FEG SEM SEI mode.

(a)

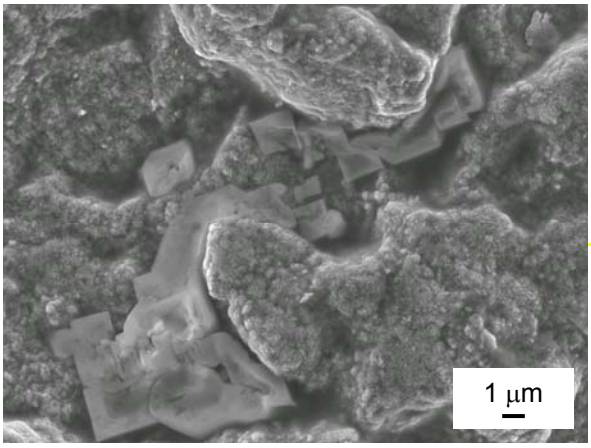

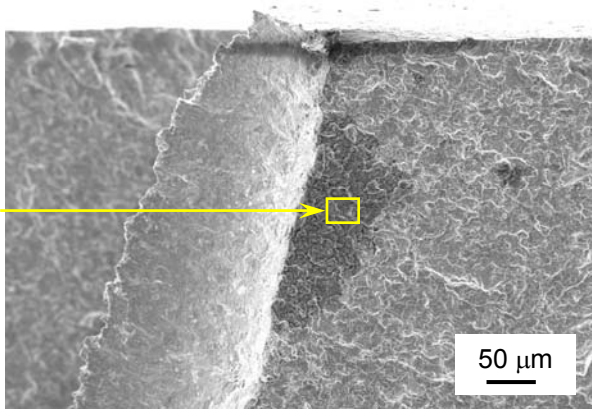

(b)

Crystal growth similar to Figure 126 (b)

Microstructural changes

Figure 127 N18 U-notch fracture surfaces, microstructural changes, in air, 1-1-1-1 load cycle, 725°C, 1020 MPa, FEG SEM SEI mode.

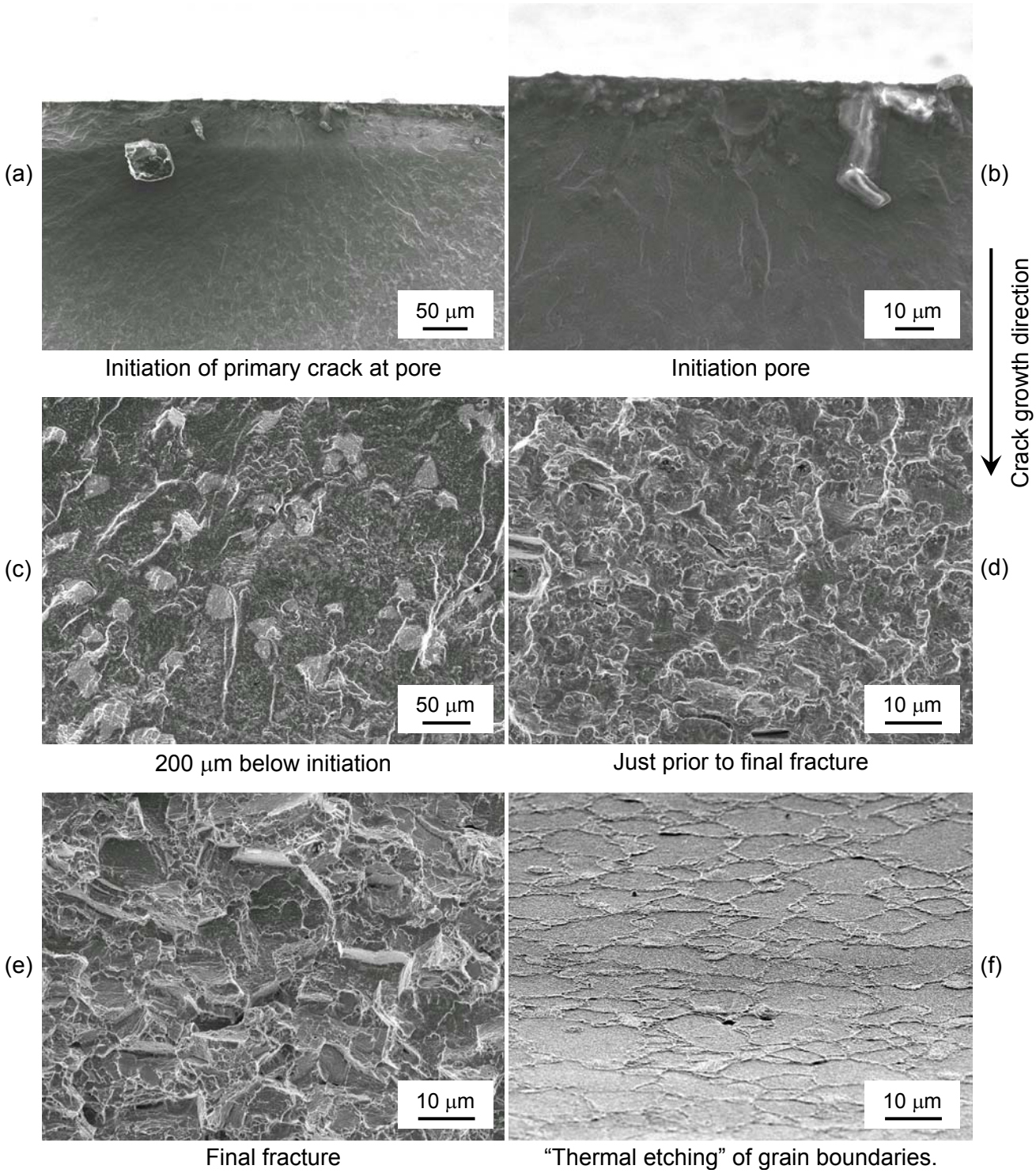

Figure 128 N18 U-notch fracture surfaces, crack initiation and propagation, in vacuum, 1-1-1-1 load cycle, 650°C, 1105 MPa, FEG SEM SEI mode.

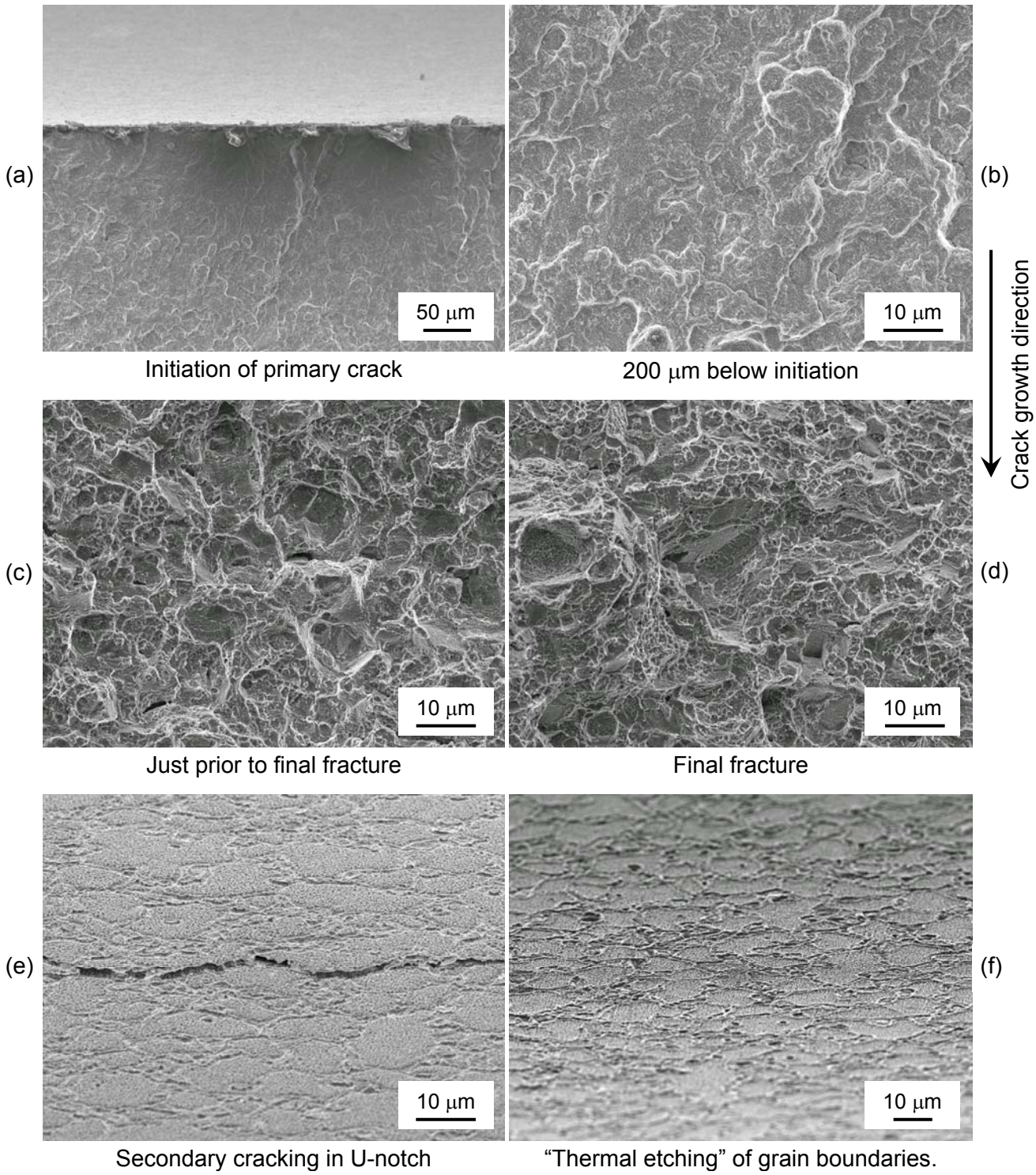

Figure 129 N18 U-notch fracture surfaces, crack initiation and propagation, in vacuum, 1-1-1-1 load cycle, 725°C, 1020 MPa, FEG SEM SEI mode.

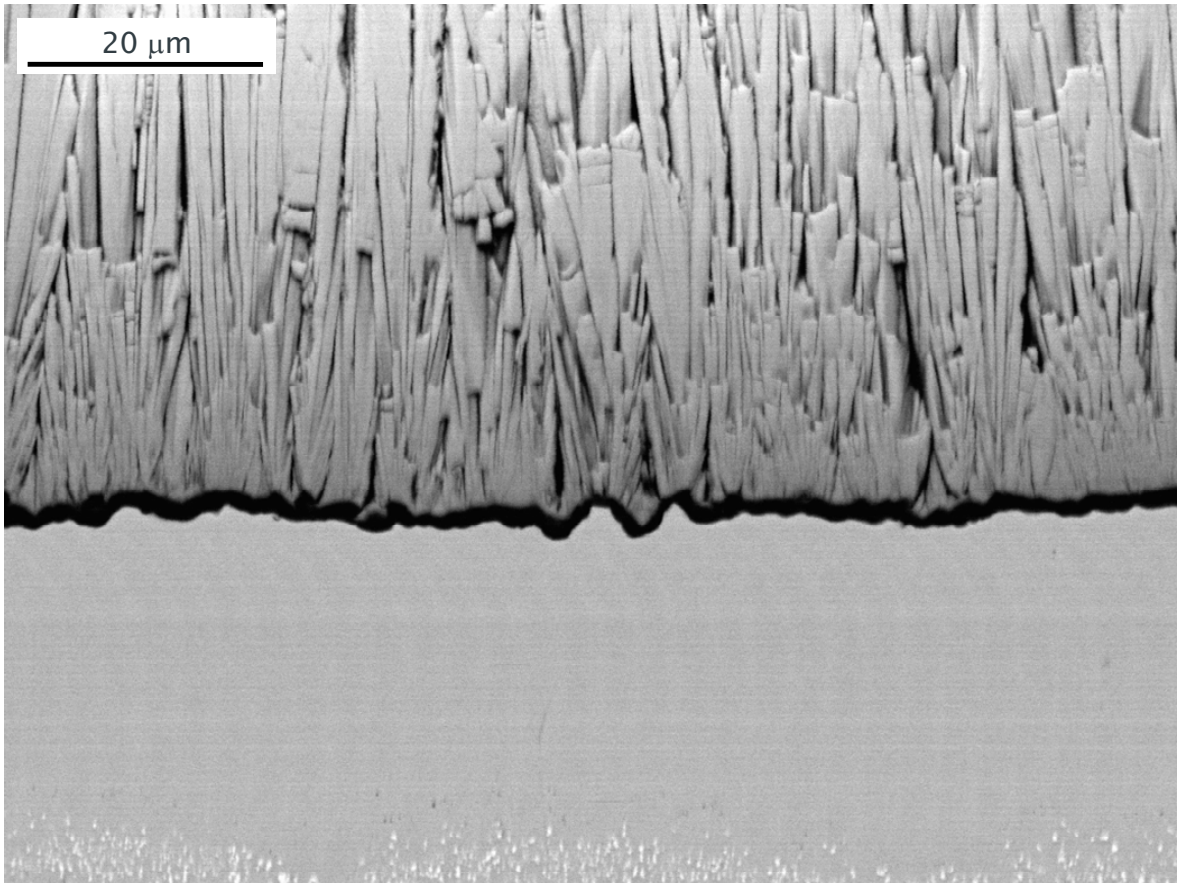

Figure 130 FEG SEM BEI mode micrograph of specimen HT08 1883 isothermal exposure for 30 hours at 1000°C.

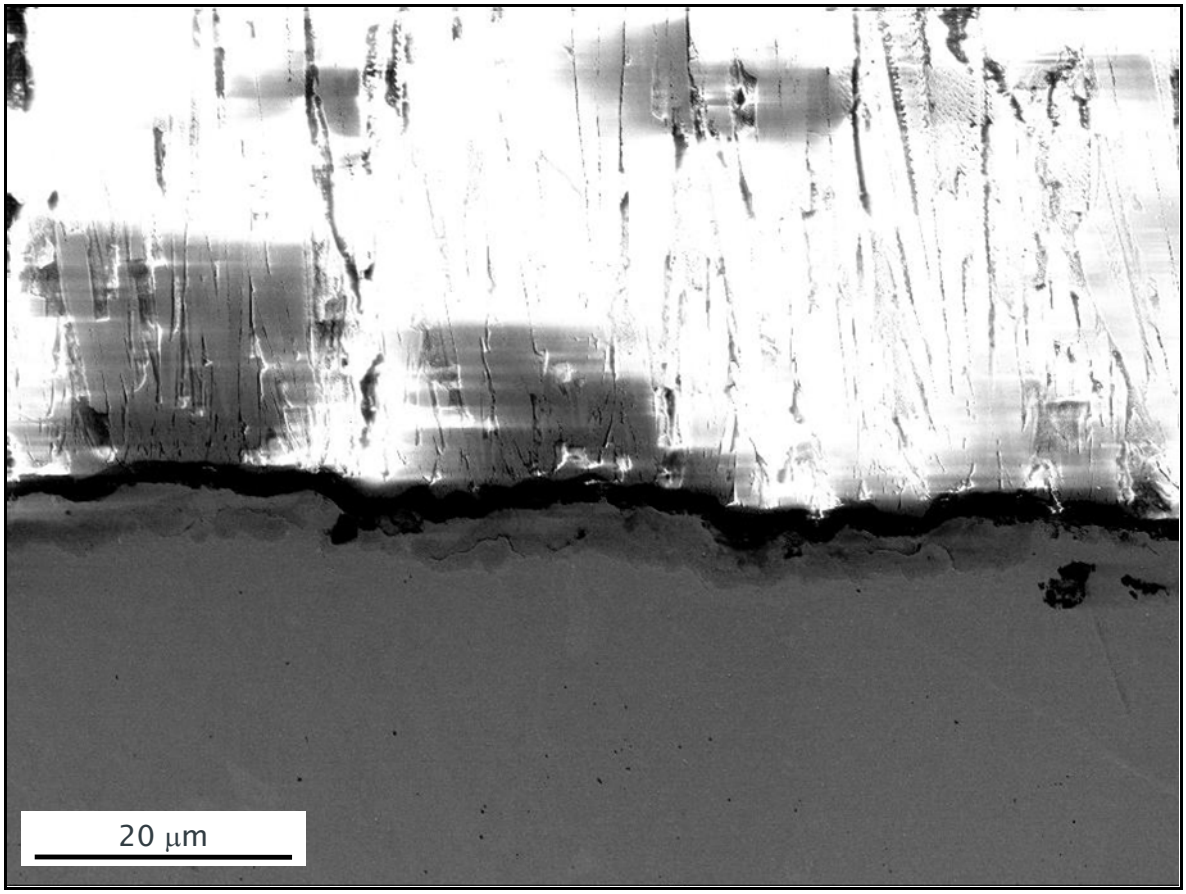

Figure 131 FEG SEM SEI mode micrograph of specimen HT08 2092 isothermal exposure for 30 hours at 1100°C. Note charging effects in the top coat.

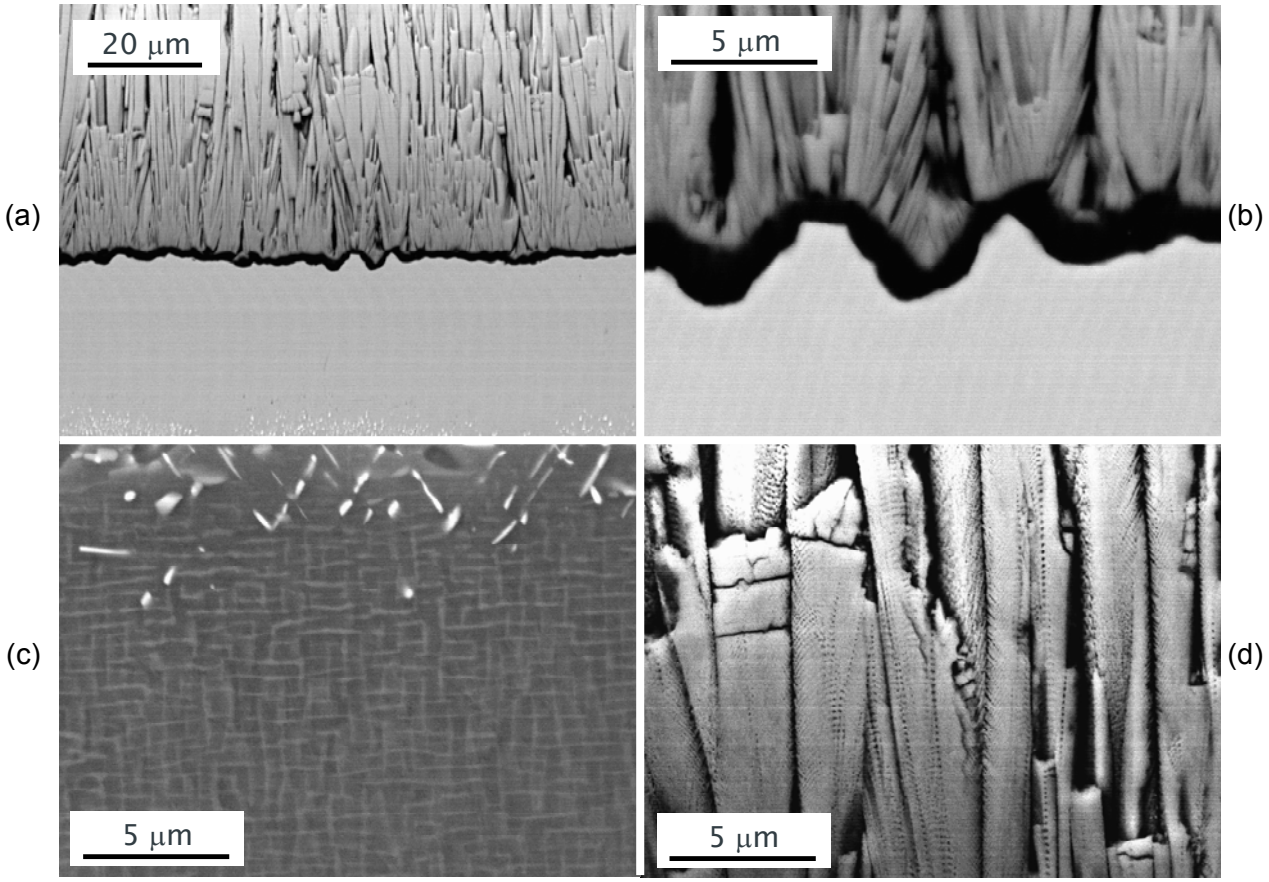

Figure 132 Specimen HT08 1883 isothermal exposure for 30 hours at 1000°C (a) TGO layer as Figure 130. (b) "Rumpling" of TGO layer, (c) Partially rafted structure of CMSX4 substrate with TCP phases, (d) Porous structure of PSZ top coat. (FEG SEM BEI mode).

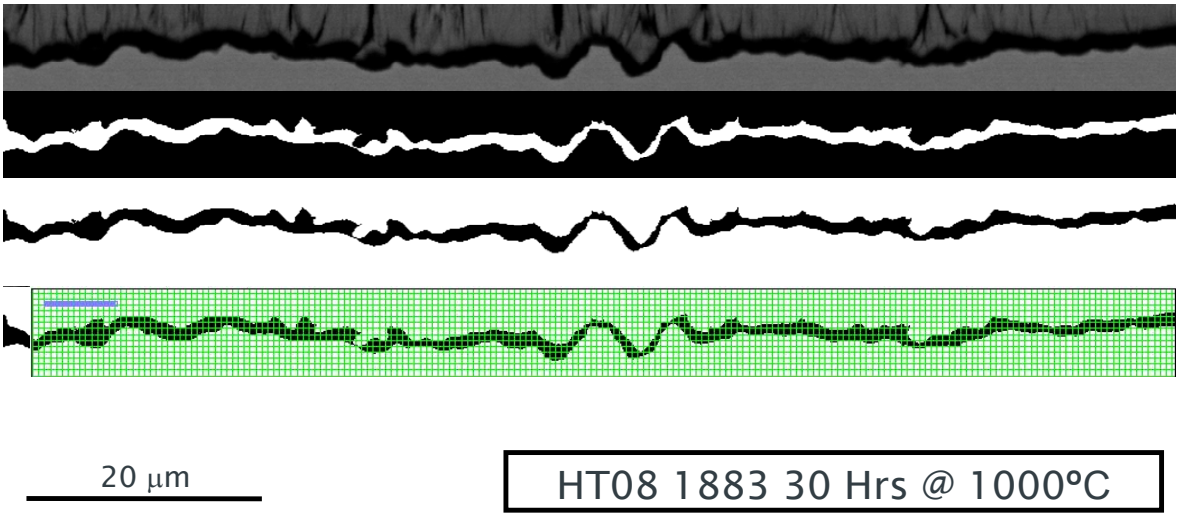

Figure 133 Example of image manipulation and manual measuring grid, specimen HT08 1883 isothermal exposure for 30 hours at 1000°C.

Table 34 Isothermal exposure testing completion status.

Nominal Exposure Time (h)	Temperature (°C)				
	950	1000	1050	1100	1150
30	30 h	30 h	30 h	30 h	30 h
100	100 h	100 h	100 h	100 h	x
300	300 h	300 h	300 h	x	x
1000	1029 h	1057 h	x	x	x
3000	3025 h	x	x	x	x

Final exposure times in hours shown, x indicates TBC spalled off during exposure

Table 35 Two stage temperature exposures testing completion status.

First Stage				
Temperature	1000°C	1050°C	1100°C	1100°C
Exposure	306 h	300 h	100 h	x
Second Stage				
Temperature	950°C	950°C	950°C	950°C
Exposure	1027 h	1002 h	1028 h	x

Final exposure times in hours shown, x indicates TBC spalled off during exposure

Table 36 Thermal cyclic exposures testing completion status.

Nominal Cycles	Temperature (°C)			
	1000	1050	1100	1150
300	300	300	300	x

Final exposure cycles shown, x indicates TBC spalled off during exposure

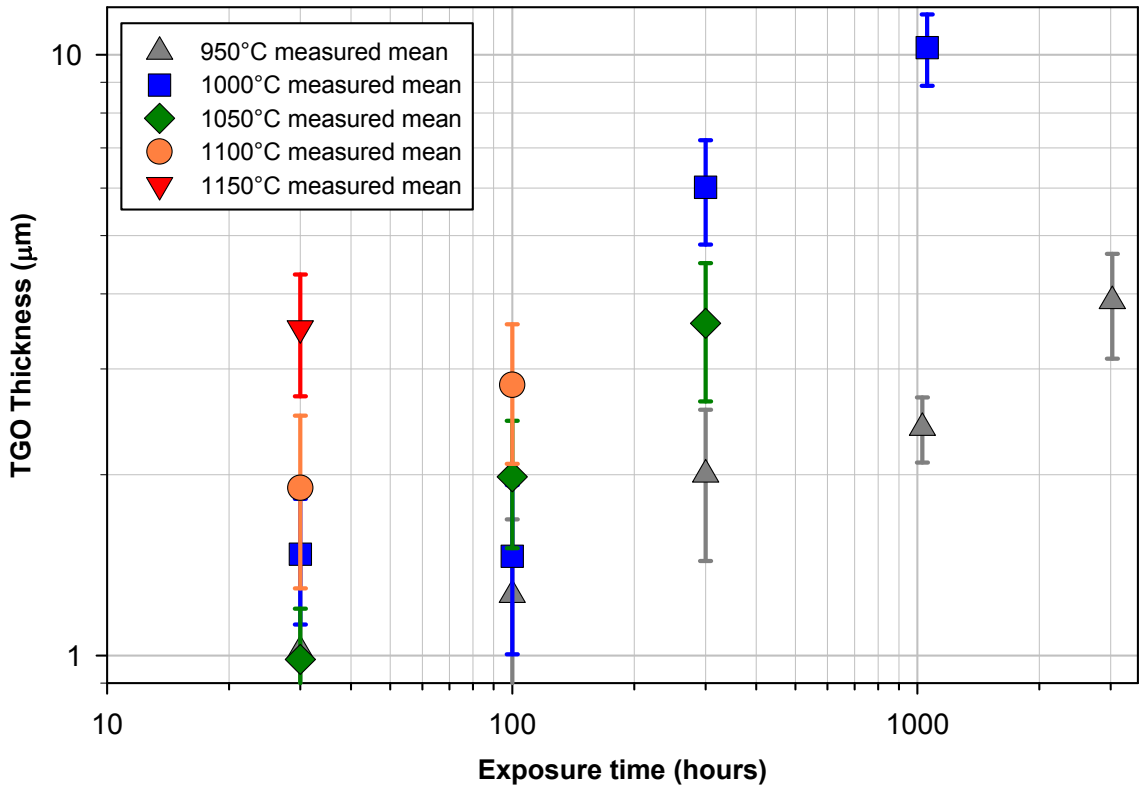

Figure 134 TGO thickness following isothermal exposure at 950°C, 1000°C, 1050°C, 1100°C and 1150°C for differing times.

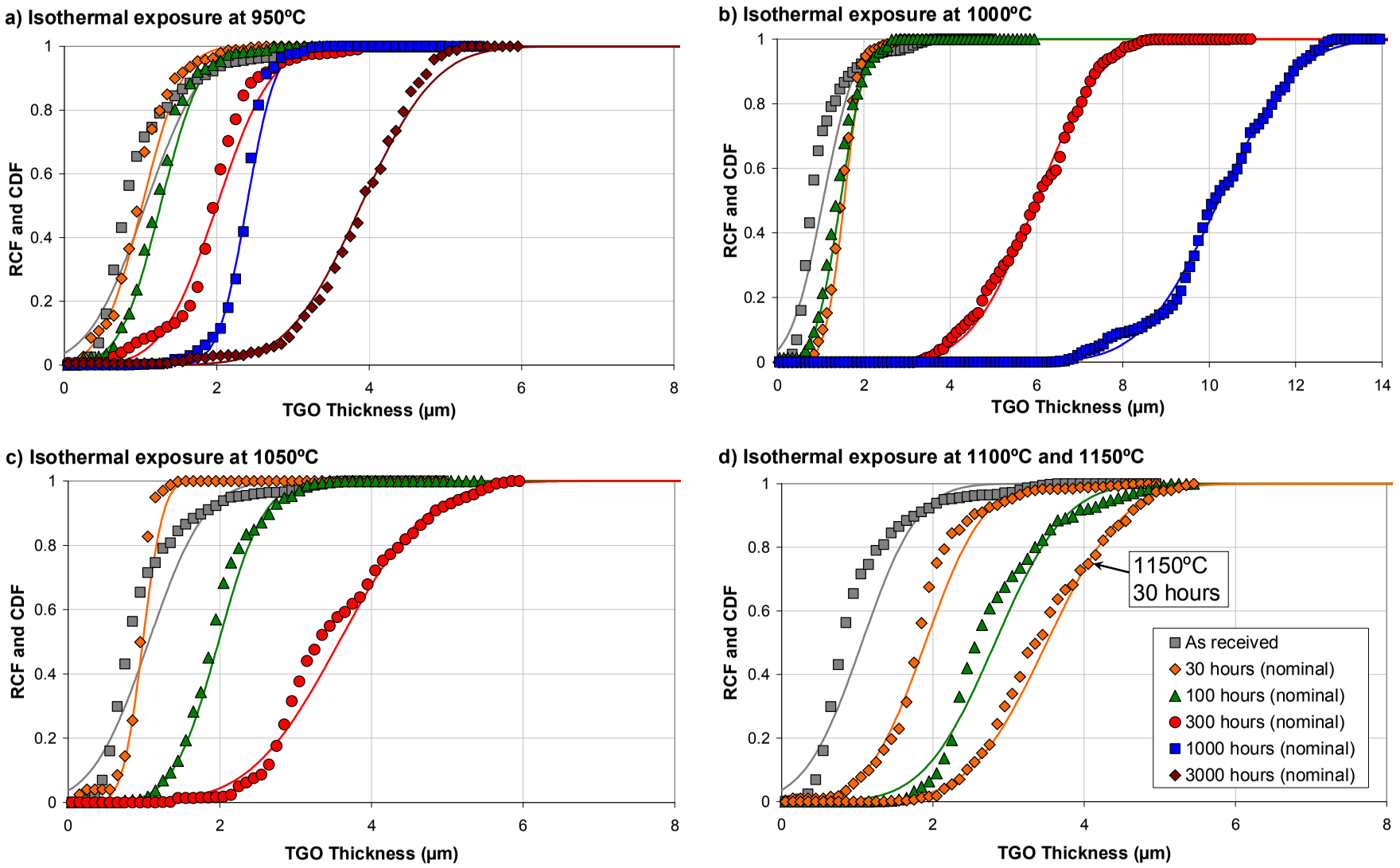

Figure 135 Relative Cumulative Frequency (RCF) and Cumulative Distribution Function (CDF) of TGO thickness following isothermal exposure at 950°C, 1000°C, 1050°C, 1100°C and 1150°C for differing times.

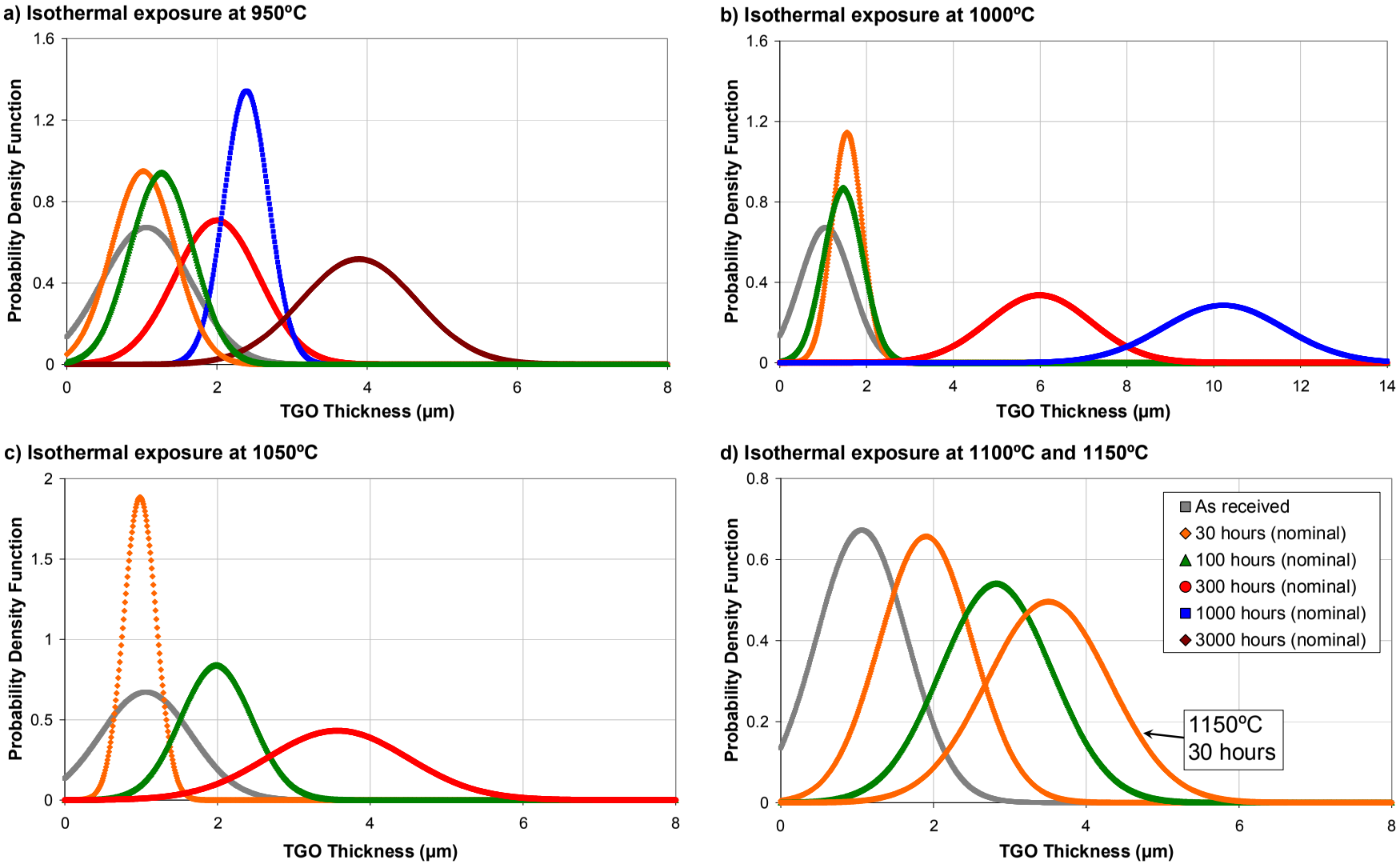

Figure 136 Probability Density Function of TGO thickness following isothermal exposure at 950°C, 1000°C, 1050°C, 1100°C and 1150°C for differing times.

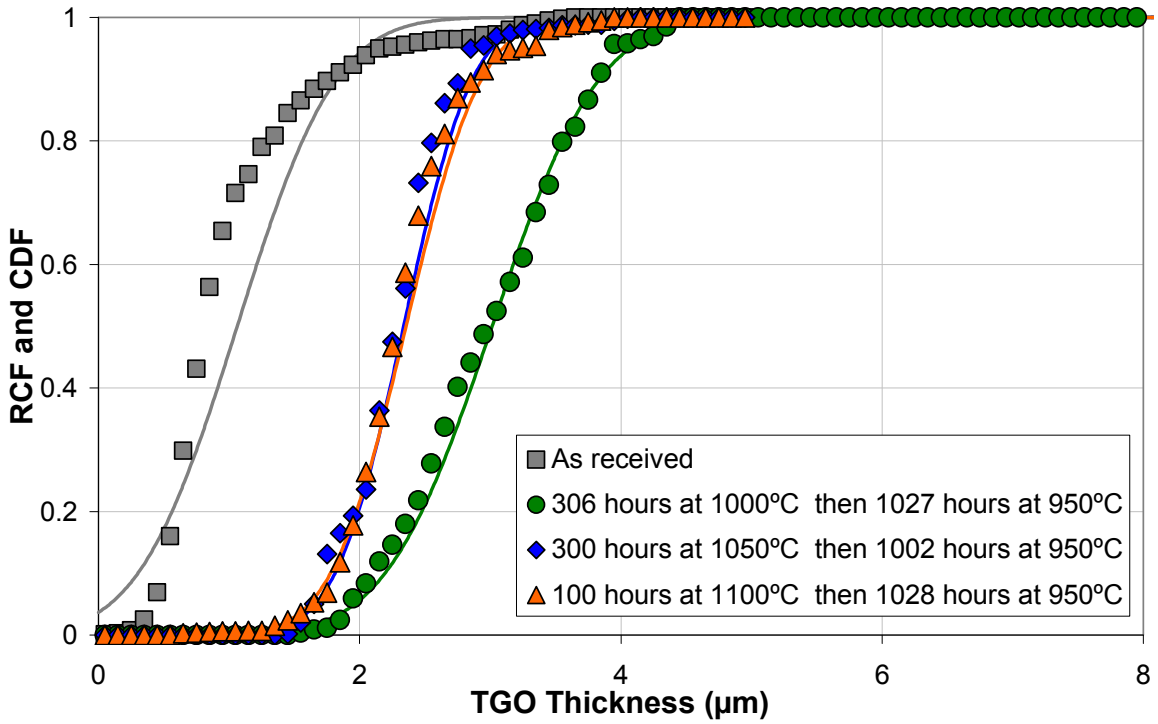

Figure 137 Relative Cumulative Frequency (RCF) and Cumulative Distribution Function (CDF) of TGO thickness following two stage temperature exposures for differing times and temperatures.

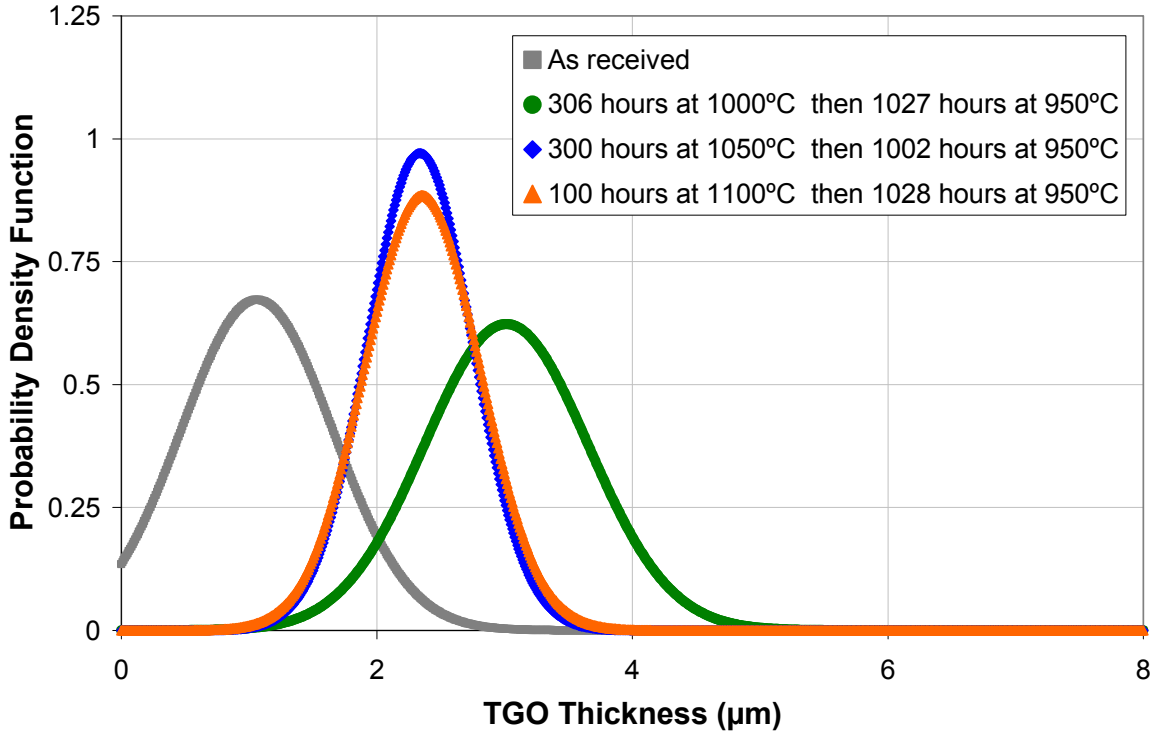

Figure 138 Probability Density Function (PDF) of TGO thickness following two stage temperature exposures for differing times and temperatures.

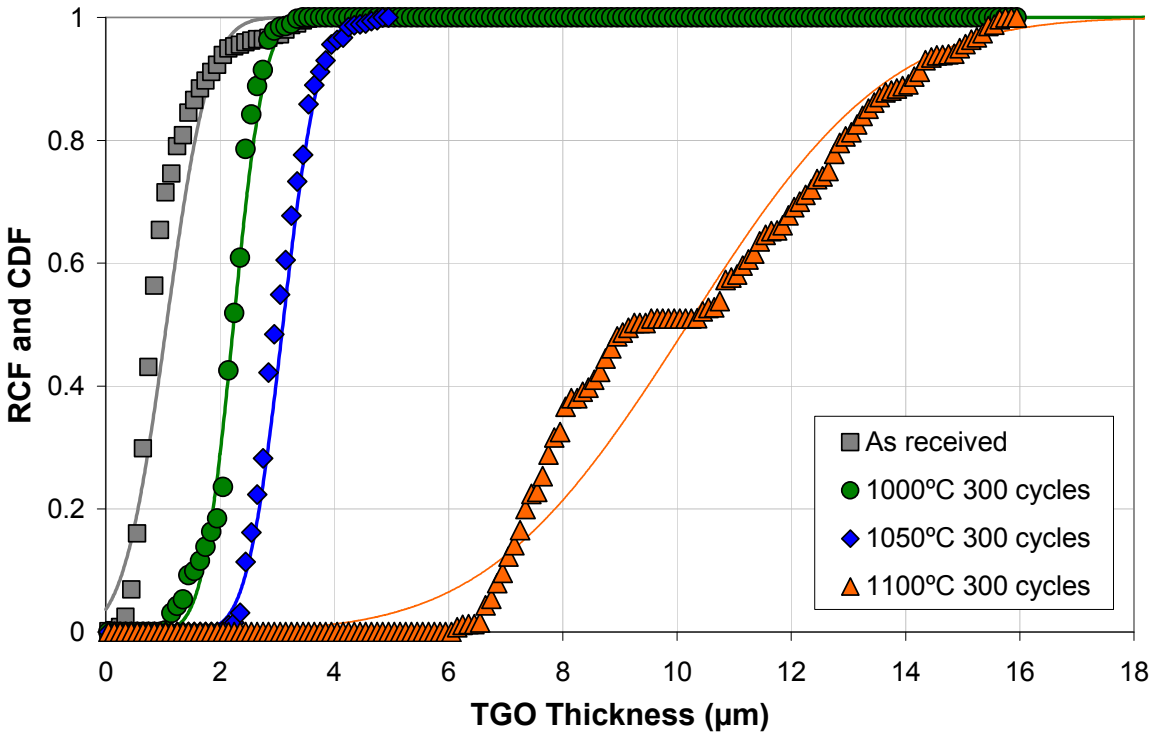

Figure 139 Relative Cumulative Frequency (RCF) and Cumulative Distribution Function (CDF) of TGO thickness following thermal cyclic exposure for 300 cycles at 1000°C, 1050°C, and 1100°C.

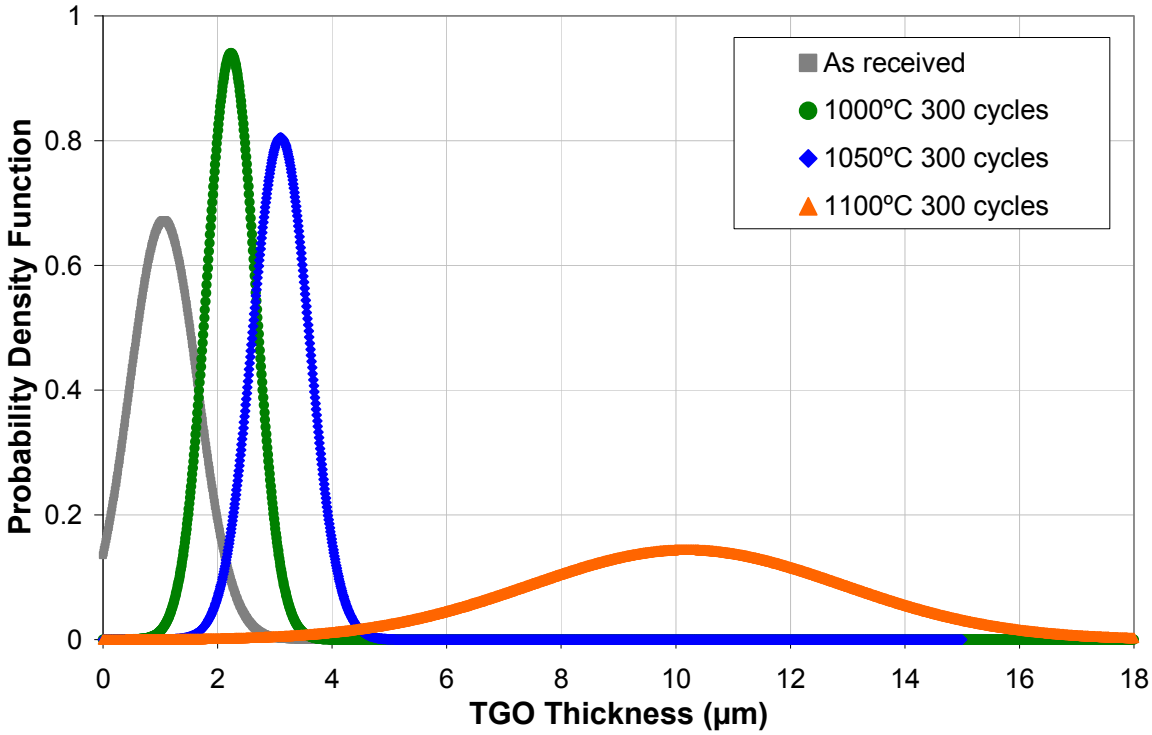

Figure 140 Probability Density Function (PDF) of TGO thickness following thermal cyclic exposure for 300 cycles at 1000°C, 1050°C, and 1100°C.

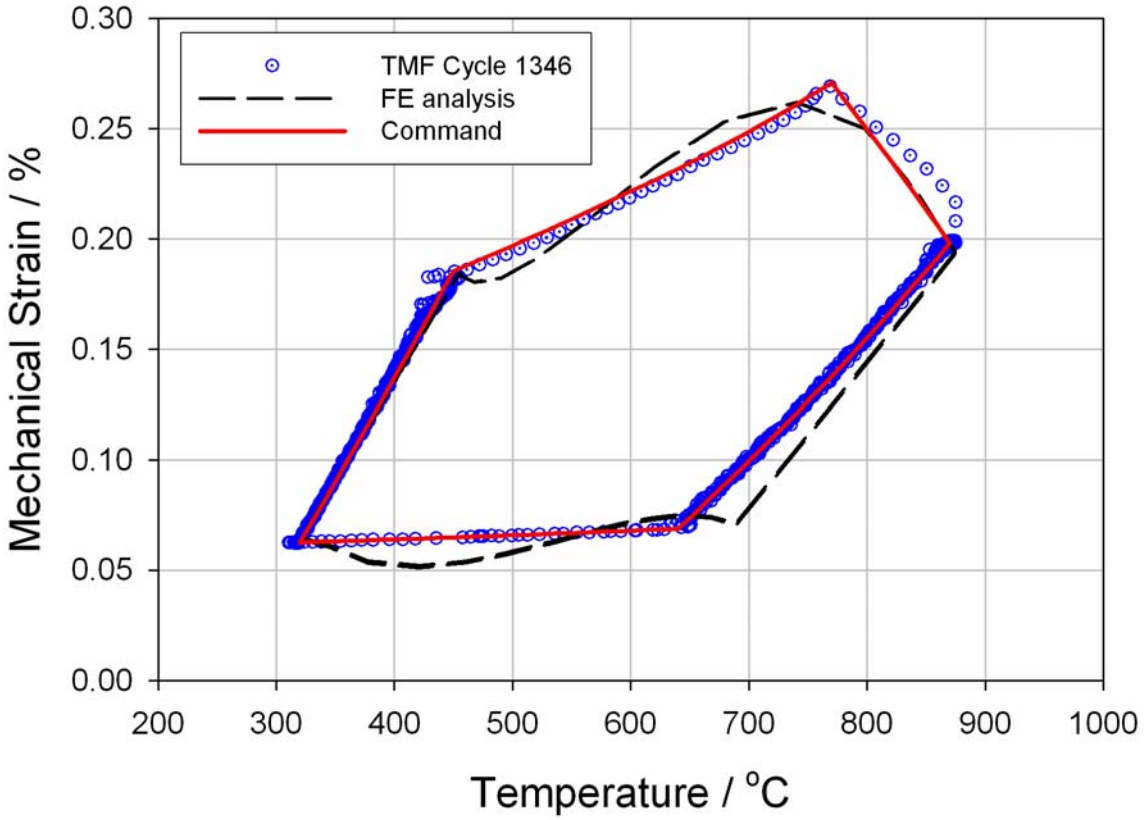

Figure 141 TMF test of specimen with no pre-exposure; Cycle 1346; Commanded and Achieved Strain versus Substrate Temperature.

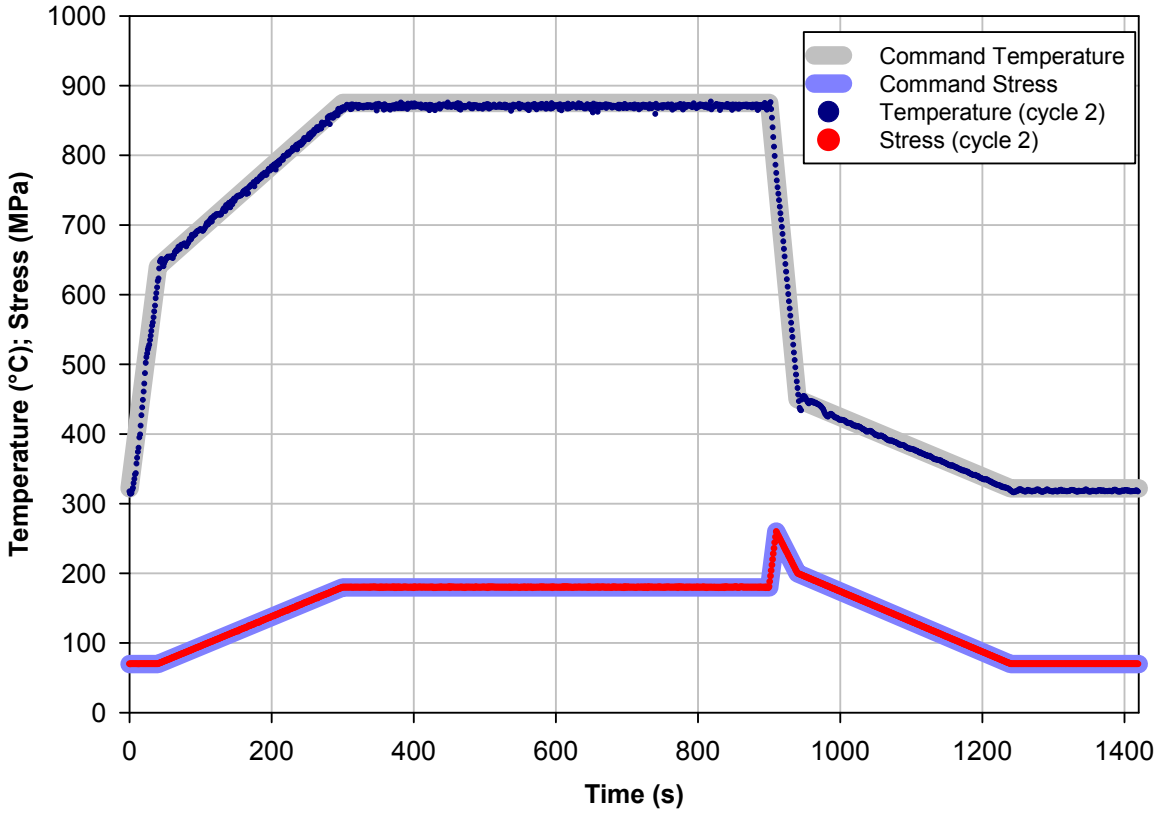

Figure 142 TMF test of specimen with no pre-exposure; Cycle 2; Commanded Substrate Temperature and Stress; Achieved Substrate Temperature and Stress; versus time.

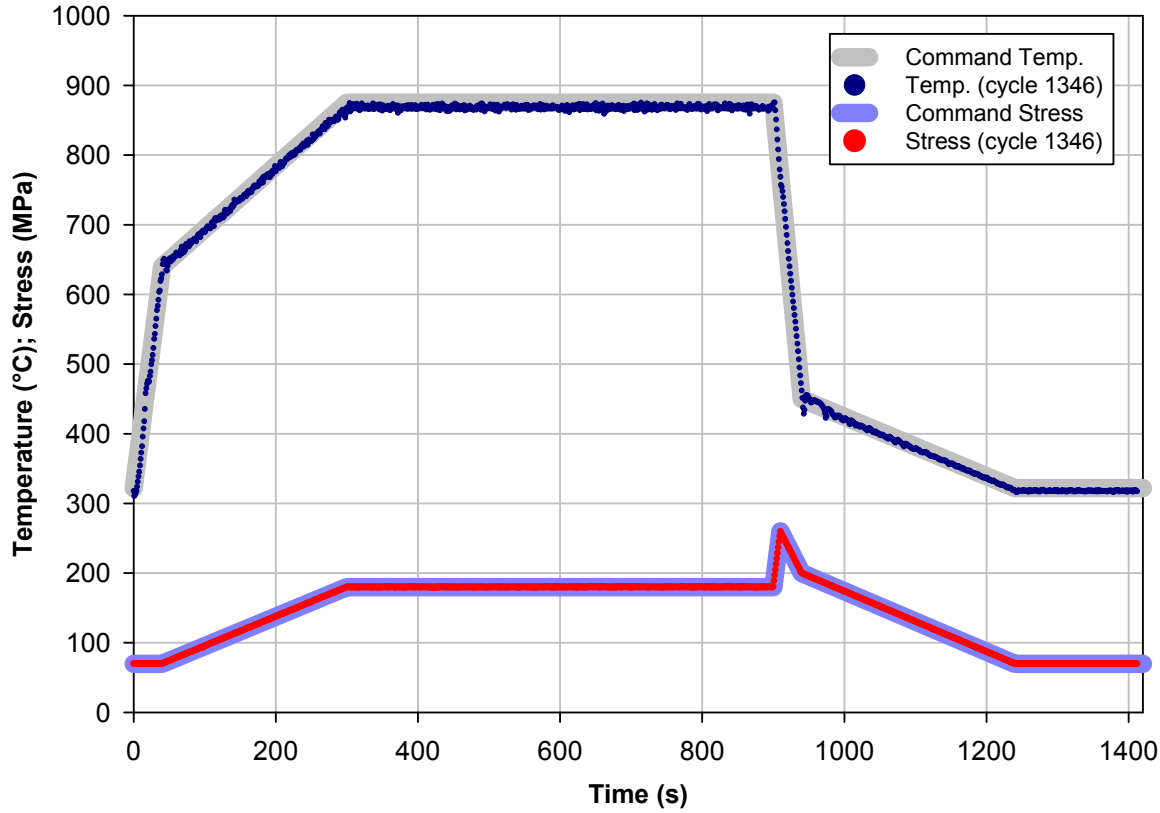

Figure 143 TMF test of specimen with no pre-exposure; Cycle 1346; Commanded Substrate Temperature and Stress; Achieved Substrate Temperature and Stress; versus time.

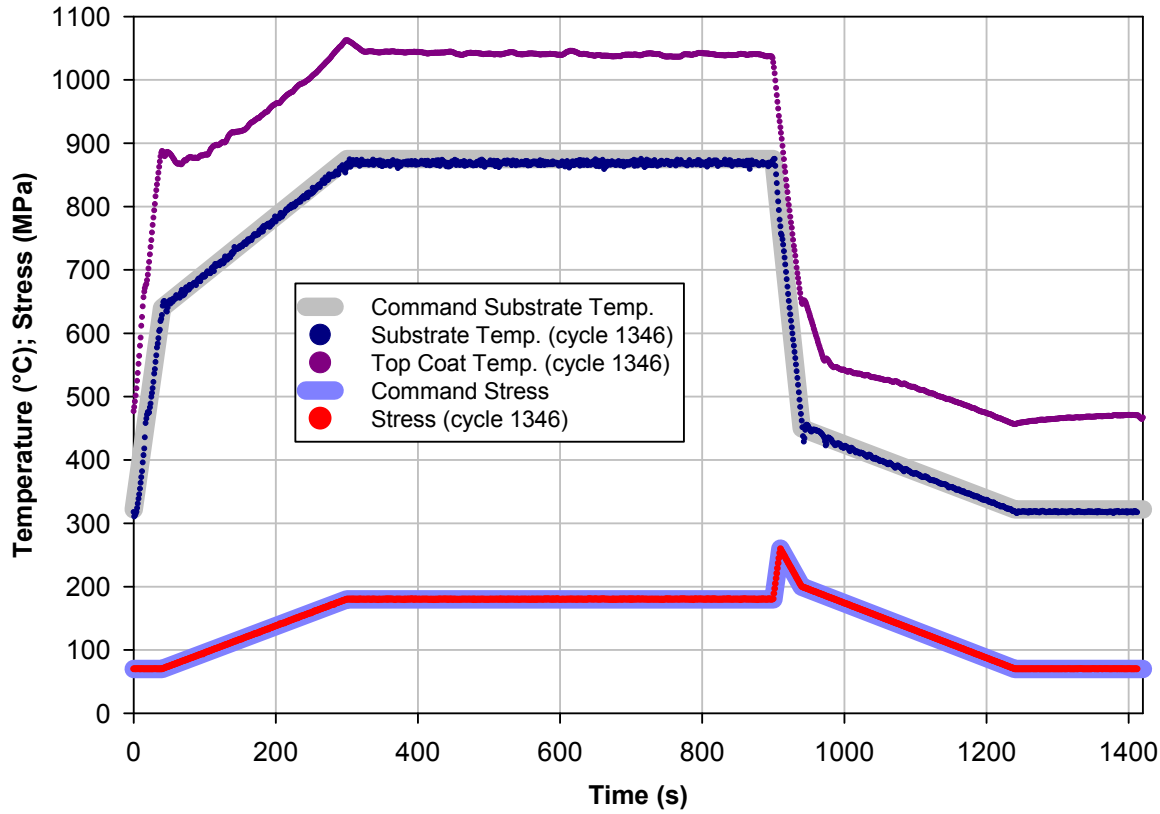

Figure 144 TMF test of specimen with no pre-exposure; Cycle 1346; Commanded Substrate Temperature and Stress; Achieved Substrate Temperature and Stress; Monitored Top Coat Temperature; versus time.

Table 37 TMF testing completion status.

Pre-exposure at 1000°C in air (h)	Total TMF Cycles completed
Nil	1346
100	1300
300	1400 (Signs of spallation from cycle 754)
900	Test not carried out

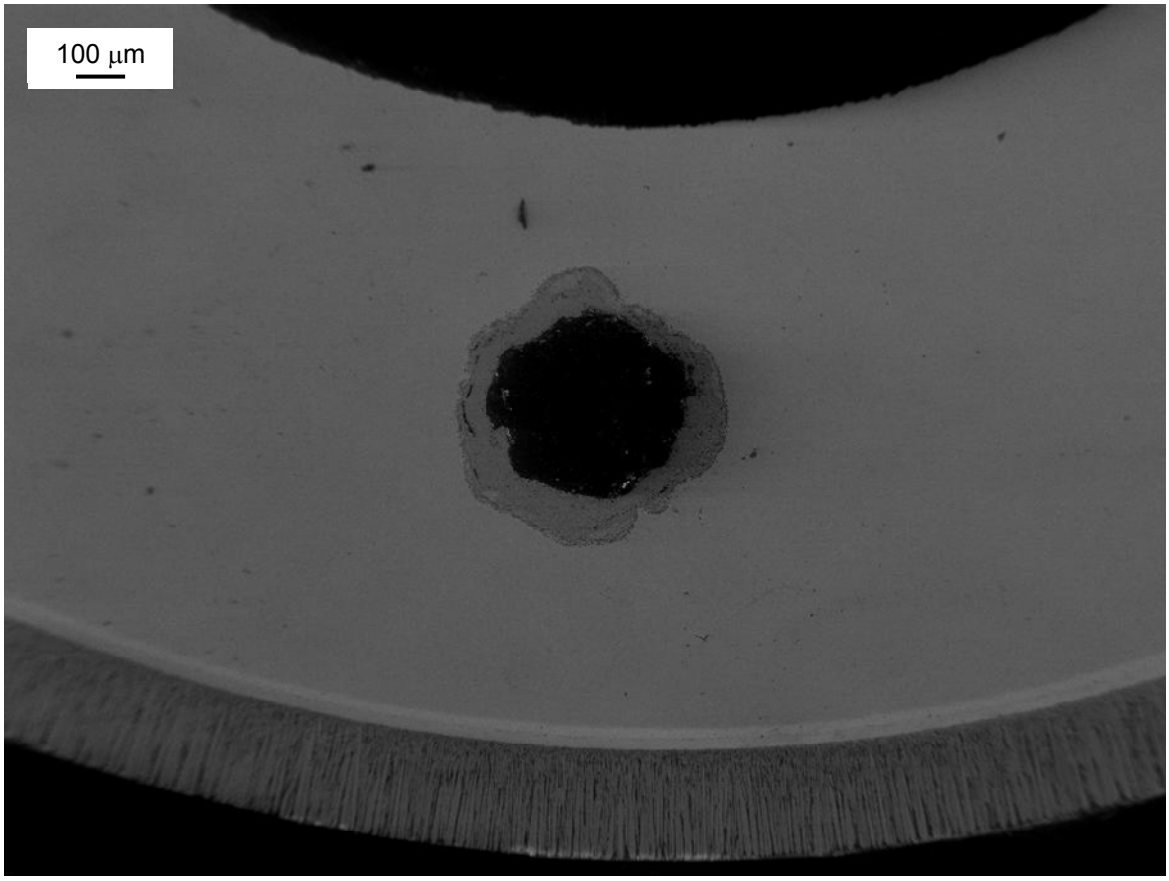

Figure 145 Section through TMF test specimen with no pre-exposure.

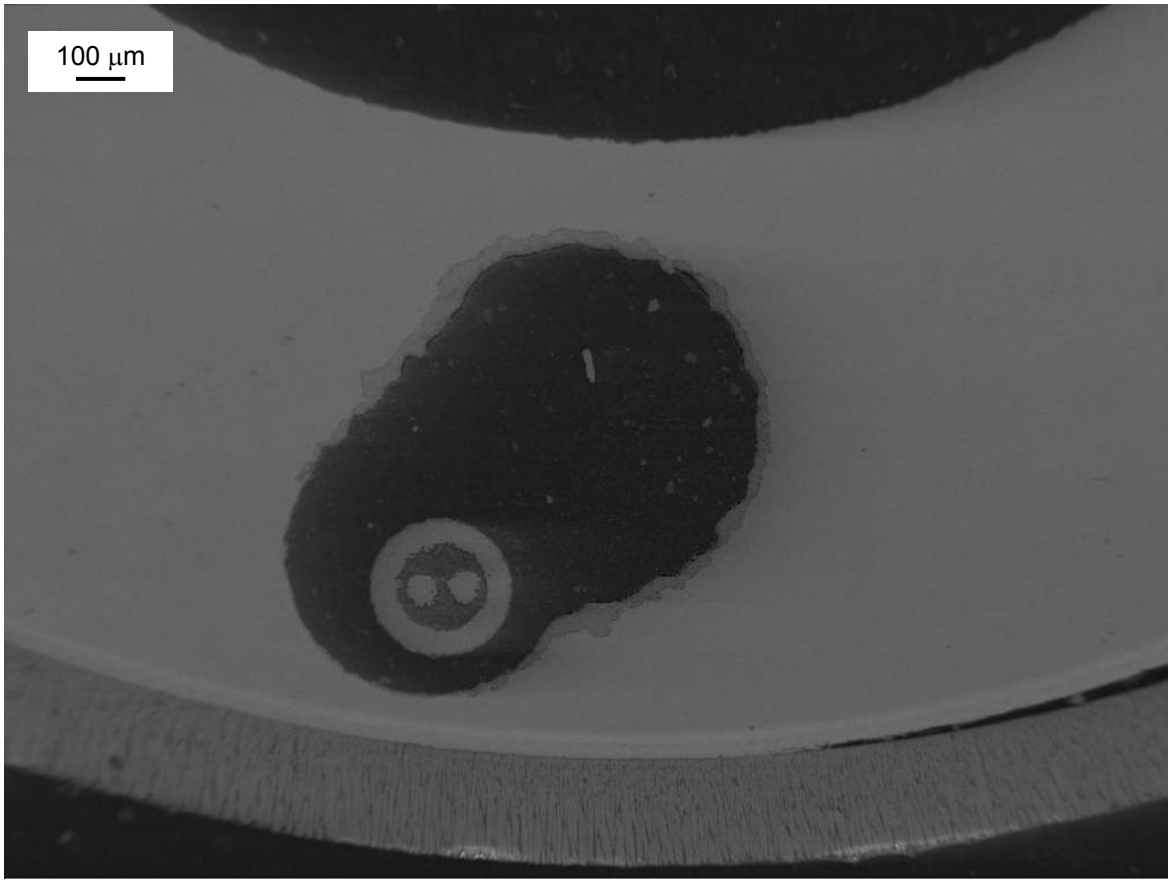

Figure 146 Section through TMF test specimen pre-exposed for 100 hours at 1000°C.

(a) Spallation of TBC in necked area (b) Close up of spallation

Figure 147 TMF test specimen pre exposed for 300 hours at 1000°C spallation started around 754 cycles.

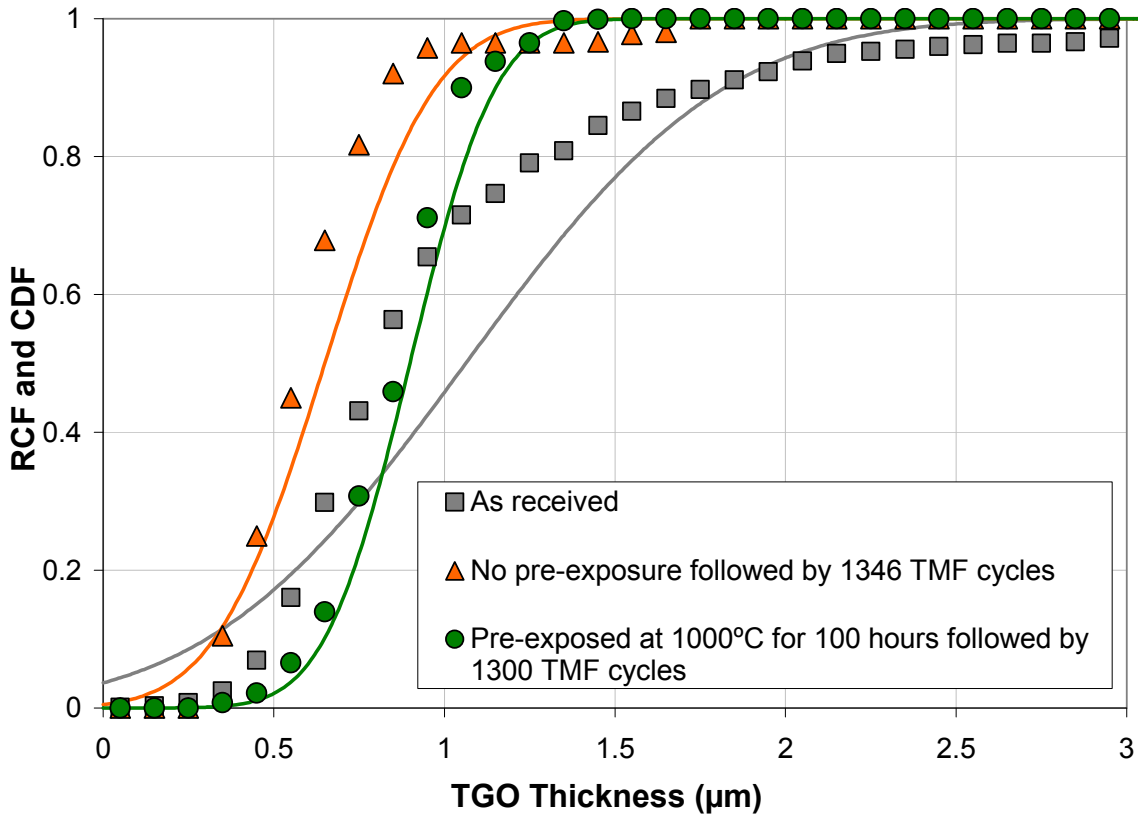

Figure 148 Relative Cumulative Frequency (RCF) and Cumulative Distribution Function (CDF) of TGO thickness following TMF testing.

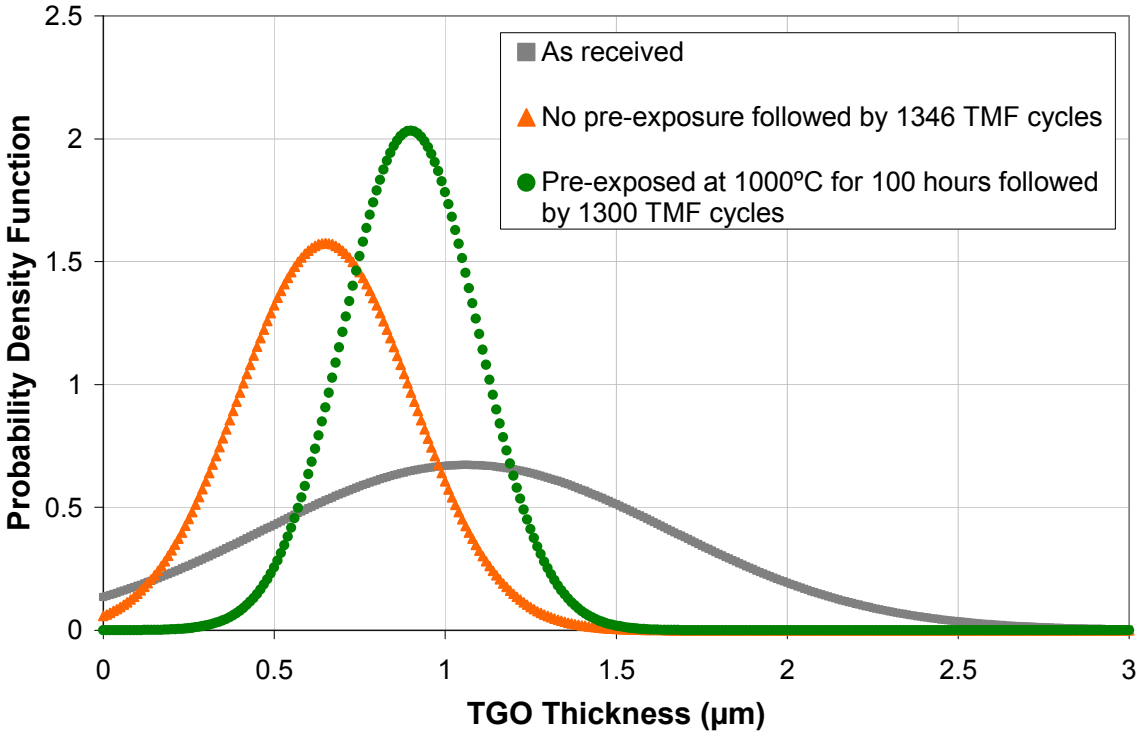

Figure 149 Probability Density Function (PDF) of TGO thickness following TMF testing.

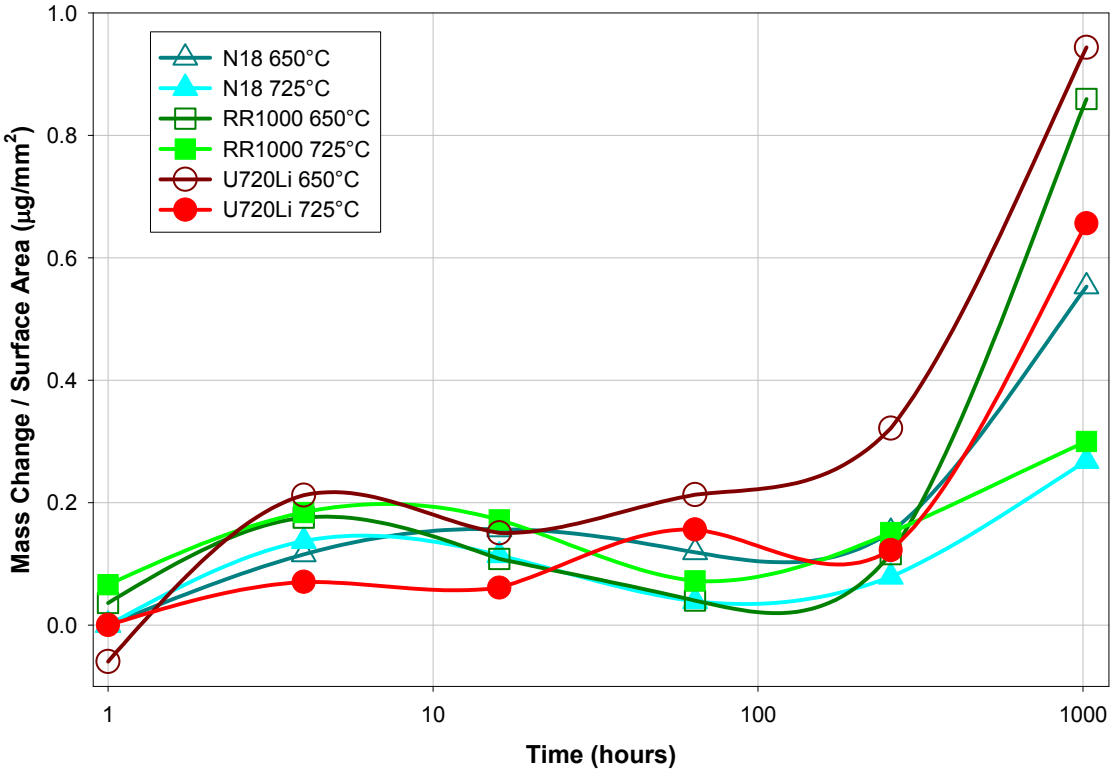

Figure 150 Oxidation Study N18, RR1000 and U720Li - Mass Change / Surface Area versus Oxidation Time.

Table 38 Tensile strength data sub-solvus heat treated LSHR at various temperatures.

Material	Tensile Strength Measure (MPa)	20°C	650°C	750°C
LSHR (sub-solvus heat treatment)[64]	0.2% proof stress	1289	1167	1118
	UTS	1742	1539	1206

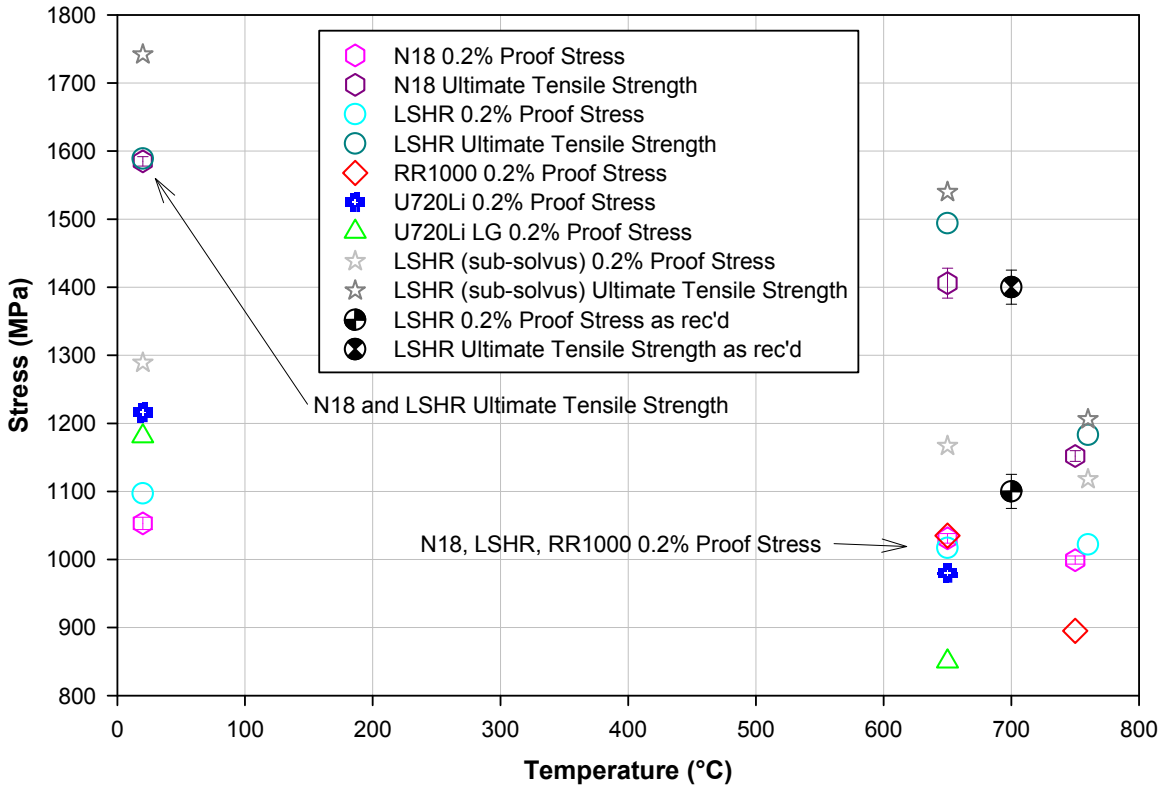

Figure 151 Tensile Strength Comparison between N18, LSHR (sub-solvus and super-solvus heat treated), RR1000, U720Li and U720Li LG.

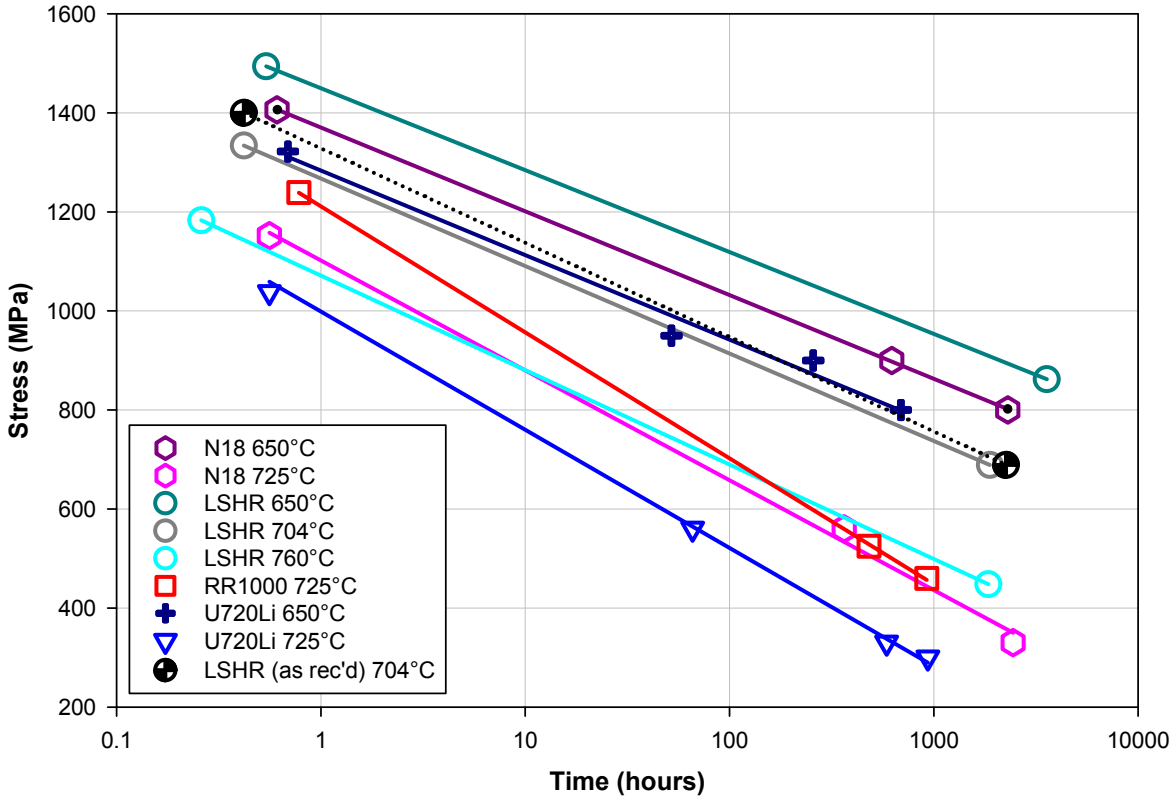

Figure 152 Creep Rupture Time Comparison between N18, LSHR (super-solvus heat treated), RR1000 and U720Li.

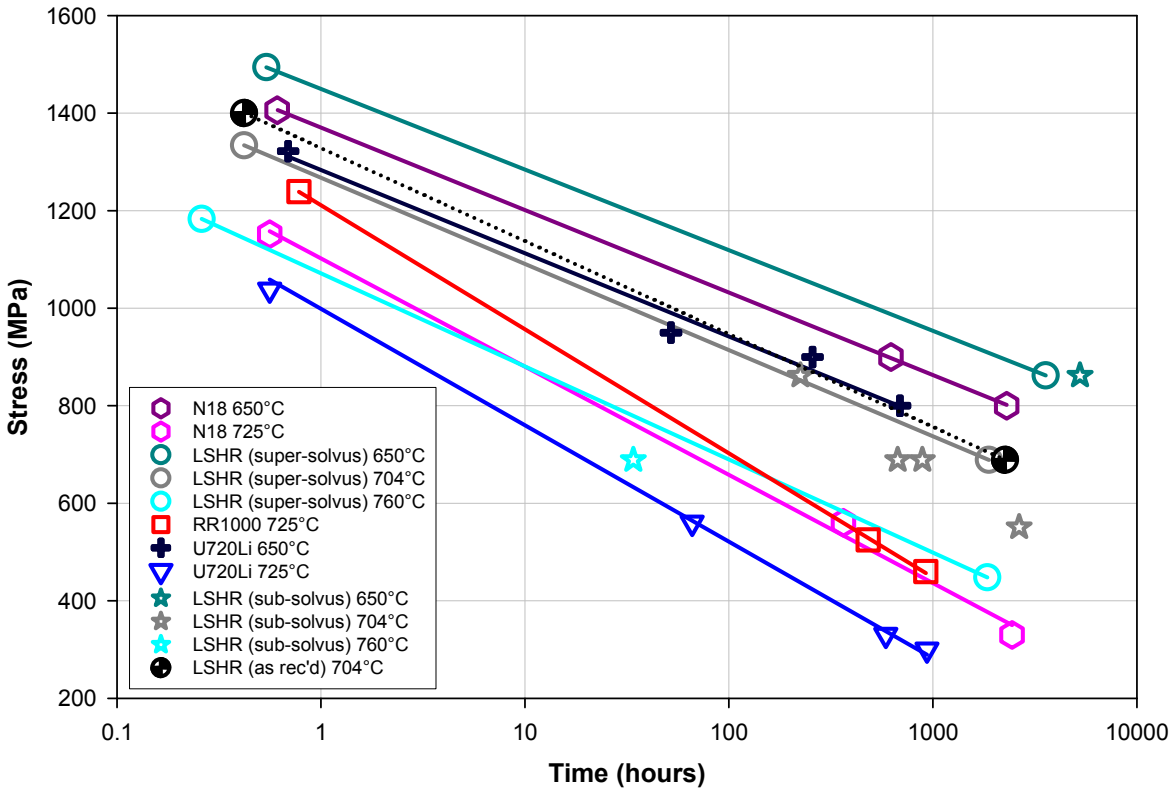

Figure 153 Creep Rupture Time Comparison between N18, LSHR (sub-solvus and super-solvus heat treated), RR1000 and U720Li.

(a)

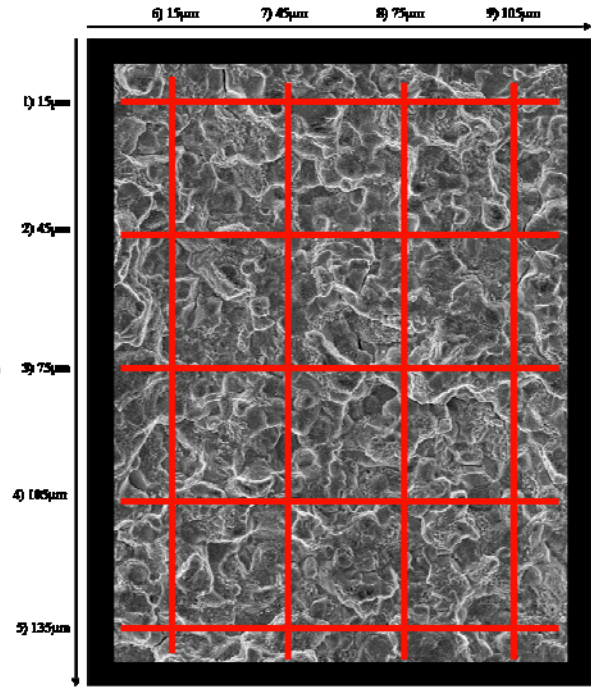

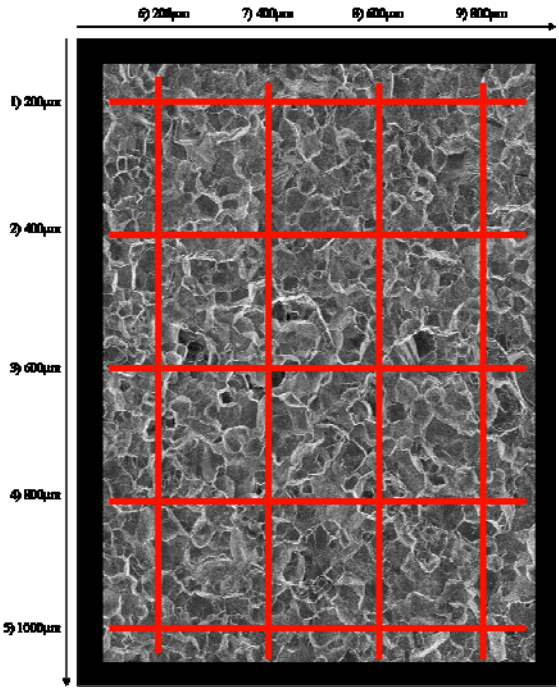

(b)

Figure 154 R_a profile measurement locations for (a) N18 and (b) LSHR, both 1-20-1-1, 650°C, Air at ΔK = 20[178].

(a)

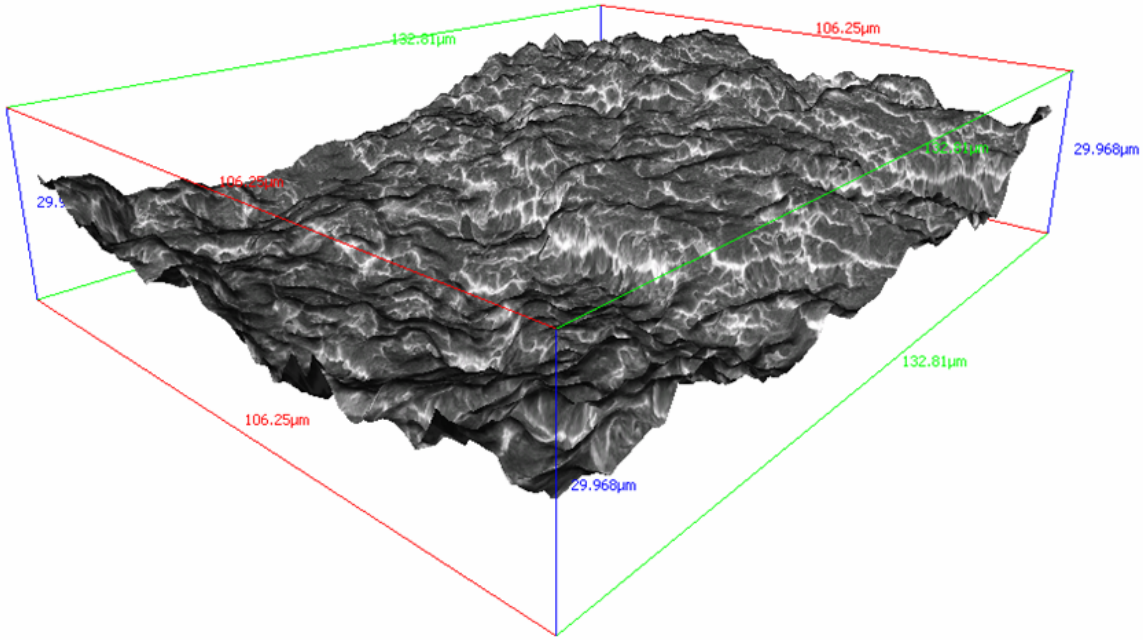

(b)

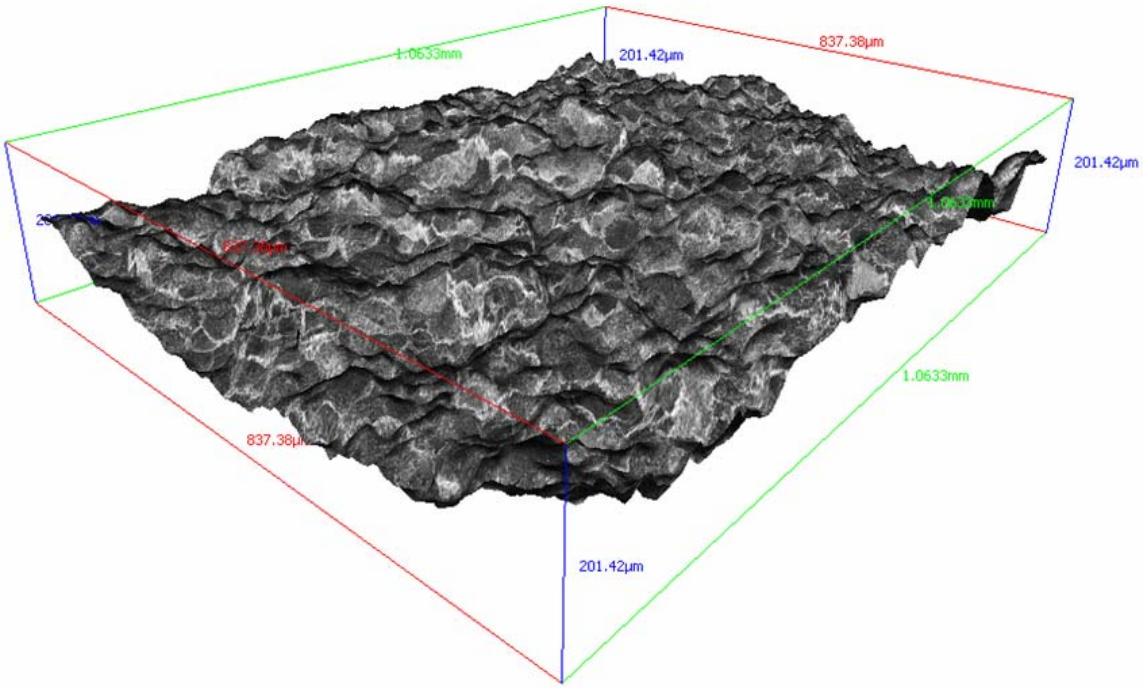

Figure 155 Three dimensional MeX® images of (a) N18 surface 1-1-1-1, 725°C, Air at ΔK = 20 MPa$\sqrt{m}$ and (b) LSHR surface 1-20-1-1, 650°C, Air at ΔK = 30 MPa$\sqrt{m}$[178].

Table 39 Long crack fracture surfaces, R_a and R_s at various ΔK for N18 and LSHR[178].

Material	Environment	Temperature, °C	Waveform	Roughness Parameter	ΔK, MPa$\sqrt{m}$		
					20	30	40
N18	Air	650	1-1-1-1	R_a, nm	121	90.5	115.6
				R_s	1.714	1.466	1.658
	Air	725	1-1-1-1	R_a, nm	102.3	128.5	136.4
				R_s	1.531	1.728	1.759
	Vacuum	725	1-1-1-1	R_a, nm	93.5	112.6	105.2
				R_s	1.507	1.605	1.528
	Air	650	1-20-1-1	R_a, nm	110.6	106.8	115.8
				R_s	1.656	1.629	1.639
	Air	725	1-20-1-1	R_a, nm	101.5	125.4	153.6
				R_s	1.542	1.693	1.962
	Vacuum	650	1-20-1-1	R_a, nm	74.7	77.9	100.7
				R_s	1.37	1.447	1.536
	Vacuum	725	1-20-1-1	R_a, nm	129.6	135.9	160.7
				R_s	1.741	1.784	1.865
LSHR	Air	650	1-20-1-1	R_a, nm	506.5	506.1	518.5
				R_s	1.874	1.907	1.959
	Air	725	1-20-1-1	R_a, nm	543.9	586.7	522.2
				R_s	1.923	2.076	1.938
	Vacuum	650	1-20-1-1	R_a, nm	629.6	601.4	497.1
				R_s	1.999	2.026	1.793
	Vacuum	725	1-20-1-1	R_a, nm	426.4	490.2	503.9
				R_s	1.664	1.83	1.896

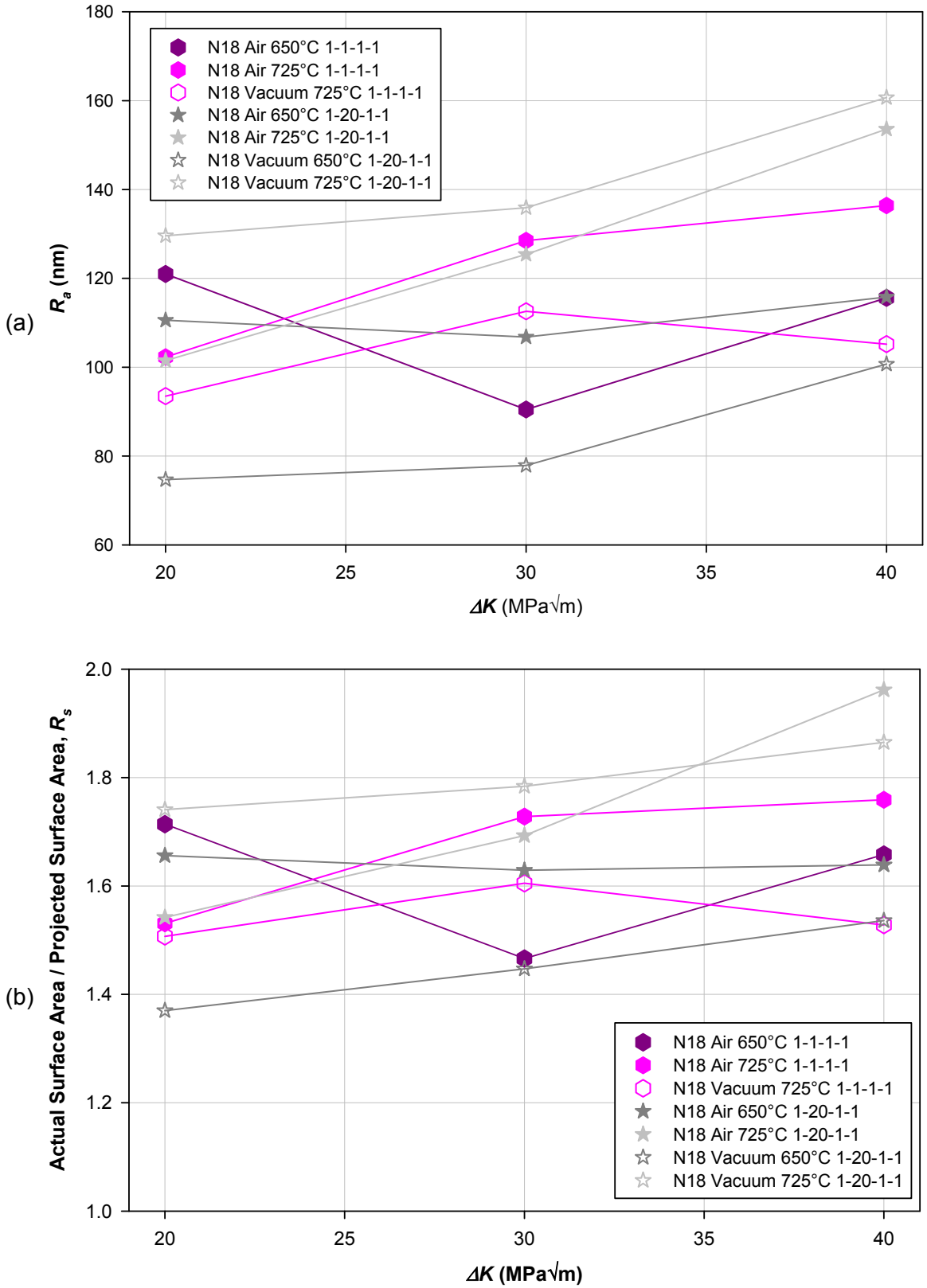

Figure 156 Roughness of N18 long crack fracture surfaces versus ΔK, (a) R_a and (b) R_s (actual surface area / projected surface area).

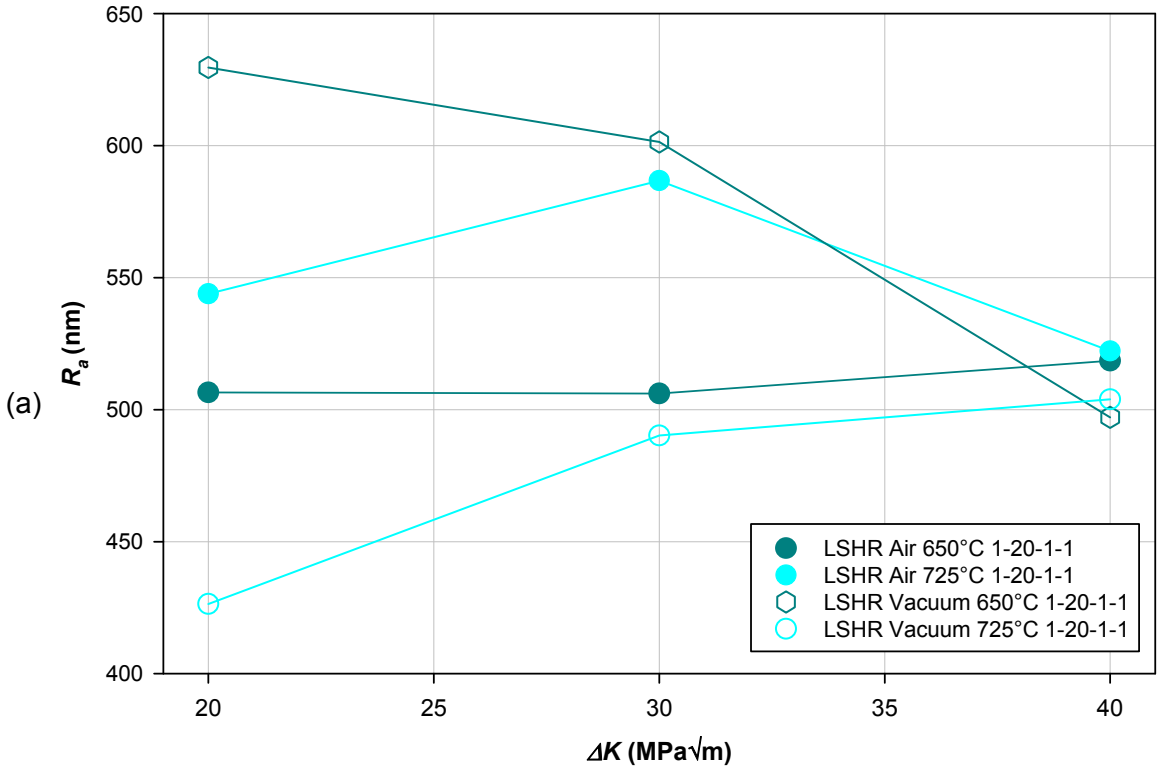

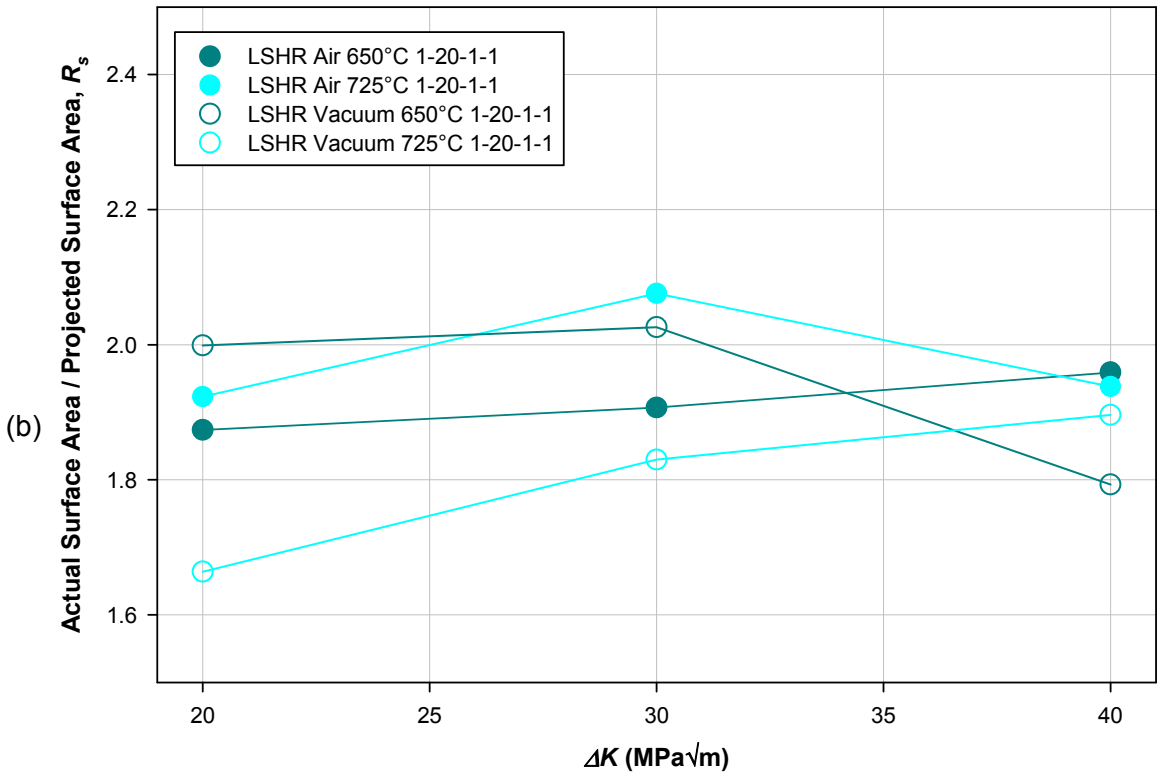

Figure 157 Roughness of LSHR long crack fracture surfaces versus ΔK, (a) R_a and (b) R_s (actual surface area / projected surface area).

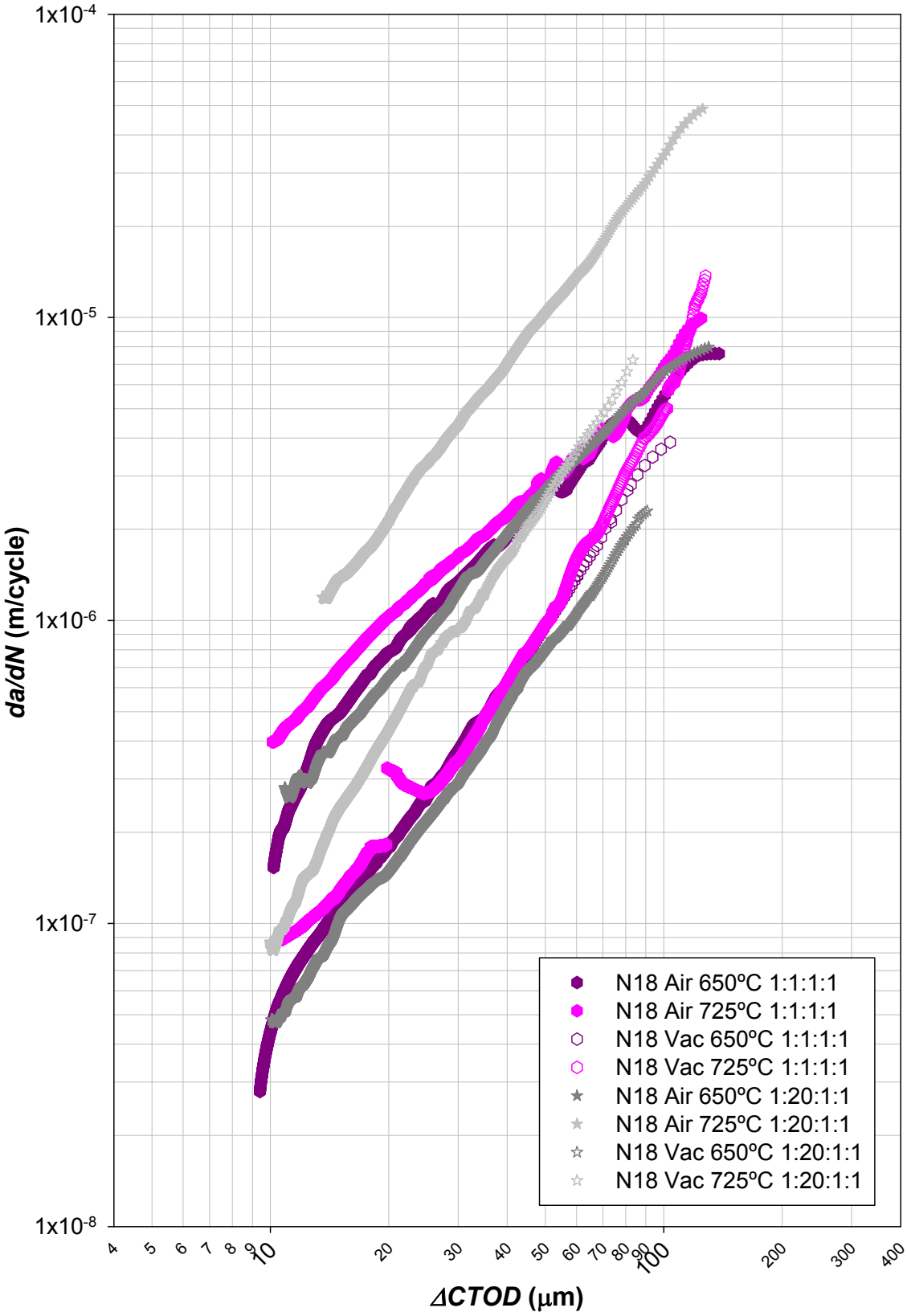

Figure 158 N18 *da/dN* vs. *ΔCTOD*, in air and vacuum at 650°C and 725°C 1-1-1-1 and 1-20-1-1 load cycles.

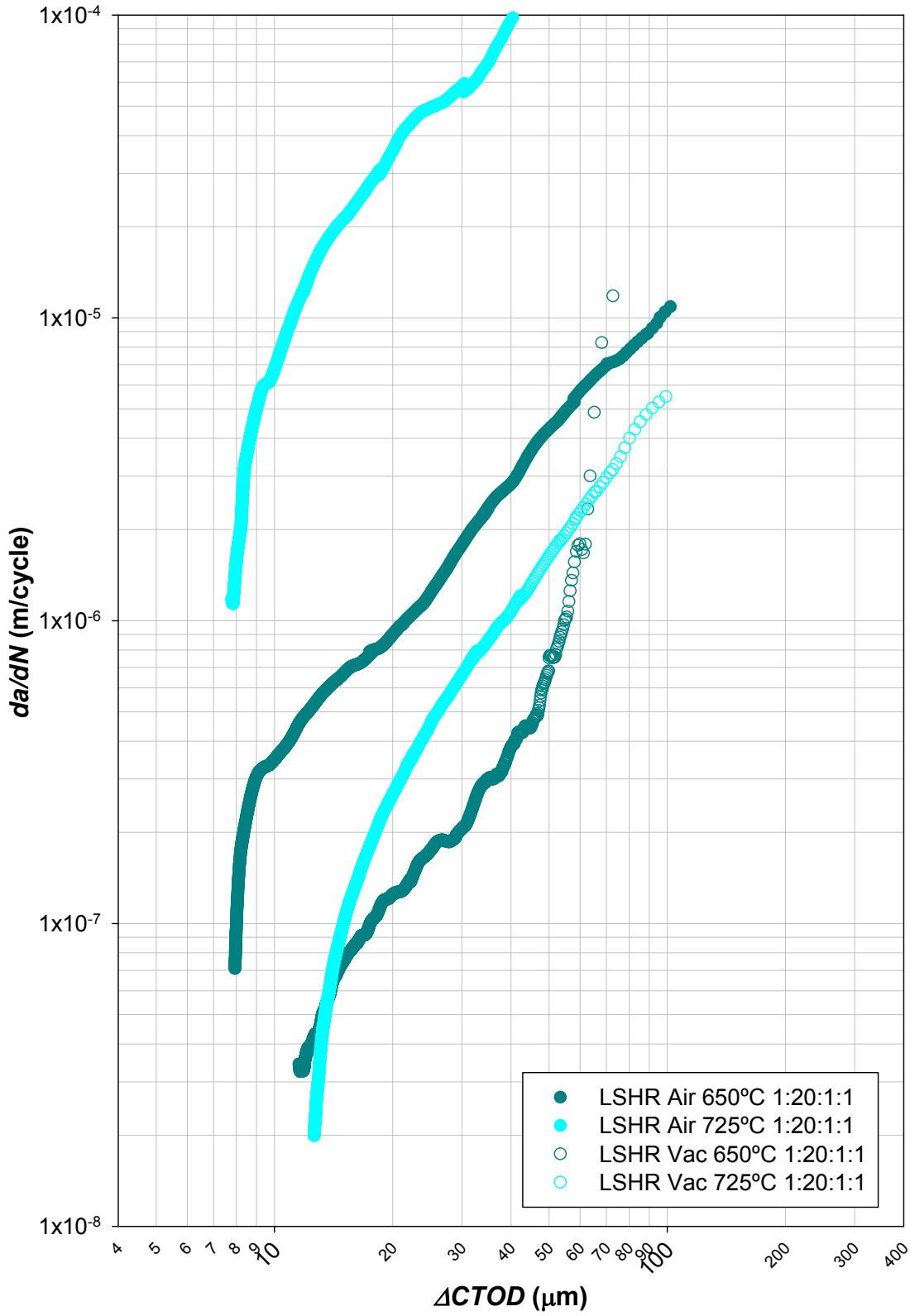

Figure 159 LSHR *da/dN* vs. *ΔCTOD*, in air and vacuum at 650°C and 725°C 1-20-1-1 load cycle.

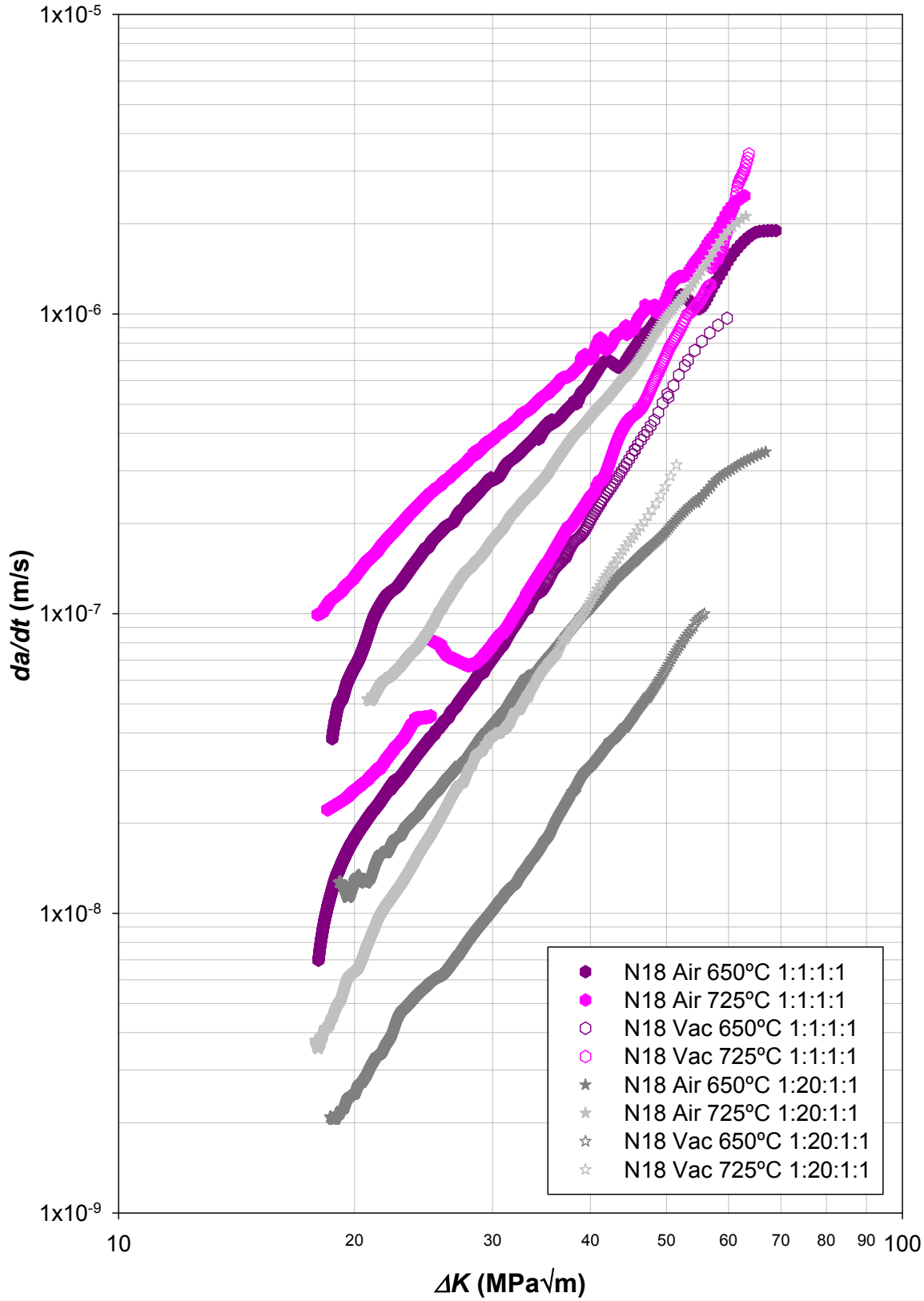

Figure 160 N18 *da/dt* vs. *ΔK*, in air and vacuum at 650°C and 725°C 1-1-1-1 and 1-20-1-1 load cycles.

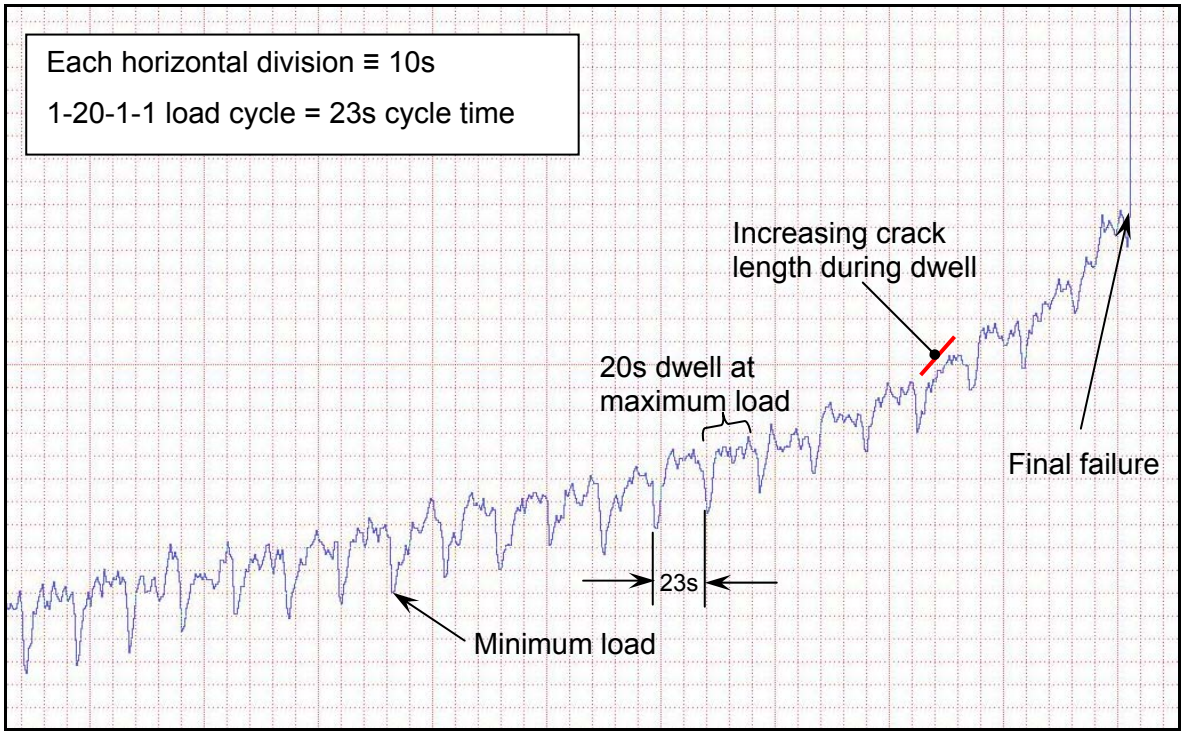

Figure 161 DATAQ data logger output showing increasing crack length during 20s dwell close to final failure.

Table 40 Activation energies for processes contributing to high temperature FCG. GB stands for grain boundary (after Starink and Reed[182]).

Process contributing to high temperature fatigue crack growth	Activation energy
Single process	
Oxidation of carbides	~250kJ/mol
Dynamic embrittlement	~250kJ/mol
Grain boundary creep	~150kJ/mol
Change in static properties	~0-60kJ/mol
Mixed processes	
Dynamic embrittlement of GBs and creep of ligaments	~250kJ/mol
GB creep failure + oxidation dominated FCG	~150-250kJ/mol
GB creep failure + non thermally activated failure	~0-150kJ/mol

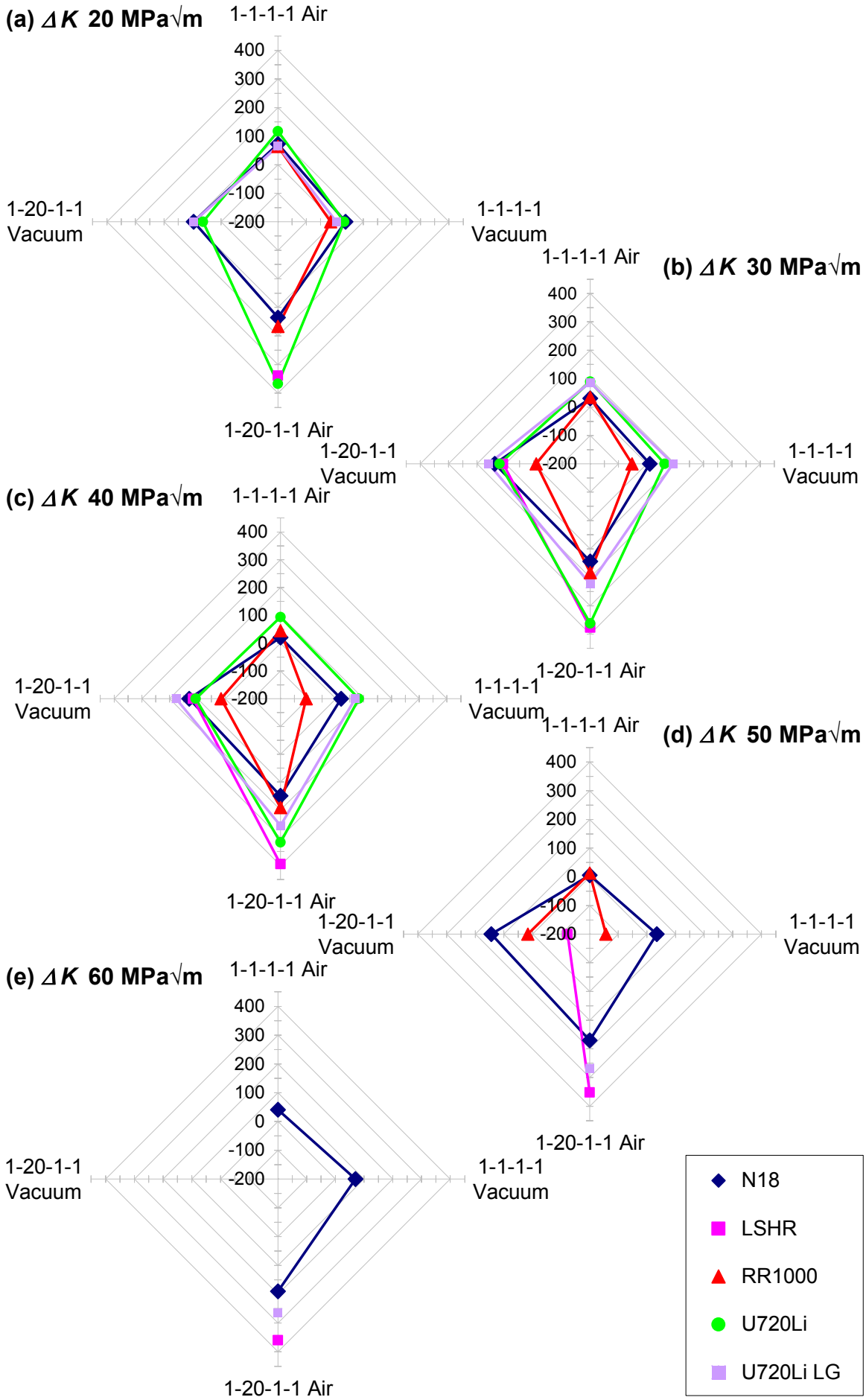

Figure 162 Apparent activation energy analysis various *ΔK* between 650°C and 725°C.

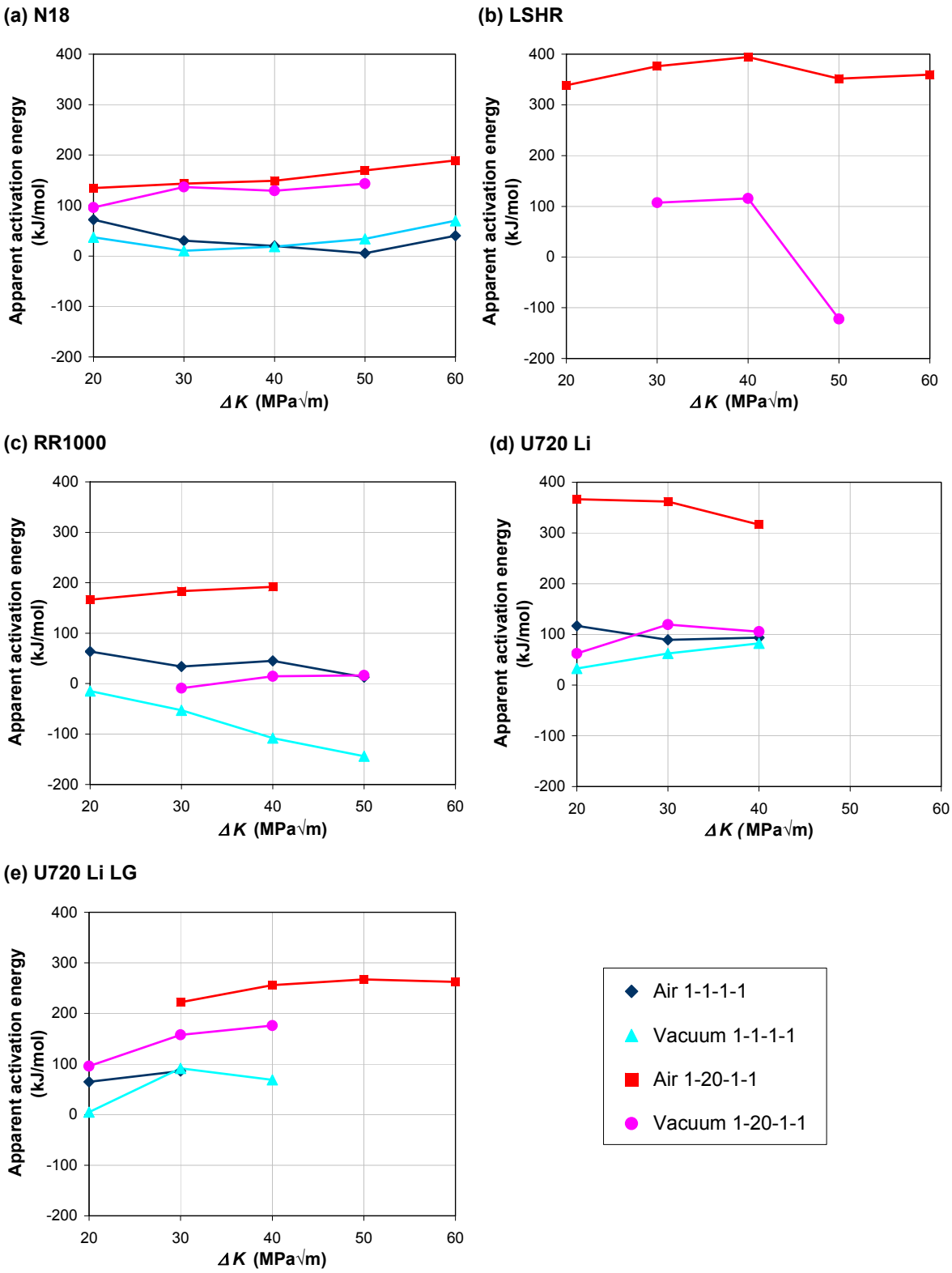

Figure 163 Apparent activation energy analysis between 650°C and 725°C.

(a)

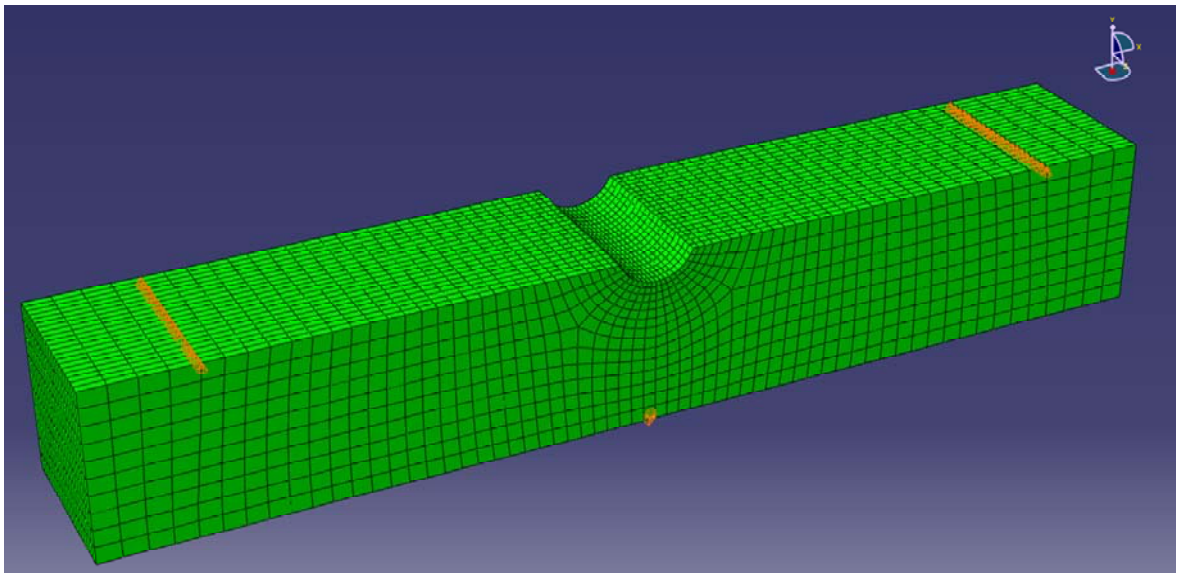

N18 U-notch finite element model mesh - 20 node quadratic hexahedral (C3D20RH type, 14200 elements, 64055 nodes). Mesh density is increased towards the notch root.

(b)

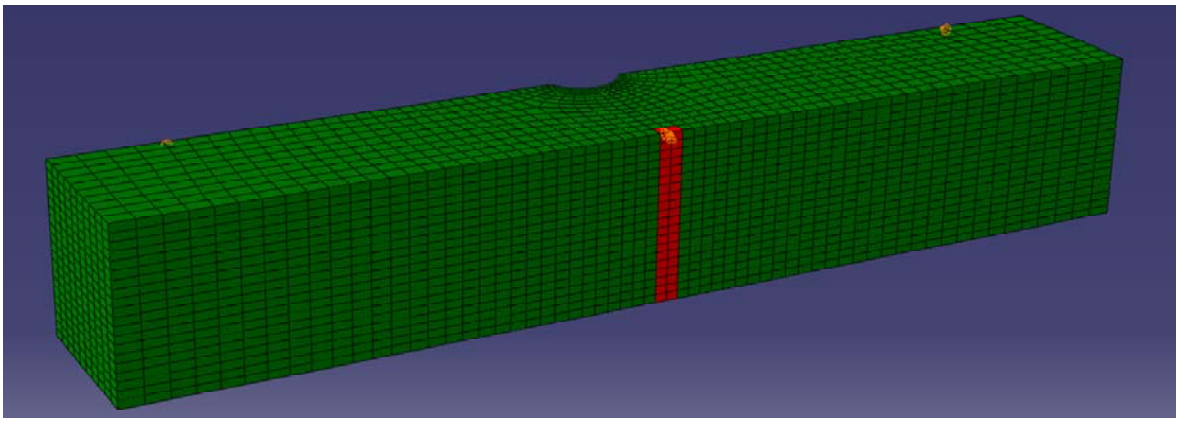

N18 U-notch finite element model mesh – Boundary conditions and loads

(c)

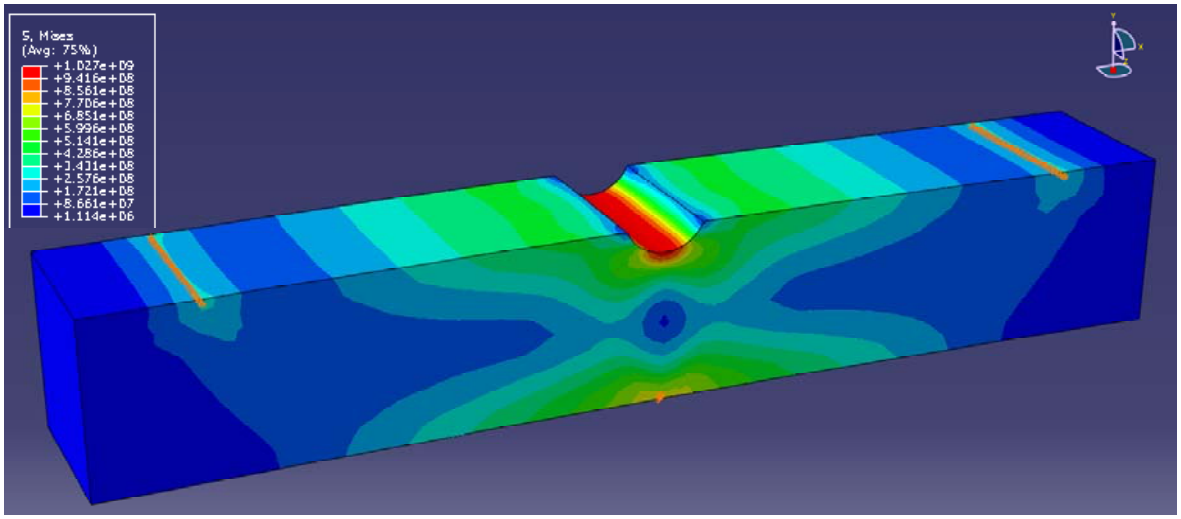

N18 U-notch finite element model – Typical von Mises Stress State (load = 6.2 kN)

Figure 164 Abaqus finite element model of N18 U-notch[186].

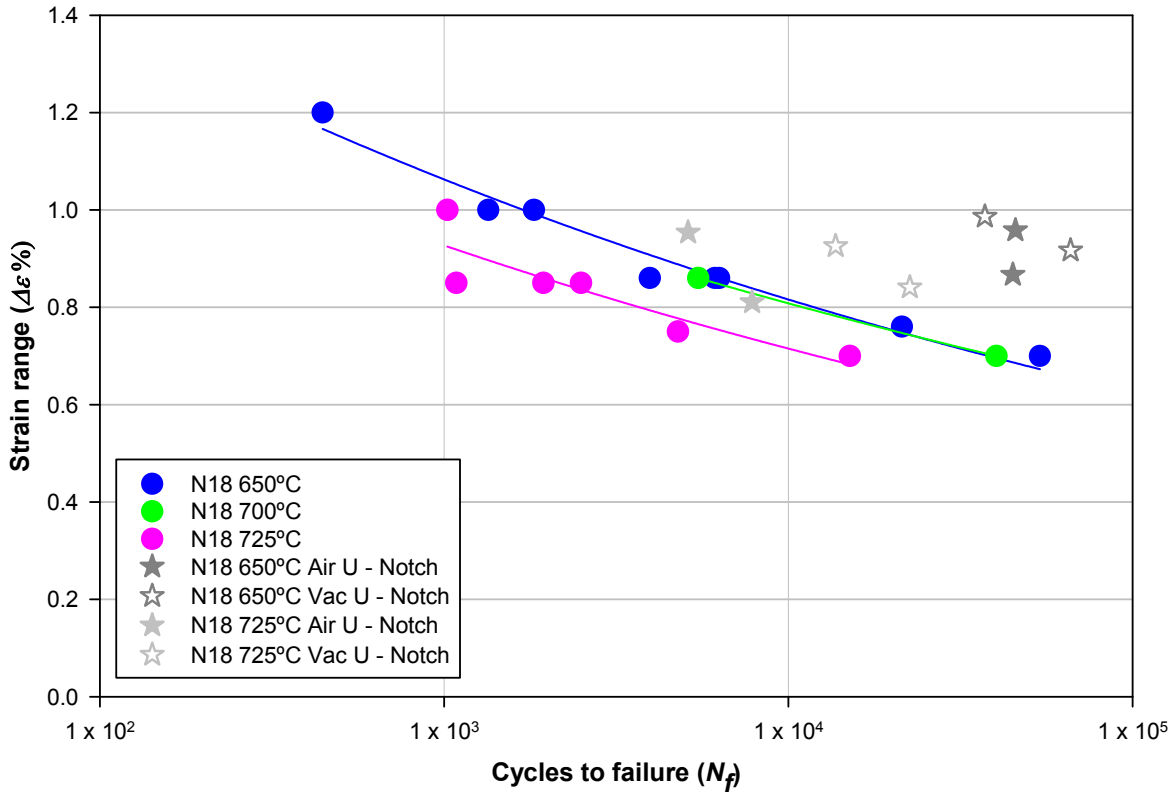

Figure 165 N18 LCF and U-notch equivalent strain range comparison.

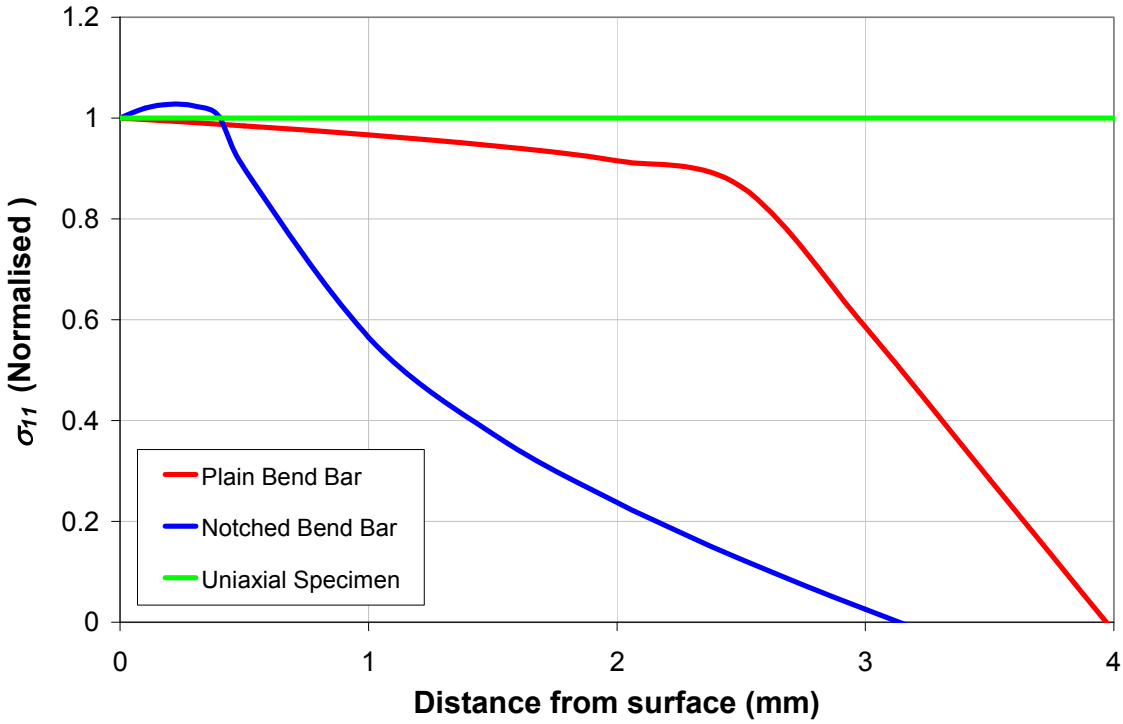

Figure 166 Typical stress states for different test specimen geometry[186].

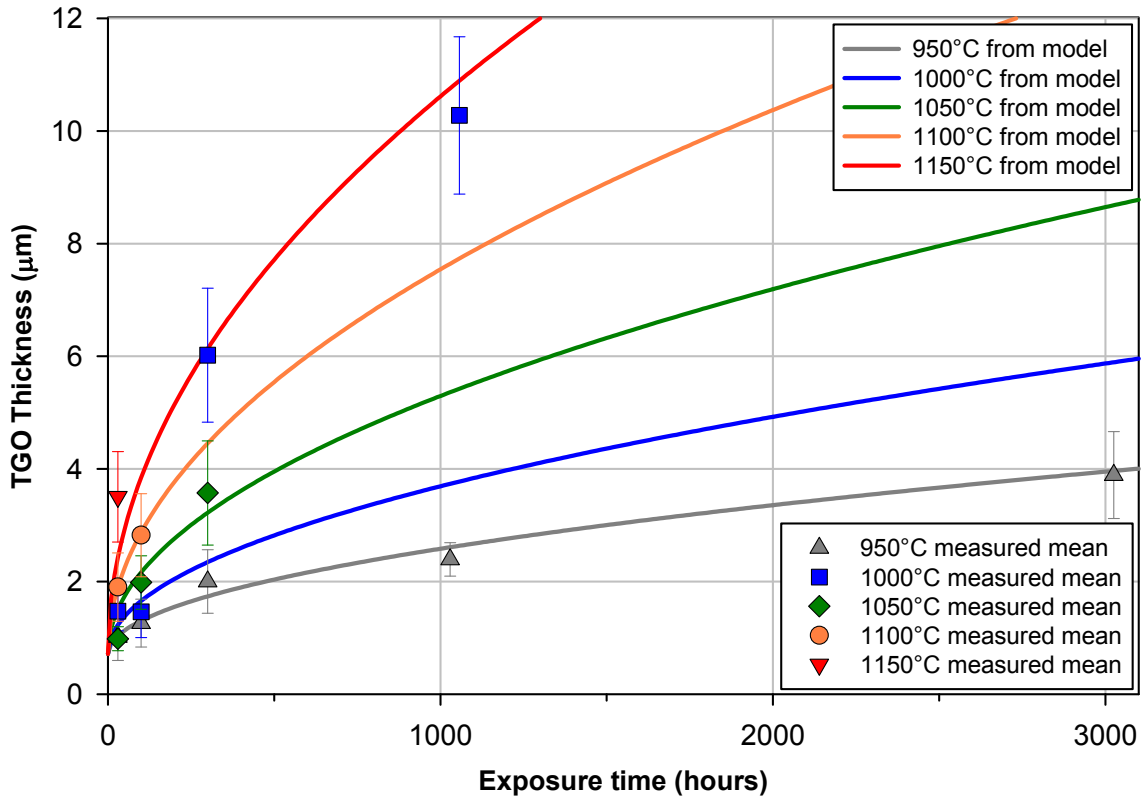

Figure 167 TGO Growth - Global parametric fit.

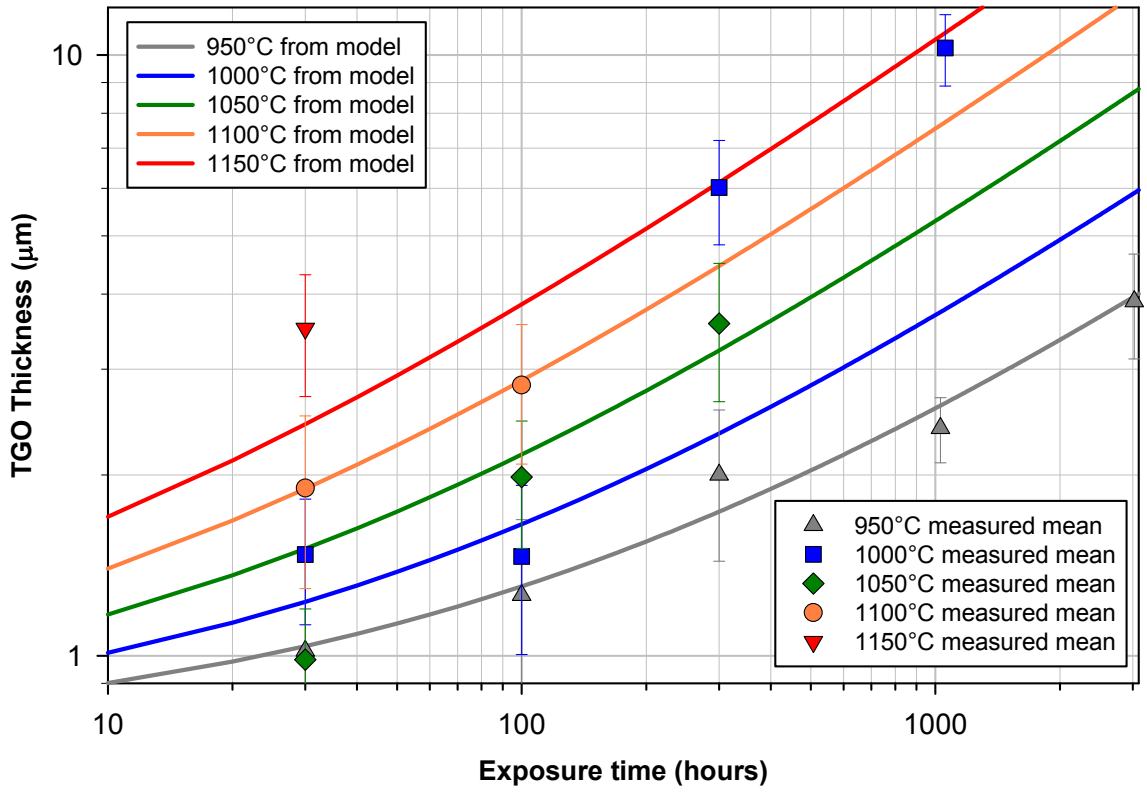

Figure 168 TGO Growth – Global parametric fit (logarithmic scales).

Table 41 Initial global fit parameters derived from isothermal diffusion based relation excluding 1000°C and 1100°C exposures and used in QinetiQ model.

Parameter	Value	Units
A	1998	μm hours^2
E	107	kJ mol^{-1}
d_0	0.767	μm

Table 42 Global fit parameters derived from isothermal diffusion based relation based on all exposures.

Parameter	Value	Units
A	8370	μm hours^2
E	121	kJ mol^{-1}
d_0	0.714	μm

Table 43 Global parametric fit to predict TGO thickness following two stage exposures at different temperatures.

Specimen	First stage exposure			Second stage exposure				
	Temp (°C)	Time (hrs)	Expected TGO thickness (μm)	Equivalent exposure time (hrs)	Temp (°C)	Time (hrs)	Equivalent total time (hrs)	Expected Final TGO thickness (μm)
1000°C 306h, 950°C 1027h	1000	306	2.36	777	950	1027	1804	3.22
1050°C 300h, 950°C 1002h	1050	300	3.22	1802	950	1002	2804	3.84
1100°C 100h, 950°C 1025h	1100	100	2.87	1335	950	1025	2363	3.59

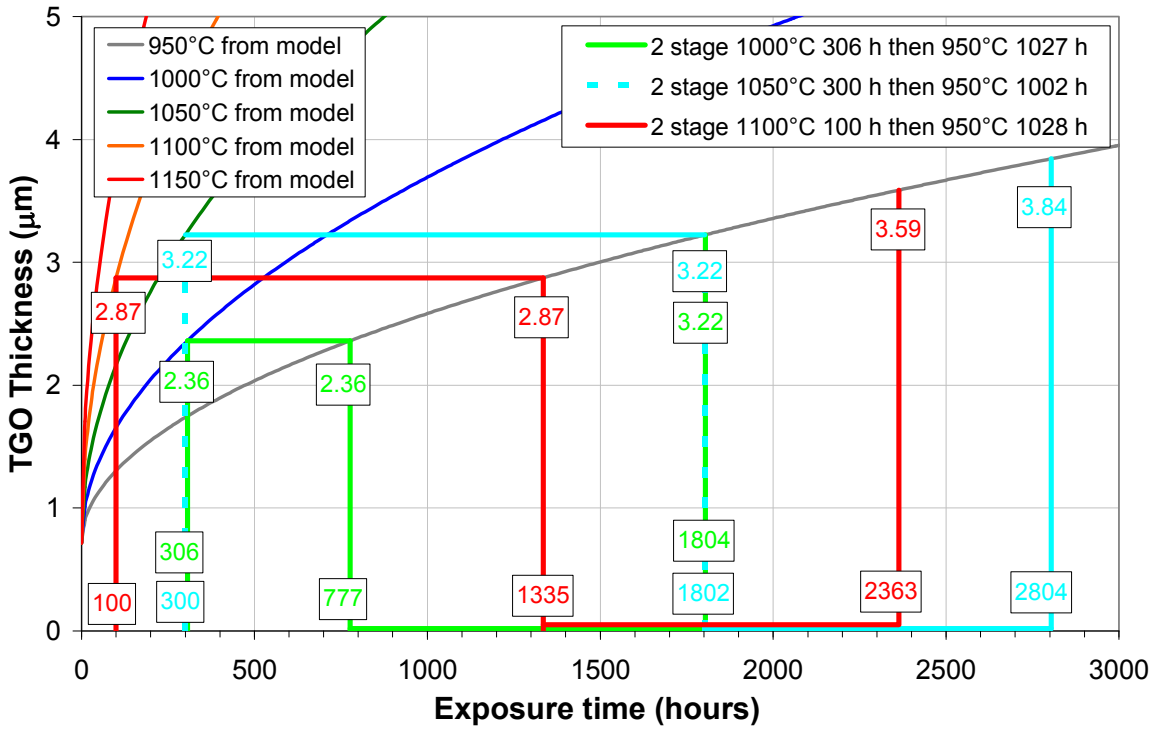

Figure 169 Global parametric fit to predict TGO thickness following two stage exposures at different temperatures.

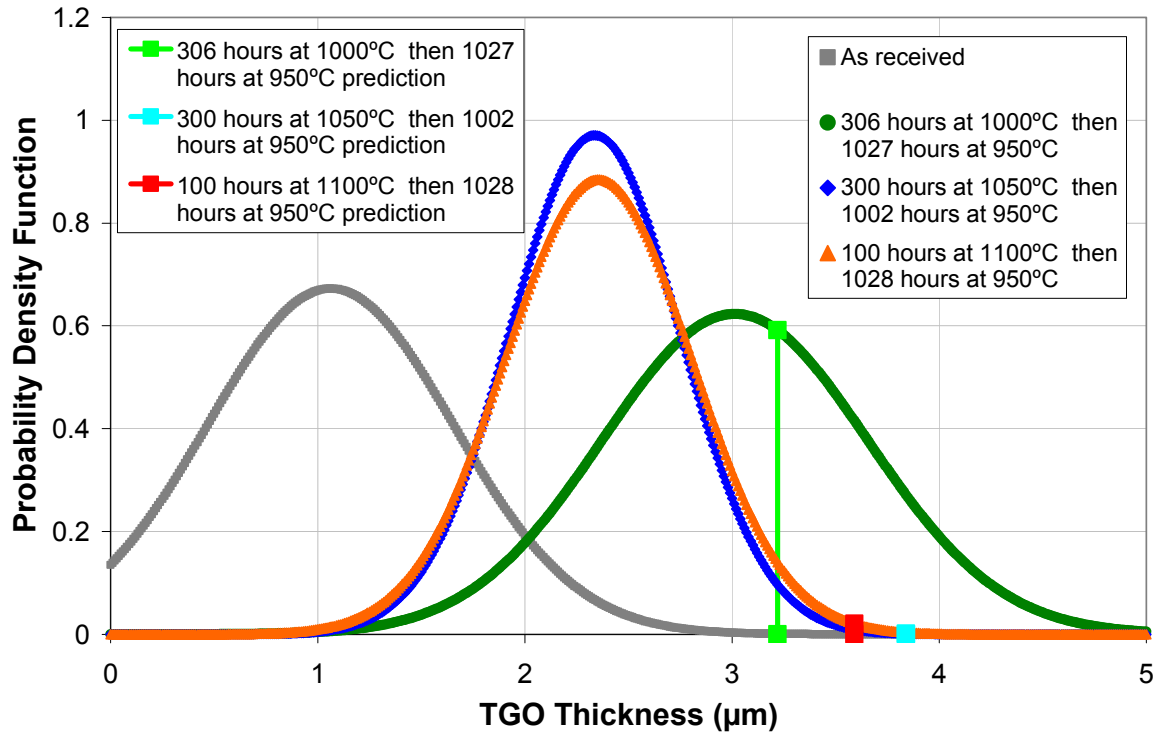

Figure 170 Comparison of two stage thermal exposure prediction of TGO thickness with two stage thermal exposure PDF.

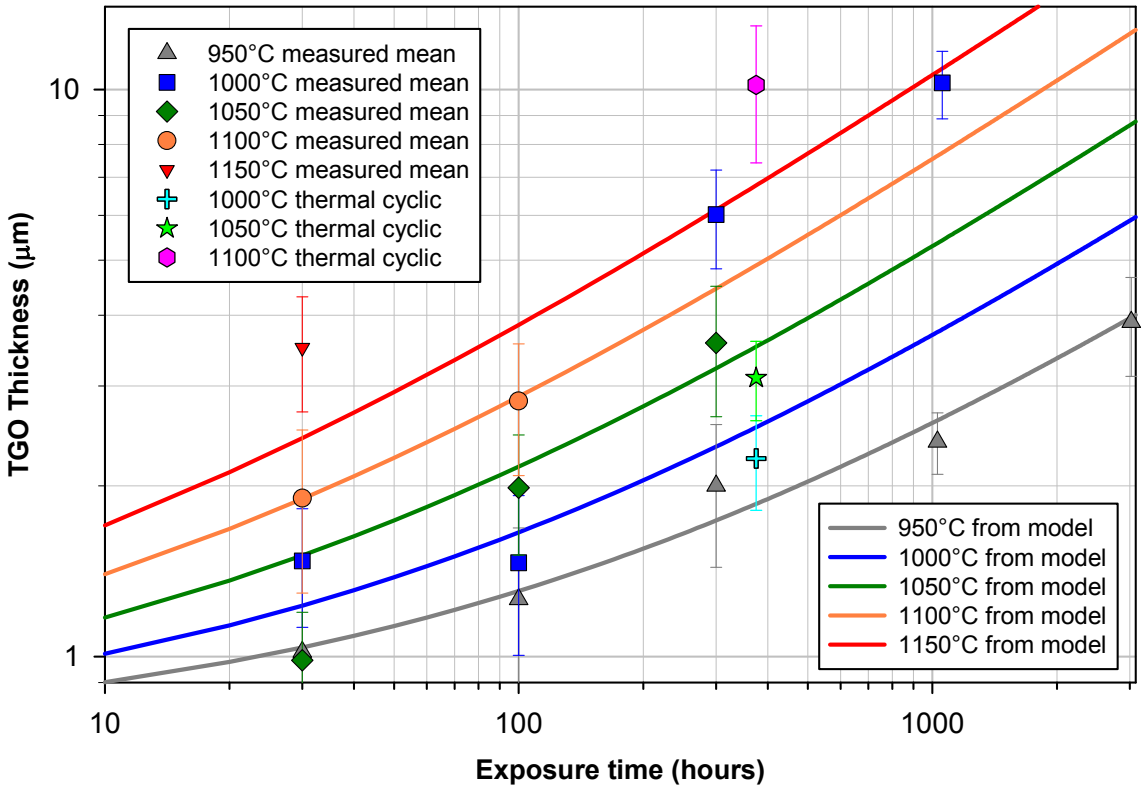

Figure 171 Thermal cyclic TGO thickness comparison with isothermal exposure (exposure time within 50°C of target temperature 300 cycles equates to 375 hours).

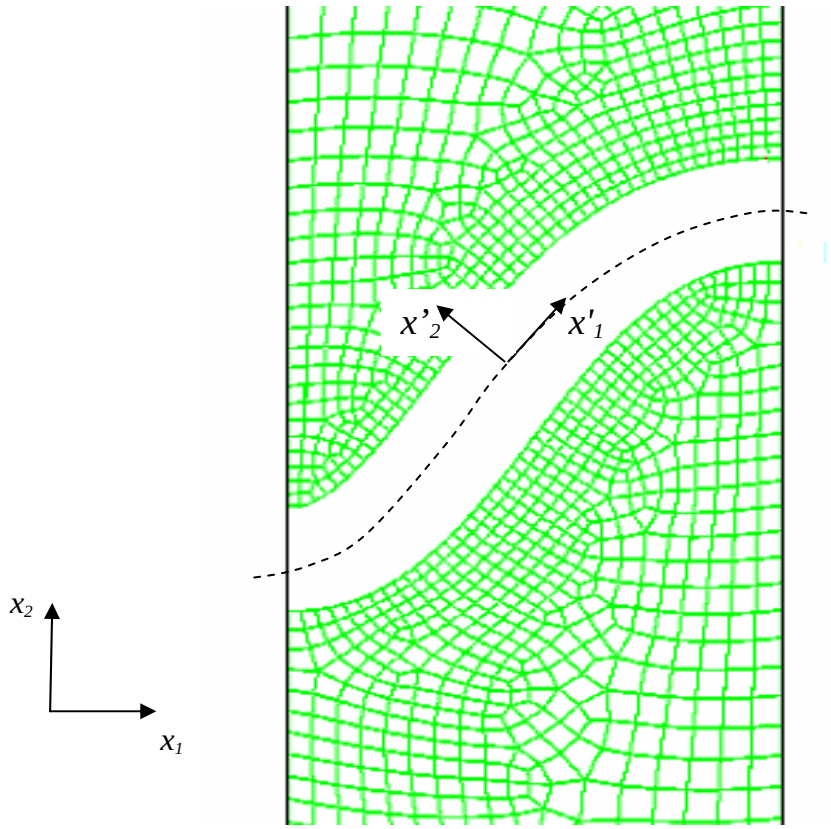

Figure 172 Definition of local coordinate system (x'_1, x'_2) and its relation to the global system (x_1, x_2)[4].

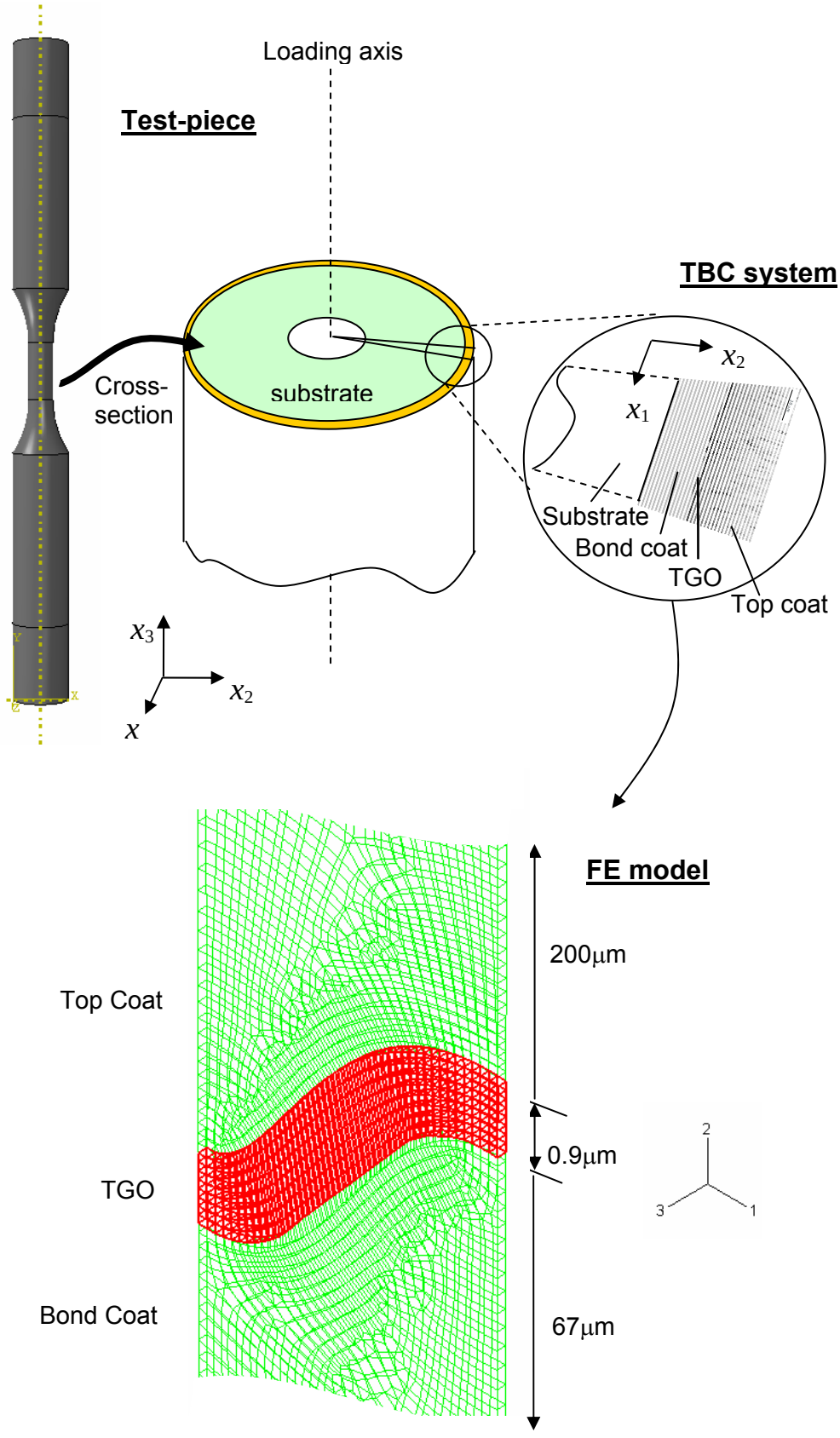

Figure 173 Model geometry and mesh near the TGO layer[4].

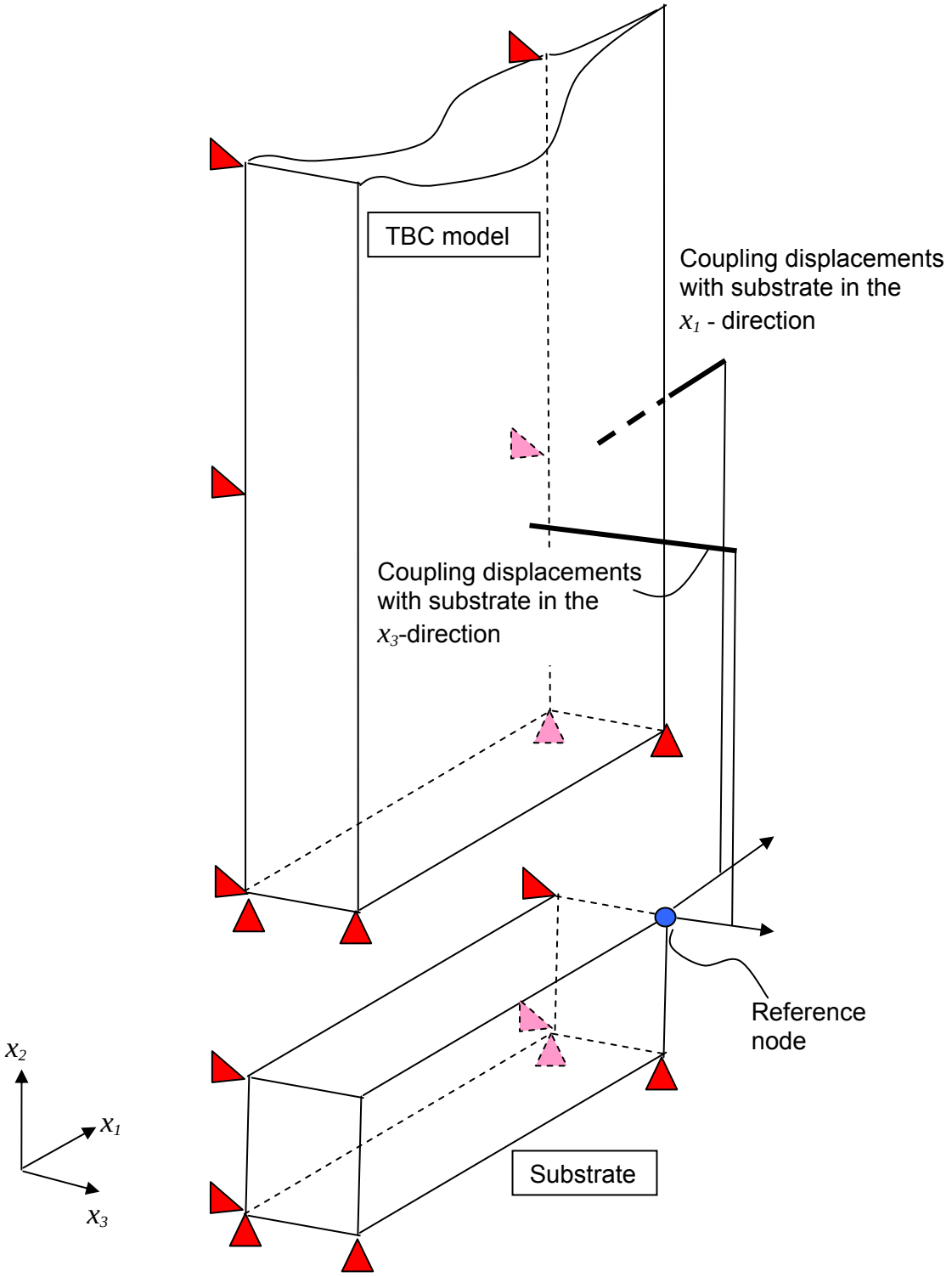

Figure 174 Model boundary conditions and definitions of constraints[4].

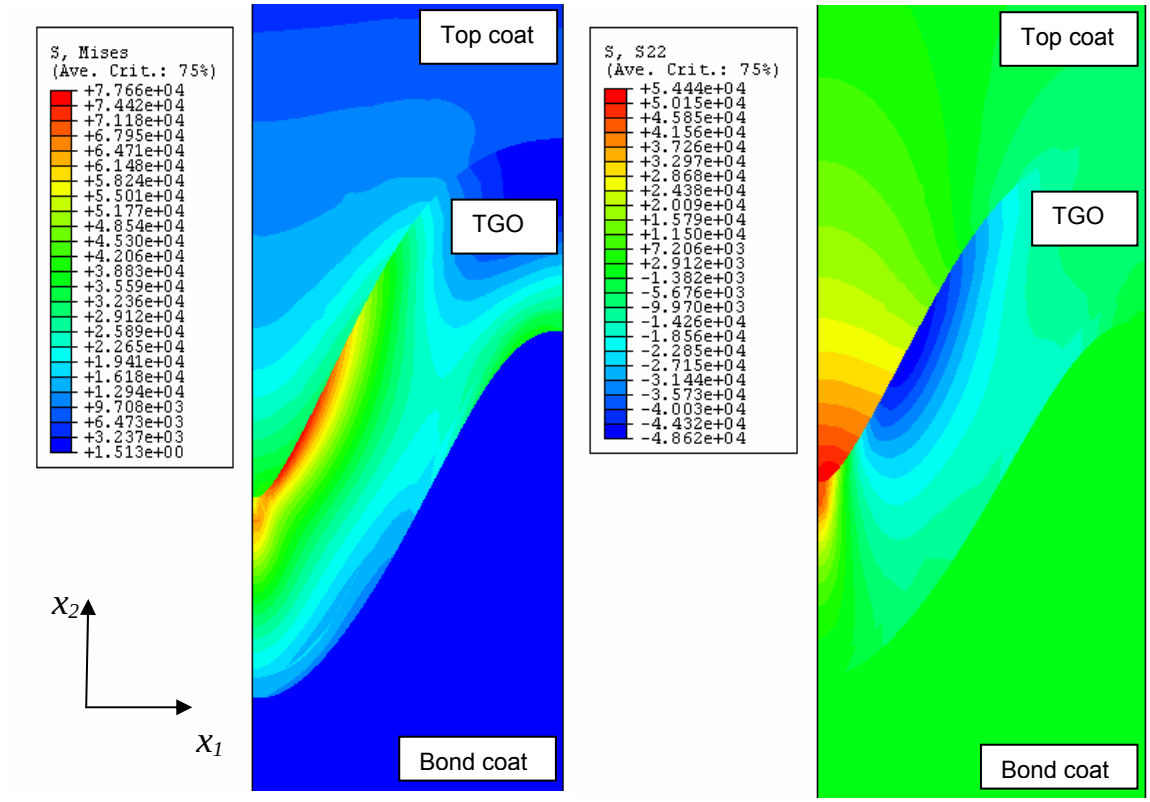

Figure 175 Mises and S22 contours after 581 hours isothermal dwell at 950°C[4].

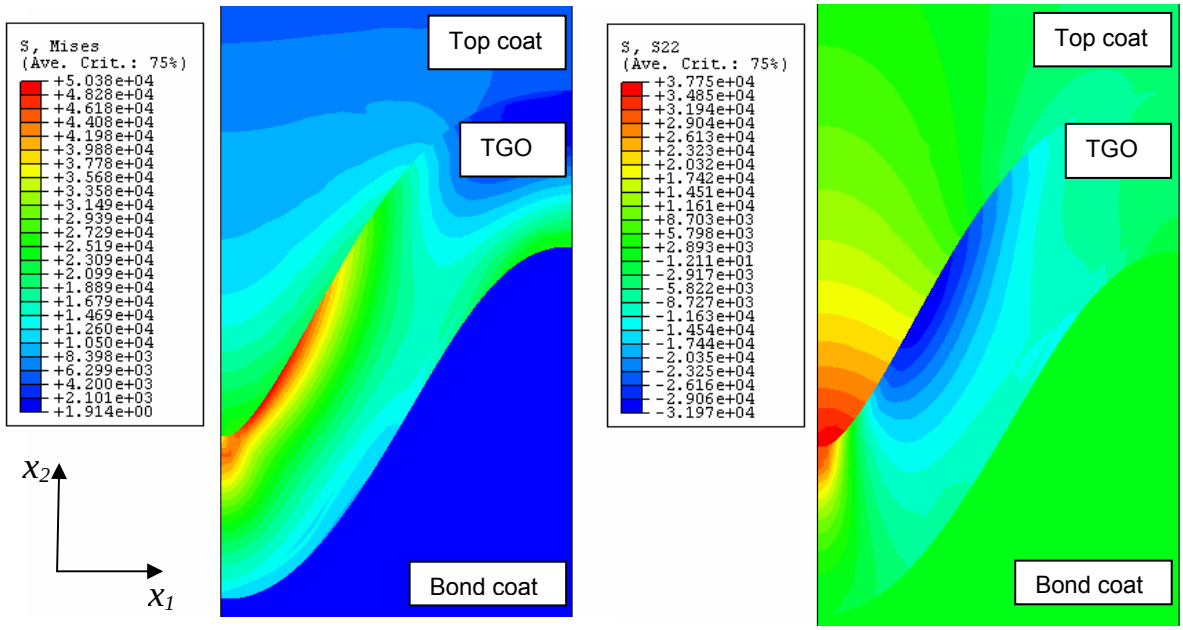

Figure 176 Mises and stress component S22 contours after 186 hours creep at 100MPa / 950°C[4].

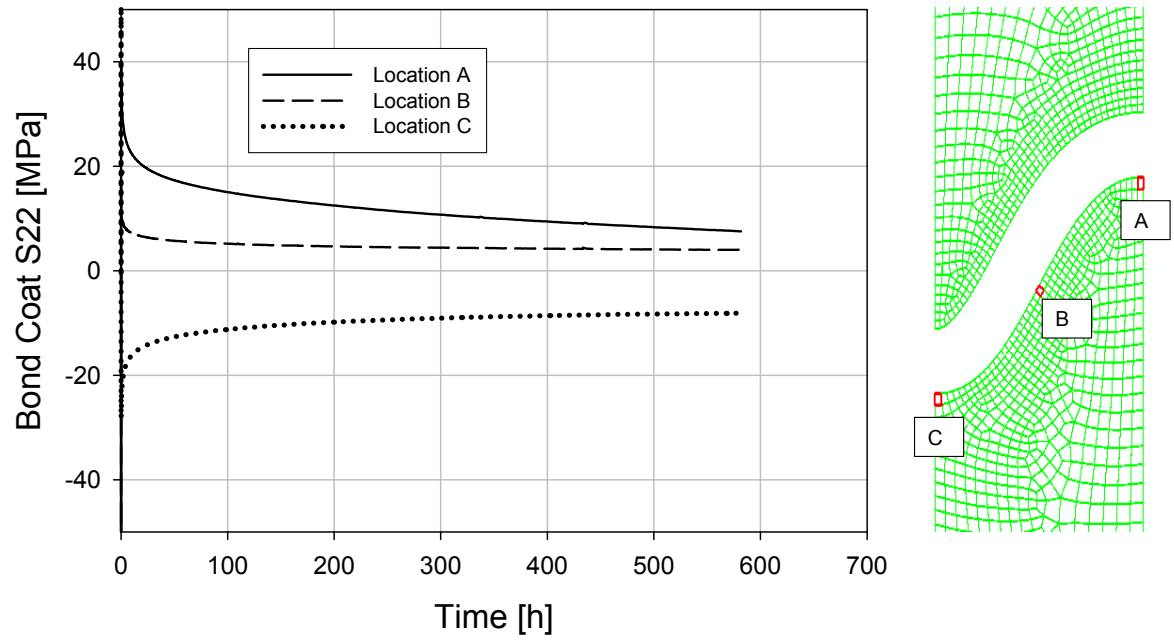

(a) Entire evolution

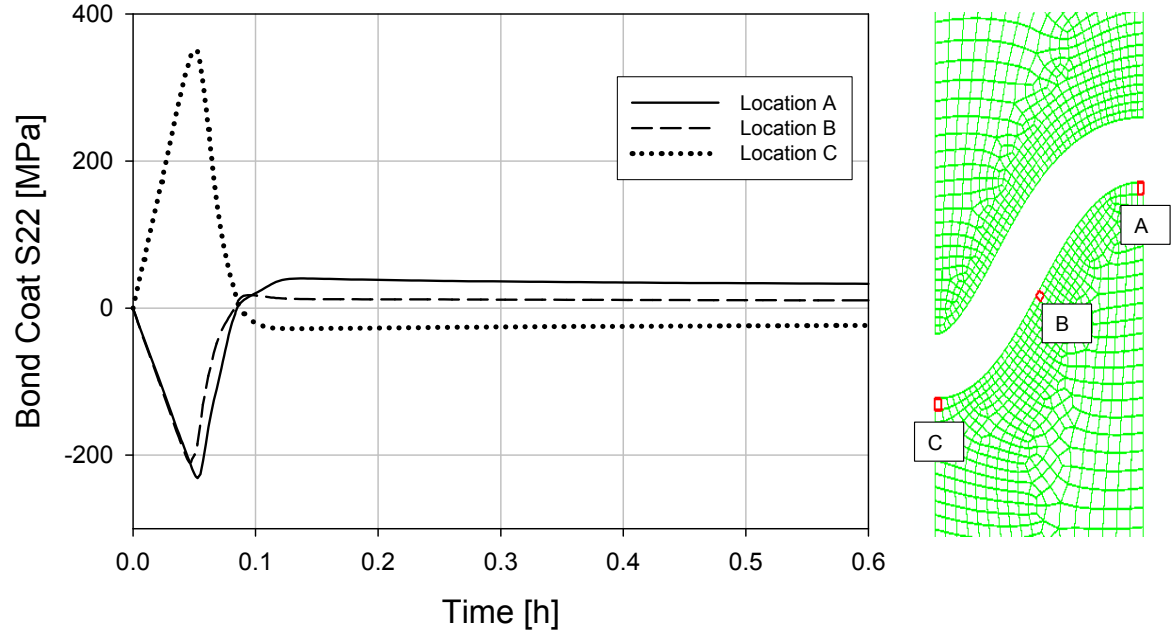

(b) Initial stages

Figure 177 Evolution of stress component S22 in the bond coat (BC) near the TGO / BC interface during 581 hours isothermal dwell at 950°C[4].

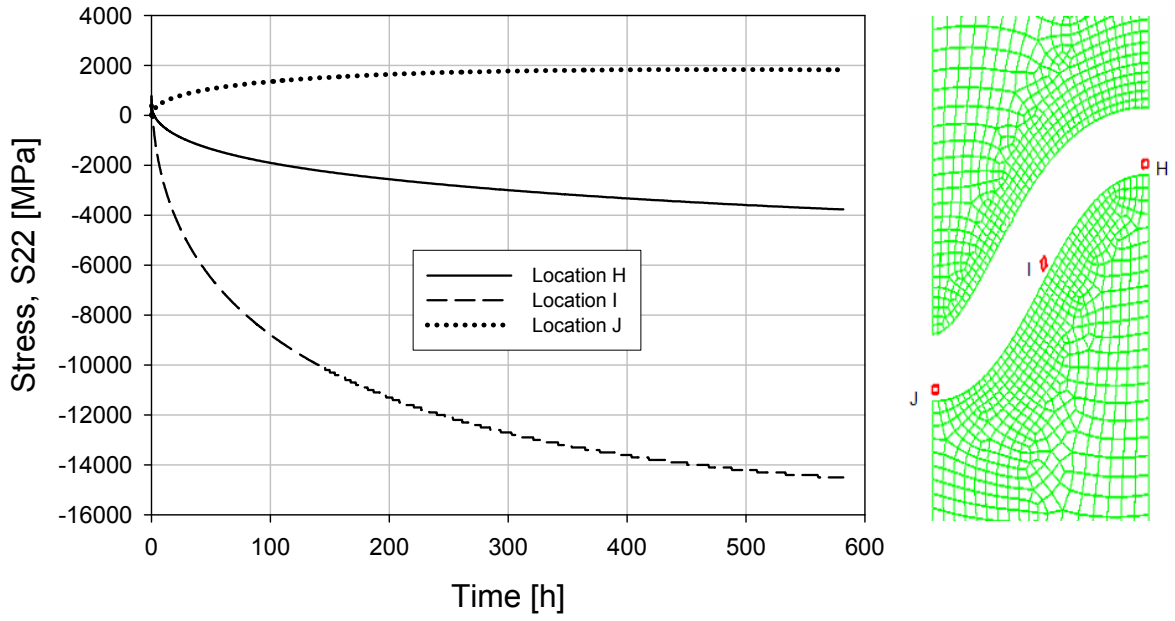

(a) Entire evolution

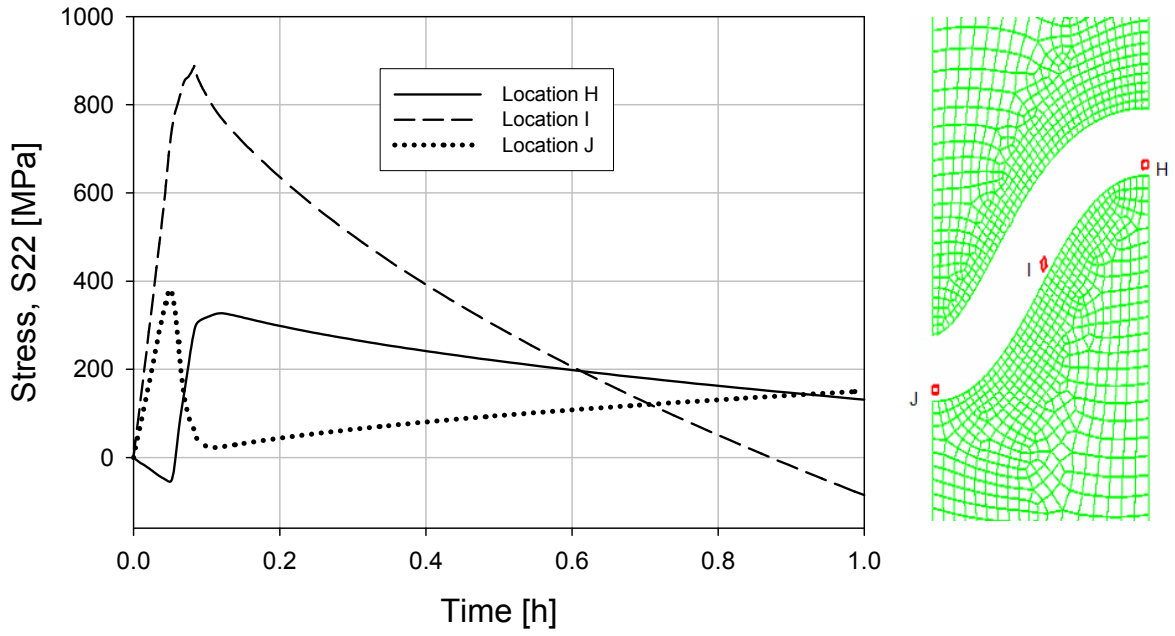

(b) Initial stages

Figure 178 Evolution of stress component S22 in the TGO near the TGO/BC interface during 581 hours isothermal dwell at 950°C[4].

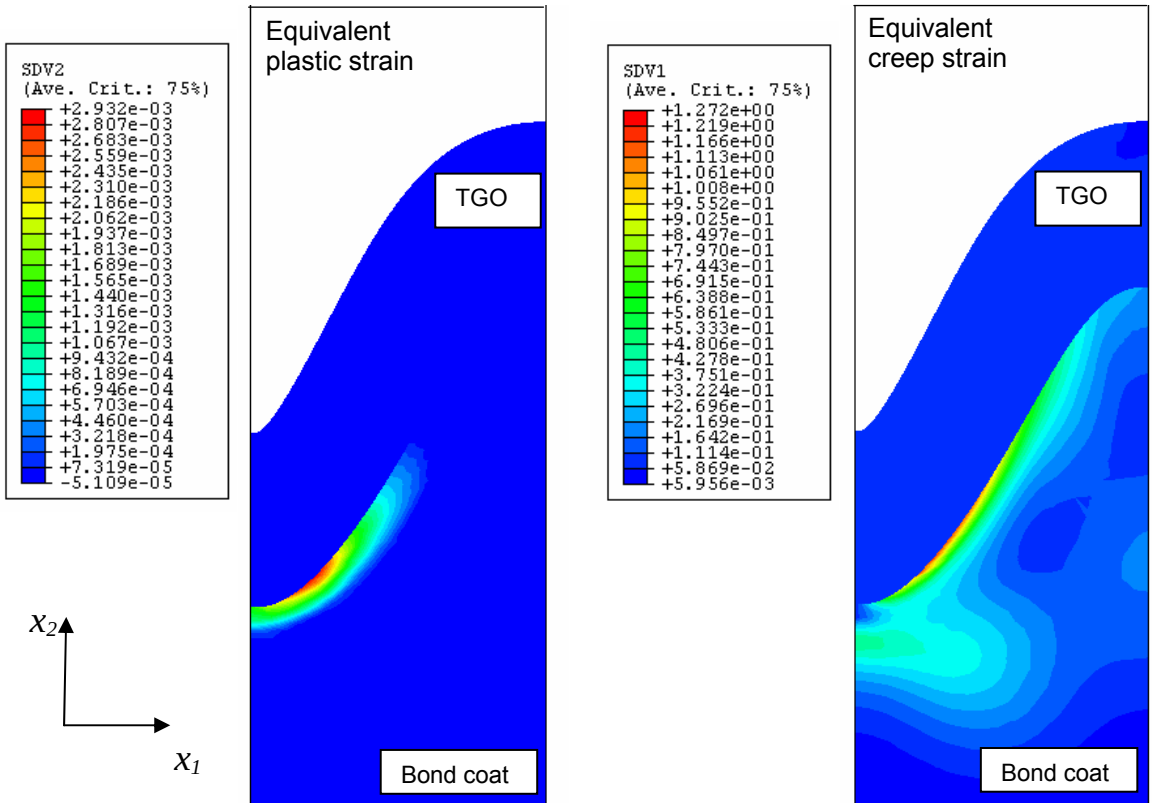

Figure 179 Equivalent plastic and creep strains after 581 hours dwell at 950°C[4].

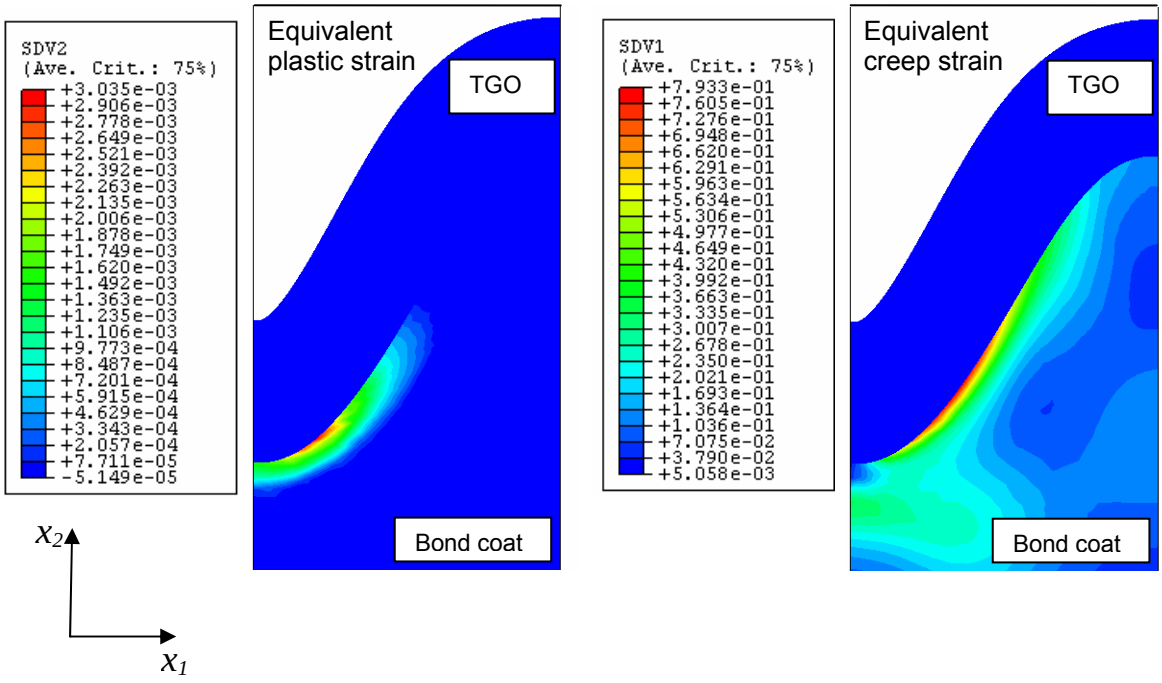

Figure 180 Equivalent plastic and creep strains after 186 hours creep at 100MPa / 950°C[4].

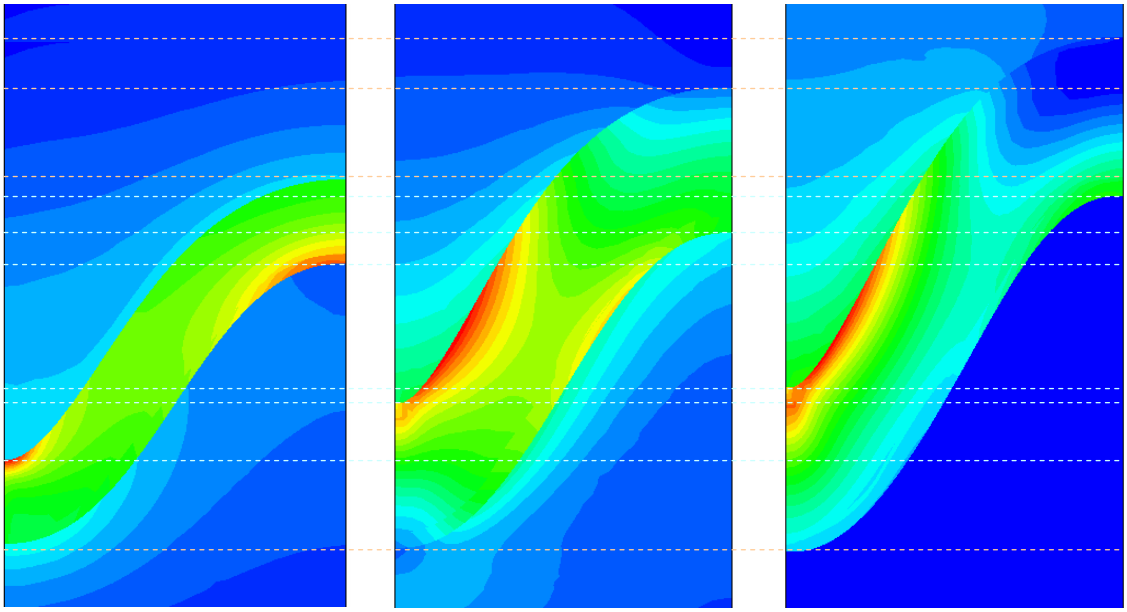

(a) Initial condition

(b) After 581 hours isothermal dwell at 950°C

(c) After 186 hours at 100 MPa at 950°C

Figure 181 TGO growth and changes in undulation[4].

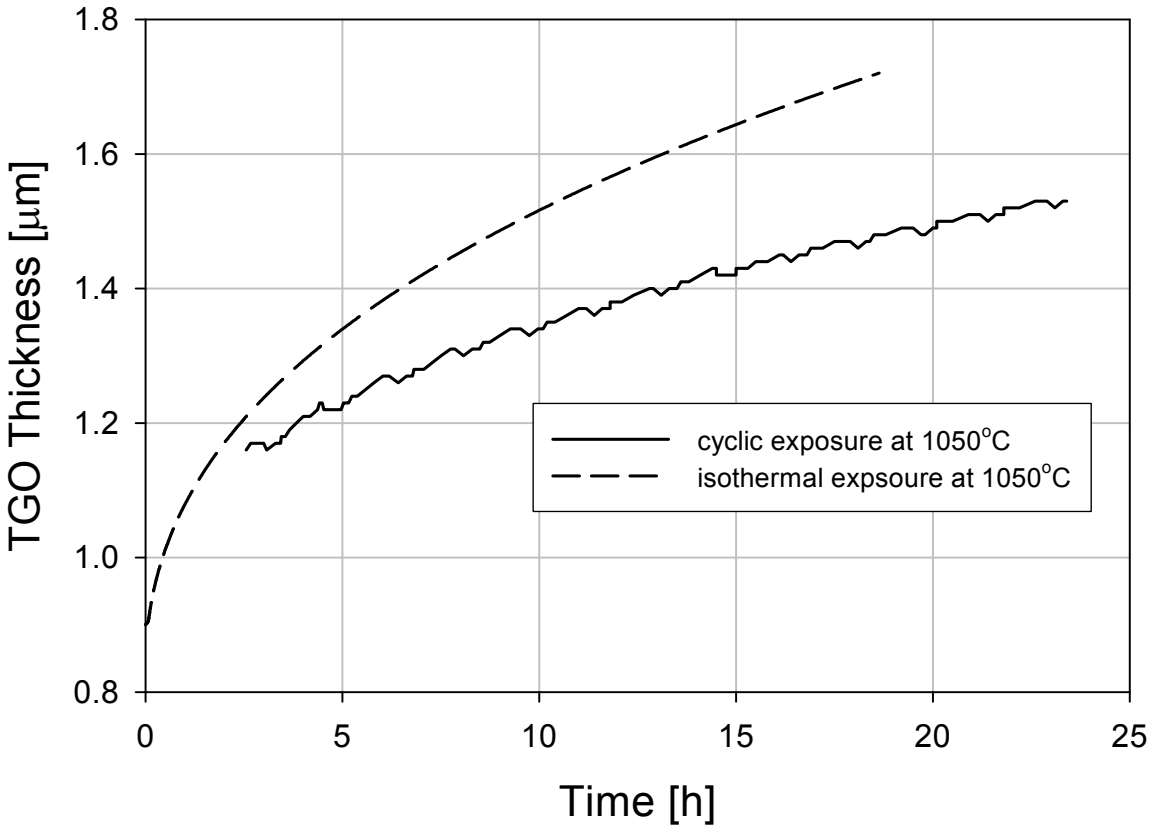

Figure 182 Finite element predictions of the TGO growth kinetics under isothermal and cyclic temperature exposures[4].

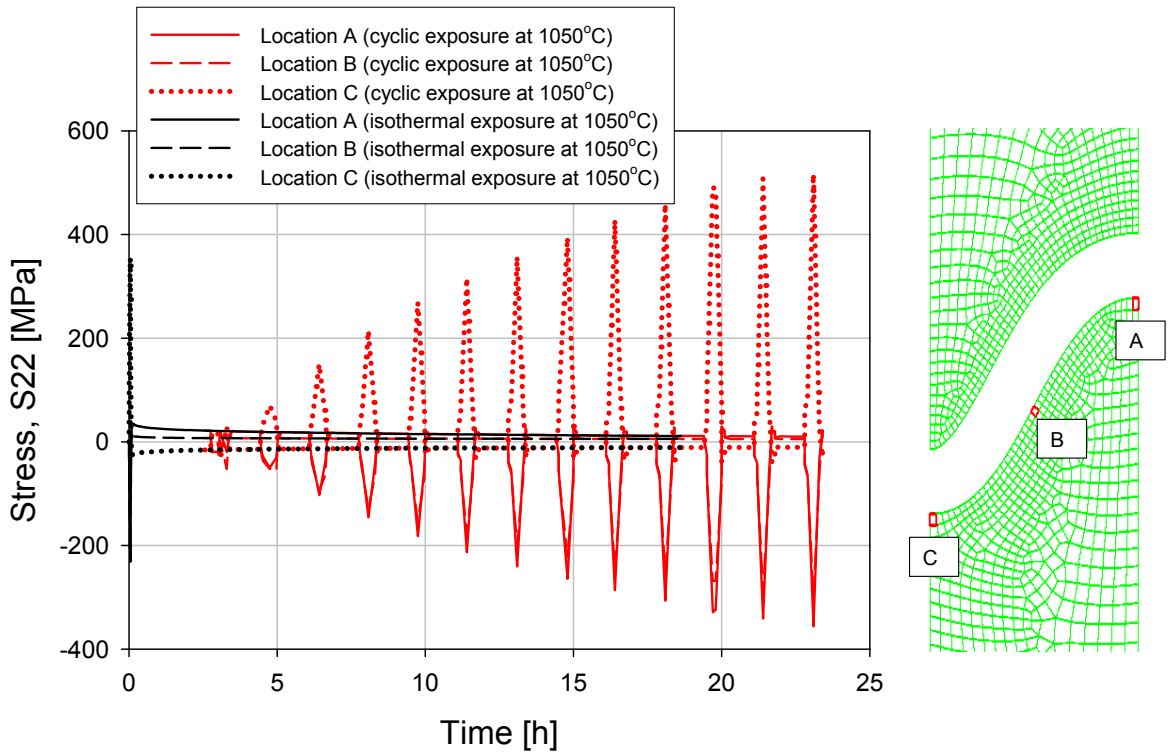

Figure 183 Evolution of stress component S22 in the BC near the TGO interface under isothermal and cyclic temperature exposures to 1050°C[4].

Cr, necessary for oxidation resistance and strengthening. For ranges of AL, Ti and Mo, Cr > 13% leads to abundant precipitation of intergranular carbides – deterioration in ductility and sensitivity to notching and cracking. Cr 11-13%

8% Co minimum for resistance to creep. Reduces γ' solvus, due to high levels of Al and Ti at least 14% is used. Maximum limited to 17% to maintain V_f of γ' for use at temperature

Due to low Nb, V_f of γ' 50% minimum

Al and Ti ratio 1:1

Ti favourably (*cf.* Al) strengthening γ' above 650ºC increases γ' solvus (check) – practical use of alloy difficult

Al + Ti 10wt% maximum

Hf complementary hardening 1% maximum – reduces solidus and raises γ' solvus

N18	Cr wt%	Co wt%	Mo wt%	Nb wt%	Ta wt%	Ti wt%	Al wt%	Hf wt%	C ppm	B ppm	Zr ppm	Ni
range	11-13	(8-17) 14-17	6-8	0-1.5	0	4-5	4-5	0-1	(0-500) 0-200	(0-500) 0-200	0-500	Bal

Nb and Ta increase σ_y for smooth creep

But detrimental to notch sensitivity and FCP at 650ºC

Ta *cf.* Nb increases density more – no Ta and 1.5% limit for Nb

Mo and W solid solution strengtheners of γ. Mo preferred – ratio of Mo in γ *cf.* γ' is 2-3 times that of W – reduces notch sensitivity under creep at 650ºC (creep performance of smooth specimen is lower) – density penalty less

Zr to counteract weakening due to possible S, limit 500 ppm to avoid forming phases with a low melting point

B and C capable of improving resistance to creep, but considering Cr and Mo used and to avoid excessive borides and carbides limit to 500 ppm

No V > strength but FCGR at 650ºC excessive

Mg, Ca, Si, Y trace levels without detriment

Appendix 2 RR1000 Patent – Alloy Composition – Summary

Characterised by Ta and combination of ranges of Cr, Mo, Ti and Al

Nb less than 0.5 wt%, preferably 0

Co (15-18.5 wt%) – no significant effect on tensile or creep strength. 15 wt% generates a minimum SFE promoting planar deformation and potential improved fcp resistance

Cr raised to improve fcp resistance without excessive TCP phases forming

Hf improves all properties

Al balanced wrt Ti to control γ' wt_f. Limited to reduce propensity for TCP phase formation.

Ti (& Al) controls wt_f of γ' and most effect on γ' solvus. Increased to counter reduced Ta to maintain tensile strength whilst controlling γ' wt_f and TCP phase formation.

RR1000 wt%	Cr	Co	Mo	Ta	Nb	V	Fe	Mn	Ti	Al	Hf	W	Re	C	B	Si	Y	Zr	Ni
min	14.35	14	4.25	1.35	0	0	0	0	3.45	2.85	0.5	0	0	0.012	0.01	0	0	0.05	Bal
max	15.15	19	5.25	2.15	0.5	0.1	1	0.15	4.15	3.15	1.0	2	1	0.033	0.025	0.2	0.1	0.07	

Mo beneficial for tensile strength and ductility at high temp, controlled to balance high Cr wrt TCP phases forming

Ta increases tensile strength, but segregates to form very stable TaC (MC), controlled to allow the MC carbide to breakdown to promote gb carbides

Roles of V, Fe, Mn W, Si, Y not discussed in patent

Nb and Re not used in any example alloys

Re strong benefit on creep resistance

C at levels to promote hot ductility and high temperature creep resistance

B reduced to levels which are beneficial to creep fcp resistance and tensile strength

Zr increased to 0.06 wt%, beneficial effect on stress rupture and creep resistance

Appendix 3 N18 Pancake Cutting Plan

Approximately three quarter size.

Cut away from existing edges and stencil marks.

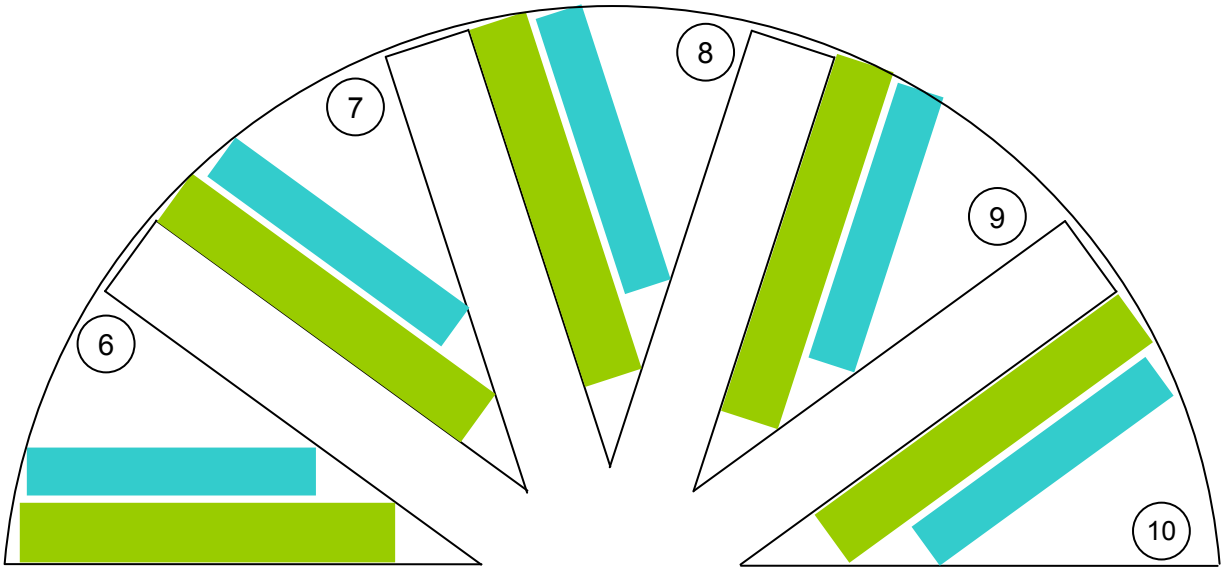

SENB Specimen

Dimensions 10 mm x 10 mm x 65 mm

Qty 2 deep from each location

Top face to be noted, notch to be cut in top face, halfway along length.

Original location to be marked on end, e.g. 6U (6 upper) 6L (6 Lower)

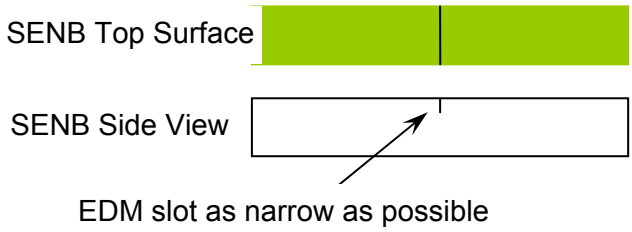

U - Notch Specimen

Dimensions 8 mm x 8 mm x 50 mm

Qty 3 deep from each location

Top face to be noted, U - notch to be cut in top face, halfway along length.

Original location to be marked on end, e.g. 6U (6 upper), 6M (6 middle), 6L (6 Lower)

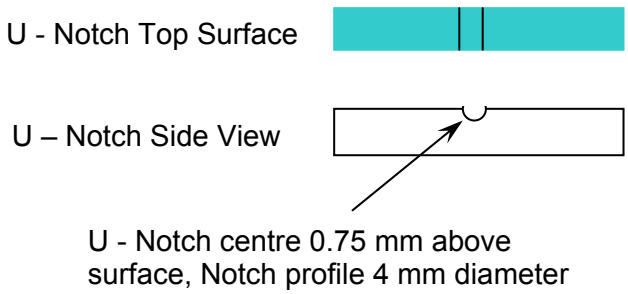

NASA LSHR SENB Specimen Cutting Drawing

All Dimensions in mm General Tolerance 0.1 mm

Drawn: Stewart Everitt Date: 21 May 2009

Contact: 07951 235783

3rd Angle Projection

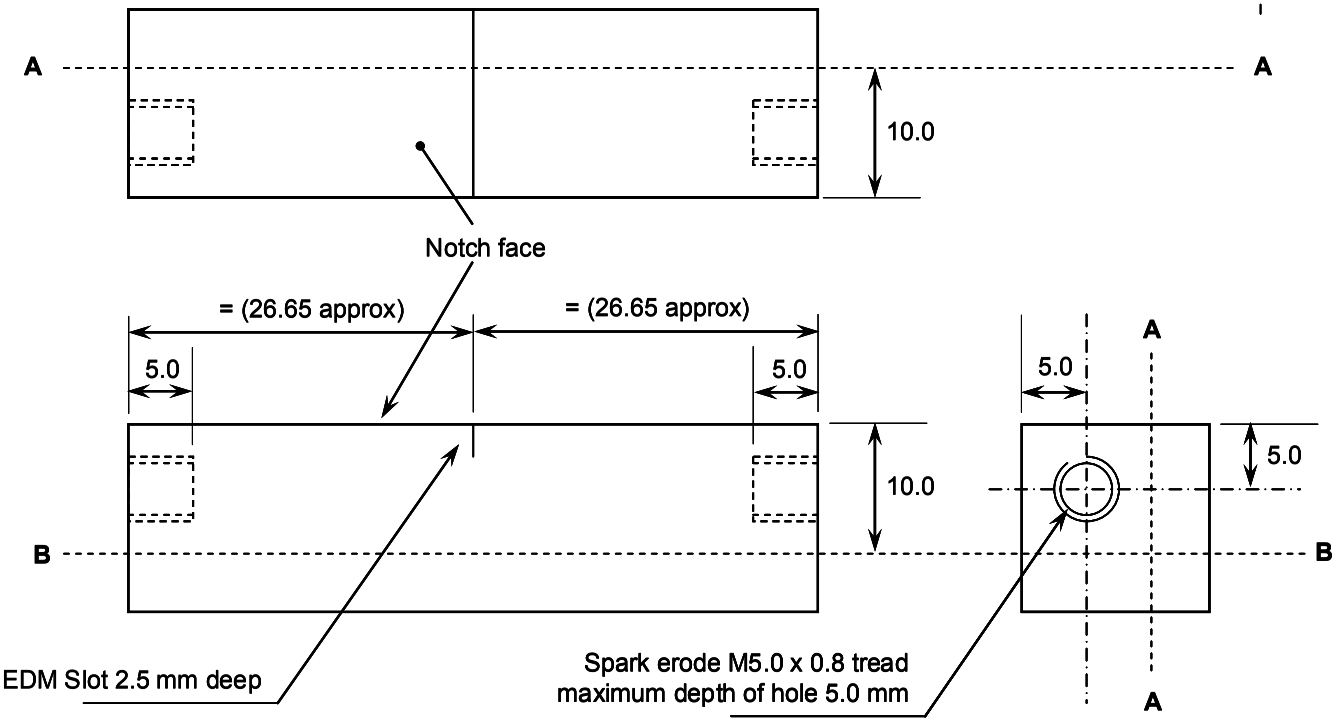

Notes:

1. **IMPORTANT!** EDM slot needs to run across notch face. This is marked by arrows pointing to it on ends and a centre pop mark on the end closest to the notch face. Identification markings are on the side face.
2. A A and B B are cut lines from supplied material
3. Maximum 5.0 mm depth of M5 hole is important
4. Please retain all offcuts with cut specimen as these will be used for metallographic analysis

Identification Centre Pops

1 = E12
2 = S12
3 = N9
4 = E5
5 = W14
6 = W7

List of References

[1] Reed, P.A.S., Wisbey, A., Everitt, S., Di Martino, I. and Brooks, J.W. (2007) 'High temperature fatigue and creep performance of N18 alloy' eds. Strang A., Banks, W.M., McColvin, G.M., Oakley, J.E., and Vanstone, R.W. *Proceedings of the Seventh International Charles Parsons Turbine Conference: Power Generation in an Era of Climate Change, 11-13 Sept. 2007, University of Strathclyde, Glasgow, UK,* IOM Communications Ltd, London, UK, 309-319.

[2] Everitt, S., Starink, M.J., Pang, H.T., Wilcock, I.M., Henderson, M.B. and Reed, P.A.S. (2007) 'A comparison of high temperature fatigue crack propagation in various sub-solvus heat treated turbine disc alloys' *Materials Science and Technology*, **23** (12) 1419-1423.

[3] Everitt, S., Starink, M.J. and Reed, P.A.S. (2008) 'Temperature and dwell dependence of fatigue crack propagation in various heat treated turbine disc alloys.' eds. Reed, R., Green, K.A., Caron, P., Gabb, T., Fahrmann, M.G., Huron, E.S. and Woodard, S.R. *Proceedings of the Eleventh International Symposium on Superalloys, 14-18 Sept. 2008, Seven Springs, Champion, Pennsylvania, USA*, TMS, 741 - 750.

[4] Basoalto, H., Everitt, S. and Vermeulen, B. (2009) 'Final Report on Thermal Barrier Coating Lifing Model.' QinetiQ Ltd. QinetiQ/08/01042 31 March 2009.

[5] Reed, R.C. (2006) *The Superalloys*, Cambridge University Press, Cambridge, UK.

[6] Gabb, T.P, Telesman, J. Kantzos, P.T. and Konkel, W.A. (2003) 'Realistic Subscale Evaluations of the Mechanical Properties of Advanced Disk Superalloys' NASA report NASA/TM-2003-212086.

[7] Gabb, T.P. (2008) Personal communication.

[8] QinetiQ Ltd. (2009) 'About Us', [online] available from: http://www.qinetiq.com/global/about_us.html [accessed 9 November 2009].

[9] Sims, C.T., Stoloff, N.S. and Hagel, W.C. (1987) *Superalloys II*, John Wiley and Sons, New York, USA.

[10] Bhadeshia, H.K.D.H. (2003) 'Nickel Based Superalloys', [online] available from: http://www.msm.cam.ac.uk/phase-trans/2003/Superalloys/superalloys.html [accessed 28 June 2006].

[11] King, J.E. (1987) 'Fatigue crack propagation in nickel-base superalloys – effects of microstructure, load ratio, and temperature' *Materials Science and Technology*, **3** (9) 750 – 764.

[12] Kattus, J.R. (1999) *Aerospace Structural Metals Handbook Ni-Base Alloy, NiCo MAR-M-247* Purdue Research Foundation, West Lafayette, Indiana, USA.

[13] Huron, E.S., Bain, K.R., Mourer, D.P., Schirra, J.J., Reynolds, P.L. and Montero, E.E (2004) 'The influence of grain boundary elements on properties and microstructures of P/M nickel base superalloys' eds. Green, K.A., Pollock, T.M., Harada, H., Howson, T.E., Reed, R., Schirra, J.J. and Watson, S. *Proceedings of the Tenth International Symposium on Superalloys, 19-23 Sept. 2004, Seven Springs, Champion, Pennsylvania, USA*, TMS, 73 - 81.

[14] Flageolet, B., Jouiad, M., Villechaise, P. and Mendez J. (2005) 'On the role of γ particles within γ' precipitates on damage accumulation in the P/M nickel –base superalloy N18' *Materials Science and Engineering A*, **399** (1-2) 199-205.

[15] Cadel, E., LeMarchand, D., Chambreland, S. and Blavette D. (2002) 'Atom probe tomography investigation of the microstructure of superalloy N18' *Acta Materialia*, **50** (5) 957-966.

[16] Betteridge, W. and Heslop, J. (1974) *The Nimonic Alloys and Other Nickel Base High-Temperature Alloys*, Edward Arnold, London, UK.

[17] Locq, D., Caron, P., Raujol, S., Pettinari-Sturmel, F., Coujou, A. and Clémen, N. (2004) 'On the Role of Tertiary γ' Precipitates in the Creep Behaviour at 700°C of a PM Disk Superalloy' *eds. Green, K.A., Pollock, T.M., Harada, H., Howson, T.E., Reed, R., Schirra, J.J. and Watson, S. Proceedings of the Tenth International Symposium on Superalloys, 19-23 Sept. 2004, Seven Springs, Champion, Pennsylvania, USA*, TMS, 179-187.

[18] Mitchell, R.J., Hardy, M.C., Preuss, M. and Tin, S. (2004) 'Development of γ' Morphology in P/M Rotor Disc Alloys during Heat Treatment' eds. Green, K.A., Pollock, T.M., Harada, H., Howson, T.E., Reed, R., Schirra, J.J. and Watson, S. *Proceedings of the Tenth International Symposium on Superalloys, 19-23 Sept. 2004, Seven Springs, Champion, Pennsylvania, USA*, TMS, 361-370.

[19] Gayda, J., Gabb, T.P. and Kantzos, P.T. (2004) 'The effect of dual microstructure heat treatment on an advanced nickel-base disk alloy' eds. Green, K.A., Pollock, T.M., Harada, H., Howson, T.E., Reed, R., Schirra, J.J. and Watson, S. *Proceedings of the Tenth International Symposium on Superalloys, 19-23 Sept. 2004, Seven Springs, Champion, Pennsylvania, USA*, TMS, 323-329.

[20] Hide, N.J., Reed, P.A.S. and Pang, H.T. (2000) 'A fundamental investigation of the effects of dwell time, grain size and environment on the high temperature fatigue and creep-fatigue resistance of turbine disc alloys' University of Southampton, UK, Final Report April 2000 Report No. PR/RA/NH/00/01/289.

[21] Pang, H.T. (2003) 'Effect of microstructure variation on turbine disc fatigue lives' PhD. Thesis, University of Southampton, UK.

[22] Di Martino, I. (2006) Personal communication, QinetiQ Ltd.

[23] Antolovich, S.D. and Jayarman, N. (1983) 'Metallurgical instabilities during the high temperature low cycle fatigue of nickel-base superalloys' *Materials Science and Engineering*, **57** (1) L9-L12.

[24] Zheng, D. and Ghonem, H. (1992) 'Influence of prolonged thermal exposure on intergranular fatigue crack growth behaviour in alloy 718 at 650°C' *Metallurgical and Materials Transactions A*, **23** (11) 3169-3171.

[25] Koul, A.K. and Wallace, W. (1983) 'Microstructural changes during long time service exposure of Udimet 500 and Nimonic115' *Metallurgical and Materials Transactions A*, **14** (1) 183-189.

[26] Hunt, D.W., Skelton, D.K. and Knowles, D.M. (2000) ' Microstructural stability and crack growth behaviour of a polycrystalline Nickel-base superalloy.' eds. Pollock, T.M., Kissinger, R.D., Bowman, R.R., Green, McLean, M., Olson, S.L., and Schirra, J.J. *Proceedings of the Ninth International*

Symposium on Superalloys, 17-21 Sept. 2000, Seven Springs, Champion, Pennsylvania, USA, TMS, 795-802.

[27] Lerch, B.A., Jayarman, N. and Antolovich, S.D. (1984) 'A study of fatigue damage mechanisms in Waspaloy from 25 to 800°C' *Materials Science and Engineering*, **66** (2) 151-166.

[28] Hayama, A.O.F., Sandim, H.R.Z., Lins, J.F.C., Hupalo, M.F. and Padilha, A.F. (2004) 'Annealing behaviour of the ODS nickel-based superalloy PM 1000' *Materials Science and Engineering: A*, **371** (1-2) 198-209.

[29] Čadek, J., Pahutová, M., Šustek, V. and Dlouhý, A. (1997) 'On the role of recovery in creep of precipitation-strengthened polycrystalline nickel-base alloys' *Materials Science and Engineering*: *A*, **238** (2) 391-398.

[30] Zamrik, S.Y. and Davis, D.C. (1990) 'Creep-fatigue damage mechanisms and life assessment of two materials: Type 316 Stainless Steel and Waspaloy' *Life Assessment and Repair: Technology for Combustion Turbine Hot Section Components, Phoenix, Arizona, USA, 17-19 Apr. 1990*, ASM International, 77-85.

[31] Subramanya Sarma, V., Sundararaman, M. and Padmanabhan, K.A. (1998) 'Effect of γ' size on room temperature low cycle fatigue behaviour of a nickel base superalloy' *Materials Science and Technology*, **14** (7). 669-675.

[32] Valsan, M., Sastry, D.H., Bhanu Sankara Rao, K. and Mannan, S.L. (1994) 'Effect of strain rate on the high-temperature low-cycle fatigue properties of a Nimonic PE-16 superalloy' *Metallurgical and Materials Transactions A*, **25** (1)159-171.

[33] Reed, P.A.S., Gale, W.F. and King J.E. (1993) 'Intrinsic threshold in polycrystalline Udimet 720' *Materials Science and Technology*, **9** (4) 281-287.

[34] Grabowski, L. and King, J.E. (1992) 'Modelling short crack growth behaviour in nickel-base superalloys' *Fatigue and Fracture of Engineering Materials and Structures (UK)*, **15** (6) 595-606.

[35] Sundararaman, M., Chen, W., Singh, V. and Wahi R.P. (1990) 'TEM investigation of γ' free bands in Nimonic PE16 under LCF loading at room temperature' *Acta Metallurgica et Materialia*, **38** (10) 1813-1822.

[36] Tong, J., Dalby, S. and Byrne, J. (2005) 'Crack growth in a new nickel-based superalloy at elevated temperature. Part III Characterisation' *Journal of Materials Science*, **40** (5) 1237-1243.

[37] Loo-Morrey, M. and Reed P.A.S (2000). 'Anomalous crack shape development (tear drop cracking) in turbine disc material Udimet 720' *Materials Science and Technology*, **16** (2) 133-146.

[38] Suresh, S. (1998) *Fatigue of Materials*, Cambridge University Press, Cambridge, UK.

[39] Blankenship, C.P. and Starke, E.A. (1993) 'Mechanical behavior of double-aged AA8090' *Metallurgical Transactions A*, **24** (4) 833-841.

[40] Jata, K.V. and Starke E.A. (1986) 'Fatigue crack growth and fracture toughness behaviour of an Al-Li-Cu alloy' *Metallurgical Transactions A*, **17** (6) 1011-1026.

[41] Blankenship, C.P., Hornbogen, E. and Starke E.A. (1993) 'Predicting slip behaviour in alloys containing shearable and strong particles' *Materials Science and Engineering: A*, **169** (1-2) 33-41.

[42] Duva, J.M., Daeubler, M.A., Starke E.A. and Luetjering G. (1998) 'Large shearable particles lead to coarse slip in particle reinforced alloys' *Acta Metallurgica*, **36**(3) 585-589.

[43] Antolovich, S.D. and Jayaraman N. (1980) 'The effect of microstructure on the fatigue behaviour of Ni-base superalloys' eds. Burke, J.J. and Weiss, V. *Proceedings of Fatigue: Environment and Temperature Effects, 14-18 July 1980*, *Bolton Landing, Lake George, NY,* Plenum, NY, 119-144.

[44] Nilsson, J.O. (1984) 'Influence of dislocation-precipitate interaction on low cycle fatigue resistance of Alloy 800 at 600°C' *Metal Science*, **18** (7) 351-355.

[45] Ghonem, H. and Zheng, D. (1992) 'Frequency interactions in high-temperature fatigue crack growth in superalloys' *Metallurgical Transactions A*, **23** (11) 3067-3072.

[46] Hide, N.J., Henderson, M.B. and Reed P.A.S. (2000) 'Effects of grain and precipitate size variation on creep-fatigue behaviour of Udimet 720 in both air and vacuum' eds. Pollock, T.M., Kissinger, R.D., Bowman, R.R., Green, McLean, M., Olson, S.L., and Schirra, J.J. *Proceedings of the Ninth International Symposium on Superalloys, 17-21 Sept. 2000, Seven Springs, Champion, Pennsylvania, USA*, TMS, 495-503.

[47] Zheng, D., Rosenberger, A. and Ghonem, H. (1993) 'Influence of prestraining on high temperature, low frequency fatigue crack growth in superalloys' *Materials Science and Engineering A:*, **161** (1) 13-21.

[48] Ghonem, H., Nicholas, T. and Pineau, A. (1993) 'Elevated temperature fatigue crack growth in alloy 718 – part II: effects of environment and material variables' *Fatigue and Fracture of Engineering Materials and Structures*, **16** (6) 577-590.

[49] Honnorat, Y. (1991) 'N18, Damage tolerant nickel-based superalloy for military aircraft turbine discs' *Materiaux et Techniques*, **79** (5-6) 19-29.

[50] Ducrocq, C.A.B., Lestrat, D.P.A., Paintendre, B., Davidson, J.H., Marty, M. and Walder, A., SNECMA, ARMINES, ONERA (1992) *'Superalloy compositions with a nickel base"* US Patent 5104614.

[51] Gabb, T.P., Gayda J., Telesman, I. and Kantzos, P.T., NASA (2005) *'Nickel Base Superalloy Turbine Disk'* US Patent 6974508.

[52] Hessell, S.J., Voice, W., James, A.W., Blackham, S.A., Small, C.J., and Winstone, M.R., Rolls-Royce (1999) *'Nickel Alloy for Turbine Engine Components'* US Patent 5897718.

[53] Sczerzenie, F.E. and Maurer, G.E. (1984) 'Development of UDIMET 720 for High Strength Disc Applications' eds. Gell, M., Kortovich, C.S., Bricknell, R.H., Kent, W.B. and Radavich, J.F. *Proceedings of the Fifth International Symposium on Superalloys, 7-11 Oct. 1984, Seven Springs, Champion, Pennsylvania, USA*, TMS, 573-580.

[54] Keefe, P.W., Mancuso, S.O. and Maurer, G.E. (1992) 'Effects of Heat Treatment and Chemistry on the Long-Term Phase Stability of a High Strength Nickel-Based Superalloy' eds. Antolovich, S.D., Stusrud, R.W., MacKay, R.A., Anton, D.L., Khan, T., Kissinger, R.D. and Klarstrom D.L. *Proceedings of the Seventh International Symposium on Superalloys, 20-24 Sept. 1992, Seven Springs, Champion, Pennsylvania, USA*, TMS, 487-496.

[55] Bain, K.R., Gambone, M.L., Hyzak, J.M. and Thomas, M.C. (1988) 'Development of Damage Tolerant Microstructures in Udimet 720' eds. Duhl, D.N., Maurer, G., Antolovich, S., Lund, C. and Reichman S. *Proceedings of the Sixth International Symposium on Superalloys, 18-22 Sept. 1988, Seven Springs, Champion, Pennsylvania, USA*, TMS, 13-22.

[56] Brooks, R.R. and Rainforth, W.M. (2000) 'The effect of microstructure on the morphology of fatigue cracks in UDIMET® 720' *Fatigue and Fracture of Engineering Materials and Structures*, **23** (9) 725–736.

[57] Moll, J.H. and Conway, J.J. (2000) 'Characteristics and Properties of As-HIP P/M Alloy 720' eds. Pollock, T.M., Kissinger, R.D., Bowman, R.R., Green, McLean, M., Olson, S.L., and Schirra, J.J. *Proceedings of the Ninth International Symposium on Superalloys, 17-21 Sept. 2000, Seven Springs, Champion, Pennsylvania, USA*, TMS, 135-142.

[58] Bryant, D.J. and McIntosh, G. (1996) 'The Manufacture and Evaluation of a Large Turbine Disc in Cast and Wrought Alloy 720 Li' eds. Kissinger, R.D., Deye, D.J., Anton, D.L. and Cetel A.D. *Proceedings of the Eighth International Symposium on Superalloys, 22-26 Sept. 1996, Seven Springs, Champion, Pennsylvania, USA*, TMS, 713-722.

[59] Jain, S.K., Ewing, B.A. and Yin, C.A. (2000) 'The Development of Improved Performance PM UDIMET® 720 Turbine Disks' eds. Pollock, T.M., Kissinger, R.D., Bowman, R.R., Green, McLean, M., Olson, S.L., and Schirra, J.J. *Proceedings of the Ninth International Symposium on Superalloys, 17-21 Sept. 2000, Seven Springs, Champion, Pennsylvania, USA*, TMS, 135-142.

[60] Sansoz, F., Brethes, B. and Pineau, A. (2002) 'Propagation of short fatigue cracks from notches in a Ni base superalloy: experiments and modelling' *Fatigue and Fracture of Engineering Materials and Structures*, **25** (1) 41-53.

[61] Gabb, T.P., Gayda, J., Telesman, J., and Garg, A. (2008) 'The Effects of Heat Treatment and Microstructure Variations on Disk Superalloy Properties at High Temperature' eds. Reed, R., Green, K.A., Caron, P., Gabb, T., Fahrmann, M.G., Huron, E.S. and Woodard, S.R. *Proceedings of the Eleventh International Symposium on Superalloys, 14-18 Sept. 2008, Seven Springs, Champion, Pennsylvania, USA* , TMS, 121-130.

[62] Pang, H.T. and Reed, P.A.S. (2007) 'Microstructure effects on high temperature fatigue crack initiation and short crack growth in turbine disc nickel-base superalloy Udimet 720Li' *Materials Science and Engineering: A*, **448** (1-2) 67-79.

[63] Mao, J., Chang, K.M., Yang, W., Ray, K.., Vaze, S.P. and Furrer, D.U. (2001) 'Cooling Precipitation and Strengthening Study in Powder Metallurgy Superalloy U720Li' *Metallurgical and Materials Transactions A*, **32** (10) 2441-2452.

[64] Gabb, T.P., Gayda, J., Telesman, J. and Kanzos, P.T. (2005) 'Thermal and Mechanical Property Characterisation of the Advanced Disk Alloy LSHR' NASA Report NASA/TM-2005-213645

[65] Telesman, J., Gabb, T.P., Garg, A., Bonacuse, P. and Gayda, J. (2008) 'Effect of Microstructure on Time Dependent Fatigue Crack Growth Behavior In a P/M Turbine Disk Alloy' eds. Reed, R., Green, K.A., Caron, P., Gabb, T., Fahrmann, M.G., Huron, E.S. and Woodard, S.R. *Proceedings of the Eleventh International Symposium on Superalloys, 14-18 Sept. 2008, Seven Springs, Champion, Pennsylvania, USA* , TMS, 807-816.

[66] Schulz, U., Leyens, C., Fritscher, K., Peters, M., Saruhan-Brings, B., Lavigne, O., Dorvaux, J., Poulain, M., Mévrel, R. and Caliez, M. (2003) 'Some recent trends in research and technology of advanced thermal barrier coatings' *Aerospace Science and* Technology, **7** (1) 73-80.

[67] Clarke, D.R. and Levi, C.G. 'Materials Design for the Next Generation Thermal Barrier Coatings' *Annual Review of Materials Research*, 2003, **33** 383-417.

[68] Nicholls, J.R. (2000) 'Designing oxidation-resistant coatings' *Journal of the Minerals, Metals and Materials Society*, **52** (1) 28-35.

[69] Busso, E.P., Lin, J., Sakurai, S. and Nakayama, M. (2001) 'A mechanistic study of oxidation-induced degradation in a plasma-sprayed thermal barrier coating system. Part I: Model formulation.' *Acta Materialia*, **49** (9) 1515-1528.

[70] Spitsberg, I. and More, K. (2006) 'Effect of thermally grown oxide (TGO) microstructure on the durability of TBCs with PtNiAl diffusion bond coats.' *Materials Science and Engineering: A* **417** (1-2) 322-333.

[71] Clarke, D.R. (2003) 'Materials selection guidelines for low thermal conductivity thermal barrier coatings' *Surface Coatings Technology*, **163-164** 67-74.

[72] Nicholls J.R., Lawson, K.J., Johnstone A. and Rickerby D.S. (2002) 'Methods to reduce the thermal conductivity of EB-PVD TBCs' *Surface and Coatings Technology*, **151-152** 383-391.

[73] Kingery, W.D. (1955) 'Factors affecting thermal stress resistance of ceramic materials' *Journal of the American Ceramic Society*, **38** (1) 3-15.

[74] Chevalier, J., Gremillard, L., Virkar, A.V. and Clarke, D.R. (2009) 'The tetragonal-monoclinic transformation in Zirconia: Lessons learned and future trends' *Journal of Amercian Ceramic Socoiety*, **92** (9) 1901-1920.

[75] Stecura, S. (1986) 'Advanced thermal barrier system bond coatings for use on nickel-, cobalt- and iron-base alloy substrates' *Thin Alloy Films*, **136** (2) 241-256.

[76] Scott, H.G. (1975) 'Phase relationships in the zirconia-yttria system' *Journal of Materials Science*, **10** (9) 1527-1535.

[77] Goward, G.W. (1998) 'Progress in coatings for gas turbine airfoils' *Surface and Coatings Technology*, **108-109** 73-79.

[78] Evans, A.G., Mumm, D.R., Hutchinson, J.W., Meier, G.H. and Pettit, F.S. (2001) 'Mechanisms controlling the durability of thermal barrier coatings' *Progress in Materials Science*, **46** (5) 505-553.

[79] Shillington, E.A.G. and Clarke D.R. (1999) 'Spalling failure of a thermal barrier coating associated with aluminum depletion in the bond-coat' *Acta Materialia*, **47** (4) 1297-1305.

[80] Üstündag, E., Zhang, Z., Stocker, M.L., Rangaswamy, P., Bourke, M.A.M., Subramanian, S., Sickafus, K.E., Roberts, J.A. and Sass, S.L. (1997) 'Influence of residual stresses on the evolution of microstructure during the partial reduction of $NiAl_2O_4$' *Materials Science and Engineering: A*, **238** (1) 50-65.

[81] Nicholls, J.R., Jaslier, Y. and Rickerby, D.S. (1997) 'Erosion and Foreign Object Damage of Thermal Barrier Coatings' *Materials Science Forum*, **251-254** 935-948.

[82] Tolpygo, V.K. and Clarke, D.R. (2003) 'Morphological evolution of thermal barrier coatings induced by cyclic oxidation' *Surface and Coatings Technology*, **163-164** 81-86.

[83] He, M.Y., Evans, A.G. and Hutchinson, J.W. (2000) 'The ratcheting of compressed thermally grown thin films on ductile substrates.' *Acta Materialia*, **48** (10) 2593-2601.

[84] Miller, R.A. (1984) 'Oxidation-Based Model for Thermal Barrier Coating Life' *Journal of the American Ceramic Society*, **67** (8) 517-524.

[85] Callister, W.D. (2000) *Materials Science and Engineering: an introduction*. John Wiley and Sons, New York, USA.

[86] Basquin, O.H. (1910) 'The exponential law of endurance tests.' *Proceedings of the American Society for Testing and Materials*, **10** 625-630.

[87] Coffin, L.F. (1954) 'A study of the effects of cyclic thermal stresses on a ductile metal.' *Transactions of the Amercian Society of Mechanical Engineers*, **76** 931-950.

[88] Manson, S.S. (1954) 'Behavior of materials under conditions of thermal stress.' National Advisory Commission on Aeronautics: Report 1170. Cleveland: Lewis Flight Propulsion Laboratory.

[89] Fournier, D. and Pineau A. (1977) 'Low cycle fatigue behavior of Inconel 718 at 298 K and 823 K' *Metallurgical and Materials Transactions A*, **8** (7) 1095-1105.

[90] Goto M. and Knowles D.M. (1998) 'Initiation and propagation behaviour of microcracks in Ni-base superalloy Udimet 720Li' *Engineering Fracture Mechanics*, **60** (1). 1-18.

[91] Miller, K.J. 'The short crack problem' (1982) *Fatigue of Engineering Materials and Structures*, **5** (3) 223-232.

[92] Wu, Z. and Sun, X. (1998) 'Multiple fatigue crack initiation, coalescence and growth in blunt notched specimens' *Engineering Fracture Mechanics*, **59** (3) 353-359.

[93] Hicks, M.A.. and Brown, C.W. (1984) 'A comparison of short crack growth behaviour in engineering alloys' ed. Beevers C.J. *Proceedings of the Second International Conference on Fatigue and Fatigue Thresholds, Birmingham, U.K., 3-7 Sept. 1984*, EMAS Publishing, 1337-1347.

[94] Stephens, R.R., Grabowski, L. and Hoeppner, D.W. (1993) 'The effect of temperature on the behaviour of short fatigue cracks in Waspaloy using an in situ SEM fatigue apparatus' *International Journal of Fatigue*, **15** (4) 273-282.

[95] Brown, C.W., King, J.E. and Hicks, M.A. (1984) 'Effects of microstructure on long and short crack growth in nickel base superalloys' *Metal Science* **18** (7) 374-380.

[96] Yates, J.R., Zhang, W. and Miller, K.J. (1993) 'The initiation and propagation behaviour of short cracks in Waspaloy subjected to bending' *Fatigue and Fracture of Engineering Materials and Structures*, **16** (3) 351-362.

[97] Kendall, J.M. and King, J.E. (1988) 'Short fatigue crack growth behaviour: data analysis effects' *International Journal of Fatigue*, **10** (3) 163-170.

[98] Mei, Z., Krenn, C.R. and Morris, J.W. (1995) 'Initiation and growth of small fatigue cracks in a Ni-base superalloy' *Metallurgical and Materials Transactions A*, **26** (8) 2063-2073.

[99] Boyd-Lee, A. and King, J.E. (1994) 'Short fatigue crack path determinants in polycrystalline Ni-base superalloys' *Fatigue and Fracture of Engineering Materials and Structures*, **17** (1) 1-14.

[100] Toh, S.F. and Rainforth, W.M. (1996) 'Fatigue of a nickel base superalloy with bimodal grain size' *Materials Science and Technology*, **12** (12) 1007-1014.

[101] Shiozawa, K. and Weertman, J.R. (1981) 'Observation of grain boundary microcracking in a nickel base superalloy after room temperature deformation' *Scripta Metallurgica*, **15** (11) 1241-1244.

[102] Healy, J.C., Grabowski, L, and Beevers, C.J. (1991) 'Short-fatigue-crack growth in a nickel-base superalloy at room and elevated temperature' *International Journal of Fatigue*, **13** (2) 133-138.

[103] Gayda, J. and Miner, R.V. (1983) 'Fatigue crack initiation and propagation in several nickel-base superalloys at 650°C' *International Journal of Fatigue*, **5** (3) 135-143.

[104] Reger, M. and Remy, L. (1988) 'High temperature, low cycle fatigue of IN100 superalloy I: influence of temperature on the low cycle fatigue behaviour' *Materials Science and Engineering A*, **101** 47-54.

[105] de Bussac, A. (1994) 'Prediction of the competition between surface and internal crack initiation in PM alloys' *Fatigue and Fracture of Engineering Materials and Structures*, **17** (11) 1319-1325.

[106] Antolovich, S.D., Rosa, E. and Pineau A. (1981) 'Low cycle fatigue of Rene 77 at elevated temperatures' *Materials Science and Engineering*, **47** (1) 47-57.

[107] Stahl, D.R., Mirdamadi, M., Zamrik, S.Y. and Antolovich S.D. (1988) 'Effect of temperature, microstructure, and stress state on the low cycle fatigue behavior of Waspaloy' eds. Soloman, H.D., Halford, G.R., Kaisand, L.R. and Leis, B.N. *ASTM STP 942, Low Cycle Fatigue, 30 Sept.-4 Oct. 1985*, *Bolton Landing, New York, USA*, ASTM, 728-750.

[108] Merrick, H.F. (1974) 'The low cycle fatigue of three wrought nickel-base alloys' *Metallurgical and Materials Transactions: B*, **5** (4) 891-897.

[109] Reed, P.A.S., Hachette, F., Thakar, D., Connolley, T. and Starink M.J. (1999) 'Creep-fatigue initiation and early crack growth in Inconel 718' eds. Ellyin, F. and Provan, J.W. *Proceedings of the Eighth International Conference on the Mechanical Behaviour of Materials, ICM8, Victoria, British Columbia, Canada, 16-21 May 1999,* **1**, 418-423.

[110] Pang, H.T. and Reed, P.A.S. (2003) 'Fatigue crack initiation and short crack growth in nickel-base turbine disc alloys – the effects of microstructure and operating parameters' *International Journal of Fatigue* **25** (9-11) 1089-1099.

[111] Davidson, D.L. and Hudak, S.J. (1995) 'The crack-tip mechanics and growth rates of small fatigue cracks in Astroloy' *Metallurgical and Materials Transactions A*, **26** (9) 2247-2257.

[112] Zabett, A.and Plumtree, A. (1995) 'Microstructural effects on the small fatigue crack behaviour of an aluminium alloy plate' *Fatigue and Fracture of Engineering Materials and Structures*, **18** (7-8) 801-809.

[113] Knott, J.F. and King, J.E. (1991) 'Fatigue in metallic alloys containing non-metallic particles' *Materials and Design,* **12** (2) 67-74.

[114] Guedou, J.Y., Lautridou, J.C. and Honnorat, Y. (1993) 'N18, Powder Metallurgy Superalloy for Disks: Development and Applications' *Journal of Materials Engineering and Performance* **2** (4) 551-556.

[115] Sansoz, F., Brethes, B. and Pineau A. (2001) 'Growth of short fatigue cracks from stress concentrations in N18 superalloy' [online] available from: http://www.uvm.edu/~fsansoz/Articles/article_N18_JP2001.pdf [accessed 30 Oct. 2006].

[116] Sansoz, F., Brethes, B. and Pineau, A. (1998) 'Short fatigue crack propagation from notches in N18 Ni based superalloy' eds. Brown, M.W., de Los Rios, E.R. and Miller, K.J. *Proceedings of The European Conference On Fracture 12*, *14-18 September 1998, University of Sheffield, UK*, EMAS Publishing, **1** 61-66.

[117] Smith, R.A., Liu, Y. and Grabowski, L. (1996) 'Short fatigue crack growth behaviour in Waspaloy at room and elevated temperatures' *Fatigue and Fracture of Engineering Materials and Structures*, **19** (12) 1505-1514.

[118] Zhang, Y.H. and Edwards, L. (1994) 'On the blocking effect of grain boundaries on small crystallographic fatigue crack growth' *Materials Science and Engineering A*, **188** (1-2) 121-132.

[119] Pommier, S., Prioul, C. and Bompard, P. (1997) 'Influence of a negative R ratio on the creep-fatigue behaviour of the N18 nickel base superalloy.' *Fatigue and Fracture of Engineering Materials and Structures*, **20** (1) 93-107.

[120] Zhang, Y.H. and Edwards, L. (1992) 'The development of plastic zones ahead of small fatigue cracks and their consequences for crack growth rate' eds. Arnberg et al. *Proceedings of the 3rd International Conference on Aluminium Alloys , Trondheim, Norway*, The Norwegian Institute of Technology, **1** 563-568.

[121] Isomoto, T. and Stoloff, N.S. (1990) 'Effect of microstructure and temperature on high cycle fatigue of powder metallurgy Astroloy' *Materials Science and Engineering: A*, **124** (2) 171-181.

[122] Reger, M. and Remy, L. (1988) 'High temperature, low cycle fatigue of IN100 superalloy II: influence of frequency and environment at high temperatures' *Materials Science and Engineering: A*, **101** 55-63.

[123] King, J.E., Venables, R.A. and Hicks, M.A. (1984) 'The effects of microstructure, temperature and R-ratio on fatigue crack propagation and threshold behaviour in two Ni-base alloys' *Proceedings of the 6th Int. Conf. on Fracture (ICF6) Advances in Fracture Research (Fracture '84), New Delhi, India, 4-10 Dec. 1984*, Pergamon Press Ltd., 2081-2089.

[124] James, L.A. (1989) 'Fatigue crack propagation in alloy 718: A review' ed. Loria, E.A. *Superalloy 718:- Metallurgy and Applications, 12-14 June 1989, Pittsburgh, Pennsylvania, USA,* TMS, 499-515.

[125] Yuen, J.L., Roy, P. and Nix, W.D. (1984) 'Effect of oxidation kinetics on the near threshold fatigue crack growth behaviour of a nickel base superalloy' *Metallurgical Transactions A*, **15** (9) 1769-1775.

[126] King, J.E. (1982) 'Surface damage and near-threshold fatigue crack growth in a Ni-base superalloy in vacuum' *Fatigue and Fracture of Engineering Materials and Structures*, **5** (2) 177-188.

[127] Loo-Morrey, M. (1997) 'Crack Growth Transitions in Udimet 720' PhD. Thesis, University of Southampton, UK.

[128] Sadananda, K.and Shahinian, P. (1985) 'Effect of environment on high temperature crack growth behaviour of several nickel-base alloys' ed. Scarberry, R.C. *Proceedings of the International Conference on Corrosion of Nickel-Base Alloys, 23-25 Oct. 1984, Cincinnati, Ohio, USA*, American Society for Testing and Materials, 101-115.

[129] Nikbin, K.M. and Webster, G.A. (1984) 'Creep-fatigue crack growth in a nickel-base superalloy' ed. Wilshire, B. and Owen, D.R.J. *Proceedings 2nd International Conference on Creep and Fracture of Engineering Materials and Structures*, *1-6 Apr. 1984*, *Swansea, U.K.,* Pineridge Press Ltd., **2** 1091-1104.

[130] Anderson, T.L. (2005) *Fracture Mechanics, Fundamentals and Applications* CRC Press, Boca Raton, Florida, USA.

[131] Winstone, M.R., Nikbin, K.M. and Webster, G.A. (1985) 'Modes of failure under creep/fatigue loading of a nickel-based superalloy' *Journal of Materials Science*, **20** (7) 2471-2476.

[132] Gayda, J., Gabb, T.P. and Miner, R.V. (1988) 'Fatigue crack propagation of nickel-base superalloys at 650°C' eds. Soloman, H.D., Halford, G.R., Kaisand, L.R. and Leis, B.N. *ASTM STP 942, Low Cycle Fatigue, 30 Sept.-4 Oct. 1985*, *Bolton Landing, New York, USA*, ASTM, 293-309.

[133] Soniak, F. and Remy, L. (1987) 'Behaviour of long and short fatigue cracks in a powder metallurgy superalloy at room and at high temperature' eds. Ritchie, R.O. and Starke, E.A *Proceedings of the Third International Conference on Fatigue and Fatigue Thresholds, June 28-July 3, 1987, Charlotesville Virginia, U.S.A*., EMAS Publishing, **1** 351-360.

[134] Hicks, M.A. and King, J.E. (1983) 'Temperature effects on fatigue thresholds and structure sensitive crack growth in a nickel-base superalloy' *International Journal of Fatigue*, **5** (2) 67-74.

[135] Byrne, J., Hall, R. and Grabowski, L. (1997) 'Elevated temperature fatigue crack growth under dwell conditions in Waspaloy' *International Journal of Fatigue*, **19** (5) 359-367.

[136] Onofrio, G. and Lupinc, V. (1998) 'High temperature fatigue crack growth behaviour of the Udimet 720Li alloy' eds. Brown, M.W., de Los Rios, E.R. and Miller, K.J. *Proceedings of The European Conference On Fracture 12*, *14-18 September 1998, University of Sheffield, UK*, EMAS Publishing, **1** 387-392.

[137] Ghonem, H., Nicholas, T. and Pineau, A. (1993) 'Elevated temperature fatigue crack growth in Alloy 718 I: effects of mechanical variables' *Fatigue and Fracture of Engineering Materials and Structures*, **16** (5) 565-576.

[138] Antunes, F.V., Ferreira, J.M., Branc, C.M. and Byrne, J. (2000) 'High temperature fatigue crack growth in Inconel 718' *Materials at High Temperatures*, **17** (4) 439-448.

[139] Lynch, S.P., Radtke, T.C. and Wicks, B.J. (1991) 'Fatigue crack growth in a nickel-based superalloy at 500-700°C' eds. Jōno, M., Inoue, T., Gakkai, N.Z. and Zaidan, K.K.S. *Mechanical behaviour of materials-VI: proceedings of the sixth international conference, 29 Jul.-2 Aug. 1991, Kyoto, Japan,29*, Pergamon Press, **4** 355-360.

[140] Lynch, S.P., Radtke, T.C., Wicks, B.J. and Byrnes, R.T. (1994) 'Fatigue crack growth in nickel-based superalloys at 500-700°C I: Waspaloy' *Fatigue and Fracture of Engineering Materials and Structures*, **17** (3) 297-311.

[141] Golwalkar, S., Stoloff, N.S. and Duquette D.J. (1982) 'The effects of frequency and hold times on fatigue crack propagation rates in a nickel base superalloy' ed. Gifkins, R.C., *Proceedings of the 6th International Conference on Strength of Metals and Alloys (ICSMA 6), 16-20 Aug. 1982, Melbourne, Australia,* Pergamon, 879-885.

[142] Mendez, J., Violan, P., Quintard, M., Marcon, G., Marty, M., Thevenin, P. and Walder A. (1993) 'Effect of environment of creep-fatigue crack propagation in turbine disc superalloys' eds. Magnin, T. and Gras, J.M., *Proceeding from Corrosion-Deformation Interactions '92, , 5-7 Oct. 1992*, *Fontainebleau, France,* Les Editions de Physique (France), 531-541.

[143] Andrieu, E. and Pineau, A. (1999) 'Study of the coupled phenomena involved in the oxidation assisted intergranular cracking of Ni based superalloys' *Journal de Physique IV*, Vol. 9 (9) Pr9-3 – Pr9-11.

[144] Zhuang, W.Z. and Swansson, N.S. (1998) 'Thermo-Mechanical Fatigue Life Prediction: A Critical Review' Australian Department of Defence, Defence Science and Technology Organisation, Report DSTO-TR-0609.

[145] Sehitoglu, H. (1992) 'Thermo-Mechanical Fatigue Life Prediction Methods' *Advances in Fatigue Lifetime Predictive Techniques*, ASTM STP 1122, 47–76.

[146] United Kingdom Ministry of Defence 'Design and Airworthiness Requirements for Service Aircraft – Part 11 – Engines' Defence Standard 00-970 Part 11 Issue 2, (2011), United Kingdom Ministry of Defence.

[147] European Aviation Safety Agency (2009) 'Certification Specifications for Engines' CS-E Amendment 2 Annex to ED Decision 2009/018/R,European Aviation Safety Agency.

[148] IncoTest certificate no. LT 0154701/01 dated 14 09 2006.

[149] Di Martino, I., Brooks, J.W., Reed, P.A. and Wisbey, A. (2007) 'Modelling the Mechanical Performance of High Temperature Nickel Alloys' eds. Strang A., Banks, W.M., McColvin, G.M., Oakley, J.E., and Vanstone, R.W. *Proceedings of the Seventh International Charles Parsons Turbine Conference: Power Generation in an Era of Climate Change, 11-13 Sept. 2007, University of Strathclyde, Glasgow, UK,* IOM Communications Ltd, London, UK, 77-88.

[150] British Standards Institution (1966) BS 4A 4:1966 'Test pieces and test methods for metallic materials for aircraft. Metric units' Milton Keynes, BSI.

[151] British Standards Institution (2002) BS ISO 12108:2002 'Metallic materials – Fatigue testing – Fatigue crack growth Method' Milton Keynes, BSI.

[152] Roberts, T. (2009) Personal communication. University of Cranfield.

[153] Vermeulen, B. and Squidd, M. (2005) 'Thermal barrier coatings under in-service TMF conditions' QinetiQ Report, QINETIQ/FST/STT/CR051167 3 March 2005.

[154] Basoalto, H.C., Hayward, D.W. and Vermeulen, B. (2007) 'Factors and Sensitivities Contributing to Thermal Barrier Coating Failure under Thermal-Mechanical Fatigue' QinetiQ Report QINETIQ/D&TS/AIR/TR0704803/1.0, 2007.

[155] Sourmail, T (2003) 'Coatings for Turbine blades' University of Cambridge [online] available from: http://www.msm.cam.ac.uk/phase-trans/2003/Superalloys/coatings/index.html [accessed 13 Oct 08].

[156] Turan, D., Hunt, D.W. and Knowles, D.M. (2007) 'Dwell time effect on fatigue crack growth of RR1000 Superalloy' *Materials Science and* Technology, **23** (2) 183-188.

[157] Decker, R.F. (1969) 'Strengthening Mechanisms in Nickel-Base Superalloys' *Steel-Strengthening Mechanisms Symposium, 5-6 May 1969, Zurich, Switzerland*, American Metal Climax Inc.

[158] Chaku, P.N. and McMahon, C.J. (1974) 'The effect of an air environment on the creep and rupture behavior of a nickel-base high temperature alloy' *Metallurgical and Materials Transactions B*, **5** (2) 441-450.

[159] Dahl, J.M., Danesi, W.F. and Gunn, R.G (1973). 'The Partitioning of Refractory Metal Elements in Hafnium-Modified Cast Nickel-Base Superalloys' *Metallurgical and Materials Transactions B*, **3** (2) 457-462.

[160] Obigodi-Ndjeng, G. (2011) 'High Temperature Oxidation and Electrochemical Investigations on Nickel-base Alloys.' DOKTOR-INGENIEUR Thesis, University of Erlangen-Nuremberg, Germany.

[161] Nielsen, R. H. (2004) 'Hafnium and Hafnium Compounds.' *Kirk-Othmer Encyclopaedia of Chemical Technology*, **13** 78-97.

[162] Huron, E.S., Bain, K.R., Mourer, D.P., Schirra, J.J., Reynolds, P.L. and Montero, E.E. (2004) 'The influence of grain boundary elements on properties and microstructures of P/M nickel base superalloys.' eds. Green, K.A., Pollock, T.M., Harada, H., Howson, T.E., Reed, R., Schirra, J.J. and Watson, S. *Proceedings of the Tenth International Symposium on Superalloys, 19-23 Sept. 2004, Seven Springs, Champion, Pennsylvania, USA*, TMS, 73-81.

[163] Flageolet, B., Villechaise, P., Jouiad, M. and Mendez J. (2004) 'Ageing characterization of the powder metallurgy superalloy N18.' eds. Green, K.A., Pollock, T.M., Harada, H., Howson, T.E., Reed, R., Schirra, J.J. and Watson, S. *Proceedings of the Tenth International Symposium on Superalloys, 19-23 Sept. 2004, Seven Springs, Champion, Pennsylvania, USA*, TMS, 371-379.

[164] Loyer-Danflou, H., Marty, M. and Walder, A. (1992) 'Formation of Serrated Grain Boundaries and Their Effect on the Mechanical Properties in a P/M Nickel Base Superalloy' eds. Antolovich, S.D., Stusrud, R.W., MacKay, R.A., Anton, D.L., Khan, T., Kissinger, R.D. and Klarstrom D.L. *Proceedings of the Seventh International Symposium on Superalloys, 20-24 Sept. 1992, Seven Springs, Champion, Pennsylvania, USA*, TMS, 63-72.

[165] Mitchell, R.J., Li, H.Y. and Huang Z.W. (2009) 'On the formation of serrated grain boundaries and fan type structures in an advanced polycrystalline nickel-base superalloy.' *Journal of Materials Processing Technology*, **209** (2) 1011-1017.

[166] Reynolds, R. (2008) 'High Temperature Performance of Aeroengine Ni-base Superalloys: Oxidation and its Relation to Fatigue' *Part III Mechanical Engineering Project,* University of Southampton, UK.

[167] Knowles, D.M. and Hunt, D.W. (2002) 'The Influence of Microstructure and Environment on the Crack Growth Behavior of Powder Metallurgy Nickel Superalloy RR1000' *Metallurgical and Materials Transactions A*, **33** (10) 3165-3172.

[168] Kofstad, P. (1988) *High Temperature Corrosion*, Elsevier Applied Science, London and New York.

[169] Abe, F., Araki, H., Yoshida, H. and Okada, M. (1987) 'The Role of Aluminium and Titanium on the Oxidation Process of a Nickel-Base Superalloy in Steam at 800°C' *Oxidation of Metals*, **27** (1/2) 21-36.

[170] Chen, J.H., Rogers, P.M. and Little, J.A. (1997) 'Oxidation Behavior of Several Chromia-Forming Commercial Nickel-Base Superalloys' *Oxidation of Metals*, **47** (5/6) 381-410.

[171] Berthod, P. (2007) 'Influence of Chromium Carbides on the High Temperature Oxidation Behaviour and on Diffusion in Nickel-Base Alloys' *Oxidation of Metals*, **68** (1/2) 77-96.

[172] Hong, J.K., Park, N.K., Kim, S.J. and Kang, C.Y. (2005) 'Microstructures of Oxidized Primary Carbides on Superalloy Inconel 718' *Material Science Forum*, **502** (1) 249-53.

[173] Raisson, C. and Davidson, J.H. (1990) 'N18, a new generation PM superalloy for critical turbine components' eds. E. Bachelet *et al., Proceedings from High Temperature Materials for Power Engineering, 24-27 Sept. 1990 Liege-Kluwer Academy, Belgium,* Kluwer Academic Publishers, 1405.

[174] Weber, M., Rodig, M., Schubert, F., Affeld, E.E. and Kraus, M. (1994) 'Influence of microstructure on the low cycle fatigue and creep-fatigue crack growth behaviour of the new PM-nickel-base superalloy N18 at elevated temperatures' ed. D. Coutsouradis et al, *Materials for Advanced Power Engineering, 3-6 Oct. 1994 Liege, Belgium,* Kluwer Academic Publishers, 961-969.

[175] Schulson, E.M, Weihs, T.P., Baker, I. and Horton J.A. (1986) 'Grain boundary accommodation of slip in Ni_3Al containing boron' *Acta Metallurgica*, **34** (7) 1395-1399.

[176] Messmer, R.P. and Briant, C.L. (1982) 'The role of chemical bonding in grain boundary embrittlement' *Acta Metallurgica*, **30** (2) 457-467.

[177] Manning, A.J., Knowles, D. and Small, C.J., Rolls-Royce (2002) *'Nickel base superalloy'* US 2002/0041821 A1.

[178] Thompson, R.S. (2010) 'Report for fractography study summer internship 2010' University of Southampton, UK.

[179] Li, X.W., Tian, J.F, Han, N.L., Kang, Y. and Wang, Z.G. (1996) 'Quantitative study of correlation between fracture surface roughness and fatigue properties of SiC/Al composites.' *Materials Letters*, **29** (4-6) 235-240.

[180] Starink, M.J., Cama, H. and Thomson, R.C. 'MC Carbides in the Hf Containing Ni Based Superalloy MarM002' *Scripta Materialia*, 1997 **38** (1) 73-80.

[181] Thomson, R.C. and Starink, M.J., Rolls-Royce (2001) *'Method of determining if an alloy article has any remaining working life'* US Patent 6219404.

[182] Starink, M.J. and Reed, P.A.S. (2008) 'Thermal activation of fatigue crack growth: Analysing the mechanisms of fatigue crack propagation in superalloys' *Materials Science and Engineering: A,* **491** (1/2) 279-289.

[183] Stoltz, R.E., and Pineau, A.G. (1978) 'Dislocation-precipitate interaction and cyclic stress-strain behavior of a γ' strengthened superalloy' *Materials Science and Engineering*, **34** (3) 275-284.

[184] Neuber, H. (1937) 'Theory of Notch Stresses', Edwards, Ann Arbor (1946) (translation of the German language version of 1937).

[185] Neuber, H. (1961) 'Theory of Stress Concentration for Shear Strained Prismatic Bodies with Nonlinear Stress-Strain Law' *Journal of Applied Mechanics, Series E*, **28 (**4) 544-550.

[186] Bray, D. (2011) 'Development of Life Assessment Methods for Power Generation Turbine Disc and Blade Materials' PhD. 9 Month Report, University of Southampton, UK.

[187] Huntz, A.M., Amiri, G.C., Evans, H.E. and Cailletaud, G. (2002) 'Comparison of oxide growth stresses in NiO film measured by defection and calculated using creep analysis or finite element modelling' *Oxidation of Metals*, **57** (5/6) 499-521.

[188] Busso, E.P., Lin, J., Sakurai, S. and Nakayama, M. (2001) 'A mechanistic study of oxidation-induced degradation in a plasma-sprayed thermal barrier coating system.: Part II: Life Prediction Model' *Acta Materialia*, **49** (9) 1529-1536.

[189] Busso, E.P, and Qian, Z.Q. (2006) 'A mechanistic study of microcracking in transversely isotropic ceramic-metal systems' *Acta Materialia*, **54** (2) 325-338.

[190] Busso, E.P., Wright, L., Evans, H.E., McCartney, L.N., Saunders, S.R.J., Osgerby, S. and Nunn, J. (2007) 'A physics-based life prediction methodology for thermal barrier coating systems' *Acta Materialia*, **55** (5) 1491-1503.

[191] Taylor, M.P., Evans, H.E., Busso, E.P. and Qian, Z.Q. (2006) 'Creep properties of a Pt–aluminide coating' *Acta Materialia*, **54** (12) 3241-3252.

[192] Cheng, J., Jordan, E.H., Barber, B. and Gell, M. (1998) 'Thermal/Residual stress in an electron beam physical deposited thermal barrier coating system' *Acta Materialia*, **46** (16) 5839-5850.

[193] Zhao, X., Wang, X. and Xiao P. (2006) 'Sintering and failure behaviour of EB-PVD thermal barrier coating after isothermal treatment' *Surface and Coatings Technology*, **200**, (20/21) 5946-5955.

[194] Abas, R.A., Hayashi, M. and Seetharaman, S. (2007) 'Thermal Diffusivity Measurements of CMSX-4 Alloy by the Laser-Flash Method' *International Journal of Thermophysics*, **28** (1) 109-122.

[195] Wisbey, A. (2007) Personal communication. QinetiQ Ltd.

[196] Hide, N. (1997) Unpublished research, University of Southampton, UK.